Copolymers to Stabilize Morphology in Conjugated Polymer-Fullerene Blends and Understanding Alkene Spacing for Repurposing Polyethylene via Alkane Metathesis and Cyclodepolymerization

by

Emily A. Mueller

A dissertation submitted in partial fulfillment
of the requirements for the degree of
Doctor of Philosophy
(Chemistry)
in the University of Michigan
2021

Doctoral Committee:

Professor Anne J. McNeil, Chair
Professor Jinsang Kim
Professor John Wolfe
Associate Professor Paul Zimmerman

Emily A. Mueller

eamuell@umich.edu

ORCID iD: 0000-0001-6984-9502

Dedication

To my family and friends for their unconditional love

and to my Grandmas, Arvilla and Betty.

Acknowledgements

There are so many people without whom this work would not be possible. I have to thank my high school science teachers, Mrs. Berg and Ms. Gavin, who made chemistry come to life for me. I also have to thank my undergraduate advisors, Prof Brad Chamberlain and Prof Olga Michels, for reaching out to me to get me involved with research, which I may never have otherwise pursued. You challenged and encouraged me at Luther and prepared me to go out into the world, not only as a chemist but as a whole person. A huge thank you to my mentors during my summer internship at 3M, Dr. Ian Dailey and Dr. Terry Sparks. I'm ever grateful for your caring attitudes as mentors and for encouraging me to apply for graduate school.

I also have to thank my mentors and colleagues at the University of Michigan. Thank you to Prof John Wolfe for letting me rotate in your lab, where I learned more than I could have imagined possible in one semester. Thank you also to Dr. Derick White, Dr. Elsa Hinds, Dr. Jordan Boothe, and Dr. Janelle Kirsh who answered all my rotation questions and taught me the ropes of graduate-level lab work. Thanks also to my collaborators for the organic photovoltaics projects, Prof Jinsang Kim, Dr. Beongsoep Song, Dr. Da Seul Yang, and Han Kim. Thank you for lending us your expertise, time, effort, and equipment to make photovoltaic devices. I absolutely must thank my advisor, Prof Anne McNeil, for your continual guidance during my graduate work across several very different projects. I'm especially grateful for your support and encouragement as I have explored different endeavors and discovered my love for science writing. I am forever indebted to my former and current labmates: Dr. Amanda Leone, Dr. Kendra Souther, Dr. Arianna

Hall, Dr. Chen Kong, Dr. Nicole Camasso, Dr. Tomohiro Kubo, Dr. Patrick Lutz, Dr. Justin Harris, Dr. Takunda Chazovachii, Morgan Young, Matthew Hannigan, Han Kim, Brianna Barbu, Gloria De La Garza, Jessica Tami, Vai Shastri, and Izzy Zelaya, for your encouragement, your support, and for engaging conversations about science, life, and everything in between. Thanks especially to Dr. Amanda Leone for your expert guidance and humor as my McNeil lab mentor. You taught me so much about conjugated polymer synthesis and set me up for a successful graduate career. A final thank you to Justin, Matt, and Takunda – I couldn't ask for better people to do grad school with and I'm grateful to count you as my friends.

I also have to thank my friends. A shoutout to the RELATE coordinator team – I loved the workshop as a participant and have had so much fun leading it with you all. Thank you especially to Joe and Deanna for being wonderful friends and for encouraging me to pursue science communication. To my friends at GCF – you have blessed me with loving community and unmeasurable support, and I am so grateful for you all. Thank you also to Jenny for being a great roommate and encouraging friend during my years in graduate school. To Madalyn, my first Michigan friend, I am grateful beyond words for your friendship and love since the beginning. An enormous thank you to my friend Claire, who is also pursuing a chemistry PhD. You have understood and supported me through everything, and I'm incredibly thankful for you. Thank you also to my Luther Ladies, who have gotten me through a global pandemic with Tuesday night chats, and to my Minnesota friends who have been there for me over so many years.

Finally, I have to thank my family: Tim, Laurie, and Thomas. You taught me to be a "rockhead" and I could not have done this without you. There are no words to describe my gratitude for your unconditional love and support.

Table of Contents

List of Charts

List of Figures

List of Schemes

List of Tables

List of Appendices

Abstract

It is indisputable that human activity has warmed Earth's oceans, land, and atmosphere, posing challenges for human and non-human life. To mitigate the effects of climate change, more sustainable technologies and systems are needed. This thesis describes research in two areas of study that each relate to sustainability: 1) conjugated polymer synthesis for application in organic photovoltaics and 2) open-loop chemical recycling of polyethylene. The first part of the thesis is motivated by the need for efficient renewable energy generation and storage technology. Conjugated polymers are promising materials for these applications because they enable devices that are flexible, lightweight, and potentially inexpensive to manufacture. Although polymer properties like molar mass and sequence can affect device performance, the scope of monomers that can be polymerized via catalyst-transfer polymerization (CTP) to control these properties remains narrow. We highlight the current state and future outlook of CTP and also demonstrate how polymers synthesized via CTP can be used to stabilize morphology and performance in organic photovoltaics (OPVs).

In Chapter 2, we outline the current limitations of CTP for synthesizing polymers for state-of-the-art devices and suggest palladium precatalysts to expand the scope of CTP. Inspired by recent examples of Pd-catalyzed CTP and by difunctionalization reactions in small-molecule cross-coupling literature, we suggest Buchwald and N-heterocyclic carbene ligated Pd precatalysts to expand the scope of monomers that can be polymerized via CTP.

In Chapter 3, we evaluate the effect of sequence, composition, and concentration for a series of conjugated copolymer additives to stabilize morphology in blends for OPVs. We used CTP to synthesize these fullerene-functionalized poly(3-hexylthiophene) (P3HT) copolymers and found that a random copolymer with 20 mol% fullerene-functionalized side chains at 8 wt% in the blend best stabilized morphology. P3HT/fullerene OPV devices with this copolymer demonstrated improved efficiencies over time with thermal annealing to mimic aging.

In Chapter 4, we evaluated our optimized copolymer additive for stabilizing higher-performing donor polymer/fullerene blends for OPVs. We found that this copolymer could stabilize morphology for multiple blends, suggesting that it could be used as a general stabilizing additive. We tested this copolymer in OPV devices for one of the blends and found that although it stabilizes morphology in devices, other factors ultimately limit performance for devices with the copolymer.

The second part of this thesis is motivated by the need for more sustainable end-of-use options for commodity plastics. While plastic production has grown exponentially over the last century, this growth has not been matched by effective waste and has resulted in thousands of tons of plastic pollution. We discuss current limitations for recycling polyethylene (PE), which is produced on the largest scale of any polymer world-wide, and outline our aims to repurpose PE waste via alkane metathesis and depolymerization to macrocycles by taking advantage of ring-chain equilibria.

In Chapter 5 we hypothesized that the quantity of alkenes formed along the PE backbone during alkane metathesis would affect cyclodepolymerization efficiency. We therefore study each step of alkane metathesis to evaluate 1) PE dehydrogenation efficiency and 2) how spacing between alkene backbones for unsaturated polyolefins affects cyclodepolymerization. We find that

lower concentrations of backbone alkenes reduce cyclodepolymerization efficiency and that dehydrogenation yields for PE are low. We describe our aims to improve PE dehydrogenation via catalyst design and also discuss the outlook for macrocyclic products that we may obtain.

Chapter 1 Introduction

The most recent assessment report from the Intergovernmental Panel on Climate Change states that greenhouse gas (e.g., CO_2, CH_4, NO_2) emission from human activities has unequivocally caused substantial changes in Earth's climate.[1] These changes include an overall warming of Earth's surface temperature, extreme storms, drought, and heatwaves that pose challenges to both human and non-human life. To mitigate climate change, new technology, political action, and improved systems are needed to reduce greenhouse gas emissions. As a framework for future action, the United Nations has put forth a list of sustainable development goals.[2] The work in this thesis uses polymer chemistry to address to two of these sustainability goals: Goal 7) to ensure access to affordable, reliable, sustainable, and modern energy for all, and Goal 12) to ensure sustainable consumption and production patterns.[2] In the first part of this thesis, we describe our work synthesizing polymeric additives to stabilize organic photovoltaics. In the second part of this thesis, we describe our efforts to repurpose polyethylene, which is produced on the largest scale of any polymer world-wide, via alkane metathesis while taking advantage of ring-chain equilibria.

1.1 Part One: Introduction to Copolymers to Stabilize Morphology in Conjugated Polymer-Fullerene Blends

There is a growing need for efficient means to generate and store renewable energy to mitigate the effects of climate change.[3] Conjugated polymers are promising materials for energy applications like batteries,[4] transistors,[5] and organic photovoltaics (OPVs)[6,7] because they can be solution processed to make flexible, lightweight, and even stretchable devices.[8,9] Conjugated polymers are also advantageous for these applications because their optical, electronic, and

morphological properties can be tuned by modifying their chemical structures.[10] For example, electron-donating or -withdrawing groups in the polymer repeat unit structure can be used to tune the bandgap, which affects both the optical absorption and the charge transfer efficiency.[11,12] The polymer molar mass, dispersity, and sequence also affect performance, although the degree to which each one of these parameters impacts different types of devices is less well understood. These parameters are challenging to study because they cannot be controlled via step-growth polymerization methods, which are commonly used to synthesize conjugated polymers for devices.[13] Controlled polymer synthesis methods are therefore needed to better understand how each parameter effects device performance and to then optimize polymer materials for given applications.

Living, chain-growth polymerization occurs when monomers are sequentially added to an active polymer chain end with fast initiation relative to propagation that occurs without termination.[14,15] This type of polymerization is ideal for precise polymer synthesis because it gives control over polymer molar mass, dispersity, and sequence. The most common living, chain-growth method to synthesize conjugated polymers is catalyst-transfer polymerization (CTP).[16,17,18] During CTP, propagation occurs through a M(0)/M(II) (where M = Ni, Pd) catalytic cycle where monomers are added to the growing chain via transmetalation and reductive elimination (Scheme 1.1). The key step that facilitates chain-growth is ring-walking, which enables the catalyst to stay associated with a single growing polymer chain. Ring-walking occurs when the metal–polymer π-complex[19] that forms after reductive elimination isomerizes, and the metal migrates to the end of a growing polymer chain. The metal then undergoes *intra*molecular oxidative addition into the C–X chain end and is thus primed for subsequent monomer addition. Because ring-walking depends

on the stability of the metal–polymer π-complex, successful CTP is highly dependent on the steric and electronic match between a given catalyst and monomer.[16b]

Scheme 1.1 Catalyst-transfer polymerization mechanism.

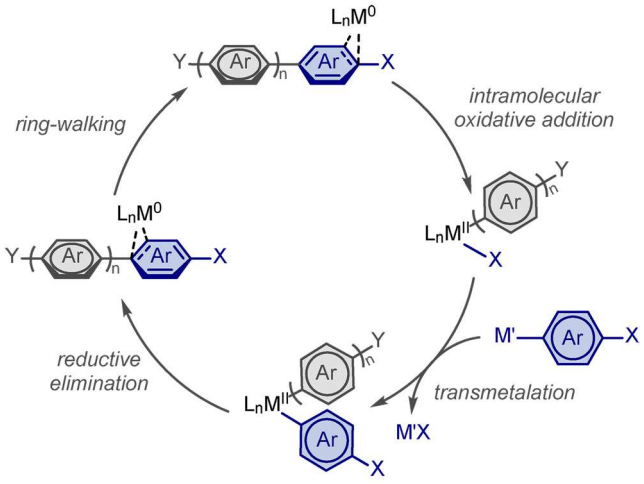

CTP is used most frequently to polymerize small, electron-rich arene monomers because these monomers form π-complexes that are stable enough for propagation to proceed without unproductive side reactions (e.g., chain-transfer[20]), yet reactive enough to avoid catalyst trapping.[21] However, the highest-performing conjugated polymers for many energy applications contain fused-ring repeat units with electron-rich and electron-poor arenes to tune the polymer bandgap and solid-state packing properties (Chart 1.1).[11] These state-of-the-art polymers have therefore almost exclusively been synthesized via step-growth methods, which has prevented control over polymer properties and is limited by batch-to-batch variability.[22] To further optimize performance for devices that employ conjugated polymers, it is necessary to expand the scope of polymers that can be synthesized via CTP.

Chart 1.1 Chemical structures of conjugated polymers used in high-performing energy devices.[23–27]

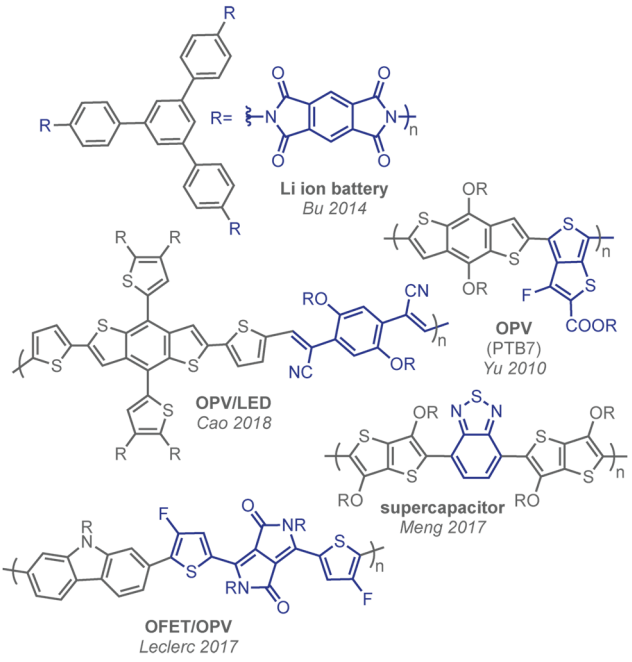

Chapter 2 of this thesis describes a potential avenue to expand CTP's scope by exploring palladium precatalysts in addition to the well-known nickel precatalysts already in use. We overview developments over the history of CTP and contrast those developments with developments in small-molecule cross-coupling. We highlight the potential advantages of palladium precatalysts for CTP and methods to identify new precatalyst/monomer pairs. Using recent examples from CTP and small-molecule cross-coupling literature, we suggest Pd ligated with Buchwald and N-heterocyclic carbene (NHC) ligands should be used to expand the scope of monomers that can be polymerized via CTP. Finally, we reflect on the remaining challenges of synthesizing polymers with structurally diverse repeat units.

One key application for conjugated polymers is OPVs.[6,7] These photovoltaic devices are advantageous for their low weight, flexibility, and potential for being manufactured inexpensively.[28] Due to improvements in conjugated polymer design over the last 25 years, power conversion efficiencies (PCEs) for OPVs have risen from 3%[29] to recent record breaking values of

> 17%.[30,31,32] Despite these improvements in device performance, however, low long-term stability remains a limitation for OPV commcialization.[28,33] One key factor that impacts device stability over time is changing morphology in the device active layer, which is composed of a physical blend of a conjugated electron-donor with a conjugated electron-acceptor.[7] Initially, nanoscale domains of each component enable effective charge separation in the device. [34] However, with aging, these initial domains phase-separate into larger (e.g., micron-scale) domains in an enthalpically-driven process, which ultimately reduces the charge separation efficiency and resulting PCE. [35,36]

A strategy to mitigate detrimental phase separation is to add a third component to the active layer blend as a compatibilizer. [37] Both small molecules[38] and polymers[39] have been used to compatibilize OPVs and, of these, block copolymers are the most common. While these additives improve device stability, few studies have evaluated how different copolymer sequences might affect the stability of device morphology or performance over time.

In Chapter 3, we evaluate how the sequence, composition, and blend concentration of copolymer additives affect morphological stability and device longevity for OPVs with poly(3-hexylthiophene) P3HT and phenyl-C_{61}-butryic acid methyl ester ($PC_{61}BM$) blended in the active layer. We employ CTP to synthesize a series of fullerene-functionalized P3HT copolymers with varying sequences (e.g., block, gradient, or random) and compositions (e.g., 20, 35, or 50 mol% fullerene-functionalization) and add them to P3HT/$PC_{61}BM$ blends at varying concentrations (e.g. 2, 5, 8 wt%) to investigate how they affect blend morphology with thermal annealing (Figure 1.1). We determined that a random copolymer with 20 mol% fullerene side-chain functionalization at 8 wt% in the blend best stabilized thin film blend morphology. We therefore evaluate this copolymer in P3HT:$PC_{61}BM$ devices and find that devices with the copolymer exhibited more stable power

conversion efficiencies than control devices. While these results are promising for the workhorse P3HT:$PC_{61}BM$ system (with PCEs of 5–6%), other donor/acceptor blends that have been developed for higher-performing OPVs (with PCEs of ~10%) also undergo phase separation that results in PCE losses over time. We hypothesized that our optimized copolymer might be miscible with the donors/acceptors used in these OPVs and could thus serve as a general compatibilizer.

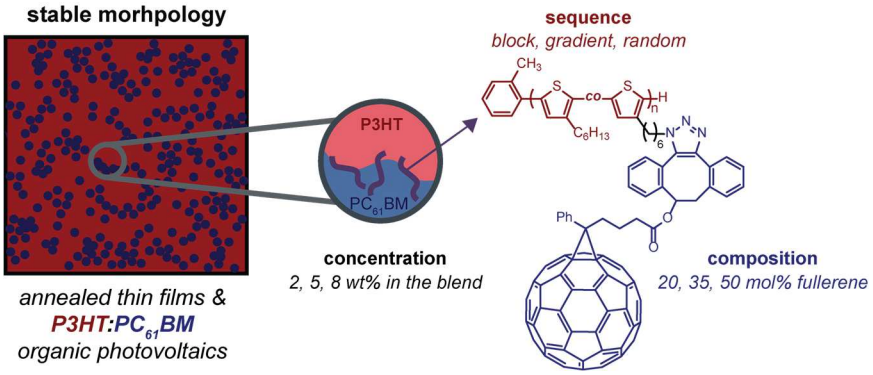

Figure 1.1 A depiction of P3HT:$PC_{61}BM$ blend morphology (left) and the structure of the copolymers and the parameters evaluated for blend stabilization (right).

In Chapter 4, we elucidate the effect that our copolymer additive has on blend morphologies for blends of three different donor polymers with phenyl-C_{71}-butyric acid methyl ester ($PC_{71}BM$) that are used in higher-performing OPVs (Figure 1.2). By annealing thin films to mimic aging, we find that our single copolymer additive stabilizes micron-scale morphology for each of these polymer/$PC_{71}BM$ blends, likely due to favorable interactions with the $PC_{71}BM$ acceptor. We also study how the copolymer affects device morphology and performance for the blend with the most promising results from thin film studies. Although we find that the copolymer stabilizes OPV device morphology, other factors including absorbance and conductivity ultimately limit device performance.

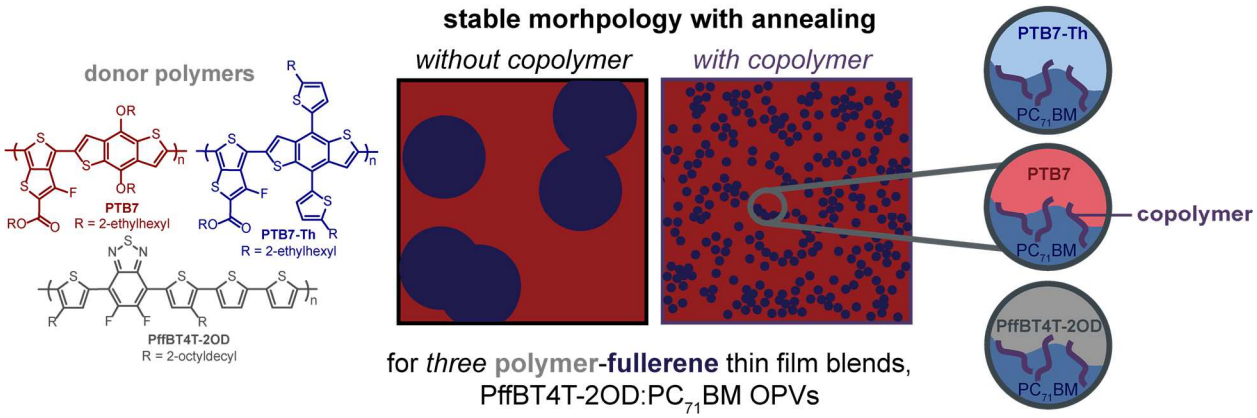

Figure 1.2 Chemical structures of the donor polymers used in this work (left),[24,40,41] a depiction of blend morphology without the copolymer (center) and blend morphology with the copolymer (right).

Overall, the first part of this thesis demonstrates the importance of controlled conjugated polymer synthesis for optimizing device performance. We use inspiration from small-molecule literature to highlight promising Pd precatalysts to expand the scope of monomers that can by polymerized via CTP. Using CTP, we systematically investigate the effect of copolymer sequence, composition, and concentration for stabilizing morphology for P3HT:$PC_{61}BM$ blends. We find that a random copolymer best stabilizes morphology for these blends and use this copolymer to stabilize PCE for annealed OPV devices. In addition, we demonstrate that this single copolymer can be used as a general additive to stabilize morphology for several donor/$PC_{71}BM$ blends, but that other factors limit device performance when the copolymer is added to non-P3HT-based OPV devices. Finally, we suggest future work to expand the utility of conjugated copolymers to stabilize morphology in non-fullerene OPVs.

1.2 Part Two: Introduction to Understanding Alkene Spacing for Repurposing Polyethylene via Alkane Metathesis and Cyclodepolymerization

Plastics have revolutionized nearly every aspect of human society – from construction to packaging, transportation, and textiles – because of their versatile physical properties.[42] Plastics

are also inexpensive to produce and are thus manufactured on an enormous scale world-wide, with an estimated 368 Mt of plastic produced in 2019 alone.[43] This large-scale production has not been matched with complementary strategies to manage the resulting plastic waste, resulting in vast quantities of plastic debris in the environment.[44] For example, one estimate suggests that 60% of all the plastic that has ever been produced has accumulated in either landfills or the natural environment.[45] In the natural environment, plastic can form microplastics, or particles of synthetic polymers ranging from 1–5000 μm in size.[46] The implications of microplastic pollution for ecosystem and human health are still being studied, but recent examples suggest adverse health effects in marine life like mussels and fish.[47,48] To mitigate the flow of plastic waste into the environment, more effective end-of-use strategies for plastic waste are needed.

Two common alternatives to landfilling plastic waste are incineration and mechanical recycling.[43] Incineration uses plastic waste as fuel to generate electricity but can generate volatile environmental pollutants,[49] especially when additives like flame retardants are present.[50] For mechanical recycling, plastics are collected, sorted from other polymers, washed to remove contaminants, physically ground into small pieces, and melt-reprocessed to form recycled products.[51] However, the recycled products rarely have comparable physical properties to those of virgin materials due to difficulties in sorting polymers, removing additives and/or contaminants, or chain-scission or cross-linking during physical processing.[5253] Due to the limitations of these methods, researchers are now focusing on new methods to recycle plastics.

Chemical recycling is an emerging strategy that treats plastic waste as a valuable feedstock for further chemical reactions.[54] In this case, plastic is collected and 1) recycled to monomer for repolymerization into the same plastic via closed-loop recycling, or 2) chemically modified and repurposed as a new material via open-loop recycling (Scheme 1.2). Either approach should limit

the amount of plastic leached into the environment and decrease reliance on fossil fuels, which are the primary feedstock for commodity plastics.[55] While closed-loop recycling is attractive in theory, it can be challenging to execute in practice. For this process to be efficient, the kinetics and thermodynamics of polymerization and depolymerization must balance to enable synthesis of polymers that are stable enough to withstand conditions for use, but with low enough energetic barriers for depolymerization into small molecules after use.[56] Polymers with heteroatoms in the backbone are more amenable to closed-loop recycling because they are susceptible to nucleophilic attack for controlled backbone degradation.[57] In contrast, commodity polyolefins have prohibitively high activation energies for decomposition to monomers (e.g., 150–300 kJ/mol at 250–400 °C for polyethylene),[58] Therefore, open-loop recycling methods are more feasible option for these materials.

Scheme 1.2 Closed-loop recycling to generate monomers (left) and open-loop recycling to generate functionalized materials (right).

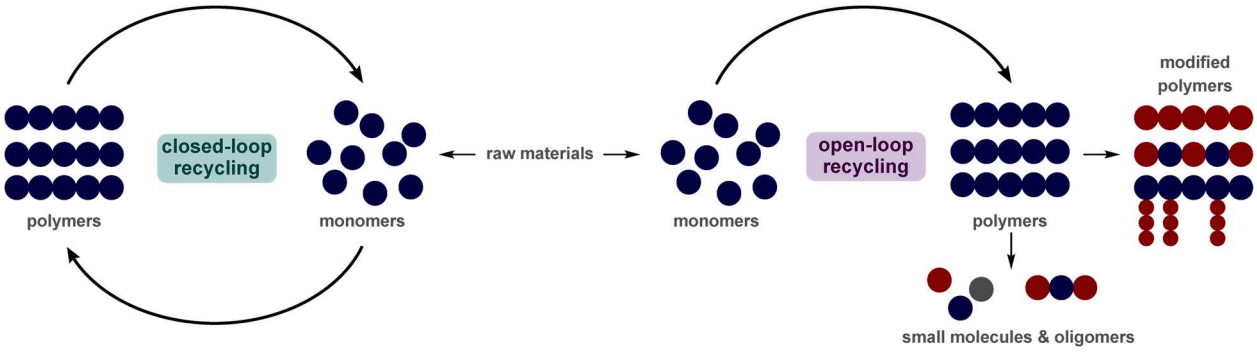

We chose to focus on open-loop recycling for polyethylene (PE) because it is produced in the largest volume of any synthetic polymer world-wide but with low recycling rates.[45] For example, of the 14.9 Mt of combined PE waste generated in the US in 2018, only 6.2% was recycled. Currently, post-consumer PE waste is recycled mechanically,[6] but open-loop recycling methods are being developed to address the limitations of mechanical recycling outlined above. One strategy is to chemically functionalize the polymer backbone and/or side-chains to obtain

value-added polymeric materials.[59,60] For example, peroxides are used to commercially to graft maleic anhydride onto the PE polymer backbone to make compatibilizers.[61] However, radical formation also induces chain-scission, which degrades the mechanical properties of the original PE.[62] Alternatively, metal-catalyzed C–H activation can be used to functionalize the PE with polar groups – like pinacol boranes[63] or a mixture of ketones, alcohols, and chlorides[64] – that modify its surface energy and adhesive properties. This method typically only affords low conversion of functionalized units (e.g., < 5 out of 100 repeat units) and is often limited to side-chain functionalization for branched PE.[63] The most common open-loop recycling strategy is to convert PE into small-molecule products via pyrolysis or hydrogenolysis (i.e., pyrolysis under H_2). These processes employ high temperatures (≥ 300 °C) to catalytically convert PE into small-molecule hydrocarbons for liquid fuels or waxes.[65,66] Although pyrolysis and hydrogenolysis effectively lower PE molar mass, they are limited by the high temperatures required and complex product mixtures that form.

Alkane metathesis is a promising alternative to pyrolysis to convert PE into short-chain alkanes because it is effective at much lower temperatures. For alkane metathesis, a dehydrogenation catalyst generates alkenes which undergo olefin-metathesis and, finally, are re-hydrogenated to obtain new alkanes with different chain lengths than the starting materials (Figure 1.3 A).[67] Two recent examples used this method to convert PE into short-chain alkanes in the presence of excess *n*-hexane or *n*-pentane at temperatures below 200 °C. [68,69] The first system used a series of homogeneous Ir catalysts paired with either a homogeneous Mo or heterogeneous Re_2O_5/Al_2O_3 olefin metathesis while the second used two heterogeneous catalysts, $SnPt/Al_2O_3$ and Re_2O_5/Al_2O_3. Promisingly, the first system successfully converted commercial PE samples into low molar mass alkanes, indicating that it was not inhibited by additives. Despite this advantage

and milder temperatures in each case, both systems produced a mixture of linear products analogous to those obtained via pyrolysis.

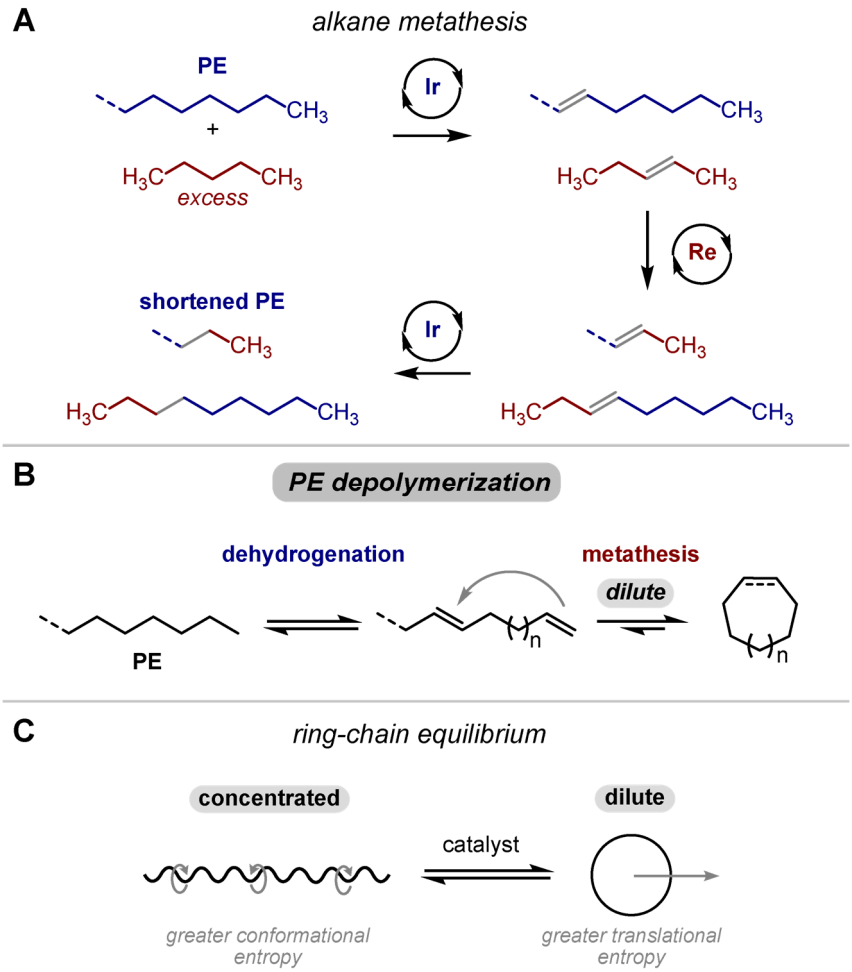

Figure 1.3 (A) Alkane metathesis of PE catalyzed by an Ir dehydrogenation catalyst and a Re olefin metathesis catalyst. (B) Depolymerization of PE via alkane metathesis under dilute conditions to obtain macrocycles (C) General scheme depicting entropy-driven ring-chain equilibria between linear and strainless cyclic species.

Inspired by these examples, we envisioned using alkane metathesis while taking advantage of ring-chain equilibria to instead convert PE into macrocyclic products (Figure 1.3, B). Equilibria between linear and cyclic species exist in any given polymerization[70] and when the cyclic species are strainless, the equilibria are governed by entropy rather than enthalpy.[71] In theory, the distribution between linear and cyclic species can thus be controlled by the dilution of the system

where concentrated conditions favor linear species for their greater conformational entropy, but dilute conditions favor macrocycles for their greater translational entropy (Figure 1.3 C).[71] In practice, this strategy has been used to "cyclodepolymerize" polycarbonates, polyesters, and alkene-containing polymers into macrocyclic species.[72,73] We therefore hypothesized that we could employ alkane metathesis under dilute conditions to depolymerize PE into macrocycles and envisioned using these macrocycles as feedstocks to generate functionalized copolymers.

In Chapter 5, we systematically investigate how the degree of PE dehydrogenation affects cyclodepolymerization with the Ir-Mo catalyst system. First, we evaluated conditions to dehydrogenate PE, because we anticipated that there may be a lower limit to the quantity of dehydrogenation needed for effective metathesis backbiting and cyclodepolymerization (Scheme 1.3 A). Second, we synthesized a series of polyolefins with varying quantities of backbone alkenes and tested depolymerization efficiency for these polymers under dilute conditions (Scheme 1.3 B). Initial results indicate that only a small percent of PE repeat units are dehydrogenated by Ir catalysts and that cyclodepolymerization efficiency decreases as the quantity of backbone alkenes decreases, as expected. Moving forward, we intend to explore a wider range of catalysts, including those that avoid precious metals, and solvents to improve PE dehydrogenation yields. Finally, we suggest future sequential dehydrogenation-cyclodepolymerization studies to cyclodepolymerize PE and discuss potential uses for the macrocyclic products.

Scheme 1.3 (A) PE dehydrogenation conditions to study the quantity of alkenes formed. (B) Metathesis cyclodepolymerization to study how alkene spacing affects the quantity and size of cyclic products.

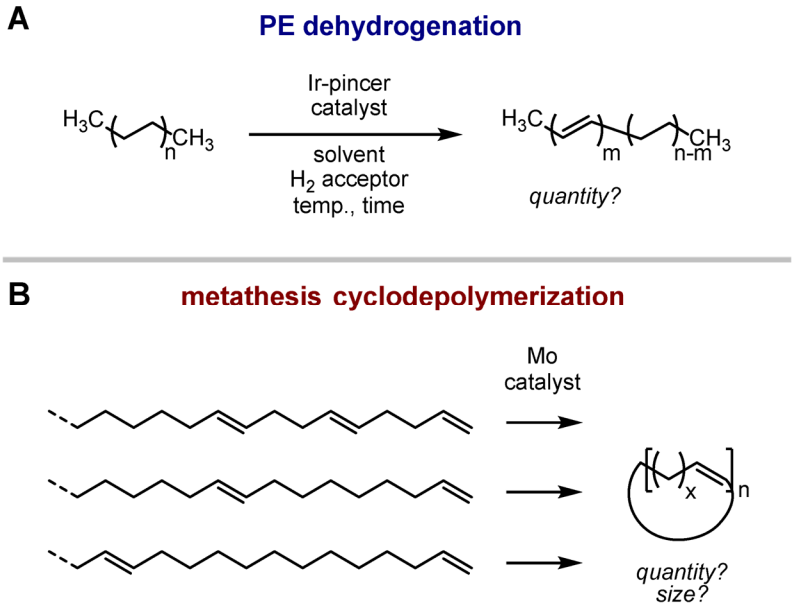

1.3 References

1 Intergovernmental Panel on Climate Change (IPCC). AR6 Climate Change 2021: The Physical Science Basis. **2021**, https://www.ipcc.ch/report/ar6/wg1/#FullReport (accessed August 24, 2021).

2 United Nations (UN). The Sustainable Development Goals Report 2021. **2021**, https://unstats.un.org/sdgs/report/2021/ (accessed August 24, 2021).

3 Durrant, P.; Ruiz, C.; Gehl Sampath, P.; Ratka, S.; Ocenic, E.; Kang, S.; Komor, P. Reaching Zero with Renewables: Eliminating CO_2 Emissions from Industry and Transport in Line with the 1.5 °C Climate Goal. **2020**, *International Renewable Energy Agency*, https://www.irena.org/publications/2020/Sep/Reaching-Zero-with-Renewables.

4 Xie, J.; Gu, P.; Zhang, Q. Nanostructured Conjugated Polymers: Toward High-Performance Organic Electrodes for Rechargeable Batteries. *ACS Energy Lett.* **2017**, *2*, 1985–1996.

5 Sirringhaus, H. 25th Anniversary Article: Organic Field-Effect Transistors: The Path Beyond Amorphous Silicon. *Adv. Mater.* **2014**, *26*, 1319–1335.

6 Chochos, C. L.; Spanos, M.; Katsouras, A.; Tatsi, E.; Drakopoulou, S.; Gregoriou, V. G.; Avgeropoulos, A. Current Status, Challenges and Future Outlook of High-Performance Polymer Semiconductors for Organic Photovoltaics Modules. *Prog. Polym. Sci.* **2019**, *91*, 51–79.

7 Lu, L.; Zheng, T.; Wu, Q.; Schneider, A. M.; Zhao, D.; Yu, L. Recent Advances in Bulk Heterojunction Polymer Solar Cells. *Chem. Rev.* **2015**, *115*, 12666–12731.

[8] Kim, T.; Kim, J.-H.; Kang, T. E.; Lee, C.; Kang, H.; Shin, M.; Wang, C.; Ma, B.; Jeong, U.; Kim, T.-S.; Kim, B. J. Flexible, Highly Efficient All-Polymer Solar Cells. *Nat. Commun. 2015 61* **2015**, *6*, 1–7.

[9] Hao, G.-P.; Hippauf, F.; Oschatz, M.; Wisser, F. M.; Leifert, A.; Nickel, W.; Mohamed-Noriega, N.; Zheng, Z.; Kaskel, S. Stretchable and Semitransparent Conductive Hybrid Hydrogels for Flexible Supercapacitors. *ACS Nano* **2014**, *8*, 7138–7146.

[10] Qiu, Z.; Hammer, B. A. G.; Müllen, K. Conjugated Polymers – Problems and Promises. *Prog. Polym. Sci.* **2020**, *100*, 101179.

[11] Holliday, S.; Li, Y.; Luscombe, C. K. Recent Advances in High Performance Donor-Acceptor Polymers for Organic Photovoltaics. *Prog. Polym. Sci.* **2017**, *70*, 34–51.

[12] Cheng, P.; Yang, Y. Narrowing the Band Gap: The Key to High-Performance Organic Photovoltaics. *Acc. Chem. Res.* **2020**, *53*, 1218–1228.

[13] Yokozawa, T.; Ohta, Y. Transformation of Step-Growth Polymerization into Living Chain-Growth Polymerization. *Chem. Rev*. **2016**, *116*, 1950−1968.

[14] Grubbs, R. B.; Grubbs, R. H. 50th Anniversary Perspective: Living Polymerization—Emphasizing the Molecule in Macromolecules. *Macromolecules* **2017**, *50* (18), 6979–6997.

[15] Cowie, J. M. G.; Arrighi, V. Polymers: Chemistry and Physics of Modern Materials, 3rd Ed. **2007**, *CRC Press*: Boca Raton, FL.

[16] For reviews see: (a) Bryan, Z. J.; McNeil, A. J. Conjugated Polymer Synthesis via Catalyst-Transfer Polycondensation (CTP): Mechanism, Scope, and Applications. *Macromolecules* **2013**, *46*, 8395−8405. (b) Leone, A. K.; McNeil, A. J. Matchmaking in Catalyst-Transfer Polycondensation: Optimizing Catalysts based on Mechanistic Insight. *Acc. Chem. Res.* **2016**, *49*, 2822−2831. (c) Aplan, M. P.; Gomez, E. D. Recent Developments in Chain-Growth Polymerizations of Conjugated Polymers. *Ind. Eng. Chem. Res.* **2017**, *56* (28), 7888–7901.

[17] Sheina, E. E.; Liu, J.; Iovu, M. C.; Laird, D. W.; McCullough, R. D. Chain Growth Mechanism for Regioregular Nickel-Initiated Cross-Coupling Polymerizations. *Macromolecules* **2004**, *37*, 3526−3528.

[18] Yokoyama, A.; Miyakoshi, R.; Yokozawa, T. Chain-Growth Polymerization for Poly(3-hexylthiophene) with a Defined Molecular Weight and a Low Polydispersity. *Macromolecules* **2004**, *37*, 1169−1171.

[19] He, W.; Patrick, B. O.; Kennepohl, P. Identifying the Missing Link in Catalyst Transfer Polymerization *Nat. Commun. **2018**, 9,* 3866.

[20] Smith, M. L.; Leone, A. K.; Zimmerman, P. M.; McNeil, A. J. Impact of Preferential π-Binding in Catalyst-Transfer Polycondensation of Thiazole Derivatives. *ACS Macro Lett.* **2016**, *5*, 1411−1415.

[21] Nojima, M.; Ohta, Y.; Yokozawa, Y. Investigation of Catalyst-Transfer Condensation Polymerization for Synthesis of Poly(pphenylenevinylene). *J. Polym. Sci., Part A: Polym. Chem*. **2014**, *52*, 2643−2653.

[22] Lee, S. M.; Park, K. H.; Jung, S.; Park, H.; Yang, C. Stepwise Heating in Stille Polycondensation Toward No Batch To-Batch Variations in Polymer Solar Cell Performance. *Nat. Commun*. **2018**, *9*, 1867.

[23] Tian, D.; Zhang, H.-Z.; Zhang, D.-S.; Chang, Z.; Han, J. Gao, X-P.; Bu, X.-H Li-Ion Storage and Gas Adsorption Properties of Porous Polyimides (PIs). *RSC Adv*., **2014**, *4*, 7506–7510.

[24] Liang, Y.; Xu, Z.; Xia, J.; Tsai, S.-T.; Wu, Y.; Li, G.; Ray, C.; Yu, L. For the Bright Future—Bulk Heterojunction Polymer Solar Cells with Power Conversion Efficiency of 7.4%. *Adv. Mater*. **2010**, *22*, E135–E138.

[25] Cao, C.; Xiao, M.; Yang, X.; Zhang, J.; Huang F.; Cao, Y. Cyanovinylene-Based Copolymers by Tin-free Knoevenagel Polycondensation for High Efficiency Polymer Solar Cells. *J. Mater. Chem. C*. **2018**, *6*, 8020–8027.

[26] Bura, T.; Beaupré, S.; Ibraikulov, O. A.; Légaré, M.-A.; Quinn, J.; Lévêque, P.; Heiser, T.; Li, Y.; Leclerc, N.; Leclerc, M. New Fluorinated Dithienyldiketopyrrolopyrrole Monomers and Polymers for Organic Electronics. *Macromolecules* **2017**, *50*, 7080–7090.

[27] Guo, Y.; Li, W.; Yu, H.; Perepichka, D.; Meng, H. Flexible Asymmetric Supercapacitors via Spray Coating of a New Electrochromic Donor–Acceptor Polymer. *Adv. Energy Mater.* **2017**, *7*, 1601623.

[28] Riede, M.; Spoltore, D.; Leo, K. Organic Solar Cells—The Path to Commercial Success. *Adv. Energy Mater.* **2021**, *11*, 2002653.

[29] Yu, G.; Gao, J.; Hummelen, J. C.; Wudl, F.; Heeger, A. J. Polymer Photovoltaic Cells: Enhanced Efficiencies via a Network of Internal Donor-Acceptor Heterojunctions. *Science* **1995**, *270* (5243), 1789–1791.

[30] Meng, L.; Zhang, Y.; Wan, X.; Li, C.; Zhang, X.; Wang, Y.; Ke, X.; Xiao, Z.; Ding, L.; Xia, R.; Yip, H. L.; Cao, Y.; Chen, Y. Organic and Solution-Processed Tandem Solar Cells with 17.3% Efficiency. *Science* **2018**, *361*, 1094–1098. https://doi.org/10.1126/science.aat2612

[31] Cui, Y.; Yao, H.; Zhang, J.; Xian, K.; Zhang, T.; Hong, L.; Wang, Y.; Xu, Y.; Ma, K.; An, C.; He, C.; Wei, Z.; Gao, F.; Hou, J. Single-Junction Organic Photovoltaic Cells with Approaching 18% Efficiency. *Adv. Mater.* **2020**, *32*, 1908205. https://doi.org/10.1002/adma.201908205

[32] Liu, Q.; Jiang, Y.; Jin, K.; Qin, J.; Xu, J.; Li, W.; Xiong, J.; Liu, J.; Xiao, Z.; Sun, K.; Yang, S.; Zhang, X.; Ding, L. 18% Efficiency Organic Solar Cells. *Sci. Bull.* **2020**, *65*, 272–275. https://doi.org/10.1016/j.scib.2020.01.001

[33] Turak, A. Device Stability in Organic Optoelectronics. In *Handbook of Organic Materials for Electronic and Photonic Devices (2nd Ed.)*; Elsevier, **2019**, 599–662. https://doi.org/10.1016/b978-0-08-102284-9.00019-x

[34] Treat, N. D.; Chabinyc, M. L. Phase Separation in Bulk Heterojunctions of Semiconducting Polymers and Fullerenes for Photovoltaics. *Annu. Rev. Phys. Chem.* **2014**, *65*, 59–81. https://doi.org/10.1146/annurev-physchem-040513-103712.

[35] Cardinaletti, I.; Kesters, J.; Bertho, S.; Conings, B.; Piersimoni, F.; D'Haen, J.; Lutsen, L.; Nesladek, M.; Van Mele, B.; Van Assche, G.; Vandewal, K.; Salleo, A.; Vanderzande, D.; Maes, W.; Manca, J. V. Toward Bulk Heterojunction Polymer Solar Cells with Thermally Stable Active Layer Morphology. *J. Photonics Energy* **2014**, *4*, 040997. https://doi.org/10.1117/1.jpe.4.040997.

[36] Savagatrup, S.; Printz, A. D.; O'Connor, T. F.; Zaretski, A. V.; Rodriquez, D.; Sawyer, E. J.; Rajan, K. M.; Acosta, R. I.; Root, S. E.; Lipomi, D. J. Mechanical Degradation and Stability of Organic Solar Cells: Molecular and Microstructural Determinants. *Energy Environ. Sci.* **2015**, *8*, 55–80. https://doi.org/10.1039/c4ee02657h

[37] Bonasera, A.; Giuliano, G.; Arrabito, G.; Pignataro, B. Tackling Performance Challenges in Organic Photovoltaics: An Overview about Compatibilizers. *Molecules* **2020**, *25*, 1–40. https://doi.org/10.3390/molecules25092200

[38] Wang, H.; Yang, L.; Lin, P.; Chueh, C.; Liu, X.; Qu, S.; Guang, S.; Yu, J.; Tang, W. A Simple Dithieno[3,2-b:2′,3′-d]Pyrrol-Rhodanine Molecular Third Component Enables Over 16.7% Efficiency and Stable Organic Solar Cells. *Small* **2021**, ASAP. https://doi.org/10.1002/smll.202007746

[39] Kipp, D.; Verduzco, R.; Ganesan, V. Block Copolymer Compatibilizers for Ternary Blend Polymer Bulk Heterojunction Solar Cells-an Opportunity for Computation Aided Molecular Design. *Molecular Systems Design and Engineering*. Royal Society of Chemistry November 28, 2016, pp 353–369. https://doi.org/10.1039/c6me00060f

[40] Liao, S.-H.; Jhuo, H.-J.; Cheng, Y.-S.; Chen, S.-A. Fullerene Derivative-Doped Zinc Oxide Nanofilm as the Cathode of Inverted Polymer Solar Cells with Low-Bandgap Polymer (PTB7-Th) for High Performance. *Adv. Mater.* **2013**, *25*, 4766–4771.

[41] Liu, Y.; Zhao, J.; Li, Z.; Mu, C.; Ma, W.; Hu, H.; Jiang, K.; Lin, H.; Ade, H.; Yan, H. Aggregation and Morphology Control Enables Multiple Cases of High-Efficiency Polymer Solar Cells. *Nat. Commun.* **2014**, *5*, 5293.

[42] Andrady, A. L.; Neal, M. A. Applications and Societal Benefits of Plastics. *Philos. Trans. R. Soc. B Biol. Sci.* **2009**, *364* (1526), 1977–1984. https://doi.org/10.1098/RSTB.2008.0304.

[43] Association of Plastic Manufacturers (Organization). Plastics – the Facts 2020. *PlasticEurope* **2020**, https://www.plasticseurope.org/en/resources/publications/4312-plastics-facts-2020 (accessed July 24, 2021).

[44] Sebille, E. van; Wilcox, C.; Lebreton, L.; Maximenko, N.; Hardesty, B. D.; Franeker, J. A. van; Eriksen, M.; Siegel, D.; Galgani, F.; Law, K. L. A Global Inventory of Small Floating Plastic Debris. *Environ. Res. Lett.* **2015**, *10*, 124006.

[45] Geyer, R.; Jambeck, J. R.; Law, K. L. Production, Use, and Fate of All Plastics Ever Made. *Sci. Adv.* **2017**, *3*, e1700782.

[46] Hale, R. C.; Seeley, M. E.; Guardia, M. J. La; Mai, L.; Zeng, E. Y. A Global Perspective on Microplastics. *J. Geophys. Res. Ocean.* **2020**, *125*, e2018JC014719.

[47] Prokić, M. D.; Radovanović, T. B.; Gavrić, J. P.; Faggio, C. Ecotoxicological Effects of Microplastics: Examination of Biomarkers, Current State and Future Perspectives. *TrAC Trends Anal. Chem.* **2019**, *111*, 37–46.

[48] Jovanović, B. Ingestion of Microplastics by Fish and Its Potential Consequences from a Physical Perspective. *Integr. Environ. Assess. Manag.* **2017**, *13*, 510–515.

[49] Wang, Z.; Wang, J.; Richter, H.; Howard, J. B.; Carlson, J.; Levendis, Y. A. Comparative Study on Polycyclic Aromatic Hydrocarbons, Light Hydrocarbons, Carbon Monoxide, and Particulate Emissions from the Combustion of Polyethylene, Polystyrene, and Poly(Vinyl Chloride). *Energy and Fuels* **2003**, *17*, 999–1013.

[50] Weber, R.; Kuch, B. Relevance of BFRs and Thermal Conditions on the Formation Pathways of Brominated and Brominated-Chlorinated Dibenzodioxins and Dibenzofurans. *Environ. Int.* **2003**, *29*, 699–710.

[51] Ragaert, K.; Delva, L.; Van Geem, K. Mechanical and Chemical Recycling of Solid Plastic Waste. *Waste Manag.* **2017**, *69*, 24–58.

[52] Hahladakis, J. N.; Velis, C. A.; Weber, R.; Iacovidou, E.; Purnell, P. An Overview of Chemical Additives Present in Plastics: Migration, Release, Fate and Environmental Impact during Their Use, Disposal and Recycling. *J. Hazard. Mater.* **2018**, *344*, 179–199.

[53] Hinsken, H.; Moss, S.; Pauquet J. R.; Zweifel, H. Degradation of polyolefins during melt processing. *Polym. Degrad. Stab.* **1991**, *34*, 279–293.

[54] Ellen MacArthur Foundation. The New Plastics Economy: Rethinking the Future of Plastics & Catalyzing Action. *Ellen MacArthur Found.* **2017**, https://www.ellenmacarthurfoundation.org/publications/the-new-plastics-economy-rethinking-the-future-of-plastics (accessed July 24, 2021).

[55] Filiciotto, L.; Rothenberg, G. Biodegradable Plastics: Standards, Policies, and Impacts. *ChemSusChem* **2021**, *14*, 56–72.

[56] Coates, G. W.; Getzler, Y. D. Y. L. Chemical Recycling to Monomer for an Ideal, Circular Polymer Economy. *Nat. Rev. Mater.* **2020**, *5*, 501–516.

[57] Worch, J. C.; Dove, A. P. 100th Anniversary of Macromolecular Science Viewpoint: Toward Catalytic Chemical Recycling of Waste (and Future) Plastics. *ACS Macro Lett.* **2020**, 1494–1506.

[58] Miranda, R.; Yang, J.; Roy, C.; Vasile, C. Vacuum Pyrolysis of Commingled Plastics Containing PVC I. Kinetic Study. *Polym. Degrad. Stab.* **2001**, *72*, 469–491.

[59] Chen, X.; Wang, Y.; Zhang, L. Recent Progress in the Chemical Upcycling of Plastic Wastes. *ChemSusChem* **2021**. DOI: 10.1002/CSSC.202100868, https://doi.org/10.1002/CSSC.202100868

[60] Plummer, C. M.; Li, L.; Chen, Y. The Post-Modification of Polyolefins with Emerging Synthetic Methods. *Polym. Chem*. **2020**, *43*, 6862–6872.

[61] Passaglia, E.; Coiai, S.; Augier, S. Control of Macromolecular Architecture during the Reactive Functionalization in the Melt of Olefin Polymers. *Prog. Polym. Sci.* **2009**, *34*, 911–947.

[62] Gloor, P. E.; Tang, Y.; Kostanska, A. E.; Hamielec, A. E. Chemical Modification of Polyolefins by Free Radical Mechanisms: A Modelling and Experimental Study of Simultaneous Random Scission, Branching and Crosslinking. *Polymer.* **1994**, *35*, 1012–1030.

[63] Bae, C.; Hartwig, J. F.; Chung, H.; Harris, N. K.; Switek, K. A.; Hillmyer, M. A. Regiospecific Side-Chain Functionalization of Linear Low-Density Polyethylene with Polar Groups. *Angew. Chemie Int. Ed.* **2005**, *44*, 6410–6413.

[64] Bunescu, A.; Lee, S.; Li, Q.; Hartwig, J. F. Catalytic Hydroxylation of Polyethylenes. *ACS Cent. Sci.* **2017**, *3* (8), 895–903.

[65] Anuar Sharuddin, S. D.; Abnisa, F.; Wan Daud, W. M. A.; Aroua, M. K. A Review on Pyrolysis of Plastic Wastes. *Energy Convers. Manag.* **2016**, *115*, 308–326.

[66] Kosloski-Oh, S. C.; Wood, Z. A.; Manjarrez, Y.; de los Rios, J. P.; Fieser, M. E. Catalytic Methods for Chemical Recycling or Upcycling of Commercial Polymers. *Mater. Horizons* **2021**, *8*, 1084–1129.

[67] Haibach, M. C.; Kundu, S.; Brookhart, M.; Goldman, A. S. Alkane Metathesis by Tandem Alkane-Dehydrogenation–Olefin-Metathesis Catalysis and Related Chemistry. *Acc. Chem. Res.* **2012**, *45*, 947–958.

[68] Jia, X.; Qin, C.; Friedberger, T.; Guan, Z.; Huang, Z. Efficient and Selective Degradation of Polyethylenes into Liquid Fuels and Waxes under Mild Conditions. *Sci. Adv.* **2016**, *2*, e1501591.

[69] Ellis, L. D.; Orski, S. V.; Kenlaw, G. A.; Norman, A. G.; Beers, K. L.; Román-Leshkov, Y.; Beckham, G. T. Tandem Heterogeneous Catalysis for Polyethylene Depolymerization via an Olefin-Intermediate Process. *ACS Sustain. Chem. Eng.* **2021**, *9*, 623–628.

[70] Ivin, K. J. Thermodynamics of Addition Polymerization. *J. Polym. Sci. A. Polym. Chem.*

[71] Jacobson, H.; Stockmayer, W. H. Intramolecular Reaction in Polycondensations. I. The Theory of Linear Systems. *J. Chem. Phys.* **2004**, *18*, 1600.

[72] Hodge, P. Recycling of Condensation Polymers via Ring-Chain Equilibria. *Polym. Adv. Technol.* **2015**, *26*, 797–803.

[73] Hodge, P. Cyclodepolymerization as a Method for the Synthesis of Macrocyclic Oligomers. *React. Funct. Polym.* **2014**, *80*, 21–32.

Chapter 2 The History of Palladium-Cross Couplings Should Inspire the Future of Catalyst-Transfer Polymerization[1]

2.1 Introduction

Designing novel materials for fuel cells, batteries, and solar panels is central to meeting society's growing needs for alternative energy sources. Semiconducting polymers are widely explored in these applications due to their inherent ability to absorb light and conduct charge. These polymers can be accessed through either oxidative coupling or transition-metal catalyzed polymerization. For the latter approach, the polymerizations proceed either through a step-growth[1,2] or chain-growth[3–6] mechanism. Living, chain-growth polymerizations are ideal because monomers are sequentially added to the polymer without termination, which enables polymers with precise molecular weights, dispersities, sequences, and end-groups to be synthesized.[7] Despite the promise of living polymerizations, advances in developing this approach for conjugated polymers has been slow relative to other polymer types.

Transition-metal catalyzed syntheses for conjugated polymers were first reported as early as 1978.[8] Remarkably, the chain-growth mechanism for some of these transformations was not revealed until 26 years later.[9,10] Thiophene polymerization catalyzed by Ni(dppp)Cl_2 was first reported by Heeger and Wudl in 1984.[11] Eight years later, McCullough demonstrated that this polymerization yielded regioregular poly(3-alkylthiophene).[12] However, it was not until 2004 that

[1] This work has been published as: Leone, A. K.,* Mueller, E. A.,* McNeil, A. J. The History of Palladium-Cross Couplings Should Inspire the Future of Catalyst-Transfer Polymerization. *J. Am. Chem. Soc.* **2018**, *140*, 15126–15139. **equal contribution*

McCullough[9] and Yokozawa[10] concurrently reported that this polymerization was living and chain-growth. These seminal reports revealed for the first time that conjugated polymers have the potential to be synthesized with control over their length, sequence and end-group functionality– an exciting advancement in the field. The discovery of this living polymerization method, now referred to as catalyst-transfer polymerization (CTP), lured the corresponding author and several others to start exploring the method's potential.

To date, CTP is still most frequently used to polymerize simple thiophene monomers with Ni(dppp)Cl_2.[5] Over the last decade, the majority of advances in CTP have been mechanistic in nature: demonstrating how the ancillary ligands, reactive ligands, and transition metal identity influence initiation and propagation.[13–19] In contrast, during the same time period most of the advances in organic electronic materials have been in structural diversification: developing new monomers to optimize optical and conductive properties as well as solid-state packing.[1,2,20–26] The dissimilar rates of development between these two fields has generated an enormous mismatch between the mechanistic insight gained for CTP and its ability to polymerize state-of-the-art, structurally diverse monomers.

To overcome this disparity, we draw inspiration from the delayed "discovery" of CTP and urge the catalysis community to ask: what are we overlooking? What potential ligands and precatalysts for CTP might *already* exist in the small-molecule or polymerization literature? Fortunately, the mechanistic insight developed over the last decade provides a detailed road map for how to identify precatalysts for CTPs. This Perspective highlights what we think should be the path forward. We begin by describing the CTP mechanism and how it enables conjugated polymers to be systematically tuned. Then, we outline why we consider palladium precatalysts to be the most promising mediators for advancing CTP. Finally, ancillary ligands that have already been

explored for Pd-mediated CTP are highlighted and used as inspiration to identify precatalysts from the small-molecule literature that we believe should be explored in future polymerizations.

2.2 Mechanism

In CTP, propagation proceeds through a M(0)/M(II) catalytic cycle, including transmetalation, reductive elimination, and oxidative addition (Scheme 2.1). The biggest difference between CTP and step-growth polymerizations is ring-walking,[18,19] wherein the catalyst remains associated with a single polymer via a metal–polymer π-bound intermediate that migrates to the C–X terminus. Intramolecular oxidative addition at the C–X bond primes the catalyst for subsequent monomer transmetalation. The cycle continues until all monomers have been added to the polymer chain. Ring-walking enables each catalyst to enchain monomers along a single polymer; therefore, polymers with targeted molecular weights, sequences, and narrow dispersities can be obtained. For propagation to proceed without unproductive pathways (e.g., chain-transfer[27] and/or termination), the catalyst and monomer identities must be matched sterically and electronically to promote stable, yet reactive, π-complexes which can efficiently ring-walk for many turnovers.

Scheme 2.1 CTP mechanism.

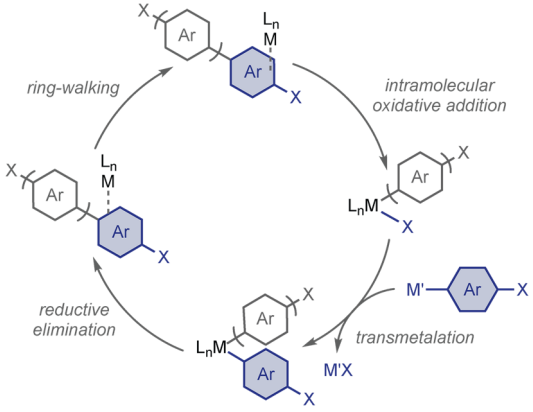

2.3 Why CTP for Organic Electronics?

CTP is advantageous for organic electronics because it enables polymers with specific molecular weights,[28] narrow dispersities, and precise sequences to be synthesized reproducibly.[7] Each of these properties can significantly impact performance, but the degree to which each parameter affects different devices is less well understood. In the past, conjugated polymers had been predominantly used in organic light-emitting diodes (OLEDs),[29,30] organic photovoltaics (OPVs),[24,25,31] and organic field-effect transistors (OFETs).[32–34] More recently, research efforts are focused on using conjugated polymers for energy storage applications such as supercapacitors,[35–38] and batteries[20,39–41] (Chart 2.1). The highest-performing conjugated polymers in these applications are almost exclusively synthesized via step-growth methods. These methods suffer from batch-to-batch variability[42] and the researcher has little control over the polymer molecular weight, dispersity, and sequence. As these variables can have an enormous impact in organic electronic applications, efforts should focus on identifying optimal polymer properties for each device.

It is well established that increasing polymer molecular weight correlates with improved organic electronic device performance, especially for OFETs and OPVs.[23,43,44] McGeehee and coworkers showed that increasing the number-average molecular weight of regioregular poly(3-hexylthiophene)'s by 10 times increased charge mobility in OFETs by 10,000 times.[45] Similar trends have been observed for high-performing donor–acceptor polymers in OPVs.[23] The effect of molecular weight in energy storage applications is less well studied.[21] The reduced solubility of high molecular weight polymer electrodes limits their dissolution, consequently improving its cycling stability.[46] To synthesize these and related high-performing polymers under current step-growth methods, long reaction times,[47] precise monomer stoichiometry,[48] and polymer

purification[49] are required. In contrast, simply altering the initial catalyst-to-monomer ratio with CTP would enable high molecular weight polymers to be targeted and obtained.

Chart 2.1 High-performing polymers synthesized via step-growth polymerization methods.[20,24,25,31,37]

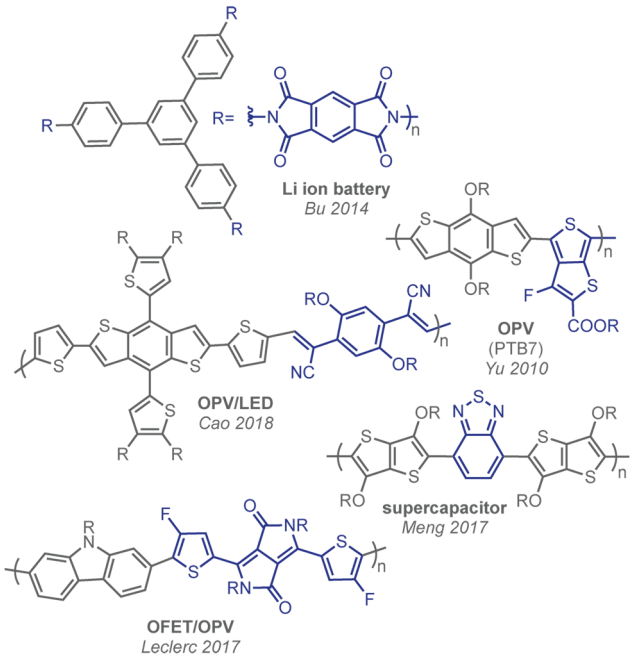

Similarly, it is challenging to target precise dispersities using step-growth methods, and therefore difficult to parse its influence on device performance. However, recent examples have shown that a broad dispersity correlates to decreased device performance. Yu and coworkers found that doubling polymer dispersity decreased device efficiency by 65% in PTB7-based OPVs (c.f., Chart 2.1).[50] They proposed that undesired homocoupled oligomers, containing donor–donor or acceptor–acceptor couplings, act as charge-trapping sites and facilitate charge recombination. The identities of these homocoupled defects were confirmed by analyzing low-performing batches using matrix assisted laser desorption-ionization time of flight mass spectrometry (MALDI-TOF-MS).[51] These homocoupled oligomer defects are challenging to remove from product mixtures even with time- and labor-intensive purifications. Identifying an optimal CTP catalyst for synthesizing donor–acceptor polymers would reduce these oligomeric contaminants and instead

yield predominantly high molecular weight polymers. In addition, by initiating with a precatalyst containing an aryl reactive ligand (e.g., $L_nM(X)(Ar)$), one can eliminate homocoupled defects altogether.[52]

Hawker and coworkers evaluated the effect of dispersity on emission by meticulously purifying thiophene oligomers to obtain monodisperse samples.[53] To evaluate dispersity effects, emission spectra from pure (Đ = 1.0) and blended (Đ =1.1–1.4) samples with the same effective molecular weight were compared. The blended samples exhibited red-shifted emission, suggesting that using conjugated polymers with even moderate dispersities could result in OLEDs with reduced color precision compared to the monodisperse samples. Combined, these select examples suggest that dispersity is directly related to organic electronic device performance. With CTP, narrow dispersities can be achieved without arduous purifications. As researchers begin to expand CTP to more complex scaffolds, it will be fascinating to see the full effect of dispersity on device performance.

Polymer sequence dramatically influences charge mobility, active layer morphology, and device longevity.[54–56] However, because non-alternating sequences are challenging to target with step-growth methods, there have been limited examples evaluating the effect of sequence (e.g., random, block, gradient) in high-performing devices.[51] Currently, OPVs are susceptible to performance decreases over time due to phase separation.[57] We used CTP to synthesize thiophene-based block, random, and gradient sequence copolymers as stabilizing additives in OPVs.[58,59] Adding 2 wt% copolymer to a poly(3-hexylthiophene):fullerene (P3HT:$PC_{61}BM$) blend suppressed phase separation by varying degrees depending on copolymer sequence. The random sequence copolymer was the best additive, improving initial device power conversion efficiency (PCE) by 29% and maintaining 75% of initial device performance after annealing for 90 min.[58]

Here, we found that sequence had a profound effect on the stability of OPVs, even for an additive only present in 2 wt% of the overall blend.

Overall, these examples stress that there should be a collective effort towards identifying CTP catalysts to synthesize the latest and best conjugated polymers in organic electronics. Then, both monomer structures and polymer sequences could be simultaneously and systematically tuned to enhance performance and longevity for specific devices.

2.4 Why Palladium?

Although CTP has many advantages, it has been largely limited to polymerizing monocyclic, electron-rich monomers.[4,5] In contrast, polymer scaffolds for organic-electronics are continually advancing, now encompassing polymers with fused-arene repeat units, electron-rich ("donor") and -deficient ("acceptor") moieties, and various functional groups (e.g., F, CN) (e.g., Chart 2.1). As such, until the monomer scope of CTP expands to include monomers with diverse functional groups and electronic properties, these complex copolymers with targeted sequences will be out of reach. It is therefore essential to identify CTP catalysts for each monomer's specific structural demands (e.g., functional groups, fused arenes, disparate electronic properties, extended π-systems) and that stay associated with the growing polymer chain.

Palladium precatalysts are promising candidates to expand CTP's monomer scope because they are ubiquitous in the small-molecule literature for coupling an array of electronically and sterically diverse substrates.[60–64] Contrasting this precatalyst library with that of CTP[5] raises the question, why have so few of these precatalysts been evaluated for polymerizing conjugated monomers? Most high-performing donor–acceptor polymers are synthesized in a step-growth manner from two difunctionalized monomers (e.g., a dihalide and a distannane) using tetrakis(triphenyl)phosphine palladium ($Pd(PPh_3)_4$).[65,66] Similar to the infancy of palladium-

catalyzed small-molecule cross-coupling,[67,68] $Pd(PPh_3)_4$ is the workhorse precatalyst for conjugated polymers and is often used despite forming undesired (e.g., homocoupled) byproducts. In Pd-catalyzed small-molecule cross-coupling, however, significant developments in catalyst design have now enabled electron-deficient and -rich substrates with unprotected functional groups to be synthesized with few side products.[60–62] While hundreds of ancillary ligands have been screened and optimized for these small-molecule cross-coupling reactions, comparatively few have been explored for synthesizing conjugated polymers, leaving a vast range of potential Pd-precatalysts for CTP (Chart 2.2)[18,19,28–127] These ligands have been specifically optimized for Pd and, as such, will likely be more successful on Pd than on Ni for CTP.[128] Herein, we highlight select examples of catalysts used in small-molecule cross-couplings as inspiration for expanding CTP.

Chart 2.2 The limited scope of ancillary ligands used in Pd-CTP since 2008. Each ligand was counted once per publication even if it was only an attempted polymerization.

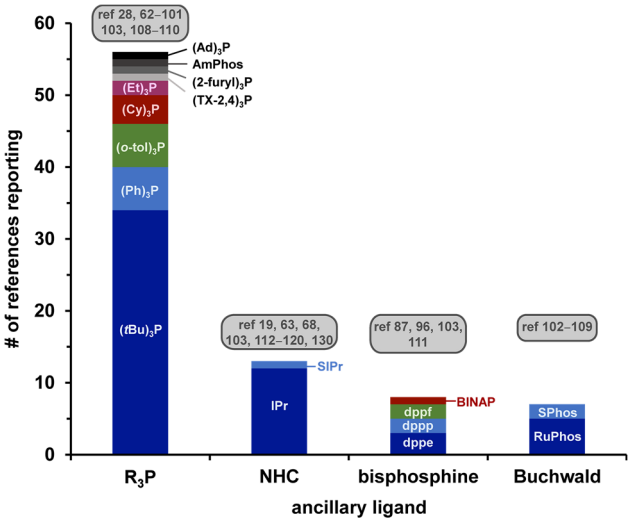

In addition to the many potential CTP precatalysts, Pd is advantageous because it has been reported to have lower ring-walking barriers than commonly used Ni catalysts.[19] This lower barrier to ring-walking could be favorable for polymerizing high-performing monomers, where the catalyst will be required to ring-walk over multiple π-bonds without dissociating, which remains

a significant challenge. We recently developed a simple method to evaluate ring-walking over polymers and found that both Ni and Pd precatalysts demonstrated efficient ring-walking over electron-rich polymers.[18] Compared to the analogous Ni precatalysts, however, Pd precatalysts were less likely to undergo unproductive pathways (i.e., ancillary ligand-based reductive elimination) at high monomer conversions when polymerizing thiophene. Additional computational evaluation by Yokozawa and coworkers indicated that Pd(IPr)(3-Clpyr)Cl_2 has lower ring-walking barriers than Ni(dppp)Cl_2, Pd(dppp)Cl_2, or Ni(IPr)PPh_3Cl_2.[19] Combined with the small-molecule precedent for coupling electron-deficient and functionalized arenes, these ring-walking mechanistic studies all suggest that Pd precatalysts should be capable of ring-walking over and polymerizing fused-arene repeat units, especially when catalyst stability is a determining factor.

Reports directly comparing Pd and Ni are rare. In cases where the comparison has been made, Pd typically outperforms Ni. In one example, Kiriy and coworkers screened various commercial Ni and Pd precatalysts for polymerizing a fused-arene monomer, fluorene.[76] The phosphine-ligated Ni precatalyst (Ni(dppp)Cl_2) undergoes unproductive reactions, whereas the phosphine-ligated Pd precatalyst (tBu_3PPdX_2) proceeded through a chain-growth pathway. Yokozawa and coworkers also found that Pd outperforms Ni when synthesizing poly(*p*-phenylene vinylene) (PPV). They hypothesized that the Ni became 'trapped' on the C=C bond in a π-complex that was too stable.[71,73] Similarly, Koeckelberghs and coworkers showed that a tBu_3P-ligated Pd precatalyst could polymerize thieno[3,2-*b*]thiophene where Ni precatalysts with a variety of ancillary ligands (e.g., dppp, dppe, depe, IPr) failed.[75] This failed polymerization was attributed to Ni trapping via a strong π-complex with the thienothiophene dimer formed in the initial reductive

elimination. These examples highlight how Pd precatalysts are particularly advantageous for polymerizing repeat units that bind too strongly with Ni precatalysts.

Many complex polymers for organic electronics contain coordinating atoms such as N and O (c.f., Chart 2.1), which are rarely present in monomers currently polymerized by CTP.[94,129–135] Previous efforts to polymerize N-containing monomers via CTP led to deleterious chain-transfer events.[27,94] Palladium has reduced oxophilicity relative to Ni which should reduce both its affinity to N and O and could therefore promote CTP. As such, we anticipate that palladium precatalysts will be useful for polymerizing monomers with coordinating atoms.

Below, we highlight recent examples of Pd-catalyzed CTP and use small-molecule cross-coupling examples as inspiration for future CTP catalyst testing. It is our hope that this Perspective will encourage polymer chemists to evaluate these precatalysts for CTP of complex monomer scaffolds, and at the same time, encourage the small-molecule catalysis community to attempt polymerizations when developing new precatalysts.

2.5 Identifying New Catalysts

We and others have used small-molecule cross-coupling as inspiration for identifying new CTP precatalysts.[117–,127] Specifically, we view difunctionalization of polyhalogenated substrates as indicative of potential CTP precatalysts. For example, in 2012 we were inspired by a report by Goldup and Larrosa showing that Pd(IPr)(3-Clpyr)Cl_2 sequentially couples two PhMgBr to various dihalogenated arenes.[136] Because PhMgBr was the limiting reagent, these results suggested that the catalyst couples the arenes via ring-walking *without dissociating*. Had dissociation occurred, mono-functionalized starting material would have been observed. By expanding these difunctionalization studies to the analogous polymerization, we found that the same precatalyst polymerizes both thiophene and phenylene monomers in a living, chain-growth manner.[127]

Difunctionalization reactions can be misleading, however, if excess organometallic coupling partner is used or if a reactivity bias preferentially generates difunctionalized products (Scheme 2.2).[137] In both cases, difunctionalized products can form even if the catalyst does not proceed through a metal–arene π-bound intermediate. When screening catalysts to polymerize a phenylene ethynylene monomer we used a small-molecule difunctionalization model system. Although one precatalyst formed di- to mono-functionalized products in a 98:2 ratio, the resulting polymerization proceeded in a step-growth manner.[137] Here, dissociated catalysts preferentially reacted with the mono-functionalized intermediate because it was more reactive than the initial dihalogenated arene.

To help ensure difunctionalized products are formed through catalyst association, ring-walking and *intra*molecular oxidative addition, a few precautionary steps should be taken. First, using substoichiometric organometallic coupling partner can reduce the number of false positives. However, reactivity differences can still lead to difunctionalized products.[137] In addition, we recommend adding a M(0) scavenger to stop dissociated catalysts from further reacting.[18] These protocols should facilitate identifying potential CTP precatalysts through small molecule difunctionalization reactions.

Scheme 2.2 Identifying potential CTP precatalysts using small-molecule difunctionalization reactions.

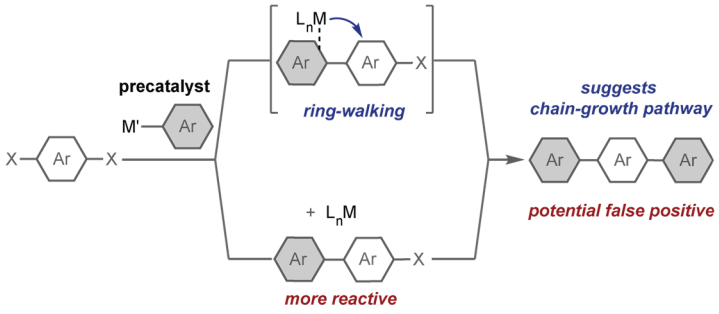

2.6 The Most Popular Pd-CTP Precatalyst

Most Pd-CTP examples use tBu_3P as the ancillary ligand for Suzuki polymerizations.[5,6] The reactive ligands in tBu_3P-ligated Pd precatalysts can be easily modified, providing an accessible handle for post-polymerization modification, or tuning the polymer's electronic properties.[28,84,86] Nevertheless, tBu_3P-ligated Pd suffers from inconsistent initiation[28,84,86,88,91,102] and turnover stability during propagation.[78] Unproductive pathways become especially detrimental if copolymer syntheses are attempted because inactive chains lead to oligomeric and/or homopolymer impurities, which are difficult to separate from the product mixture.[138] To circumvent these shortcomings, recent research efforts have been directed towards identifying alternative ancillary ligand scaffolds.

Tris(1-adamantyl)phosphine (Ad_3P) was identified as a promising ancillary ligand for Pd-catalyzed Suzuki-CTP of fluorene- and phenylene-based monomers with a range of steric properties.[115] The Ad_3P ancillary ligand is sterically similar to tBu_3P but it is more Lewis basic.[139] This property could improve CTP relative to tBu_3P because increased electron-donation has been shown to stabilize the metal–polymer π-bound intermediate and promote productive CTP pathways.[13,14] Using an Ad_3P-Pd precatalyst, polymers with approximately theoretical molecular weights could be synthesized with narrow dispersities, suggesting that the polymerization proceeds via CTP.[115] Furthermore, polymers could be end-capped *in situ* to generate a single detectable set of end-groups, indicating the catalyst was still polymer-bound and stable at high monomer conversions. These initial results using Ad_3P-ligated Pd to polymerize a range of monomers indicate potential for synthesizing structurally diverse polymers. Nevertheless, alternative electronically diverse monomer scaffolds have yet to be explored with this precatalyst.

A small-molecule cross-coupling precedent also supports the potential that Ad_3P-ligated Pd precatalysts have for polymerizing diverse monomer scaffolds. Carrow and coworkers generated an air-tolerant Ad_3P-ligated precatalyst that was used to synthesize various fluorinated bi- and triaryls under mild, Suzuki conditions (Scheme 2.3).[140] Heteroarenes could be difunctionalized with fluorinated arenes in excellent yields (>95%). Although these difunctionalization experiments were done using excess $PinBC_6F_5$, these methods were expanded to various fluorinated substrates, which could translate to fluorinated monomers for CTP. Fluorine-functionalized monomers are important in organic electronics because the fluorine substituents lower the polymer's highest occupied molecular orbital (HOMO) level, which facilitates charge transfer. For example, Yan and coworkers developed a benzothiadiazole/thiophene polymer with fluorinated thiophenes for OPVs which resulted in an overall PCE of 10.8% (c.f., Scheme 2.3).[141]

Scheme 2.3 (top) Ad_3P-ligated Pd-catalyzed small-molecule difunctionalization reaction of benzothiadiazole and fluorinated arenes.[140] (bottom) High-performing polymer containing benzothiadiazole and fluorinated-thiophene units.[141]

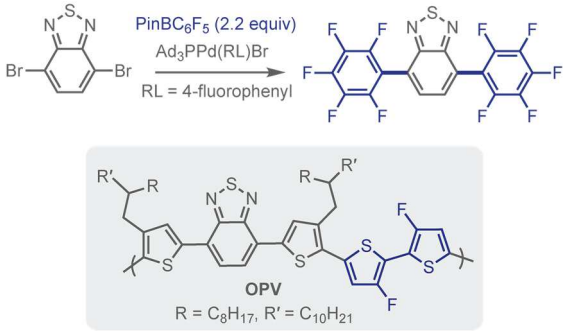

The Ad_3P ligand is one example of how modifying ancillary ligand electronic properties may significantly improve polymerization efficiency and potentially expand monomer scope. However, Ad_3P-ligated Pd is relatively nascent even for small-molecule cross-coupling.[139,140] In contrast, there have been decades of research on biarylphosphine (Buchwald ligands)[60] and N-heterocyclic carbenes (NHCs).[62] Many modifications to the original compounds have been made to optimize their small-molecule cross-coupling efficiency.[60,61] Nevertheless, these ancillary

ligands have scarcely been used in CTP. Based on preliminary CTP examples (discussed below), it is evident that these tunable ligands could be exactly what is needed to match catalyst/monomer pairings, promote catalyst association, and significantly advance CTP.

2.7 The Future: Buchwald Ligands

Dialkylbiarylphosphine ancillary ligands developed by Buchwald and co-workers are widely used for cross-coupling sterically hindered and/or electronically dissimilar molecules.[60] Buchwald ancillary ligand modularity has enabled them to be designed to meet the demands of various substrates, promoting highly efficient cross-coupling systems (Chart 2.3). We expect that Buchwald ancillary ligands could also promote CTP of electron-poor and complex monomers. The few examples using Buchwald-type ligands in CTP[109–114] should inspire both the small-molecule and polymer communities to start evaluating more of these ligands for CTP.

Chart 2.3 Select Buchwald precatalysts and ancillary ligands.[60,149,152]

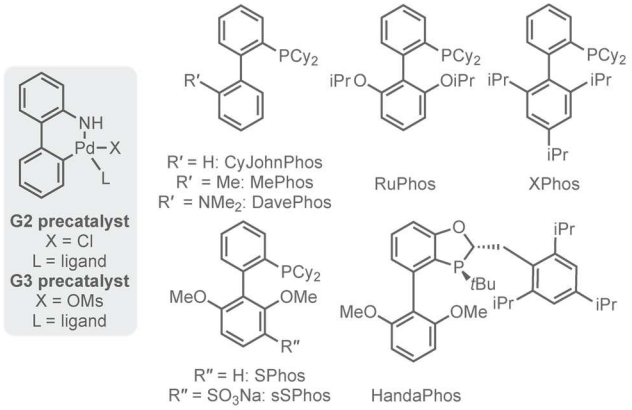

Recently, Choi and coworkers showed that both RuPhos and SPhos G3 Pd precatalysts outperformed XPhos- or tBu_3P-ligated Pd precatalysts when polymerizing BPin-thiophene monomers.[109] Mechanistic analysis revealed that when ligated to Pd, both RuPhos and SPhos mediated a living, chain-growth polymerization, affording polymers with consistently narrow dispersities (Đ = 1.08–1.45), and excellent end-group fidelity (>95%), indicating each catalyst

generates a single polymer and is stable throughout polymerization. In addition, an SPhos-ligated Pd precatalyst was also used to synthesize copolymers with a MIDA-boronate-based thiophene monomer. For Suzuki-CTP to occur using a protected boron-transmetalating agent (e.g., BPin or MIDA boronate), the protecting group must be hydrolyzed. The resulting boronic acid is then capable of transmetalating to the precatalyst. In small-molecule cross-coupling, there are examples of utilizing boron-transmetalating groups that hydrolyze at different rates to control the coupling order.[142] Similarly, Choi and coworkers used these rate differences to generate block copolymers in one pot (i.e., without sequential monomer addition). Here, adding SPhos-ligated Pd to a solution of MIDA boronate-thiophene and BPin-thiophene resulted in block copolymers because BPin-thiophene hydrolyzes faster and is polymerized first (Scheme 2.4). Then, the MIDA boronate-thiophene hydrolyzes and is added to the polymer chain. Although these examples are limited to thiophene monomers, they use relatively unexplored precatalysts and copolymerization methods. Future efforts should focus on exploring the versatility of these hydrolysis rate-dependent methods with Buchwald ligands and alternative monomer scaffolds.

Scheme 2.4 Generating block copolymers based on monomer reactivity differences using SPhos-ligated Pd.[109]

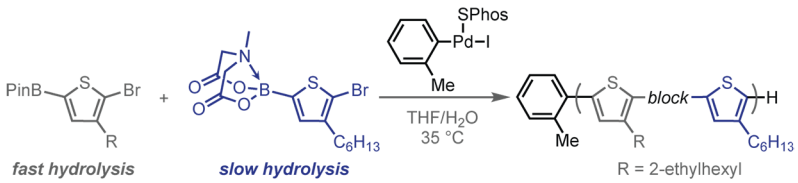

There are also several examples using Buchwald ancillary ligands in the postulated "preferential oxidative addition" chain-growth polymerizations.[110–114] Here, after reductive elimination the catalyst is believed to dissociate from the polymer but preferentially undergo oxidative addition back into a polymer's terminal C–X bond. The dissociated catalysts react with polymers rather than monomers because of either monomer deactivation or diffusion control. In

the monomer deactivation approach, the monomer's electron-rich metal-carbon bond decreases the reactivity of the neighboring C–Br bond towards oxidative addition with Pd. In contrast, the polymers no longer have a deactivating Zn–C bond, and enable the catalyst to react more quickly with the C–Br bond. The monomer-deactivation approach has been used by Koeckelberghs and coworkers to synthesize homopolymers, diblock, and triblock copolymers consisting of various combinations of thiophene, selenophene, and fluorene via a RuPhos-ligated Pd catalyst.[111–114] In the diffusion control mechanism, immediately after dissociating, the Pd(0) species is closer to polymer than monomer and therefore preferentially reacts with and continues extending the polymer. Moore and coworkers used an SPhos-ligated Pd catalyst to polymerize an extended arene monomer via the diffusion method which yields a hyperbranched polymer (Scheme 2.5).[110] Similar branched, porous polymers are advantageous for Li-ion battery cathodes (Scheme 2.5).[20] In both the monomer deactivation and diffusion control examples, Buchwald ancillary ligands outperformed others (e.g., PPh_3, dppf, P(o-tolyl)$_3$, IPr) for promoting pseudo-chain growth behavior. If the catalyst does dissociate, Buchwald ligands are advantageous because they can stabilize the Pd(0) center before re-association and continue monomer enchainment on the active polymer chain.

Scheme 2.5 (top) Synthesizing extended arene polymers using Buchwald ancillary ligand SPhos.[110] (bottom) Example of an extended arene polymer in Li-ion batteries.[20]

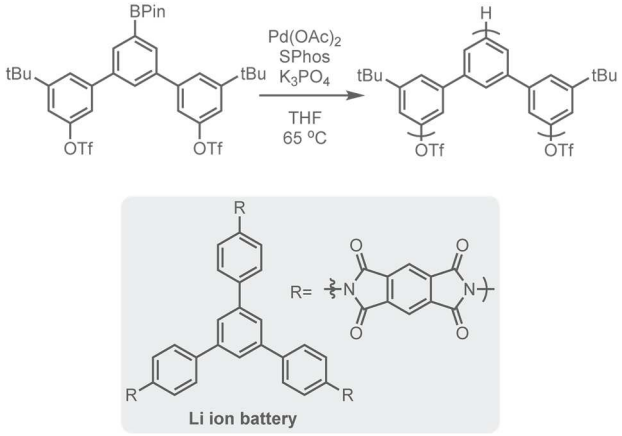

While these examples both expand the Pd-CTP ancillary ligand scope and generate interesting polymer sequences/architectures, they are still limited to polymerizing electron-rich monomers. To polymerize donor–acceptor monomers, it will be important to identify precatalysts capable of polymerizing electron deficient monomers. For this, we turn to the small-molecule literature for inspiration.

Electron deficient units are desirable for organic electronics but they are challenging to couple in both the polymer and small-molecule literature. Since most Pd-catalyzed CTPs are Suzuki-type polymerizations, we looked to the Suzuki coupling small-molecule literature for inspiration. A key challenge for Suzuki cross-coupling is that electron-deficient boronates are prone to protodeborylation.[143,144] Precatalysts that quickly couple electron-deficient boronates result in fewer undesired byproducts and, therefore, are promising candidates for improving CTP of electron-deficient monomers. In a select small-molecule example, Huber and Bulfield found that strong σ-donating Buchwald ancillary ligands with cyclohexyl substituents (c.f., see Chart 2.3) could enable Pd-catalyzed cross-coupling of perfluoroarene boronic acids in high yields with few undesired products.[144] This method could be extended to neopentyl glycol boronic esters and MIDA-boronates as well (Scheme 2.6). The more sterically demanding and slower-hydrolyzing boron nucleophiles required less sterically encumbered ancillary ligands (e.g., DavePhos, CyJohnPhos, and MePhos) to achieve high yields. Similarly, the less hindered ancillary ligands DavePhos and CyJohnPhos were optimal for coupling *ortho*- or *meta*-substituted substrates. These examples demonstrate how matching the ancillary ligand steric and electronic properties to the substrate resulted in successful cross-couplings for challenging substrates. These ancillary ligand trends should be considered when designing hydrolysis-rate dependent copolymerizations[109] and polymerizing fluorinated monomers, which feature prominently in high-performing OPVs and

OFETs. For example, adding fluorine to a carbazole/thieno[3,2-b]thiophene-diketopyrrolopyrrole-based monomer increased charge mobility in OFETs as well as PCE in OPVs by >2 times.[31] Combined with the increasing number of fluorinated high-performing materials, these cross-coupling examples suggest that Buchwald ligands could promote polymerizing fluorinated units via CTP.

Scheme 2.6 (top) Matching Buchwald ligands to fluoroarene, boronic acids.[144] (bottom) Example of a high-performing polymer with fluorine substituents.[31]

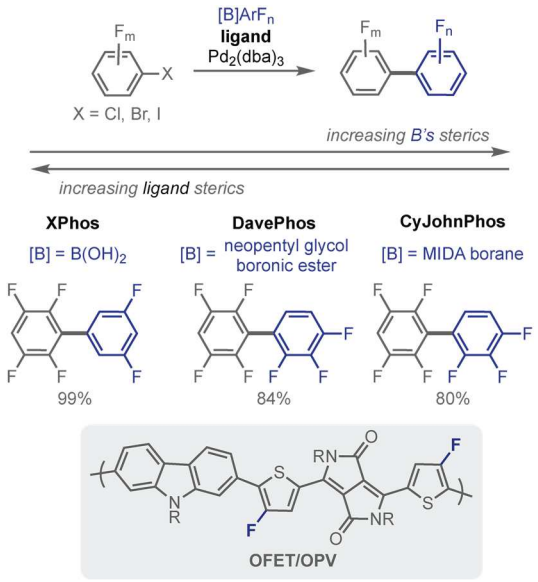

Polymers with nitrogen-containing repeat units are used in organic electronics (e.g., battery anodes[145]) but have been challenging to polymerize via CTP[129–134] because the standard Ni-based precatalysts are susceptible to chain-transfer.[27,94] In contrast, Buchwald-ligated Pd-precatalysts have been used extensively to couple nitrogen-containing small-molecules.[146] The sterically encumbering ancillary ligands SPhos and XPhos were both efficient at coupling pyridine, pyrazine, and indole moieties of varying electronic properties in good to excellent yields (Scheme 2.7).[146] The more sterically hindered XPhos ligand improved Negishi and Suzuki cross-coupling efficiency of N-containing heterocycles with electron-deficient (hetero)arenes.[146,147] Accordingly,

SPhos- and/or XPhos-ligated Pd provide potential routes to polymerize electronically diverse N-containing monomers via CTP.

For Suzuki cross-coupling reactions, water is typically added to facilitate transmetalation.[148] but can be disadvantageous for catalyst stability. Adding sulfonate groups to ligands improves catalyst solubility in aqueous solutions while maintaining catalyst stability. The sulfonated-SPhos (sSPhos)-ligated Pd-precatalyst efficiently coupled substrates containing various unprotected functional groups in excellent yields.[149] These small-molecule cross-coupling examples with sSPhos-ligated Pd suggests that monomers with reactive functional groups (e.g., OH) could be polymerized without protection in a living, chain-growth manner, eliminating the need for post-polymerization modifications.

Scheme 2.7 Identifying optimal Buchwald ligands for coupling arenes with coordinating atoms.[146,147,149] (bottom) Examples of polymers containing N and reactive functional groups.[150,151]

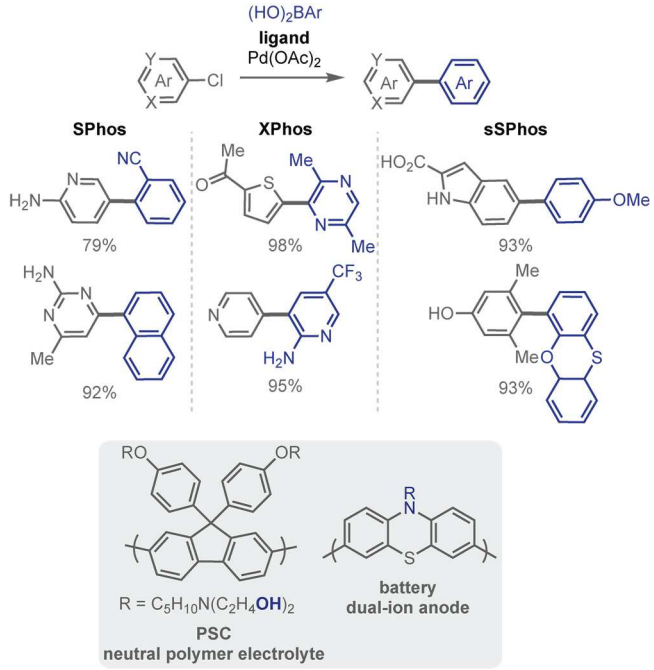

Sonogashira-[77,116,137]and Heck[74]-CTP examples are rare; however, alkynyl and alkenyl moieties are found in organic electronics. One challenge when polymerizing these functionalities is catalyst trapping at the triple or double bond. A mechanistic study conducted by Yokozawa and

coworkers suggested that Pd precatalysts were less likely to get trapped on these π-bonds than Ni precatalysts.[73] However, when applying tBu_3P-ligated Pd, disproportionation occurred. Using more sterically encumbering Buchwald ancillary ligands could destabilize these Pd-π interactions and facilitate ring-walking. Recently, a HandaPhos-ligated Pd precatalyst was used in di- and tri-functionalization reactions (Scheme 2.8).[152] Although excess alkynyl-coupling partner was used, these results suggest HandaPhos could be a good ancillary ligand for Sonogashira-CTP.

Overall, these select examples demonstrate the versatility and promise of Buchwald ancillary ligands for polymerizing electron-deficient and N-containing monomers as well as those with reactive functional groups, assuming the catalyst stays associated with growing polymer chains.

Scheme 2.8 HandaPhos-ligated Pd catalyzed difunctionalization reaction.[152] (bottom) Examples of conjugated polymers that could be accessed through Sonogashira-CTP.[153]

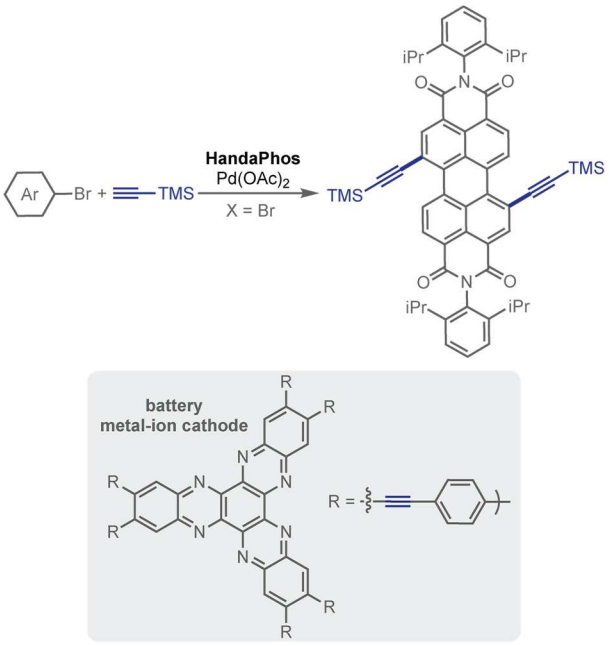

2.8 The Future: N-Heterocyclic Carbenes (NHCs)

N-heterocyclic carbenes are promising ancillary ligands for CTP because their tunable properties have enabled sterically hindered and electronically dissimilar small molecules to be coupled.[63,154] The steric and electronic properties of NHCs can be easily modified, which has resulted in a library of compounds with a range of Tolman electronic parameters and buried volumes (Chart 2.4).[155,156] In most cases, NHCs are more Lewis basic (electron-donating) than phosphines,[157] which based on previous mechanistic insight,[13,14] suggests that NHCs should be good ancillary ligands for CTP. There are even fewer NHC than Buchwald ligand examples that exist in the CTP literature. We believe that this area is ripe for further exploration.

Currently, the only NHC ancillary ligands used in Pd-CTP are IPr and SIPr. [18,19,70,75,110,119–127] The unsaturated analogue, IPr, promotes CTP of various simple monomer scaffolds with a range of transmetalating agents (e.g., magnesium, boron, and tin). Additionally, $AuPtBu_3$- and ZnCl-based thiophene have been polymerized, but these systems deviate from living, chain-growth behavior at high monomer conversions.[126] As the field advances towards complex monomer scaffolds, this versatility in transmetalating-agent nucleophilicity will be advantageous for polymerizing monomers with electrophilic functional groups. In addition, IPr-ligated Pd precatalysts are often air-stable, which is an advantageous yet relatively unexplored property in the CTP field. The saturated analogue, SIPr, outperformed IPr in Murahashi-CTP of thiophene, however this catalyst system has not been explored further.[120]

Polymerizing alternative monomers with a more expansive range of electronic properties will likely require tuning the NHCs' electronic and steric properties. For example, altering σ-donating and π-accepting abilities of the ancillary ligand could dramatically impact the stability and reactivity of the metal–polymer π-complex. When studying ring-walking, we observed that

increasing electron density in the metal/ancillary ligand pair promoted ring-walking along higher molecular weight polymers.[18] Despite this data and other mechanistic insight,[13,14,17,19] the orbital-electronic demands for catalyst association during ring-walking and propagation remain relatively undefined.

Chart 2.4 NHC-ligated Pd precatalysts.[154,158,168,169]

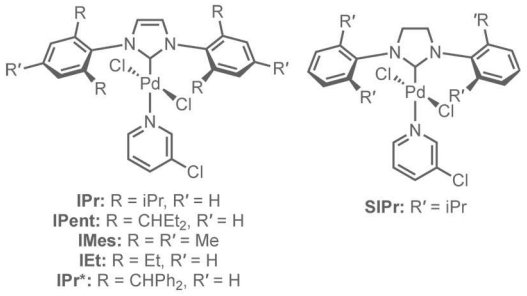

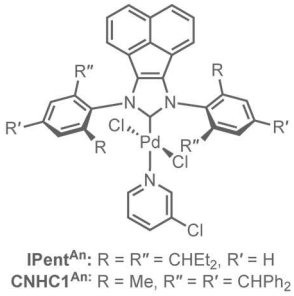

Designing precatalysts for CTP based on their π-accepting ability alone is unexplored, but ligands with these properties have already been synthesized. For example, Cavello and coworkers have deconstructed the effects of both π-accepting and σ-donating properties for many NHCs (Chart 2.5).[158] Alternatively, replacing one N with a quaternary carbon yields cyclic (alkyl)(amino)carbene (CAACs) which have both increased σ-donating and π-accepting properties relative to most NHC ancillary ligands, both of which could be advantageous for ring-walking (Chart 2.6).[159] Replacing the alkyl substituent in CAACs with an aryl group yields cyclic (aryl)(amino)carbene (CAArCs), which demonstrate similar electronic but different steric properties relative to CAACs.[160] Combined, both CAACs and CAArCs provide a range of ancillary

ligand parameters for both small-molecule cross-coupling and CTP that have yet to be explored by either community (Chart 2.6).

Chart 2.5 Examples of NHCs with varied electronic properties.[158]

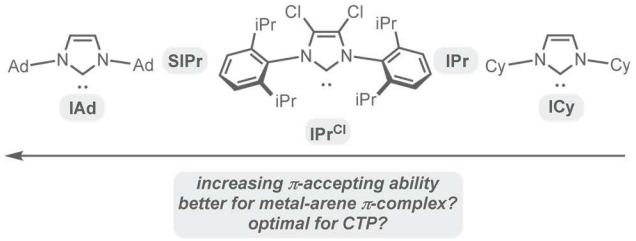

Fully conjugated block copolymers have been underutilized in organic electronics in part because they are inaccessible through step-growth methods. In addition, block copolymer synthesis via CTP has been mostly limited to electronically similar monomers. However, the IPr-ligated Pd precatalyst (Pd(IPr)(3-Clpyr)Cl_2) has shown promise for copolymerizing electronically diverse monomers. For example, block copolymers of thiophene and phenylene have been synthesized using this precatalyst,[127] a process for which bisphosphine-Ni precatalysts fail.[161] The ability of IPr-ligated Pd to transition between monomers with different electronic properties suggests it could stay associated to and polymerize donor–acceptor monomers or gradient sequence copolymers via CTP.

Chart 2.6 Select examples of CAACs[159] and CAArCs.[160]

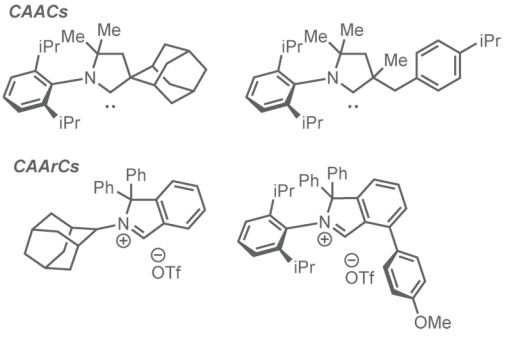

In light of these promising initial results with two NHC ancillary ligands, we have identified alternative NHC scaffolds with potential for CTP. For example, Goldup and Larrosa

have demonstrated that in addition to IPr-ligated Pd, increasing the steric encumbrance around Pd using IPent results in a precatalyst optimal for difunctionalizing a range of substrates with substoichiometric PhMgBr, outperforming IPr, IMes, IEt, and IPr* (c.f., Chart 2.4 and Scheme 2.9).[162] One particularly promising example formed difunctionalized carbazole, a commonly used motif in high-performing polymers,[2,21,163] in 85% yield. These experiments suggest IPent-ligated Pd forms a stable π-bound intermediate and should be evaluated for CTP.

Scheme 2.9 (top) IPent-ligated Pd-catalyzed difunctionalization reaction.[162] (bottom) Examples of structurally diverse polymers containing carbazole for high performing organic electronics.[163,164]

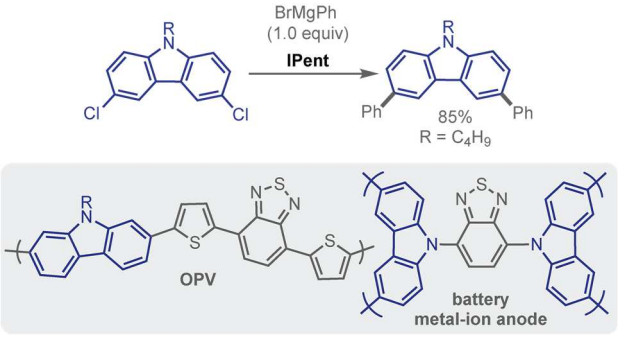

When selecting an ancillary ligand, it is critical to identify steric properties that will match each monomer's demands. The IPr-ligated Pd precatalyst has precedent for polymerizing both 3HT regioisomers[18] which suggests that NHC ancillary ligands could polymerize monomers with bulky side-chains. Side-chains are used to solubilize high molecular weight polymers and influence solid-state packing.[2,165–167] Furthermore, adding functional groups (e.g., thiophenes,[22] esters,[24] and/or cyanides[25]) to side-chains can improve device performance and/or stability. In some cases, electron-deficient monomers are less soluble than analogous electron-rich monomers and therefore require sterically encumbering, branched side chains.[27] Here, we highlight a potential precatalyst that has demonstrated efficient coupling of sterically hindered arenes. Liu and coworkers recently reported an NHC-ligated precatalyst (IPent^{An}) that demonstrated similar steric properties but increased electron-donating ability relative to IPr.[168] Although no

difunctionalization reactions were reported, IPent^{An} coupled various heteroaromatic and sterically encumbered substrates in high yields. When coupling two, bis-*ortho*-substituted substrates, IPent^{An} generated the desired product in 92% yield whereas using IPr or IPent ancillary ligands resulted in considerably less efficient systems (0% and 50% yield, respectively), suggesting that increased electron-donation could facilitate sterically encumbered couplings. Further increasing the NHC's steric properties yields CNHC1^{An} (c.f., Chart 2.4), which affords difunctionalized heteroaromatic compounds in excellent yields via Suzuki cross-coupling, albeit using excess boron-coupling partners (Scheme 2.10).[169] Combined, these results suggest that increasing the steric encumbrance around Pd could facilitate CTP of more hindered and even N-containing monomers. This progression in NHC ligand design also demonstrates how modest adjustments to the ancillary ligand framework can significantly influence reaction outcomes. Overall, the wide-ranging design capability for NHC ligands make them promising candidates for future Pd-CTP precatalysts.

Scheme 2.10 (top) Examples of bulky yet flexible NHCs for cross-coupling N-containing and sterically hindered substrates.[168,169] (bottom) Example of a conjugated polymer containing sterically encumbered side-chains.[170]

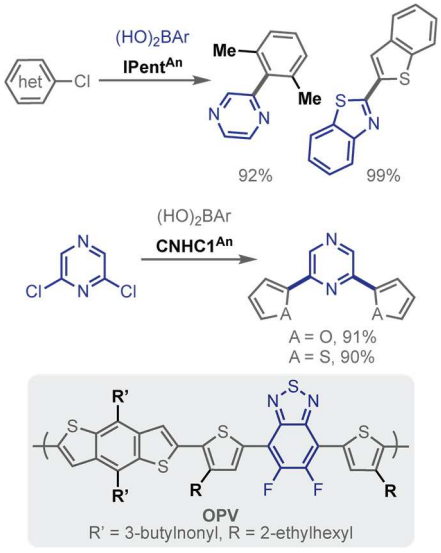

2.9 Reflection

This Perspective was borne out of frustration. Fourteen years after the initial discovery, CTP is still extraordinarily limited in its scope.[7] All the mechanistic insight gained during this time has not translated efficiently into better catalysts. We wrote this call-to-action with the hope that it will inspire others to work on these challenges with us. Why not just do it ourselves? The reality is that synthesizing the more complex monomers for evaluating a potential precatalyst is challenging and time-consuming. For example, to synthesize a donor–acceptor monomer, each unit needs to first be desymmetrized (to prevent oligomerization or polymerization) and then coupled (Scheme 2.11). Then, another desymmetrization needs to take place so that a reactive C–X bond and a transmetalating agent can be installed on opposing ends. The cartoon version seems simple, but the challenges lie in both over- or under-functionalization, and its resulting impact on the subsequent polymerization.

Scheme 2.11 Generic depiction of routes to an AB-functionalized donor/acceptor monomer and potential starting reagents.

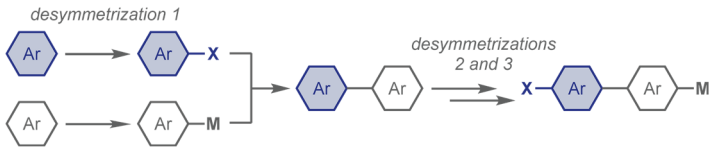

The vast and impressive work in ligand design and evaluation performed by the small-molecule cross-coupling community serves as inspiration for the future of CTP. Here, we presented ways to find these catalysts and we matched specific Pd-precatalysts with high-performing monomers. Great strides will be necessary to develop these polymerizations, which may not always extrapolate perfectly from the small-molecule examples due to the additional requirement of catalyst association. We encourage the catalysis field, small-molecule and polymer chemists alike, to help us develop the next generation of CTP precatalysts. The impact of this

collective effort will be enormous. Polymer macrostructure impacts device performance, with molecular weight, dispersity, and sequence each playing a significant role. Developing living, chain-growth methods for accessing these materials should enable polymers to be optimized for each device. Someday we imagine commercial, conjugated polymer-based devices that help meet the world's growing energy demands.

2.10 References

[1] Holliday, S.; Li, Y.; Luscombe, C. K. Recent Advances in High Performance Donor-Acceptor Polymers for Organic Photovoltaics. *Prog. Polym. Sci.* **2017**, *70*, 34–51.

[2] Lu, L.; Zheng, T.; Wu, Q.; Schneider, A. M.; Zhao, D.; Yu, L. Recent Advances in Bulk Heterojunction Polymer Solar Cells. *Chem. Rev.* **2015**, *115*, 12666–12731.

[3] Bryan, Z. J.; McNeil, A. J. Conjugated Polymer Synthesis via Catalyst-Transfer Polycondensation (CTP): Mechanism, Scope, and Applications. *Macromolecules* **2013**, *46*, 8395−8405.

[4] Yokozawa, T.; Ohta, Y. Transformation of Step-Growth Polymerization into Living Chain-Growth Polymerization. *Chem. Rev.* **2016**, *116*, 1950−1968.

[5] Leone, A. K.; McNeil, A. J. Matchmaking in Catalyst-Transfer Polycondensation: Optimizing Catalysts based on Mechanistic Insight. *Acc. Chem. Res.* **2016**, *49*, 2822−2831.

[6] Baker, M. A.; Tsai, C.-H.; Noonan, K. J. T. Diversifying Cross-Coupling Strategies, Catalysts and Monomers for the Controlled Synthesis of Conjugated Polymers. *Chem. Eur. J.* **2018**, *24*, 13708–13088.

[7] Lutz, J. P.; Hannigan, M. D.; McNeil, A. J. Polymers Synthesized via Catalyst-Transfer Polymerization and Their Applications. *Coord. Chem. Rev.* **2018**, *376*, 225–247.

[8] Yamamoto, T.; Hayashi, Y.; Yamamoto, A. A Novel Type of Polycondensation Utilizing Transition Metal-Catalyzed C–C Coupling. I. Preparation of Thermostable Polyphenylene Type Polymers. *Bull. Chem. Soc. Jpn.* **1978**, *51*, 2091–2097.

[9] Sheina, E. E.; Liu, J.; Iovu, M. C.; Laird, D. W.; McCullough, R. D. Chain Growth Mechanism for Regioregular Nickel-Initiated Cross-Coupling Polymerizations. *Macromolecules* **2004**, *37*, 3526−3528.

[10] Yokoyama, A.; Miyakoshi, R.; Yokozawa, T. Chain-Growth Polymerization for Poly(3-hexylthiophene) with a Defined Molecular Weight and a Low Polydispersity. *Macromolecules* **2004**, *37*, 1169−1171.

[11] Kobayashi, M.; Chen, J.; Chung, T.-C.; Moraes, F.; Heeger, A. J.; Wudl, F. Synthesis and Properties of Chemically Coupled Poly(thiophene). *Synth. Met.* **1984**, *9*, 77–86.

[12] McCullough, R. D.; Lowe, R. D. Enhanced Electrical Conductivity in Regioselectively Synthesized Poly(3-alkylthiophenes). *J. Chem. Soc., Chem. Commun.* **1992**, *0*, 70–72.

[13] Lee, S. R.; Bryan, Z. J.; Wagner, A. M.; McNeil, A. J. Effect of Ligand Electronic Properties on Precatalyst Initiation and Propagation in Ni-Catalyzed Cross-Coupling Polymerizations. *Chem. Sci.* **2012**, *3*, 1562−1566.

[14] Bryan, Z. J.; McNeil, A. J. Evidence for a Preferential Intramolecular Oxidative Addition in Ni-Catalyzed Cross-Coupling Reactions and their Impact on Chain-Growth Polymerizations. *Chem. Sci*. **2013**, *4*, 1620−1624.

[15] Leone, A. K.; Souther, K. D.; Vitek, A. K.; LaPointe, A. M.; Coates, G. W.; Zimmerman, P. M.; McNeil, A. J. Mechanistic Insight into Thiophene Catalyst-Transfer Polymerization Mediated by Nickel Diimine Catalysts. *Macromolecules* **2017**, *50*, 9121−9127.

[16] Hall, A. O.; Lee, S. R.; Bootsma, A. N.; Bloom, J. W. G.; Wheeler, S. E.; McNeil, A. J. Reactive Ligand Influence on Initiation in Phenylene Catalyst-Transfer Polymerization. *J. Polym. Sci., Part A: Polym. Chem*. **2017**, *55*, 1530−1535.

[17] Lanni, E. L.; McNeil, A. J. Mechanistic Studies on Ni(dppe)Cl_2-Catalyzed Chain-Growth Polymerizations: Evidence for Rate-Determining Reductive Elimination. *J. Am. Chem. Soc.* **2009**, *131*, 16573− 16579.

[18] Leone, A. K.; Goldberg, P. K.; McNeil, A. J. Ring-Walking in Catalyst-Transfer Polymerization. *J. Am. Chem. Soc*. **2018**, *140*, 7846–7850.

[19] Mikami, K.; Nojima, M.; Masumoto, Y.; Mizukoshi, Y.; Takita, R.; Yokozawa, T.; Uchiyama, M. Catalyst-Dependent Intrinsic Ring-Walking Behavior on π-face of Conjugated Polymers. *Polym. Chem*. **2017**, *8*, 1708−1713.

[20] Tian, D.; Zhang, H.-Z.; Zhang, D.-S.; Chang, Z.; Han, J. Gao, X-P.; Bu, X.-H Li-Ion Storage and Gas Adsorption Properties of Porous Polyimides (PIs). *RSC Adv*., **2014**, *4*, 7506–7510.

[21] Schon, T. B.; McAllister, B. T.; Li P.-F..; Seferos, D. S. The Rise of Organic Electrode Materials for Energy Storage. *Chem. Soc. Rev*. **2016**, *45*, 6345–6404.

[22] Li, S.; Ye, L.; Zhao, W.; Yan, H.; Yang, B.; Liu, D.; Li, W.; Ade, H.; Hou. J. A Wide Band Gap Polymer with a Deep Highest Occupied Molecular Orbital Level Enables 14.2% Efficiency in Polymer Solar Cells *J. Am. Chem. Soc.* **2018**, *140*, 7159–7167.

[23] Bartelt, J. A.; Douglas, J. D.; Mateker, W. R.; El Labban, A.; Tassone, C. J.; Toney, M. F.; Fréchet, J. M. J.; Beaujuge, P. M.; McGehee, M. D. Controlling Solution-Phase Polymer Aggregation with Molecular Weight and Solvent Additives to Optimize Polymer-Fullerene Bulk Heterojunction Solar Cells. *Adv. Mater*. **2014**, *4*, 1301733.

[24] Liang, Y.; Xu, Z.; Xia, J.; Tsai, S.-T.; Wu, Y.; Li, G.; Ray, C.; Yu, L. For the Bright Future—Bulk Heterojunction Polymer Solar Cells with Power Conversion Efficiency of 7.4%. *Adv. Mater*. **2010**, *22*, E135–E138

[25] Cao, C.; Xiao, M.; Yang, X.; Zhang, J.; Huang F.; Cao, Y. Cyanovinylene-Based Copolymers by Tin-free Knoevenagel Polycondensation for High Efficiency Polymer Solar Cells. *J. Mater. Chem. C*. **2018***, 6*, 8020–8027.

[26] Grimsdale, A. C.; Chan, K. L.; Martin, R. E.; Jokisz, P. G.; Holmes, A. B. Synthesis of Light-Emitting Conjugated Polymers for Applications in Electroluminescent Devices. *Chem. Rev*. **2009**, *109*, 897−1091.

[27] Smith, M. L.; Leone, A. K.; Zimmerman, P. M.; McNeil, A. J. Impact of Preferential π-Binding in Catalyst-Transfer Polycondensation of Thiazole Derivatives. *ACS Macro Lett*. **2016**, *5*, 1411−1415.

[28] Zhang, H.-H.; Peng, W.; Dong, J.; Hu, Q.-S. *t*-Bu_3P-Coordinated 2-Phenylaniline-Based Palladacycle Complex/ArBr as Robust Initiators for Controlled Pd(0)/*t*-Bu_3P-Catalyzed Suzuki Cross-Coupling Polymerization of AB-Type Monomers. *ACS Macro Lett.* **2016**, *5*, 656−660.

[29] Vandana, T.; Kannan, P. Blue and Green Light Emitting Polyarylpyrazolines Luminogens Containing Anthracene and Thiophene Units. *J. Photochem. Photobiol. A.* **2018**, *359*, 64–72.

[30] Hellerich, E. S.; Intemann, J. J.; Cai, M.; Liu, R.; Ewan, M. D.; Tlach, B. C.; Jeffries-EL, M.; Shinar, R.; Shinar, J. Fluorescent Polymer Guest:Small Molecule Host Solution-Processed OLEDs. *J. Mater. Chem. C*. **2013**, *1*, 5191–5199.

[31] Bura, T.; Beaupré, S.; Ibraikulov, O. A.; Légaré, M.-A.; Quinn, J.; Lévêque, P.; Heiser, T.; Li, Y.; Leclerc, N.; Leclerc, M. New Fluorinated Dithienyldiketopyrrolopyrrole Monomers and Polymers for Organic Electronics. *Macromolecules* **2017**, *50*, 7080–7090.

[32] Sirringhaus, H. 25th Anniversary Article: Organic Field-Effect Transistors: The Path Beyond Amorphous Silicon. *Adv. Mater.* **2014**, *26*, 1319–1335.

[33] Ma, J.; Liu, Z.; Yao, J.; Wang, Z.; Zhang, G.; Zhang, X.; Zhang, D. Improving Ambipolar Semiconducting Properties of Thiazole-Flanked Diketopyrrolopyrrole-Based Terpolymers by Incorporating Urea Groups in the Side-Chains. *Macromolecules* **2018**, *51*, 6003–6010.

[34] Kim, Y.; Hwang, H.; Kim, N.-K.; Hwang, K.; Park, J.-J.; Shin, G.-I.; Kim, D.-Y. π-Conjugated Polymers Incorporating a Novel Planar Quinoid Building Block with Extended Delocalization and High Charge Carrier Mobility. *Adv. Mater*. **2018**, *30*, 1706557.

[35] DiCarmine, P. M.; Schon, T. B.; McCormick, T. M.; Klein, P. P.; Seferos, D. S. Donor–Acceptor Polymers for Electrochemical Supercapacitors: Synthesis, Testing, and Theory. *J. Chem. Phys. C.* **2014**, *118*, 8295–8307.

[36] Ju, X.; Kong, L.; Zhao, J.; Bai, G. Synthesis and Electrochemical Capacitive Performance of Thieno[3,4–*b*] Pyrazine-Based Donor–Acceptor Type Copolymers Used as Supercapacitor Electrode Material. *Electrochim. Acta* **2017**, *238*, 36–48.

[37] Guo, Y.; Li, W.; Yu, H.; Perepichka, D.; Meng, H. Flexible Asymmetric Supercapacitors via Spray Coating of a New Electrochromic Donor–Acceptor Polymer. *Adv. Energy Mater.* **2017**, *7*, 1601623.

[38] Estrada, L. A.; Liu, D. Y.; Salazar, D. H.; Dyer, A. L.; Reynolds, J. R. Poly[Bis-EDOT-Isoindigo]: An Electroactive Polymer Applied to Electrochemical Supercapacitors. *Macromolecules* **2012**, *45*, 8211–8220.

[39] Wu, J.; Rui, X.; Wang, C.; Pei, W.-B.; Lau, R.; Yan, Q.; Zhang, Q. Nanostructured Conjugated Ladder Polymers for Stable and Fast Lithium Storage Anodes with High-Capacity. *Adv. Energy Mater.* **2015**, *5*, 1402189.

[40] Kim, Y. J.; Wu, W.; Chun, S.-E.; Whitacre, J. F.; Bettinger, C. J. Catechol-Mediated Reversible Binding of Multivalent Cations in Eumelanin Half-Cells. *Adv. Mater*. **2014**, *26*, 6572–6579.

[41] Peterson, B. M.; Ren, D.; Shen, L.; Wu, Y.-C. M.; Ulgut, B.; Coates, G. W.; Abruña, H. D.; Fors, B. P. Phenothiazine-Based Polymer Cathode Materials with Ultrahigh Power Densities for Lithium Ion Batteries. *ACS App. Energy Mater.* **2018**, *1*, 3560–3564.

[42] Lee, S. M.; Park, K. H.; Jung, S.; Park, H.; Yang, C. Stepwise Heating in Stille Polycondensation Toward No Batch-To-Batch Variations in Polymer Solar Cell Performance. *Nat. Commun.* **2018**, *9*, 1867.

[43] Kline, R. J.; McGehee, M. D.; Kadnikova, E. N.; Liu, J. Fréchet, J. M. J.; Toney, M. F. Dependence of Regioregular Poly(3-hexylthiophene) Film Morphology and Field-Effect Mobility on Molecular Weight. *Macromolecules* **2005**, *38*, 3312–3319.

[44] Katsouras, A.; Gasparini, N.; Koulogiannis, C.; Spanos, M.; Ameri, T.; Brabec, C. J.; Chochos, C. L.; Avgeropoulos, A. Systematic Analysis of Polymer Molecular Weight Influence on the Organic Photovoltaic Performance. *Macromol. Rapid Commun.* **2015**, *36*, 1778–1797.

[45] Kline, R. S.; McGehee, M. D.; Kadnikova, E. N.; Liu, J.; Fréchet, J. M. J. Controlling the Field-Effect Mobility of Regioregular Polythiophene by Changing the Molecular Weight. *Adv. Mater.* **2003**, *15*, 1519–1522.

[46] Song, Z.; Qian, Y.; Gordin, M. L.; Tang, D.; Xu, T.; Otani, M.; Zhan, H.; Zhou, H.; Wang, D. Polyanthraquinone as a Reliable Organic Electrode for Stable and Fast Lithium Storage. *Angew. Chem. Int. Ed.* **2015**, *54*, 13947–13951.

[47] Ma, P.; Wen, S.; Wang, C.; Guo, W.; Shen, L.; Dong, W.; Lu, J.; Ruan, S. Optimization of PDTS-DTffBT-Based Solar Cell Performance through Control of Polymer Molecular Weight. *J. Phys. Chem. C*, **2016**, *120*, 19513–19520.

[48] Li, W.; Yang, L.; Tumbleston, J. R.; Yan, L.; Ade, H.; You, W. Controlling Molecular Weight of a High Efficiency Donor–Acceptor Conjugated Polymer and Understanding Its Significant Impact on Photovoltaic Properties. *Adv. Mater*. **2014**, *26*, 4456–4462.

[49] Meager, I.; Shahid Ashraf, R.; Nielsen, C. B.; Donaghey, J. E.; Huang, Z.; Bronstein, H.; Durrant, J. R.; McCulloch, I. Power Conversion Efficiency Enhancement in Diketopyrrolopyrrole Based Solar Cells Through Polymer Fractionation. *J. Mater. Chem. C*, **2014**, *2*, 8593–8598.

[50] Lu, L.; Zheng, T.; Xu, T.; Zhao, D.; Yu, L. Mechanistic Studies of Effect of Dispersity on the Photovoltaic Performance of PTB7 Polymer Solar Cells. *Chem. Mater*. **2015**, *27*, 537–543.

[51] Vangerven, T.; Verstappen, P.; Drijkoningen, J.; Dierckx, W.; Himmelberger, S.; Salleo, A.; Vanderzande, D.; Maes, W.; Manca, J. V. Molar Mass versus Polymer Solar Cell Performance: Highlighting the Role of Homocouplings. *Chem. Mater*. **2015**, *27*, 3726−3732.

[52] Bronstein, H. A.; Luscombe, C. K. Externally Initiated Regioregular P3HT with Controlled Molecular Weight and Narrow Polydispersity. *J. Am. Chem. Soc.* **2009**, *131*, 12894–12895.

[53] Lawrence, J.; Goto, E.; Ren, J. M.; McDearmon, B.; Kim, D. S.; Ochiai, Y.; Clark, P. G.; Laitar, D.; Higashihara, T.; Hawker, C. J. A Versatile and Efficient Strategy to Discrete Conjugated Oligomers. *J. Am. Chem. Soc.* **2017**, *139*, 13735–13739.

[54] Kipp, D.; Verduzco, R.; Ganesan, V. Block Copolymer Compatibilizers for Ternary Blend Polymer Bulk Heterojunction Solar Cells–an Opportunity for Computation Aided Molecular Design. *Mol. Syst. Des. Eng.* **2016**, *1*, 353–369.

[55] Yuan, K.; Chen, L.; Chen, Y. Nanostructuring Compatibilizers of Block Copolymers for Organic Photovoltaics. *Polym. Int.* **2014**, *63*, 593–606.

[56] Cheng, P.; Zhan, X. Versatile Third Components for Efficient and Stable Organic Solar Cells. *Mater. Horiz.* **2015**, *2*, 462–485.

[57] Rafique, S.; Abdullah, S. M.; Sulaiman, K.; Iwamoto, M. Fundamentals of Bulk Heterojunction Organic Solar Cells: An Overview of Stability/Degradation Issues and Strategies for Improvement. *Renew. Sust. Energy Rev.* **2018**, *84*, 43–53.

[58] Kong, C.; Song, B.; Mueller, E. A.; Kim, J.; McNeil, A. J. *Submitted*.

[59] Palermo, E. F.; Darling, S. B.; McNeil, A. J. π-Conjugated Gradient Copolymers Suppress Phase Separation and Improve Stability in Bulk Heterojunction Solar Cells. *J. Mater. Chem. C.* **2014**, *2*, 3401–3406.

[60] Martin, R.; Buchwald, S. L. Palladium-Catalyzed Suzuki−Miyaura Cross-Coupling Reactions Employing Dialkylbiaryl Phosphine Ligands. *Acc. Chem. Res*. **2008**, *41*, 1461–1473.

[61] Phan, N. T. S.; Van Der Sluys, M.; Jones, C. W. On the Nature of the Active Species in Palladium Catalyzed Mizoroki–Heck and Suzuki–Miyaura Couplings – Homogeneous or Heterogeneous Catalysis, A Critical Review. *Adv. Synth. Catal*. **2006**, *348*, 609–679.

[62] Nasielski, J.; Hadei, N.; Achonduh, G.; Assen, E.; Kantchev, E. A. B.; O'Brien, C. J.; Lough, A.; Organ, M. G.; Structure–Activity Relationship Analysis of Pd–PEPPSI Complexes in Cross-Couplings: A Close Inspection of the Catalytic Cycle and the Precatalyst Activation Model. *Chem. Eur. J.* **2010**, *16*, 10844–10853.

[63] Marion, N.; Nolan, S. P. Well-Defined N-Heterocyclic Carbenes-Palladium(II) Precatalysts for Cross-Coupling Reactions. *Acc. Chem. Res.* **2008**, *41*, 1440–1449.

[64] Fu, G. C. The Development of Versatile Methods for Palladium-Catalyzed Coupling Reactions of Aryl Electrophiles through the Use of P(*t*-Bu)$_3$ and PCy$_3$ as Ligands. *Acc. Chem. Res.* **2008**, *41*, 1555–1564.

[65] Zhao, W.; Li, S.; Yao, H.; Zhang, S.; Zhang, Y.; Yang, B.; Hou, J. Molecular Optimization Enables over 13% Efficiency in Organic Solar Cells. *J. Am. Chem. Soc.* **2017**, *139*, 7148–7151.

[66] Yamashita, Y.; Hinkel, F.; Marszalek, T.; Zajaczkowski, W.; Pisula, W.; Baumgarten, M.; Matsui, H.; Müllen, K.; Takeya, J. Mobility Exceeding 10 cm^2/(V·s) in Donor–Acceptor Polymer Transistors with Band-like Charge Transport. *Chem. Mater.*, **2016**, *28*, 420–424.

[67] Suzuki, A. Cross-Coupling Reactions of Organoboranes: An Easy Way to Construct C–C Bonds (Nobel Lecture). *Angew. Chem. Int. Ed*. **2011**, *50*, 6723–6737.

[68] Miyaura, N.; Suzuki, A. Palladium-Catalyzed Cross-Coupling Reactions of Organoboron Compounds. *Chem. Rev.,* **1995***, 95*, 2457–2483.

[69] Terayama, K.; Goto, E.; Higashihara, T. Nonstoichiometric Stille Coupling Polycondensation via an Intramolecular Pd(0) Catalyst Transfer Using Excess Phthalimide Monomer. *Macromol. Chem. Phys.* **2018**, *219*, 1800175.

[70] Zhang, H.-H.; Zhu, Y.-X.; Wang, W.; Zhu, J.; Bonnesen, P. V.; Hong, K. Controlled Synthesis of *Ortho*, *Para*-Alternating Linked Polyarenes *via* Catalyst-Transfer Suzuki Coupling Polymerization. *Polym. Chem.* **2018**, *9*, 3342–3346.

[71] Nojima, M.; Kamigawara, T.; Ohta, Y.; Yokozawa, T. Catalyst-Transfer Suzuki–Miyaura Condensation Polymerization of Stilbene Monomer: Different Polymerization Behavior Depending on Halide and Aryl Group of ArPd(*t*Bu$_3$P)X Initiator. *J. Polym. Sci. A. Polym. Chem.* **2018,** DOI: 10.1002/pola.29169.

[72] Kang, S.; Todd, A. D.; Paul, A.; Lee, S. Y.; Bielawski, C. W. Controlled Syntheses of Poly(phenylene ethynylene)s with Regiochemically-Tuned Optical Band Gaps and Ordered Morphologies. *Macromolecules* **2018**, *51*, 5972–5978.

[73] Nojima, M.; Ohta, Y.; Yokozawa, Y. Investigation of Catalyst-Transfer Condensation Polymerization for Synthesis of Poly(*p*-phenylenevinylene). *J. Polym. Sci. Part A. Polym. Chem.* **2014**, *52*, 2643–2653.

[74] Nojima, M.; Saito, R.; Ohta, Y.; Yokozawa, T. Investigation of Mizoroki-Heck Coupling Polymerization as Catalyst-Transfer Condensation Polymerization for Synthesis of Poly(*p*-phenylenevinylene). *J. Polym. Sci. A. Polym. Chem.* **2015**, *53*, 543–551.

[75] Willot, P.; Koeckelberghs, G. Evidence for Catalyst Association in the Catalyst Transfer Polymerization of Thieno[3,2-*b*]thiophene. *Macromolecules* **2014**, *47*, 8548−8555.

[76] Tkachov, R.; Senkovskyy, V.; Beryozkina, T.; Boyko, K.; Bakulev, V.; Lederer, A.; Sahre, K.; Voit, B.; Kiriy, A. Palladium-Catalyzed Chain-Growth Polycondensation of AB-type Monomers: High Catalyst Turnover and Polymerization Rates. *Angew. Chem. Int. Ed.* **2014**, *53*, 2402–2407.

[77] Kang, S.; Ono, R. J.; Bielawski, C. W. Controlled Catalyst Transfer Polycondensation and Surface-Initiated Polymerization of *p*-Phenyleneethynylene-Based Monomer. *J. Am. Chem. Soc*. **2013**, *135*, 4984–4987.

[78] Verswyvel, M.; Hoebers, C.; De Winter, J.; Gerbaux, P.; Koeckelberghs, G. Study of the Controlled Chain-Growth Polymerization of Poly(3,6-phenanthrene). *J. Polym. Sci. A. Polym. Chem.* **2013**, *51*, 5067 −5074.

[79] Kamigawara, T.; Sugita, H.; Mikami, K.; Ohta, Y.; Yokozawa, T. Intramolecular Transfer of Pd Catalyst on Carbon–Carbon Triple Bond and Nitrogen–Nitrogen Double Bond in Suzuki–Miyaura Coupling Reaction. *Catalysts* **2017**, *7*, 195.

[80] Grisorio, R.; Suranna, G. P. Impact of Precatalyst Activation on Suzuki-Miyaura Catalyst-Transfer Polymerizations: New Mechanistic Scenarios for Pre-transmetalation Events. *ACS Macro Lett.* **2017**, *6*, 1251–1256.

[81] Nojima, M.; Ohta, Y.; Yokozawa, T. Additive-controlled Switching from Abnormal to Normal Unstoichiometric Suzuki–Miyaura Polycondensation for Poly(biphenylenevinylene). *Chem. Lett.* **2017**, *46*, 35–37.

[82] Tokita, Y.; Katoh, M.; Ohta, Y.; Yokozawa, T. Mechanistic Investigation of Catalyst-Transfer Suzuki–Miyaura Condensation Polymerization of Thiophene–Pyridine Biaryl Monomers with the Aid of Model Reactions. *Chem. Eur. J*. **2016**, *22*, 17436–17444.

[83] Nojima, M.; Kosaka, K.; Kato, M.; Ohta, Y.; Yokozawa, T. Alternating Intramolecular and Intermoleular Catalyst-Transfer Suzuki–Miyaura Condensation Polymerization: Synthesis of Boronate-Terminated π-Conjugated Polymers Using Excess Dibromo Monomers. *Macromol. Rapid Commun*. **2016**, *37*, 79−85.

[84] Zhang, H.-H.; Hu, Q.-S.; Hong, K. Accessing Conjugated Polymers with Precisely Controlled Heterobisfunctional Chain Ends *via* Post-Polymerization Modification of the OTf Group and Controlled Pd(0)/*t*-Bu_3P-Catalyzed Suzuki Cross-Coupling Polymerization. *Chem. Commun.* **2015**, *51*, 14869–14872.

[85] He, L.-Y.; Urrego-Riveros, S.; Gates, P. J.; Näther, C.; Brinkmann, M.; Abetz, V.; Staubitz, A. Synthesis of poly(thiophene-*alt*-pyrrole) from a Difunctionalized Thienylpyrrole by Kumada Polycondensation. *Tetrahedron* **2015**, *71*, 5399–5406.

[86] Zhang, H.-H.; Xing, C.-H.; Hu, Q.-S.; Hong, K. Controlled Pd(0)/*t*-Bu_3P-Catalyzed Suzuki Cross-Coupling Polymerization of AB-Type Monomers with ArPd(*t*-Bu_3P)X or $Pd_2(dba)_3$/*t*-Bu_3P/ArX as the Initiator. *Macromolecules* **2015**, *48*, 967–978.

[87] Nojima, M.; Ohta, Y.; Tokozawa, T. Structural Requirements for Palladium Catalyst Transfer on a Carbon–Carbon Double Bond. *J. Am. Chem. Soc.* **2015**, *137*, 5682–5685.

[88] Grisorio, R.; Mastrorilli, P.; Suranna, G. P. A $Pd(AcO)_2$/*t*-Bu_3P/K_3PO_4 Catalytic System for the Control of Suzuki Cross-Coupling Polymerization. *Polym. Chem*. **2014**, *5*, 4304–4310.

[89] Kosaka, K.; Ohta, Y.; Yokozawa, T. Influence of the Boron Moiety and Water on Suzuki–Miyaura Catalyst-Transfer Condensation Polymerization. *Macromol. Rapid Commun*. **2015**, *36*, 373−377.

[90] Tkachov, R.; Komber, H.; Rauch, S.; Lederer, A.; Oertel, U.; Häußler, L.; Voit, B.; Kiriy, A. One-Pot Synthesis of All-Conjugated Block-Like Bisthiophene–Naphthalenediimide/Fluorene Copolymer. *Macromolecules* **2014**, *47*, 4994–5001.

[91] Zhang, H.-H.; Xing, C.-H.; Hu, Q.-S. Controlled Pd(0)/*t*-Bu_3P-Catalyzed Suzuki Cross-Coupling Polymerization of AB-Type Monomers with PhPd(*t*-Bu_3P)I or $Pd_2(dba)_3$/*t*-Bu_3P/ArI as the Initiator. *J. Am. Chem. Soc.* **2012**, *134*, 13156–13159.

[92] Elmalem, E.; Biedermann, F.; Johnson, K.; Friend, R. H.; Huck, W. T. S. Synthesis and Photophysics of Fully π-Conjugated Heterobis-Functionalized Polymeric Molecular Wires via Suzuki Chain-Growth Polymerization. *J. Am. Chem. Soc.* **2012**, *134*, 17769–17777.

[93] Huddleston, N. E.; Sontag, S. K.; Bilbrey, J. A.; Sheppard, G. R,; Locklin, J. Palladium-Mediated Surface-Initiated Kumada Catalyst Polycondensation: A Facile Route Towards Oriented Conjugated Polymers. *Macromol. Rapid Commun*. **2012**, *33*, 2115−2120.

[94] Nanashima, Y.; Shibata, R.; Miyakoshi, R.; Yokoyama, A,; Yokozawa, T. Investigation of Catalyst-Transfer Condensation Polymerization for the Synthesis of *n*-Type π-Conjugated Polymer, Poly(2-dioxaalkylpyridine-3,6-diyl). *J. Polym. Sci., A: Polym. Chem.* **2012**, *50*, 3628–3640.

[95] Yokozawa, T.; Suzuki, R.; Nojima, M.; Ohta, Y.; Yokoyama, A. Precision Synthesis of Poly(3-hexylthiophene) from Catalyst-Transfer Suzuki–Miyaura Coupling Polymerization. *Macromol. Rapid Commun.* **2011**, *32*, 801–806.

[96] Elmalem, E.; Kiriy, A.; Huck, W. T. S. Chain-Growth Suzuki Polymerization of n-Type Fluorene Copolymers. *Macromolecules* **2011**, *44*, 9057–9061.

[97] Yokozawa, T.; Kohno, H.; Ohta, Y.; Yokoyama, A. Catalyst-Transfer Suzuki−Miyaura Coupling Polymerization for Precision Synthesis of Poly(*p*-phenylene). *Macromolecules* **2010**, *43*, 7095–7100.

[98] Huang, W.; Su, L.; Bo, Z. Hyperbranched Polymers with a Degree of Branching of 100% Prepared by Catalyst Transfer Suzuki−Miyaura Polycondensation. *J. Am. Chem. Soc*. **2009**, *131*, 10348–10349.

[99] Beryozkina, T.; Boyko, K.; Khanduyeva, N.; Senkovskyy, V.; Horecha, M.; Oertel, U.; Simon, F.; Stamm, M.; Kiriy, A. Grafting of Polyfluorene by Surface-Initiated Suzuki Polycondensation. *Angew. Chem. Int. Ed*. **2009**, *48*, 2695–2698.

[100] Yokoyama, A.; Suzuki, H.; Kubota, Y.; Ohuchi, K.; Higashimura, H.; Yokozawa, T. Chain-Growth Polymerization for the Synthesis of Polyfluorene via Suzuki–Miyaura Coupling Reaction from an Externally Added Initiator Unit. *J. Am. Chem. Soc.* **2007**, *129*, 7236–7237.

[101] Michinori, S.; Hiroyoshi, N.; Masahiro, M. Synthesis and Helical Structure of Oligo(quinoline-2,3-diyl)s. *Chem. Lett.* **2007**, *36*, 1036−1037.

[102] Zhang, S.; Zhang, Z.; Fu. H.; Li, X.; Zhan, H.; Cheng, Y. Synthesis of Polyfluorene Containing Simple Functional End Group with Aryl Palladium(II) Complexes as Initiators. *J. Organometal. Chem*. **2016**, *825–826*, 100–113.

[103] Mao, Y.; Wang, Y.; Lucht, B. L. Regiocontrolled Synthesis of Poly(3-alkylthiophene)s by Grignard Metathesis. *J. Polym. Sci., A: Polym. Chem* **2004**, *42*, 5538–5547.

[104] Zhang, Z.; Hu, P.; Li, X.; Zhan, H.; Cheng, Y. Investigation of Suzuki–Miyaura Catalyst-Transfer Polycondensation of AB-type Fluorene Monomer Using Coordination-Saturated Aryl Pd(II) Halide Complexes as Initiators. *J. Polym. Sci., Part A: Polym. Chem*. **2015**, *53*, 1457–1463.

[105] Goto, E.; Ando, S.; Ueda, M.; Higashihara, T. Nonstoichiometric Stille Coupling Polycondensation for Synthesizing Naphthalene-Diimide-Based π-Conjugated Polymers. *ACS Macro Lett.* **2015**, *4*,1004–1007.

[106] Grisorio, R.; Suranna G. P.; Mastrorilli P. Chain-Growth Versus Step-Growth Mechanisms for the Suzuki–Heck Polymerisation of Fluorenyldibromides with Potassium Vinyl Trifluoroborate. *Chem. Euro. J*. **2010**, *16*, 8054–8061.

[107] Sun, H.; Zhang, S.; Yang, Y.; Li, X.; Zhan, H.; Cheng, Y. Excellent Control of Perylene Diimide End Group in Polyfluorene via Suzuki Catalyst Transfer Polymerization. *Macromol. Chem. Phys.* **2016**, *217*, 2726–2735.

[108] Fu, H.; Li, J.; Zhang, Z.; Zhan, H.; Li, X.; Cheng, Y. Synthesis of Novel Polyfluorene with Defined Group in the Center Using Aryl Dipalladium Complex as an Initiator. *J. Organomet. Chem.* **2013**, *738*, 55–58.

[109] Seo, K.-B.; Lee, I.-H.; Lee, J.; Choi, I.; Choi, T.-L. A Rational Design of Highly Controlled Suzuki–Miyaura Catalyst-Transfer Polycondensation for Precision Synthesis of Polythiophenes and their Block Copolymers: Marriage of Palladacycle Precatalysts with MIDA-boronates. *J. Am. Chem. Soc.* **2018**, *140*, 4335−4343.

[110] Xue, Z.; Finke, A. D.; Moore, J. S. Synthesis of Hyperbranched Poly(*m*-phenylene)s via Suzuki Polycondensation of a Branched AB_2 Monomer. *Macromolecules* **2010**, *43*, 9277–9282

[111] Verswyvel, M.; Verstappen, P.; De Cremer, L.; Verbiest, T.; Koeckelberghs, G. Development of a Universal Chain-Growth Polymerization Protocol of Conjugated Polymers: Toward a Variety of All-Conjugated Block-Copolymers. *J. Polym. Sci., A: Polym. Chem.* **2011**, *49*, 5339–5349.

[112] Willot,P.; Steverlynck, J.; Moerman, D.; Leclère, P.; Lazzaroni, R.; Koeckelberghs, G. Poly(3-alkylthiophene) with Tuneable Regioregularity: Synthesis and Self-Assembling Properties. *Polym. Chem*. **2013**, *4*, 2662–2671.

[113] Verswyvel, M.; Steverlynck, J.; Mohamed, S. H.; Trabelsi, M.; Champagne, B.; Koeckelberghs, G. All-Conjugated ABC-*block*-copolymer Formation with a Varying Sequence via an Unassociated Catalyst. *Macromolecules* **2014**, *47*, 4668–4675.

[114] Hardeman, T.; Koeckelberghs, G. The Synthesis of Poly(thiophene-*co*-fluorene) Gradient Copolymers. *Macromolecules* **2015**, *48*, 6987–6993

[115]Dong, J.; Guo, H.; Hu, Q.-S. Controlled Pd(0)/Ad_3P-Catalyzed Suzuki Cross-Coupling Polymerization of AB-Type Monomers with Ad_3P-Coordinated Acetanilide-Based Palladacycle Complex as Initiator. *ACS Macro Lett.* **2017**, *6*, 1301–1304.

[116] Su, M.; Liu, N.; Wang, Q.; Wang, H.; Yin, J.; Wu, Z.-Q. Facile Synthesis of Poly(phenyleneethynylene)-*block*-Polyisocyanide Copolymers via Two Mechanistically Distinct, Sequential Living Polymerizations Using a Single Catalyst. *Macromolecules* **2016**, *49*, 110–119.

[117] Kosaka, K.; Uchida, T.; Mikami, K.; Ohta, Y.; Yokozawa, T. AmPhos Pd-Catalyzed Suzuki–Miyaura Catalyst-Transfer Condensation Polymerization: Narrower Dispersity by Mixing the Catalyst and Base Prior to Polymerization *Macromolecules* **2018**, *51*, 364−369.

[118] Bhatt, M. P.; Magurudeniya, H. D.; Sista, P.; Sheina, E. E.; Jeffries-EL, M.; Janesko, B. G.; Mccullough, R. D.; Stefan, M. C Role of the Transition Metal in Grignard Metathesis Polymerization (GRIM) of 3-Hexylthiophene. *J. Mater. Chem. A*. **2013**, *1*, 12841–12849.

[119] Fuji, K.; Tamba, S.; Shono, K.; Sugie, A.; Mori, A. Murahashi Coupling Polymerization: Nickel(II)−N-Heterocyclic Carbene Complex-Catalyzed Polycondensation of Organolithium Species of (Hetero)arenes. *J. Am. Chem. Soc.* **2013***, 135,* 12208–12211.

[120] Shono, K.; Sumino, Y.; Tanaka, S.; Tamba, S.; Mori, A. Polythiophene Synthesis *via* Halogen Dance. *Org. Chem. Front*., **2014**, *1*, 678–682.

[121] Sui, A.; Shi, X.; Tian, H.; Geng, Y.; Wang, F. Suzuki−Miyaura Catalyst-Transfer Polycondensation with Pd(IPr)$(OAc)_2$ as the Catalyst for the Controlled Synthesis of Polyfluorenes and Polythiophenes. *Polym. Chem*. **2014**, *5*, 7072−7080.

[122] Qiu, Y.; Mohin, J.; Tsai, C.-H.; Tristram-Nagle, S.; Gil, R. R.; Kowalewski, T.; Noonan, K. J. T. Stille Catalyst-Transfer Polycondensation Using Pd-PEPPSI-IPr for High-Molecular-Weight Regioregular Poly(3-hexylthiophene). *Macromol. Rapid Commun*. **2015**, *36*, 840−844.

[123] Zhang, H-H.; Ma, C.; Bonnesen, P. V.; Zhu, J.; Sumpter, B. G.; Carrillo, J-M. Y.; Yin, P.; Wang, Y.; Li, A-P.; Hong, K. Helical Poly(5-alkyl-2,3-thiophene)s: Controlled Synthesis and Structure Characterization. *Macromolecules*, **2016**, *49*, 4691–4698.

[124] Suraru, S.-L.; Lee, J. A.; Luscombe, C. K. Preparation of an Aurylated Alkylthiophene Monomer via C −H Activation for Use in Pd-PEPPSI-iPr Catalyzed-Controlled Chain Growth Polymerization. *ACS Macro Lett*. **2016**, *5*, 533−536.

[125] Qiu, Y.; Worch, J. C.; Fortney, A.; Gayathri, C.; Gil, R. R.; Noonan, K. J. T. Nickel-Catalyzed Suzuki Polycondensation for Controlled Synthesis of Ester-Functionalized Conjugated Polymers. *Macromolecules* **2016**, *49*, 4757−4762.

[126] Hardeman, T.; Koeckelberghs, G.; Synthesis of Conjugated Copolymers by Combining Different Coupling Reactions. *Polym. Chem*., **2017**, *8*, 3999–4004.

[127] Bryan, Z. J.; Smith, M. L.; McNeil, A. J. Chain-Growth Polymerization of Aryl Grignards Initiated by A Stabilized NHC-Pd Precatalyst. *Macromol. Rapid Commun*. **2012**, *33*, 842−847.

[128] Wu, K.; Doyle, A. G. Parameterization of Phosphine Ligands Demonstrates Enhancement of Nickel Catalysis via Remote Steric Effects.. *Nat. Chem.* **2017**, *9*, 779–784.

[129] Pammer, F.; Passlack, U. Head-to-Tail Regioregular Polythiazole Prepared via Kumada-Coupling Polycondensation. *ACS Macro Lett*. **2014**, *3*, 170−174.

[130] Senkovskyy, V.; Tkachov, R.; Komber, H.; John, A.; Sommer, J.-U.; Kiriy, A. Mechanistic Insight into Catalyst-Transfer Polymerization of Unusual Anion-Radical Naphthalene Diimide Monomers: An Observation of Ni(0) Intermediates. *Macromolecules* **2012**, *45*, 7770−7777.

[131] Nanashima, Y.; Yokoyama, A.; Yokozawa, T. Synthesis of Novel Blue-Light-Emitting Polypyridine. *J. Polym. Sci., Part A: Polym. Chem.* **2012**, *50*, 1054−1061.

[132] Senkovskyy, V.; Tkachov, R.; Komber, H.; Sommer, M.; Heuken, M.; Voit, B.; Huck, W. T. S.; Kataev, V.; Petr, A.; Kiriy, A. Chain-Growth Polymerization of Unusual Anion-Radical Monomers Based on Naphthalene Diimide: A New Route to Well-Defined n-Type Conjugated Copolymers. *J. Am. Chem. Soc.* **2011**, *133*, 19966−19970.

[133] Wen, L.; Duck, B. C.; Dastoor, P. C.; Rasmussen, S. C. Poly(2,3-dihexylthieno[3,4-*b*]pyrazine) via GRIM Polymerization: Simple Preparation of a Solution Processable, Low-Band-Gap Conjugated Polymer. *Macromolecules* **2008**, *41*, 4576−4578.

[134] Pammer, F.; Jäger, J.; Rudolf, B.; Sun, Y. Soluble Head-to-Tail Regioregular Polythiazoles: Preparation, Properties, and Evidence for Chain-Growth Behavior in the Synthesis via Kumada-Coupling Polycondensation. *Macromolecules* **2014**, *47*, 5904−5912.

[135] Nanashima, Y.; Yokoyama, A.; Yokozawa, T. Synthesis of Well-Defined Poly(2-alkoxypyridine-3,5-diyl) via Ni-Catalyst-Transfer Condensation Polymerization. *Macromolecules* **2012**, *45*, 2609−2613.

[136] Larrosa, I.; Somoza, C.; Banquy, A.; Goldup, S. M. Two Flavors of PEPPSI-IPr: Activation and Diffusion Control in a Single NHC Ligated Pd Catalyst? *Org. Lett.* **2011**, *13*, 146−149

[137] Bryan, Z. J.; Hall, A. O.; Zhao, C. T.; Chen, J.; McNeil, A. J. Limitations of Using Small Molecules to Identify Catalyst-Transfer Polycondensation Reactions. *ACS Macro Lett*. **2016**, *5*, 69 −72.

[138] Souther, K. D.; Leone, A. K.; Vitek, A. K.; Palermo, E. F.; LaPointe, A. M.; Coates, G. W.; Zimmerman, P. M.; McNeil, A. J. Trials and Tribulations of Designing Multitasking Catalysts for Olefin/Thiophene Block Copolymerizations. *J. Polym. Sci., A: Polym. Chem*. **2018**, *56*, 132–137.

[139] Chen, L.; Ren, P.; Carrow, B. P.; Tri(1-adamantyl)phosphine: Expanding the Boundary of Electron Releasing Character Available to Organophosphorus Compounds. *J. Am. Chem. Soc*. **2016**, *138*, 6392–6395.

[140] Chen, L.; Francis, H.; Carrow, B. P. An "On-Cycle" Precatalyst Enables Room-Temperature Polyfluoroarylation Using Sensitive Boronic Acids. *ACS Catal*. **2018**, *8*, 2989–2994.

[141] Liu, Y.; Zhao, J.; Li, Z.; Mu, C.; Ma, W.; Hu, H.; Jiang, K.; Lin, H.; Ade, H.; Yan, H. Aggregation and Morphology Control Enables Multiple Cases of High-Efficiency Polymer Solar Cells. *Nat. Commun*. **2014**, *5*, 5293.

[142] Fyfe, J. W. B.; Fazakerley, N. J.; Watson, A. J. B. Chemoselective Suzuki–Miyaura Cross-Coupling via Kinetic Transmetallation. *Angew. Chem. Int. Ed.* **2017**, *56*, 1249 –1253.

[143] Lennoxa, A. J. J.; Lloyd-Jones, G. C. Selection of Boron Reagents for Suzuki–Miyaura Coupling. *Chem. Soc. Rev.*, **2014**, *43*, 412–443.

[144] Bulfield, D.; Huber, S. M. Synthesis of Polyflourinated Biphenyls; Pushing the Boundaries of Suzuki−Miyaura Cross Coupling with Electron-Poor Substrates. *J. Org. Chem*. **2017**, *82*, 13188–13203.

[145] Yang, L; Mihali, V.-A.; Brandell, D.; Strømme, M.; Sjödin, M. Conjugated Pyridine-Based Polymers Characterized as Conductivity Carrying Components in Anode Materials. *J. Phys. Chem. C*, **2014**, *118*, 25956–25963.

[146] Billingsley, K. L.; Anderson, K. W.; Buchwald, S. L. A Highly Active Catalyst for Suzuki–Miyaura Cross-Coupling Reactions of Heteroaryl Compounds. *Angew. Chem. Int. Ed.* **2006**, *45*, 3484 –3488.

[147] Yang, Y.; Oldenhuis, N. J.; Buchwald, S. L. Mild and General Conditions for Negishi Cross-Coupling Enabled by the Use of Palladacycle Precatalysts. *Angew. Chem., Int. Ed*. **2013**, *52*, 615–619.

[148] Thomas, A. A.; Denmark, S. E. Pre-transmetalation Intermediates in the Suzuki-Miyaura Reaction Revealed: The Missing Link. *Science* **2016**, *352*, 329–332.

[149] Anderson, K. W.; Buchwald, S. L. General Catalysts for the Suzuki–Miyaura and Sonogashira Coupling Reactions of Aryl Chlorides and for the Coupling of Challenging Substrate Combinations in Water. *Angew. Chem. Int. Ed*. **2005**, *44*, 6173–6177.

[150] Godget-Bar, T.; Leprêtre, J.-C.; Le Bacq, O.; Sanchez, J.-Y.; Deronzier, A.; Pasturel, A. Electrochemical and *ab initio* Investigations to Design a New Phenothiazine Based Organic Redox Polymeric Material for Metal-Ion Battery Cathodes. *Phys. Chem. Chem. Phys.,* **2015**, *17*, 25283–25296.

[151] Xu, W.; Zhang, X.; Hu, Q.; Zhao, L.; Teng, X.; Lai, W.-Y.; Xia, R.; Nelson, J.; Huang, W.; Bradley, D. D. C. Fluorene-Based Cathode Interlayer Polymers for High Performance Solution Processed Organic Optoelectronic Devices. *Org. Electron*. **2014**, *15*, 1244−1253.

[152] Handa, S.; Smith, J. D.; Zhang, Y.; Takale, B. S.; Gallou, F. Lipshutz, B. H. Sustainable HandaPhos-*ppm* Palladium Technology for Copper-Free Sonogashira Couplings in Water under Mild Conditions. *Org. Lett*. **2018**, *20*, 542–545.

[153] Xu, F.; Chen, X.; Tang, Z.; Wu, D.; Fu, R.; Jiang, D. Redox-Active Conjugated Microporous Polymers: a New Organic Platform for Highly Efficient Energy Storage. *Chem. Commun*. **2014**, *50*, 4788−4790.

[154] Valente, C.; Çalimsiz, S.; Hoi, K. H.; Mallik, D.; Sayah, M.; Organ, M. G. The Development of Bulky Palladium NHC Complexes for the Most-Challenging Cross-Coupling Reactions. *Angew. Chem. Int. Ed*. **2012**, *51*, 3314–3332.

[155] Nelson, D. J.; Nolan, S. P. Quantifying and Understanding the Electronic Properties of *N*-Heterocyclic Carbenes. *Chem. Soc. Rev*., **2013**, *42*, 6723–6753.

[156] Gómez-Suárez, A.; Nelson, D. J.; Nolan, S. P. Quantifying and Understanding the Steric Properties of *N*-Heterocyclic Carbenes. *Chem. Commun.*, **2017**, *53*, 2650–2660.

[157] Antonova, N. S.; Carbó, J. J.; Poblet, J. M. Quantifying the Donor–Acceptor Properties of Phosphine and N-Heterocyclic Carbene Ligands in Grubbs' Catalysts Using a Modified EDA Procedure Based on Orbital Deletion. *Organometallics* **2009**, *28*, 4283–4287.

[158] Vummaleti, S. V. C.; Nelson, D. J.; Poater, A.; Gómez-Suárez, A.; Cordes, D. B.; Slawin, A. M. Z.; Nolan, S. P.; Cavallo, L. What Can NMR Spectroscopy of Selenoureas and Phosphinidenes Teach Us About the □-Accepting Abilities of N-Heterocyclic Carbenes? *Chem. Sci*. **2015**, *6*, 1895–1904.

[159] Frey, G. D.; Dewhurst, R. D.; Kousar, S.; Donnadieu, B.; Bertrand, G. (Alkyl)(Amino)Carbene Gold(I) Complexes: A Synthetic and Structural Investigation. *J. Organomet. Chem*. **2008,** *693*, 1674–1682.

[160] Rao, B.; Tang, H.; Zeng, X.; Liu, L.; Melaimi, M.; Bertrand, G. Cyclic (Amino)(aryl)carbenes (CAArCs) as Strong σ-Donating and π-Accepting Ligands for Transition Metals. *Angew. Chem. Int. Ed*. **2015**, *54*, 14915–14919.

[161] Miyakoshi, R.; Yokoyama, A.; Yokozawa, T. Importance of the Order of Successive Catalyst-transfer Condensation Polymerization in the Synthesis of Block Copolymers of Polythiophene and Poly(*p*-phenylene). *Chem. Lett.* **2008**, *37*, 1022−1023.

[162] Groombridge, B. J.; Goldup, S. M.; Larrosa, I. Selective and General Exhaustive Cross-Coupling of Dichloroarenes with a Deficit of Nucleophiles Mediated by a Pd–NHC Complex. *Chem. Commun*. **2015**, *51*, 3832–3834.

[163] Zhang, S.; Huang, W.; Hu, P.; Huang, C.; Shang, C.; Zhang, C.; Yang R.; Cui, G. Conjugated Microporous Polymers with Excellent Electrochemical Performance for Lithium and Sodium Storage. *J. Mater. Chem. A*, **2015**, *3*, 1896–1901.

[164] Park, S. H.; Roy, A.; Beaupre, S.; Cho, S.; Coates, N.; Moon, J. S.; Moses, D.; Leclerc, M.; Lee, K.; Heeger, A. J. Bulk Heterojunction Solar Cells with Internal Quantum Efficiency Approaching 100% *Nat. Photonics* **2009**, *3*, 297–302.

[165] Liang, Y.; Feng, D.; Wu, Y.; Tsai, S.–T.; Li, G.; Ray, C.; Yu, L. Highly Efficient Solar Cell Polymers Developed via Fine-Tuning of Structural and Electronic Properties. *J. Am. Chem. Soc*. **2009**, *131*, 7792–7799.

[166] Cabanetos, C.; El Labban, A.; Bartelt, J. A.; Douglas, J. D.; Mateker, W. R. Fréchet, J. M.; McGehee, M. D.; Beaujuge, P. M. Linear Side Chains in Benzo[1,2-*b*:4,5-*b*′]dithiophene–Thieno[3,4-*c*]pyrrole-4,6-dione Polymers Direct Self-Assembly and Solar Cell Performance *J. Am. Chem. Soc.* **2013**, *135*, 4656–4659.

[167] Wang, X.; Deng, W.; Chen, Y.; Wang, X.; Ye, P.; Wu, X.; Yan, C.; Zhan, X.; Liu, F.; Huang, H. Fine-Tuning Solid State Packing and Significantly Improving Photovoltaic Performance of Conjugated Polymers Through Side Chain Engineering *via* Random Polymerization. *J. Mater. Chem. A*, **2017**, *5*, 5585–5593.

[168] Lu, D.-D.; He, X.-X.; Liu, F.-S. Bulky Yet Flexible Pd-PEPPSI-IPentAn for the Synthesis of Sterically Hindered Biaryls in Air. *J. Org. Chem*. **2017**, *82*, 10898−10911.

[169] Ouyang, J-S.; Li, Y.-F.; Huang, F.-D.; Lu, D-D.; Liu, F.-S.The Highly Efficient Suzuki–Miyaura Cross-Coupling of (Hetero)aryl Chlorides and (Hetero)arylboronic Acids Catalyzed by "Bulky-yet-Flexible" Palladium–PEPPSI Complexes in Air. *Chem. Cat. Chem.* **2018**, *10*, 371 –375.

[170] Stuart, A. C.; Tumbleston, J. R.; Zhou, H.; Li, W.; Liu, S.; Ade, H.; You, W. Fluorine Substituents Reduce Charge Recombination and Drive Structure and Morphology Development in Polymer Solar Cells. *J. Am. Chem. Soc.* **2013**, *135*, 1806−1815.

Chapter 3 Random Copolymers Outperform Gradient and Block Copolymers in Stabilizing Organic Photovoltaics[2]

3.1 Introduction

The National Renewable Energy Lab (NREL) has been tracking the "best" photovoltaic cells since 1976, highlighting growth trends in promising materials and technologies.[1] Conjugated polymer-based solar cells exhibit some of the lowest efficiencies on this chart, but are considered "emerging" materials because of their advantageous properties, including transparency, flexibility, and low weight.[2] In addition, the solution-based processing methods used for device fabrication are commercially appealing.[3] As a consequence, many researchers continue searching for organic materials with higher efficiencies.

Most organic photovoltaics are constructed from a blend of two materials: a conjugated polymer electron donor and a small molecule electron acceptor. The optoelectronic properties and device performance are dictated by the chemical structures of both components as well as the blend morphology. Recent advances in both donor and acceptor structures have led to organic devices with efficiencies that rival amorphous silicon.[4,5] As an example, Hou et. al. described a novel blend with a record-breaking 14.2% efficiency.[4b] This device has not yet been certified by NREL due to

[2] This work has been published as: Kong, C.; Song, B.; Mueller, E. A.; Kim, J.; McNeil, A. J. Random Copolymers Outperform Gradient and Block Copolymers in Stabilizing Organic Photovoltaics. *Adv. Funct. Mater.* **2019**, *29*, 1900467. C. Kong synthesized the polymers, performed optical microscopy studies, and contributed to writing, B. Song made and tested devices and contributed to writing, E. A. Mueller performed DSC experiments and contributed to writing, J. Kim and A. J. McNeil contributed intellectually and contributed to writing.

its instability. In a corresponding highlight article, Hou suggests that conjugated polymer-based devices may reach 18–20% efficiency within the next few years.[6]

With efficiencies on the rise, many researchers are focusing on improving device longevity. Due to changes in the active layer morphology, organic photovoltaic devices gradually lose efficiency over time.[7] The initial active layer morphology consists of nanoscale phase-separated poly(3-hexylthiophene) (P3HT) and phenyl-C_{61}-butyric acid methyl ester ($PC_{61}BM$) domains. These domains coalesce, increasing in size over time due to enthalpically-driven phase separation.[8] The net result is that the power conversion efficiencies (PCE) dramatically decrease, reducing the device utility.

To attenuate this detrimental process, researchers are investigating compatibilizers – a third component added to the blend to stabilize the morphology through noncovalent interactions.[9] To be effective, the compatibilizer should minimize the overall free energy by localizing at the donor/acceptor interface, lowering the interfacial tension and suppressing domain coalescence. The compatibilizer can impart additional beneficial properties to the device, such as a broader and stronger absorption profile as well as more efficient exciton dissociation and charge transport, all of which would contribute to a higher PCE.[9]

Both small molecules[10] and polymers[11,12] have been used as compatibilizers with moderate success. The majority of polymer compatibilizers have been diblock copolymers containing repeat units that are structurally similar to the donor and acceptor.[12] A prototypical example is a rod–coil diblock copolymer with a conjugated segment (the rod) that resembles the donor polymer and a nonconjugated segment (the coil) with a side-chain group that interacts with the acceptor. One limitation of this approach is that the coil segment is frequently an insulating material, which lowers the effective concentration of absorbing and electroactive species in the device. Rod–rod

diblock copolymers wherein both segments are conjugated have also been used.[12] These copolymers can facilitate exciton dissociation and charge transport as well. Although adding these tailored compatibilizers provides longer-lasting devices, no studies have elucidated the impact of sequence (e.g., block vs gradient) or composition (e.g., 50:50 vs 25:75) on compatibilization.

To address this knowledge gap, we have been exploring alternative copolymer sequences (i.e., random[13] and gradient[14,15] copolymers) as compatibilizers in blends. For example, we reported that gradient copolymer compatibilizers led to smaller domain sizes than the analogous block and random copolymers in homopolymer blends.[14] Gradient copolymers, with their gradual compositional change, were best at interacting with both homopolymer domains to lower the interfacial energy. In related work, we found that a gradient copolymer could stabilize photovoltaic devices containing P3HT and $PC_{61}BM$, with little change in efficiency over extended thermal annealing times (> 60 min at 150 °C).[15]

Herein, we expand on this work by examining the influence of copolymer sequence (random, diblock, and gradient), composition (comonomer ratio), and concentration on the stabilization of P3HT:$PC_{61}BM$ blends. All copolymers attenuated phase separation during thermal annealing. Their compatibilizing abilities depended on copolymer sequence, with gradient and random sequences outperforming the analogous diblock sequences. Further studies showed that the random copolymer gave a higher and longer-lasting PCE than the blend without copolymer. These improvements were due to the random copolymer's ability to stabilize the morphology, as well as facilitate exciton dissociation and charge transport. Combined, these results suggest that random copolymers are the best compatibilizers for stabilizing organic photovoltaics.

3.2 Results and Discussion

3.2.1 Synthesis and Characterization of Copolymer Additives

Nine copolymers were targeted each with a different sequence and/or composition. The copolymers had a poly(3-hexylthiophene) backbone with varying quantities and distributions of side-chain fullerenes. Catalyst-transfer polymerization (CTP)[16] was used to access all copolymers with random, gradient, and block sequences, narrow dispersities (Đ), and high regioregularities (Scheme 3.1). Polymers with approximately the same number-average molecular weights (M_n) were targeted by using the same monomer/catalyst ratio for each polymerization. Using a precatalyst with an ortho-tolyl reactive ligand[15,17,18] ensured unidirectional propagation and led to polymers with tolyl/H end-groups. Activated (5-bromo-4-hexylthiophen-2-yl)magnesium chloride (HT) and (5-bromo-4-(6-bromohexyl)thiophen-2-yl)magnesium chloride (BrHT) were chosen as monomers to generate polymers with specified reactive side-chain distributions. Using this approach, we synthesized random, gradient, and diblock[19] copolymers with three different theoretical HT:BrHT ratios (80:20, 65:35, and 50:50; Appendix 1, pp 146–168).[15]

Scheme 3.1 Copolymer synthesis with random, block, and gradient distributions of Br-functionalized side chains.

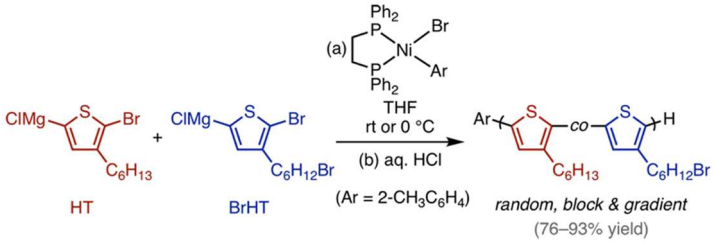

The gradient copolymers were prepared by initiating HT polymerization and then gradually adding BrHT. The block copolymers were prepared by adding precatalyst to a solution containing HT; once the HT consumption reached >90%, BrHT was added. The random copolymers were prepared by adding precatalyst to a solution containing both HT and BrHT. A random (rather than statistical) sequence was obtained due to the similar monomer reactivities.[14e] The cumulative mole fraction incorporation of BrHT (f_{BrHT}) versus the copolymer's normalized chain length was

evaluated by running an independent set of polymerizations where aliquots were periodically removed (Figure 3.1). As anticipated, the random copolymer showed a consistent, cumulative HT:BrHT ratio, whereas the block and gradient copolymers showed a changing HT:BrHT ratio consistent with the time-dependent changes in relative monomer concentrations during the reaction.

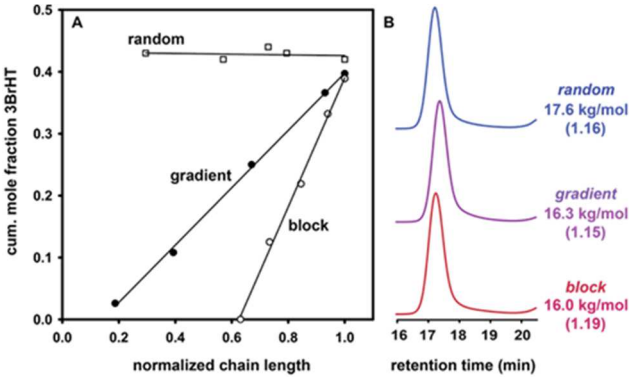

Figure 3.1 (A) Plot of the cumulative BrHT mole fraction in each copolymer versus its normalized chain length with a total monomer feed ratio of 60:40 HT:BrHT.[20] (B) GPC traces for the polymers obtained at normalized chain length = 1 (Mn and Đ are shown).

For each copolymer, a chain length of 80 thiophene units was targeted using a monomer/catalyst ratio of 80/1, which would give theoretical M_n of ~14–15 kg/mol depending on the BrHT mole fraction. The experimental M_n ranged from 18–22 kg/mol, consistent with the known overestimation of gel-permeation chromatography (GPC) by a factor of ~1.3× when using polystyrene calibration standards (Table 3.1).[21] As anticipated for CTP, each copolymer sample exhibited low dispersity (Đ = 1.11–1.24) and high regioregularity (Appendix 1, pp 158–175). In addition, the mole fraction of BrHT incorporated into the copolymer (f_{BrHT}) matched the experimental feed ratios, implying that their conversion rates were similar.

Table 3.1 Data for copolymers with Br-functionalized side chains.

	block			random			gradient		
BrHT:HT (mol:mol)	50:50	35:65	20:80	50:50	35:65	20:80	50:50	35:65	20:80
M_n (kg/mol)	18.8	19.1	19.5	21.1	21.4	21.7	20.7	22.1	18.9
Đ	1.19	1.17	1.15	1.24	1.23	1.22	1.15	1.11	1.19
f_{BrHT}	0.52	0.36	0.21	0.51	0.35	0.21	0.53	0.34	0.20

Two postpolymerization reactions were used to append fullerene units onto the copolymer side chains. The first reaction used sodium azide to substitute the side-chain bromine with an azide, generating a reactive handle for the click reaction (Scheme 3.2).[15,22] Subsequent ^{1}H NMR spectroscopic analysis revealed quantitative conversion of the Br to N_3. In addition, there were no significant changes in the GPC profiles.

Scheme 3.2 Post-polymerization reaction to generate random, block and gradient copolymers with N_3-functionalized side chains. ^{1}H NMR spectra and GPC traces of the random copolymer (20 mol%) before and after the reaction.

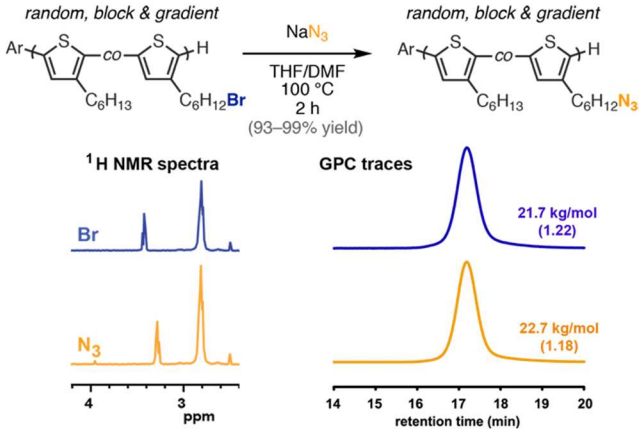

The second reaction involved an azide–alkyne "click" reaction to install the fullerene moieties onto the side chain. In our previous work, we used the copper-catalyzed azide–alkyne cycloaddition;[15a] however, crosslinked polymers were obtained when the azide concentration exceeded 10 mol%. To prevent this deleterious side-reaction, we employed the strain-promoted

azide–alkyne cycloaddition (SPAAC) that proceeds without a copper catalyst.[23] This approach involved five linear steps to synthesize the strained alkyne fullerene derivative, with a 14% overall yield from commercial starting materials (Scheme 3.3, Appendix 1, pp 127–133). Although low yielding, most alternative methods for grafting fullerene to P3HT require harsher conditions, including [3+2] cycloadditions,[12f,12h,24] 1,3-dipolar cycloadditions,[12a,25] and S_N2 reactions.[26] In contrast, the Steglich esterification[27] and Diels-Alder cycloaddition[28] represent mild alternatives to SPAAC for grafting fullerenes to P3HT. Our route began with ring-expansion of dibenzosuberenone followed by reduction with sodium borohydride.[29] Subsequent dibromination followed by a double elimination with lithium diisopropylamide afforded dibenzocyclooctynol (DIBO) in moderate yield.[29] In a separate step, the methyl ester of $PC_{61}BM$ was converted to the corresponding acid via hydrolysis.[30] Esterifying this acid with DIBO in the presence of *N,N'*-diisopropylcarbodiimide yielded the click-ready fullerene derivative $PC_{61}B$-DIBO.[15]

Scheme 3.3 Synthetic route to generate $PC_{61}B$-DIBO from dibenzosubrenone and $PC_{61}BM$.

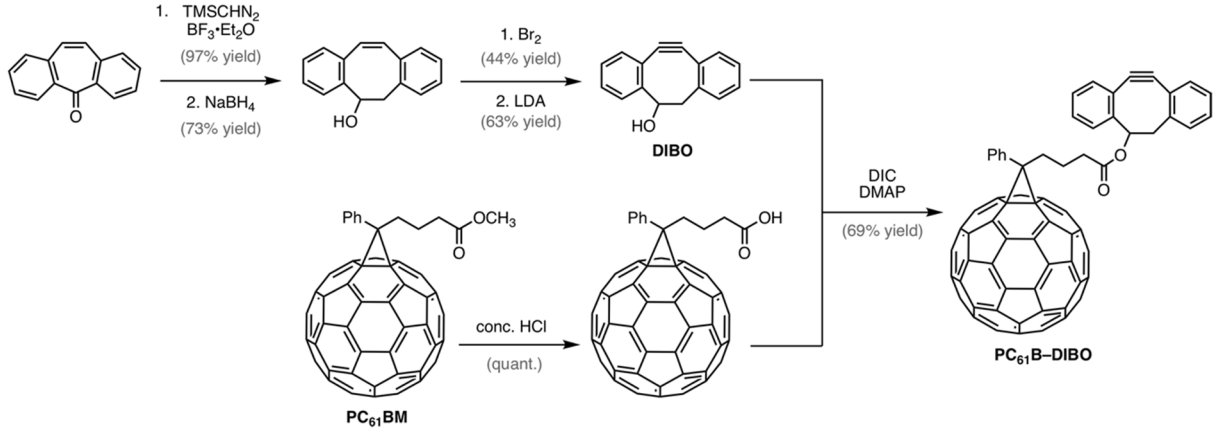

Each of the nine copolymers were functionalized with fullerene via SPAAC by stirring the azide-functionalized copolymer with $PC_{61}BM$-DIBO at room temperature over 48 h (Scheme 3.4, Appendix 1, pp 176–181).[31,32] The fullerene-loaded copolymers were characterized using IR spectroscopy to confirm >95% azide conversion via disappearance of the peak at 2091 cm^{-1}.[33]

Comparing the copolymers to a fullerene-functionalized small-molecule analog (Appendix 1, pp 134 and 144) via ^{1}H NMR spectroscopy supported cycloadduct formation. Multiple stereo- and regioisomers were generated due to both the racemic **PC_{61}B-DIBO** and the non-regioselective reaction. Combined, these results indicate that fullerene-functionalized copolymers with varying sequences and compositions were obtained.

Scheme 3.4 Post-polymerization transformation to generate random, block and gradient copolymers with fullerene-functionalized side chains. IR spectra and GPC traces of the block copolymer (20 mol%) before and after the reaction.

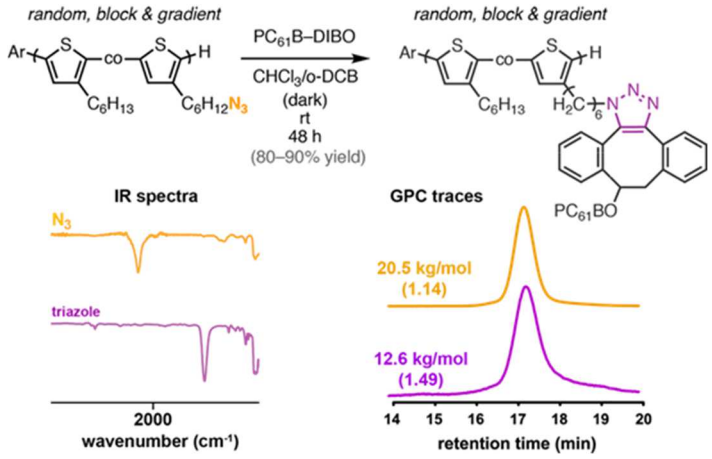

3.2.2 Quantifying Phase Separation in Blends

As noted above, one of the biggest challenges for polymer-based photovoltaics is their unstable active layer morphologies,[7] which form micrometer-scale domains with reduced interfacial area over time. We hypothesized that fullerene-functionalized P3HT copolymers could enthalpically stabilize P3HT:PC_{61}BM blends, minimizing their micrometer-scale phase separation. To test this hypothesis, we examined the thermal stability of P3HT:PC_{61}BM blends with and without each copolymer additive using optical microscopy.

The benchmark was set by annealing P3HT:PC_{61}BM (1:1 wt:wt) blends for 1 h at 150 °C. Subsequent optical microscope images revealed needle-shaped PC_{61}BM aggregates[34] (≈5–30 mm

length and ≈1 mm width) occupying 11.4% of the film area (Figure 3.2A). Next, blends with different copolymer sequences and compositions were codeposited with P3HT:$PC_{61}BM$ at several different concentrations. After thermal annealing, optical microscope images revealed that all copolymer additives led to reduced sizes and densities of $PC_{61}BM$ aggregates (Figure 3.2B–D, Appendix 1, Figures A1.51–A1.54).

Plotting these data as a function of the copolymer variables revealed that the random and gradient sequences outperformed the diblock sequence regardless of the composition or concentration (Figure 3.2E). We suspect that this effect is entropic in origin, wherein the gradient and random copolymers have more low-energy orientations at the interface (than the block) due to their mixed composition. When comparing copolymers of the same sequence and composition but at different concentrations in the blend (e.g., 2 vs 8 wt%), we found that higher copolymer concentrations were better, presumably because more of the interfacial area can be stabilized under these conditions. When comparing copolymers with the same sequences but different compositions (e.g., random 50 vs 20 mol%), the higher fullerene loading exhibited *more* phase separation. In this case, less compatibilizer is added to the blend when the fullerene-loading is higher because the average "repeat unit" mass is higher; consequently, less interfacial area is stabilized under these conditions. In total, these data suggested that the most stable devices would be obtained with random and/or gradient copolymers at 20 mol% fullerene loading and at 8 wt% concentration in the blend.

These conclusions are further supported by UV/vis spectroscopic data collected on selected films before and after thermal annealing (Appendix 1, Figure A1.55). The blend with no additive showed substantial phase separation after annealing as evidenced by a drop in the $PC_{61}BM$ signal (due to crystallization) and an increase in the P3HT peak intensity (due to demixing). In contrast, a blend

containing random copolymer (20 mol% fullerene, at 8 wt% concentration) showed no change in the $PC_{61}BM$ intensity and only a small increase in P3HT intensity after thermal annealing.

Combined, these results indicate that all copolymers suppress phase separation in P3HT:$PC_{61}BM$ blends, presumably by serving as an interfacial compatibilizer. One alternative explanation is that the copolymer increases the glass transition temperature of the blend (T_g^{blend}), which would minimize phase separation at the temperatures studied herein. To evaluate this hypothesis, the T_g^{blend} was measured for blends with and without added copolymer via differential scanning calorimetry (DSC). Blends without the copolymers exhibited a weak, broad T_g^{blend} at 42 °C, consistent with previous reports (Appendix 1, Figure A1.69).[35] In contrast, blends containing the copolymer additive did not exhibit a discernable T_g^{blend}, regardless of sample mass, scan rate, scan range, and even with a modulated temperature profile (Appendix 1, pp 195–197). At this time, the precise mechanism for the stabilization remains unclear.

Among the 28 films examined, the random and gradient copolymers showed the least macroscale phase separation overall. Because the random copolymer with 20 mol% fullerene side chains and at 8 wt% concentration was both the best compatibilizer and the easiest to access synthetically, we focused the following device studies on this copolymer alone, comparing P3HT:$PC_{61}BM$ blends with and without it.

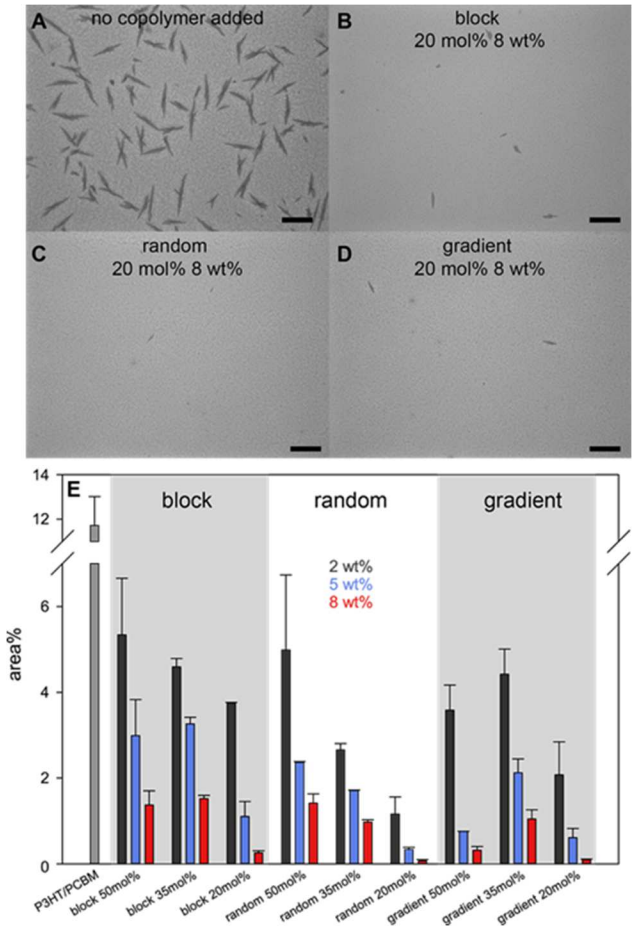

Figure 3.2 (A–D) Optical microscope images of P3HT:copolymer additive:$PC_{61}BM$ blends after annealing at 150 °C for 1 h (scale bar = 30 μm). (E) The relative area% of $PC_{61}BM$ aggregates within each blend as a function of the copolymer sequence, composition, and concentration.

3.2.3 Device Performance and Longevity

The PCE depends on the efficiencies of absorption and exciton dissociation, as well as the electron and hole mobilities. Although we anticipated that the random copolymer devices would have a more stable PCE during annealing due to the copolymer's morphology-stabilizing properties, it was unclear what effect the copolymer additive would have on the other processes that contribute to PCE. To elucidate its effect, photovoltaic devices were fabricated using an inverted device architecture: glass/ITO/ZnO/polymer blend/MoO_3/Ag (Appendix 1, pp 125–126).[36] The polymer blend was prepared by spin-casting a P3HT:$PC_{61}BM$ solution with or without

random copolymer additive to achieve a final thickness of ~175 nm (Appendix 1, pg 125). Photovoltaic measurements were performed under simulated AM 1.5G conditions both before and after annealing. To obtain statistically significant results, each data point represents an average of six measurements obtained from three different devices fabricated on two different substrates.

Devices containing the random copolymer additive exhibited an unexpectedly higher initial PCE (3.1 ± 0.2%) than the control device (2.4 ± 0.2%) (Figure 3.3A, Appendix 1, Figures A1.56 and A1.57). The observed PCE increase is largely attributable to a higher fill factor (FF), which is proportional to the maximum power available from a solar cell (Figure 3B). This FF difference is not due to an increase in the absorption efficiency because the copolymer has a nearly identical absorption spectrum to the P3HT:$PC_{61}BM$ blend (Appendix 1, Figure A1.62). We hypothesized that the copolymer might instead facilitate exciton dissociation because its highest occupied molecular orbital (HOMO) and lowest unoccupied molecular orbital (LUMO) levels both lie between those of P3HT and $PC_{61}BM$, providing an "energy cascade" (Figure 3.3C, Appendix 1, Figures A1.62 and A1.63).[37] In addition, we observed that the electron current was significantly higher in the blends containing the random copolymer than those with none (202 ± 47 pA/μm^2 vs 88 ± 11 pA/μm^2, Appendix 1, Figure A1.64).[38] This increased electron mobility may be due to better charge migration away from the interface through the fullerene units in the copolymer (Scheme 5). To support this hypothesis, we compared the series resistances (R_s), which reflects the overall device resistance (Figure 3.3D).

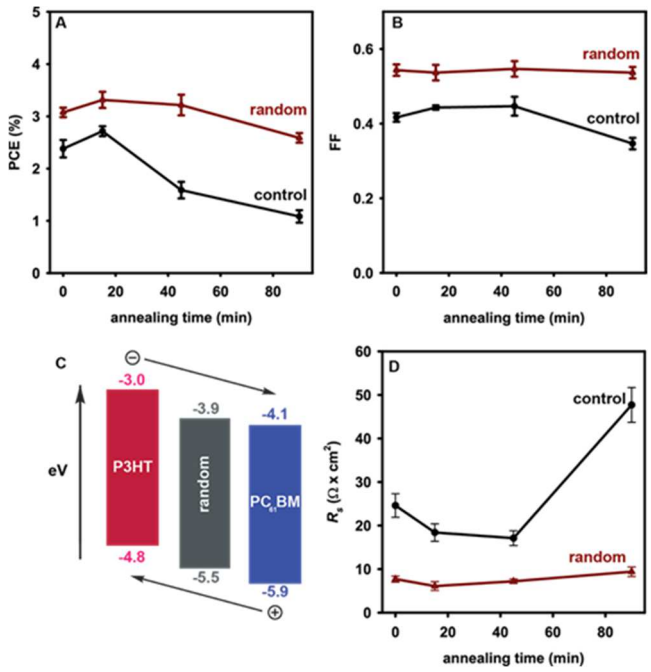

Figure 3.3 Plots of the (A) power conversion efficiency (PCE), (B) fill factor (FF), and (D) series resistance (R_s) versus annealing time for P3HT:$PC_{61}BM$ devices with and without random copolymer. (C) Schematic comparing the HOMO/LUMO levels of the copolymer relative to P3HT and $PC_{61}BM$.

The device containing random copolymer exhibited a significantly lower series resistance, consistent with the notion that the copolymer plays an active role in exciton dissociation and electron percolation. Finally, atomic force microscope images revealed that the films containing random copolymer exhibited smaller feature sizes with larger interfacial area than the control (Appendix 1, Figure A1.65). More interfacial area should translate to more efficient exciton dissociation, and an ensuing higher PCE. To summarize these studies, the random copolymer had an unanticipated beneficial impact on the initial device PCE by enhancing both exciton dissociation and electron percolation and mobility.

Scheme 3.5 Proposed percolation pathway in which electron mobility is facilitated at the interface by the side chain fullerenes on the random copolymer.

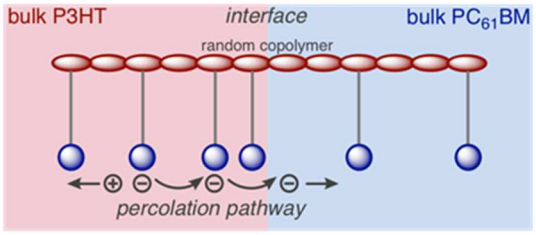

To determine device stabilities over time, thermal studies were performed by annealing the active layer at 150 °C before MoO_3/Ag deposition. Devices containing random copolymer significantly outlasted and outperformed the control devices (Figure 3.3 and Appendix 1, Figures A1.56–A1.59). After annealing for 90 min the control device lost >50% of its initial PCE; however, the random copolymer-containing device lost just 15% of its initial PCE (Figure 3A). The biggest change in the control device was a significant drop (>50%) in the short-circuit current (J_{sc}), which reflects charge generation and collection processes (Appendix 1, Figure A1.57). This result can be rationalized in conjunction with the micrometer-scale phase segregation occurring during this time. These morphological changes reduce the donor/acceptor interfacial area, decreasing the exciton dissociation efficiency. This conclusion is supported by the changes in *Rs*,[39] which for the control device increases from 24.6 to 47.7 Ω×cm^2 after annealing (Figure 3.3D). Combined, these data suggest that by stabilizing the active layer morphology, the random copolymer compatibilizer also stabilizes the device PCE.

Although the random copolymer led to a longer-lasting device, a minor but significant drop in PCE was observed. The culprit was a decrease in open-circuit voltage (V_{oc}, Appendix 1, Figure A1.57), which reflects the amount of charge recombination. Further analysis showed that the reverse bias saturation current (J_0),[40] which also reflects the amount of charge recombination, was one order of magnitude higher with random copolymer present (Appendix 1, Figure A1.61). The

theoretical V_{oc} change expected from this J_0 difference is ≈ 0.07 *V,* consistent with the experimental differences in V_{oc} (Appendix 1, pg 189). Combined, the V_{oc} drop and increased J_0 imply that after annealing the copolymer additive facilitates some charge recombination.

3.3 Conclusions

While PCEs have been on the rise for organic photovoltaics, the poor longevity of these devices remains a concern. We demonstrated that a random copolymer additive can both enhance longevity and improve efficiency. Other areas for future exploration include understanding the increased charge recombination that occurs after annealing as well as how the transport layer interfaces are affected by compatibilizer. Overall, this approach to stabilize organic photovoltaics should be generalizable, and our future efforts are focused on applying it toward higher efficiency conjugated polymer-based devices.

3.4 References

---

[1] National Renewable Energy Lab, Best Research-cell Efficiencies, https://www.nrel.gov/pv/assets/images/efficiency-chart.png, accessed: June 2018

[2] For recent reviews, see: (a) G. Zhang, J. Zhao, P. C. Y. Chow, K. Jiang, J. Zhang, Z. Zhu, J. Zhang, F. Huang, H. Yan, *Chem. Rev.* **2018**, *118*, 3447–3507. (b) J. Hou, O. Inganäs, R. H. Friend, F. Gao, *Nature Mater.* **2018**, *17*, 119–128. (c) S. Holliday, Y. Li, C. K. Luscombe, *Prog. Polym. Sci.* **2017**, *70*, 34–51. (d) H. Huang, L. Yang, B. Sharma, *J. Mater. Chem. A* **2017**, *5*, 11501–11517. (e) Y. Gao, M. Liu, Y. Zhang, Z. Liu, Y. Yang, L. Zhao, *Polymers* **2017**, *9*, 39. (f) Z. Hu, L. Ying, F. Huang, Y. Cao, *Sci. China Chem.* **2017**, *60*, 571–582. (g) S. Xiao, Q. Zhang, W. You, *Adv. Mater.* **2017**, *29*, 1601391. (h) L. Ying, F. Huang, G. C. Bazan, *Nature Commun.* **2017**, *8*, 14047.

[3] (a) F. C. Krebs, N. Espinosa, M. Hösel, R. R. Søndergaard, M. Jørgensen, *Adv. Mater.* **2014**, *26*, 29–39. (b) R. R. Søndergaard, M. Hösel, F. C. Krebs, *J. Polym. Sci. Part B: Polym. Phys.* **2013**, *51*, 16–34. (c) R. Søndergaard, M. Hösel, D. Angmo, T. T. Larsen-Olsen, F. C. Krebs, *Mater. Today* **2012**, *15*, 36–49.

[4] For reviews and recent examples of fullerene-free devices, see: (a) G. Zhang, J. Zhao, P. C. Y. Chow, K. Jiang, J. Zhang, Z. Zhu, J. Zhang, F. Huang, H. Yan, *Chem. Rev.* **2018**, 118, 3447–3507. (b) S. Li, L. Ye, W. Zhao, H. Yan, B. Yang, D. Liu, W. Li, H. Ade, J. Hou, *J. Am. Chem. Soc.* **2018**, *140*, 7159–7167. (c) Z. Fei, F. D. Eisner, X. Jiao, M. Azzouzi, J. A. Röhr, Y. Han, M. Shahid, A. S. R. Chesman, C. D. Easton, C. R. McNeill, T. D. Anthopoulos, J. Nelson, M. Heeney, *Adv. Mater.* **2018**, *30*, 1705209. (d) P. Cheng, G. Li, X. Zhan, Y. Yang, *Nature Photonics*

2018, *12*, 131–142. (e) X. Xu, T. Yu, Z. Bi, W. Ma, Y. Li, Q. Peng, *Adv. Mater*. **2018**, *30*, 1703973. (f) W. Zhao, S. Li, H. Yao, S. Zhang, Y. Zhang, B. Yang, J. Hou, *J. Am. Chem. Soc.* **2017**, *139*, 7148–7151. (g) W. Chen, Q. Zhang, *J. Mater. Chem. C* **2017**, *5*, 1275–1302.

[5] For reviews and examples of fullerene-containing devices, see: (a) J. Zhao, S. Zhao, Z. Xu, D. Song, B. Qiao, D. Huang, Y. Zhu, Y. Li, Z. Li, Z. Qin, *ACS Appl. Mater. Interfaces* DOI: 10.1021/acsami.8b07342. (b) C. Xu, M. Wright, N. K. Elumalai, M. A. Mahmud, D. Wang, V. R. Goncales, M. B. Upama, F. Haque, J. J. Gooding, A. Uddin. *Appl. Phys. A* **2018**, *124*, 449. (c) Y. Liu, M. Sheri, M. D. Cole, T. Emrick, T. P. Russell, *Angew. Chem. Int. Ed*. **2018**, *57*, DOI: 10.1002/anie.201803748. (d) J. Zhang, R. Xue, G. Xu, W. Chen, G.-Q. Bian, C. Wei, Y. Li, Y. Li, *Adv. Funct. Mater.* **2018**, *28*, 1705847. (e) X. Liu, L. Nian, K. Gao, L. Zhang, L. Qing, Z. Wang, L. Ying, Z. Xie, Y. Ma, Y. Cao, F. Liu, J. Chen. *J. Mater. Chem. A* **2017**, *5*, 17619–17631. (f) C. Li, H. Zhu, Y. Wang, H. Liu, S. Hu, F. Wang, B. Zhang, S. Dai, Z. Tan, *Nano Energy* **2017**, *31*, 201–209. (g) J. Huang, J. H. Carpenter, C.-Z. Li, J.-S. Yu, H. Ade, A. K.-Y. Jen, *Adv. Mater.* **2016**, *28*, 967–974. (h) J. Zhao, Y. Li, G. Yang, K. Jiang, H. Lin, H. Ade, W. Ma, H. Yan, *Nat. Energy* **2016**, *1*, 15027.

[6] K. Bourzac, *C&EN Global Enterp*. **2018**, *96 (22)*, 7–7.

[7] For reviews on stability (including, but not limited to, morphological stability), see: (a) S. Rafique, S. M. Abdullah, K. Sulaiman, M. Iwamoto, *Renew. Sust. Energy Rev.* **2018**, *84*, 43–53. (b) S. A. Gevorgyan, I. M. Heckler, E. Bundgaard, M. Corazza, M. Hösel, R. R. Søndergaard, G. A. dos Reis Benatto, M. Jørgensen, F. C. Krebs, *J. Phys. D: Appl. Phys.* **2017**, *50*, 103001. (c) W. R. Mateker, M. D. McGehee, *Adv. Mater.* **2017**, *29*, 1603940. (d) P. Cheng, X. Zhan, *Chem. Soc. Rev.* **2016**, *45*, 2544–2582. (e) S. Lizin, S. Van Passel, E. De Schepper, W. Maes, L. Lutsen, J. Manca, D. Vanderzande, *Energy Environ. Sci.* **2013**, *6*, 3136–3149. (f) M. Jørgensen, K. Norrman, S. A. Gevorgyan, T. Tromholt, B. Andreasen, F. C. Krebs, *Adv. Mater.* **2012**, *24*, 580–612.

[8] (a) B. Kuei, E. D. Gomez, *Soft Matter* **2017**, *13*, 49–67. (b) F. S. Bates, *Science* **1991**, *251*, 898–905.

[9] For recent reviews, see: (a) P. Cheng, X. Zhan, *Mater. Horiz.* **2015**, *2*, 462–485. (b) Goubard, G. Wantz, *Polym. Int.* **2014**, *63*, 1362–1367.

[10] For recent examples, see: (a) M. Xiao, K. Zhang, Y. Jin, Q. Yin, W. Zhong, F. Huang, Y. Cao, Nano Energy **2018**, 48, 53–62. (b) G. Sai-Anand, A. Dubey, A.-I. Gopalan, S. Venkatesan, S. Ruban, K. M. Reza, J. Choi, K. S. Lakhi, B. Xu, Q. Qiao, A. Vinu, Sol. Energy Materials and Sol. Cells **2018**, 182, 246–254. (c) A. Rahmanudin, X. A. Jeanbourquin, S. Hänni, A. Sekar, E. Ripaud, L. Yaoa, K. Sivula, J. Mater. Chem. A **2017**, 5, 17517–17524. (d) H. Li, K. Lu, Z. Wei, Adv. Energy Mater. **2017**, 7, 1602540. (d) P. Cheng, C. Yan, T-K. Lau, J. Mai, X. Lu, X. Zhan, Adv. Mater. **2016**, 28, 5822–5829. (e) P. Cheng, Q. Shi and X. Zhan, Acta Chim. Sin. **2015**, 73, 252–256. (f) W. Zhou, J. Shi, L. Lv, L. Chen and Y. Chen, Phys. Chem. Chem. Phys. **2015**, 17, 387–397. (g) J. Yang, W. He, K. Denman, Y. Jiang and Y. Qin, J. Mater. Chem. A **2015**, 3, 2108–2119. (h) Q. An, F. Zhang, L. Li, J. Wang, Q. Sun, J. Zhang, W. Tang and Z. Deng, ACS Appl. Mater. Interfaces **2015**, 7, 3691–3698. (i) W. Nie, G. Gupta, B. K. Crone, F. Liu, D. L. Smith, P. P. Ruden, C.-Y. Kuo, H. Tsai, H.-L. Wang, H. Li, S. Tretiak and A. D. Mohite, Adv. Sci. **2015**, 2, 1500024. (j) S. Wang, Y. Qu, S. Li, F. Ye, Z. Chen, X. Yang, Adv. Funct. Mater. **2015**, 25, 748–757.

[11] For recent reviews, see: (a) D. Kipp, R. Verduzco, V. Ganesan, *Mol. Syst. Des. Eng.* **2016**, *1*, 353–369. (b) K. Yuan, L. Chen, Y. Chen, *Polym. Int.* **2014**, *63*, 593–606. (c) See also, ref 9a.

[12] For recent examples, see: (a) C. Sartorio, V. Campisciano, C. Chiappara, S. Cataldo, M. Scopelliti, M. Gruttadauria, F. Giacalone, B. Pignataro, *J. Mater. Chem. A* **2018**, *6*, 3884–3498. (b) Y. Sun, P. Pitliya, C. Liu, X. Gong, D. Raghavan, A. Karim, *Polymer* **2017**, *113*, 135–146. (c) D. Kipp, O. Wodo, B. Ganapathysubramanian, V. Ganesan, *Sol. Energy Mater. Sol. Cell* **2017**, *161*, 206–218. (d) F. Lombeck, A. Sepe, R. Thomann, R. H. Friend, M. Sommer, *ACS Nano* **2016**, *10*, 8087–8096. (e) H. Fujita, T. Michinobu, S. Fukuta, T. Koganezawa, T. Higashihara, *ACS Appl. Mater. Interfaces* **2016**, *8*, 5484–5492. (f) S. Kakogianni, A. K. Andreopoulou, J. K. Kallitsis, *Polymers* **2016**, *8*, 440. (g) D. Kipp, V. Ganesan, *Macromolecules* **2016**, *49*, 5137–5144. (h) S. Kakogianni, M. A. Lebedeva, G. Paloumbis, A. K. Andreopoulou, K. Porfyrakis, J. K. Kallitsis, *RSC Adv.* **2016**, *6*, 98306–98316. (i) J. W. Mok, D. Kipp, L. R. Hasbun, A. Dolocan, J. Strzalka, V. Ganesan, R. Verduzco, *J.*

Mater. Chem. A **2016**, *4*, 14804–14813. (j) J. Liu, X. Zhu, J. Li, J. Shen, G. Tu, *RSC Adv.* **2016**, *6*, 61934–61943. (k) K. H. Park, Y. An, S. Jung, H. Park, C. Yang, *Energy Environ. Sci.* **2016**, *9*, 3464–3471. (l) E. Bicciocchi, M. Haeussler, E. Rizzardo, A. D. Scully, K. P. Ghiggino, *J. Polym. Sci., Part A: Polym. Chem.* **2015**, *53*, 888–903. (m) M. Raïssi, H. Erothu, E. Ibarboure, H. Cramail, L. Vignau, E. Cloutet, R. C. Hiorns *J. Mater. Chem. A* **2015**, *3*, 18207–18221. (m) D. Kipp, J. Mok, J. Strzalka, S. B. Darling, V. Ganesan, R. Verduzco, *ACS Macro Lett.* **2015**, *4*, 867–871.

[13] A. Li, J. Amonoo, B. Huang, P. K. Goldberg, A. J. McNeil, P. F. Green, *Adv. Funct. Mater.* **2014**, *24*, 5594–5602.

[14] (a) J. A. Amonoo, A. Li, G. E. Purdum, M. E. Sykes, B. Huang, E. F. Palermo, A. J. McNeil, M. Shtein, Y.-L. Loo, P. F. Green, *J. Mater. Chem. A* **2015**, *3*, 20174–20184. (b) E. F. Palermo, A. J. McNeil, In *Sequence-Controlled Polymers: Synthesis, Self-Assembly, and Properties*, (Eds: H. Baltes, W. Göpel, J. Hesse), ACS Symposium Series, American Chemical Society, Washington, DC **2014**, Ch. 19. (c) E. F. Palermo, H. L. van der Laan, A. J. McNeil, *Polym. Chem.* **2013**, *4*, 4606–4611. (d) E. F. Palermo, A. J. McNeil, *Macromolecules* **2012**, *45*, 5948–5955. (e) J. R. Locke, A. J. McNeil, *Macromolecules* **2010**, *43*, 8709–8710.

[15] E. F. Palermo, S. B. Darling, A. J. McNeil, *J. Mater. Chem. C* **2014**, *2*, 3401–3406.

[16] For recent reviews, see: (a) M. A. Baker, C.-H. Tsai, K. J. T. Noonan, *Chem. Eur. J.* **2018**, *24*, DOI: 10.1002/chem.201706102. (b) A. K. Leone, A. J. McNeil, *Acc. Chem. Res.* **2016**, *49*, 2822–2831. (c) T. Yokozawa, Y. Ohta, *Chem. Rev.* **2016**, *116*, 1950–1968. (d) R. Grisorio, G. P. Suranna, *Polym. Chem.* **2015**, *6*, 7781–7795. (e) Z. J. Bryan, A. J. McNeil, *Macromolecules* **2013**, *46*, 8395–8405.

[17] (a) H. A. Brontstein, C. K. Luscombe, *J. Am. Chem. Soc.* **2009**, *131*, 12894–12895. (b) N. Doubina, A. Ho, A. K.-Y. Jen, C. K. Luscombe, *Macromolecules* **2009**, *42*, 7670–7677. (c) V. Senkovskyy, R. Tkachov, T. Beryozkina, H. Komber, U. Oertel, M. Horecha, V. Bocharova, M. Stamm, S. A. Gevorgyan, F. C. Krebs, A. Kiriy, *J. Am. Chem. Soc.* **2009**, *131*, 16445–16453. (d) V. Senkovskyy, M. Sommer, R. Tkachov, H. Komber, W. T. S. Huck, A. Kiriy, *Macromolecules* **2010,** *43*, 10157–10161.

[18] See also: (a) A. O. Hall, S. R. Lee, A. N. Bootsma, J. W. G. Bloom, S. E. Wheeler, A. J. McNeil, *J. Polym. Sci., Part A: Polym. Chem.* **2017**, *55*, 1530–1535. (b) S. R. Lee, J. W. G. Bloom, S. E. Wheeler, A. J. McNeil, *Dalton Trans.* **2013**, *42*, 4218–4222. (c) E. L. Lanni, A. J. McNeil, *J. Am. Chem. Soc.* **2009**, *131*, 16573–16579.

[19] For a related structure, see: S. H. Chan, C. S. Lai, H. L. Chen, C. Ting, C. P. Chen, *Macromolecules* **2011**, *44*, 8886–8891.

[20] All copolymerizations presented in Figure 1.1 were conducted under N_2 (outside the glovebox) at 0 °C so that the slower reaction rate would enable adequate time between aliquots.

[21] M. Wong, J. Hollinger, L. M. Kozycz, T. M. McCormick, Y. Lu, D. C. Burns, D. S. Seferos, *ACS Macro Lett.* **2012**, *1*, 1266–1269.

[22] See also: L. Zhai, R. L. Pilston, K. L. Zaiger, K. K. Stokes, R. D. McCullough, *Macromolecules* **2003**, *36*, 61–64.

[23] For a recent review, see: C. J. Pickens, S. N. Johnson, M. M. Pressnall, M. A. Leon, C. J. Berkland, *Bioconjugate Chem.* **2018**, *29*, 686–701.

[24] S.-H. Chan, C.-S. Lai, H.-L. Chen, C. Ting, C.-P. Chen, *Macromolecules* **2011**, *44*, 8886–8891.

[25] M. Li, P. Xu, J. Yang, S. Yang, *J. Mater. Chem.* **2010**, *20*, 3953–3960.

[26] (a) F. Pierini, M. Lanzi, P. Nakielski, S. Pawlowska, O. Urbanek, K. Zembrzcyki, T. A. Kowalewski, *Macromolecules* **2017**, *50* 13, 4972–4981. (b) M. Lanzi, E. Salatelli, T. Benelli, D. Caretti, L. Giorgini, F. P. Di-Nicola, *J. Appl. Polym. Sci.* **2015**, *132*, 42121.

[27] M. Chen, M. Li, H. Wang, S. Qu, X. Zhao, L. Xie, S. Yang, *Polym. Chem.* **2013**, *4*, 550–557.

[28] B. Yameen, T. Puerchkhauer, J. Ludwig, I. Ahmed, O. Altintas, L. Fruk, A. Colsmann, C. Barner-Kowollik, *Small* **2014**, *10*, 3091–3098.

[29] N. E. Mbua, J. Guo, M. A. Wolfert, R. Steet, G.-J. Boons *ChemBioChem* **2011**, *12*, 1912–1921.

[30] S. P. Singh, CH. P. Kumar, G. D. Sharma, R. Kurchania, M. S. Roy, *Adv. Funct. Mater.* **2012**, *22*, 4087–4095.

[31] S. Wang, X. Yang, W. Zhu, L. Zou, K. Zhang, Y. Chen, F. Xi, *Polymer* **2014**, *55*, 4812–4819.

[32] Copolymers with >50 mol% side-chain fullerenes were largely insoluble in THF and not pursued further.

[33] An exothermic peak was observed at temperatures >150 °C during DSC analysis of some fullerene-functionalized copolymers (SI Figures S66–S67). After DSC analysis, the samples were completely insoluble in $CDCl_3$. We tentatively attributed this non-reversible event to a crosslinking reaction involving side-chain azides (<5% by IR spectroscopy) reacting with fullerene. Fortunately, this reaction does not occur if the copolymer samples are heated to the device annealing temperature (150 °C). After DSC analysis, the resulting copolymers fully dissolve in $CDCl_3$ and the ^{1}H NMR spectra are identical to the samples before analysis (SI Figure S67).

[34] A. Torreggiani, F. Tinti, A. Savoini, M. Melchiorre, R. Po, N. Camaioni, *Org. Photonics Photovolt.* **2014**, *2*, 50–58.

[35] (a) J. Zhao, A. Swinnen, G. Van Assche, J. Manca, D. Vanderzande, B. Van Mele, *J. Phys. Chem. B* **2009**, *113*, 1587–1591. (b) P. E. Hopkinson, P. A. Staniec, A. J. Pearson, A. D. F. Dunbar, T. Wang, A. J. Ryan, R. A. L. Jones, D. G. Lidzey, A. M. Donald, *Macromolecules* **2011**, *44*, 2908–2917. (a) H. Chen, J. Chen, W. Yin, X. Yu, M. Shao, K. Xiao, K. Hong, D. L. Pickel, W. M. Kochemba, S. M. Kilbey II, M. Dadmun, *J. Mater. Chem. A* **2013**, *1*, 5309–5319.

[36] Z. He, C. Zhong, S. Su, M. Xu, H. Wu, Y. Cao, *Nature Photonics* **2012**, *6*, 591–595.

[37] (a) J. Hou, Z. Tan, Y. Yan, Y. He, C. Yang, Y. Li, *J. Am. Chem. Soc.* **2006**, *128*, 4911–4916. (b) Y. He, G. Zhao, B. Peng, Y. Li, *Adv. Funct. Mater.* **2010**, *20*, 3383–3389.

[38] Note that blends containing 12 wt% random copolymer exhibited lower electron mobilities than the 8 wt% blend, and lower hole mobilities than the control devices, suggesting there is an upper limit to additive concentration on its beneficial effects (SI Figures S56–S57). We suspect that at these higher concentrations the copolymer may disrupt the P3HT crystallization within its "pure" domain.

[39] M.-S. Kim, B.-G. Kim, J. Kim, *ACS Appl. Mater. Interfaces* **2009**, *1*, 1264–1269.

[40] (a) J. D. Zimmerman, X. Xiao, C. K. Renshaw, S. Wang, V. V. Diev, M. E. Thompson, S. R. Forrest, *Nano Lett.* **2012**, *12*, 4366–4371. (b) W. J. Potscavage, Jr., A. Sharma, B. Kippelen, *Acc. Chem. Res.* **2009**, *42*, 1758–1767. (c) C. G. Shuttle, A. Maurano, R. Hamilton, B. O'Regan, J. C. de Mello, J. R. Durrant, *Appl. Phys. Lett.* **2008**, *93*, 183501.

Chapter 4 A Fullerene-Functionalized Poly(3-hexylthiophene) Additive Stabilizes Conjugated Polymer-Fullerene Blend Morphologies[3]

4.1 Introduction

Over the last three decades, organic photovoltaics (OPVs) have emerged as a promising solar energy technology because they can be flexible, lightweight, and fabricated via inexpensive methods.[1–4] In a typical OPV device, the photoactive layer is an interpenetrating blend of an electron-donor and an electron-acceptor material, either of which can be small molecules or polymers.[5] To improve power conversion efficiencies (PCEs), researchers have tuned the chemical structures of the donor and acceptor materials to optimize their bandgaps. The most common donor/acceptor pair for OPVs has been poly(3-hexylthiophene) (P3HT) as a donor paired with phenyl-C_{61}-butyric acid methyl ester ($PC_{61}BM$) as the acceptor, which typically achieves PCEs of 3–5%.[6,7] In the last decade, researchers have shifted away from P3HT in favor of conjugated polymers with alternating electron-rich and electron-poor units along the backbone to improve visible light absorption and optimize the bandgap for charge transfer with a given acceptor.[8,9] Over the last ten years, a variety of donor polymers have been designed that enable PCEs around 10%,[10,11] with some examples of record-breaking PCEs greater than 17% for tandem[12] and single-junction devices[13,14] in the last two years.

[3] This work is accepted for publication in *ACS Appl. Polym. Mater.* as: Kim, D.;* Mueller, E. A.;* Yang, D. S.; Fagnani, D. E.; Kim, J.; McNeil, A. J. Fullerene-Functionalized Poly(3-hexylthiophene) Additive Stabilizes Conjugated Polymer-fullerene Blend Morphologies. **equal contribution* D. Kim made and analyzed devices and contributed to writing, E. A. Mueller synthesized the copolymer, made and analyzed thin films, and contributed to writing, D. S. Yang made and analyzed devices, D. E. Fagnani contributed intellectually, J. Kim and A. J. McNeil contributed intellectually and to writing.

Despite improvements in device PCE, long-term stability remains a central challenge to OPV commercialization.[1,15] One factor impacting long-term stability is detrimental changes in the blend morphology over time. Initially, the physically blended donor and acceptor form a kinetically trapped morphology with nanoscale domains of each pure component and, depending on the donor/acceptor pair, an additional amorphous mixed phase.[16] This nanoscale morphology is important for effective charge separation because photogenerated excitons, which must migrate to domain interfaces to separate into holes and electrons, have diffusion lengths of less than 50 nm. [17–19] In an enthalpically-driven process, the initial domains phase-separate into larger (e.g., micron-scale) domains with aging, which reduces the charge separation efficiency.[20,21] Phase separation is particularly problematic for blends that contain fullerenes, some of the most common acceptors, which diffuse throughout the active layer more easily than polymers.[22] Thus, measures to prevent active layer phase separation are necessary to maintain high PCE over time.

One method to stabilize device morphology is to add a compatibilizer as a third component into the active layer blend.[23,24] The compatibilizer localizes at the interface between immiscible phases, lowers the interfacial tension, and increases the interfacial adhesion.[25,26] Both small molecules[27–31] and polymers[32–42] have been used to stabilize domain sizes in active layer blends. In our previous work, we used a fullerene-functionalized P3HT copolymer to stabilize P3HT:$PC_{61}BM$ blend morphologies.[43] We investigated how the copolymer sequence (e.g., random, gradient, block), composition (e.g., 20, 35, 50 mol% fullerene side-chains), and concentration in the blend (e.g., 2, 5, 8 wt%) affected blend morphology over time. We found that a random copolymer with 20 mol% fullerene-functionalized side chains at 8 wt% in the blend was best at preventing micron-scale phase separation in annealed thin film blends and OPVs. In our work, and in other examples,[32,36,38,39,44] tailored compatibilizers were synthesized to match the

specific donor and acceptor in the active layer of the OPV. Synthesizing custom compatibilizers is time-intensive and impractical for complex donor polymers. To circumvent this challenge, we hypothesized that our P3HT copolymer additive might be miscible with other conjugated polymers and serve as a general compatibilizer.

To test this hypothesis, we investigated how the fullerene-functionalized P3HT additive impacts morphology for three different blends of phenyl-C_{71}-butyric acid methyl ester ($PC_{71}BM$) with one of the following conjugated polymers (Chart 4.1): poly[[4,8-bis[(2-ethylhexyl)oxy]benzo[1,2-b:4,5-b0]dithiophene-2,6-diyl][3-fluoro-2-[(2-ethylhexyl)-carbonyl]-thieno-[3,4-b]thiophene-diyl]] (PTB7),[45] poly[4,8-bis(5-(2-ethylhexyl)thiophen-2-yl)benzo[1,2-b;4,5-b′]dithiophene-2,6-diyl-alt-(4-(2-ethylhexyl)-3-fluorothieno[3,4-b]thiophene-)-2-car-boxylate-2-6-diyl] (PTB7-Th),[46] and poly[(5,6-difluoro-2,1,3-benzothiadiazol-4,7-diyl)-alt-(3,3‴-di(2-octyldodecyl)-2,2′;5′,2″;5″,2‴-quaterthiophen-5,5‴-diyl)] (PffBT4T-2OD).[47] Each of these donor polymers was selected because it has a reported PCE ≥ 10% with $PC_{71}BM$. We found that the fullerene-functionalized P3HT copolymer suppresses micron-scale phase separation for all three blends, likely by inhibiting $PC_{71}BM$ aggregation rather than via traditional blend compatibilization. Further studies showed that OPV devices fabricated with the PffBT4T-2OD:$PC_{71}BM$ blend showed the active layer morphology was stabilized when the copolymer was added. We also investigated factors beyond morphology that could affect device performance. Overall, our results demonstrate that a fullerene-functionalized P3HT copolymer additive can stabilize different conjugated polymer thin film blends and prevent phase separation in the active layer of PffBT4T-2OD:$PC_{71}BM$ devices.

Chart 4.1 Chemical structures of the donor polymers, the acceptor, and the additives used in this study.[48–50]

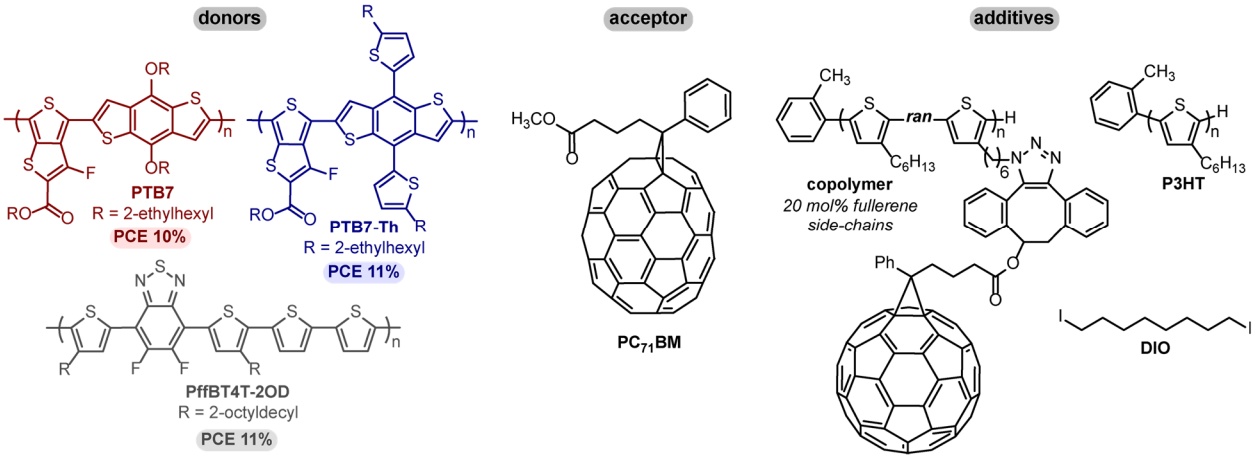

4.2 Results and Discussion

The copolymer additive was synthesized and characterized as reported in our previous studies to obtain 21 mol% side-chain functionalization, M_n = 21.0 kg/mol and Đ = 1.15 (Appendix 2, pgs 214–218, Figures A2.12-A2.16).[43] To probe the morphological stability of each system without any additives, we prepared and thermally annealed thin film blends of each donor (PTB7, PTB7-Th, or PffBT4T-2OD) with $PC_{71}BM$. The blend compositions PTB7 or PTB7-Th:$PC_{71}BM$ (1.0:1.5),[48,49] and PffBT4T-2OD:$PC_{71}BM$ (1.0:1.2)[50] films were chosen based on previously reported optimized blend ratios for OPVs. The films were annealed under vacuum for 0–180 min at 200 °C to accelerate the aging process (Appendix 2, pp 231–238). Phase separation was quantified via optical microscopy, wherein the percent area that was filled with dark micron-scale $PC_{71}BM$ crystallites was determined using ImageJ (Appendix 2, pp 238–249).[51] The PTB7 blends had significantly fewer aggregates (1.4 ± 0.8 area%) compared to the PTB7-Th (22 ± 3 area%) and PffBT4T-2OD (39.9 ± 0.9 area%) blends after 180 min of annealing (Figure 2.1, left). This smaller degree of phase separation may be due to the reduced crystallinity of PTB7 (Figure A2.42).[52,53] To understand how the copolymer additive affected these morphological changes, thin films were

prepared with 8 wt% of the copolymer, annealed, and analyzed with the same method described above. In all cases, the aggregate area percent was reduced when the copolymer was added: 0.15 ± 0.02 area % (PTB7), 0.7 ± 0.1 area % (PTB7-Th), and 1.8 ± 0.2 area % (PffBT4T-2OD) (Figure 1, right). In contrast, films with lower copolymer loading (4 wt%) exhibited more phase separation (Appendix 2, Figure A2.18): 0.35 ± 0.03 area % (PTB7), 15 ± 1 area % (PTB7-Th), and 27.7 ± 0.1 area % (PffBT4T-2OD), consistent with our previous studies.[43] Because optical microscopy only probes phase separation on the micron-scale, it is likely that nanoscale phase separation is still occurring. Indeed, in previous reports for similar systems (e.g., PTB7, PTB7-Th with $PC_{71}BM$), nanoscale phase separation was observed prior to or concomitant with micron-scale phase separation.[54] As such, our results indicate that phase separation is occurring at a slower rate with the copolymer present. Overall, these results suggest that the copolymer could be a generalizable additive for stabilizing blends of multiple conjugated polymers with $PC_{71}BM$.

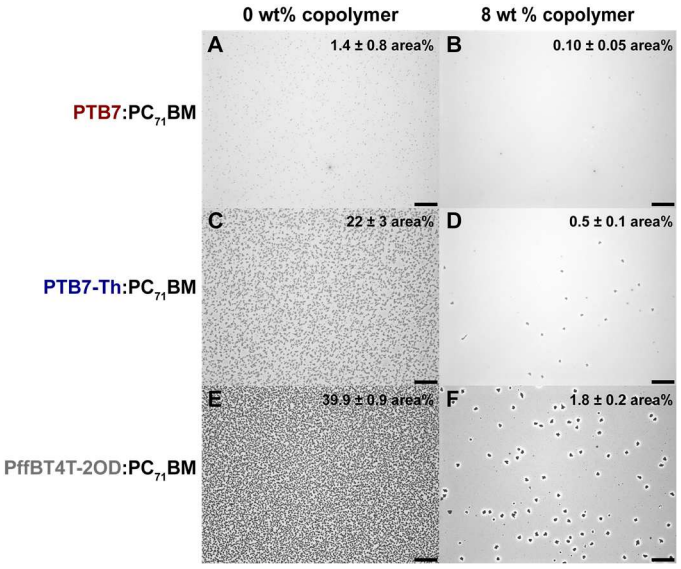

Figure 4.1 Optical microscope images of PTB7 (A, B), PTB7-Th (C, D), and PffBT4T-2OD (E, F) blended with $PC_{71}BM$ and 0 wt % (left) or 8 wt% (right) copolymer. All films were annealed under vacuum for 180 min at 200 °C. Scale bars represent 30 μm.

We then benchmarked the performance of our additive against diiodooctane (DIO), which is commonly used to optimize as-cast morphology by reducing domain sizes for PTB7[45,55] and

PTB7-Th[56] while increasing domain sizes for PffBT4T-2OD[57] with $PC_{71}BM$. These optimal as-cast morphologies may still be far from thermodynamic equilibrium, resulting in phase separation over time.[54] Indeed, we found that blends with 3 vol% DIO, the volume ratio typically used in devices,[48–50] still underwent phase separation, albeit by reduced amounts compared to no additives (cf. Figures 4.2A and 4.2C). By comparison, the thin films with copolymer gave the least amount of phase separation for all three donor polymers (Figure 4.2B). In addition, we analyzed thin films with 8 wt% P3HT to investigate whether adding a similar conjugated polymer without fullerene-functionalized side chains could stabilize the blend morphology, a strategy that has been successful for ternary OPVs.[58] Blends with P3HT (Figure 4.2D) exhibited similar amounts of phase separation to blends without any additives (Figure 4.2A), indicating that the fullerene-functionalized side chains on the copolymer are necessary to minimize micron-scale aggregates. In all cases, the stability of blends with the copolymer or with the copolymer and DIO was greater than the others, demonstrating that the copolymer was the most effective additive for limiting micron-scale phase separation in these blends.

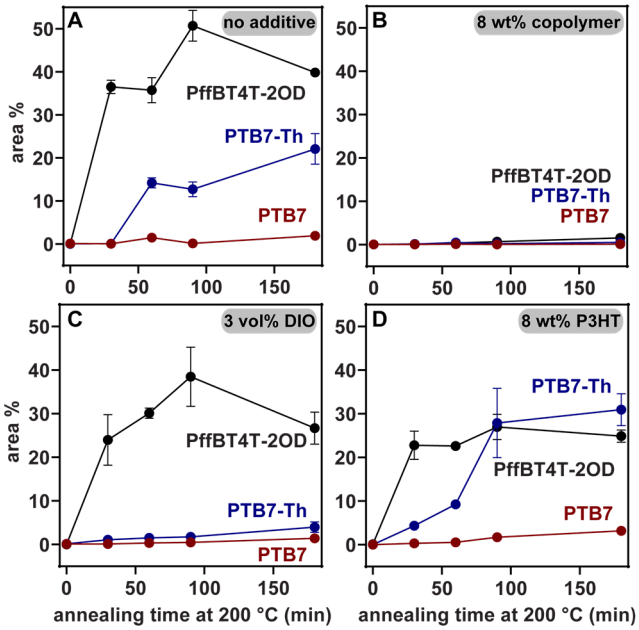

Figure 4.2 Area percent of $PC_{71}BM$ aggregates for thin film blends of PTB7 (red), PTB7-Th (blue), or PffBT4T-2OD (grey) with (A) no additive, (B) copolymer, (C) DIO, or (D) P3HT. All films were annealed at 200 °C under vacuum. Each data point represents the average from 3 images.

Because fewer micron-scale aggregates were observed in copolymer-containing films, we hypothesized that the copolymer was compatibilizing the blend morphology. More specifically, we hypothesized that the copolymer additive would localize at the interface between the donor and acceptor phases due to favorable miscibility with each one.[25] To test this hypothesis, we determined the surface free energies (γ) of each blend component to qualitatively assess their miscibility, where components with similar surface free energies would be more miscible with each other.[59–62] Surface contact angles of water and glycerol were measured for neat thin films and used to calculate the surface free energy of each blend component (Table 4.1, Appendix 2, pp 248–255). Because both the solvents and the method used to calculate surface energy can affect the results,[63] we analyzed the relative differences in surface energy between each material that we studied. The three donor polymers studied had similar surface free energies of 21.9 mJ/m2 (PTB7), 21.4 mJ/m2 (PTB7-Th), and 19.2 mJ/m2 (PffBT4T-2OD) and these surface energies were

significantly lower than the surface energy of 28.0 mJ/m2 for PC71BM, consistent with previous reports.[60–66] Interestingly, the surface free energy of the copolymer (27.8 mJ/m^2) was nearly identical to that of $PC_{71}BM$, suggesting that the copolymer has enhanced miscibility with $PC_{71}BM$.[62] For comparison, the surface energy of P3HT was determined by the same method to be 20.8 mJ/m^2, which is more similar to that of the other donor polymers studied.

Table 4.1 Measured surface free energies (γ) and calculated wetting coefficients (ω_c), as well as calculated Flory-Huggins interaction parameters (χ).

material	γ_i^{total}(mJ/m^2)	copolymer ω_c[a]	$\chi_{i,copolymer}K$[b]
PTB7	21.9	–0.94	0.36
PTB7-Th	21.4	–0.94	0.50
PffBT4T-2OD	19.2	–0.96	0.87
$PC_{71}BM$	28.0	-	0.0036
copolymer	27.8	-	-
P3HT	20.8	-	-

[a] *for copolymer in donor:$PC_{71}BM$ blend*

[b] *K is a proportionality constant (SI pg S47)*[67,68]

To investigate whether the copolymer was localized at the interface between the donor and acceptor, the surface energies were used to calculate a wetting coefficient, ω_c, for an additive in a binary blend.[69] This unitless parameter is derived from the differences in interfacial surface energy for the additive with each component of the blend. When $\omega_c < -1$, the additive is localized in the $PC_{71}BM$ phase, when $-1 \leq \omega_c \leq 1$, the additive is localized at the interface between the phases in a blend, and when $\omega_c > 1$ the additive is localized in the donor phase. The wetting coefficient calculated for the copolymer additive in each blend was –0.94 (PTB7 and PTB7-Th) or –0.96 (PffBT4T-2OD), indicating that the copolymer may have had some degree of interface localization

but likely is preferentially localized in the $PC_{71}BM$ phase (Table 1). For comparison, the wetting coefficients calculated for P3HT in the donor-acceptor blends were 1.37 (PTB7), 1.19 (PTB7-Th), and 0.63 (PffBT4T-2OD) demonstrating that without the fullerene-functionalized side chains, P3HT likely localizes in the donor phase or at the interface (Appendix 2, Table A2.13). These results, combined with the optical microscopy studies, suggest that the copolymer is selectively inhibiting $PC_{71}BM$ aggregation to stabilize blend morphology. One possible mechanism for this stabilization is that the copolymer acts as nucleating agent for $PC_{71}BM$.[70] By introducing nucleation sites for $PC_{71}BM$, the copolymer would increase the rate of $PC_{71}BM$ nucleation relative to crystal growth and limit crystal size to the nanoscale.[71,72] If relevant, this process could be observed via differential scanning calorimetry (DSC) by an increase in $PC_{71}BM$ crystallization temperature.[65] However, $PC_{71}BM$ crystallization was not observed in DSC thermograms of PffBT4T-2OD:$PC_{71}BM$ blends with or without the copolymer, nor for blends of $PC_{71}BM$ with 8 wt% of the copolymer (Appendix 2, Figure A2.40–A2.41), suggesting that this mechanism is unlikely. Alternatively, the copolymer may be acting in a similar manner to poly-fullerenes[73] or oligo-fullerenes[74,75] by preventing the small molecule $PC_{71}BM$ from diffusing and crystallizing to form aggregates. Indeed, annealing films of just $PC_{71}BM$ (i.e., without the donor polymer) with 8 wt% copolymer additive or with 8 wt% P3HT for 180 min at 200 °C revealed micron-scale aggregates for the P3HT films alone (Appendix 2, Figure A2.38). This result demonstrates that the copolymer likely has favorable interactions with the $PC_{71}BM$ that prevent $PC_{71}BM$ diffusion and aggregation in the thin films.

To further investigate the miscibility of the copolymer with each blend component, the Flory-Huggins interaction parameters (χ) were estimated (Appendix 2, pp 254–255).[63–77] This parameter is directly proportional to the enthalpy of mixing for amorphous liquids, with lower

values indicating an increased thermodynamic preference for mixing.[78,79] These values can provide a qualitative comparison of the copolymer interactions with each component. Notably, the copolymer additive displays a very small Flory-Huggins interaction parameter with $PC_{71}BM$, indicating thermodynamically favorable mixing with $PC_{71}BM$ (Table 4.1). This result further supports that the conclusion that the copolymer additive is likely attenuating $PC_{71}BM$ aggregate formation during annealing.

To summarize, annealed thin films of several conjugated polymers blended with $PC_{71}BM$ exhibit less macroscale phase separation with 8 wt% of a fullerene-functionalized P3HT copolymer additive. From the surface contact angle analysis, we found that the copolymer additive may localize at the interface between donor polymer and $PC_{71}BM$ phases but more likely localizes with $PC_{71}BM$. Although we do not directly observe copolymer miscibility with $PC_{71}BM$, the lack of macroscale phase separation in annealed copolymer/$PC_{71}BM$ thin films indicates that the copolymer likely stabilizes the blends by preventing $PC_{71}BM$ aggregation. Taken together, these results suggest that the copolymer could be a general additive for stabilizing donor-$PC_{71}BM$ blends.

To investigate the copolymer's impact on OPV device performance, we fabricated devices with and without the copolymer for the PffBT4T-2OD:$PC_{71}BM$ blend (Appendix 2, pp 257–258). This blend was chosen because it exhibited the most dramatic reduction in micron-scale aggregates when annealed with the copolymer in the thin film studies (cf. Figures 4.1 and 4.2). An inverted device architecture (glass/ITO/ZnO/polymer blend/MoO_3/Ag, Appendix 2, Figure A2.44) was used because it enables higher PCE than a conventional architecture.[80] The polymer blend was prepared by spin-casting a PffBT4T-2OD:$PC_{71}BM$ solution with or without 8 wt% of the copolymer additive to achieve a final thickness of 215 ± 10 nm, where the weight ratio of

polymer(s):$PC_{71}BM$ was 1.0:1.2.[81] Photovoltaic measurements were performed under simulated AM 1.5G conditions both before and after annealing. Each data point represents an average of six measurements obtained from three different devices fabricated on two different substrates. Devices with the copolymer exhibited an initial PCE of 6.0 ± 0.2 % while devices without copolymer showed an initial PCE of 9.3 ± 0.2% (Table 4.2).

Table 4.2 The power conversion efficiency (PCE), fill factor (*FF*), open circuit voltage (V_{OC}), and short circuit current (J_{SC}) for PffBT4T-2OD:$PC_{71}BM$ devices with 0 wt% and 8 wt% copolymer.

copolymer (wt%)	PCE (%)	FF	J_{SC} (mA/cm^2)	V_{OC} (V)
0	9.3 ± 0.2	0.7 ± 0.0	18.3 ± 0.3	0.7 ± 0.0
8	6.0 ± 0.2	0.6 ± 0.0	14.4 ± 0.7	0.7 ± 0.0

Before studying the thermal stability of devices with or without copolymer, we investigated the discrepancy in the initial PCE between the two types of blends. The open-circuit voltage (V_{OC}) was similar with or without the copolymer but the fill factor (*FF*) and the short circuit current (J_{SC}) both decreased with copolymer addition. Both of these parameters depend on the absorption efficiency, therefore the lower performance with the copolymer could be due a reduction in absorption. Indeed, the UV spectrum for the blend containing copolymer exhibited lower overall absorption than the blend without the copolymer (Figure 4.3A (corrected for film thickness) and Appendix 2, Figure A2.50B (uncorrected)), presumably due to the lower molar absorptivity of the copolymer, the lower concentration of PffBT4T-2OD in the blend, and a slightly reduced film thickness with the copolymer (146 ± 2 nm) than without (156.4 ± 0.6 nm). The lower initial PCE with the copolymer additive is not likely due to changes in charge separation efficiency because the bandgap of the copolymer is intermediate between that of PffBT4T-2OD and $PC_{71}BM$ (Appendix 2, Figure A2.43). Instead, the lower initial PCE with the copolymer additive could also

be due to a reduction in charge mobility. To test this hypothesis, triboindentation was used to measure the electron current in the active layer (50 nm depth) for films with and without the copolymer (Figure 3B and Appendix 2, Figure A2.44). These studies revealed that the copolymer-containing active layer had lower electron current, suggesting that the copolymer impedes current when localized in or near the $PC_{71}BM$ phase. In addition to these factors, differences in the initial nanoscale morphology might also lead to differences in the initial PCE with or without the copolymer. However, energy-filtered transmission electron microscopy revealed qualitatively similar nanoscale morphologies for unannealed films with and without the copolymer (Appendix 2, Figure A.251). Taken together, these data suggest that a lower absorption efficiency along with reduced electron mobility, rather than changes in nanoscale morphology, led to the lower initial PCE with copolymer addition.

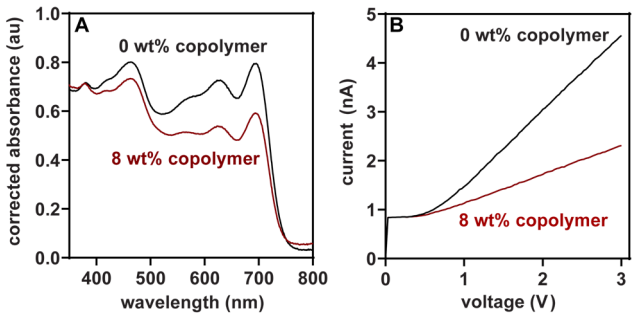

Figure 4.3 (A) UV-vis spectra of thin films with 0% (black) and 8 wt% (red) copolymer, adjusted to account for differences in film thickness. (The uncorrected spectra can be found in Appendix 2, Figure A2.50.) (B) Plot of electron current versus voltage for devices with 0% (black) and 8 wt% (red) copolymer.

To evaluate device stability over time, thermal studies were performed by annealing the devices at 200 °C before MoO_3/Ag deposition. Based on our thin-film studies, we expected that the devices containing the copolymer additive would have better thermal stability over time than devices without the copolymer. However, both samples exhibited lower PCEs after annealing for 90 min at 200 °C. Optical microscope images revealed that both samples underwent significant

macroscale phase separation during annealing (Appendix, Figure A2.47). To attenuate this effect, we reduced the annealing temperature to 150 °C to better quantify the impact of the copolymer additive over time. After annealing for 30 min, the PCE for devices without copolymer dropped significantly (from 9.3 ± 0.2% to 2.6 ± 0.2%, Figure 4A). In contrast, the PCE for devices with the copolymer underwent a much smaller decrease (from 6.0 ± 0.2 % to 2.9 ± 0.2%). After annealing at 180 min, the devices without copolymer fully degraded and were unmeasurable while devices with the copolymer maintained a PCE of 3.2 ± 0.4%.

The biggest difference in parameters between the two types of devices were in the V_{OC} changes over time; more specifically, the V_{OC} in the device without copolymer dropped steadily while copolymer-containing device showed minimal changes even at 180 min (Figure 4.4B). Additionally, optical microscopy images showed macroscale aggregates in the devices without copolymer (80 area%) while the copolymer-containing devices had no observable macroscale phase separation after annealing for 180 min (Figure 4.4D). These data suggest that the phase separation observed in devices without the copolymer likely facilitates charge recombination leading to a reduced V_{OC},[82,83] which is supported by the smaller shunt resistance of the annealed devices without the copolymer (Appendix 2, Figure A2.46F, Table A2.15). In contrast, devices with the copolymer maintain their V_{OC} and shunt resistance during annealing.[84] Combined, these data suggest that the copolymer additive prevents macroscale phase separation resulting better stability in V_{OC} of the OPV devices.

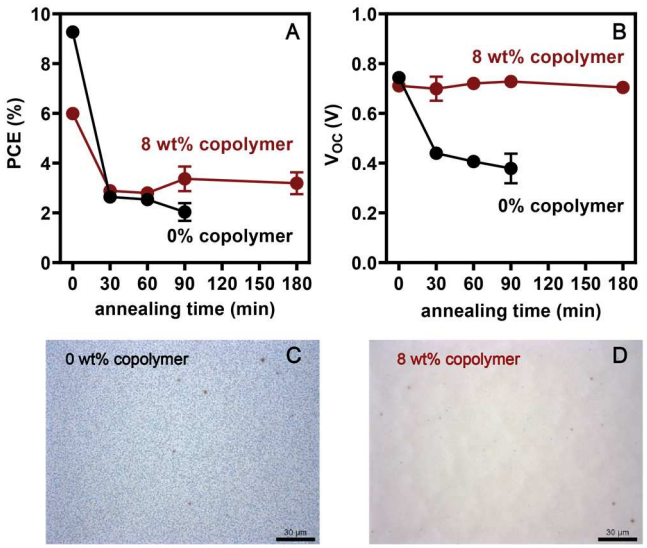

Figure 4.4 Plots of the (A) power conversion efficiency (PCE) and (B) open-circuit voltage (V_{OC}) for the PffBT4T-2OD:$PC_{71}BM$ OPV devices during annealing at 150 °C with 0 wt% (black) or 8 wt% (red) copolymer. Optical microscope images of unmasked portions of the PffBT4T-2OD:$PC_{71}BM$ OPV devices after 180 min of annealing at 150 °C with (C) 0 wt% or (D) 8 wt% copolymer. Scale bars represent 30 μm.

4.3 Conclusion

In this work, we employ a fullerene-functionalized P3HT copolymer additive to stabilize the morphology for blends of three different donor polymers (PTB7, PTB7-Th, and PffBT4T-2OD) with $PC_{71}BM$. In all thin film blends, micron-scale aggregation was reduced when the copolymer was added, suggesting that the copolymer may be a general stabilizing additive. Based on surface energy analysis, the copolymer likely exhibits favorable miscibility with $PC_{71}BM$, rather than being interfacially active, and inhibits $PC_{71}BM$ aggregation upon thermal annealing. When the copolymer was added to PffBT4T-2OD:$PC_{71}BM$ devices, however, lower initial power conversion efficiencies were observed, due to reduced absorption and electron current. For annealed devices, the PCE decreased with increasing annealing time regardless of copolymer addition, although the relative PCE loss was smaller for devices with the copolymer. Furthermore, micron-scale aggregates only formed in devices without the copolymer after 180 min of annealing. Combined, these results suggest that the copolymer could be used as a general additive to stabilize

the morphology of donor/acceptor blends and, when used, other factors besides morphology impact device performance.

4.4 References

[1] Riede, M.; Spoltore, D.; Leo, K. Organic Solar Cells—The Path to Commercial Success. *Adv. Energy Mater.* **2021**, *11*, 2002653.

[2] Li, Y.; Xu, G.; Cui, C.; Li, Y. Flexible and Semitransparent Organic Solar Cells. *Adv. Energy Mater.* **2018**, *8*, 1701791.

[3] Wang, Q.; Xie, Y.; Soltani-Kordshuli, F.; Eslamian, M. Progress in Emerging Solution-Processed Thin Film Solar Cells - Part I: Polymer Solar Cells. *Renew. Sustain. Energy Rev.* **2016**, *56*, 347–361.

[4] Guo, J.; Min, J. A Cost Analysis of Fully Solution-Processed ITO-Free Organic Solar Modules. *Adv. Energy Mater.* **2019**, *9*, 1802521.

[5] Lu, L.; Zheng, T.; Wu, Q.; Schneider, A. M.; Zhao, D.; Yu, L. Recent Advances in Bulk Heterojunction Polymer Solar Cells. *Chem. Rev.* **2015**, *115*, 12666–12731.

[6] Wadsworth, A.; Hamid, Z.; Bidwell, M.; Ashraf, R. S.; Khan, J. I.; Anjum, D. H.; Cendra, C.; Yan, J.; Rezasoltani, E.; Guilbert, A. A. Y.; Azzouzi, M.; Gasparini, N.; Bannock, J. H.; Baran, D.; Wu, H.; de Mello, J. C.; Brabec, C. J.; Salleo, A.; Nelson, J.; Laquai, F.; McCulloch, I. Progress in Poly (3-Hexylthiophene) Organic Solar Cells and the Influence of Its Molecular Weight on Device Performance. *Adv. Energy Mater.* **2018**, *8*, 1801001.

[7] Dang, M. T.; Hirsch, L.; Wantz, G. P3HT:PCBM, Best Seller in Polymer Photovoltaic Research. *Adv. Mater.* **2011**, *23*, 3597–3602.

[8] Holliday, S.; Li, Y.; Luscombe, C. K. Recent Advances in High Performance Donor-Acceptor Polymers for Organic Photovoltaics. *Prog. Polym. Sci.* **2017**, *70*, 34–51.

[9] Hou, J.; Park, M. H.; Zhang, S.; Yao, Y.; Chen, L. M.; Li, J. H.; Yang. Bandgap and Molecular Energy Level Control of Conjugated Polymer Photovoltaic Materials Based on Benzo[l,2-b:4,5-B′]Dithiophene. *Macromolecules* **2008**, *41*, 6012–6018.

[10] National Renewable Energy Lab, Best Research-Cell Efficiencies, https://www.nrel.gov/pv/assets/images/efficiency-chart.png (accessed: February 2021).

[11] Green, M.; Dunlop, E.; Hohl-Ebinger, J.; Yoshita, M.; Kopidakis, N.; Hao, X. Solar Cell Efficiency Tables (Version 57). *Prog. Photovoltaics Res. Appl.* **2021**, *29*, 3–15.

[12] Meng, L.; Zhang, Y.; Wan, X.; Li, C.; Zhang, X.; Wang, Y.; Ke, X.; Xiao, Z.; Ding, L.; Xia, R.; Yip, H. L.; Cao, Y.; Chen, Y. Organic and Solution-Processed Tandem Solar Cells with 17.3% Efficiency. *Science* **2018**, *361*, 1094–1098.

[13] Cui, Y.; Yao, H.; Zhang, J.; Xian, K.; Zhang, T.; Hong, L.; Wang, Y.; Xu, Y.; Ma, K.; An, C.; He, C.; Wei, Z.; Gao, F.; Hou, J. Single-Junction Organic Photovoltaic Cells with Approaching 18% Efficiency. *Adv. Mater.* **2020**, *32*, 1908205.

[14] Liu, Q.; Jiang, Y.; Jin, K.; Qin, J.; Xu, J.; Li, W.; Xiong, J.; Liu, J.; Xiao, Z.; Sun, K.; Yang, S.; Zhang, X.; Ding, L. 18% Efficiency Organic Solar Cells. *Sci. Bull.* **2020**, *65*, 272–275.

[15] Turak, A. Device Stability in Organic Optoelectronics. In *Handbook of Organic Materials for Electronic and Photonic Devices (2nd Ed.)*; Elsevier, **2019**, 599–662.

[16] Treat, N. D.; Chabinyc, M. L. Phase Separation in Bulk Heterojunctions of Semiconducting Polymers and Fullerenes for Photovoltaics. Annu. Rev. Phys. Chem. 2014, 65, 59–81.

[17] Yu, G.; Gao, J.; Hummelen, J. C.; Wudl, F.; Heeger, A. J. Polymer Photovoltaic Cells: Enhanced Efficiencies via a Network of Internal Donor-Acceptor Heterojunctions. *Science.* **1995**, *270*, 1789-1791.

[18] Shaw, P. E.; Ruseckas, A.; Samuel, I. D. W. Exciton Diffusion Measurements in Poly(3-Hexylthiophene). *Adv. Mater.* **2008**, *20*, 3516–3520.

[19] Hedley, G. J.; Ward, A. J.; Alekseev, A.; Howells, C. T.; Martins, E. R.; Serrano, L. A.; Cooke, G.; Ruseckas, A.; Samuel, I. D. W. Determining the Optimum Morphology in High-Performance Polymer-Fullerene Organic Photovoltaic Cells. *Nat. Commun.* **2013**, *4*, 2867.

[20] Cardinaletti, I.; Kesters, J.; Bertho, S.; Conings, B.; Piersimoni, F.; D'Haen, J.; Lutsen, L.; Nesladek, M.; Van Mele, B.; Van Assche, G.; Vandewal, K.; Salleo, A.; Vanderzande, D.; Maes, W.; Manca, J. V. Toward Bulk Heterojunction Polymer Solar Cells with Thermally Stable Active Layer Morphology. *J. Photonics Energy* **2014**, *4*, 040997.

[21] Savagatrup, S.; Printz, A. D.; O'Connor, T. F.; Zaretski, A. V.; Rodriquez, D.; Sawyer, E. J.; Rajan, K. M.; Acosta, R. I.; Root, S. E.; Lipomi, D. J. Mechanical Degradation and Stability of Organic Solar Cells: Molecular and Microstructural Determinants. *Energy Environ. Sci.* **2015**, *8*, 55–80.

[22] Kronholm, D. F.; Hummelen, J. C. Fullerene-Based Acceptor Materials. In *Organic Photovoltaics*; Wiley-VCH Verlag GmbH & Co. KGaA: Weinheim, Germany, **2009**, 153–178.

[23] Bonasera, A.; Giuliano, G.; Arrabito, G.; Pignataro, B. Tackling Performance Challenges in Organic Photovoltaics: An Overview about Compatibilizers. *Molecules* **2020**, *25*, 1–40.

[24] P. Cheng, X. Zhan. Versatile Third Components for Efficient and Stable Organic Solar Cells. *Mater. Horiz.* **2015**, *2*, 462–485.

[25] Di Lorenzo, M. L.; Frigione, M. Compatibilization Criteria and Procedures for Binary Blends: A Review. *J. Polym. Eng.* **1997**, *17*, 429–460.

[26] Koning, C.; Van Duin, M.; Pagnoulle, C.; Jerome, R. Strategies for Compatibilization of Polymer Blends. *Prog. Polym. Sci.* **1998**, *23*, 707–757.

[27] Wang, H.; Yang, L.; Lin, P.; Chueh, C.; Liu, X.; Qu, S.; Guang, S.; Yu, J.; Tang, W. A Simple Dithieno[3,2-b:2′,3′-d]Pyrrol-Rhodanine Molecular Third Component Enables Over 16.7% Efficiency and Stable Organic Solar Cells. *Small* **2021**, ASAP.

[28] Liu, L.; Zhang, H.; Xiao, B.; Liu, Y.; Xu, B.; Wang, C.; Wen, S.; Zhou, E.; Chen, G.; Im, C.; Tian, W. Effects of BTA2 as the Third Component on the Charge Carrier Generation and Recombination Behavior of PTB7:$PC_{71}BM$ Photovoltaic System. *Front. Chem. Sci. Eng.* **2021**. 15, 127-137.

[29] Xu, B.; Sai-Anand, G.; Unni, G. E.; Jeong, H. M.; Kim, J. S.; Kim, S. W.; Kwon, J. B.; Bae, J. H.; Kang, S. W. Pyridine-Based Additive Optimized P3HT:$PC_{61}BM$ Nanomorphology for Improved Performance and Stability in Polymer Solar Cells. *Appl. Surf. Sci.* **2019**, *484*, 825–834.

[30] Xiao, M.; Zhang, K.; Jin, Y.; Yin, Q.; Zhong, W.; Huang, F.; Cao, Y. Low Temperature Processed High-Performance Thick Film Ternary Polymer Solar Cell with Enhanced Stability. *Nano Energy* **2018**, *48*, 53–62.

[31] Cheng, P.; Yan, C.; Lau, T.-K.; Mai, J.; Lu, X.; Zhan, X. Molecular Lock: A Versatile Key to Enhance Efficiency and Stability of Organic Solar Cells. *Adv. Mater.* **2016**, *28*, 5822–5829.

[32] Sivula, K.; Ball, Z. T.; Watanabe, N.; Fréchet, J. M. J. Amphiphilic Diblock Copolymer Compatibilizers and Their Effect on the Morphology and Performance of Polythiophene:Fullerene Solar Cells. *Adv. Mater.* **2006**, *18*, 206–210. https://doi.org/10.1002/adma.200501787

[33] Yang, C.; Lee, J. K.; Heeger, A. J.; Wudl, F. Well-Defined Donor-Acceptor Rod-Coil Diblock Copolymers Based on P3HT Containing C60: The Morphology and Role as a Surfactant in Bulk-Heterojunction Solar Cells. *J. Mater. Chem.* **2009**, *19*, 5416–5423. https://doi.org/10.1039/b901732a

[34] Lee, J. U.; Jung, J. W.; Emrick, T.; Russell, T. P.; Jo, W. H. Morphology Control of a Polythiophene-Fullerene Bulk Heterojunction for Enhancement of the High-Temperature Stability of Solar Cell Performance by a New Donor-Acceptor Diblock Copolymer. *Nanotechnology* **2010**, *21*, 105201. https://doi.org/10.1088/0957-4484/21/10/105201

[35] Kipp, D.; Verduzco, R.; Ganesan, V. Block Copolymer Compatibilizers for Ternary Blend Polymer Bulk Heterojunction Solar Cells-an Opportunity for Computation Aided Molecular Design. *Molecular Systems Design and Engineering*. Royal Society of Chemistry November 28, 2016, pp 353–369.

[36] Wang, M.; Sun, J.; Cai, X.; Huang, Y.; Li, F. Morphology Modulation of Organic Photovoltaics with Block Copolymer Additive Based on Rational Design Strategies. *Org. Electron.* **2021**, *88*, 106020.

[37] Li, Z.; Yan, L.; Shan, J.; Gu, H.; Lin, Y.; Wang, Y.; Tan, H.; Ma, C.-Q. Organic Amines as Targeting Stabilizer at the Polymer/Fullerene Interface for Polymer:PC $_{61}$ BM Solar Cells. *Energy Technol.* **2020**, *8*, 2000266.

[38] Su, Y.-A.; Maebayashi, N.; Fujita, H.; Lin, Y.-C.; Chen, C.-I.; Chen, W.-C.; Michinobu, T.; Chueh, C.-C.; Higashihara, T. Development of Block Copolymers with Poly(3-Hexylthiophene) Segments as Compatibilizers in Non-Fullerene Organic Solar Cells. *ACS Appl. Mater. Interfaces* **2020**, *12*, 12083–12092.

[39] Seibers, Z. D.; Collier, G. S.; Hopkins, B. W.; Boone, E. S.; Le, T. P.; Gomez, E. D.; Kilbey, S. M. Tuning Fullerene Miscibility with Porphyrin-Terminated P3HTs in Bulk Heterojunction Blends. *Soft Matter* **2020**, *16*, 9769–9779.

[40] Saito, M.; Tamai, Y.; Ichikawa, H.; Yoshida, H.; Yokoyama, D.; Ohkita, H.; Osaka, I. Significantly Sensitized Ternary Blend Polymer Solar Cells with a Very Small Content of the Narrow-Band Gap Third Component That Utilizes Optical Interference. *Macromolecules* **2020**. 53, 10623-10635.

[41] Yang, T.; Ma, R.; Cheng, H.; Xiao, Y.; Luo, Z.; Chen, Y.; Luo, S.; Liu, T.; Lu, X.; Yan, H. A Compatible Polymer Acceptor Enables Efficient and Stable Organic Solar Cells as a Solid Additive. *J. Mater. Chem. A.* **2020**, *8*, 17706–17712.

[42] Yang, D.; Cao, B.; Körstgens, V.; Saxena, N.; Li, N.; Bilko, C.; Grott, S.; Chen, W.; Jiang, X.; Heger, J. E.; Bernstorff, S.; Müller-Buschbaum, P. Tailoring Morphology Compatibility and Device Stability by Adding PBDTTPD-COOH as Third Component to Fullerene-Based Polymer Solar Cells. *ACS Appl. Energy Mater.* **2020**, *3*, 2604–2613.

[43] Kong, C.; Song, B.; Mueller, E. A.; Kim, J.; McNeil, A. J. Random Copolymers Outperform Gradient and Block Copolymers in Stabilizing Organic Photovoltaics. *Adv. Funct. Mater.* **2019**, *29*, 1900467.

[44] Lutz, J. P.; Hannigan, M. D.; McNeil, A. J. Polymers Synthesized via Catalyst-Transfer Polymerization and Their Applications. *Coord. Chem. Rev.* **2018**, *376*, 225–247.

[45] Liang, Y.; Xu, Z.; Xia, J.; Tsai, S.-T.; Wu, Y.; Li, G.; Ray, C.; Yu, L. For the Bright Future-Bulk Heterojunction Polymer Solar Cells with Power Conversion Efficiency of 7.4%. *Adv. Mater.* **2010**, *22*, E135–E138.

[46] Liao, S.-H.; Jhuo, H.-J.; Cheng, Y.-S.; Chen, S.-A. Fullerene Derivative-Doped Zinc Oxide Nanofilm as the Cathode of Inverted Polymer Solar Cells with Low-Bandgap Polymer (PTB7-Th) for High Performance. *Adv. Mater.* **2013**, *25*, 4766–4771.

[47] Liu, Y.; Zhao, J.; Li, Z.; Mu, C.; Ma, W.; Hu, H.; Jiang, K.; Lin, H.; Ade, H.; Yan, H. Aggregation and Morphology Control Enables Multiple Cases of High-Efficiency Polymer Solar Cells. *Nat. Commun.* **2014**, *5*, 5293.

[48] Ouyang, X.; Peng, R.; Ai, L.; Zhang, X.; Ge, Z. Efficient Polymer Solar Cells Employing a Non-Conjugated Small-Molecule Electrolyte. *Nat. Photonics* **2015**, *9*, 520–524.

[49] Huang, J.; Carpenter, J. H.; Li, C.-Z.; Yu, J.-S.; Ade, H.; Jen, A. K.-Y. Highly Efficient Organic Solar Cells with Improved Vertical Donor-Acceptor Compositional Gradient Via an Inverted Off-Center Spinning Method. *Adv. Mater.* **2016**, *28*, 967–974.

[50] Yan, Y.; Li, W.; Cai, F.; Cai, J.; Huang, Z.; Gurney, R. S.; Liu, D.; Lidzey, D. G.; Pearson, A. J.; Wang, T. Correlating Nanoscale Morphology with Device Performance in Conventional and Inverted PffBT4T-2OD:$PC_{71}BM$ Polymer Solar Cells. *ACS Appl. Energy Mater.* **2018**, *1*, 3505–3512.

[51] Campoy-Quiles, M.; Ferenczi, T.; Agostinelli, T.; Etchegoin, P. G.; Kim, Y.; Anthopoulos, T. D.; Stavrinou, P. N.; Bradley, D. D. C.; Nelson, J. Morphology Evolution via Self-Organization and Lateral and Vertical Diffusion in Polymer:Fullerene Solar Cell Blends. *Nat. Mater.* **2008,** 7, 158–164.

[52] Hammond, M. R.; Kline, R. J.; Herzing, A. A.; Richter, L. J.; Germack, D. S.; Ro, H. W.; Soles, C. L.; Fischer, D. A.; Xu, T.; Yu, L.; Toney, M. F.; Delongchamp, D. M. Molecular Order in High-Efficiency Polymer/Fullerene Bulk Heterojunction Solar Cells. *ACS Nano* **2011**, *5*, 8248–8257.

[53] Collins, B. A.; Li, Z.; Tumbleston, J. R.; Gann, E.; Mcneill, C. R.; Ade, H. Absolute Measurement of Domain Composition and Nanoscale Size Distribution Explains Performance in PTB7:$PC_{71}BM$ Solar Cells. *Adv. Energy Mater.* **2013**, *3* (1), 65–74.

[54] Dkhil, S. Ben; Pfannmöller, M.; Saba, M. I.; Gaceur, M.; Heidari, H.; Videlot-Ackermann, C.; Margeat, O.; Guerrero, A.; Bisquert, J.; Garcia-Belmonte, G.; Mattoni, A.; Bals, S.; Ackermann, J. Toward High-Temperature Stability of PTB7-Based Bulk Heterojunction Solar Cells: Impact of Fullerene Size and Solvent Additive. *Adv. Energy Mater.* **2017**, *7*, 1601486.

[55] Lou, S. J.; Szarko, J. M.; Xu, T.; Yu, L.; Marks, T. J.; Chen, L. X. Effects of Additives on the Morphology of Solution Phase Aggregates Formed by Active Layer Components of High-Efficiency Organic Solar Cells. *J. Am. Chem. Soc.* **2011**, *133*, 20661–20663.

[56] Song, X.; Gasparini, N.; Baran, D. The Influence of Solvent Additive on Polymer Solar Cells Employing Fullerene and Non-Fullerene Acceptors. *Adv. Electron. Mater.* **2018**, *4*, 1700358.

[57] Zhang, Y.; Parnell, A. J.; Pontecchiani, F.; Cooper, J. F. K.; Thompson, R. L.; Jones, R. A. L.; King, S. M.; Lidzey, D. G.; Bernardo, G. Understanding and Controlling Morphology Evolution via DIO Plasticization in PffBT4T-2OD/$PC_{71}BM$ Devices. *Sci. Rep.* **2017**, *7*, 44269.

[58] Landerer, D.; Mertens, A.; Freis, D.; Droll, R.; Leonhard, T.; Schulz, A. D.; Bahro, D.; Colsmann, A. Enhanced Thermal Stability of Organic Solar Cells Comprising Ternary D-D-A Bulk-Heterojunctions. *npj Flex. Electron.* **2017**, *1*, 11.

[59] Gao, M.; Liang, Z.; Geng, Y.; Ye, L. Significance of Thermodynamic Interaction Parameters in Guiding the Optimization of Polymer:Nonfullerene Solar Cells. Chem. Commun. 2020, 56, 12463–12478.

[60] Kim, J. S.; Lee, Y.; Lee, J. H.; Park, J. H.; Kim, J. K.; Cho, K. High-Efficiency Organic Solar Cells Based on End-Functional-Group-Modified Poly(3-Hexylthiophene). Adv. Mater. 2010, 22, 1355–1360.

[61] Liu, Y.; Tang, D.; Zhang, K.; Huang, P.; Wang, Z.; Zhu, K.; Li, Z.; Yuan, L.; Fan, J.; Zhou, Y.; Song, B. Tuning Surface Energy of Conjugated Polymers via Fluorine Substitution of Side Alkyl Chains: Influence on Phase Separation of Thin Films and Performance of Polymer Solar Cells. ACS Omega 2017, 2, 2489–2498.

[62] Sun, Y.; Chien, S. C.; Yip, H. L.; Chen, K. S.; Zhang, Y.; Davies, J. A.; Chen, F. C.; Lin, B.; Jen, A. K. Y. Improved Thin Film Morphology and Bulk-Heterojunction Solar Cell Performance through Systematic Tuning of the Surface Energy of Conjugated Polymers. J. Mater. Chem. 2012, 22, 5587–5595.

[63] Shimizu, R. N.; Demarquette, N. R. Evaluation of Surface Energy of Solid Polymers Using Different Models. J. Appl. Poly. Sci. 2000, 76, 1831–1845.

[64] Ohori, Y.; Fujii, S.; Kataura, H.; Nishioka, Y. Improvement of Bulk Heterojunction Organic Solar Cells Based on PTB7:PC61BM with Small Amounts of P3HT. Jpn. J. Appl. Phys. 2015, 54, 04DK09.

[65] Wang, C.; Zhang, W.; Meng, X.; Bergqvist, J.; Liu, X.; Genene, Z.; Xu, X.; Yartsev, A.; Inganäs, O.; Ma, W.; Wang, E.; Fahlman, M. Ternary Organic Solar Cells with Minimum Voltage Losses. Adv. Energy Mater. 2017, 7, 1700390.

[66] Li, W.; Cai, J.; Cai, F.; Yan, Y.; Yi, H.; Gurney, R. S.; Liu, D.; Iraqi, A.; Wang, T. Achieving over 11% Power Conversion Efficiency in PffBT4T-2OD-Based Ternary Polymer Solar Cells with Enhanced Open-Circuit-Voltage and Suppressed Charge Recombination. Nano Energy 2018, 44, 155–163.

[67] Clark, M. D.; Jespersen, M. L.; Patel, R. J.; Leever, B. J. Predicting Vertical Phase Segregation in Polymer-Fullerene Bulk Heterojunction Solar Cells by Free Energy Analysis. *ACS Appl. Mater. Interfaces* **2013**, *5*, 4799–4807.

[68] Nilsson, S.; Bernasik, A.; Budkowski, A.; Moons, E. Morphology and Phase Segregation of Spin-Casted Films of Polyfluorene/PCBM Blends. *Macromolecules* **2007**, *40*, 8291–8301.

[69] Sumita, M.; Sakata, K.; Asai, S.; Miyasaka, K.; Nakagawa, H. Dispersion of Fillers and the Electrical Conductivity of Polymer Blends Filled with Carbon Black. *Polym. Bull.* **1991**, *25*, 265–271.

[70] Lindqvist, C.; Bergqvist, J.; Feng, C.-C.; Gustafsson, S.; Bäcke, O.; Treat, N. D.; Bounioux, C.; Henriksson, P.; Kroon, R.; Wang, E.; Sanz-Velasco, A.; Kristiansen, P. M.; Stingelin, N.; Olsson, E.; Inganäs, O.; Andersson, M. R.; Müller, C. Fullerene Nucleating Agents: A Route Towards Thermally Stable Photovoltaic Blends. *Adv. Energy Mater.* **2014**, *4*, 1301437.

[71] Lindqvist, C.; Sanz-Velasco, A.; Wang, E.; Bäcke, O.; Gustafsson, S.; Olsson, E.; Andersson, M. R.; Müller, C. Nucleation-Limited Fullerene Crystallisation in a Polymer-Fullerene Bulk-Heterojunction Blend. *J. Mater. Chem. A* **2013**, *1*, 7174–7180.

[72] Richards, J. J.; Rice, A. H.; Nelson, R. D.; Kim, F. S.; Jenekhe, S. A.; Luscombe, C. K.; Pozzo, D. C. Modification of PCBM Crystallization via Incorporation of C_{60} in Polymer/Fullerene Solar Cells. *Adv. Funct. Mater*. **2013**, *23*, 514–522.

[73] Dowland, S. A.; Salvador, M.; Perea, J. D.; Gasparini, N.; Langner, S.; Rajoelson, S.; Ramanitra, H. H.; Lindner, B. D.; Osvet, A.; Brabec, C. J.; Hiorns, R. C.; Egelhaaf, H. J. Suppression of Thermally Induced Fullerene Aggregation in Polyfullerene-Based Multiacceptor Organic Solar Cells. *ACS Appl. Mater. Interfaces* **2017**, *9*, 10971–10982.

[74] Ramanitra, H. H.; Dowland, S. A.; Bregadiolli, B. A.; Salvador, M.; Santos Silva, H.; Bégué, D.; Graeff, C. F. O.; Peisert, H.; Chassé, T.; Rajoelson, S.; Osvet, A.; Brabec, C. J.; Egelhaaf, H. J.; Morse, G. E.; Distler, A.; Hiorns, R. C. Increased Thermal Stabilization of Polymer Photovoltaic Cells with Oligomeric PCBM. *J. Mater. Chem. C* **2016**, *4*, 8121–8129.

[75] Wong, H. C.; Li, Z.; Tan, C. H.; Zhong, H.; Huang, Z.; Bronstein, H.; McCulloch, I.; Cabral, J. T.; Durrant, J. R. Morphological Stability and Performance of Polymer-Fullerene Solar Cells under Thermal Stress: The Impact of Photoinduced PC60BM Oligomerization. *ACS Nano* **2014**, *8*, 1297–1308.

[76] Li, Q.; Wang, L. M.; Liu, S.; Zhan, X.; Zhu, T.; Cao, Z.; Lai, H.; Zhao, J.; Cai, Y.; Xie, W.; Huang, F. Impact of Donor-Acceptor Interaction and Solvent Additive on the Vertical Composition Distribution of Bulk Heterojunction Polymer Solar Cells. *ACS Appl. Mater. Interfaces* **2019**, *11*, 45979–45990.

[77] Khlyabich, P. P.; Rudenko, A. E.; Thompson, B. C.; Loo, Y. L. Structural Origins for Tunable Open-Circuit Voltage in Ternary-Blend Organic Solar Cells. *Adv. Funct. Mater.* **2015**, *25*, 5557–5563.

[78] Flory, P. J. *Principles of Polymer Chemistry*. Cornell University Press: Ithaca, NY, 1953.

[79] Rubinstein, M.; Colby, R. H. "Thermodynamics of Mixing," *Polymer Physics*. Oxford University Press: New York, NY, **2003**, 137–170.

[80] He, Z.; Zhong, C.; Su, S.; Xu, M.; Wu, H.; Cao, Y. Enhanced power-conversion efficiency in polymer solar cells using an inverted device structure. *Nature Photonics* **2012**, *6*, 591–595.

[81] Wang, T.; Brédas, J.-L. Organic Photovoltaics: Understanding the Preaggregation of Polymer Donors in Solution and Its Morphological Impact. *J. Am. Chem. Soc.* **2021**, 143, 1822–1835.

[82] Kim, B.-G.; Jeong, E. J.; Park, H. J.; Bilby, D.; Guo, L. J.; Kim, J. Effect of Polymer Aggregation on the Open Circuit Voltage in Organic Photovoltaic Cells: Aggregation-induced Conjugated Polymer Gel and its Application for Preventing Open Circuit Voltage Drop. *ACS Appl. Mater. Interfaces* **2009**, 3, 674–680.

[83] Vandewal, K.; Tvingstedt, K.; Gadisa, A.; Inganäs, O.; Manca, J. V. On the Origin of the Open-Circuit Voltage of Polymer-Fullerene Solar Cells. *Nature Mater.* **2009**, 8, 904–909.

[84] Kim, M. S.; Kim, B. G.; Kim, J. The Effective Variables to Control the Fill Factor of Organic Photovoltaic Cells. *ACS Appl. Mater. Interfaces* **2009**, 1, 1264–1629.

Chapter 5 Evaluating the Degree of Unsaturation Needed for Alkane Metathesis-Cyclodepolymerization of Polyethylene

5.1 Introduction

Polyethylene (PE) is produced on the largest scale of any commodity polymer world-wide.[1] The largest demand for PE-based consumer products is for packaging, most of which is discarded after a single use into landfills or incinerators.[1,2] The consequences of the current model for plastic production and use are 1) a dependence on fossil fuel feedstocks and 2) thousands of tons of plastic waste entering the natural environment, where the plastic breaks down into microplastics that can harm microorganism, animal, and human health.[3,4]

Mechanical recycling is one strategy to divert PE waste from entering the natural environment, but little PE waste (e.g., 6.2% of combined HDPE and LDPE waste in the US from 2018)[5] is recycled this way because of several key limitations. For mechanical recycling the PE is collected, sorted from other polymers, washed to remove contaminants, physically ground into small pieces, and melt reprocessed to form new products.[6] Difficulties in separating polymers, including high- versus low-density PE, and in removing additives and contaminants prevent recycled materials from having comparable physical properties to pristine materials.[6,7] Another challenge is that the physical process of grinding and melt-reprocessing can induce chain scission, which reduces the PE melt-flow index and makes it more difficult to process.[8,9,10] Thus, new recycling methods are needed to improve both recycling rates and the quality of recycled PE.

A more sustainable option would be to treat PE waste as a valuable feedstock and to chemically repurpose it. The most common way to chemically repurpose PE is via pyrolysis, which converts long-chain polymers into shorter solid, liquid, and/or gaseous alkanes with heat and catalysts (e.g., zeolites and/or Lewis acids).[11] Hydrogenolysis is a similar process to break down PE, but under an H_2 atmosphere.[12] With the exception of a few recent reports that employ Pt catalysts,[13,14] pyrolysis and hydrogenolysis are usually energy intensive, requiring temperatures ≥ 300 °C.[11] Another drawback of this process is that a complex mixture of products is formed, which would require purification before entering the market.[11]

Alkane metathesis is an alternate strategy that to transform PE into short-chain alkanes at lower temperatures than pyrolysis (e.g., 125 °C).[15] In alkane metathesis, the substrate is dehydrogenated to form alkenes which then undergo olefin cross metathesis followed by re-hydrogenation. Alkane metathesis was originally reported by Burnett and Hughes using heterogeneous Pt and W catalysts in tandem at 425 °C for dehydrogenation and olefin metathesis, respectively.[16] Later work developed by Basset and coworkers used a single solid-supported Ta or W hydride catalyst, each of which can perform both dehydrogenation and olefin metathesis reactions.[17] Most recently, homogeneous Ir "pincer" catalysts have been used to perform dehydrogenation reactions in tandem with either homogeneous Mo-alkylidene or heterogeneous Re-oxide catalysts that perform olefin metathesis.[18,19] The third method has been used to depolymerize PE, including commercial PE sources like disposable shopping bags, in the presence of excess n-hexane.[20] The depolymerization produced a mixture of short- to medium-length linear alkenes, similar to pyrolysis products, but obtained at 125 °C (Scheme 5.1, top).

Scheme 5.1 Alkane metathesis with n-hexane to transform PE into short-chain alkanes (top),[20] and alkane metathesis and cyclodepolymerization to transform PE into macrocycles (bottom).

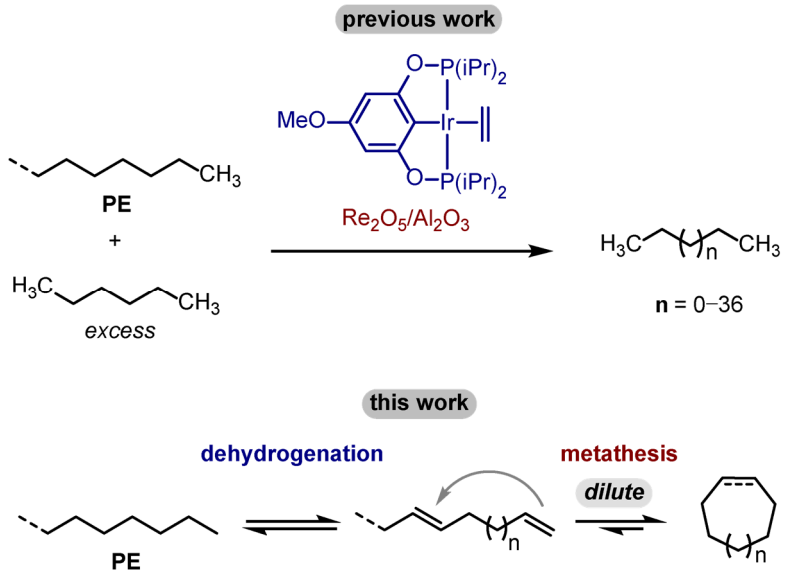

Instead of degrading PE by pairing it with excess short alkanes, we hypothesized that we could take advantage of ring-chain equilibria to induce backbiting reactions between dehydrogenated repeat units and/or chain ends to form macrocyclic alkenes (Scheme 5.1, bottom). The theory to describe the equilibrium distribution of macrocyclic and linear species was developed by Jacobsen and Stockmeyer.[21] Their results, which match empirical findings,[22,23] demonstrate that the concentration of macrocyclic species is proportional to the system volume and that the concentration of rings of size x at equilibrium is proportional to $x^{-5/2}$.[21] Because the enthalpy change between cyclic and linear species is negligible, the equilibria between them are therefore driven by entropy and can be controlled by dilution. Linear species are favored under concentrated conditions because they have higher conformational entropy due to free chain ends. Conversely, macrocyclic species are favored under high dilutions because they have greater translational entropy in solution and because a greater number of molecules are formed. In addition, backbiting reactions (versus intramolecular reactions) are kinetically favored under dilute conditions.[22] Manipulating system dilution has been used both to synthesize olefin-containing

polymers via entropy-driven ring-opening polymerization (ED-ROMP)[24] and macrocycles with specific sizes via cyclodepolymerization (CDP),[25] so we anticipated that we could use dilute conditions to cyclodepolymerize dehydrogenated PE into cyclic species via ring-closing metathesis.

Previous studies suggest that equilibrium concentrations of cyclic species may be low for polyolefins with low degrees of unsaturation due to increased chain stiffness and thus inefficient backbiting.[26,27] Therefore, we expected that depolymerization efficiency would decrease with fewer alkenes along the PE backbone and hypothesized that the alkene concentration needed for effective cyclodepolymerization may have a lower limit, which is important because previously reported yields for PE dehydrogenation are low (ca. 4%).[28] We tested this hypothesis by isolating each fundamental step of the alkane metathesis reaction and studying: 1) dehydrogenation efficiency for low molar mass PE and 2) depolymerization for polyolefins with known quantities and spacin of backbone alkenes (Scheme 5.2). For the first step, we evaluated three Ir pincer catalysts for PE dehydrogenation by monitoring alkene formation with NMR spectroscopy (Scheme 5.2A). For the second step, we evaluated ring-closing metathesis cyclodepolymerization for polymers with varying quantities of backbone alkenes under dilute conditions (Scheme 5.2B). By isolating and evaluating each step of the reaction, we identified PE dehydrogenation as a limiting factor for successful alkane-metathesis-cyclodepolymerization and will focus on improving the yield for this step in future work.

Scheme 5.2 (A) PE dehydrogenation conditions to study the quantity of alkenes formed. (B) Metathesis cyclodepolymerization to study how alkene spacing affects the quantity and size of cyclic products.

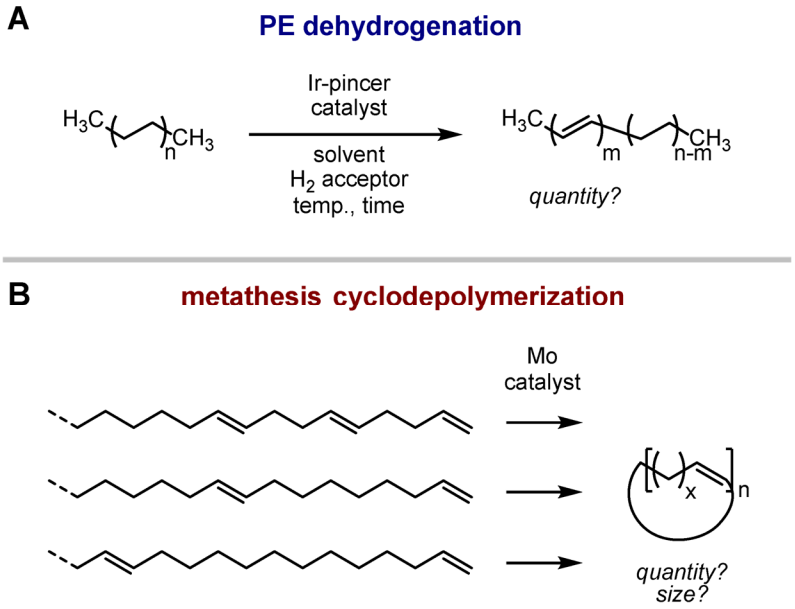

5.2 Results and Discussion

5.2.1 Polyethylene Dehydrogenation

Because only low quantities of alkenes (ca. 4 % of total repeat units) have been previously reported for PE dehydrogenation,[28] we first isolated and attempted to optimize this reaction with three Ir pincer catalysts (Chart 5.1). We chose low molar mass, high-density PE (M_n = 4.25 kg/mol) as our test substrate because it is soluble in aromatic solvents at moderate temperatures and contains few branch points, which may slow metathesis reactions.[29] We began our investigation with ***t*BuPOCOP** because it forms alkenes at internal positions,[30] which are more prevalent in PE than in small molecule linear alkanes. Reacting PE (2.4 mmol) with ***t*BuPOCOP** (0.47 mol%) and norbornene (NBE) (6.6 mol%) as an H_2 acceptor in d_6-benzene yielded only 2.5% dehydrogenated units as observed by ^{1}H NMR spectroscopy, in reasonable agreement with previous reports (Scheme 5.3, Table 5.1, entry 1).[28] Increasing the temperature to 175 °C and time to 54 h only

moderately improved the yield (Table 5.1, entry 2). Increasing the NBE loading at high temperatures did not increase the amount of dehydrogenated repeat units (Table 5.1, entry 3). We also attempted dehydrogenation using *tert*-butylethylene (TBE) as an alternative H_2 acceptor but noticed only an increase in bumping during the reaction due to its low boiling point (41 °C) of TBE (Table 5.1, entry 4).

Chart 5.1 Ir catalysts evaluated for PE dehydrogenation.

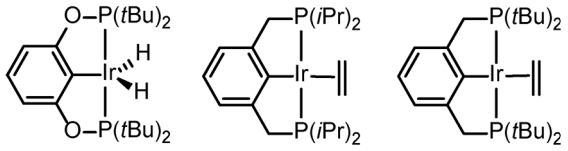

***t*BuPOCOP** ***i*PrPCP** ***t*BuPCP**

Scheme 5.3 General scheme for PE dehydrogenations with Ir catalysts and NBE.

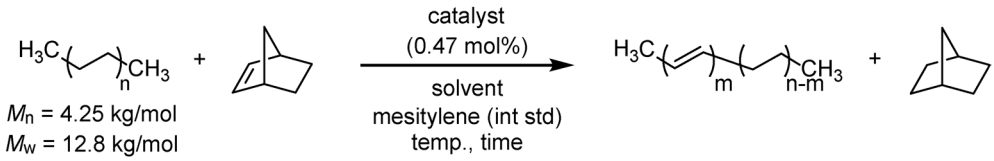

M_n = 4.25 kg/mol
M_w = 12.8 kg/mol

Table 5.1 Experimental conditions for PE dehydrogenation

entry	substrate	catalyst	solvent	H_2 acceptor	eq. H_2 acceptor	temp. (°C)	time (h)	dehydrogenation (%)[a]	H_2 acceptor conversion (%)
1	PE	tBuPOCOP	d_6-benzene	NBE	0.066	150	44	2.4	70
2	PE	tBuPOCOP	d_6-benzene	NBE	0.066	175	54	3.6	83
3	PE	tBuPOCOP	d_6-benzene	NBE	0.132	175	54	1.6	34
4	PE	tBuPOCOP	d_6-benzene	TBE	0.066	150	24	2.8	82
5	PE	tBuPCP	d_6-benzene	NBE	-	150	16	0.4	-
6	PE	tBuPCP	d_6-benzene	NBE	0.066[b]	150	54	2.2	quant
7	PE	iPrPCP	d_6-benzene	NBE	-	150	16	0.2	-
8	PE	iPrPCP	d_6-benzene	NBE	0.061[b]	150	54	0.4	quant
9	PE	tBuPCP	d_{10}-*p*-xylene	NBE	0.066	150	24	10.9	quant
10	PE	iPrPCP	d_{10}-*p*-xylene	NBE	0.066	150	24	2.0	quant
11	-	tBuPCP	d_6-benzene	NBE	0.066	150	24	-	47
12	COA	tBuPCP	d_6-benzene	NBE	0.066	150	18	4.8	quant

[a] *from ^{1}H NMR*
[b] *added after 16 h*

We also attempted PE dehydrogenation with ***t*BuPCP** and ***i*PrPCP** because these catalysts have high reported turnover numbers for alkane metathesis and dehydrogenation, respectively.[18,31] Dehydrogenation with ***t*BuPCP** was comparable to dehydrogenation with ***t*BuPOCOP** (Table 5.1, entries 1 and 6) and dehydrogenation with ***i*PrPCP** was negligible, due to catalyst degradation which was observed via ^{31}P NMR spectroscopy (Table 5.1, entry 8, Appendix 3, Figure A3.14). We also attempted dehydrogenation reactions in d_{10}-*p*-xylene instead of d_6-benzene to minimize the effects of solvent boiling and to remove any possibility of aryl C–H activation, which has been reported at rt for unhindered arenes (e.g., benzene, toluene, *m*-xylene but not *p*-xylene) with ***t*BuPCP** and ***t*BuPOCOP**.[3233] In addition, d_{10}-*p*-xylene was used in a previous report of PE dehydrogenation.[28] With this solvent, we indeed observed a higher percentage dehydrogenation and the maximum quantity was achieved with ***t*BuPCP** (10.9 %) rather than ***i*PrPCP** (Table 5.1, entries 9 and 10). The reason for the large increase in dehydrogenation with ***t*BuPCP** is unclear but could be attributed to improved PE solubility, reduced aryl solvent C–H addition to the catalyst,[32] or reduced solvent boiling in the NMR tube.

H_2 acceptor

In an ideal case of dehydrogenation, each mol of NBE consumed should correspond to one mol of alkene product because the hydrogen acceptor reduces the catalyst to turn over the catalytic cycle (Scheme 5.4). We initially chose low NBE loading (6.6 mol%) based on previously reported conditions for PE dehydrogenation[28] and previous reports indicating that high H_2 acceptor to catalyst ratios inhibit catalysis due to the formation of off-cycle olefin-bound intermediates.[34] We observed that relatively high % NBE conversion for reactions with 6.6 mol% NBE (60–100%) despite dehydrogenation yields lower than 6.6%, indicating that the consumed NBE does not directly correspond to PE dehydrogenation. In reactions with ***t*BuPOCOP**, formation of a species

with a ^{31}P NMR resonance at 181 ppm was observed even at t = 0 h (Appendix 3, Figures A3.7–3.9), which has similar chemical shift to ethylene-bound[18] and cyclooctene-bound[35] intermediates for this catalyst. This species could correspond to an olefin- or NBE-bound catalyst intermediate (Scheme 5.4, right), which may explain high NBE conversion. Low conversion of PE could be due to the NBE inhibiting catalytic turnover,[34,36] although POCOP-ligated Ir catalysts are less susceptible to inhibition by high H_2 acceptor concentrations than PCP analogues.[37] An alternate explanation is that the 14 e^- catalytically active Ir intermediate (Scheme 5.4, **III**) does form, but that a high barrier to PE coordination and/or oxidative addition prevents productive catalysis.

Scheme 5.4 The catalytic cycle for PE dehydrogenation, including the off-cycle intermediate **Ir-NBE**

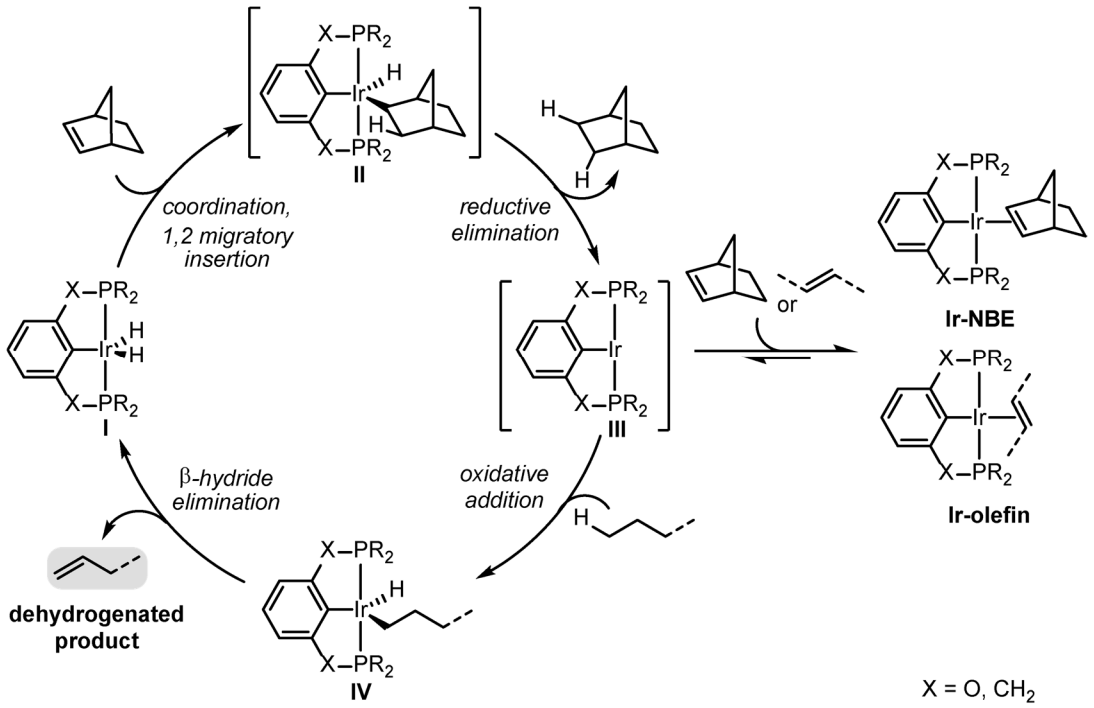

Control reactions

Control reactions were also performed to evaluate catalyst stability under our conditions. In the absence of PE, decomposition of ***t*BuPCP** was observed via ^{1}H and ^{31}P NMR spectroscopy (Table 5.1, entry 11, Appendix 3, Figure A3.17). Likewise, catalyst degradation was observed after

16 h for reactions with ***t*BuPCP** and ***i*PrPCP** but without any H_2 acceptor, and negligible PE dehydration was observed (Table 5.1, entries 5 and 7, Appendix 3, Figures A3.11 and A3.13). In an additional test of catalyst stability, dehydrogenation of model substrate cyclooctane (COA) was also performed with ***t*BuPCP**. In this case, only a 4.9% yield of cyclooctene was obtained despite quantitative conversion of NBE, likely due to catalyst degradation (Table 5.1, entry 12, Appendix 3, Figure A3.18). While this yield is similar to one previous report,[37] future work will focus on using lower temperatures and sequentially adding aliquots of NBE at shorter reaction times to improve the yield of dehydrogenated PE.

5.2.2 Cyclodepolymerization of Polyolefins with Varying Degrees of Unsaturation

To determine how the extent of dehydrogenation would affect depolymerization efficiency, we synthesized polyolefins with defined concentrations of alkenes along the backbone as test substrates (Chart 5.2). We used either ring-opening metathesis of commercially available cyclic monomers or acyclic diene metathesis (ADMET) polymerization[38] of diene monomers to synthesize polymers with 6–16 methylene units between alkenes along the backbone in good to moderate yields (Appendix 3 pp 266–268, Figures A3.3–3.6). We also compared our synthetic polymers with two commercial samples of poly-1,4-butadiene (PBD) – either PBD containing all *cis* repeat units (***c*PBD**), which is known to depolymerize to cyclic trimers, [39–42] or PBD containing a mixture of 1,4-*cis* (36%), 1,4-*trans* (55%), and 1,2-addition (9%) repeat units (***ct*PBD**).

Chart 5.2 Polyolefins with specific alkene spacing for depolymerization experiments.

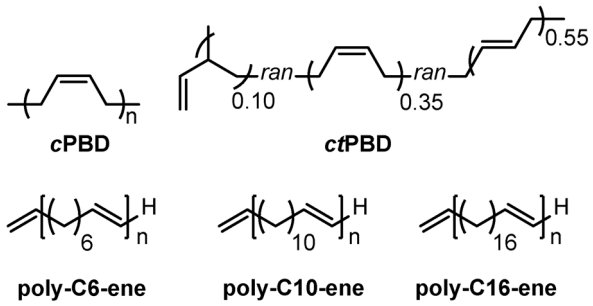

To investigate depolymerization conditions and products, we made dilute solutions of each polymer ([repeat unit] = 0.05 M) in toluene and reacted each one with Schrock's catalyst, **Mo-1** (Scheme 5.5). We chose **Mo-1** because it is used in tandem with iridium pincer catalysts for alkane metathesis.[18] In general, as the number of methylene spacers increased, depolymerization was less efficient (Figure 5.1).[43] For both reactions with commercial PBD, near complete reduction of the molar mass was observed with SEC (Table 5.2, entries 1 and 2). For both reactions, GC analysis revealed clean formation of the cyclic trimer 1,5,9-cyclododecatriene, similar to previous reports,[40,41,42] although the ratio of product to internal GC standard was slightly lower for *ct*PBD (0.29:1.00) compared to *c*PBD (0.34:1.00) (Appendix 3, Table A3.3). These results suggest that the *cis*- versus *trans*- conformation of the polymer alkenes do not significantly impact molar mass reduction, although they may impact the product distribution. For *ct*PBD, it is possible that species that were not observable by GC remained due to the 9% 1,2-addition repeat units that may have prevented further conversion to the cyclic trimer product.

Scheme 5.5 General scheme for cyclodepolymerization of polymers with different quantities of methylene spacers.

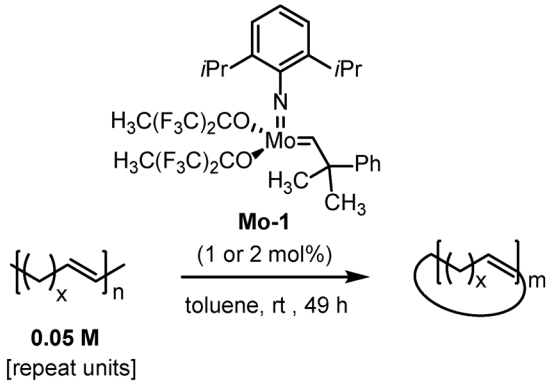

Table 5.2 Cyclodepolymerization conditions and molar mass data for polyolefins with **x** methylene units per repeat unit.

entry	x	conc. (M)	temp (°C)	cat.	cat. mol%	initial M_n (kg/mol)	initial M_w (kg/mol)	final M_n (kg/mol)	final M_w (kg/mol)
1	2[a]	0.05	25	**Mo-1**	2	116	338	0.671	0.968
2	2[b]	0.05	25	**Mo-1**	2	183	434	0[d]	0[d]
3	6	0.05	25	**Mo-1**	2	102	208	0.792	2.02
4	10	0.05	25	**Mo-1**	2	24.2	34.8	0[d]	0[d]
5	16	0.1	25	**Mo-1**[c]	1	2.48	3.38	1.03	2.42

a *c*PBD

b *ct*PBD

c in paraffin wax

d outside the SEC calibration curve range

The molar mass also greatly decreased for polymers with 6 and 10 methylene units between alkenes. For these polymers, the molar mass reduction was accompanied by concomitant formation of cyclic monomers (poly-C10-ene only), dimers, and trimers (Figure 5.1 B). In addition, cyclic species with molar masses that correspond to cyclic dimers plus or minus one or two -CH_2-units were also observed (Appendix 3, Figures A3.24 and A3.25). These species could arise from double-bond isomerization during polymerization or depolymerization. Although the molar mass decreased by SEC, the quantity of cyclic products formed for either of these polymerizations was less than for depolymerizations with PBD (Appendix 3, Table A3.3). For the polymer with 16 methylene units in between alkenes, minimal depolymerization was observed under our initial conditions via SEC (Table 3.2, entry 5). Taken together, these results demonstrate that

depolymerization efficiency drops for polymers with greater spacing between alkenes, as expected. These results also suggest that ≤ 10 methylene units between alkenes (i.e., ≥ 17% dehydrogenation of PE) is needed for effective cyclodepolymerization and that dehydrogenation conditions should target at least this quantity of alkene formation.

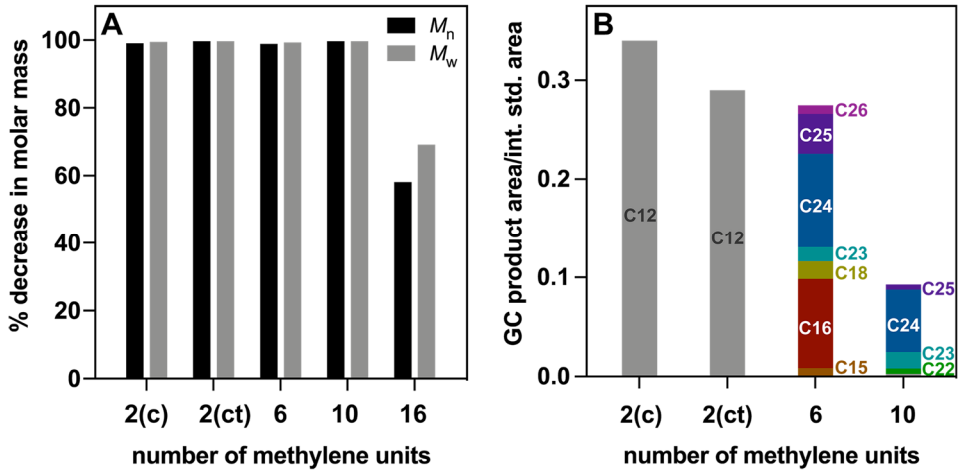

Figure 5.1 (A) Change in molar mass after depolymerization under dilute conditions for polymers with varying methylene units between backbone alkenes. (B) The distribution of depolymerization products observed by GC, plotted as a ratio of product peak area over the internal standard (durene) peak area. The numbers "CX" correspond to the number of C atoms in each observed product, determined by GC-MS.

5.2.3 Alkane Metathesis of Polyethylene

To assess if higher concentrations of alkenes are indeed necessary for successful depolymerization during alkane metathesis, a sequential dehydrogenation-metathesis reaction was attempted with PE (Scheme 5.6). The PE was initially reacted with ***t*BuPOCOP** and NBE to yield 2% dehydrogenation (Table 5.1, entry 1). After dehydrogenation, the reaction mixture was diluted in toluene to obtain a repeat unit concentration of 0.05 M. The resulting mixture was reacted with **Mo-1** for 16 h at 25 °C, but the molar mass was not reduced nor were cyclic species observed in the GC-MS chromatogram (Appendix 3, Figure A3.20). Together with our cyclodepolymerization

results, these findings suggest that higher yields of dehydrogenated PE will be needed for successful depolymerization to macrocycles.

Scheme 5.6 Sequential dehydrogenation and alkane metathesis of PE.

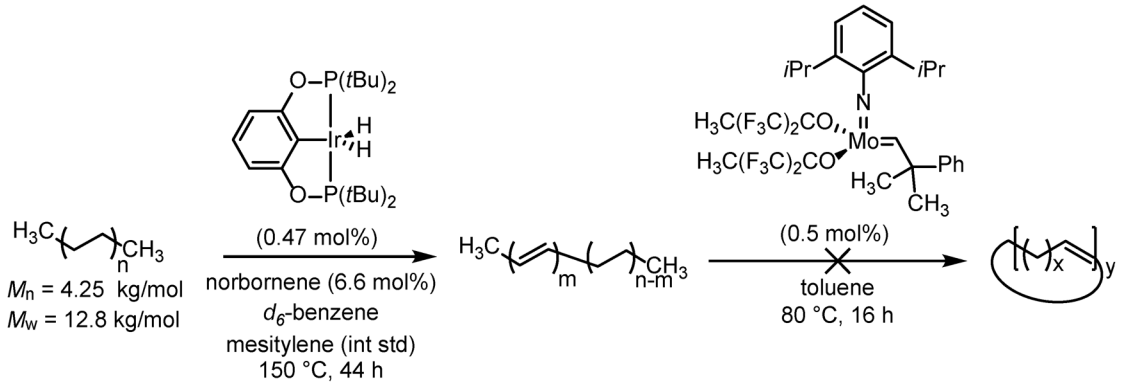

5.3 Conclusion

In this chapter, we isolate each step of alkane metathesis, dehydrogenation and olefin metathesis, to understand how the quantity of alkenes along a PE backbone affect cyclodepolymerization. Overall, our results indicate that the extent of dehydrogenation of PE is a key factor for effective alkane metathesis-cyclodepolymerization. Specifically, our depolymerization reactions indicate that greater than 17% of PE repeat units need to be dehydrogenated for molar mass reduction and concomitant cyclic oligomer formation. Unfortunately, in our hands only low yields of PE dehydrogenation (ca. 3%) with a maximum of 10% were achieved using Ir pincer catalysts ***t*BuPOCOP**, ***t*BuPCP**, or ***i*PrPCP**. Of these catalysts, the highest yields were achieved for catalysts with *t*Bu-substituted phosphines. Higher yields were also obtained in the higher-boiling solvent, d_{10}-*p*-xylene. Because our depolymerization studies indicated that higher concentrations of backbone alkenes are needed, future work will focus on modifying the pincer ligand scaffold with *p*-methoxy groups, to increase catalyst activity.[37] This modification will also provide a functional handle for stabilizing the catalyst on a solid support to

stabilize the catalyst and increase overall turnover numbers.[44] The long-term goal of this work is to develop a system to convert PE to macrocycles that we can use as feedstocks for copolymerization with functionalized cyclooctenes to obtain copolymers with polar functional groups that are challenging to access via current methods. We describe the potential limitations and future outlook for this work in Chapter 6.

5.4 References

1 Geyer, R.; Jambeck, J. R.; Law, K. L. Production, Use, and Fate of All Plastics Ever Made. *Sci. Adv.* **2017**, *3*, e1700782.

2 PlasticsEurope and EPRO. Plastics – the Facts 2020. **2020**, https://www.plasticseurope.org/en/resources/publications/4312-plastics-facts-2020 (accessed July 31, 2020)

3 Hale, R. C.; Seeley, M. E.; Guardia, M. J. La; Mai, L.; Zeng, E. Y. A Global Perspective on Microplastics. *J. Geophys. Res. Ocean.* **2020**, *125* (1), e2018JC014719.

4 Prokić, M. D.; Radovanović, T. B.; Gavrić, J. P.; Faggio, C. Ecotoxicological Effects of Microplastics: Examination of Biomarkers, Current State and Future Perspectives. *TrAC Trends Anal. Chem.* **2019**, *111*, 37–46.

5 United States Enviromental Protection Agency (US EPA). Advancing Sustainable Materials Management: Facts 2018 Tables and Figures. **2020**. https://www.epa.gov/sites/default/files/2021-01/documents/2018_tables_and_figures_dec_2020_fnl_508.pdf (Accessed August 4, 2021).

6 Ragaert, K.; Delva, L.; Van Geem, K. Mechanical and Chemical Recycling of Solid Plastic Waste. *Waste Manag.* **2017**, *69*, 24–58.

7 Hahladakis, J. N.; Velis, C. A.; Weber, R.; Iacovidou, E.; Purnell, P. An Overview of Chemical Additives Present in Plastics: Migration, Release, Fate and Environmental Impact during Their Use, Disposal and Recycling. *J. Hazard. Mater.* **2018**, *344*, 179–199.

8 Hinsken, H.; Moss, S.; Pauquet J. R.; Zweifel, H. Degradation of polyolefins during melt processing. *Polym. Degrad. Stab.* **1991**, *34*, 279–293.

9 Oblak, P.; Gonzalez- Gutierrez, J.; Zupancic, B.; Aulova, A.; Emri, I. Processability and mechanical properties of extensively recycled high density polyethylene. *Polym. Degrad. Stab*. **2015**, *114*, 133–145.

10 Jin, H.; Gonzalez-Gutierrez, J.; Oblak, P.; Zupančič, B.; Emri, I. The Effect of Extensive Mechanical Recycling on the Properties of Low Density Polyethylene. *Polym. Degrad. Stab.* **2012**, *97*, 2262–2272.

11 Anuar Sharuddin, S. D.; Abnisa, F.; Wan Daud, W. M. A.; Aroua, M. K. A Review on Pyrolysis of Plastic Wastes. *Energy Convers. Manag.* **2016**, *115*, 308–326.

[12] Kosloski-Oh, S. C.; Wood, Z. A.; Manjarrez, Y.; de los Rios, J. P.; Fieser, M. E. Catalytic Methods for Chemical Recycling or Upcycling of Commercial Polymers. *Mater. Horizons* **2021**, *8*, 1084–1129.

[13] Celik, G.; Kennedy, R. M.; Hackler, R. A.; Ferrandon, M.; Tennakoon, A.; Patnaik, S.; LaPointe, A. M.; Ammal, S. C.; Heyden, A.; Perras, F. A.; Pruski, M.; Scott, S. L.; Poeppelmeier, K. R.; Sadow, A. D.; Delferro, M. Upcycling Single-Use Polyethylene into High-Quality Liquid Products. *ACS Cent. Sci.* **2019**, *5*, 1795–1803.

[14] Zhang, F.; Zeng, M.; Yappert, R. D.; Sun, J.; Lee, Y.-H.; LaPointe, A. M.; Peters, B.; Abu-Omar, M. M.; Scott, S. L. Polyethylene Upcycling to Long-Chain Alkylaromatics by Tandem Hydrogenolysis/Aromatization. *Science* **2020**, *370*, 437–441.

[15] Haibach, M. C.; Kundu, S.; Brookhart, M.; Goldman, A. S. Alkane Metathesis by Tandem Alkane-Dehydrogenation–Olefin-Metathesis Catalysis and Related Chemistry. *Acc. Chem. Res.* **2012**, *45*, 947–958.

[16] Burnett, R. L.; Hughes, T. R. Mechanism and Poisoning of the Molecular Redistribution Reaction of Alkanes with a Dual-Functional Catalyst System. *J. Catal.* **1973**, *31*, 55–64.

[17] Vidal, V.; Théolier, A.; Thivolle-Cazat, J.; Basset, J.-M. Metathesis of Alkanes Catalyzed by Silica-Supported Transition Metal Hydrides. *Science* **1997**, *276*, 99–102.

[18] Goldman, A. S.; Roy, A. H.; Huang, Z.; Ahuja, R.; Schinski, W.; Brookhart, M. Catalytic Alkane Metathesis by Tandem Alkane Dehydrogenation-Olefin Metathesis. *Science* **2006**, *312*, 257–261.

[19] Huang, Z.; Rolfe, E.; Carson, E. C.; Brookhart, M.; Goldman, A. S.; El-Khalafy, S. H.; MacArthur, A. H. R. Efficient Heterogeneous Dual Catalyst Systems for Alkane Metathesis. *Adv. Synth. Catal.* **2010**, *352*, 125–135.

[20] Jia, X.; Qin, C.; Friedberger, T.; Guan, Z.; Huang, Z. Efficient and Selective Degradation of Polyethylenes into Liquid Fuels and Waxes under Mild Conditions. *Sci. Adv.* **2016**, *2*, e1501591.

[21] Jacobson, H.; Stockmayer, W. H. Intramolecular Reaction in Polycondensations. I. The Theory of Linear Systems. *J. Chem. Phys.* **2004**, *18*, 1600.

[22] Höcker, H.; Reimann, W.; Reif, L.; Riebel, K. Kinetics and Thermodynamic Aspects of the Metathesis Reaction of Cycloolefins Considering Particularly the Molecular Weight Distribution of the Products. *J. Mol. Catal.* **1980**, *8*, 191–202.

[23] Reif, L.; Höcker, H. Kinetics and Thermodynamics of the Metathesis Reaction of Cycloolefins. 2. Molecular Weight Distribution. *Macromolecules* **1984**, *17*, 952–956.

[24] Pearce, A. K.; Foster, J. C.; O'Reilly, R. K. Recent Developments in Entropy-Driven Ring-Opening Metathesis Polymerization: Mechanistic Considerations, Unique Functionality, and Sequence Control. *J. Polym. Sci. Part A Polym. Chem.* **2019**, *57*, 1621–1634.

[25] Hodge, P. Recycling of Condensation Polymers via Ring-Chain Equilibria. *Polym. Adv. Technol.* **2015**, *26*, 797–803.

[26] Höcker, H.; Reimann, W.; Reif, L.; Riebel, K. Kinetics and Thermodynamic Aspects of the Metathesis Reaction of Cycloolefins Considering Particularly the Molecular Weight Distribution of the Products. *J. Mol. Catal.* **1980**, *8*, 191–202.

[27] Höcker, H. The Metathesis Reaction — a Route to the Synthesis of Elastomeric Polymers and a Scientific Challenge. *Die Angew. Makromol. Chemie* **1981**, *100*, 87–97.

[28] Ray, A.; Zhu, K.; Kissin, Y. V.; Cherian, A. E.; Coates, G. W.; Goldman, A. S. Dehydrogenation of Aliphatic Polyolefins Catalyzed by Pincer-Ligated Iridium Complexes. *Chem. Commun.* **2005**, *27*, 3388–3390.

[29] Kirkland, T. A.; Grubbs, R. H. Effects of Olefin Substitution on the Ring-Closing Metathesis of Dienes. *J. Org. Chem.* **1997**, *62*, 7310–7318.

[30] Kumar, A.; Zhou, T.; Emge, T. J.; Mironov, O.; Saxton, R. J.; Krogh-Jespersen, K.; Goldman, A. S. Dehydrogenation of N-Alkanes by Solid-Phase Molecular Pincer-Iridium Catalysts. High Yields of α-Olefin Product. *J. Am. Chem. Soc.* **2015**, *137*, 9894–9911.

[31] Liu, F.; Pak, E. B.; Singh, B.; Jensen, C. M.; Goldman, A. S. Dehydrogenation of N-Alkanes Catalyzed by Iridium "pincer" Complexes: Regioselective Formation of α-Olefins. *J. Am. Chem. Soc.* **1999**, *121*, 4086–4087.

[32] Kanzelberger, M.; Singh, B.; Czerw, M.; Krogh-Jespersen, K.; Goldman, A. S. Addition of C-H Bonds to the Catalytically Active Complex (PCP)Ir (PCP = H3-2,6-((t)Bu2PCH2)2C6H3). *J. Am. Chem. Soc.* **2000**, *122*, 11017–11018.

[33] Göttker-Schnetmann, I.; White, P. S.; Brookhart, M. Synthesis and Properties of Iridium Bis(Phosphinite) Pincer Complexes (p-XPCP)IrH 2, (p-XPCP)Ir(CO), (p-XPCP)Ir(H)(Aryl), and {(p-XPCP)Ir}H 2{μ-N 2} and Their Relevance in Alkane Transfer Dehydrogenation. *Organometallics* **2004**, *23*, 1766–1776.

[34] Gupta, M.; Hagen, C.; Flesher, R. J.; Kaska, W. C.; Jensen, C. M. A Highly Active Alkane Dehydrogenation Catalyst: Stabilization of Dihydrido Rhodium and Iridium Complexes by a P-C-P Pincer Ligand. *Chem. Commun.* **1996**, *17*, 2083–2084.

[35] Göttker-Schnetmann, I.; Brookhart, M. Mechanistic Studies of the Transfer Dehydrogenation of Cyclooctane Catalyzed by Iridium Bis(Phosphinite) p-XPCP Pincer Complexes. *J. Am. Chem. Soc.* **2004**, *126*, 9330–9338.

[36] Renkema, K. B.; Kissin, Y. V.; Goldman, A. S. Mechanism of Alkane Transfer-Dehydrogenation Catalyzed by a Pincer-Ligated Iridium Complex. *J. Am. Chem. Soc.* **2003**, *125*, 7770–7771.

[37] Göttker-Schnetmann, I.; White, P.; Brookhart, M. Iridium Bis(Phosphinite) p-XPCP Pincer Complexes: Highly Active Catalysts for the Transfer Dehydrogenation of Alkanes. *J. Am. Chem. Soc.* **2004**, *126*, 1804–1811.

[38] Caire da Silva, L.; Rojas, G.; Schulz, M. D.; Wagener, K. B. Acyclic Diene Metathesis Polymerization: History, Methods and Applications. *Prog. Polym. Sci.* **2017**, *69*, 79–107.

[39] Dewaele, A.; Renders, T.; Yu, B.; Verpoort, F.; Sels, B. F. Depolymerization of 1,4-polybutadiene by Metathesis: High Yield of Large Macrocyclic Oligo(butadiene)s by Ligand Selectivity Control. *Catal. Sci. Technol.* **2016**, *6*, 7708–7717.

[40] Thorn-Csányi, E.; Ruhland, K. Quantitative Description of the Metathesis Polymerization/Depolymerization Equilibrium in the 1,4-Polybutadiene System, 1. Influence of Feed Concentration and Temperature. *Macromol. Chem. Phys.* **1999**, *200*, 1662–1671.

[41] Thorn- Csányi, E.; Ruhland, K. Quantitative Description of the Metathesis Polymerization/Depolymerization Equilibrium in the 1,4-Polybutadiene System, 2. Unusual Behavior at Lower Temperature. *Macromol. Chem. Phys.* **1999**, *200*, 2245–2249.

[42] Thorn-Csányi, E.; Ruhland, K. Quantitative Description of the Metathesis Polymerization/Depolymerization Equilibrium in the 1,4-Polybutadiene System, 3. Influence of the Solvent. *Macromol. Chem. Phys.* **1999**, *200*, 2606–2611.

[43] Note: response factors were not calculated for the cyclic products, so we cannot report quantitative yields. Because we've found that response factors for linear alkanes tend to increase with increasing molar mass (see also Gorocs, N.; Mudri, D.; Mátyási, J.; Balla, J. The Determination of GC–MS Relative Molar Responses of Some *n*-Alkanes and Their Halogenated Analogues *J. Chromatogr. Sci.* **2013**, *51*, 138–145.) we anticipate that our reported peak areas are overestimations of the actual quantitative yield.

[44] Huang, Z.; Rolfe, E.; Carson, E. C.; Brookhart, M.; Goldman, A. S.; El-Khalafy, S. H.; MacArthur, A. H. R. Efficient Heterogeneous Dual Catalyst Systems for Alkane Metathesis. *Adv. Synth. Catal.* **2010**, *352*, 125–135.

Chapter 6 Conclusions

6.1 Part One: Conclusion to Copolymers to Stabilize Morphology in Conjugated Polymer-Fullerene Blends

Conjugated polymers are promising materials for energy storage and generation applications because of their optical, conductive, and physical properties. These properties directly depend on the structural characteristics of the polymer like the repeat unit identity and the polymer sequence, end groups, and molar mass. New repeat unit structures are continually being developed,[1] but control over polymer molar mass and sequence depends on the match between catalyst and monomer[2] and therefore remains a challenge. In this part of the thesis, we aimed to highlight the importance and limitations of conjugated polymer synthesis via catalyst-transfer polymerization (CTP) for energy generating and storing applications. We then used CTP to synthesize additives for stabilizing morphology in organic photovoltaics (OPVs).

In Chapter 2, we described our perspective on using palladium precatalysts to expand the scope of CTP. Bidentate-phospine nickel catalysts are still most prevalent for CTP, despite the fact that they polymerize a limited scope of arene monomers, which are usually electron-rich. However, many of the conjugated polymers for state-of-the-art organic electronics contain both electron-rich and -poor units and fused arenes that make them challenging to synthesize via CTP. To expand the scope of CTP to include these donor-acceptor (D-A) polymers, we suggested Buchwald or N-heterocyclic amine ligated palladium precatalysts based on existing Pd-catalyzed CTPs and on difunctionalization reactions of small-molecule arenes. Indeed, a recent example

from Choi and coworkers demonstrated statistical and block copolymerization of 3,4-propylenedioxythiophene, benzotriazole, quinoxaline monomers using RuPhos and SPhos ligated Pd catalysts via Suzuki-CTP.[3] The statistical polymers in this example are a promising step towards synthesizing D-A polymers via CTP with a pair of monomers based on reactivity differences, rather than a single D-A monomer, which is challenging to synthesize due to the multiple desymmetrizations required (Scheme 6.1). For example, future work could focus on expanding the scope of slow-hydrolyzing but electron-rich boronate monomers that could be copolymerized with fast-hydrolyzing electron-poor monomers to achieve alternating D-A conjugated polymers with well-defined molar masses via Suzuki-CTP. We anticipate that catalysts with both σ-donating and π-accepting capabilities, like cyclic amino alkyl or aryl carbenes,[4,5] could enable polymerization of these electronically diverse monomers.

Scheme 6.1 (A) Synthesis via desymmetrization to achieve a single donor-acceptor monomer for CTP. (B) Synthesis of boronate monomers with differing reactivity for alternating polymerization via CTP.

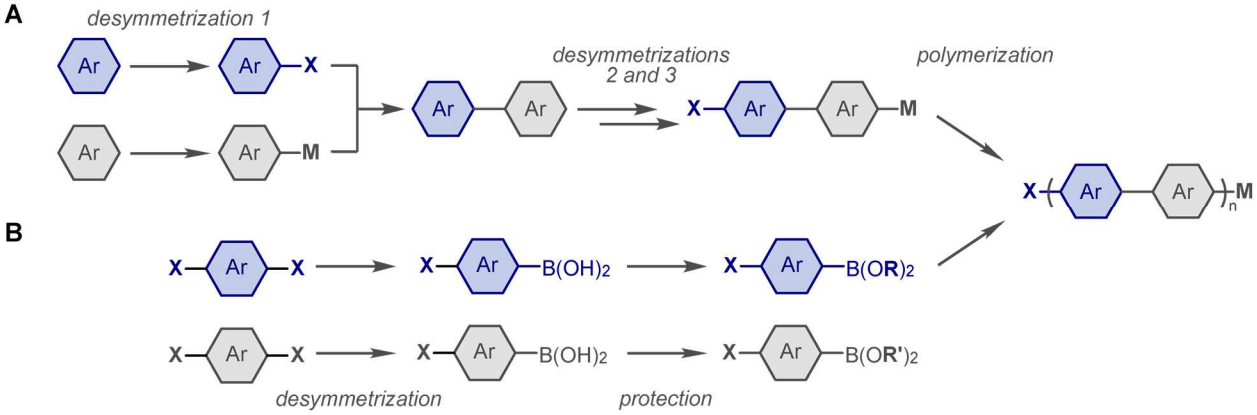

In Chapters 3 and 4, we described our efforts to stabilize the active layer morphology and performance for organic photovoltaics (OPVs). In Chapter 3, we used CTP to synthesize fullerene-functionalized poly(3-hexylthioene) copolymer additives and studied their effect on the morphology of P3HT:$PC_{61}BM$ blends (Figure 6.1). We used optical microscopy to study the effect of copolymer sequence (e.g., block, gradient, random), composition (e.g. 20, 35, 50 mol%

functionalization), and concentration in the blend (e.g., 2, 5, 8 wt%) on blend morphology over time with thermal annealing. We found that a random copolymer with 20 mol% functionalized side-chains at 8 wt% in the blend best stabilized the morphology and increased performance in P3HT:$PC_{61}BM$ devices that were annealed to mimic aging.

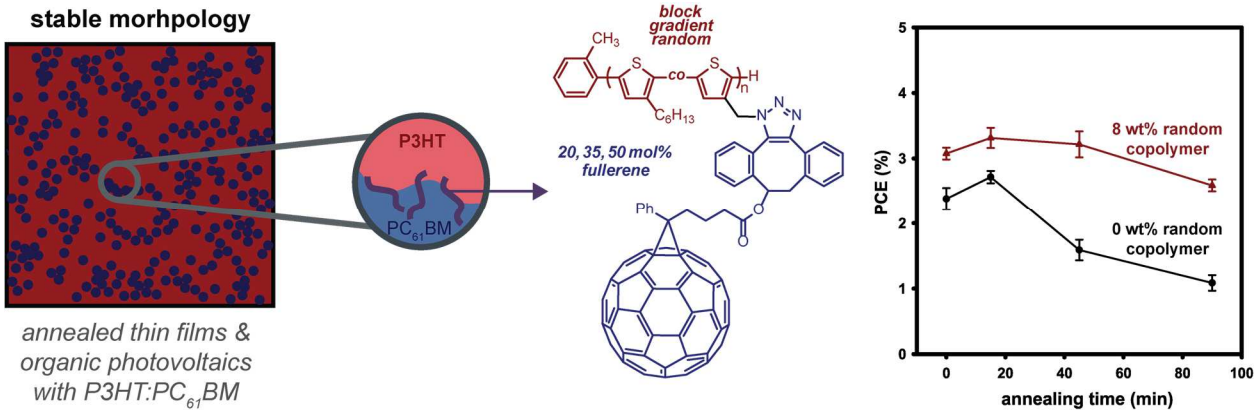

Figure 6.1 A depiction of thin film blend morphology for the P3HT:$PC_{61}BM$ blend (left), the structure of copolymers synthesized via CTP for stabilizing P3HT:$PC_{61}BM$ blends (middle), and stabilized PCE for P3HT:$PC_{61}BM$ OPVs with copolymer addition (right).

In Chapter 4, we found that the same copolymer could also stabilize morphology in blends of high-performing donor polymers (PTB7, PTB7-Th, and PffBT4T-2OD) with $PC_{71}BM$, suggesting that this copolymer could be a general stabilizing additive (Figure 6.3). We found that the copolymer has similar surface energy to $PC_{71}BM$, likely mixing with the $PC_{71}BM$ to prevent aggregation during annealing. In PffBT4T-2OD:$PC_{71}BM$ OPV devices, however, device power conversion efficiency (PCE) was limited with the copolymer due to decreased absorbance and electron conductivity in the active layer. Future work could focus on applying the copolymer additive to OPV systems with non-fullerene acceptors, which have been developed in recent years to improve optical absorption and PCE.[6] Both thiophene-containing copolymers[7] and fullerenes[8] have been used as additives in non-fullerene OPVs to stabilize performance over time. We thus anticipate that our copolymer additive may be well-suited to stabilize these systems, especially in systems where the non-fullerene acceptor has similar surface energy to the copolymer.

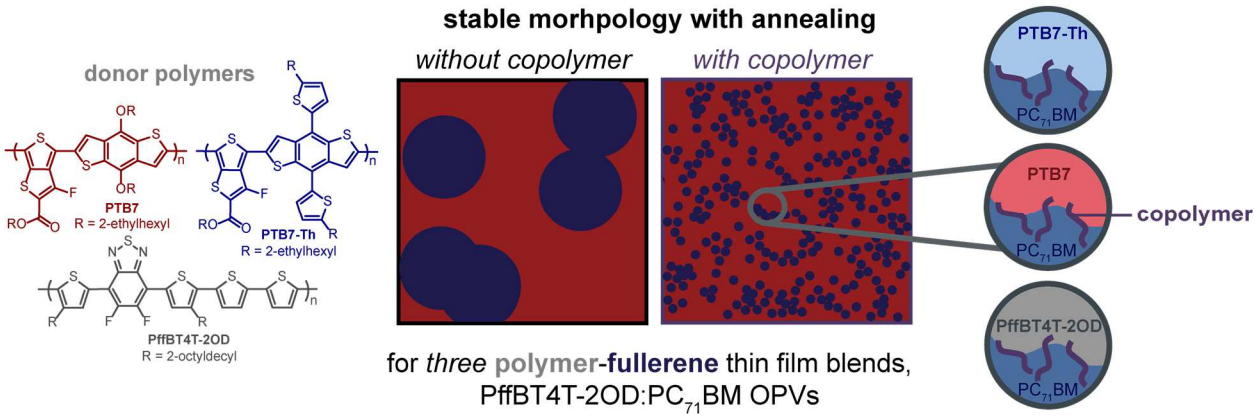

Figure 6.2 Structures of donor polymers in high performing blends and schematic of blend stabilization with the copolymer synthesized in Chapter 2.

Overall, this part of the thesis highlights the importance of control over conjugated polymer properties like sequence and molar mass for organic electronic applications. We highlight the current limitations of CTP, a living, chain-growth method to synthesize conjugated polymers, and suggest Pd precatalysts to expand the scope of monomers that can be polymerized via this method. Using CTP, we synthesized fullerene-functionalized poly(3-hexylthiophene) copolymers and use them to stabilize morphology in several blends of conjugated polymers with fullerenes that are used in OPVs. We found that the sequence, composition, and concentration of the copolymer in the blend affects the morphological stability of the blend. We found that a random copolymer best stabilizes morphology in P3HT:$PC_{61}BM$ blends and that it could stabilize several other blends of donor polymers with $PC_{71}BM$, suggesting that it could be used as a general stabilizing additive. As the development of conjugated polymers for energy storage and energy generating devices continues, controlled polymer synthesis should play a role in developing novel materials to improve device performance and stability.

6.2 Part Two: Conclusion to Understanding Alkene Spacing for Repurposing Polyethylene via Alkane Metathesis and Cyclodepolymerization

Plastics have improved global quality of life by revolutionizing food systems, transportation, medicine, and construction. Global plastic production has increased exponentially over the last century, with an estimated 368 million tons of plastic produced globally in 2019.[9] Of global plastic, polyethylene (PE) is the polymer that has been produced on the largest scale world-wide.[10] PE is also discarded at high rates and made up the largest share (42%) of US plastic waste generated in 2018, yet only a small fraction of that PE waste (6.2%) was recycled.[11] Limitations to current recycling methods include poor retention of PE physical properties after processing, difficulties in separating PE from other polymer types, contaminants, and additives,[12] as well as high temperatures needed to transform PE into small-molecule hydrocarbons by pyrolysis.[13] This part of the thesis describes our aim to circumvent these limitations by chemically recycling PE via alkane metathesis reactions under dilute conditions to form macrocyclic products.

In Chapter 5, we describe our efforts to study how unsaturation along the PE backbone would affect PE cyclodepolymerization. We hypothesized that there may be a lower limit to the quantity of alkenes needed for effective depolymerization and therefore studied each step of alkane metathesis to evaluate 1) conditions for PE dehydrogenation and 2) ring-closing metathesis depolymerization efficiency for polyolefins with varying quantities of alkenes along the backbone (Scheme 6.2).

Scheme 6.2 (A) PE dehydrogenation conditions to study the quantity of alkenes formed. (B) Metathesis cyclodepolymerization to study how alkene spacing affects the quantity and size of cyclic products.

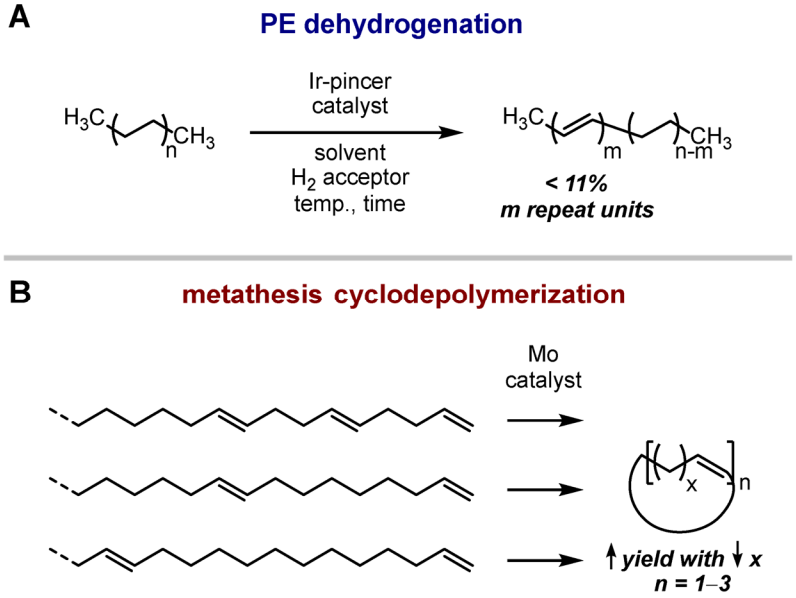

We first investigated conditions for PE dehydrogenation with a series of Ir catalysts (Chart 6.1, top) and obtained only low yields (≤ 11%) of dehydrogenation. We observed species that may correspond to olefin-bound Ir complexes for reactions with the ***t*BuPOCOP** catalyst and catalyst degradation after long times (16–24 h) for the ***t*BuPCP** and ***i*PrPCP** catalysts, which may explain low dehydrogenation yields. In our cyclodepolymerization studies, we found that depolymerization efficiency decreased with decreasing quantities of alkanes along the backbone. This result was evidenced by the smaller quantity of observable cyclic products via GC-MS with decreasing alkene concentration and by the fact that only polymers with ≤10 methylene units between alkenes (i.e., ≥ 17% dehydrogenation) showed a significant decrease in molecular weight. Overall, our results suggest that there is indeed a lower limit of alkenes needed for effective PE cyclodepolymerization.

Chart 6.1 Ir pincer catalysts studied in this work (top) and for future dehydrogenation reactions of PE (bottom).

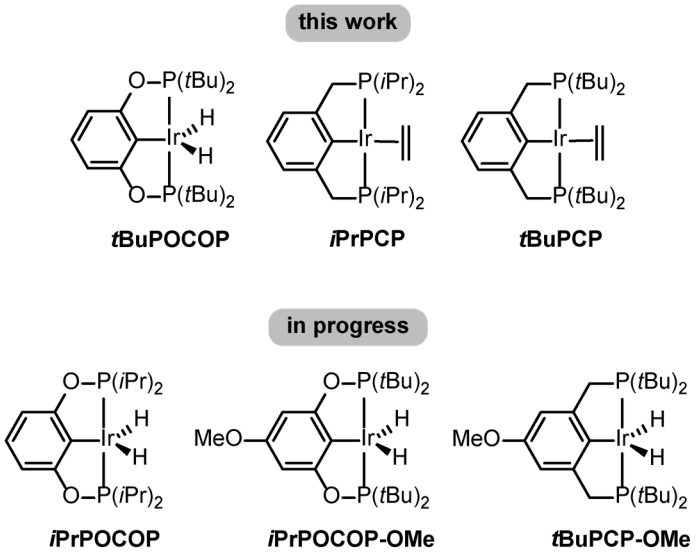

To improve dehydrogenation yield, we will first focus on improving catalyst stability. Work is currently underway to synthesize catalysts with *p*-methoxy functionalized ligands, which are not only more active for alkane dehydrogenation than unfunctionalized analogues but can also be appended to a Al_2O_3 solid support to improve catalyst lifetimes (Chart 6.1, bottom).[14,15,16] Another strategy to improve yield would be to modify the ***t*BuPOCOP** phosphine alkyl groups to *i*Pr rather than *t*Bu groups, which should make the catalyst more active by reducing steric hinderance at the Ir center (Chart 6.1, bottom).[17,18]

While we originally anticipated combining both dehydrogenation and metathesis in one pot, doing so limits catalyst choice. For example, in the original report of alkane metathesis with Ir catalysts, Grubbs-type olefin metathesis catalysts could not be used because they deactivated the Ir catalysts, which formed catalytically inactive Cl-bound Ir species.[19] Keeping dehydrogenation and metathesis reactions separate would enable us to use Grubbs type metathesis catalysts that are more air tolerant than Mo-alkylidines and that have been used to control the size distribution of macrocyclic products.[20] In addition, keeping each reaction separate would ensure

that the macrocyclic species we obtain contain alkenes, which would enable us to use them as a feedstock for ring-opening metathesis polymerization (ROMP).[21] Our long-term goal is to copolymerize the macrocycles with cyclooctenes to generate functionalized copolymers under concentrated conditions (Scheme 6.3, top). We anticipate that reactivity differences between the moderately-strained cyclooctenes and strainless macrocycles will allow us to generate di- and tri-block copolymers initially, with PE segments and segments that contain polar functional groups, or blocky copolymers over time as metathesis scrambling reactions occur (Scheme 6.3, bottom).[22,23] Our repurposing route would enable us to access this class of polymers, which are advantageous due to their adhesive properties and toughness,[24] without the custom catalysts and/or harsh conditions that are typically required.[25]

Scheme 6.3 Repurposing macrocycles from PE depolymerization via ROMP to generate copolymers with segments containing polar functional groups (top). Anticipated polymer sequences due to differences in reactivity between strainless macrocycles and cyclooctenes (bottom).

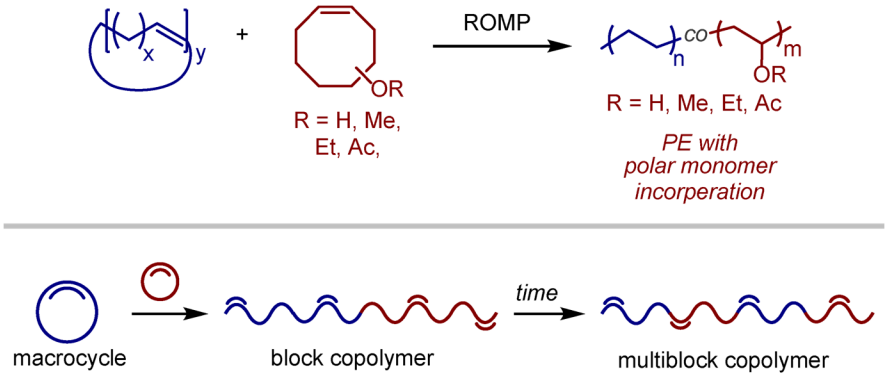

This part of the thesis describes our efforts to chemically repurpose PE, treating it as a valuable feedstock for synthesizing functional materials. We demonstrate that PE dehydrogenation is a limiting step in alkane metathesis and cyclodepolymerization and anticipate that optimization of this step will improve the overall process. This work provides just one avenue to expand the options for open-loop recycling of PE. More broadly, we recognize one limitation of this work is the precious-metal catalysts that we employ. While these catalysts are the current state-of-the-art

for alkane dehydrogenation, future work in catalytic recycling methods for commodity plastics should focus on earth-abundant metal catalysts instead. Furthermore, the scientific research being done to develop improved recycling methods should be paired with political action to balance the economic costs of plastic recycling and to improve recycling infrastructure.[26,27] This combined effort can establish more sustainable systems for plastic waste management.

Overall, this thesis describes our efforts to address challenges in renewable energy and in plastic waste disposal. In the first part of the thesis, we describe the limitations and future outlook for synthesizing conjugated polymers via CTP and synthesize conjugated copolymers as additives to stabilize morphology in OPVs, finding that a random copolymer can stabilize multiple polymer/fullerene blends. In the second part of the thesis, we determine that increased alkene spacing decreases efficiency for open-loop PE recycling via alkane metathesis and cyclodepolymerization and outline future work to improve PE dehydrogenation. Each part of this thesis addresses a challenge in sustainable development – renewable energy (part 1) or plastic pollution (part 2). This work is part of a broader effort to develop the technologies and systems that are needed to mitigate the detrimental effects of human-caused climate change. With concerted effort across disciplines, we can sustain improved quality of life far into the future.

6.3 References

[1] Liu, Q.; Jiang, Y.; Jin, K.; Qin, J.; Xu, J.; Li, W.; Xiong, J.; Liu, J.; Xiao, Z.; Sun, K.; Yang, S.; Zhang, X.; Ding, L. 18% Efficiency Organic Solar Cells. *Sci. Bull.* **2020**, *65* (4), 272–275.

[2] Leone, A. K.; McNeil, A. J. Matchmaking in Catalyst-Transfer Polycondensation: Optimizing Catalysts based on Mechanistic Insight. *Acc. Chem. Res.* **2016**, *49*, 2822−2831.

[3] Lee, J.; Kim, H.; Park, H.; Kim, T.; Hwang, S.-H.; Seo, D.; Chung, T. D.; Choi, T.-L. Universal Suzuki–Miyaura Catalyst-Transfer Polymerization for Precision Synthesis of Strong Donor/Acceptor-Based Conjugated Polymers and Their Sequence Engineering. *J. Am. Chem. Soc.* **2021**, *143*, 11180–11190.

[4] Frey, G. D.; Dewhurst, R. D.; Kousar, S.; Donnadieu, B.; Bertrand, G. (Alkyl)(Amino)Carbene Gold(I) Complexes: A Synthetic and Structural Investigation. *J. Organomet. Chem*. **2008**, *693*, 1674−1682.

[5] Rao, B.; Tang, H.; Zeng, X.; Liu, L.; Melaimi, M.; Bertrand, G. Cyclic (Amino)(aryl)carbenes (CAArCs) as Strong σ-Donating and π-Accepting Ligands for Transition Metals. *Angew. Chem., Int. Ed*. **2015**, *54*, 14915−14919.

[6] Liu, W.; Xu, X.; Yuan, J.; Leclerc, M.; Zou, Y.; Li, Y. Low-Bandgap Non-Fullerene Acceptors Enabling High-Performance Organic Solar Cells. *ACS Energy Lett.* **2021**, *6*, 598–608.

[7] Su, Y.-A.; Maebayashi, N.; Fujita, H.; Lin, Y.-C.; Chen, C.-I.; Chen, W.-C.; Michinobu, T.; Chueh, C.-C.; Higashihara, T. Development of Block Copolymers with Poly(3-Hexylthiophene) Segments as Compatibilizers in Non-Fullerene Organic Solar Cells. *ACS Appl. Mater. Interfaces* **2020**, *12*, 12083–12092.

[8] Kim, T.; Choi, J.; Kim, H. J.; Lee, W.; Kim, B. J. Comparative Study of Thermal Stability, Morphology, and Performance of All-Polymer, Fullerene-Polymer, and Ternary Blend Solar Cells Based on the Same Polymer Donor. *Macromolecules* **2017**, *50*, 6861–6871.

[9] PlasticsEurope and EPRO. Plastics – the Facts 2020. **2020**, https://www.plasticseurope.org/en/resources/publications/4312-plastics-facts-2020 (accessed July 31, 2020).

[10] Geyer, R.; Jambeck, J. R.; Law, K. L. Production, Use, and Fate of All Plastics Ever Made. *Sci. Adv.* **2017**, *3*, e1700782.

[11] United States Enviromental Protection Agency (US EPA). *Advancing Sustainable Materials Management: Facts 2018, Tables and Figures.* **2020**, https://www.epa.gov/sites/default/files/2021-01/documents/2018_tables_and_figures_dec_2020_fnl_508.pdf (accessed July 31, 2020).

[12] Ragaert, K.; Delva, L.; Van Geem, K. Mechanical and Chemical Recycling of Solid Plastic Waste. *Waste Manag.* **2017**, *69*, 24–58.

[13] Anuar Sharuddin, S. D.; Abnisa, F.; Wan Daud, W. M. A.; Aroua, M. K. A Review on Pyrolysis of Plastic Wastes. *Energy Convers. Manag.* **2016**, *115*, 308–326.

[14] Zhu, K.; Achord, P. D.; Zhang, X.; Krogh-Jespersen, K.; Goldman, A. S. Highly Effective Pincer-Ligated Iridium Catalysts for Alkane Dehydrogenation. DFT Calculations of Relevant Thermodynamic, Kinetic, and Spectroscopic Properties. *J. Am. Chem. Soc.* **2004**, *126*, 13044–13053.

[15] Göttker-Schnetmann, I.; White, P. S.; Brookhart, M. Synthesis and Properties of Iridium Bis(Phosphinite) Pincer Complexes (p-XPCP)IrH 2, (p-XPCP)Ir(CO), (p-XPCP)Ir(H)(Aryl), and {(p-XPCP)Ir}H 2{μ-N 2} and Their Relevance in Alkane Transfer Dehydrogenation. *Organometallics* **2004**, *23*, 1766–1776.

[16] Huang, Z.; Rolfe, E.; Carson, E. C.; Brookhart, M.; Goldman, A. S.; El-Khalafy, S. H.; MacArthur, A. H. R. Efficient Heterogeneous Dual Catalyst Systems for Alkane Metathesis. *Adv. Synth. Catal.* **2010**, *352*, 125–135.

[17] Liu, F.; Pak, E. B.; Singh, B.; Jensen, C. M.; Goldman, A. S. Dehydrogenation of N-Alkanes Catalyzed by Iridium "pincer" Complexes: Regioselective Formation of α-Olefins. *J. Am. Chem. Soc.* **1999**, *121*, 4086–4087.

[18] Morales-Morales, D.; Redón, R.; Yung, C.; Jensen, C. M. Dehydrogenation of Alkanes Catalyzed by an Iridium Phosphinito PCP Pincer Complex. *Inorganica Chim. Acta* **2004**, *357*, 2953–2956.

[19] Goldman, A. S.; Roy, A. H.; Huang, Z.; Ahuja, R.; Schinski, W.; Brookhart, M. Catalytic Alkane Metathesis by Tandem Alkane Dehydrogenation-Olefin Metathesis. *Science* **2006**, *312*, 257–261.

[20] Dewaele, A.; Renders, T.; Yu, B.; Verpoort, F.; Sels, B. F. Depolymerization of 1,4-Polybutadiene by Metathesis: High Yield of Large Macrocyclic Oligo(Butadiene)s by Ligand Selectivity Control. *Catal. Sci. Technol.* **2016**, *6*, 7708–7717.

[21] Pearce, A. K.; Foster, J. C.; O'Reilly, R. K. Recent Developments in Entropy-Driven Ring-Opening Metathesis Polymerization: Mechanistic Considerations, Unique Functionality, and Sequence Control. *J. Polym. Sci. Part A Polym. Chem.* **2019**, *57*, 1621–1634.

[22] Xie, M.; Wang, W.; Ding, L.; Liu, J.; Yang, D.; Wei, L.; Zhang, Y. Cleavable Multiblock Copolymer Synthesized by Ring-Opening Metathesis Copolymerization of Cyclooctene and Macrocyclic Olefin and Its Hydrolysis to Give Carboxyl-Telechelic Polymer. *J. Polym. Sci. Part A: Polym. Sci.* **2010**, *48*, 380–388.

[23] Norwalk, J. A.; Fang, C.; Short, A. L.; Weiss, R. M.; Swisher, J. H.; Liu, P. Meyer, T. Y. Sequence-Controlled Polymers Through Entropy-Driven Ring-Opening Metathesis Polymerization: Theory, Molecular Weight Control, and Monomer Design. *J. Am. Chem. Soc.* **2019**, *141*, 5741–5752.

[24] Boffa, L. S.; Novak, B. M. Copolymerization of Polar Monomers with Olefins Using Transition-Metal Complexes. *Chem. Rev.* **2000,** *100*, 1479–1494.

[25] Keyes, A.; Alhan, Basbug Alhan, H. E.; Ordonez, E.; Ha, U.; Beezer, D. B.; Dau, H.; Liu, Y.-S.; Tsogtgerel, E.; Jones, G. R.; Harth, E. Olefins and Vinyl Polar Monomers: Bridging the Gap for Next Generation Materials. *Angew. Chem. Int. Ed.* **2019**, *58*, 12370–12391.

[26] Vogt, B. D.; Stokes, K.; Kumar, S. K. Why Is Recycling of Postconsumer Plastics so Challenging ? **2021**, ASAP DOI: 10.1021/acsapm.1c00648.

[27] da Costa, J. P. The 2019 Global Pandemic and Plastic Pollution Prevention Measures: Playing Catch-Up. *Sci. Total Environ.* **2021**, *774*, 145806.

Appendices

Appendix 1 for Random Copolymers Outperform Gradient and Block Copolymers in Stabilizing Organic Photovoltaics

A1.1 Materials

Flash chromatography was performed on SiliCycle silica gel (40–63 μm). Thin layer chromatography was performed on MACHEREY-NAGEL TLC plates (pre-coated with 0.20 mm silica gel 60 with fluorescent indicator UV254). $Ni(COD)_2$ was purchased from Strem Chemicals. Lithium diisopropylamide (LDA, 2.0 M in THF/n-heptane/ethylbenzene, 59/28/13 v/v) was purchased from Acros Organics. 2,5-Dibromo-3-hexylthiophene (DB3HT) was purchased from ArkPharm and purified by dissolving in hexanes, decoloring with carbon powder, stirring for 2 h, filtering through a plug of silica gel and concentrating in vacuo. [6,6]-phenyl C_{61}-butyric acid methyl ester ($PC_{61}BM$) was purchased from Nano-C Inc. N-Bromosuccinimide (NBS) was purchased from Sigma Aldrich, recrystallized from water and dried over P_2O_5. Isopropylmagnesium chloride (iPrMgCl, 2.0 M in THF, 25 mL), Molybdenum(VI) oxide, (MoO_3, 99.97% trace metals basis), zinc acetate dihydrate ($Zn(OAc)_2•2H_2O$), and 2-methoxyethanol (2ME) were purchased from Sigma Aldrich. Silver pellets (Ag, 99.99% purity) were purchased from Kurt J. Lesker Company. MoO_3 and Ag pellets were loaded into an Angstrom Engineering AMOD thermal evaporation chamber. All other reagent grade materials and solvents were purchased from Sigma Aldrich, Acros Organics, Alfa Aesar, or Fisher and used without further purification unless otherwise noted. THF was dried and deoxygenated using an mBraun Innovative Technology solvent purification system composed of activated alumina, a copper catalyst, and molecular sieves. Any water used for reactions or work-ups was deionized. The glovebox in which

specified procedures were carried out was an MBraun LABmaster 130 with a N_2 atmosphere and H_2O levels below 4 ppm. Compounds **S1**,[1] **S2**,[1] **S3**,[2] and **S4**–**S7**[3] were prepared using modified literature procedures.

A1.2 General Experimental

NMR Spectroscopy: ^{1}H, ^{13}C and ^{31}P spectra for all compounds were acquired in deuterated solvents on a Varian MR400 operating at 400, 100, and 162 MHz or a Varian VNMRS 500 operating at 500, 126, and 202 MHz, respectively. For ^{1}H and ^{13}C spectra, the chemical shift data are reported in units of δ (ppm) relative to tetramethylsilane (TMS) and referenced with residual solvent. For 31P spectra, the chemical shift data are reported in units of δ (ppm) relative to 85% H_3PO_4 in H_2O. All NMR spectra were recorded at r.t.

Mass Spectrometry: HRMS data were obtained on a Micromass AutoSpec Ultima Magnetic Sector mass spectrometer.

Infrared Spectroscopy: IR data were recorded using Thermo Scientific Nicolet iS50 FT-IR spectrometer.

Matrix-Assisted Laser Desorption/Ionization Mass Spectrometry: Matrix-assisted laser desorption/ionization time of flight mass spectrometry (MALDI-TOF-MS) was carried out on a Bruker AutoFlex Speed MALDI-TOF in positive-ion reflectron mode using using *trans*-2-[3-(4-*tert*-butylphenyl)-2-methyl-2-propenylidene]malononitrile (DCTB) as a matrix. Samples were prepared by dissolving a 2.5 μL of a 1 mg/mL solution of polymer in THF/toluene (99:1 v/v) in 2.5–10 μL of 1 M DCTB in $CHCl_3$. Samples were diluted in DCTB in varying ratios (to ensure

good signal/noise) and then spotted on a MALDI 96-well plate and air dried. The data were analyzed using flexAnalysis.

Gel Permeation Chromatography: Polymer molecular weights were determined by comparison with polystyrene standards (Varian, EasiCal PS-2 MW 580–377,400) at 40 °C in THF on a Malvern Viscotek GPCMax VE2001 equipped with two Viscotek LT-5000L 8 mm (ID) × 300 mm (L) columns and analyzed with Viscotek TDA 305 (with UV-PDA Detector Model 2600). All data shown refer to the absorbance at 254 nm. Samples were dissolved in THF/toluene (99:1 v/v) (with mild heating), and passed through a 0.2 μm PTFE filter prior to analysis.

Gas Chromatography: Gas chromatography was carried out using a Shimadzu GC 2010 containing a Shimadzu SHRX5 (crossbound 5% diphenyl–95% dimethyl polysiloxane; 15 m, 0.25 mm ID, 0.25 μm df) column.

Thin Film Preparation: Fused silica wafers (from University Wafer) were cut into square substrates (~1.5 cm x 1.5 cm) and cleaned via rubbing with undiluted Hellmanex III followed by rinsing with DI water. The substrates were then sonicated for 15 min in each of the following solvents: DI water, acetone, and iPrOH. The clean substrates were then dried in an oven at 80 °C for 8 h and stored in a clean petri dish wrapped in aluminum foil. P3HT, $PC_{61}BM$, and copolymer were each dissolved separately in 1,2-dichlorobenzene (*o*-DCB) (30 mg/mL) and stirred at 60 °C for 2 h. The solutions were then combined (1:1:X, P3HT:$PC_{61}BM$:copolymer, 30 mg/mL overall), stirred for 18 h at 60 °C, filtered, then spin-casted onto the clean silica substrate at 800 rpm for 3 min. The thin films were characterized with optical microscopy and UV-Vis spectroscopy before

and after thermal annealing in a vacuum oven (–711.2 mmHg) at 150 °C for 60 min. Thin film thickness was determined by variable-angle spectroscopic ellipsometry by spin-casting onto silicon wafers. Near-infrared (1100 nm–1600 nm) spectroscopic data were recorded by J.A. Woollam M-2000 ellipsometer followed by thickness measurement by Cauchy-model fitting.[4]

Optical Microscopy: The annealed thin film samples were examined using a Leica DMCB optical microscope with a 40× objective lens. Images were recorded with an attached QICAM Fast 1394 digital video camera and analyzed with ImageJ.

Image Processing with ImageJ: Images were saved as .tiff files to open in the ImageJ software. Once loaded, the images were converted to black and white by clicking "Image" and selecting "Color," then "Split Channels" from the dropdown menu. Three images were generated and the "(blue)" channel image was selected for further analysis. The image background was subtracted by clicking "Process" then "Subtract Background" from the dropdown menu which opened a new window. The default rolling ball radius (50 pixels) was used and "light background" was checked to ensure even background subtraction. In the "Image" tab, "Adjust" then "Threshold" were selected, opening a new window showing the minimum and maximum threshold limits for detecting particles (dark domains), now depicted in red on the image. Selecting "Apply" defined the particle sizes/areas and displayed them in black on the image. To calculate the black particle percent area, "Analyze" then "Analyze Particles" was selected. In the resulting window, the size was set to "0.0005-infinity" then "display results," "summary," "include holes" and "clear results" were checked and "OK" was selected. The tabulated data points and results summary (with % area of particles relative to whole image), each appeared in separate windows.

UV-Vis Spectroscopy: UV-Vis spectra of thin films were acquired using a Thermo Scientific Evolution 220 UV-Vis spectrophotometer.

Cyclic Voltammetry (CV): The electrochemical measurements were performed on a CH Instruments electrochemical analyzer. A glassy carbon electrode, Pt wire, and Ag/AgCl electrode were used as the working, counter, and reference electrodes, respectively. A ferrocene/ferrocenium (Fc/Fc+) redox couple was used as the internal standard which is assumed to have an absolute energy level of -4.8 eV.[5]

Bulk Heterojunction Solar Cell Device Fabrication and Measurement: All processing was completed in an ultra-high puritiy (<1ppm of H_2O and O_2) glovebox from LC Technology Solutions, INC. Solar cell devices have the following inverted structure: glass/ITO/ZnO(40 nm)/blend/MoO_3(20 nm)/Ag(100 nm). The indium tin oxide (ITO) substrate was cleaned with detergent, sonicated in DI water, acetone, and iPrOH for 10 min each, then exposed to 245 nm ultraviolet light under oxygen flow for 15 min. ZnO sol–gel solution was prepared by dissolving zinc acetate dihydrate ($Zn(OAc)_2 \bullet 2H_2O$, Sigma Aldrich) in 2-methoxyethanol (2ME, Sigma Aldrich) (0.5 M). Monoethanolamine (0.5 M) was added as a stabilizer and the mixture was vigorously stirred at 60 °C for 4 h. The solution was then cooled to rt and aged for > 24 h. The prepared ZnO solution was spin-casted on ITO coated glass substrates at 3000 rpm for 60 s, followed by thermal annealing in air at 150 °C for 20 min. Polymer solutions were prepared as described above in *o*-DCB and heated at 60 °C for 12 h before spin-casting in an ultra-high purity (< 1 ppm of H_2O and O_2) N_2 glovebox. The polymer solutions were spin-casted at 800 rpm for 180

s, generating thin films (175 ± 10 nm). After spin-casting the polymers, the films were either thermally annealed (for 15, 45, 90 min) then transferred, or directly transferred to an Angstrom Engineering AMOD thermal evaporation chamber. Molybdenum masks with 1 mm radius circular openings were placed on the sample, determining 3.14 mm^2 of the device size. MoO_3 and Ag were evaporated onto the film at a rate of 1 Å/s under the base pressure of 3×10^{-7} torr.

J-V characteristics of the devices were recorded by a HP 4156a semiconductor parameter analyzer. The transparent glass/ITO side was illuminated with simulated AM 1.5G at 1 sun intensity (100 mW/cm^2). The intensity of the solar simulator was calibrated by the National Renewable Energy Laboratory (NREL)-traceable Si reference cell. The reverse bias saturation current (J_o) was obtained from the *J-V* curve at -1 bias voltage in the dark. The series resistance (Rs) of each device was extracted from the inverse slope of the *J-V* curve at the open circuit voltage (V_{OC}).

Conductive Atomic Force Microscopy (c-AFM): An Asylum Research MFP-3D atomic force microscope was used for both phase images and conductive-tip atomic force microscopy (c-AFM) images. Phase images of the spin-casted polymer (175 nm) on ITO/ZnO (40 nm) were obtained under tapping mode. The c-AFM images were obtained under the contact-mode using a Pt-Ir5-coated tip (spring constant 0.2 N/m). For the hole or electron current measurements, the spin-casted polymer (175 nm) on ITO/MoO_3 (10 nm) or ITO/ZnO (40 nm) was scanned under 1.5 V of applied bias in reference to an ITO substrate. The average current and standard deviation were obtained from the current distribution over a 1×2 μm scanned area.

Differential Scanning Calorimetry (DSC): All DSC experiments were performed under nitrogen on a TA Instruments Q2000 differential scanning calorimeter equipped with a TA RCS cooling accessory. The C60-functionalized copolymers were weighed directly into low-mass aluminum Tzero DSC pans with hermeneutic lids. Solutions of P3HT, copolymer, and $PC_{61}BM$ for blends were prepared the same way as for thin films. The solutions were then drop cast while hot through a 0.2 μm PTFE filter onto clean glass substrates and the solvent was removed *in vacuo* over 24 h. The dried films were then scraped from the glass substrates onto weigh paper and the resulting solid was weighed into low-mass aluminum Tzero DSC pans with hermeneutic lids. All sample masses were ~3.2 mg. The temperature was ramped at a rate of 10 °C/min for heating up to 150 °C or 295 °C and cooling to –60 °C over three cycles. The third cycle was used for analysis.

A1.3 Small Molecule Synthetic Procedures

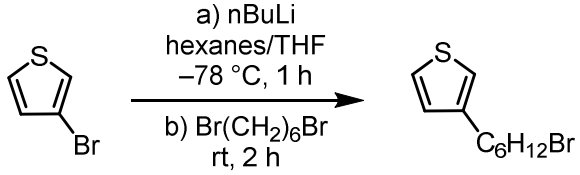

S1

3-(6-bromohexyl)thiophene (S1). To a 200 mL oven-dried Schlenk flask under N_2 were added 3-bromothiophene (2.00 mL, 21.3 mmol, 1.00 equiv) and dry, degassed hexanes (50 mL). The flask was cooled to –78 °C. A solution of n-butyllithium in hexanes (2.65 M, 7.70 mL, 20.4 mmol, 0.96 equiv) was added dropwise over 10 min and the solution was stirred for an additional 10 min. Then THF (5 mL) was injected dropwise over 15 min and the solution was stirred for an additional 1 h. During this time, a white precipitate formed in a transparent, yellow supernatant. The supernatant was removed via cannula transfer and replaced with hexanes/THF (10/1 v/v, 55 mL). 1,6-Dibromohexane (13.1 mL, 85.2 mmol, 4.0 equiv) was then added. The slurry was warmed to r.t. and stirred for 2 h. The reaction was quenched with saturated aq. $NaHCO_3$ (50 mL) and extracted

with Et_2O (100 mL). The organic layer was washed with water (100 mL) and brine (100 mL), dried over $MgSO_4$, treated with decolorizing carbon, filtered, and concentrated *in vacuo* to give a viscous orange oil. Excess 1,6-dibromohexane was removed by distillation (0.20 torr, 55 °C) and the remaining oil was purified by silica gel column chromatography (EtOAc/hexane gradient from 0/100 to 2/98 v/v) to obtain a clear, colorless oil (2.2 g, 42%). HRMS (EI): Calcd. for $C_{10}H_{15}BrS$ $[M]^+$ 246.0078; found, 246.0084.

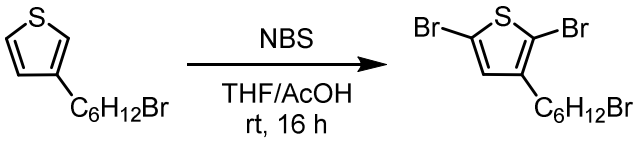

S1 **S2**

2,5-dibromo-3-(6-bromohexyl)thiophene (S2). To an oven-dried 100 mL round-bottom flask were added S1 (2.40 g, 9.71 mmol, 1.00 equiv), THF (25 mL) and AcOH (25 mL). Recrystallized NBS (4.32 g, 24.3 mmol, 2.50 equiv) was added and the solution was stirred at r.t. for 16 h. The reaction was quenched using saturated aq. $NaHCO_3$ (50 mL) and extracted with Et_2O (100 mL). The organic layer was washed with water (100 mL) and brine (100 mL), dried over $MgSO_4$, filtered, and concentrated *in vacuo*. The resulting orange oil was purified by silica gel column chromatography (EtOAc/hexane gradient from 1/99 to 4/96 v/v) to obtain a clear, colorless oil (3.0 g, 77%). HRMS (EI): Calcd. for $C_{10}H_{13}Br_3S$ $[M]^+$ 401.8288; found, 401.8283.

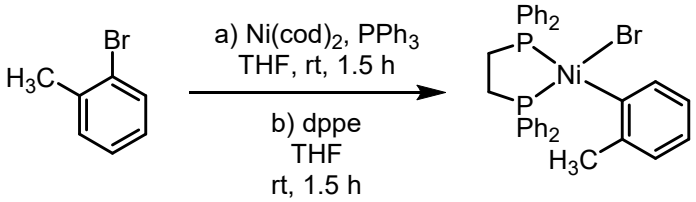

S3

(*o*-tolyl)(1,2-bis(diphenylphosphino)ethane)nickel bromide (S3). $Ni(cod)_2$ (275 mg, 1.00 mmol, 1.00 equiv) and PPh_3 (538 mg, 2.05 mmol, 2.05 equiv) were added to a 20 mL vial equipped with a stir bar in the glovebox. To this vial was added THF (5 mL) and the solution was stirred for

5 min. Then 2-bromotoluene (132 μL, 1.10 mmol, 1.10 equiv) was added and the solution was stirred at r.t. for 1.5 h. Then, 1,2-bis(diphenylphosphino)ethane (dppe) (438 mg, 1.10 mmol, 1.10 equiv) was added and stirred for 1.5 h. Hexane (15 mL) was slowly added as the top layer and the mixture was cooled to –35 °C for 24 h. The resultant yellow precipitate was isolated by filtration inside the glovebox, washed with hexanes (10 mL) and recrystallized from CH_2Cl_2/hexanes (20 mL) at –35 °C to afford a fine yellow powder (375 mg, 60%). HRMS (EI): Calcd. For $C_{33}H_{31}BrNiP_2$ $[M]^+$ 626.0438; found, 626.0447.

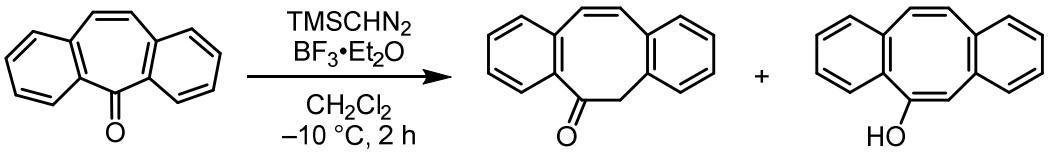

S4 **S4'**

6*H*-Dibenzo[a,e]cyclooctatrien-5-one (S4). In a N_2 flushed 100 mL round-bottom flask was added dibenzosuberenone (3.10 g, 15.0 mmol, 1.00 equiv) and $BF_3 \cdot OEt_2$ (2.80 mL, 22.7 mmol, 1.50 equiv) in CH_2Cl_2 (30 mL). The solution was cooled to –10 °C. A 0.75 M solution of trimethylsilyl diazomethane in CH_2Cl_2 (32.0 mL, 24.0 mmol, 1.60 equiv) was added to the solution dropwise over 1 h and then stirred at –10 °C for an additional 2 h. Then AcOH (0.2 mL) was added to quench the reaction. The mixture was poured into ice water (150 mL). The aqueous layer was extracted with CH_2Cl_2 (3 x 100 mL) and the combined organic layers were washed with brine (100 mL), dried over $MgSO_4$, and filtered. The filtrate was concentrated *in vacuo* and the crude product was purified by silica gel column chromatography (hexanes/CH_2Cl_2 gradient from 90/10 to 30/70, v/v) to give dibenzocyclooctenone (**S4**) as a white solid (1.13 g, 34%) and dibenzocyclooctadienol (**S4'**) as a viscous transparent liquid (2.1 g, 63%). HRMS (EI): Calcd. For $C_{16}H_{12}O$ $[M]^+$ 220.0888; found, 220.0884.

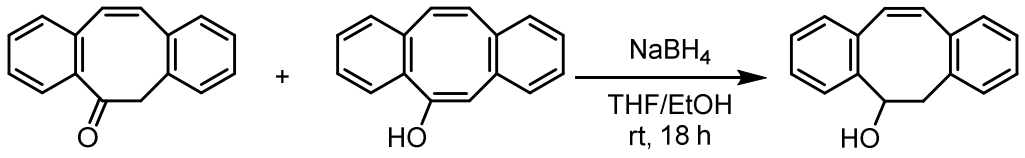

S4 **S4'** **S5**

5,6-Dihydro-dibenzo[a,e]cycloocten-5-ol (S5). Sodium borohydride (0.388 g, 10.3 mmol, 2.00 equiv) was slowly added to a stirred solution of **S4**/**S4'** (1.13 g, 5.13 mmol, 1.00 equiv) in THF/EtOH (1/1, v/v, 60 mL). The reaction was stirred at r.t. for 18 h, then quenched by slow addition of AcOH (0.5 mL). The mixture was concentrated *in vacuo*, and the yellow residue was dissolved in CH_2Cl_2 (50 mL) and washed with brine (50 mL). The aqueous layer was extracted with CH_2Cl_2 (4 x 50 mL). The combined organic layers were dried over $MgSO_4$, treated with decolorizing carbon, filtered and concentrated *in vacuo* to give a white solid (723 mg, 63%). HRMS (EI): Calcd. For $C_{16}H_{14}O$ $[M]^+$ 222.1045; found, 222.1046.

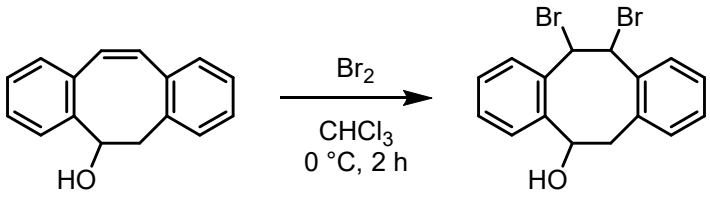

S5 **S6**

11,12-Dibromo-5,6,11,12-tetrahydro-dibenzo[a,e]cycloocten-5-ol (S6). Into a N_2 filled round-bottom flask was added **S5** (0.642 g, 2.89 mmol, 1.00 equiv) in $CHCl_3$ (15 mL) and the resulting solution was cooled to 0 °C using an ice-water bath. A solution of Br_2 (0.150 mL, 2.93 mmol, 1.01 equiv) in $CHCl_3$ (5 mL) was added dropwise over 3 minutes. After stirring for 2 h, the resulting solution was quenched with saturated aq. $Na_2S_2O_3$ (20 mL), and washed with water (20 mL) and brine (20 mL). The organic layer was dried over $MgSO_4$, filtered, and concentrated *in vacuo*, affording a yellow oil. The crude product was purified by silica gel column chromatography

(CH_2Cl_2/hexanes gradient from 5/95 to 70/30 v/v) to obtain a viscous, colorless oil (480 mg, 44%). HRMS (EI): Calcd for $C_{16}H_{13}BrO$ $[M–HBr]^+$ 300.0150; found, 300.0156.

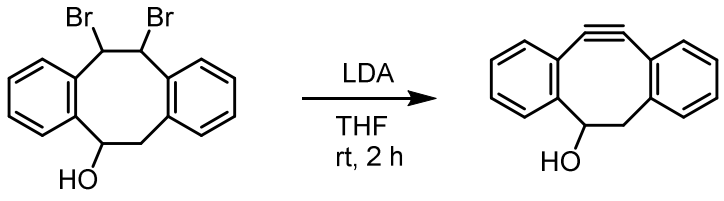

S6 **S7**

5,6-Dihydro-11,12-didehydro-dibenzo[a,e]cycloocten-5-ol (S7). Under an N_2 atmosphere, **S6** (480 mg, 1.26 mmol, 1.00 equiv) was dissolved in THF (15 mL) at r.t. and a solution of commercial lithium diisopropylamide (LDA) (2.0 M in THF, 2.50 mL, 5.00 mmol, 4.00 equiv) was added dropwise over 5 min. The reaction solution was stirred for 2 h, and then quenched by the dropwise addition of water (0.5 mL). The resulting mixture was concentrated *in vacuo* and the resulting yellow oil residue was purified by silica gel column chromatography (hexanes/CH_2Cl_2 gradient from 75/25 to 0/100, v/v) to give a white solid (174 mg, 63%). HRMS (EI): Calcd. For $C_{16}H_{11}O$ $[M–H]^+$ 219.0810; found, 219.0806.

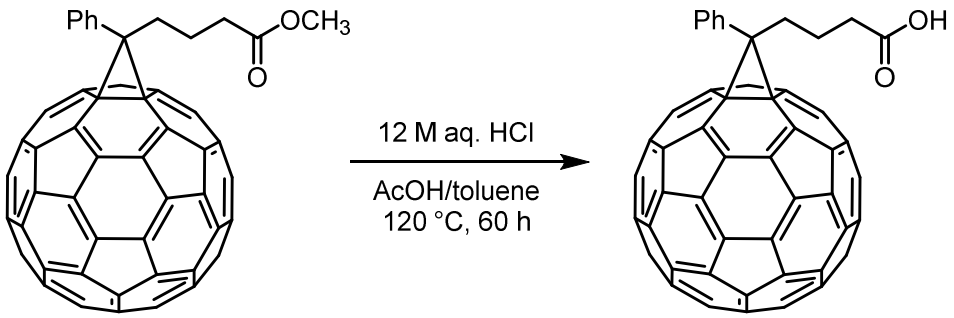

PCBM **S8**

phenyl-C_{61}-butyric acid (S8). Phenyl-C_{61}-butyric acid methyl ester (PCBM) (550 mg, 0.604 mmol, 1.00 equiv) was dissolved in toluene (80 mL) and AcOH (40 mL) in a 350 mL bomb flask then aq. HCl (12 M, 20 mL) was added. The flask was sealed and heated to 120 °C for 60 h with vigorous stirring. The mixture was then cooled to r.t. The now heterogeneous organic layer was

separated from the aquous layer and filtered. The resulting brown solid was washed sequentially with MeOH, acetone, toluene, and Et_2O (30 mL each), to afford a brown powder (541 mg, quant). The product was carried to the next step without further purification. HRMS (ESI-): Calcd. For $C_{71}H_{11}O_2$ $[M–H]^-$ 895.0765; found, 895.0750.

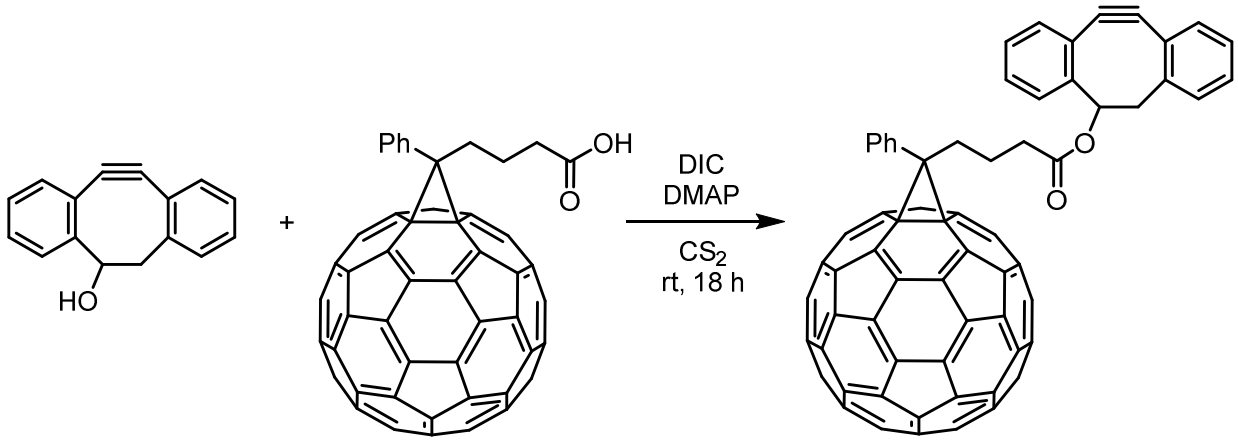

S7 **S8** **S9**

PCB-DIBO (S9). Under an N_2 atmosphere, **S8** (300 mg, 0.334 mmol, 1.00 equiv) was suspended in CS_2 (15 mL) in a 50 mL round-bottom flask. Then **7** (81 mg, 0.37 mmol, 1.1 equiv) and 4-dimethylaminopyridine (41 mg, 0.34 mmol, 1.0 equiv) were added, followed by diisopropylcarbodiimide (DIC) (57 µL, 0.37 mmol, 1.1 equiv). The reaction was stirred at r.t. in the dark for 18 h and then quenched with H_2O (1 mL). Then the organic layer was washed with H_2O (20 mL) and brine (20 mL), then concentrated *in vacuo*. The resulting brown solid was purified by silica gel column chromatography (CH_2Cl_2/hexane gradient from 10/90 to 100/0 v/v), affording a dark brown powder (300 mg, 82%). MALDI-TOF-MS: Calcd. For $C_{87}H_{22}O_2$ [M] 1099.162; found,1100.422.

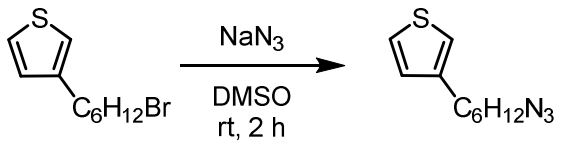

S1 **S10**

3-(6-azidohexyl)thiophene (S10). In a 20 mL vial equipped with a stir bar, **S1** (288 mg, 1.17 mmol, 1.00 equiv) was dissolved in DMSO (5 mL). Sodium azide (160 mg, 2.46 mmol, 2.10 equiv) was then added. The reaction mixture was stirred for 10 min and then sonicated for 3 min to facilitate sodium azide dissolution. Then the solution was stirred for 2 h at r.t. before quenching with H_2O (5 mL). The mixture was extracted with Et_2O (3 x 10 mL). The combined organic layers were washed with brine (10 mL), dried over $MgSO_4$, filtered, and concentrated *in vacuo*. The oil was purified by silica gel column chromatography (hexanes/EtOAc gradient from 100/0 to 90/10, v/v) to give a yellow oil (207 mg, 85%). HRMS (EI): Calcd. For $C_{10}H_{15}NS$ $[M–N_2]^+$ 181.092; found, 181.0921.

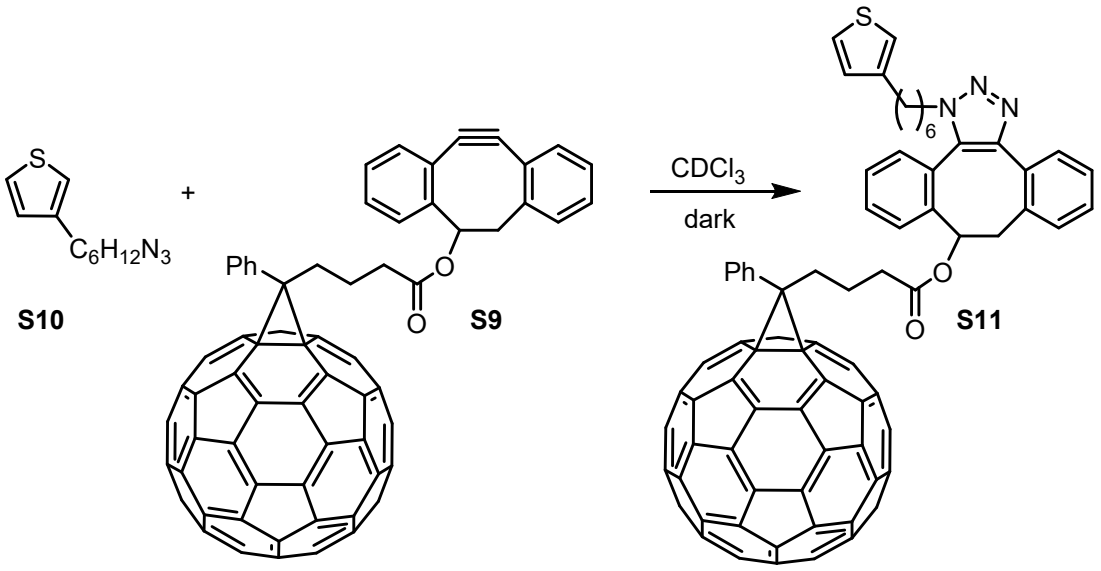

3AHT-PCB-DIBO (S11). In a 20 mL vial, **S9** (25.6 mg, 0.0233 mmol, 1.00 equiv) and **S10** (5.2 mg, 0.025 mmol, 1.10 equiv) were added. Then $CDCl_3$ (1.5 mL) was added and the solution was transferred to a NMR tube. ^1H NMR spectra were collected at 10 min, 8 h, 29 h and 43 h. At 29 h, **S10** (2 mg, 0.010 mmol, 0.4 equiv) was added to the NMR tube and then an additional spectrum was acquired to show starting material peak reappearance. IR spectra were also collected at 8 h and at 29 h (after the second addition of **S10**). The resulting solution was concentrated *in vacuo* and the resulting solid was purified by silica gel column chromatography (CH_2Cl_2/MeOH gradient from 100/0 to 90/10 v/v) to give a dark brown solid that was a mixture of regioisomers (23.3 mg, 76%). MALDI-TOF-MS: Calcd. For $C_{97}H_{37}N_3O_2S$ [M] 1308.264; found 1308.894.

A1.4 Small Molecule NMR Spectra

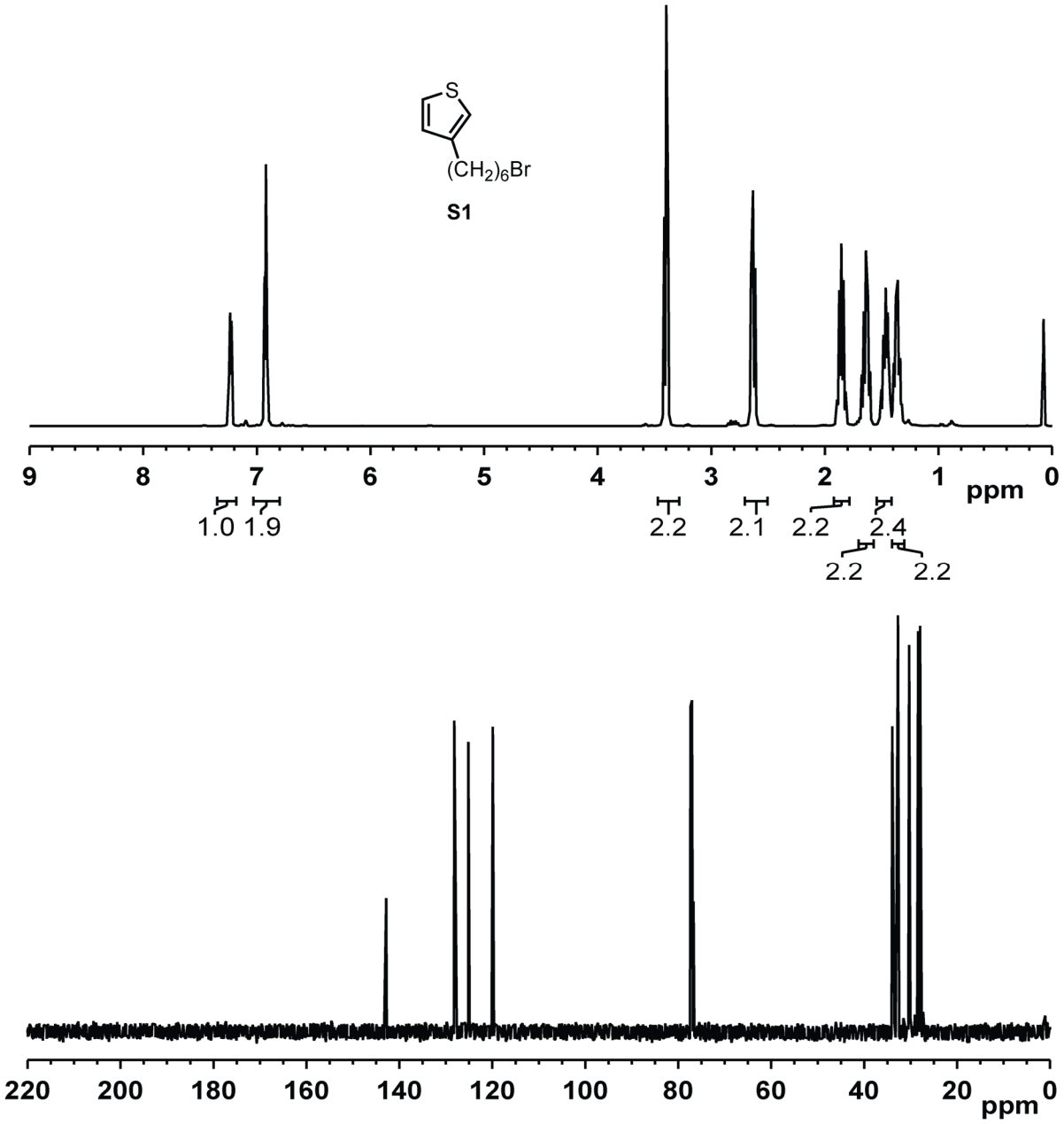

Figure A1.1 NMR spectra for **S1**. ^{1}H NMR (400 MHz, $CDCl_3$) δ 7.23 (dd, J = 4.8, 2.9 Hz, 1H), 6.92 (m, 2H), 3.40 (t, J = 6.8 Hz, 2H), 2.63 (t, J = 7.6 Hz, 2H), 1.86 (m, 2H), 1.64 (m, 2H), 1.46 (m, 2H), 1.36 (m, 2H). ^{13}C NMR (100 MHz, $CDCl_3$) δ 142.84, 128.19, 125.16, 119.89, 33.96, 32.71, 30.32, 30.11, 28.38, 27.97.

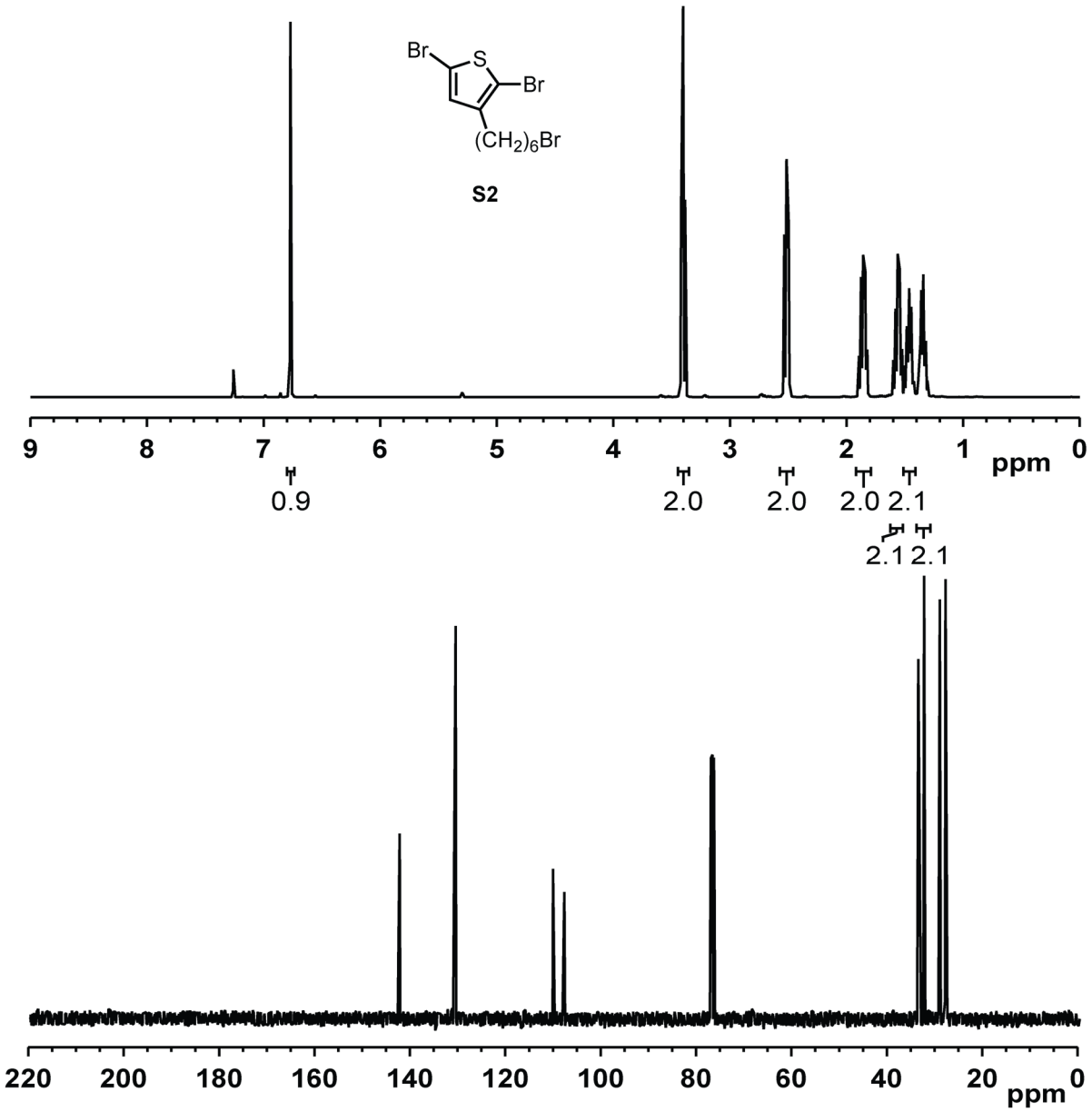

Figure A1.2 NMR spectra for **S2**. ^{1}H NMR (400 MHz, $CDCl_3$) δ 6.77 (s, 1H), 3.40 (t, J = 6.8 Hz, 2H), 2.52 (t, J = 7.6 Hz, 2H), 1.86 (m, 2H), 1.56 (m, 2H), 1.46 (m, 2H), 1.35 (m, 2H). ^{13}C NMR (100 MHz, $CDCl_3$) δ 142.59, 130.86, 110.44, 108.07, 33.86, 32.64, 29.35, 29.29, 28.15, 27.87.

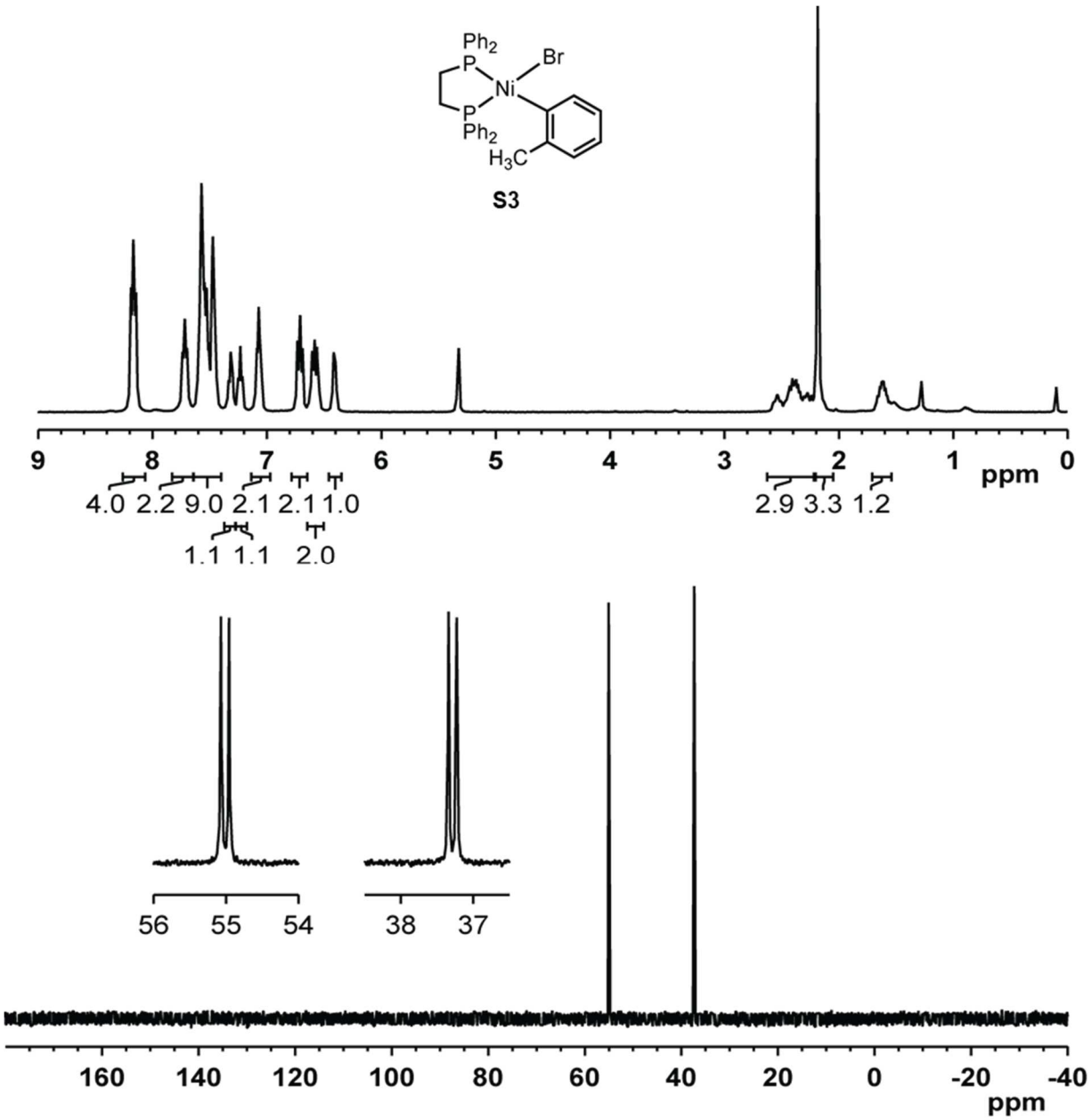

Figure A1.3 NMR spectra for **S3**. ^{1}H NMR (400 MHz, CD_2Cl_2) δ 8.16 (m, 4H), 7.72 (app t, J = 8.3 Hz, 2H), 7.51 (m, 9H), 7.31 (app t, J = 7.2 Hz, 1H), 7.23 (app t, J = 6.4 Hz, 1H), 7.07 (app t, J = 6.5 Hz, 2H), 6.71 (m, 2H), 6.58 (m, 2H), 6.41 (d, J = 6.6 Hz, 1H), 2.39 (m, 3H), 2.18 (s, 3H), 1.61 (m, 1H). ^{31}P NMR (162 MHz, CD_2Cl_2) δ 55.01 (d, J = 18.3 Hz), 37.28 (d, J = 18.2 Hz).

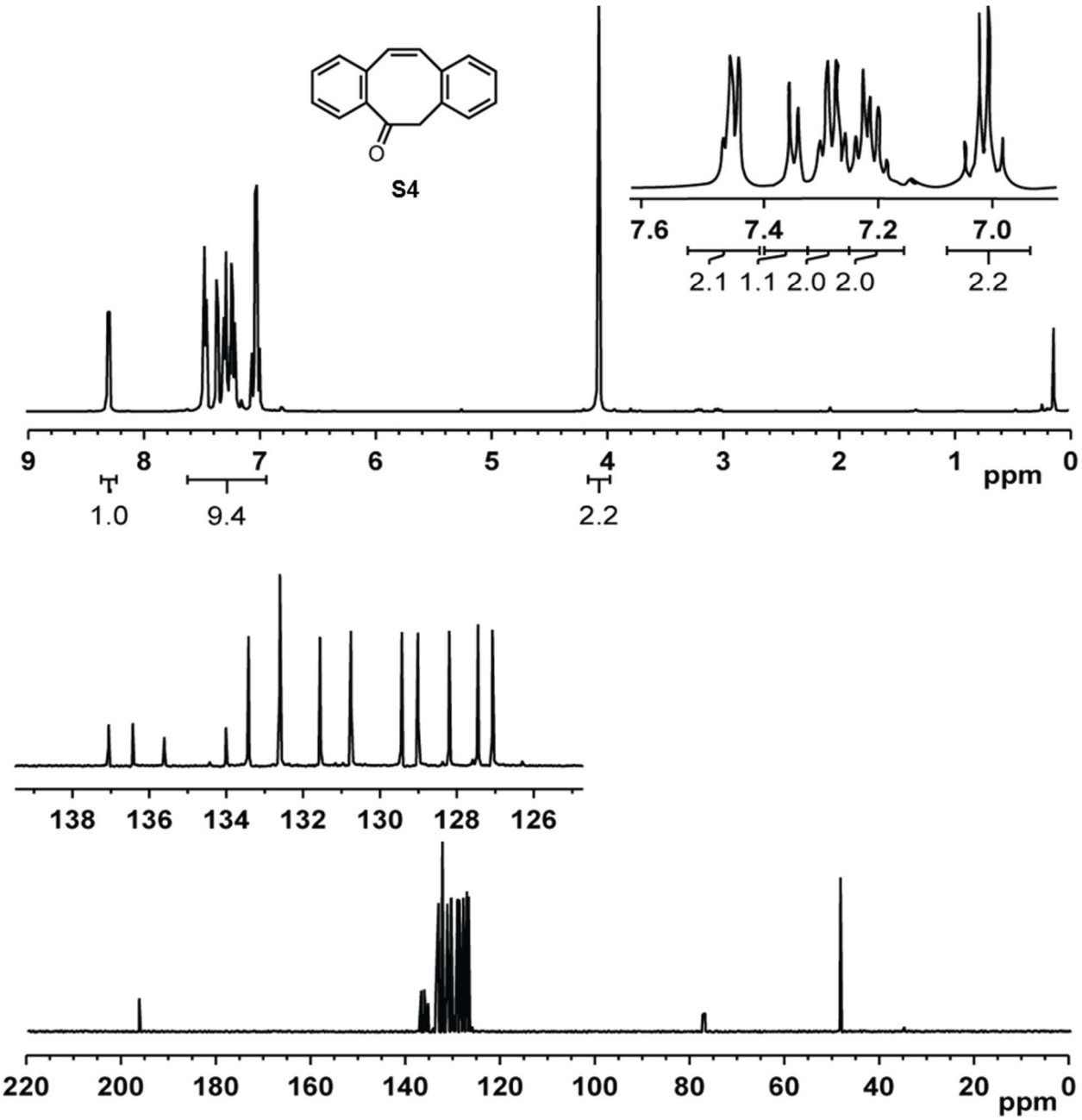

Figure A1.4 NMR spectra for **S4**. ^{1}H NMR (500 MHz, $CDCl_3$) δ 8.29 (d, J = 8.0 Hz, 1H), 7.46 (m, 2H), 7.35 (d, J = 7.7 Hz, 1H), 7.28 (m, 2H), 7.21 (m, 2H), 7.02 (m, 2H), 4.06 (s, 2H). ^{13}C NMR (126 MHz, $CDCl_3$) δ 196.58, 137.06, 136.43, 135.61, 134.01, 133.42, 132.60, 131.56, 130.76, 129.43, 129.01, 128.20, 127.45, 127.07, 48.60.

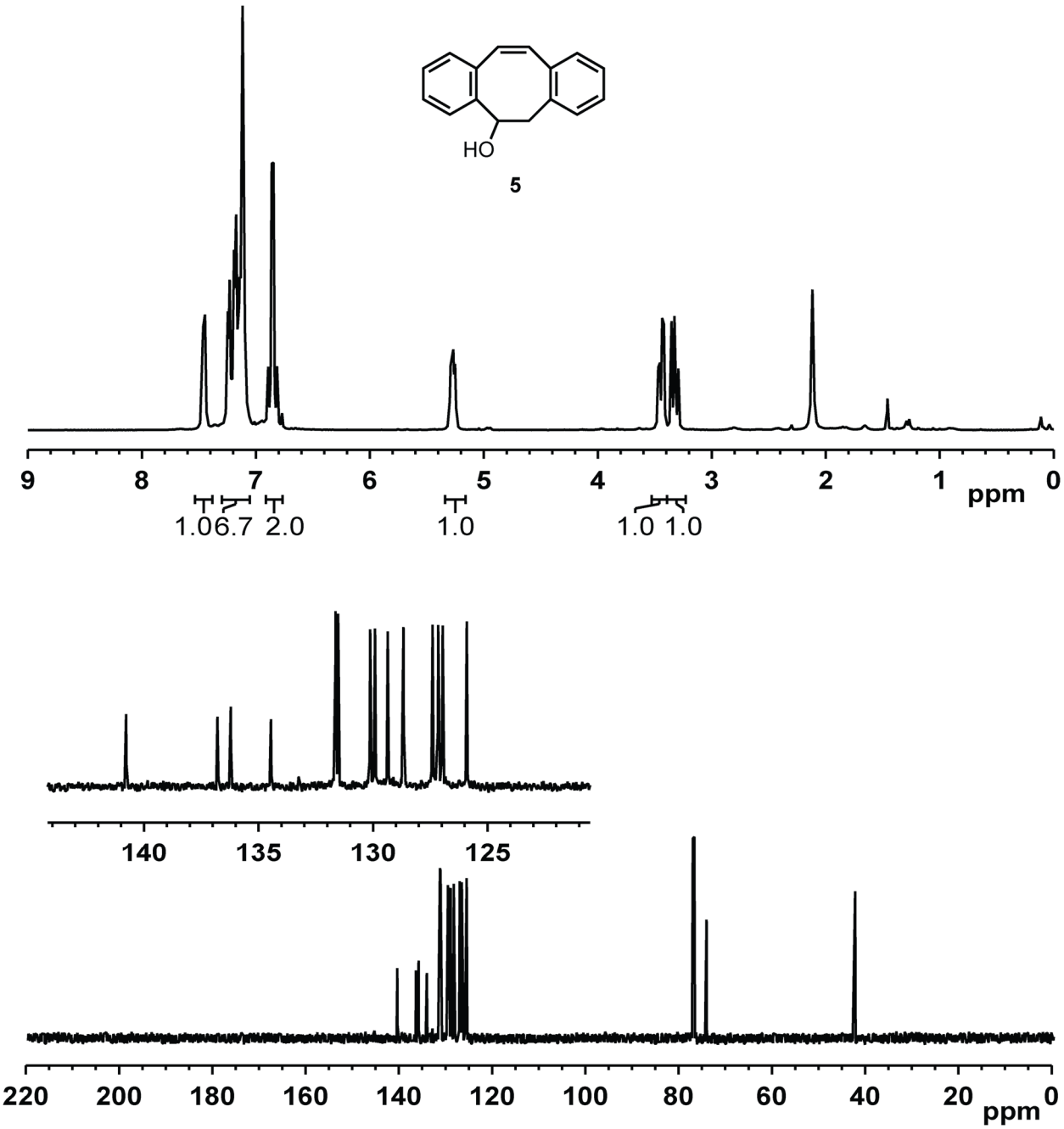

Figure A1.5 NMR spectra for **S5**. ^{1}H NMR (400 MHz, $CDCl_3$) δ 7.48 (m, 1H), 7.17 (m, 7H), 6.84 (m, 2H), 5.27 (dd, J = 9.6, 6.3 Hz, 1H), 3.45 (dd, J = 13.7, 6.1 Hz, 1H), 3.32 (dd, J = 13.6, 10.2 Hz, 1H). *Acetone, ■ H_2O, ▲ grease. ^{13}C NMR (100 MHz, $CDCl_3$) δ 140.78, 136.79, 136.21, 134.46, 131.63, 131.53, 130.12, 129.91, 129.36, 128.67, 127.40, 127.15, 126.96, 125.91, 74.46, 42.59.

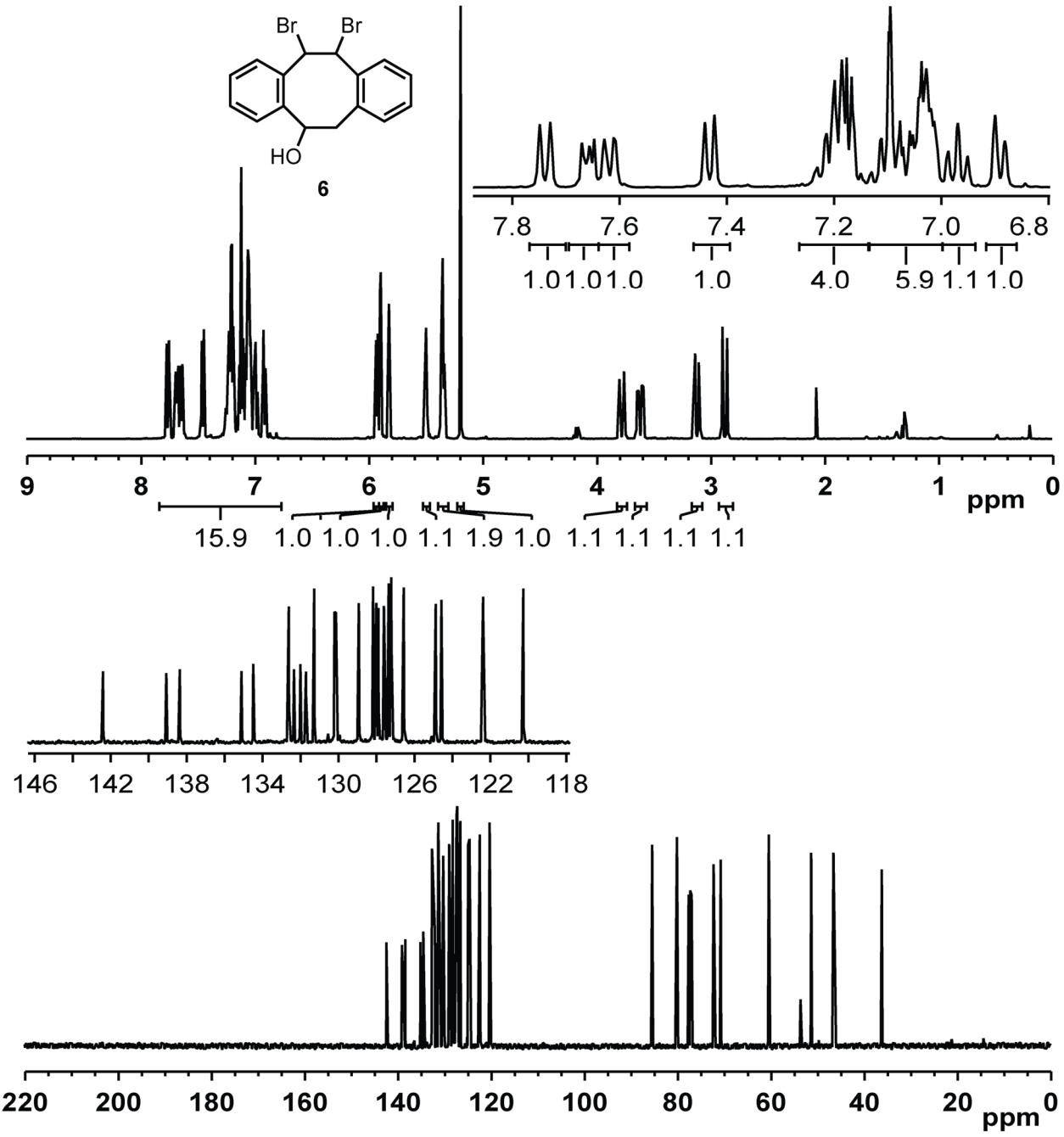

Figure A1.6 NMR spectra for **S6** (a 1:1 mixture of diastereomers). ^{1}H NMR (400 MHz, CD_2Cl_2) δ 7.74 (d, *J* = 7.8 Hz, 1H), 7.66 (m, 1H), 7.62 (d, *J* = 7.0 Hz, 1H), 7.43 (d, *J* = 7.2 Hz, 1H), 7.23-7.18 (m, 4H), 7.01-7.11 (m, 6H), 6.97 (t, *J* = 7.2 Hz, 1H), 6.89 (d, *J* = 7.4 Hz, 1H), 5.90 (d, *J* = 5.5 Hz, 1H), 5.87 (d, *J* = 2.2 Hz, 1H), 5.80 (s, 1H), 5.47 (t, *J* = 3.2 Hz, 1H), 5.33 (t, *J* = 5.0 Hz, 2H), 5.17 (s, 1H), 3.75 (dd, *J* = 16.1, 1.2 Hz, 1H), 3.59 (dd, *J* = 16.4, 6.2 Hz, 1H), 3.10 (dd, *J* = 16.1, 3.7 Hz, 1H), 2.85 (d, *J* = 16.4 Hz, 1H). ^{13}C NMR (100 MHz, $CDCl_3$) δ 142.40, 139.07, 138.36, 135.11, 134.49, 132.62, 132.35, 132.01, 131.72, 131.28, 130.21, 130.14, 128.93, 128.18, 128.01, 127.90, 127.61, 127.36, 127.22, 126.57, 124.88, 124.58, 122.39, 120.27, 85.40, 80.09, 72.24, 70.70, 60.40, 51.31, 46.53, 36.16. *EtOAc

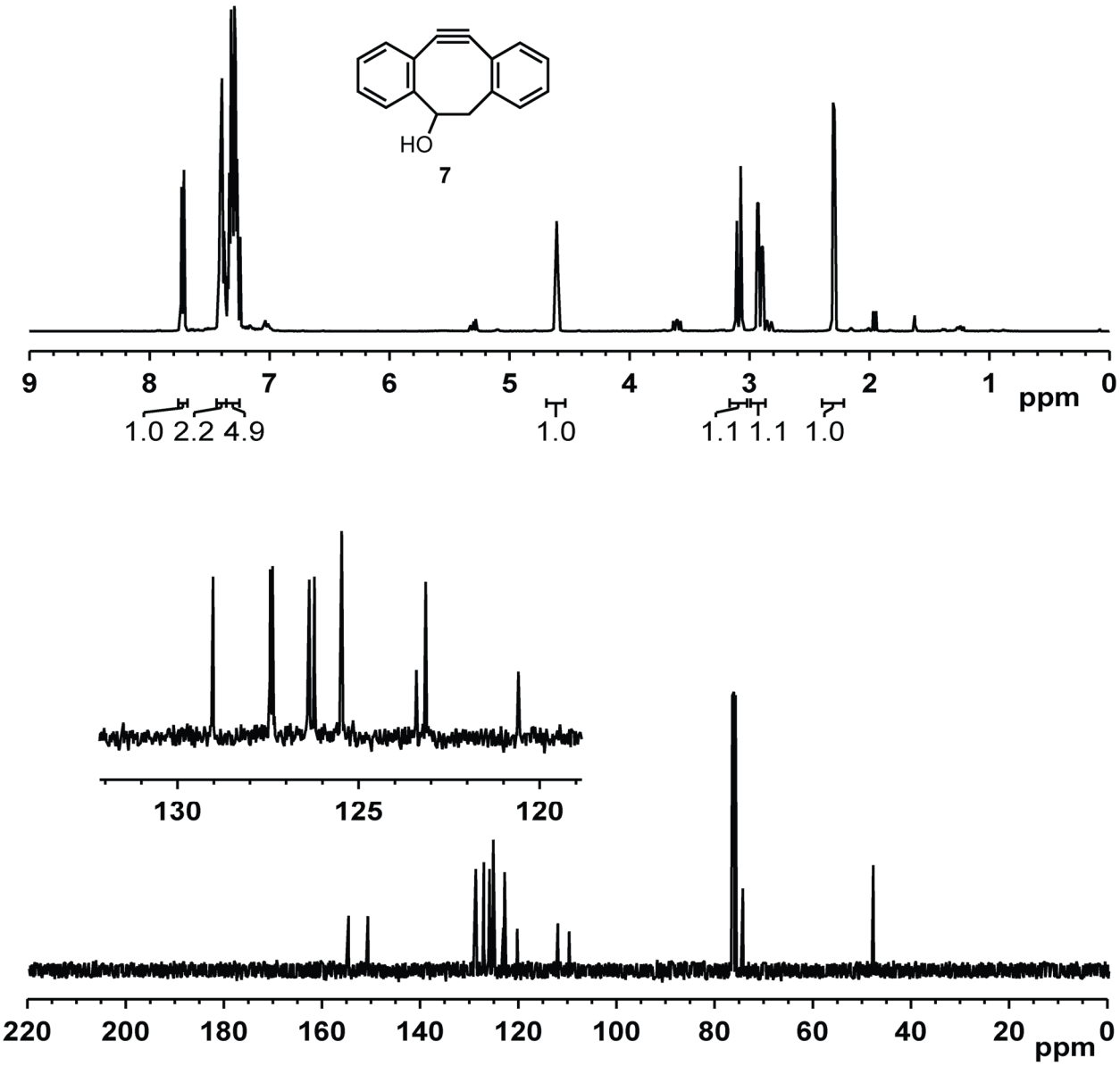

Figure A1.7 NMR spectra for **S7**. ^{1}H NMR (400 MHz, $CDCl_3$) δ 7.72 (d, *J* = 7.8 Hz, 1H), 7.40 (m, 2H), 7.30 (m, 5H), 4.60 (bs, 1H), 3.09 (dd, *J* = 14.7, 2.1 Hz, 1H), 2.91 (dd, *J* = 14.7, 3.7 Hz, 1H), 2.30 (d, *J* = 4.6 Hz, 1H). ^{13}C NMR (100 MHz, $CDCl_3$) δ 155.67, 151.75, 129.76, 128.18, 128.11, 127.10, 126.96, 126.20, 126.19, 124.14, 123.88, 121.33, 113.04, 110.73, 75.34, 48.78. *unknown and unresolvable impurity

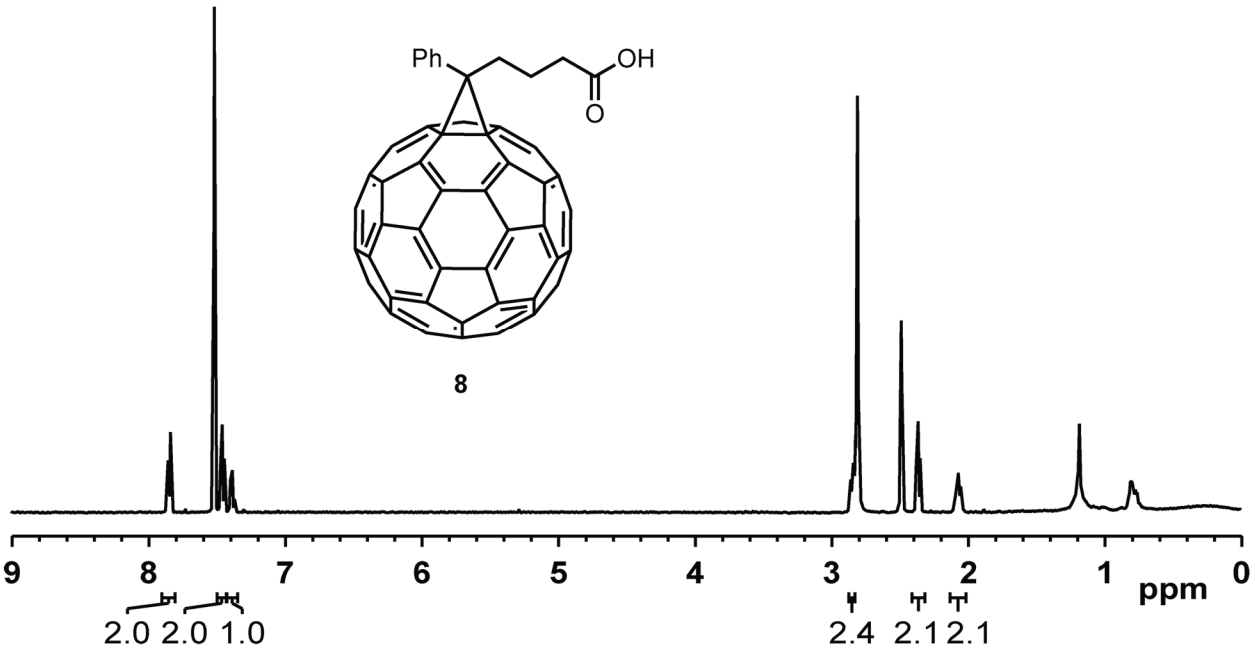

Figure A1.8 NMR spectrum for **S8**. ^{1}H NMR (500 MHz, $CDCl_3$/DMSO-d_6/CS_2 3:1:1) δ 7.84 (d, J = 7.3 Hz, 2H), 7.46 (m, 2H), 7.38 (m, 1H), 2.84 (m, 2H), 2.36 (t, J = 7.6 Hz, 2H), 2.07 (m, 2H). *grease

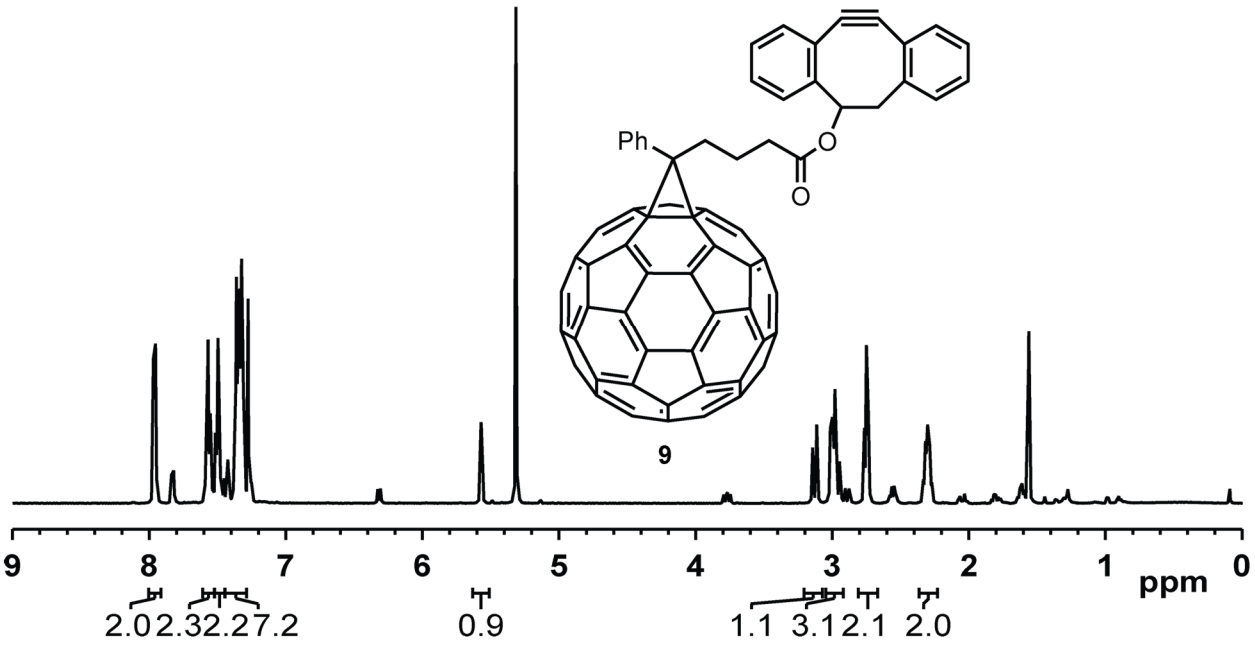

Figure A1.9 NMR spectrum for S9. ^{1}H NMR (500 MHz, $CDCl_3$) δ 7.96 (d, J = 8.0 Hz, 2H), 7.56 (m, 2H), 7.50 (m, 2H), 7.35 (m, 7H), 5.57 (s, 1H), 3.13 (m, 1H), 2.98 (m, 3H), 2.75 (t, J = 7.3 Hz, 2H), 2.31 (m, 2H). *unknown and unresolvable impurity. ■DCM

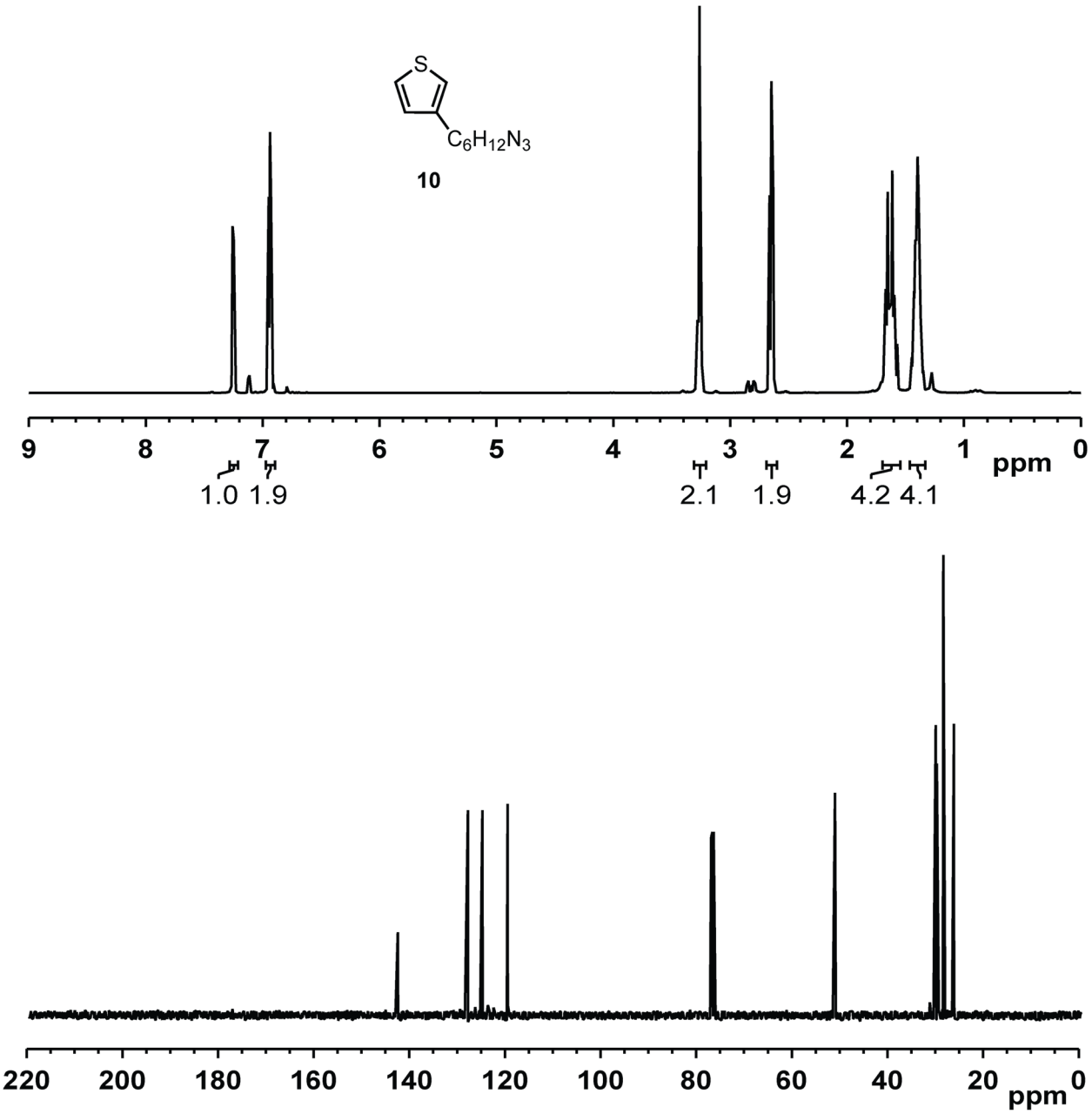

Figure A1.10 NMR spectrum for **S10**. ^{1}H NMR (500 MHz, $CDCl_3$) δ 7.25 (dd, *J* = 4.8, 3.0 Hz, 1H), 6.94 (m, 2H), 3.26 (t, *J* = 6.9 Hz, 2H), 2.65 (t, *J* = 7.7 Hz, 2H), 1.63 (m, 4H), 1.40 (m, 4H). ^{13}C NMR (126 MHz, $CDCl_3$) δ 142.86, 128.19, 125.17, 119.89, 51.42, 30.37, 30.13, 30.12, 28.78, 26.55. *unknown and unresolvable impurity, ■grease

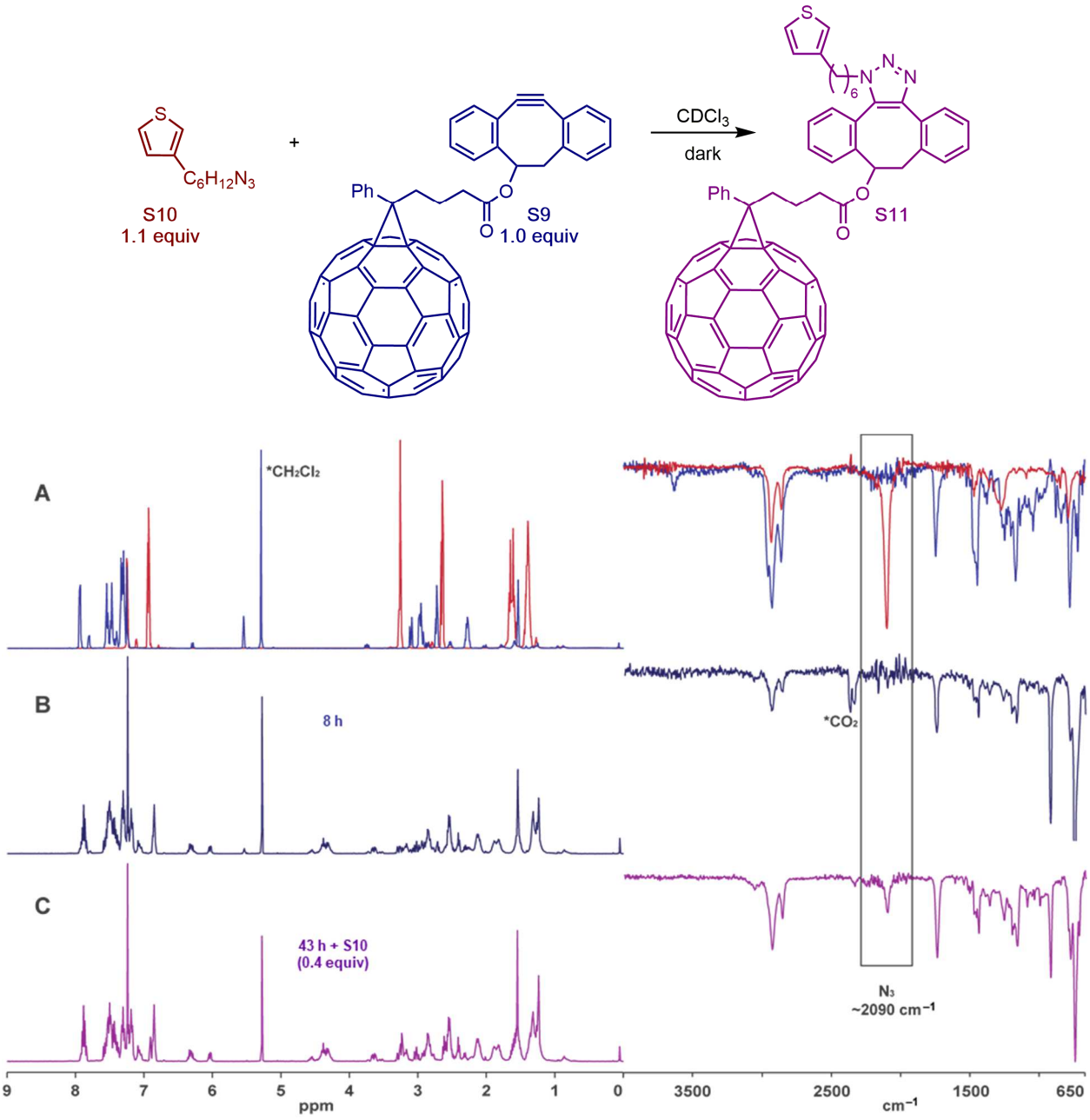

Figure A1.11 ^{1}H NMR (left) and IR (right) spectra for (A) **S10** (red) and **S9** (blue) overlay. (B) Reaction solution at 8 h with unreacted **S9**. (C) After 29 h additional **S10** (0.4 equiv) was added and the spectrum shows reaction solution after 43 h with unreacted **S10**. Note that two regioisomers of the triazole are formed in the click reaction.

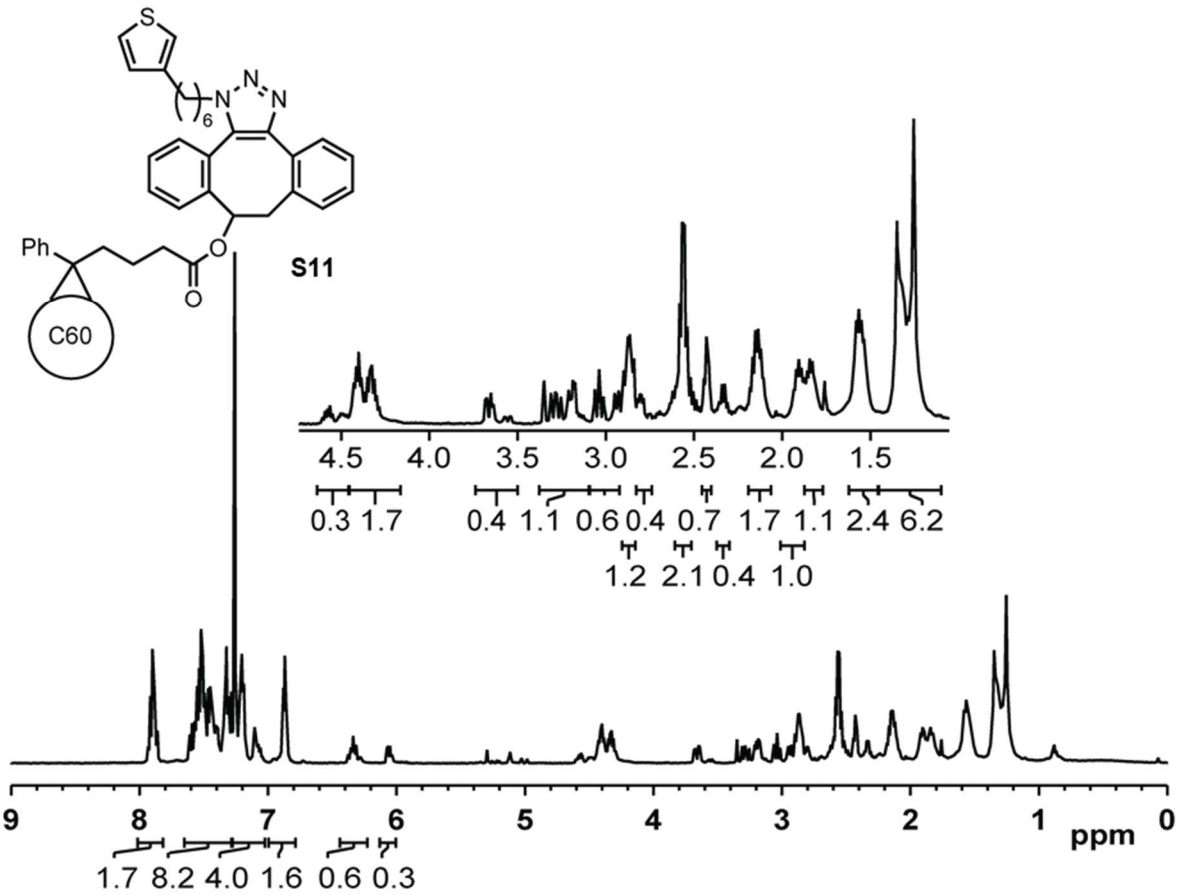

Figure A1.12 NMR spectrum for **S11** (a mixture of regioisomers and diastereomers). ^{1}H NMR (500 MHz, $CDCl_3$) δ 7.89 (m, 2H), 7.46 (m, 8H), 7.19 (m, 4H), 6.87 (m, 2H), 6.33 (m, 0.6H), 6.05 (m, 0.3H), 4.58 (m, 0.3H), 4.36 (m, 1.7H), 3.61 (m, 0.4H), 3.25 (m, 1H), 3.00 (m, 0.6H), 2.87 (m, 1H), 2.80 (m, 0.4H), 2.56 (q, J = 7.3 Hz, 2H), 2.43 (t, J = 7.3 Hz, 0.7H), 2.33 (q, J = 7.2 Hz, 0.4H), 2.14 (m, 1.7H), 1.90 (m, 1H), 1.84 (m, 1H), 1.57 (m, 2H), 1.31 (m, 6H).

A1.5 Polymerization Procedures and Data

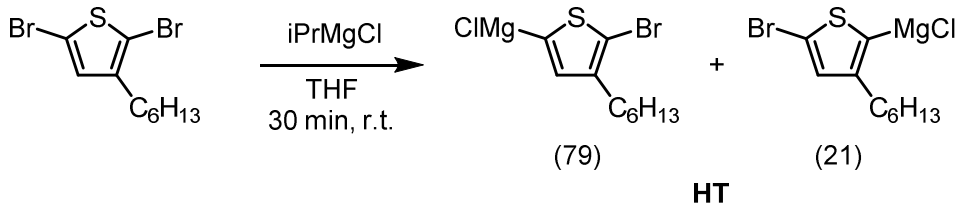

3HT monomer activation. In the glovebox, 2,5-dibromo-3-hexylthiophene (117 mg, 0.359 mmol, 1.00 equiv) was dissolved in THF (3 mL) in an 8 mL vial equipped with a stir bar. iPrMgCl (2.0 M in THF, 160 µL, 0.32 mmol, 0.89 equiv) was added and stirred at r.t. for 30 min. An aliquot (0.5 mL) was quenched with 6 M aq. HCl (0.1 mL), extracted with $CHCl_3$ (2 x 1 mL), dried over $MgSO_4$, filtered, and analyzed by GC, showing a mixture of **HT** regioisomers in a 79:21 ratio. Note that only the major regioisomer undergoes polymerization with precatalyst **S3**, giving highly regioregular materials. Fresh solution of **HT** was synthesized before every polymerization.

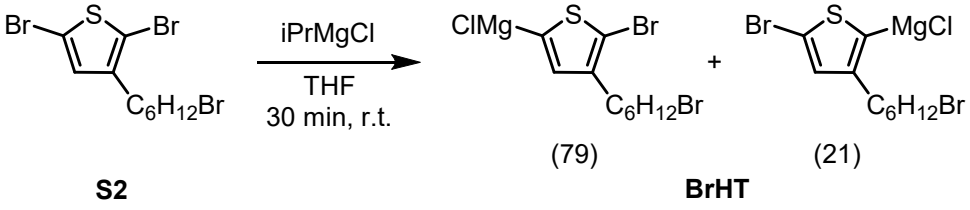

BrHT monomer activation. In the glovebox, **S2** (149 mg, 0.368 mmol, 1.00 equiv) was dissolved in THF (3 mL) in an 8 mL vial equipped with a stir bar. iPrMgCl (2.0 M in THF, 160 µL, 0.320 mmol, 0.87 equiv) was added and the reaction stirred at r.t. for 30 min. An aliquot (0.5 mL) was quenched with 6 M aq. HCl (0.1 mL), extracted with $CHCl_3$ (2 x 1 mL), dried over $MgSO_4$, filtered and analyzed by GC, showing a mixture of **BrHT** regioisomers in a 79:21 ratio. Note that only the major regioisomer undergoes polymerization with precatalyst **S3**, giving highly regioregular materials. Fresh solution of **BrHT** was synthesized before every polymerization.

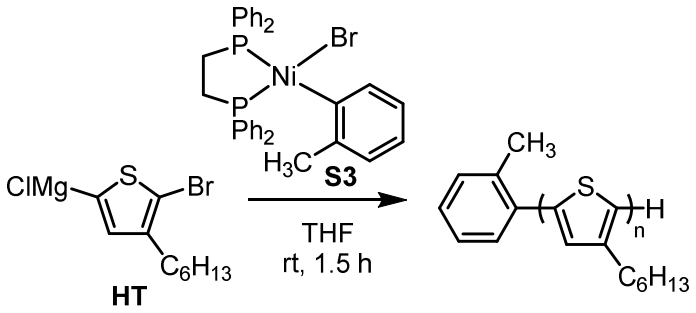

Poly(3-hexylthiophene) (P3HT): To an oven-dried 500 mL round-bottom flask, a 0.17 M solution of HT (15 mL, 2.5 mmol, 250 equiv) in THF was added and diluted with THF (250 mL). A 0.010 M solution of precatalyst S3 (1.0 mL, 0.010 mol, 1.0 equiv) in THF was injected and the solution was stirred at r.t. for 1.5 h. The polymerization was quenched with 6 M aq. HCl (30 mL), and precipitated with MeOH (200 mL). The precipitate was collected on filter paper and purified by Soxhlet extraction sequentially with acetone, MeOH, hexane, CH2Cl2 and CHCl3. The CHCl3 fraction was dried in vacuo to afford P3HT as a dark purple solid (374 mg, 80%). Gel permeation chromatography (GPC) after purification: Mn = 61.8 kg/mol, Đ = 1.26.

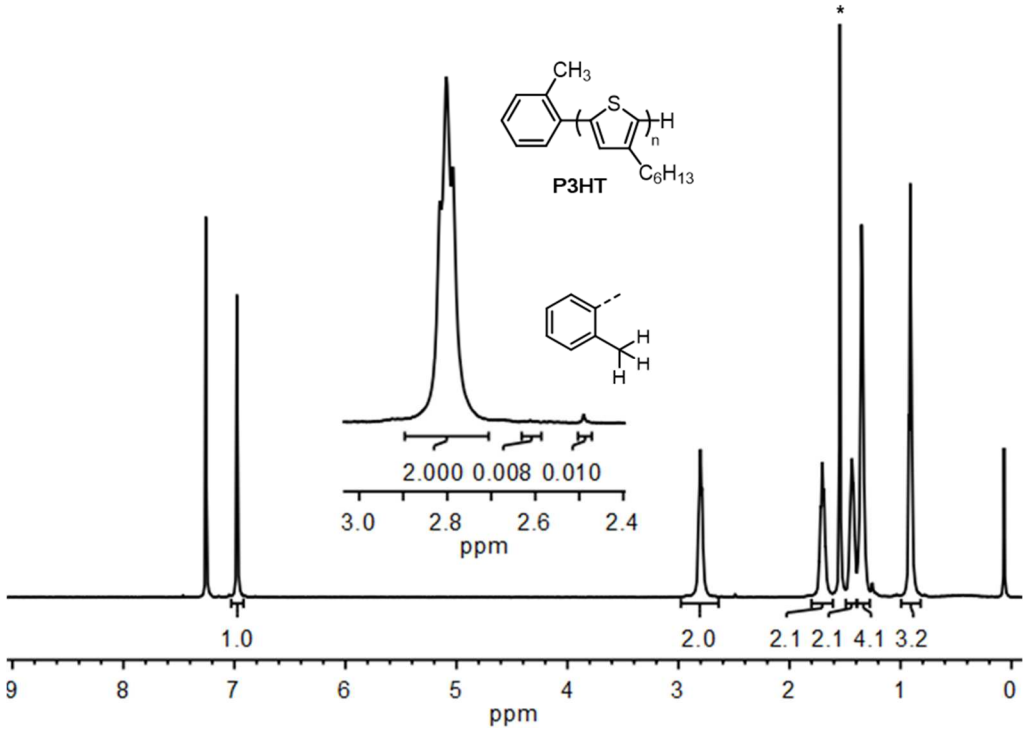

Figure A1.13 NMR spectrum for **P3HT**. ^{1}H NMR (500 MHz, $CDCl_3$) δ 6.98 (s, 1H), 2.80 (t, J = 7.9 Hz, 2H), 1.71 (m, 2H), 1.43 (m, 2H), 1.35 (m, 4H), 0.99 (m, 3H). ^{1}H NMR shows >99% regioregularity and M_n = 49.8 kg/mol based on end-group analysis (inset). The M_n obtained by GPC is an overestimation by a factor of 1.2, in reasonable agreement with a previous report.[6] *H_2O

A1.5.1 Copolymers for Compositional Studies

Poly(3-hexylthiophene-*grad*-3-(6-bromohexyl)thiophene)60:40 (grad40$_{Br}$). In the glovebox, to an oven-dried 50 mL Schlenk flask, a 0.122 M solution of **HT** (2.40 mL, 0.293 mmol, 54.0 equiv) in THF was added and diluted with THF (10 mL). The Schlenk flask was capped and removed from the glovebox, put under N_2 and cooled to 0 °C. In a 20 mL vial, a 0.0863 M solution of **BrHT** (1.70 mL, 0.147 mmol, 27.0 equiv) in THF was added and diluted with THF (1.3 mL). The solution of **BrHT** was taken out of the glovebox with a syringe and affixed to the syringe pump. A 0.010

M solution of precatalyst **S3** (0.54 mL, 5.4 μmol, 1.0 equiv) in THF was taken out of the glovebox in a plastic syringe and injected to the solution of **3HT**. After 2 min 48 s, the syringe pump was activated to inject **BrHT** at a rate of 0.1 mL/min. Aliquots (2 mL) were removed at 7, 17, 35 (addition completed), 69 and 108 min (reaction completed) and quenched with 6 M aq. HCl (2 mL). The resulting solution was then extracted with $CHCl_3$ (3 x 2 mL). The combined organic layers were dried over $MgSO_4$, filtered, and concentrated *in vacuo* to afford crude polymer. The samples were analyzed by GC for monomer conversion and GPC for M_n. Then these samples were purified (see below) and analyzed by ^1H NMR spectroscopy to determine the cumulative mole fraction of **BrHT**.

Purification of aliquots for NMR spectroscopic analysis: The first aliquot was purified using silica gel column chromatography (CH_2Cl_2/hexane gradient from 0/100 to 100/0 v/v). The crude polymers from the remaining aliquots were dissolved in a minimal amount of $CHCl_3$ and precipitated with cold MeOH (10 mL). The resulting mixture was centrifuged for 15 min, the clear supernatant was decanted and the reddish purple precipitate was collected and dried *in vacuo*.

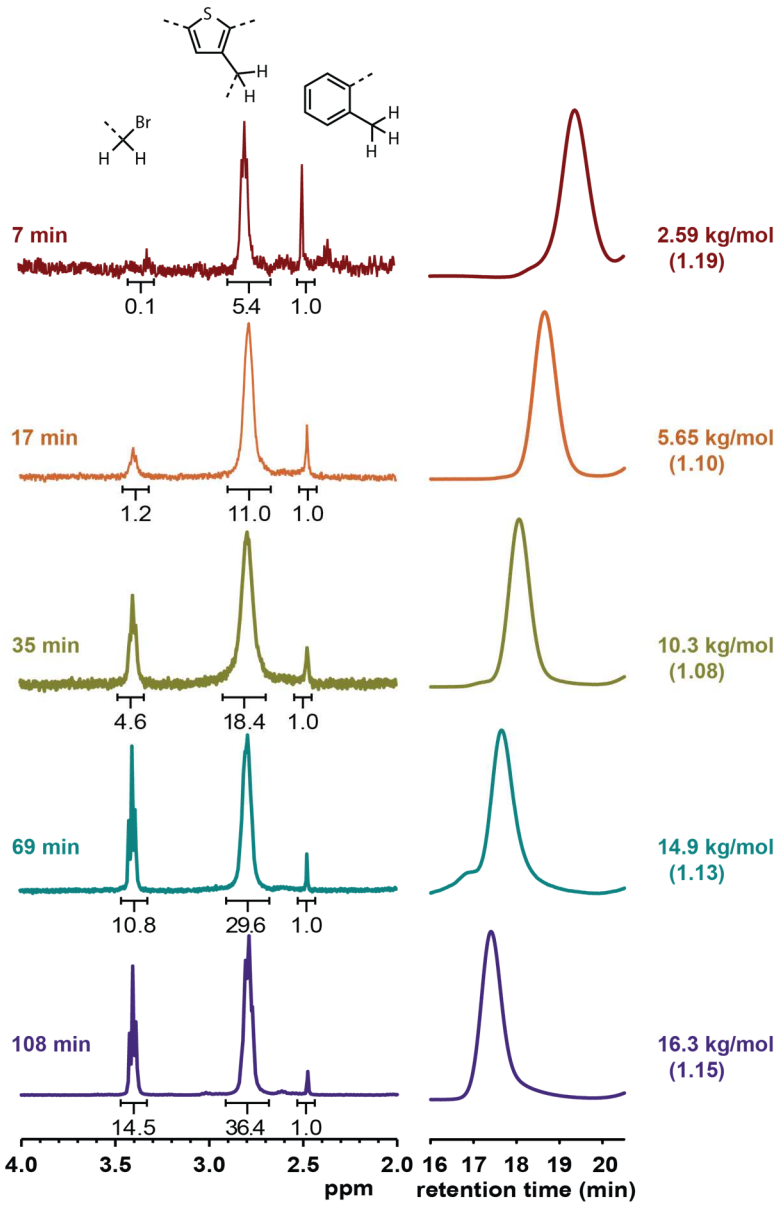

Figure A1.14 ^{1}H NMR spectra (left) and GPC curves (right) for aliquots drawn during the synthesis of **grad40$_{Br}$**. GPC data are labeled with M_n (top) and Đ (in parenthesis, bottom).

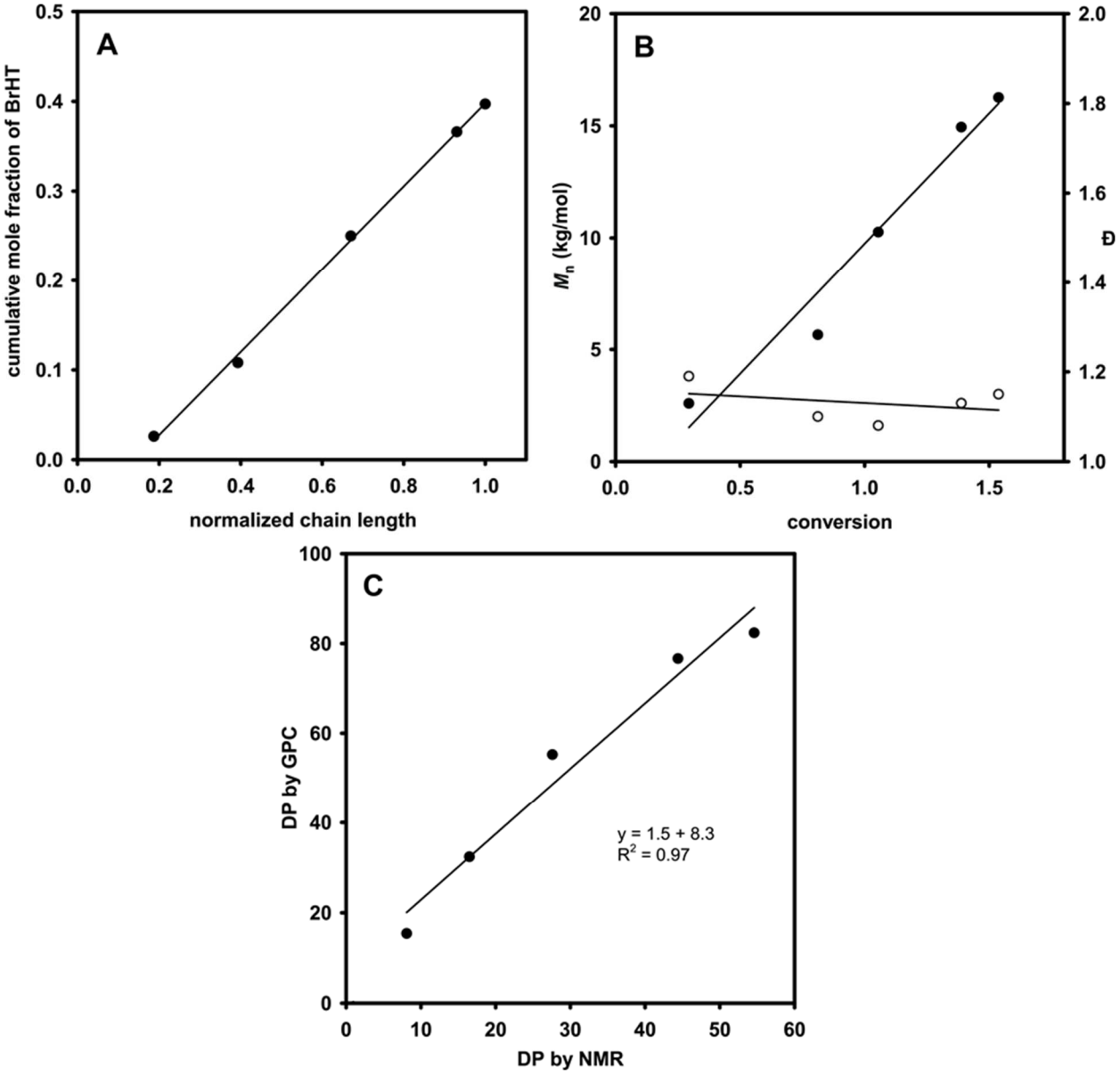

Figure A1.15 (A) Plot of the cumulative mole fraction of monomer **BrHT** in **grad40$_{Br}$** as a function of normalized chain length, (B) M_n (filled circles, ●) and Đ (open circles, ○) versus % conversion, and (C) comparison of the degree of polymerization (DP) obtained by GPC and ^{1}H NMR spectroscopic analysis of end groups. DP = M_n/ average repeat unit MW. Comparing the results of these two methods, it appears that GPC overestimates the DP of these copolymers by a factor of approximately 1.5, in reasonable agreement with a previous report.[6]

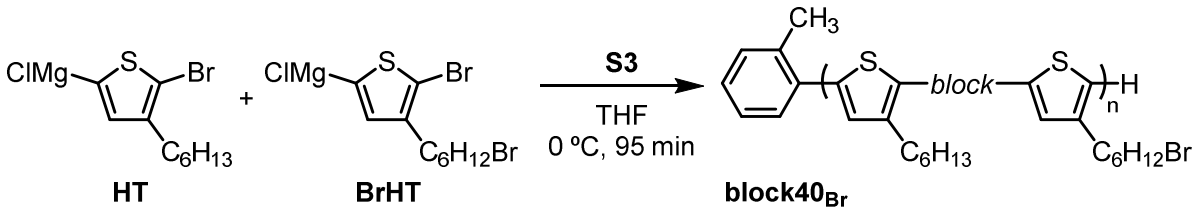

HT **BrHT** **block40$_{Br}$**

Poly(3-hexylthiophene-*block*-3-(6-bromohexyl)thiophene)60:40 (block40$_{Br}$). In the glovebox, to an oven-dried 50 mL Schlenk flask, a 0.123 M solution of **HT** (3.00 mL, 0.369 mmol, 48.0 equiv) in THF was added and diluted with THF (25 mL). The Schlenk flask was capped and removed from the glovebox, put under N_2 and cooled to 0 °C. A 0.010 M solution of precatalyst **S3** (0.77 mL, 7.7 μmol, 1.0 equiv) in THF was added to the solution of **HT**. After 30 min, a 0.123 M solution of **BrHT** (2.00 mL, 0.246 mmol, 32 equiv) in THF was injected into the reaction solution. Aliquots (2 mL) were removed at 12, 34, 40, 50, 66 and 95 min (reaction completed), and quenched with 6 M aq. HCl (2 mL). The resulting solutions were then extracted with $CHCl_3$ (3 x 2 mL). The combined organic layers were dried over $MgSO_4$, filtered, and concentrated *in vacuo* to afford crude polymer. The samples were analyzed by GC for monomer conversion and GPC for M_n. Then these samples were purified (see page S25) and analyzed by ^1H NMR spectroscopy to determine the cumulative mole fraction of **BrHT**.

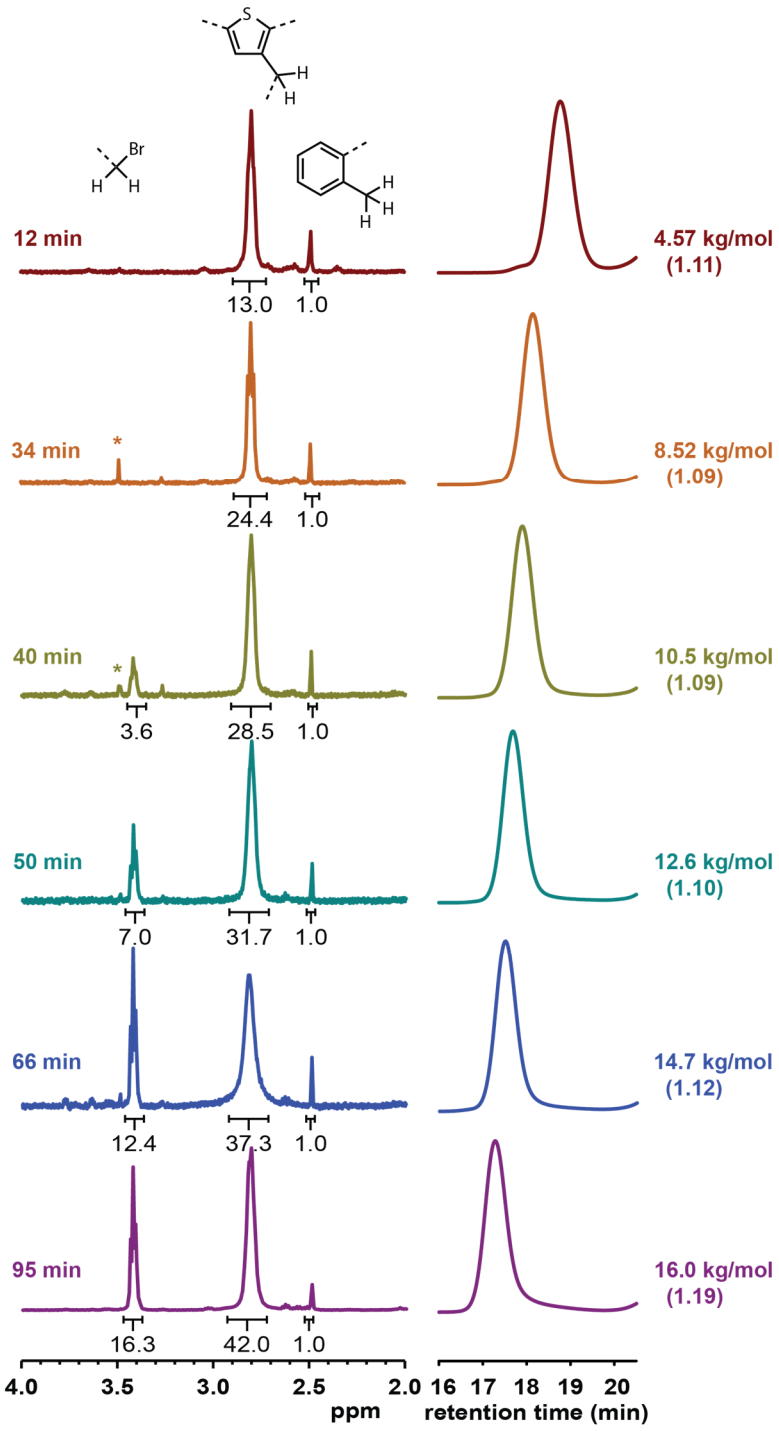

Figure A1.16 ^{1}H NMR spectra (left) and GPC curves (right) for aliquots drawn during synthesis of **block40$_{Br}$** at various times. (* labeled as residual solvents, 3.49 ppm for MeOH.) GPC data is labeled with M_n (top) and Đ (in parenthesis, bottom).

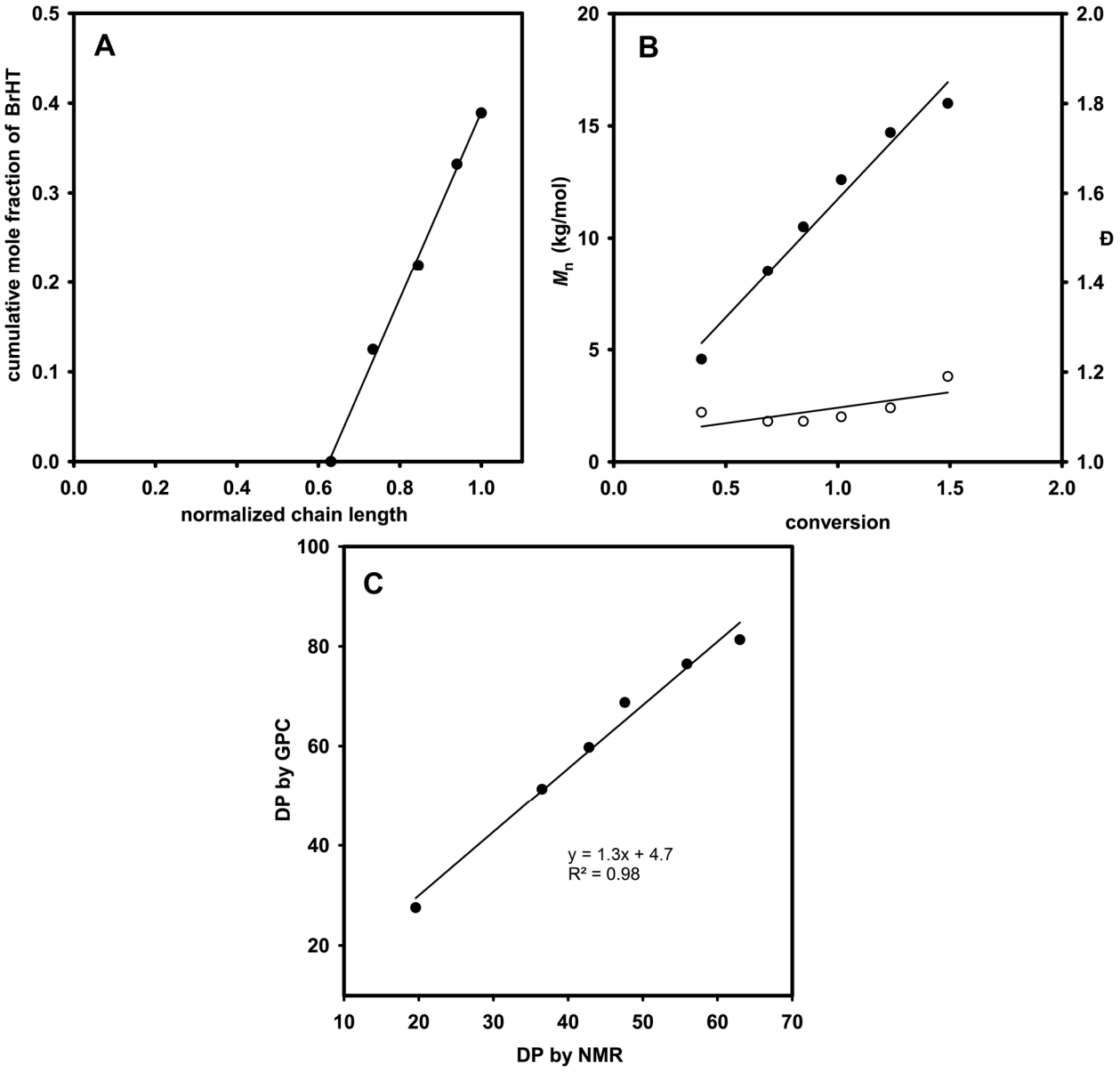

Figure A1.17 (A) Plot of the cumulative mole fraction of monomer **BrHT** in **block40$_{Br}$** as a function of normalized chain length, (B) M_n (filled circles, ●) and Đ (open circles, ○) versus % conversion, and (C) comparison of the degree of polymerization (DP) obtained by GPC and ^{1}H NMR spectroscopic analysis of end groups. DP = M_n/ average repeat unit MW. Comparing the results of these two methods, it appears that GPC overestimates the DP of these copolymers by a factor of approximately 1.3, in reasonable agreement with a previous report.[6]

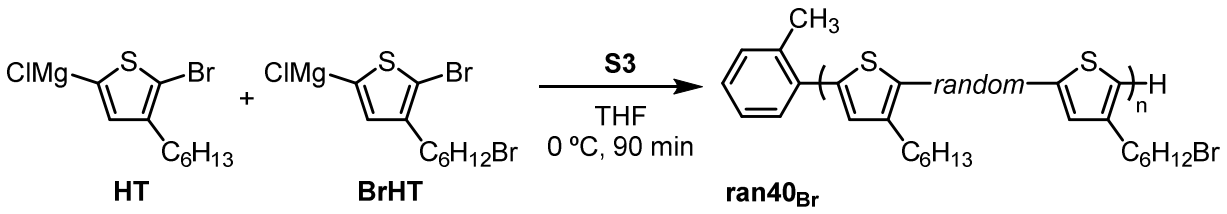

Poly(3-hexylthiophene-*random*-3-(6-bromohexyl)thiophene)60:40 (ran40$_{Br}$). In the glovebox, to an oven-dried 50 mL Schlenk flask, a 0.131 M solution of **HT** (2.20 mL, 0.288 mmol, 48.0 equiv) in THF and a 0.103 M solution of **BrHT** (1.87 mL, 0.192 mmol, 32.0 equiv) in THF were added and diluted with THF (15 mL). The Schlenk flask was capped and removed from glovebox, put under N_2 and cooled to 0 °C. Then a 0.010 M solution of precatalyst **S3** (0.60 mL, 6.0 μmol, 1.0 equiv) in THF was added. Aliquots (2 mL) were taken at 11, 25, 45, 60 and 90 min (reaction completed), and the reaction was quenched with 6 M aq. HCl (2 mL). The resulting solution was then extracted with $CHCl_3$ (3 x 2 mL). The combined organic layers were dried over $MgSO_4$, filtered, and concentrated *in vacuo* to afford crude polymer. The samples were analyzed by GC for monomer conversion and GPC for M_n. Then these samples were purified (see page S25) and analyzed by ^{1}H NMR spectroscopy to determine the cumulative mole fraction of **BrHT**.

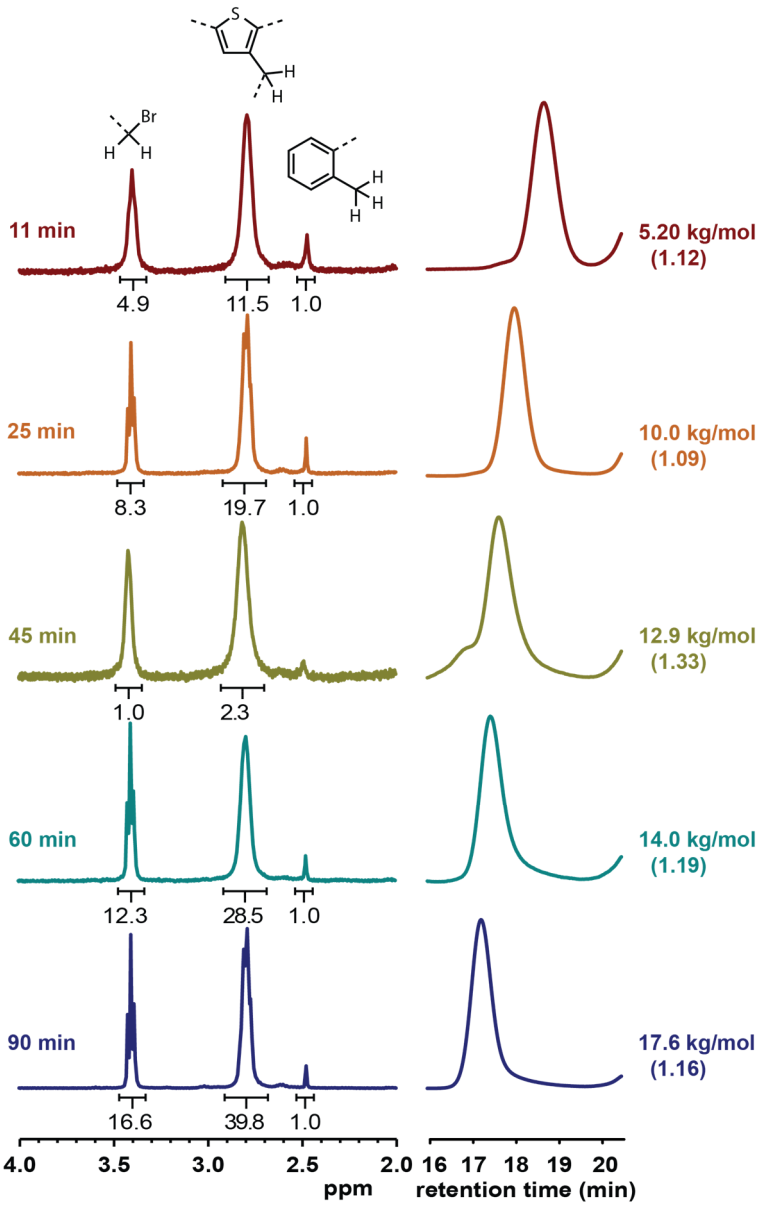

Figure A1.18 ^{1}H NMR spectra (left) and GPC curves (right) for aliquots drawn during the synthesis of **ran40$_{Br}$** at various times. GPC data is labeled with M_n (top) and Đ (in parenthesis, bottom).

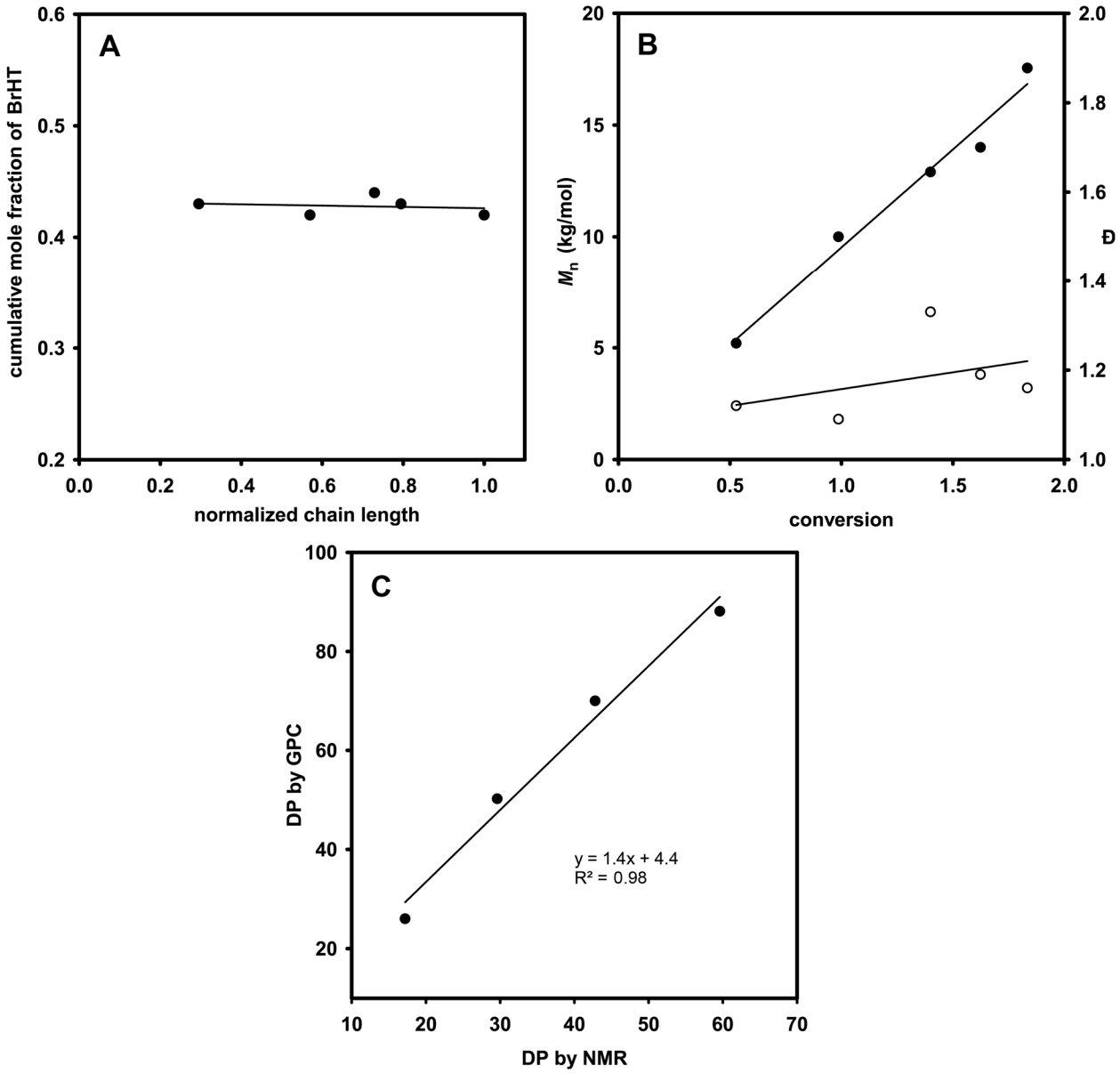

Figure A1.19 (A) Plot of the cumulative mole fraction of monomer **BrHT** in **ran40$_{Br}$** as a function of normalized chain length, (B) M_n (filled circles, ●) and Đ (open circles, ○) versus % conversion, and (C) comparison of the degree of polymerization (DP) obtained by GPC and ^{1}H NMR spectroscopic analysis of end groups. DP = M_n/ average repeat unit MW. Comparing the results of these two methods, it appears that GPC overestimates the DP of these copolymers by a factor of approximately 1.4, in reasonable agreement with a previous report.[6]

A1.5.2 Copolymers for Further Studies

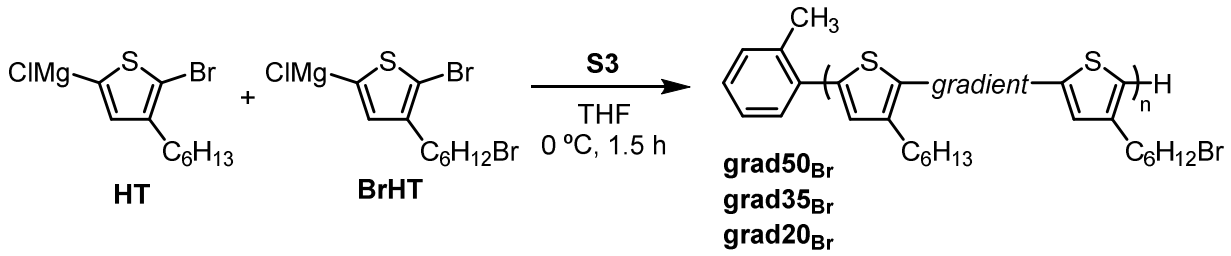

poly(3-hexylthiophene-*grad*-3-(6-bromohexyl)thiophene) (grad50$_{Br}$). In the glovebox, to an oven-dried 25 mL Schlenk flask, a 0.0810 M solution of **HT** (2.80 mL, 0.227 mmol, 40.0 equiv) in THF was added and diluted with THF (15 mL). The Schlenk flask was capped and removed from the glovebox, put under N_2 and cooled to 0 °C. In a 20 mL vial, a 0.0810 M solution of **BrHT** (2.80 mL, 0.227 mmol, 40.0 equiv) in THF was added and diluted with THF (0.2 mL). The solution of **BrHT** was taken out of the glovebox in a syringe and affixed to a syringe pump. A 0.010 M solution of pre-catalyst **S3** (0.56 mL, 5.6 μmol, 1.0 equiv) in THF was taken out of the glovebox in a plastic syringe and injected to the solution of **3HT**. Then the syringe pump was activated to inject **BrHT** at a rate of 0.1 mL/min. After 90 min, the polymerization was quenched with 6 M aq HCl (15 mL), extracted with $CHCl_3$ (3 x 20 mL), dried over $MgSO_4$, filtered, and concentrated *in vacuo* to afford a reddish purple solid. The solid was then dissolved in a minimal amount of $CHCl_3$ (1.5 mL) and precipitated into cold MeOH (50 mL). The mixture was centrifuged and the supernatant was decanted. Then, the precipitate was suspended in MeOH (30 mL) with sonication and was collected by centrifugation, decanting, and drying the pellet under vacuum, affording a purple solid (79.1 mg, 85%). Gel permeation chromatography (GPC) after purification: M_n = 20.7 kg/mol, Đ = 1.15.

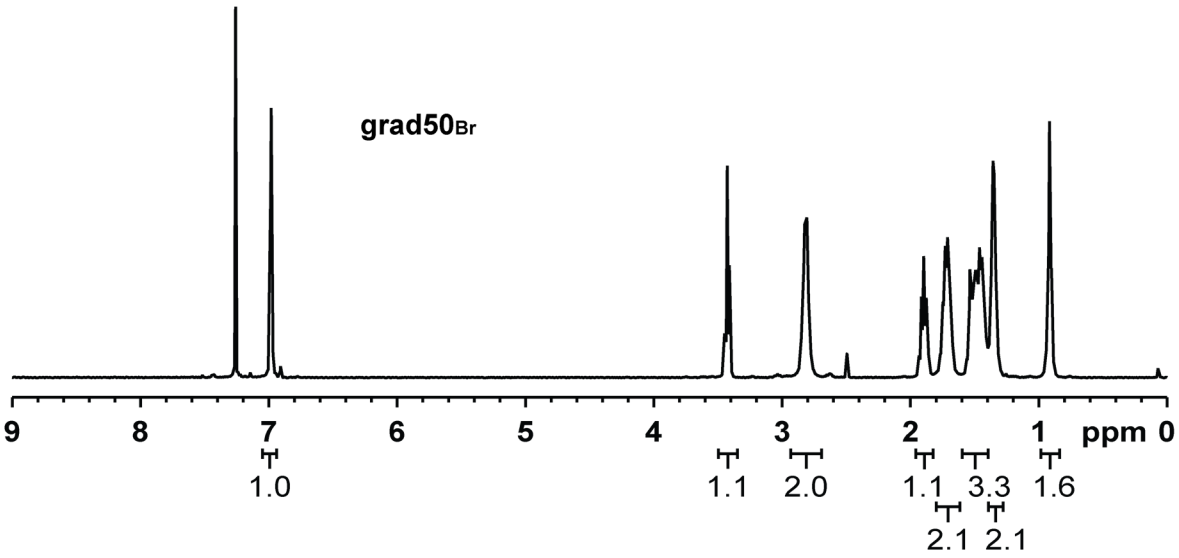

Figure A1.20 NMR spectrum for **grad50$_{Br}$**. ^{1}H NMR (400 MHz, $CDCl_3$) δ 6.98 (s, 1H), 3.43 (t, 1H), 2.82 (bs, 2H), 1.90 (m, 1H), 1.70 (m, 2H), 1.49 (m, 3H), 1.35(m, 2H), 0.92 (bs, 1.5H).

poly(3-hexylthiophene-*grad*-3-(6-bromohexyl)thiophene) (grad35$_{Br}$). In the glovebox, to an oven-dried 25 mL Schlenk flask, a 0.0953 M solution of **HT** (2.80 mL, 0.267 mmol, 52.0 equiv) in THF was added and diluted with THF (15 mL). The Schlenk flask was capped and removed from glovebox, put under N_2 and cooled to 0 °C. In a 20 mL vial, a 0.0762 M solution of **BrHT** (1.90 mL, 0.145 mmol, 28.0 equiv) in THF was added and diluted with THF (1.1 mL). The solution of **BrHT** was taken out of the glovebox with a syringe affixed to a syringe pump. A 0.010 M solution of precatalyst **S3** (0.51 mL, 5.1 μmol, 1.0 equiv) in THF was taken out of the glovebox in a plastic syringe and injected to the solution of **3HT**. After 2 min, the syringe pump was activated to inject **BrHT** at a rate of 0.1 mL/min. After 90 min, the polymerization was quenched with 6 M aq. HCl (15 mL), extracted with $CHCl_3$ (3 x 20 mL) and dried over $MgSO_4$, filtered, and concentrated *in vacuo* to afford a reddish purple solid. The solid was then dissolved in minimal amount of $CHCl_3$ (1.5 mL) and precipitated into cold MeOH (50 mL). The mixture was centrifuged and the supernatant was decanted. Then, the precipitate was suspended in MeOH (30 mL) with sonication and was collected by centrifugation, decanting, and drying the pellet under vacuum,

affording a purple solid (65.1 mg, 82%). Gel permeation chromatography (GPC) after purification: M_n = 22.1 kg/mol, Đ = 1.11.

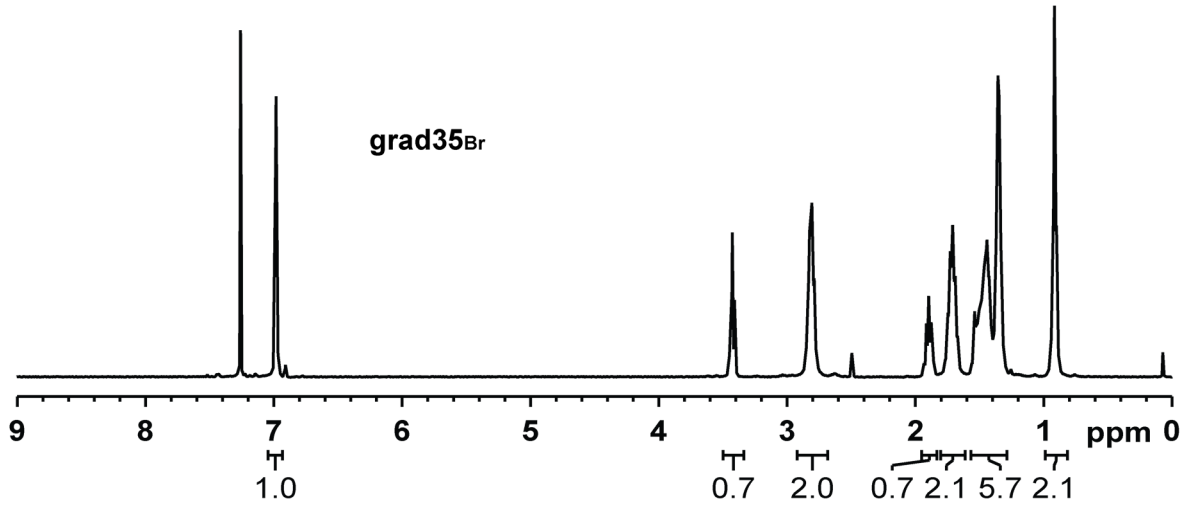

Figure A1.21 NMR spectrum for grad35$_{Br}$. ^{1}H NMR (400 MHz, $CDCl_3$) δ 6.98 (s, 1H), 3.43 (m, 0.7H), 2.81 (m, 2H), 1.90 (q, 0.7H), 1.70 (m, 2H), 1.42 (m, 5.7H), 0.92 (t, 2H).

poly(3-hexylthiophene-*grad*-3-(6-bromohexyl)thiophene): grad20$_{Br}$ In the glovebox, to an oven-dried 25 mL Schlenk flask, a 0.112 M solution of **HT** (3.80 mL, 0.424 mmol, 65.0 equiv) in THF was added and diluted with THF (20 mL). The Schlenk flask was capped and removed from the glovebox, put under N_2 and cooled to 0 °C. In a 20 mL vial, a 0.0689 M solution of **BrHT** (1.50 mL, 0.103 mmol, 16.0 equiv) in THF was added and diluted with THF (1.5 mL). The solution of **BrHT** was taken out of the glovebox in a syringe and affixed to a syringe pump. A 0.010 M solution of precatalsyt **S3** (0.65 mL, 6.5 μmol, 1.0 equiv) in THF was taken out of the glovebox in a plastic syringe and injected to the solution of **HT**. After 5 min, the syringe pump was activated to inject **BrHT** at a rate of 0.1 mL/min. After 90 min, the polymerization was quenched with 6 M aq. HCl (15 mL), extracted with $CHCl_3$ (3 x 20 mL) and dried over $MgSO_4$, filtered, and concentrated *in vacuo* to afford a reddish purple solid. The solid was then dissolved in minimal amount of $CHCl_3$ (1.5 mL) and precipitated into cold MeOH (50 mL). The precipitate was collected on filter paper and purified by Soxhlet extraction sequentially with acetone, MeOH,

hexane, CH_2Cl_2 and $CHCl_3$. The $CHCl_3$ fraction was dried *in vacuo* to afford a purple solid (72.7 mg, 76%). Gel permeation chromatography (GPC) after purification: M_n = 19.0 kg/mol, Đ = 1.18.

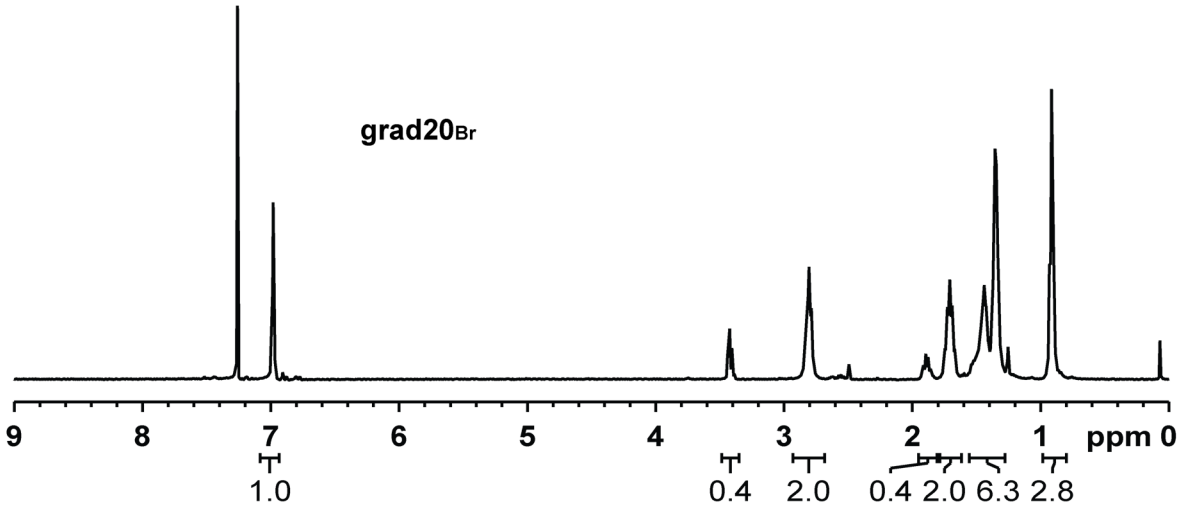

Figure A1.22 NMR spectrum for grad20$_{Br}$. ^{1}H NMR (400 MHz, $CDCl_3$) δ 6.98 (s, 1H), 3.42 (t, 0.4H), 2.81 (t, 2H), 1.89 (m, 0.4H), 1.71 (t, 2H), 1.39 (m, 6H), 0.92 (t, 2.4H).

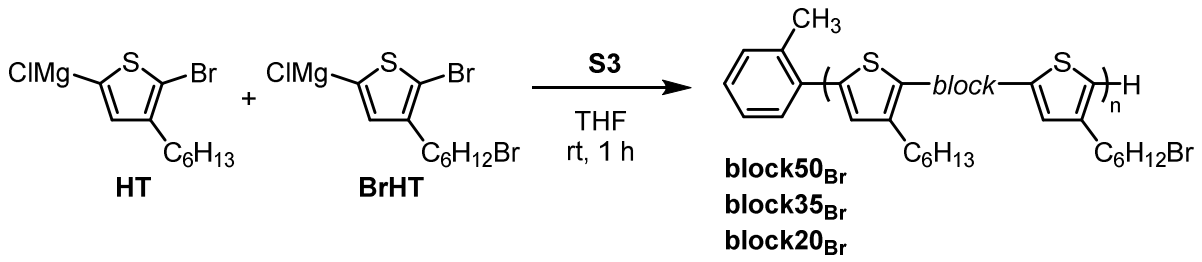

poly(3-hexylthiophene-*block*-3-(6-bromohexyl)thiophene) (block50$_{Br}$). In the glovebox, to a 20 mL vial, a 0.103 M solution of **HT** (1.50 mL, 0.154 mmol, 40.0 equiv) in THF was added and diluted with THF (12 mL). A 0.010 M solution of precatalyst **S3** (0.38 mL, 3.8 μmol, 1.0 equiv) in THF was added and stirred at r.t. for 30 min. Then a 0.0823 M solution of **BrHT** (1.87 mL, 0.154 mmol, 40.0 equiv) in THF was added and the solution stirred for 30 min. The polymerization was quenched with 6 M aq. HCl (5 mL) and precipitated into cold MeOH (50 mL). The precipitate was collected on filter paper and purified by Soxhlet extraction sequentially with acetone, MeOH, hexane, CH_2Cl_2 and $CHCl_3$. The $CHCl_3$ fraction was dried *in vacuo* to afford a purple solid (50.0 mg, 79%). Gel permeation chromatography (GPC) after purification: M_n = 18.8 kg/mol, Đ = 1.19.

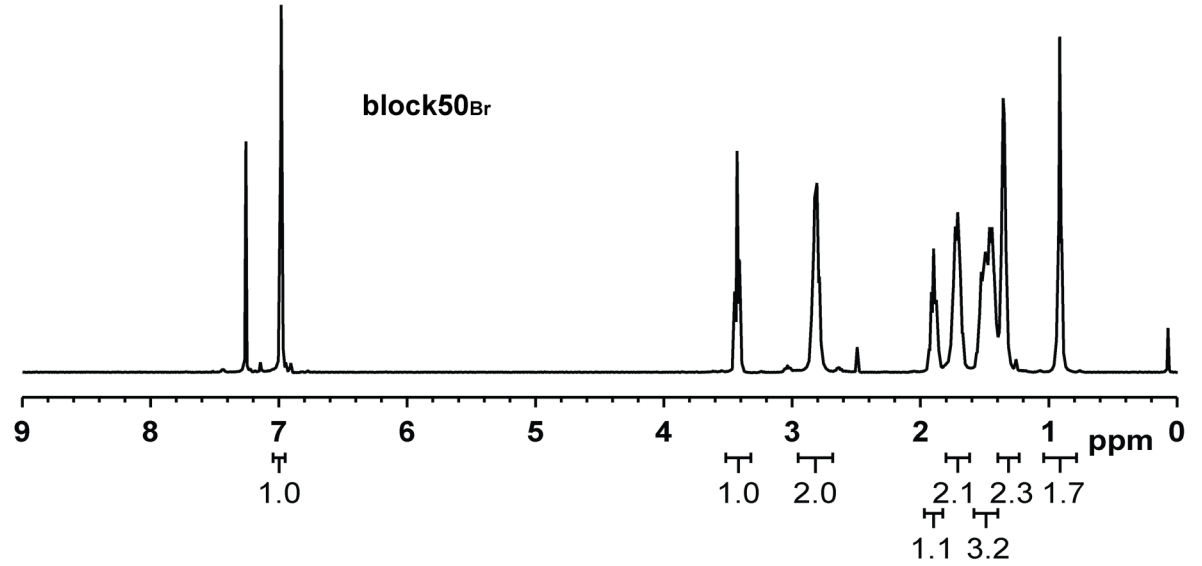

Figure A1.23 NMR spectrum for **block50$_{Br}$**. ^{1}H NMR (400 MHz, $CDCl_3$) δ 6.99 (s, 1H), 3.43 (t, 1H), 2.81 (t, 2H), 1.90 (q, 1H), 1.70 (m, 2H), 1.48 (m, 3H), 1.35 (m, 2H), 0.92 (t, 1.5H).

poly(3-hexylthiophene-*block*-3-(6-bromohexyl)thiophene): block35$_{Br}$

In the glovebox, to a 20 mL vial, a 0.103 M solution of **HT** (2.00 mL, 0.206 mmol, 53.0 equiv) in THF was added and diluted with THF (12 mL). A 0.010 M solution of precatalyst **S3** (0.39 mL, 3.9 μmol, 1.0 equiv) in THF was added and stirred at r.t. for 30 min. Then a 0.0823 M solution of **BrHT** (1.34 mL, 0.110 mmol, 28.0 equiv) in THF was added and the solution stirred for 30 min. The polymerization was quenched with 6 M aq. HCl (5 mL) and precipitated into cold MeOH (50 mL). The precipitate was collected on filter paper and purified by Soxhlet extraction sequentially with acetone, MeOH, hexane, CH_2Cl_2 and $CHCl_3$. The $CHCl_3$ fraction was dried *in vacuo* to afford a purple solid (49.2 mg, 80%). Gel permeation chromatography (GPC) after purification: M_n = 19.1 kg/mol, Đ = 1.17.

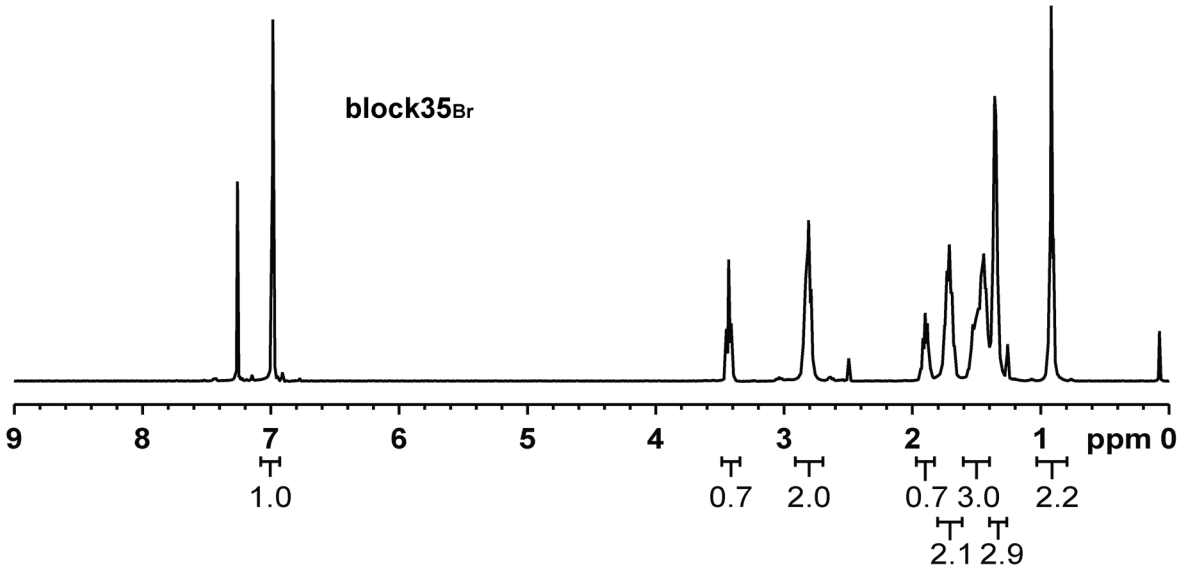

Figure A 1.24 NMR spectrum for **block35$_{Br}$**. ^{1}H NMR (400 MHz, $CDCl_3$) δ 6.98 (s, 1H), 3.43 (t, 0.7H), 2.81 (t, 2H), 1.90 (q, 0.7H), 1.70 (m, 2H), 1.47 (m, 3H), 1.35 (m, 3H), 0.92 (t, 2H).

poly(3-hexylthiophene-*block*-3-(6-bromohexyl)thiophene) (block20$_{Br}$). In the glovebox, to a 20 mL vial, a 0.103 M solution of **HT** (2.40 mL, 0.247 mmol, 65.0 equiv) in THF was added and diluted with THF (12 mL). A 0.010 M solution of precatalyst **S3** (0.38 mL, 3.8 μmol, 1.0 equiv) in THF was added and stirred at r.t. for 30 min. Then a 0.083 M solution of **BrHT** (0.75 mL, 0.062 mmol, 16.0 equiv) in THF was added and the solution stirred for 30 min. The polymerization was quenched with 6 M aq. HCl (5 mL) and precipitated into cold MeOH (50 mL). The precipitate was collected on filter paper and purified by Soxhlet extraction sequentially with acetone, MeOH, hexane, CH_2Cl_2 and $CHCl_3$. The $CHCl_3$ fraction was dried *in vacuo* to afford a purple solid (48.4 mg, 86%). Gel permeation chromatography (GPC) after purification: M_n = 19.5 kg/mol, Đ = 1.15.

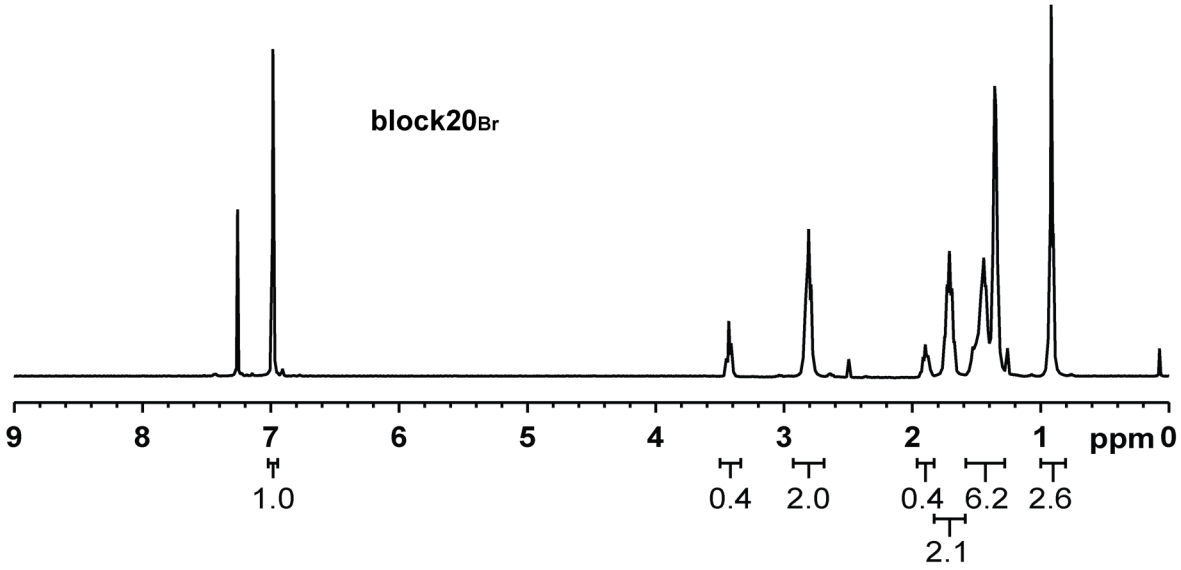

Figure A1.25 NMR spectrum for **block20$_{Br}$**. ^{1}H NMR (400 MHz, $CDCl_3$) δ 6.98 (s, 1H), 3.43 (t, 0.4H), 2.81 (t, 2H), 1.90 (q, 0.4H), 1.71 (t, 2H), 1.39 (m, 6H), 0.92 (t, 2.4H).

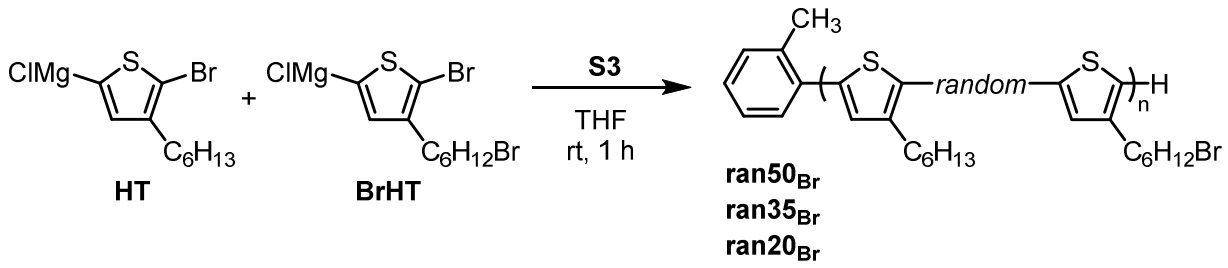

poly(3-hexylthiophene-*random*-3-(6-bromohexyl)thiophene) (ran50$_{Br}$). In the glovebox, to a 20 mL vial, was added a 0.110 M solution of **HT** (1.50 mL, 0.165 mmol, 40.0 equiv) in THF and a 0.142 M solution of **BrHT** (1.16 mL, 0.164 mmol, 40.0 equiv) in THF and diluted with THF (12 mL). A 0.010 M solution of precatalyst **S3** (0.41 mL, 4.1 μmol, 1 equiv) in THF was then added and the solution was stirred at r.t. for 1 h. The polymerization was quenched with 6 M aq. HCl (5 mL), extracted with $CHCl_3$ (3 x 5 mL) and dried *in vacuo* to afford the crude polymer as a dark purple solid. The solid was then dissolved in minimal amount of $CHCl_3$ (1.5 mL) and precipitated into cold MeOH (50 mL). The mixture was centrifuged and the supernatant was decanted. Then, the precipitate was suspended in MeOH (30 mL) with sonication and was collected by centrifugation, decanting, and drying the pellet under vacuum, affording a purple solid (64.7 mg, 96%). Gel permeation chromatography (GPC) after purification: M_n = 21.1 kg/mol, Đ = 1.24.

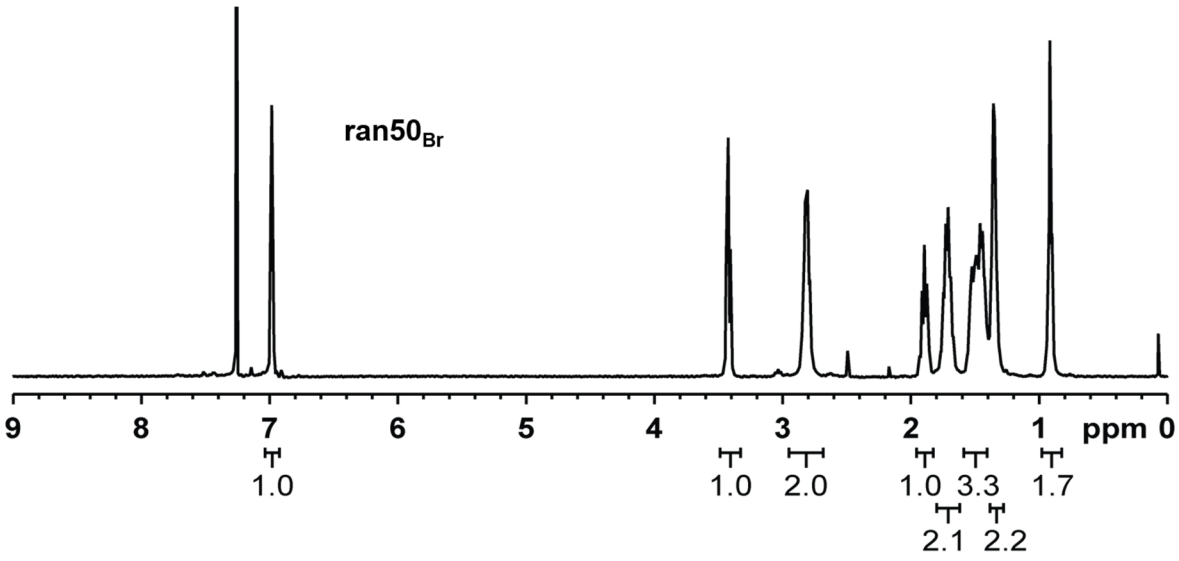

Figure A1.26 NMR spectrum for **ran50$_{Br}$**. ^{1}H NMR (400 MHz, $CDCl_3$) δ 6.98 (s, 1H), 3.42 (t, 1H), 2.81 (m, 2H), 1.90 (q, 1H), 1.70 (m, 2H), 1.47 (m, 3H), 1.35 (m, 2H), 0.92 (t, 1.5H).

poly(3-hexylthiophene-*random*-3-(6-bromohexyl)thiophene) (ran35$_{Br}$). In the glovebox, to a 20 mL vial, was added a 0.110 M solution of **HT** (1.60 mL, 0.176 mmol, 52.0 equiv) in THF and a 0.142 M solution of **BrHT** (0.670 mL, 0.095 mmol, 28.0 equiv) in THF and diluted with THF (12 mL). A stock solution of **S3** (10 mM in THF, 0.41 mL, 4.1 μmol, 1 equiv) was then added and the solution was stirred at r.t. for 1 h. The polymerization was quenched with 6 M aq. HCl (5 mL), extracted with $CHCl_3$ (3 x 5 mL) and dried *in vacuo* to afford the crude polymer as a dark purple solid. The solid was then dissolved in minimal amount of $CHCl_3$ (1.5 mL) and precipitated into cold MeOH (50 mL). The mixture was centrifuged and the supernatant was decanted. Then, the precipitate was suspended in MeOH (30 mL) with sonication and was collected by centrifugation, decanting, and drying the pellet under vacuum, affording a purple solid (53.6 mg, 93%). Gel permeation chromatography (GPC) after purification: M_n = 21.4 kg/mol, Đ = 1.23.

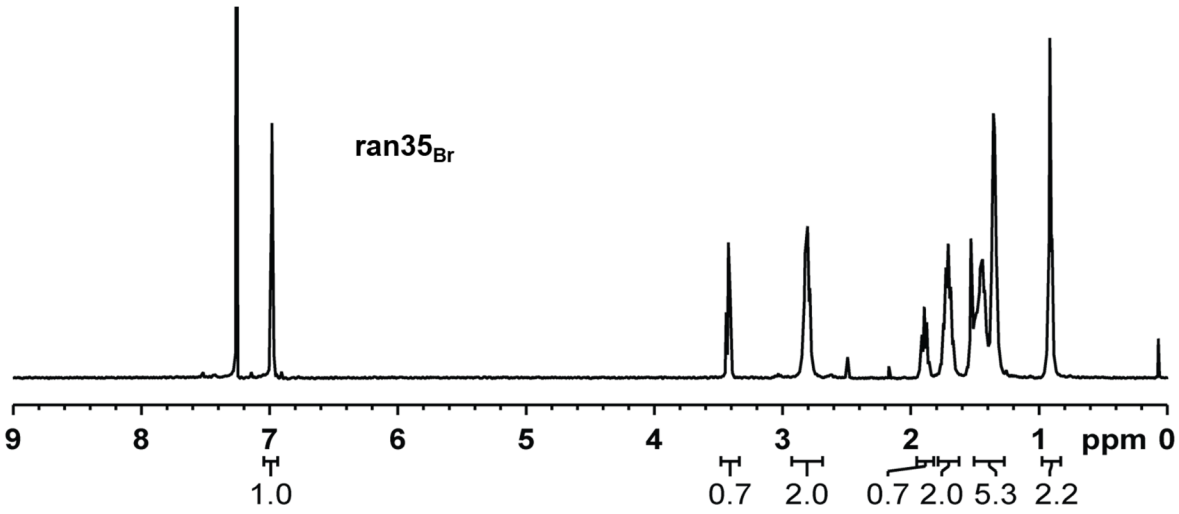

Figure A1.27 NMR spectra for **ran35$_{Br}$**. ^{1}H NMR (400 MHz, $CDCl_3$) δ 6.98 (s, 1H), 3.42 (t, 0.7H), 2.81 (q, 2H), 1.89 (q, 0.7H), 1.70 (m, 2H), 1.39 (m, 5.3H), 0.92 (t, 2H).

poly(3-hexylthiophene-*random*-3-(6-bromohexyl)thiophene) (ran20$_{Br}$). In the glovebox, to a 20 mL vial, was added a 0.110 M solution of **HT** (2.00 mL, 0.220 mmol, 65.0 equiv) in THF and a 0.142 M solution of **BrHT** (0.390 mL, 0.055 mmol, 16.0 equiv) in THF and diluted with THF (12 mL). A stock solution of **S3** (10 mM in THF, 0.41 mL, 4.1 μmol, 1 equiv) was then added and

the solution was stirred at r.t. for 1 h. The polymerization was quenched with 6 M aq. HCl (5 mL), extracted with $CHCl_3$ (3 x 5 mL) and dried *in vacuo* to afford the crude polymer as a dark purple solid. The solid was then dissolved in minimal amount of $CHCl_3$ (1.5 mL) and precipitated into cold MeOH (50 mL). The mixture was centrifuged and the supernatant was decanted. Then, the precipitate was suspended in MeOH (30 mL) with sonication and was collected by centrifugation, decanting, and drying the pellet under vacuum, affording a purple solid (49.4 mg, 89%). Gel permeation chromatography (GPC) after purification: M_n = 21.7 kg/mol, Đ = 1.22.

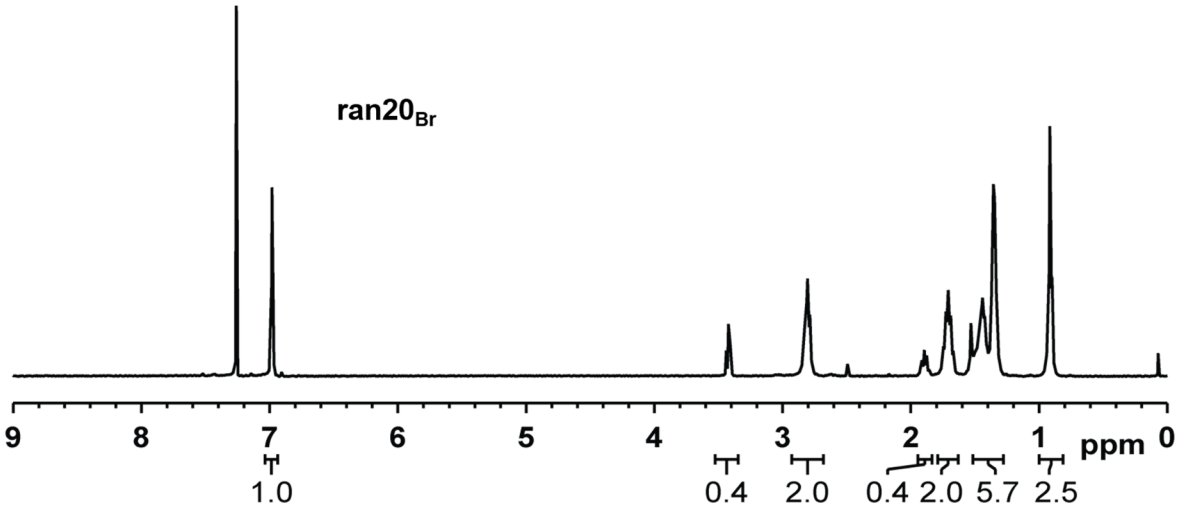

Figure A1.28 NMR spectrum for **ran20$_{Br}$**: ^{1}H NMR (400 MHz, $CDCl_3$) δ 6.98 (s, 1H), 3.42 (t, 0.4H), 2.81 (t, 2H), 1.89 (q, 0.4H), 1.71 (m, 2H), 1.39 (m, 5.6H), 0.92 (t, 2.4H).

A1.6 Post-Polymerization Procedures and Data

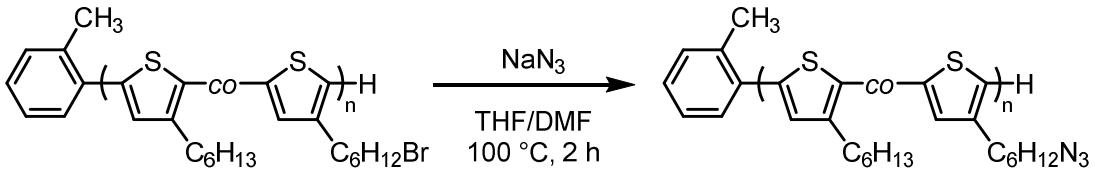

grad/block/ran$_{Br}$ **grad/block/ran$_{N3}$**

General procedure: The precursor polymer (~40 mg, 1.0 equiv) was dissolved in THF (30 mL) in a 100 mL round bottom flask equipped with a reflux condenser. The solution was heated to 60 °C for 5 min to give a bright orange solution. A solution of sodium azide (~80 mg, 10 equiv) in DMF (15 mL) was added dropwise over 1 min. Then the flask was protected from light using aluminum foil, the temperature was increased to 100 °C and the mixture was stirred for 2 h. After removing THF by rotary evaporation, the resulting suspension was precipitated in cold MeOH (100 mL), centrifuged, and the supernatant was decanted. Then, the precipitate was suspended in MeOH (30 mL) with sonication and separated by centrifugation, decanting, and drying the pellet under vacuum for 18 h at r.t. in the dark, affording a purple solid (yields: 93% – 99%).

poly(3-hexylthiophene-*grad*-3-(6-azidohexyl)thiophene)

grad50$_{N3}$: **grad50$_{Br}$** (30.3 mg) was used to afford purple solid (27.3 mg, 99%). GPC after purification: M_n = 21.3 kg/mol, Đ = 1.15.

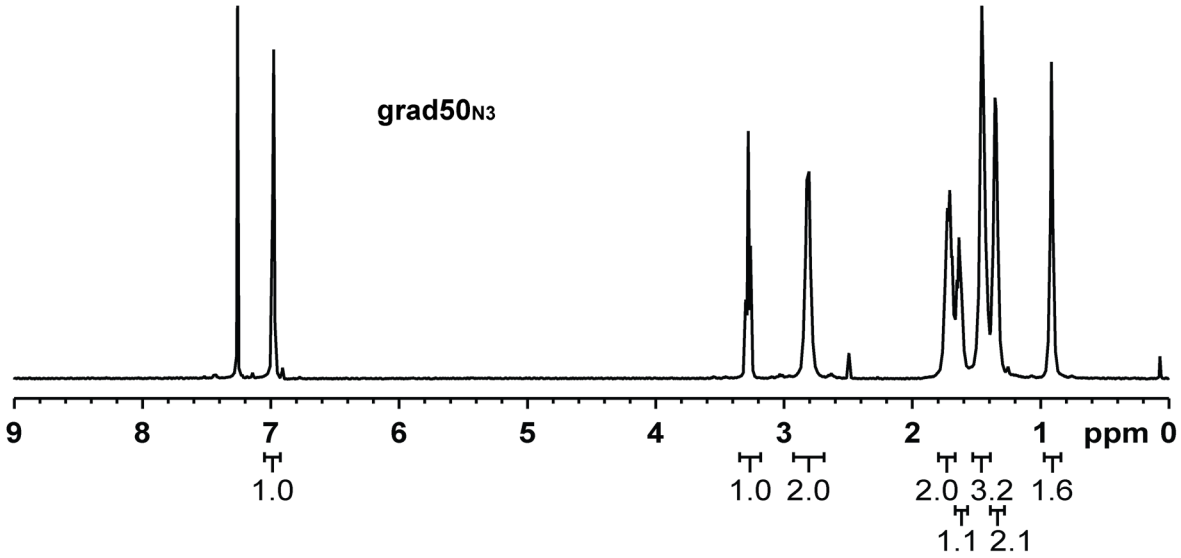

Figure A1.29 NMR spectrum for **grad50$_{N3}$**. ^{1}H NMR (400 MHz, $CDCl_3$) δ 6.98 (s, 1H), 3.28 (t, 1H), 2.81 (q, 2H), 1.70 (m, 2H), 1.64 (m, 1H), 1.46 (m, 3H), 1.35 (m, 2H), 0.92 (t, 1.5H).

grad35$_{N3}$: **grad35$_{Br}$** (33.9 mg) was used to afford purple solid (31.3 mg, 99%). GPC after purification: M_n = 22.1 kg/mol, Đ = 1.12.

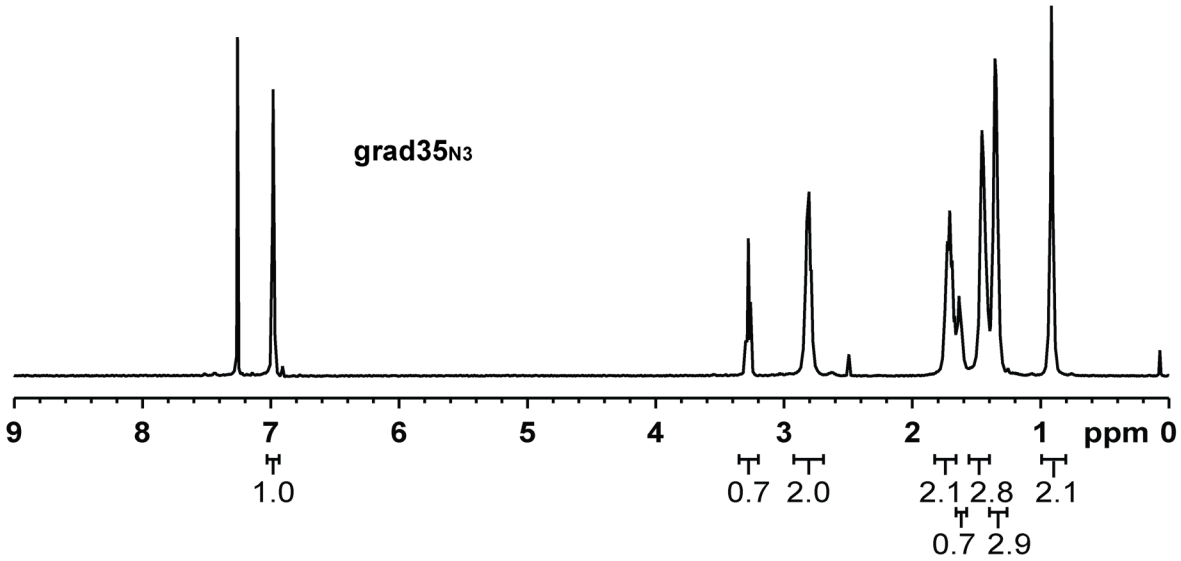

Figure A1.30 NMR spectrum for **grad35$_{N3}$**: ^{1}H NMR (400 MHz, $CDCl_3$) δ 6.98 (s, 1H), 3.28 (t, 0.7H), 2.81 (t, 2H), 1.71 (q, 2H), 1.63 (m, 0.7H), 1.45 (m, 3H), 1.35 (m, 3H), 0.91 (m, 2H).

grad20$_{N3}$: **grad20$_{Br}$** (46.8 mg) was used to afford purple solid (44.1 mg, 99%). GPC after purification: M_n = 18.8 kg/mol, Đ = 1.21.

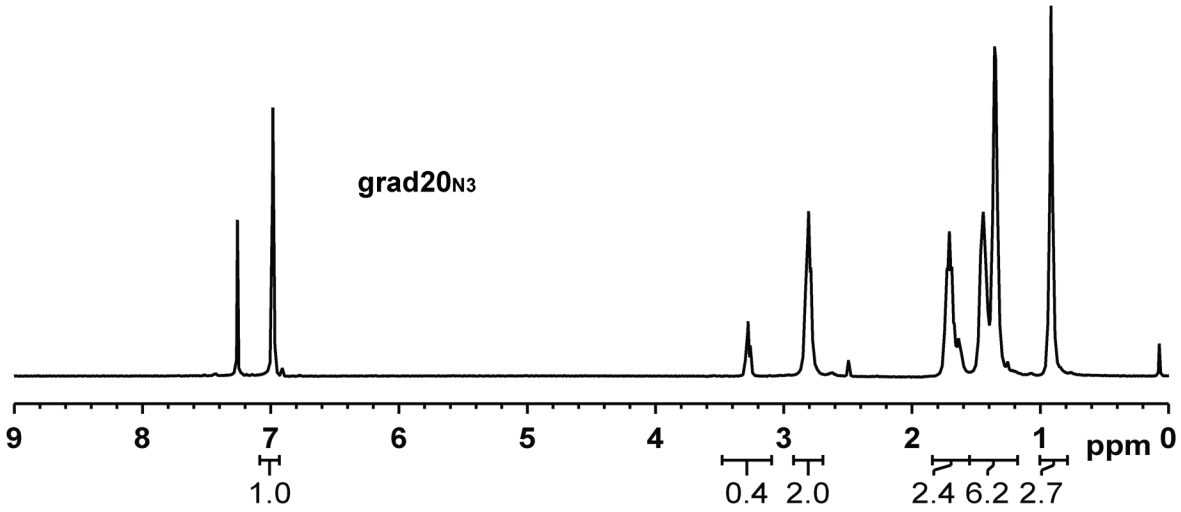

Figure A1.31 NMR spectrum for grad20$_{N3}$: ^{1}H NMR (400 MHz, $CDCl_3$) δ 6.98 (s, 1H), 3.28 (t, 0.4H), 2.81 (t, 2H), 1.67 (m, 2H), 1.40 (m, 6H), 0.92 (t, 2.4H).

poly(3-hexylthiophene-*block*-3-(6-azidohexyl)thiophene)

block50$_{N3}$: **block50$_{Br}$** (33.6 mg) was used to afford purple solid (30.1 mg, 99%). GPC after purification: M_n = 19.8 kg/mol, Đ = 1.19.

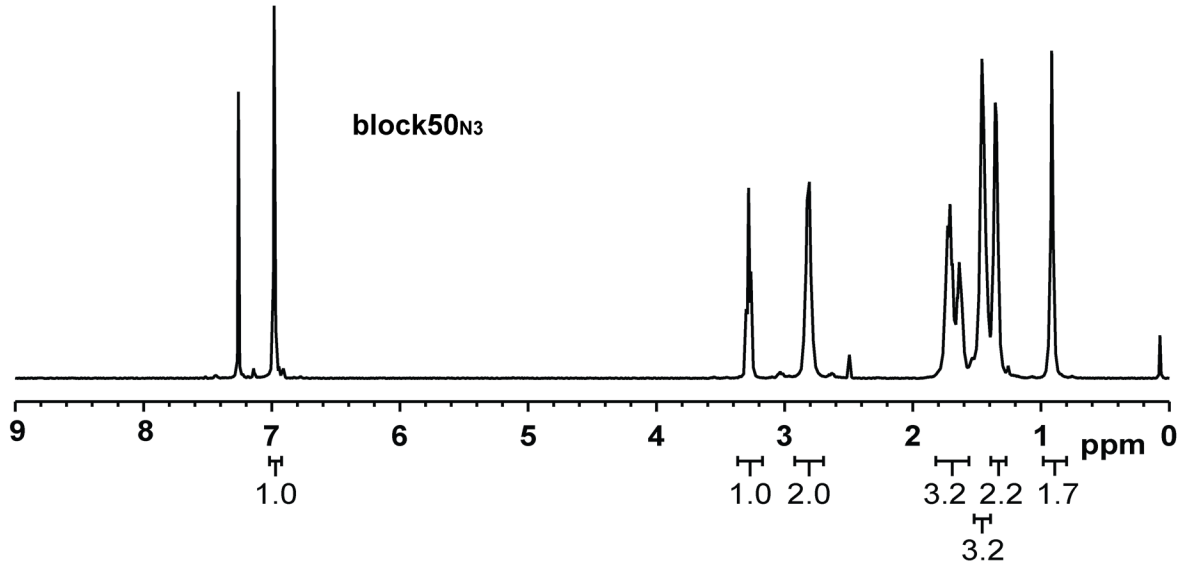

Figure A1.32 NMR spectrum for **block50$_{N3}$**: ^{1}H NMR (400 MHz, $CDCl_3$) δ 6.98 (s, 1H), 3.28 (t, 1H), 2.81 (t, 2H), 1.67 (m, 3H), 1.46 (m, 3H), 1.35 (m, 2H), 0.92 (t, 1.5H).

block35$_{N3}$: **block35$_{Br}$** (31.5 mg) was used to afford purple solid (29.1 mg, 99%). GPC after purification: M_n = 19.6 kg/mol, Đ = 1.17.

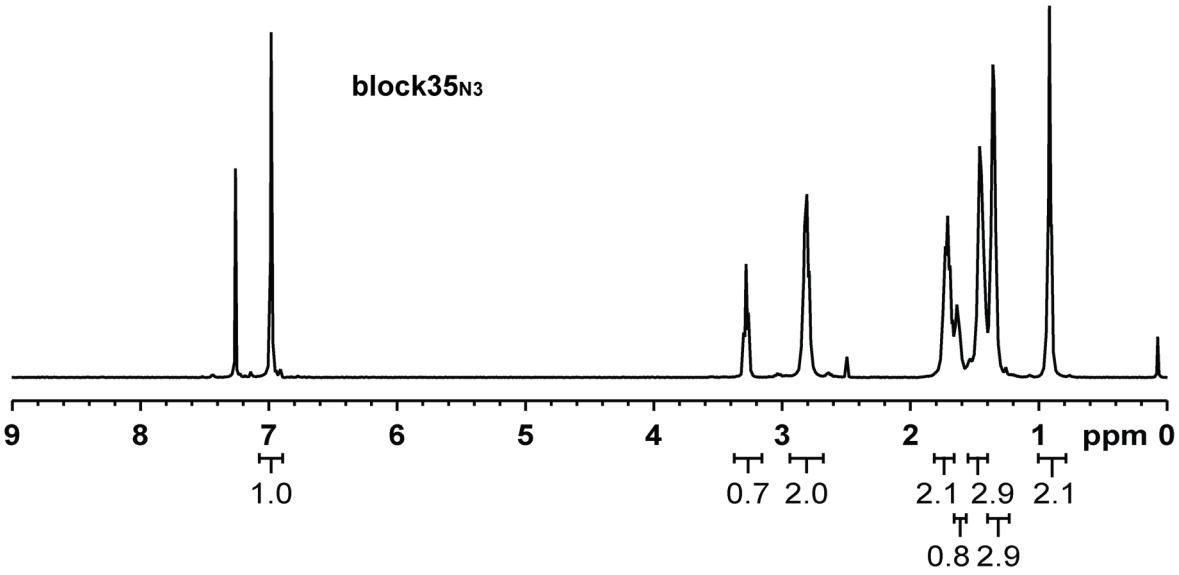

Figure A1.33 NMR spectra for **block35$_{N3}$**: ^{1}H NMR (400 MHz, $CDCl_3$) δ 6.98 (s, 1H), 3.28 (t, 0.7H), 2.81 (t, 2H), 1.70 (m, 2H), 1.64(m, 0.8H), 1.46 (m, 3H), 1.35 (m, 3H), 0.92 (t, 2H).

block20$_{N3}$: **block20$_{Br}$** (38.1 mg) was used to afford purple solid (36.0 mg, 99%). GPC after purification: M_n = 20.5 kg/mol, Đ = 1.14.

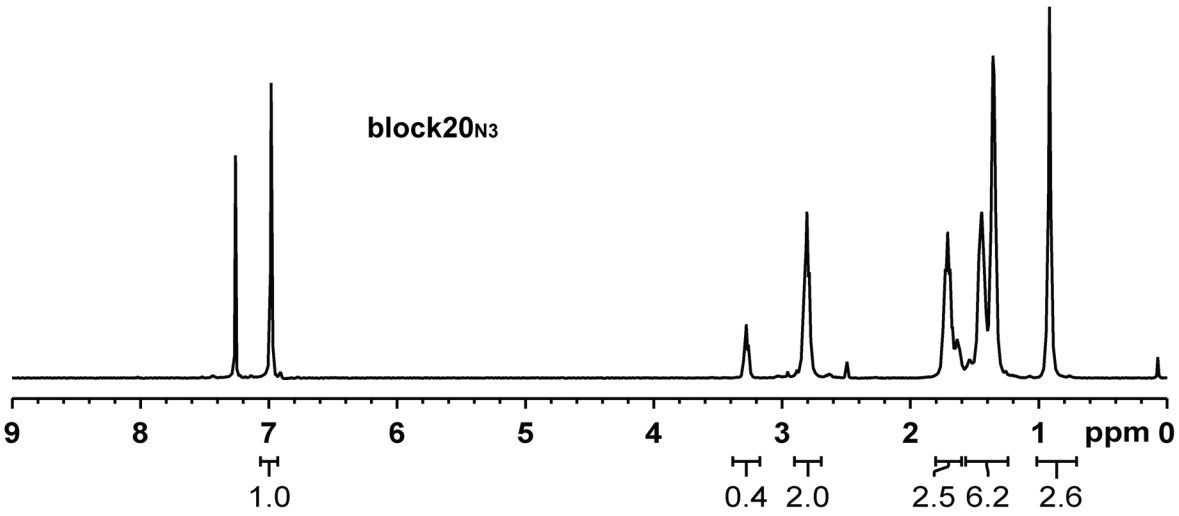

Figure A1.34 NMR spectrum for **block20$_{N3}$**: ^{1}H NMR (400 MHz, $CDCl_3$) δ 6.98 (s, 1H), 3.28 (t, 0.4H), 2.81 (t, 2H), 1.71 (m, 2H), 1.40 (m, 6H), 0.92 (t, 2.4H).

poly(3-hexylthiophene-*random*-3-(6-azidohexyl)thiophene)

ran50$_{N3}$: **ran50$_{Br}$** (49.9 mg) was used to afford purple solid (42.2 mg, 93%). GPC after purification: M_n = 21.5 kg/mol, Đ = 1.26.

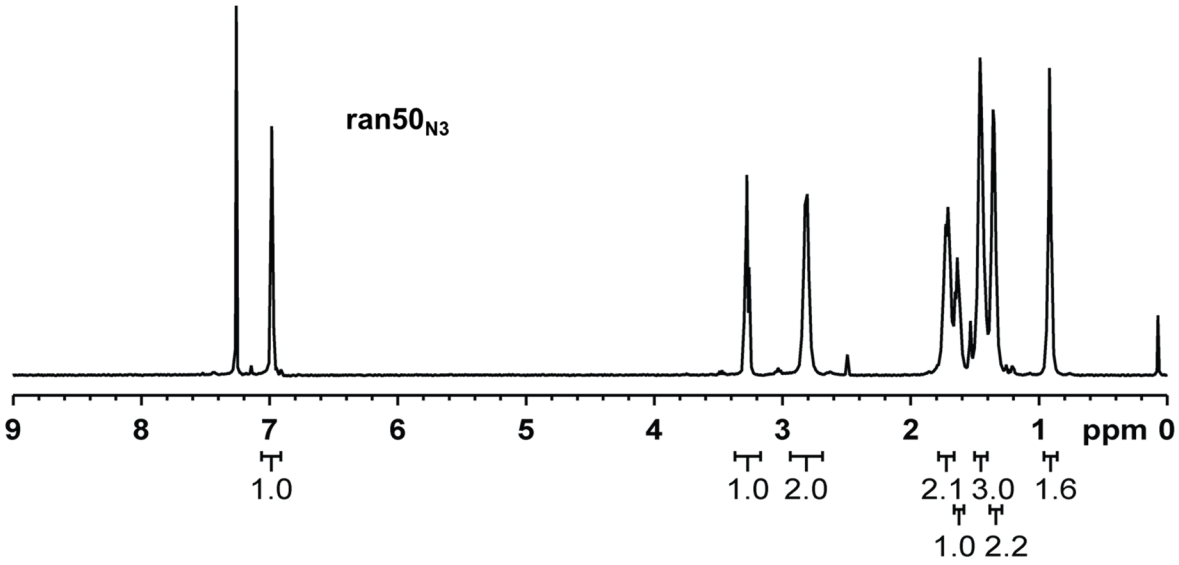

Figure A1.35 NMR spectrum for **ran50$_{N3}$**: ^{1}H NMR (400 MHz, $CDCl_3$) δ 6.98 (s, 1H), 3.28 (t, 1H), 2.82 (q, 2H), 1.71 (q, 2H), 1.64 (m, 1H), 1.46 (m, 3H), 1.35 (m, 2H), 0.92 (t, 1.5H).

ran35$_{N3}$: **ran35$_{Br}$** (42.7 mg) was used to afford purple solid (37.3 mg, 93%). GPC after purification: M_n = 21.8 kg/mol, Đ = 1.24.

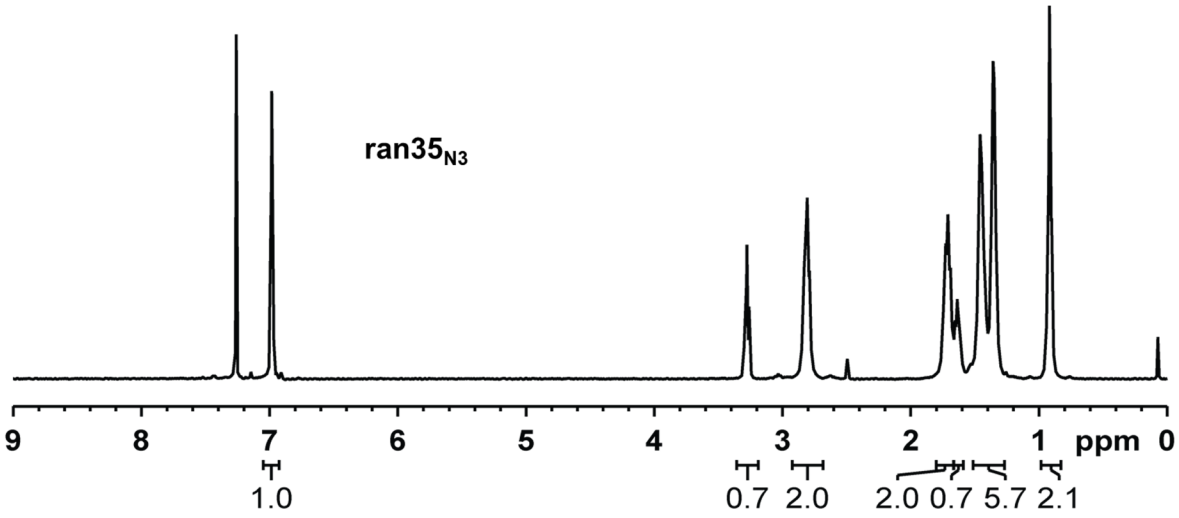

Figure A1.36 NMR spectrum for **ran35$_{N3}$**: ^{1}H NMR (400 MHz, $CDCl_3$) δ 6.98 (s, 1H), 3.28 (t, 0.7H), 2.81 (t, 2H), 1.71 (q, 2H), 1.64 (m, 0.7H), 1.40 (m, 5.3H), 0.92 (t, 2H).

ran20$_{N3}$: **ran20$_{Br}$** (35.8 mg) was used to afford purple solid (33.1 mg, 97%). GPC after purification: M_n = 22.7 kg/mol, Đ = 1.18.

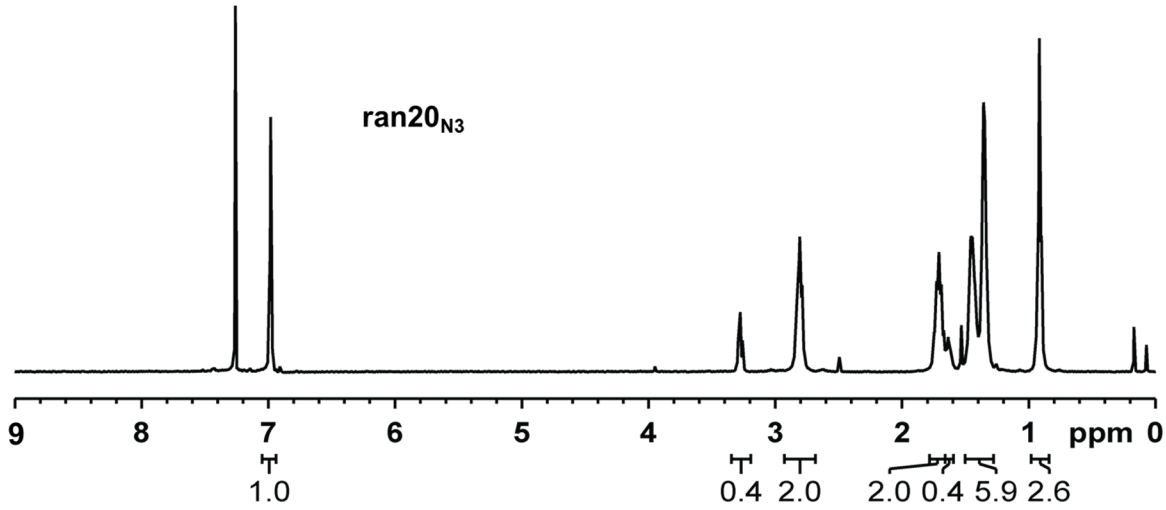

Figure A 1.37 NMR spectrum for **ran20$_{N3}$**: ^{1}H NMR (400 MHz, $CDCl_3$) δ 6.98 (s, 1H), 3.28 (t, 0.4H), 2.81 (t, 2H), 1.71 (q, 2H), 1.64 (m, 0.4H), 1.40 (m, 5.9H), 0.92 (t, 2.6H).

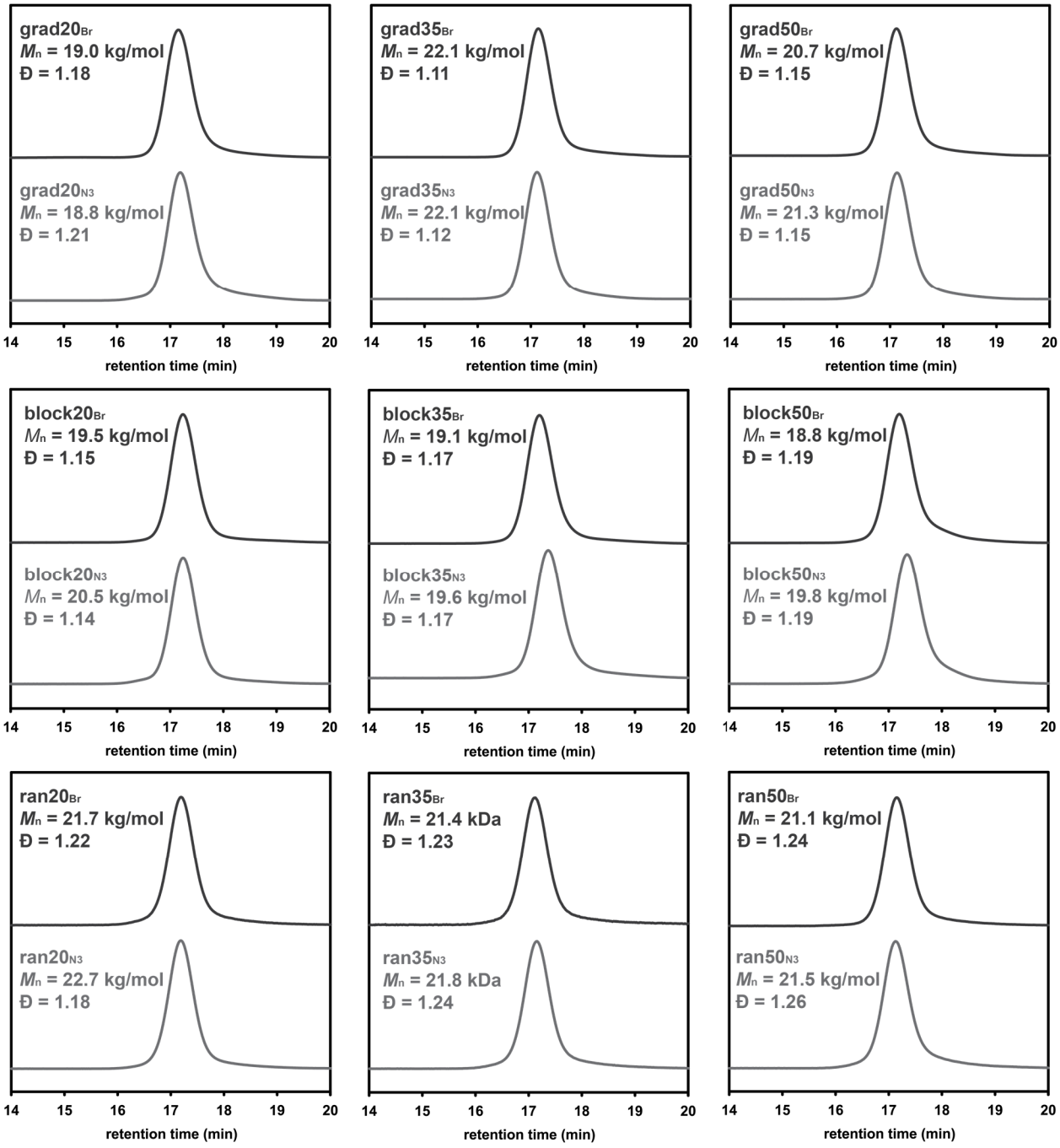

Figure A1.38 GPC traces of copolymers before (**grad/block/ran$_{Br}$**) and after conversion to **grad/block/ran$_{N3}$**.

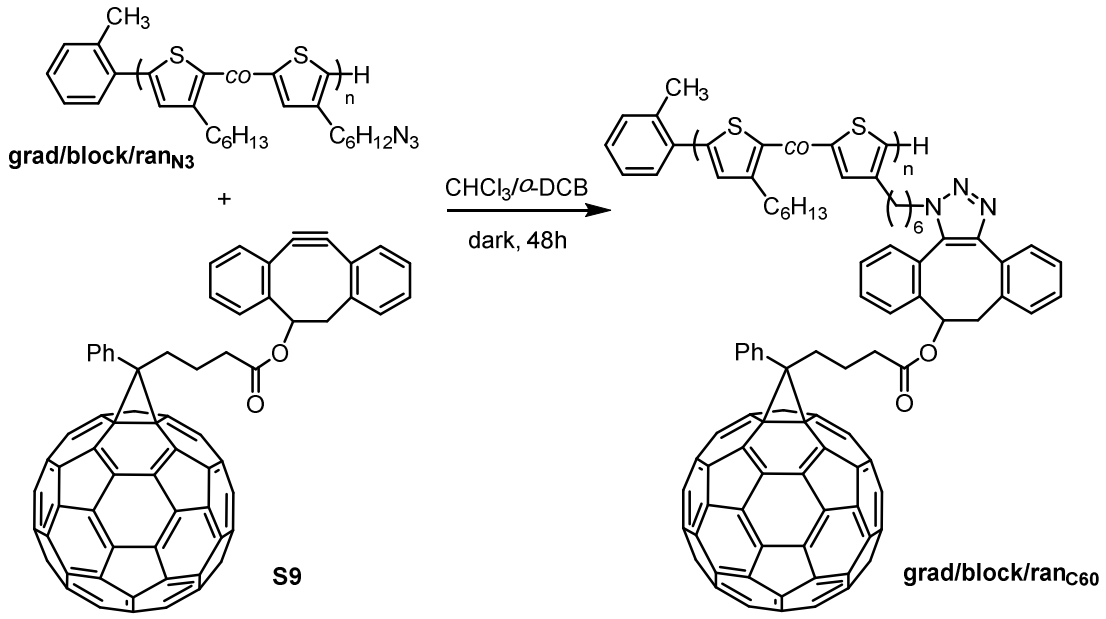

General Procedure: In a 20 mL vial, copolymer **grad/block/ran$_{N3}$** (~10-20 mg, 1.0 equiv of N_3) and **S9** (~30-50 mg, 1.5 equiv) were dissolved in $CHCl_3$ (15 mL) and *o*-DCB (1 mL) and stirred at r.t. in the dark for 48 h. Then the solution was concentrated, redissolved in a minimal amount of $CHCl_3$ and precipitated in a mixture of DCM/MeOH (30 mL v/v 1/1). The precipitate was collected on filter paper and purified by Soxhlet extraction sequentially with CH_2Cl_2 and $CHCl_3/CS_2$. The $CHCl_3/CS_2$ fraction was condensed *in vacuo* to afford a brown solid (80–90%).

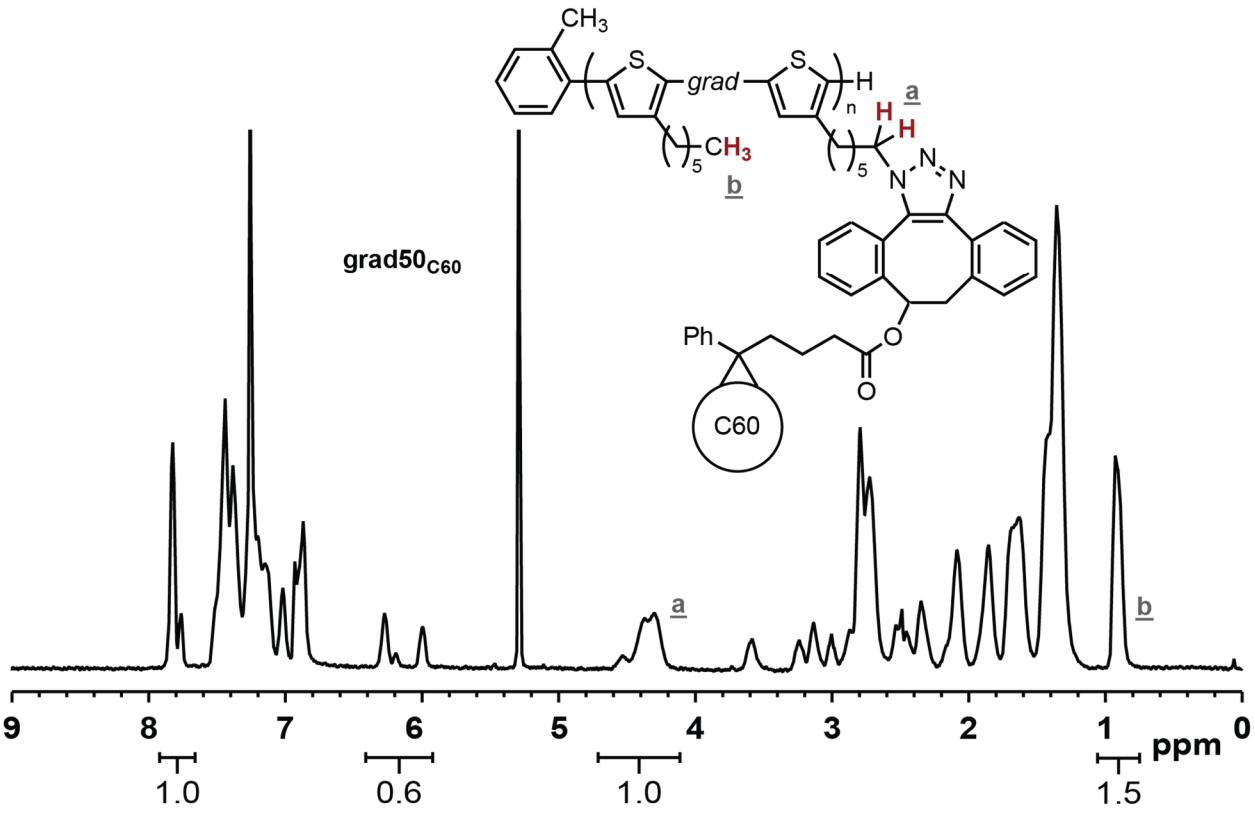

Figure A1.39 ^{1}H NMR spectrum for **grad50**$_{C60}$.

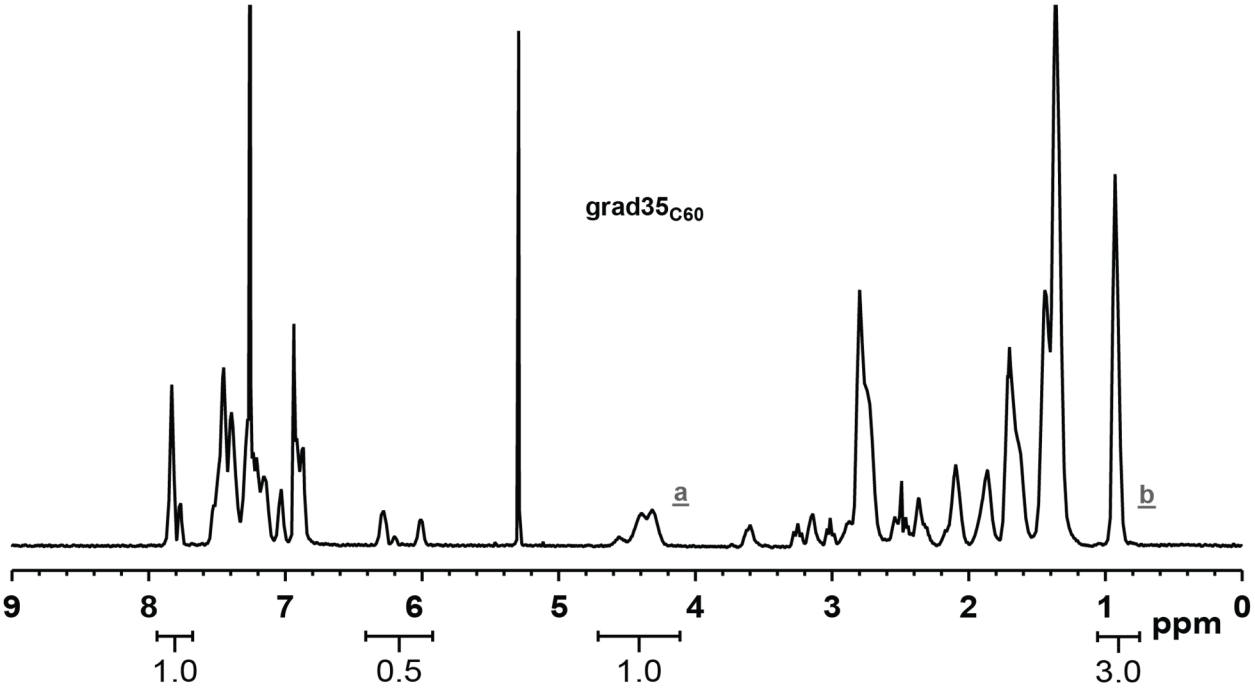

Figure A1.40 ^{1}H NMR spectrum for **grad35**$_{C60}$.

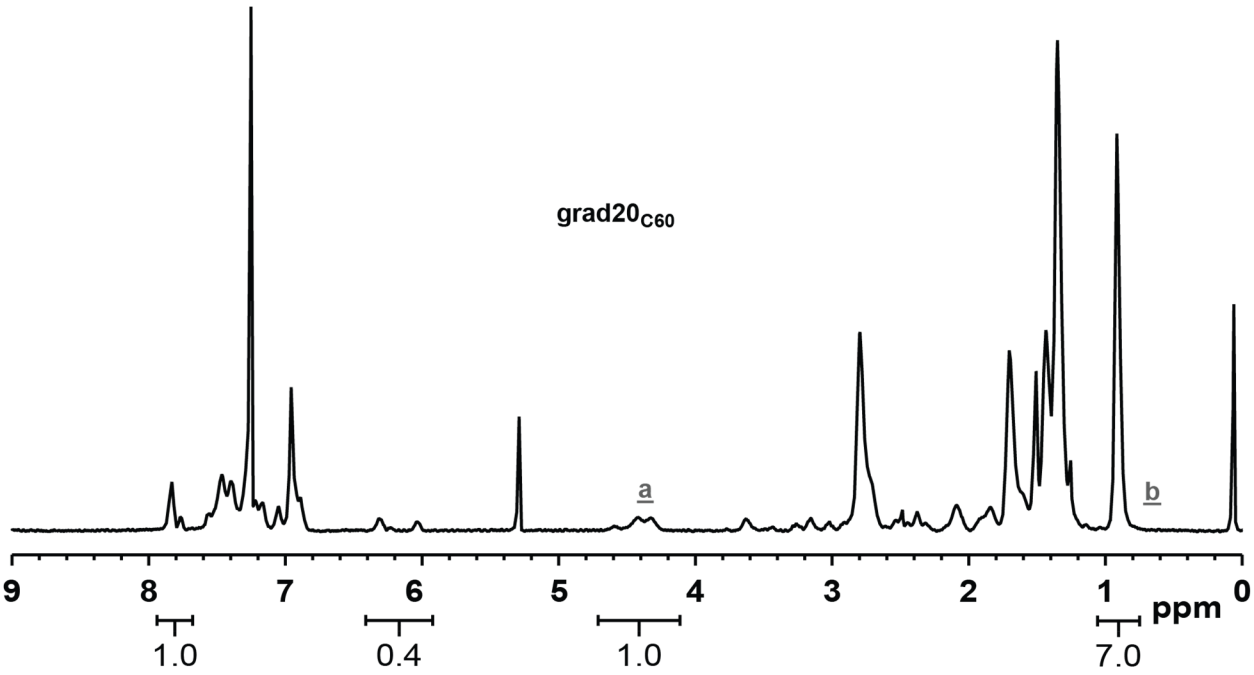

Figure A1.41 ^{1}H NMR spectrum for **grad20**$_{C60}$.

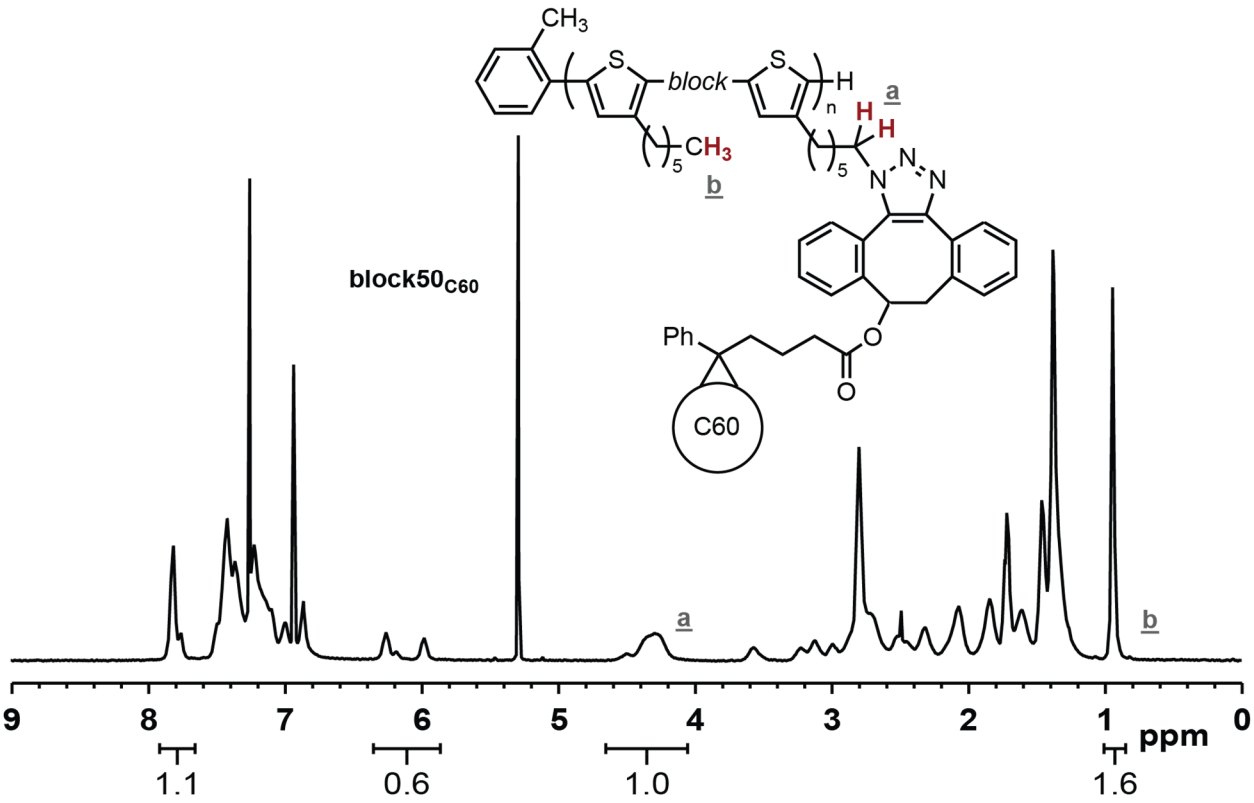

Figure A1.42 ^{1}H NMR spectrum for **block50**$_{C60}$.

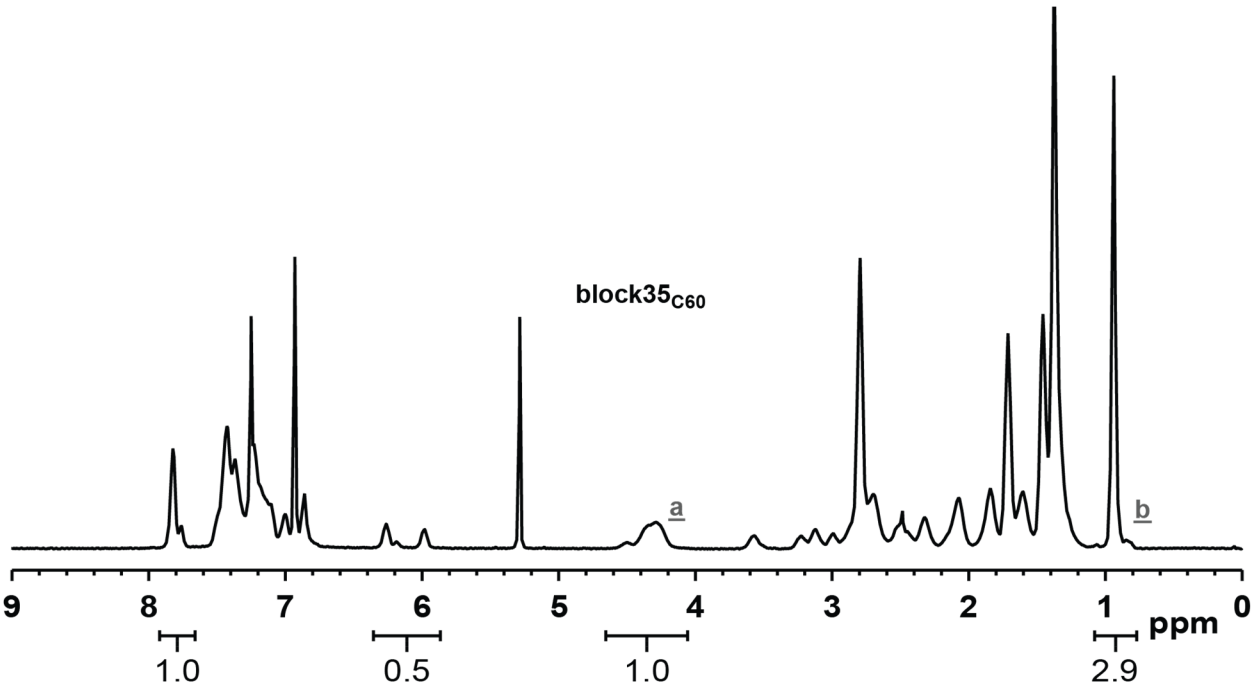

Figure A1.43 ^{1}H NMR spectrum for **block35**$_{C60}$.

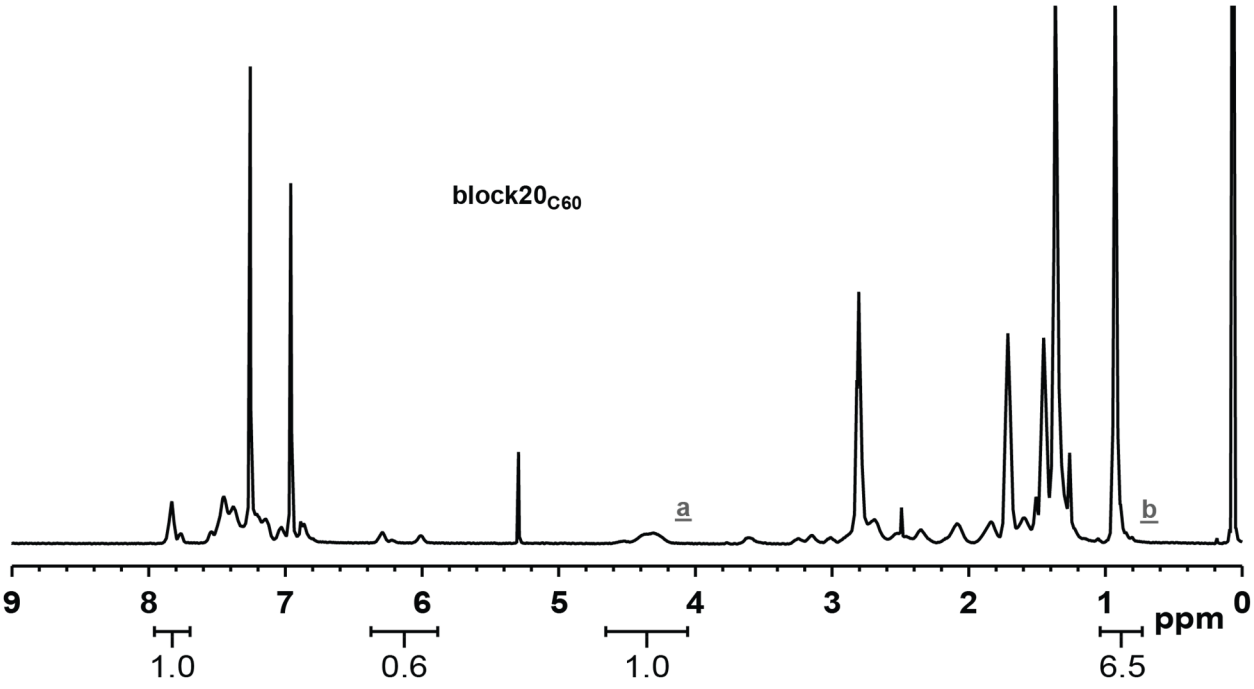

Figure A1.44 ^{1}H NMR spectrum for **block20**$_{C60}$.

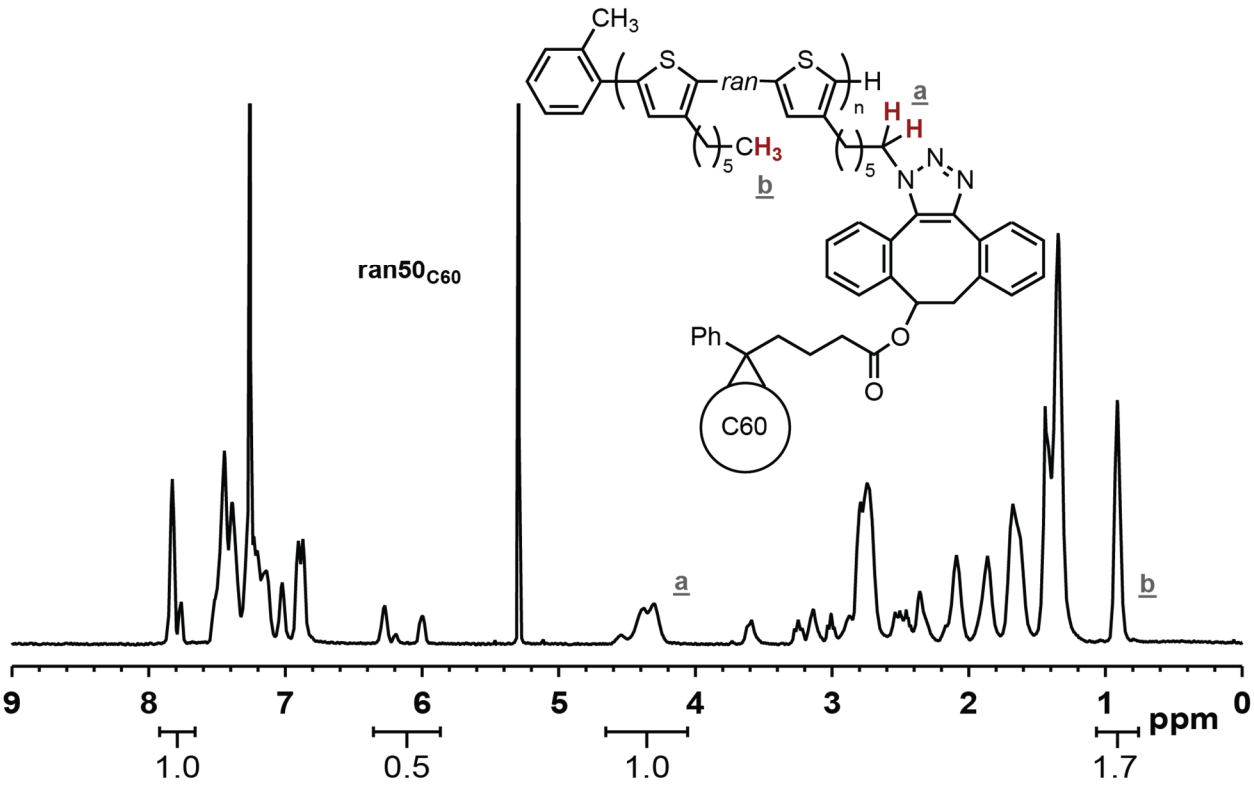

Figure A1.45 ^{1}H NMR spectrum for **ran50**$_{C60}$.

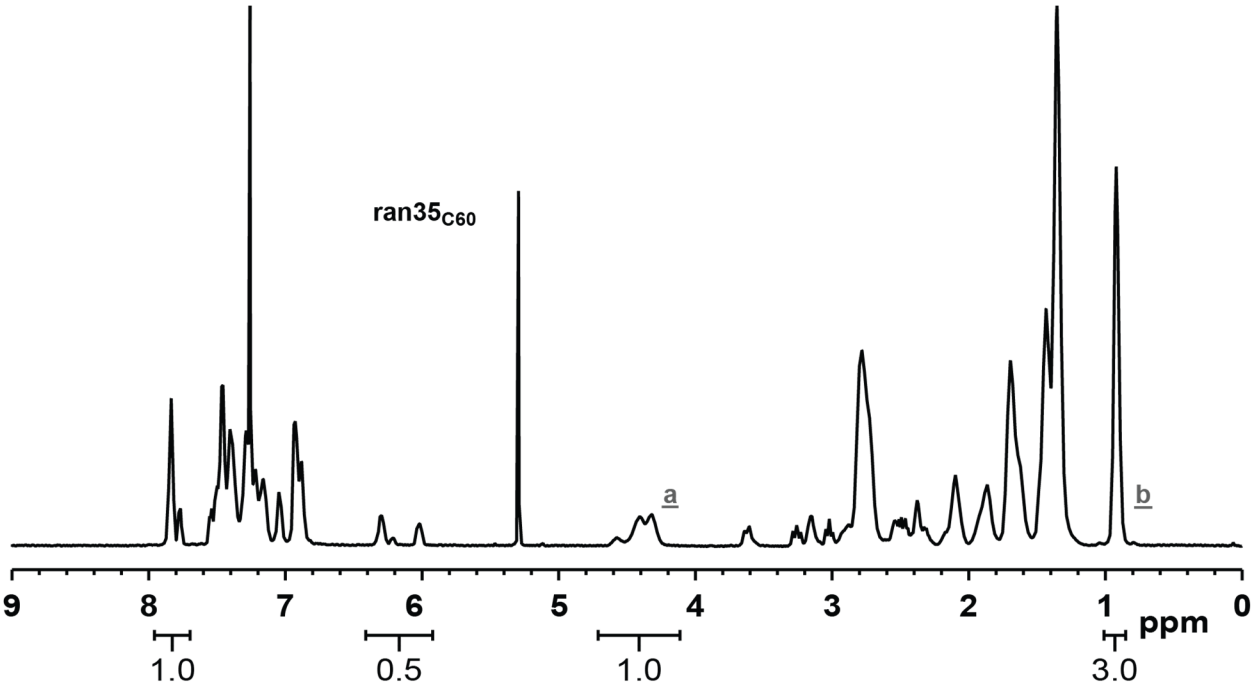

Figure A1.46 ^{1}H NMR spectrum for **ran35**$_{C60}$.

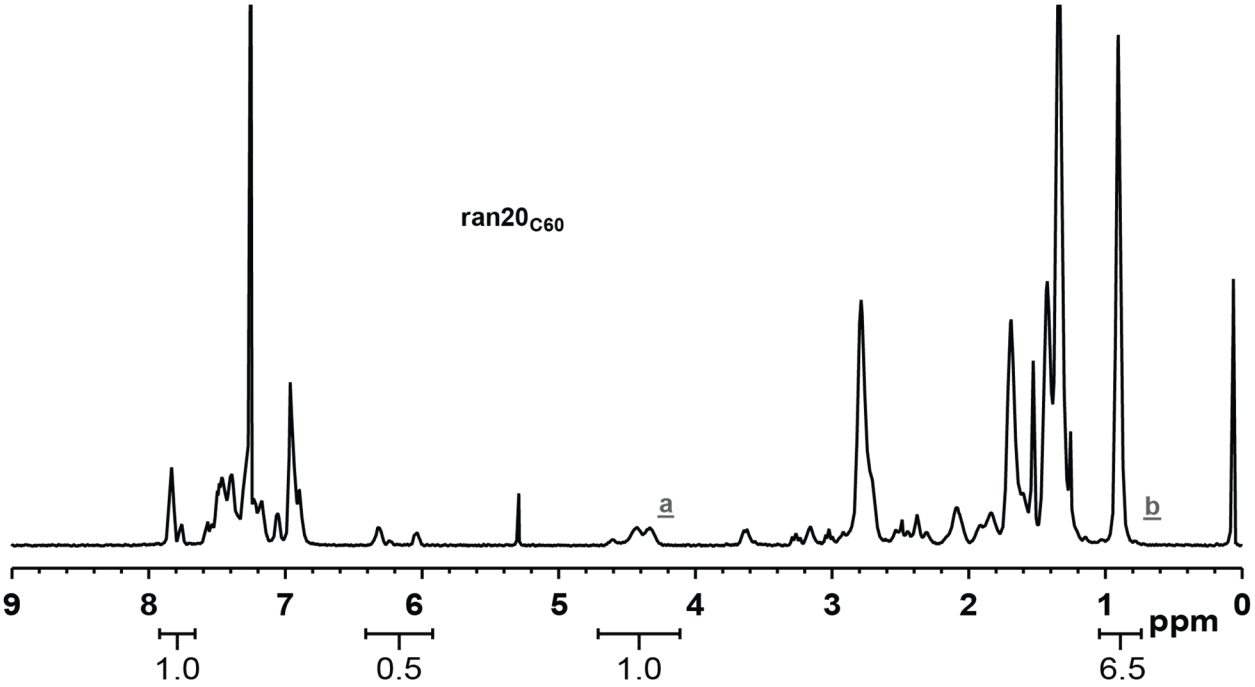

Figure A1.47 ^{1}H NMR spectrum for **ran20$_{C60}$**.

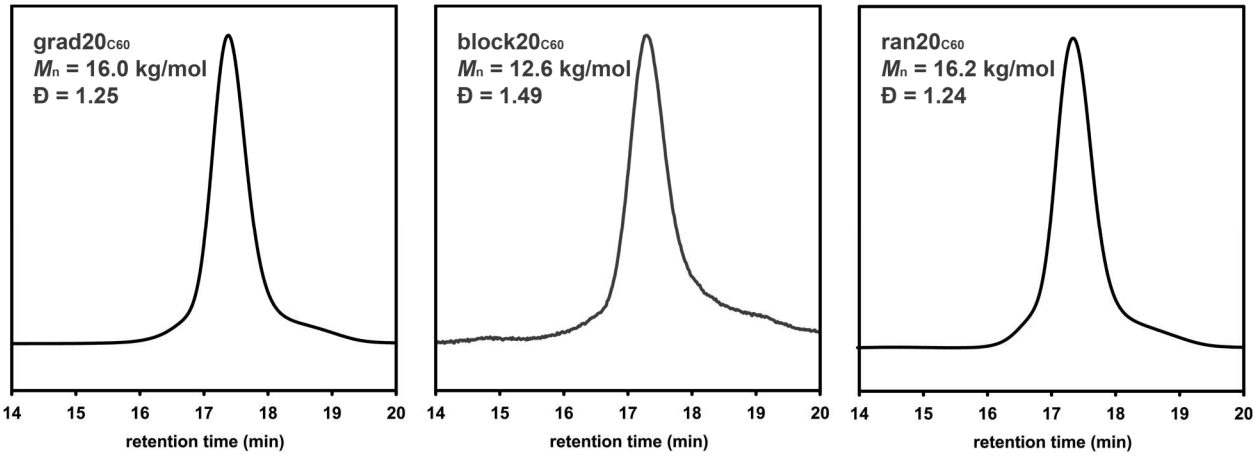

Figure A1.48 GPC trace of copolymers **grad20$_{C60}$**, **block20$_{C60}$**, and **ran20$_{C60}$**.

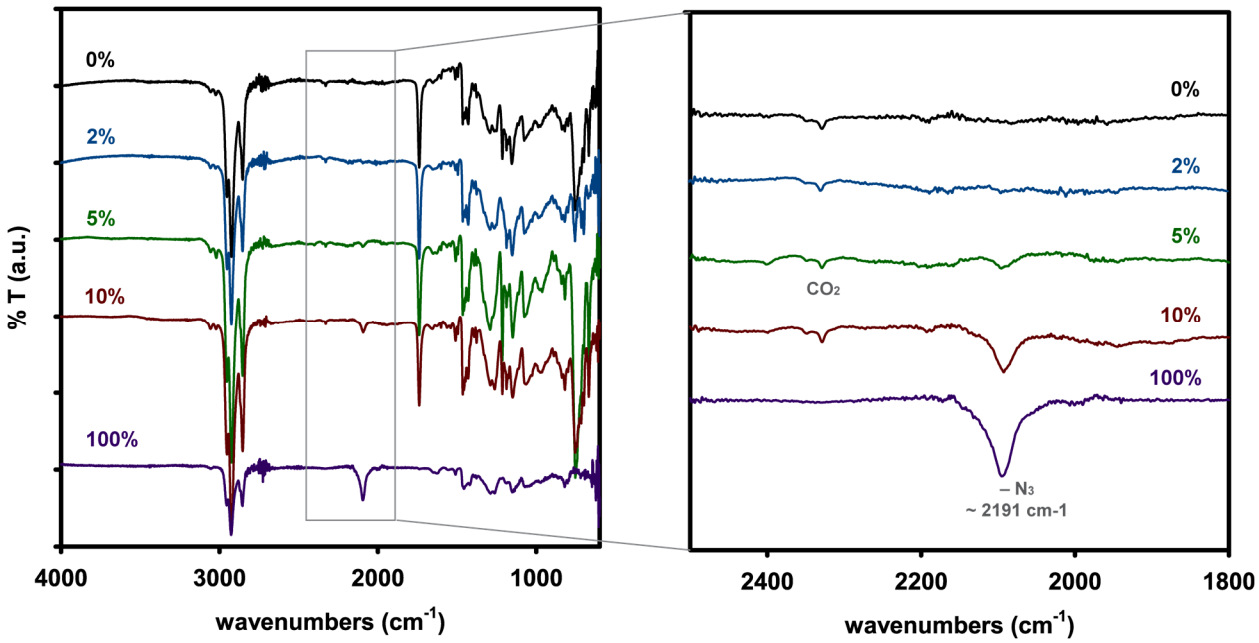

Figure A1.49 FTIR spectrum data for a solution of **P3HT** and **PCBM** (3.5 mg/mL in $CHCl_3$, 1:1 wt:wt) with **block20**$_{N3}$ at indicated wt%.

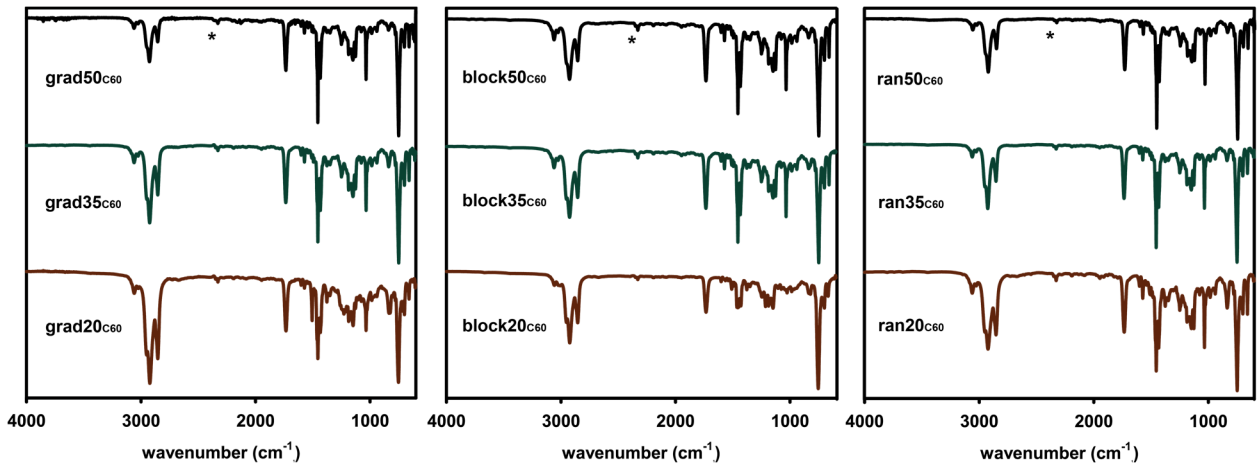

Figure A1.50 FTIR spectrum data for completed SPAAC reaction containing grad/block/ran$_{C60}$ and unreacted PCB-DIBO. *CO_2

A1.7 Optical Microscopy Images

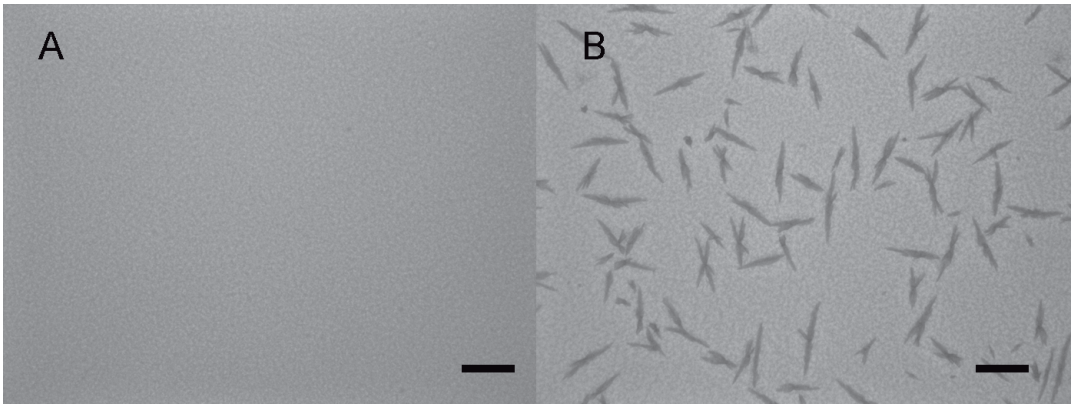

Figure A1.51 Optical microscopy images of **P3HT/PCBM** thin films (A) before and (B) after annealing for 60 min at 150 °C. Scale bar represents 30 μm.

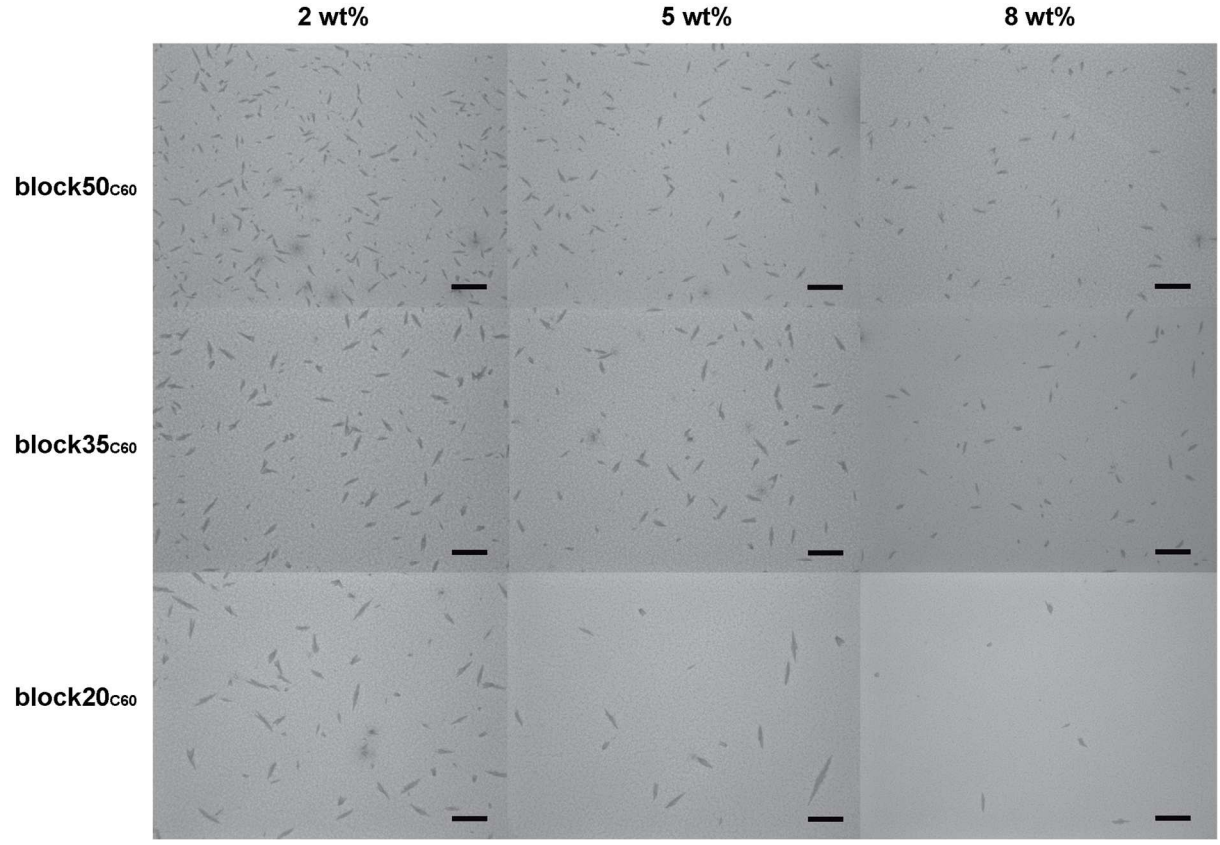

Figure A1.52 Optical microscopy images of **P3HT:PC$_{61}$BM** thin films with 2 wt%, 5 wt%, and 8 wt% of **block20$_{C60}$**, **block35$_{C60}$**, or **block50$_{C60}$** after annealing for 60 min at 150 °C. Scale bar represents 30 μm.

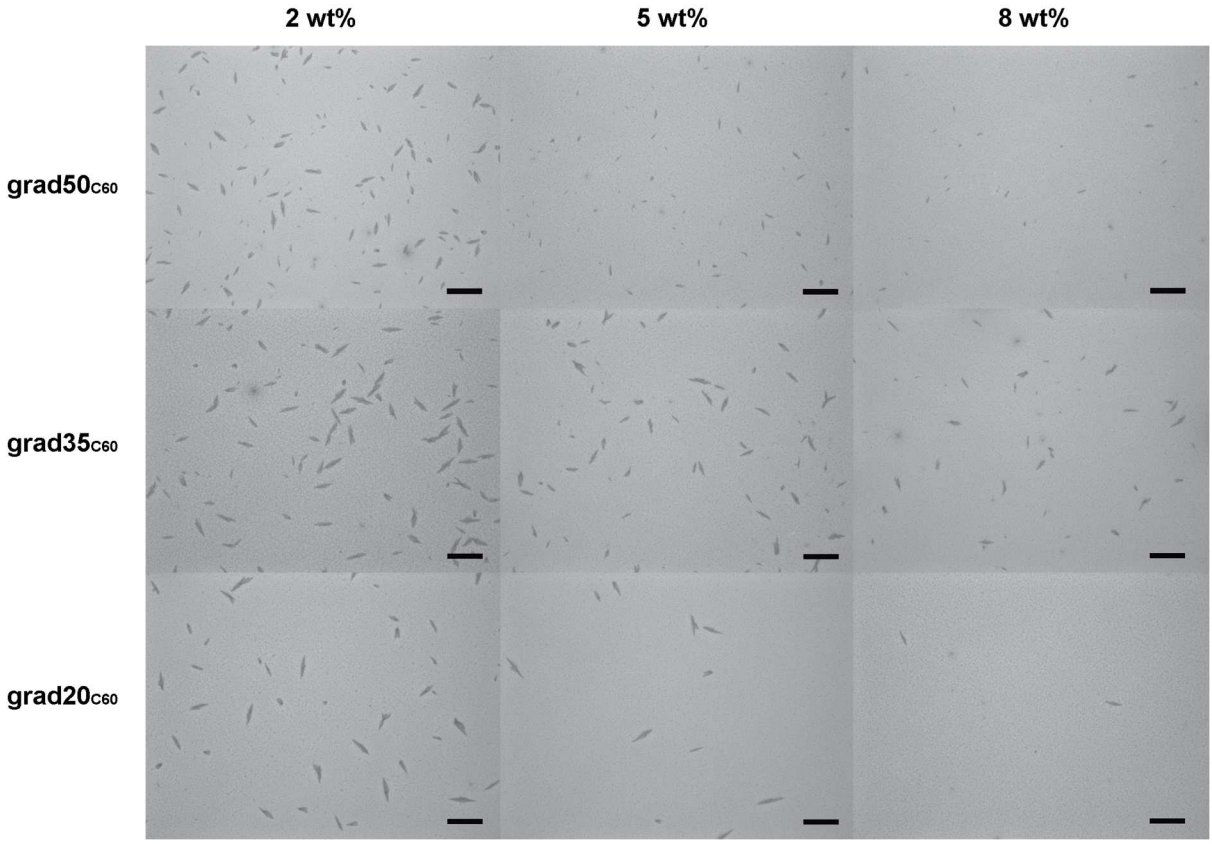

Figure A1.53 Optical microscopy images of **P3HT:PC$_{61}$BM** thin films with 2 wt%, 5 wt%, and 8 wt% of **grad20$_{C60}$**, **grad35$_{C60}$**, or **grad50$_{C60}$** after annealing for 60 min at 150 °C. Scale bar represents 30 μm.

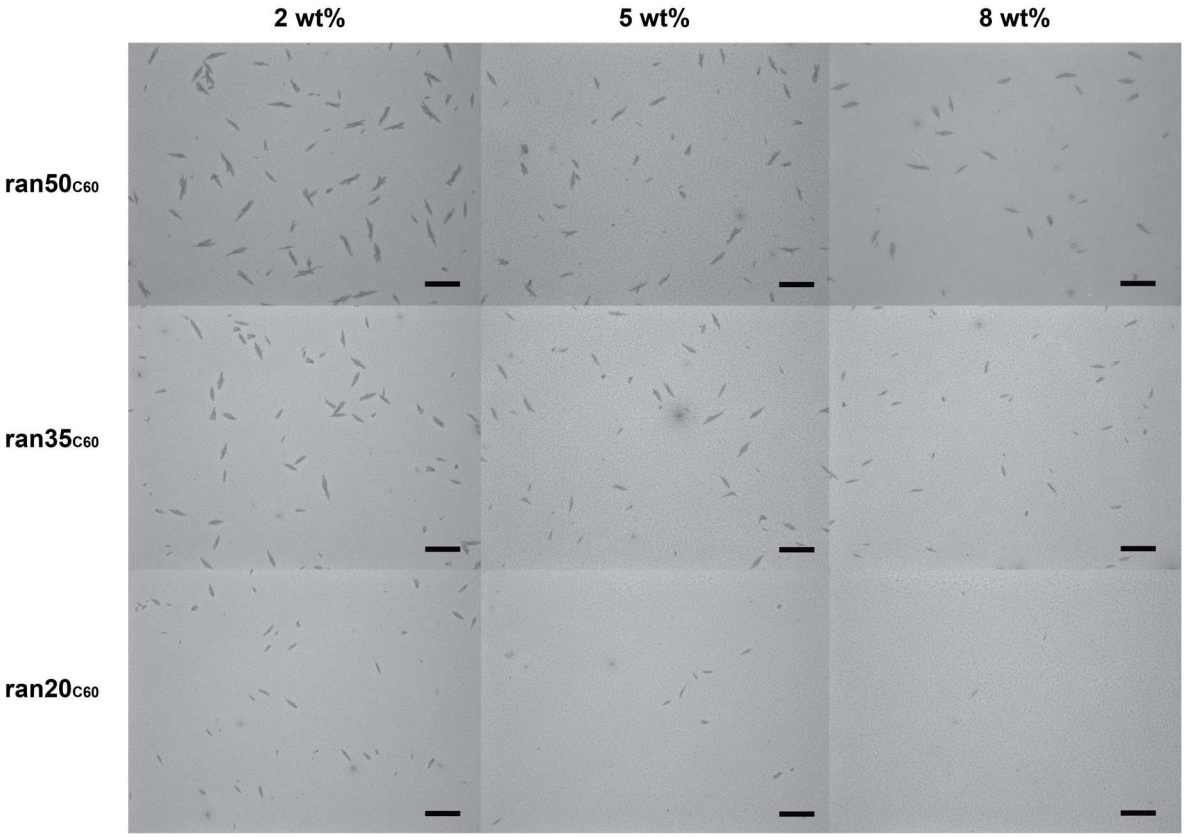

Figure A1.54 Optical microscopy images of **P3HT:PC$_{61}$BM** thin films with 2 wt%, 5 wt%, and 8 wt% of **ran20$_{C60}$**, **ran35$_{C60}$**, or **ran50$_{C60}$** after annealing for 60 min at 150 °C. Scale bar represents 30 μm.

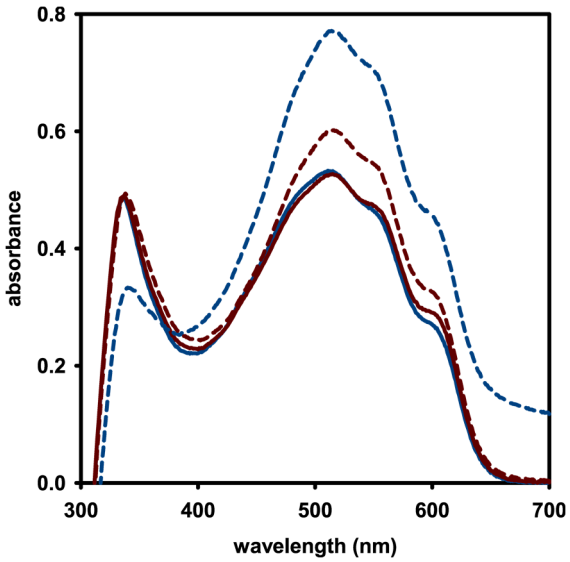

Figure A1.55 UV-Vis spectra of **P3HT:PC$_{61}$BM** thin films on quartz with 0 (blue) or 8 (red) wt% **ran20$_{C60}$** after 0 (solid) or 60 (dashed) min of annealing at 150 °C.

A1.8 Photocurrent and Device Performance Data

A1.8.1 Concentration Influence

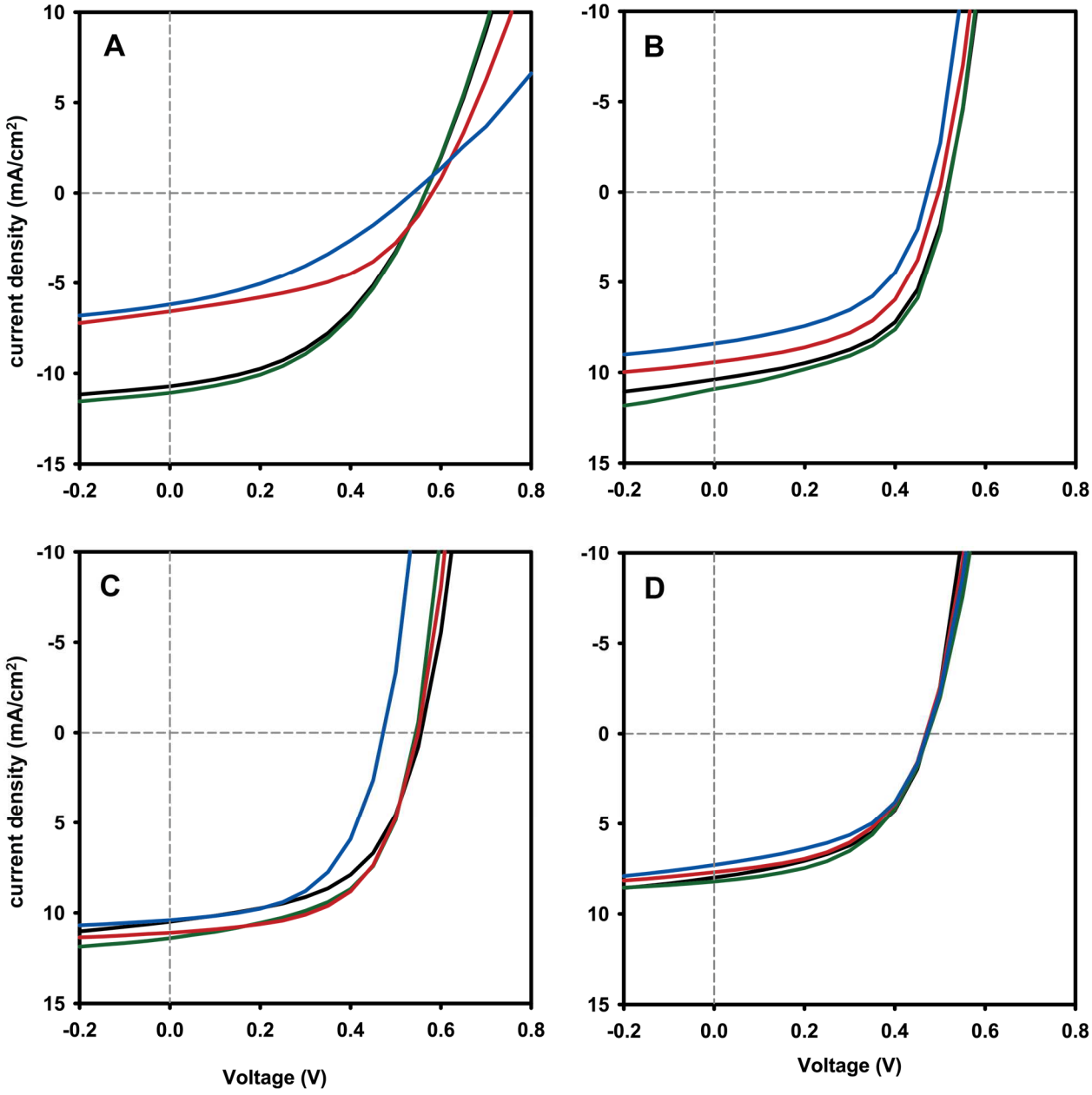

Figure A1.56 Current-voltage characteristics for the bulk heterojunction devices. The device active layer is composed of **P3HT:PC$_{61}$BM** blend with (A) 0 wt%, (B) 2 wt%, (C) 8 wt%, (D) 12 wt% **ran20**$_{C60}$ copolymer additive. Thermal annealing at 150 °C for 0 min (black), 15 min (green), 45 min (red), 60 min (blue).

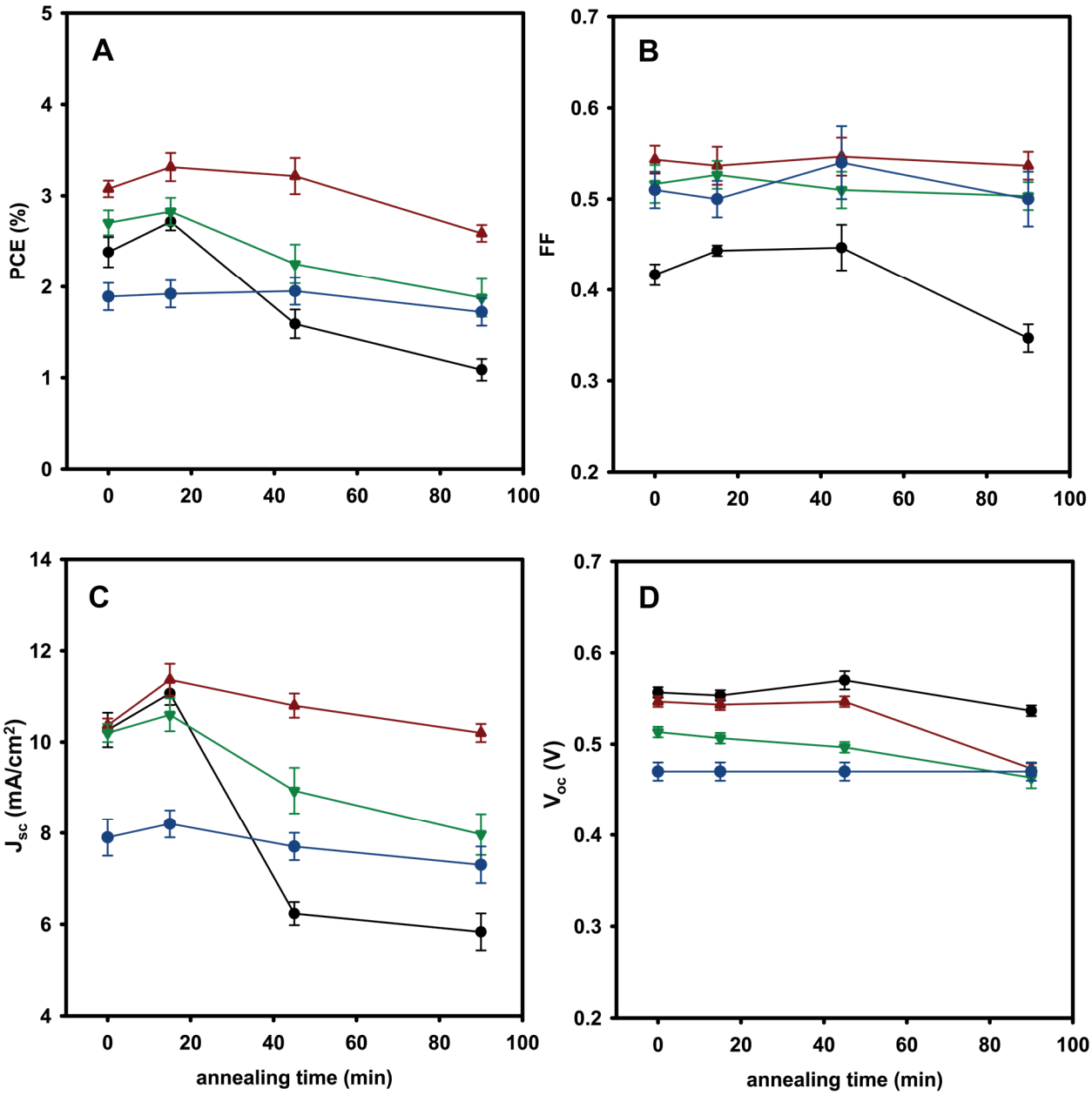

Figure A1.57 Performance data for bulk heterojunction devices with active layers composed P3HT:$PC_{61}BM$ blend with 0 (black circles ●), 2 (green triangles ▼), 8 (red triangles ▲), and 12 (blue circles ●) wt% **ran20**$_{C60}$. (A) PCE, (B) FF, (C) J_{sc}, and (D) V_{oc} as a function of annealing time at 150 °C.

A1.8.2 Composition Influence

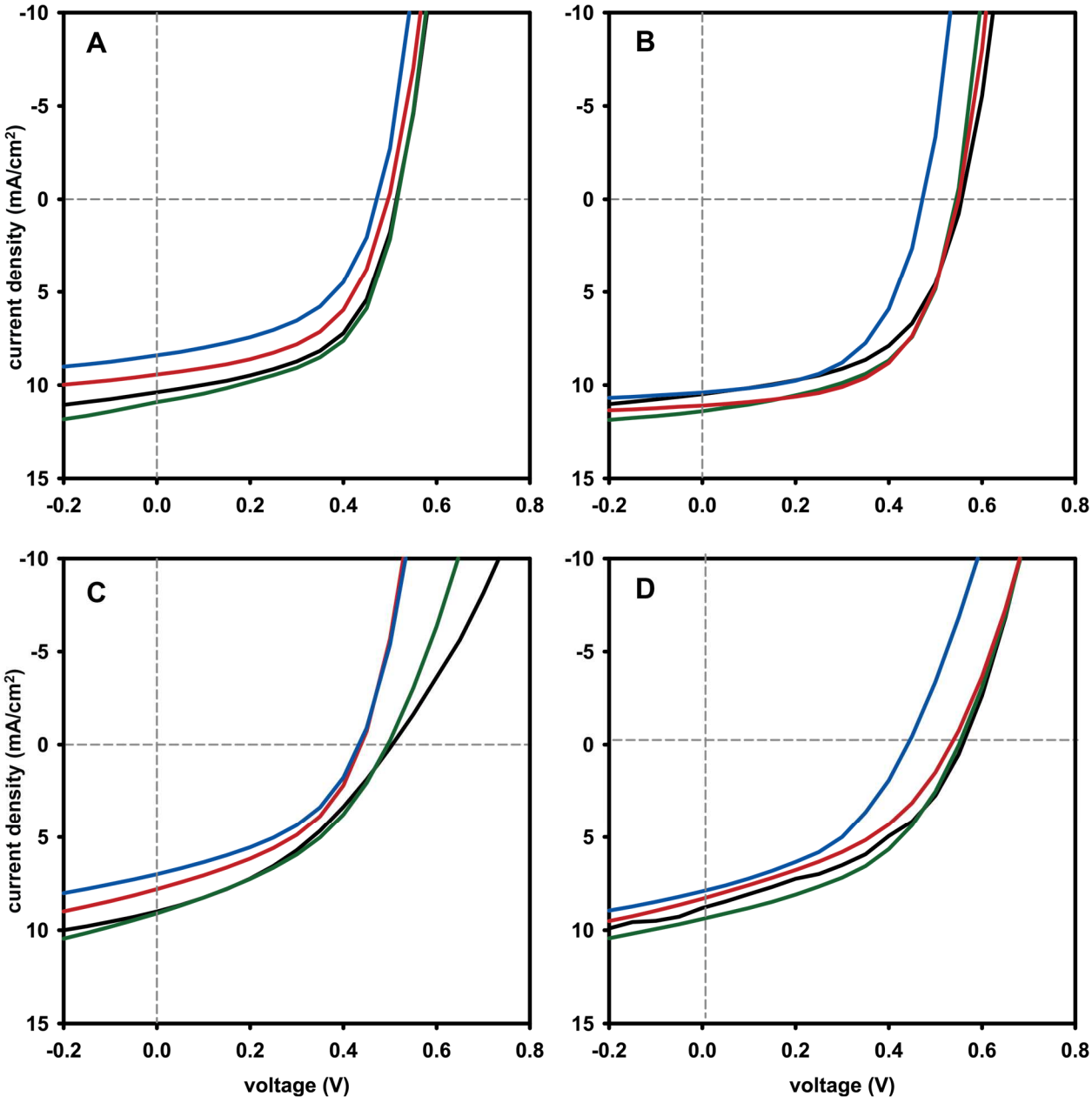

Figure A1.58 Current-voltage characteristics for the bulk heterojunction devices. The device active layer is composed of P3HT:$PC_{61}BM$ blend with (A) 2 wt%, (B) 8 wt% **ran20**$_{C60}$, or (C) 2 wt%, (D) 8 wt% **ran50**$_{C60}$ copolymer additive. Thermal annealing is at 150 °C for 0 min (black), 15 min (green), 45 min (red), 60 min (blue).

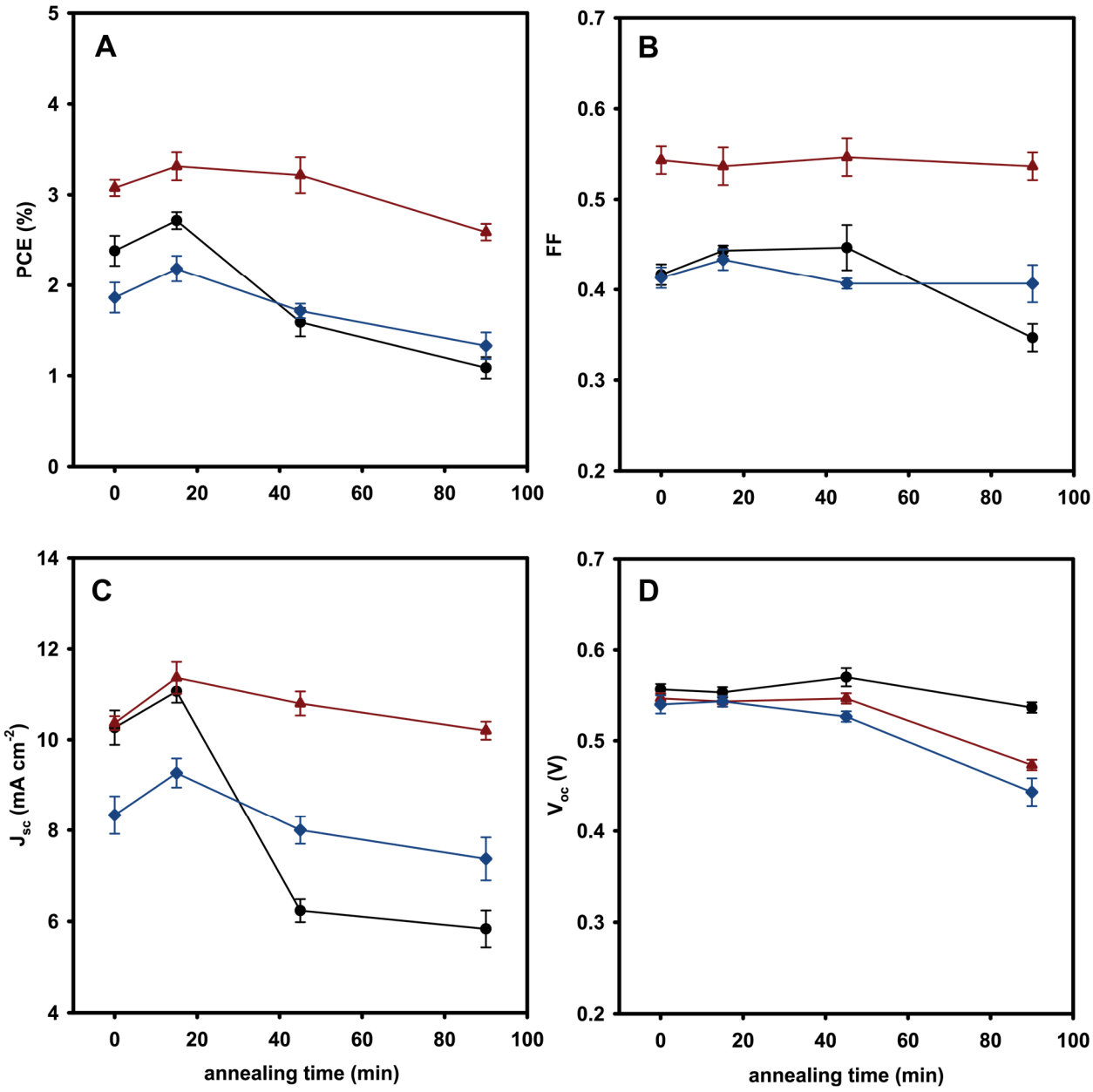

Figure A1.59 Performance data for bulk heterojunction devices with active layers composed P3HT:$PC_{61}BM$ with 0 (black circles ●), 8 wt% ran20$_{C60}$ (red triangles ▲), or 8 wt% **ran50$_{C60}$** (blue diamonds ◆) copolymer additive. (A) PCE, (B) FF, (C) J_{sc}, and (D) V_{oc} as a function of annealing time at 150 °C.

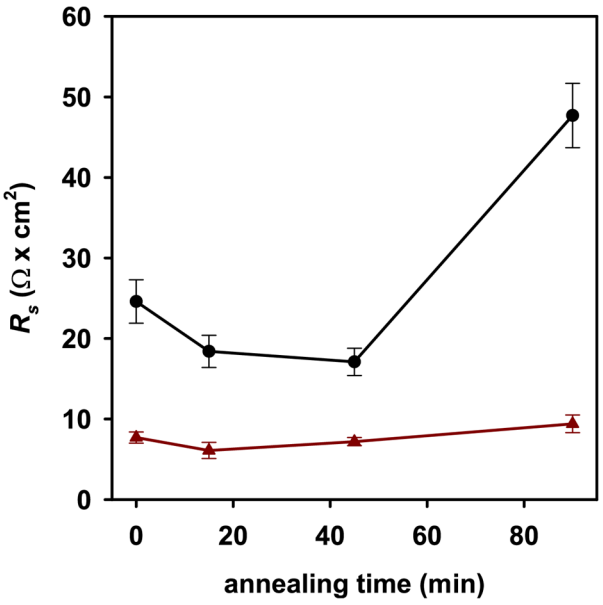

Figure A1.60 Series resistance (R_s) for bulk heterojunction solar cells as a function of annealing time at 150 °C containing 0 (black circles ●) or 8 wt% (red circles ●) **ran20$_{C60}$** in the **P3HT:PC$_{61}$BM** blend.

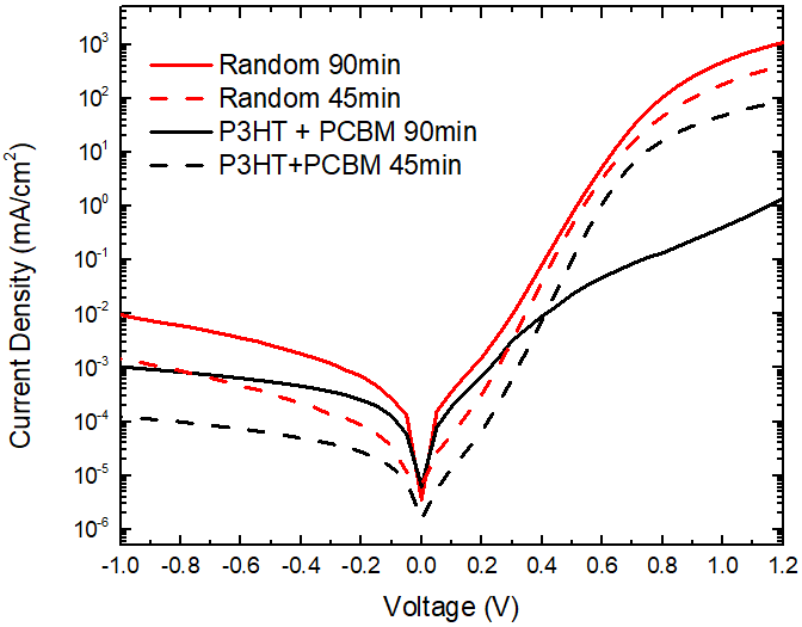

Figure A1.61 The *J-V* characteristics in the dark for solar cell devices with **P3HT:PC$_{61}$BM** blends containing 0 (black) or 8 (red) wt% **ran20$_{C60}$** after annealing at 150 °C for 45 (dashed) and 90 (solid) mins.

A1.8.3 Derivation and Calculation for Change in V_{OC} from Change in J_{OC}:

The V_{oc} for **ran20$_{C60}$** is given in equation S1,[7]

$$V_{oc_1} = \Delta E_{HL} - nk_BTln\left(\frac{J_{o_1}}{J_{sc_1}}\right) \quad \text{(S1)}$$

The V_{oc} for P3HT:$PC_{61}BM$ is given in equation S2

$$V_{\mathrm{oc}_2} = \Delta E_{HL} - nk_BT\ln\left(\frac{J_{\mathrm{o}_2}}{J_{\mathrm{sc}_2}}\right) \quad \text{(S2)}$$

The reverse bias saturation current for the device with **ran20$_{C60}$** is approximately 1 order of magnitude greater than that of the P3HT:$PC_{61}BM$ device.

$$J_{o_1} \cong 10\left(J_{o_2}\right) \quad \text{(S3)}$$

The difference in V_{oc} between the **ran20$_{C60}$** and P3HT:$PC_{61}BM$ devices can be calculated by subtracting equation S2 from S1.

$$\Delta V_{oc} = nk_BT\left[\ln\left(\frac{J_{o_1}}{J_{sc_1}}\right) - \ln\left(\frac{J_{o_2}}{J_{sc_2}}\right)\right] \quad \text{(S4)}$$

Using the relationship in equation S3 and simplifying gives equation S5.

$$\Delta V_{oc} = nk_BT\ln\left(\frac{10J_{sc_2}}{J_{sc_1}}\right) \quad \text{(S5)}$$

Substituting measured values for J_{sc_1} and J_{sc_2}, and approximating $n \cong 1.5$ (where n is the diode ideality factor approximated for P3HT: $PC_{61}BM$ after annealing)[8] gives the approximate difference in V_{oc} between the **ran20$_{C60}$** and P3HT:$PC_{61}BM$ devices:

$\Delta V_{oc} \cong 0.07\ V$

A1.9 HOMO/LUMO Determination

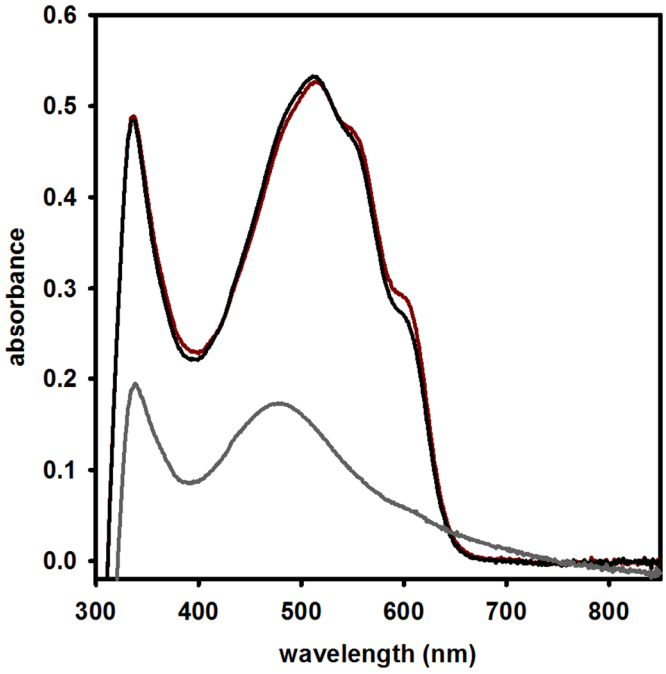

Figure A1.62 UV-Vis spectra of neat **ran20$_{C60}$** (grey) and P3HT:$PC_{61}BM$ thin films on quartz with 0 (black) and 8 (red) wt% **ran20$_{C60}$**. The spectrum of neat **ran20$_{C60}$** was used to calculate the optical bandgap (E_g^{opt}) (see page S67).

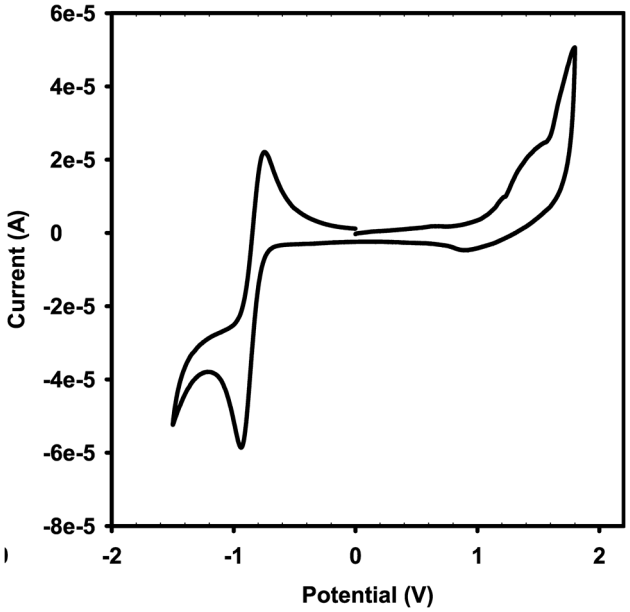

Figure A1.63 Cyclic voltammogram of **ran20$_{C60}$** (1 mg/mL in $CHCl_3$) which was used to determine the HOMO of the copolymer (see page S67).

A1.9.1 Calculation of the HOMO/LUMO

P3HT:

Values for the HOMO (-4.76 eV) and E_g^{opt} (1.80 eV) of P3HT were used.[9] The LUMO (-2.96 eV) was then calculated by adding the E_g^{opt} to the HOMO:

$$-4.76 \text{ eV} + 1.80 \text{ eV} = -2.96\text{eV} \quad \text{(S6)}$$

$PC_{61}BM$:

The value for the HOMO (-5.93 eV) was obtained from reference 10. The E_g^{opt} (1.87 eV) of $PC_{61}BM$ was calculated from the approximate optical absorption edge (~660 nm).[10] The LUMO (-4.06 eV) was then calculated by adding the E_g^{opt} to the HOMO:

$$-5.93 \text{ eV} + 1.87 \text{ eV} = -4.06 \text{ eV} \quad \text{(S7)}$$

ran20$_{C60}$:

The HOMO (-5.5 eV) was calculated from the electrochemical onset potential. The E_g^{opt} (1.6 eV) was calculated from the optical absorption edge. The LUMO (-3.9 eV) was then calculated by adding the E_g^{opt} to the HOMO:

$$-5.5 \text{ eV} + 1.6 \text{ eV} = -3.9 \text{ eV} \quad \text{(S8)}$$

A1.10 Atomic Force Microscopy (AFM) Data

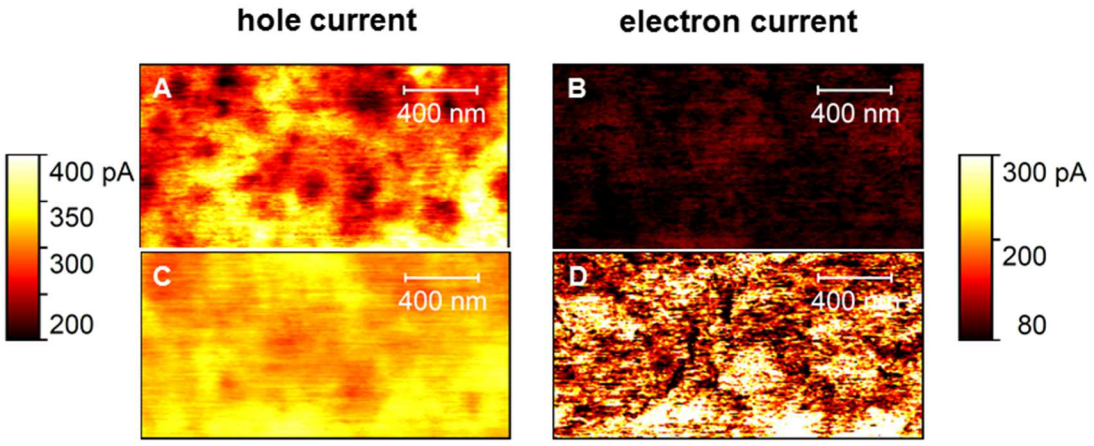

Figure A1.64 conductive-Atomic Force Microscopy (c-AFM) phase images of the active layer blend. The hole current was measured for **P3HT:PC$_{61}$BM** blends with (A) 0, or (C) 8 wt% ran20$_{C60}$ spin-casted onto ITO/MoO_3 (scale bar at left corresponds to images A, C). The electron current was measured for active layer blends with (B) 0, or (D) 8 wt% **ran20$_{C60}$** spin-casted onto ITO/ZnO (scale bar at right corresponds to images B, D).

Table A1.1 Hole and electron current data from c-AFM of **P3HT:PC$_{61}$BM** blends with 0 or 8 wt% **ran20$_{C60}$**.

wt% ran20$_{C60}$	hole current (pA/μm^2)	electron current (pA/μm^2)
0	292 ± 37	88 ± 11
8	319 ± 15	202 ± 47

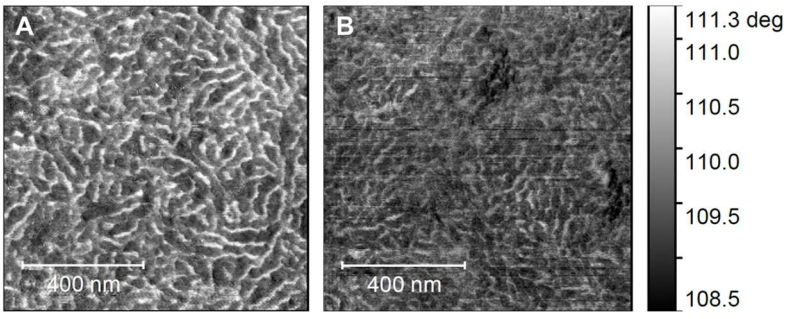

Figure A1.65 Atomic force microscopy phase images depicting surface morphology of **P3HT:PC$_{61}$BM** blends with (A) 0 and (B) 8 wt% **ran20$_{C60}$**.

A1.11 Differential Scanning Calorimetry (DSC) Data

The T_g can be difficult to observe in semicrystalline materials like **P3HT**, **$PC_{C61}BM$**, and blends of both because only a small fraction of each material is amorphous.[11] To measure the thermal glass transition temperatures (T_g) of the fullerene functionalized copolymers and optimal blends, a variety of DSC conditions were screened:

Standard DSC

- Pan and lid type (Tzero and Tzero Low-Mass pans, Tzero and Tzero Hermetic lids)
- Sample mass (1–8 mg)
- Scan rate (5, 10, 20 °C/min)
- Initial temperature (anneal at -60 °C or 150 °C before beginning scan cycles)
- Minimum temperature (-80, -60, -40, 0 °C)
- Maximum temperature (150, 295 °C)
- Isotherm length at minimum/maximum temperatures (1, 5 min)

Modulated Temperature DSC (MDSC)

- Pan and lid type (Tzero and Tzero Low-Mass pans, Tzero Hermetic lids)
- Sample mass (1–8 mg)
- Period (60 s)
- Amplitude (0.398, 0.400, 0.500, 0.738)
- Minimum temperature (-80, -60 °C)
- Maximum temperature (150, 295 °C)
- Ramp rate (2.0, 2.5 °C/min)

A1.11.1 Copolymer Cross-Linking at High Temperatures

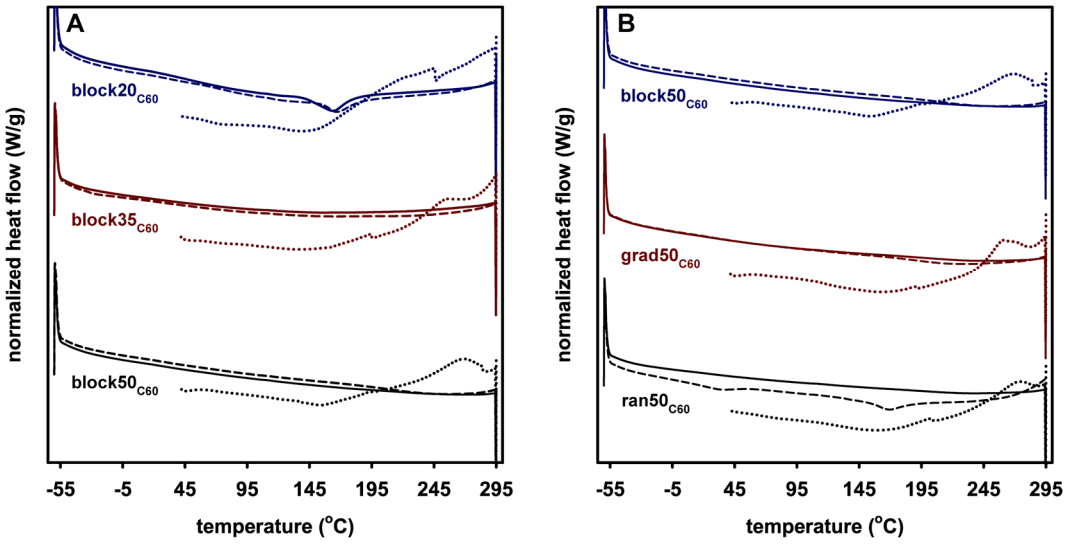

Figure A1.66 Standard DSC heating thermograms for fullerene-functionalized copolymers with (A) varying composition and (B) varying sequence. The initial (dotted) heating ramp shows cross-linking at temperatures >150 °C as a broad exothermic peak. The second (dashed) and third (solid) heating ramps show minimal to no thermal transitions, as would be expected for cross-linked material. The exothermic direction is up for all thermograms.

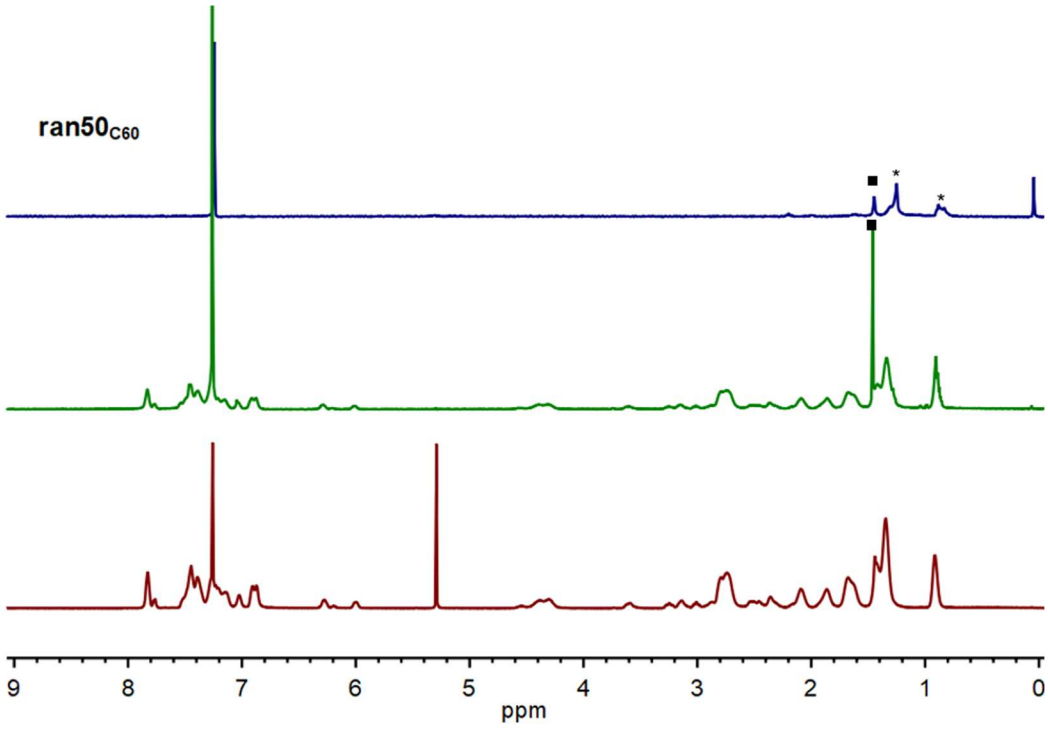

Figure A1.67 A sample ^{1}H NMR spectrum depicting ran50$_{C60}$ copolymers before (red) and after DSC scans with maximum temperatures of 150 °C (green), and 295 °C (blue). ■ H_2O, *grease

A1.11.2 Fullerene-Functionalized Copolymers and Optimal Blends

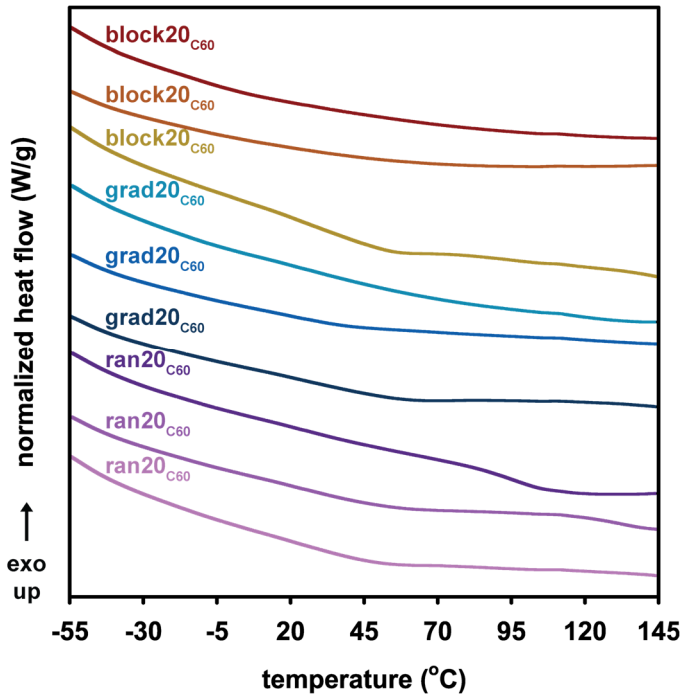

Figure A1.68 Standard DSC thermograms of all fullerene-functionalized copolymers showing the 3rd heating ramp. Most copolymers did not display a thermal glass transition temperature (T_g). The T_g for **ran20**$_{C60}$ is 99 °C.

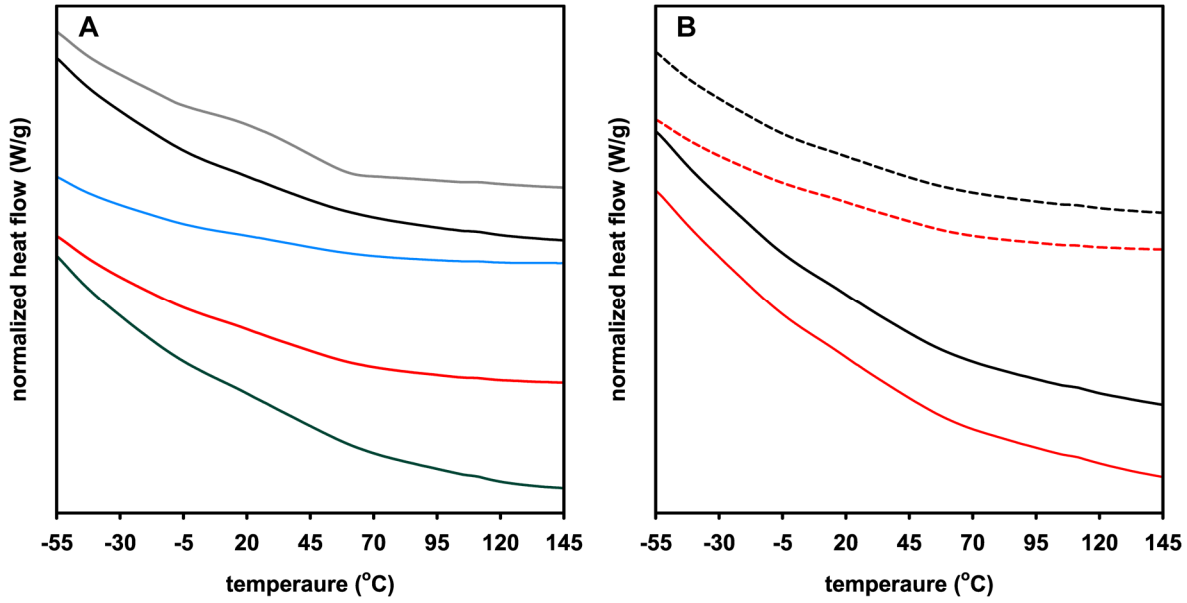

Figure A1.69 Standard DSC thermograms of optimal blends to study (A) concentration influence for **ran20**$_{C60}$ and (B) composition influence by comparing **ran20**$_{C60}$ (dashed) and **ran50**$_{C60}$ (solid). The copolymers were present in 0 (grey), 2 (black), 5 (blue), 8 (red), or 12 (green) wt% of the blend.

A1.12 References

[1] R. S. Loewe, P. C. Ewbank, J. S. Liu, L. Zhai, R. D. McCullough, Macromolecules 2001, 34, 4324–4333.

[2] (a) E. L. Lanni, A. J. McNeil, *Macromolecules* **2010**, *43*, 8039–8044. (b) S. R. Lee, J. W. G. Bloom, S. E. Wheeler, A. J. McNeil *Dalton Trans* **2013**, *42*, 4218–4222. (c) S. R. Lee, Z. J. Bryan, A. M. Wagner, A. J. McNeil, *Chem Sci* **2012**, *3*, 1562–1566.

[3] N. E. Mbua, J. Guo, M. A. Wolfert, R. Steet, G.-J. Boons, *ChemBioChem*, **2011**, *12*, 1912–1921.

[4] M. S. White, D. C. Olson, S. E. Shaheen, N. Kopidakis, D. S. Ginley, *Appl. Phys. Lett.* **2006**, *89*, 143517/1-143517/3.

[5] Z. Liu, E. Shi, Y. Wan, N. Li, D. Chen, Q. Xu, H. Li, J. Lu, K. Zhang, L. Wang, *J. Mater. Chem. C* **2015**, *3*, 2033.

[6] M. Wong, J. Hollinger, L. M. Kozycz, T. M. McCormick, Y. J. Lu, D. C. Burns, D. S. Seferos, *ACS Macro Lett* **2012**, *1*, 1266–1269.

[7] N. C. Giebink, G. P. Wiederrecht, M. R. Wasielewski, S. R. Forrest, *Phys. Rev. B* **2010**, *82*, 155305.

[8] E. Voroshazi, B. Verreet, T. Aernouts, P. Heremans, P. *Sol. Energy Mater. Sol. Cells* **2011**, *95*, 1303–1307.

[9] J. Hou, Z. Tan, Y. Yan, Y. He, C. Yang, Y. Li *J. Am. Chem. Soc.* **2006**, *128*, 4911–4916.

[10] Y. He, G. Zhao, B. Peng, Y. Li *Adv. Funct. Mater.* **2010**, *20*, 3383–3389.

[11] J. Zhao, A. Swinnen, G. Van Assche, J. Manca, D. Vanderzande, B. Van Mele, *J. Phys. Chem. B*, **2009**, *113*, 1587–1591.

Appendix 2 for A Fullerene-Functionalized Poly(3-hexylthiophene) Additive Stabilizes Conjugated Polymer-Fullerene Blend Morphologies

A2.1 Polymer and Fullerene Chemical Structures

Chart A2.1 Chemical structures of the donor polymers poly[[4,8-bis[(2-ethylhexyl)oxy]benzo[1,2-b:4,5-b0]dithiophene-2,6-diyl][3-fluoro-2-[(2-ethylhexyl)-carbonyl]-thieno-[3,4-b]thiophene-diyl]] (**PTB7**), poly[4,8-bis(5-(2-ethylhexyl)thiophen-2-yl)benzo[1,2-b;4,5-b′]dithiophene-2,6-diyl-alt-(4-(2-ethylhexyl)-3-fluorothieno[3,4-b]thiophene-)-2-car-boxylate-2-6-diyl)] (**PTB7-Th**), and poly[(5,6-difluoro-2,1,3-benzothiadiazol-4,7-diyl)-alt-(3,3‴-di(2-octyldodecyl)-2,2′;5′,2″;5″,2‴-quaterthiophen-5,5‴-diyl)] (**PffBT4T-2OD**), the acceptor phenyl-C_{71}-butyric acid methyl ester (**$PC_{71}BM$**), and the copolymer, poly(3-hexylthiophene) (**P3HT**), and diiodooctane (**DIO**) additives used in this work.

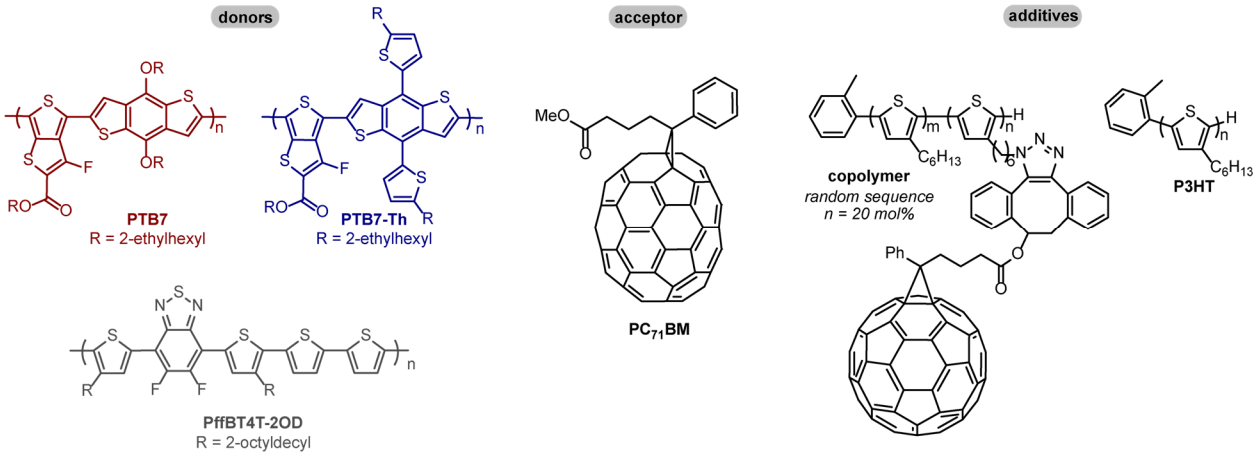

A2.2 Materials

Flash chromatography was performed on SiliCycle silica gel (40–63 μm). Thin-layer chromatography was performed on MACHEREY-NAGEL TLC plates (pre-coated with 0.20 mm silica gel 60 with fluorescent indicator UV254). Fused silica wafers were purchased from University Wafer and cut into square substrates (1.5 x 1.5 cm). Glass and indium tin oxide (ITO)/glass substrates (1.8 x 1.8 x 0.7 cm, ITO 15 Ω) were purchased from Luminescence

Technology Corporation. Pure-C on copper TEM grids were purchased from Ted Pella Corporation.

$Ni(COD)_2$ was purchased from Strem Chemicals. Lithium diisopropylamide (LDA, 2.0 M in THF/n-heptane/ethylbenzene, 59/28/13 v/v) was purchased from Sigma Aldrich. 2,5-Dibromo-3-hexylthiophene (DB3HT) was purchased from ArkPharm and purified by dissolving in hexanes, stirring for 2 h with decolorizing carbon, filtering through a plug of silica gel, and concentrating in vacuo. N-bromosuccinimide (NBS) was purchased from Sigma Aldrich, recrystallized from water, and dried over P_2O_5. Isopropylmagnesium chloride (iPrMgCl, 2.0 M in THF, 25 mL), diiodooctane (DIO) (98%, containing Cu as a stabilizer), and PEDOT:PSS (3–4% suspension in H_2O) were purchased from Sigma Aldrich. Compounds **S1–S9**, **ran20$_{Br}$**, **ran20$_{N3}$**, and **copolymer** were prepared using modified literature procedures.[1] All monomer solutions for polymerizations were titrated with salicylaldehyde phenylhydrazone to obtain the active Grignard concentration.[2]

The polymers **PTB7** (lot # YY13230DC), **PTB7-Th** (lot # YY171760CH), and **PffBT4T-2OD** (lot # YY13086CB, YY13250CB, and YY13250CH) were purchased from 1-Material – Organic Nano Electronic. [6,6]-phenyl-C_{61}-butyric acid methyl ester ($PC_{61}BM$, lot # RC160930) and [6,6]-phenyl-C_{71}-butyric acid methyl ester ($PC_{71}BM$, lot # TC200702) were purchased from Nano-C Inc. *N*-, Molybdenum(VI) oxide, (MoO_3, 99.97% trace metals basis), zinc acetate dihydrate ($Zn(OAc)_2•2H_2O$), and 2-methoxyethanol (2ME) were purchased from Sigma Aldrich. Silver pellets (Ag, 99.99% purity) were purchased from Kurt J. Lesker Company.

Tetrahydrofuran (THF) was dried and deoxygenated using an Innovative Technology (IT) solvent purification system composed of activated alumina, a copper catalyst, and molecular sieves. All water used was deionized. All other reagent grade materials and solvents were purchased from Sigma Aldrich, Acros Organics, Alfa Aesar, or Fisher and used without further purification unless otherwise noted. The glovebox in which synthetic procedures were carried out was an MBraun LABmaster 130 with a N_2 atmosphere. The glovebox in which device fabrication was carried out was an ultra-high puritiy (<1ppm of H_2O and O_2) glovebox from LC Technology Solutions, INC.

A2.3 General Experimental

NMR Spectroscopy: Unless otherwise noted, ^{1}H, ^{13}C and ^{31}P NMR spectra were acquired at room temperature in deuterated solvents. For ^{1}H NMR spectra, a relaxation delay of 1 s was used for small molecules and 10 s was used for polymers. For ^{1}H and ^{13}C NMR spectra, the chemical shift data are reported in units of δ (ppm) relative to tetramethylsilane (TMS) and referenced to residual solvent. For ^{31}P spectra, the chemical shift data are reported in units of δ (ppm) relative to 85% H_3PO_4 in H_2O. Multiplicities are reported as follows: singlet (s), doublet (d), doublet of doublets (dd), triplet (t), quartet (q), multiplet (m), broad signal (br).

High Resolution Mass Spectrometry (HRMS): High-resolution mass spectrometry data were obtained on a Micromass AutoSpec Ultima Magnetic Sector mass spectrometer.

Fourier-Transform Infrared (FTIR) Spectroscopy: FTIR spectroscopy data were obtained on a Thermo-Nicolet IS-50 using the attenuated total reflectance (ATR) accessory on neat samples.

Gas Chromatography: Gas chromatography was carried out using a Shimadzu GC 2010 containing a Restek RXI-5MS (crossbound 5% diphenyl–95% dimethyl polysiloxane; 15 m, 0.25 mm ID, 0.25 μm df) column.

Size-Exclusion Chromatography (SEC): For SEC analysis, all polymers were dried under vacuum overnight, dissolved (~0.5 mg polymer/mL) in THF spiked with trace toluene (<1 vol%) with mild heating if necessary, and filtered through a 0.2 μm PTFE filter.

SEC was performed with THF as the eluent at 40 °C and at a flow rate of 1.0 mL/min on two different instruments. The data presented correspond to the absorbance at 254 nm with the maximum intensity normalized to 1.

SEC #1: Malvern Viscotek GPCMax VE2001 equipped with two Viscotek LT-5000L 8 mm (ID) × 300 mm (L) columns, and Viscotek TDA 305 and Viscotek PDA detectors. Apparent molar masses were calculated using 9 polystyrene standards from 377,400 g/mol to 580 g/mol.

SEC #2: Shimadzu GPC/SEC equipped with two Styragel HT 7.8 mm (ID) x 300 mm (L) columns and a PSS Gram column 8 mm (ID) x 300 mm (L), and a RI (refractive index) detector and an UV diode array detector. Apparent molar masses were calculated using polystyrene standards from 1,000,000 g/mol to 92 g/mol.

SEC #3: Same instrument as #2 (Shimadzu GPC/SEC) equipped with different columns (three Phenomenex Phenogel™ 10 µm Linear (2), LC Column 300 x 7.8 mm). Apparent molar masses were calculated using polystyrene standards from 1,000,000 g/mol to 92 g/mol.

Differential Scanning Calorimetry (DSC): DSC was performed under N_2 on a TA Instruments DSC Q2000 equipped with a TA RCS cooling accessory. Neat solid samples (~4–5 mg) were placed in aluminum Tzero Low-Mass Hermetic pans and sealed with Tzero Hermetic lids using a TA Instruments crimper. Blend samples were drop cast from a 19.8 mg/mL solution in *ortho*-dichlorobenzene/chlorobenzene (*o*-DCB/CB 50/50, v/v) into aluminum Tzero Hermetic pans, dried *in vacuo* overnight and sealed with Tzero Hermetic lids using a TA Instruments crimper. Samples were cycled between 0 °C and 350 °C at a ramp rate of 10 °C/min with 5 min isotherms at the minimum/maximum temperatures.

Substrate Cleaning: Substrates for films and devices were cleaned via scrubbing with undiluted Hellmanex III Detergent then rinsing with DI water. The substrates were then sonicated for 15 min in each of the following solvents: DI water, acetone, and iPrOH. Clean substrates were then dried in an oven at 140 °C for 16 h and stored in a clean petri dish wrapped in aluminum foil.

Optical Microscopy: Thin film samples were examined using a Leica DMCB optical microscope with a 40x objective lens. Images were recorded with an attached QICAM Fast 1394 digital video camera and analyzed with ImageJ.

Image Analysis with ImageJ: Images were saved as .tiff files to open in the ImageJ software. Once loaded in the software, images were converted to black and white by clicking "Image" and selecting "Color," then "Split Channels" from the dropdown menu. Three images were generated and the "(blue)" (**PTB7**, **PTB7-Th**) or "(green)" (**PffBT4T-2OD**) channel image was selected for further analysis. The image background was subtracted by clicking "Process" then "Subtract Background" from the dropdown menu which opened a new window. In the new window, default rolling ball radius (50 pixels) was used and "light background" was checked to ensure even background subtraction. In the "Image" tab, "Adjust" then "Threshold" were selected, opening a new window showing the minimum and maximum threshold limits for detecting particles (dark domains), now depicted in red on the image. Selecting "Apply" defined the particle sizes/areas and displayed them in black on the image. To calculate the black particle percent area, "Analyze" then "Analyze Particles" was selected. In the resulting window, the size was set to "0.0001-infinity" then "display results," "Summary," "Include Holes" and "Clear Results" were checked and "OK" was selected. The tabulated data points and results summary (with % area of particles relative to whole image), each appeared in separate windows.

Surface Contact Angle Goniometry: The surface contact angles were measured for water and glycerol and calculated with CAM 100 KSV Instrumental Ltd software. The surface contact angles were calculated by averaging angles from 10 frames for each droplet, three droplets per film, and at least three films. The surface energies were calculated using the Wu Harmonic Mean method (see pp 248–249).[3,4]

Variable-angle Spectroscopic Ellipsometry: Thin film thicknesses were determined by variable-angle spectroscopic ellipsometry of films on silicon wafers. Near-infrared (1100 nm–1600 nm) spectroscopic data were recorded by J.A. Woollam M-2000 ellipsometer followed by thickness measurement by Cauchy-model fitting.[5]

Ultraviolet-visible (UV-vis) Spectroscopy: UV-vis spectra of thin films were acquired using a Thermo Scientific Evolution 220 UV-vis spectrophotometer.

Bulk Heterojunction Solar Cell Device Fabrication and Measurement: Solar cell devices have the following inverted structure: glass/ITO/ZnO(40 nm)/blend/MoO_3(20 nm)/Ag(100 nm). The indium tin oxide (ITO) substrates were cleaned as described on page 201, then exposed to 245 nm ultraviolet light under oxygen flow for 15 min. 0.5 M ZnO sol–gel solution was prepared by dissolving (2.195 g, 0.01 mol) of zinc acetate dihydrate ($Zn(OAc)_2*_2H_2O$) in 20 mL of 2-methoxyethanol (2ME). A (0.611 g, 0.01 mol) of monoethanolamine was added into the stock solution as a stabilizer and the mixture was stirred at 60 °C for 4 h. The solution was then cooled to rt and aged for > 24 h. An aliquot of the ZnO solution (80 μL) was spin-cast on ITO-coated glass substrates at 3000 rpm for 60 s, followed by thermal annealing in air at 150 °C for 20 min. Polymer solutions were prepared as described for optical microscopy (pp 227–232) and stirred at 60 °C for 12 h before spin-casting under N_2. An aliquot of the hot polymer solution (100 μL) was spin-cast at 800 rpm for 180 s, generating thin films (215 ± 10 nm) as measured with spectroscopic ellipsometry. After spin-casting the polymers, the films were either directly transferred or thermally annealed (for 10, 30, 60, 90, 180 min) then transferred to an Angstrom Engineering AMOD thermal evaporation chamber containing MoO_3 and Ag pellets. Molybdenum masks with

1 mm radius circular openings were placed on the sample to form devices with a total area of 3.14 mm^2. MoO_3 and Ag were evaporated sequentially onto the film at a rate of 1 Å/s under the base pressure of 3×10^{-7} torr.

J-V characteristics of the devices were recorded by a HP 4156a semiconductor parameter analyzer. The transparent glass/ITO side was illuminated with simulated AM 1.5G at 1 sun intensity (100 mW/cm^2). The intensity of the solar simulator was calibrated by the National Renewable Energy Laboratory (NREL)-traceable Si reference cell. The reverse bias saturation current (J_o) was obtained from the *J-V* curve at -1 bias voltage in the dark. The series resistance (R_s) of each device was extracted from the inverse slope of the *J-V* curve at the open circuit voltage (V_{OC}).

Energy-filtered Transmission Electron Microscopy (EF-TEM): Energy-filtered transmission electron microscopy (EF-TEM) was carried out on a JEOL 3100R05 Double Cs Corrected TEM/STEM operating at 300 kV, which was equipped with a Gatan Quantum 969 Imaging Filter (GIF) with a K2 direct electron detector. A pair of low-loss EF-TEM images were acquired for 5 s using a 5 eV wide energy selecting slit centered at 19 and 29 eV. Maximum contrast was then produced by dividing the lower energy loss image by that of the higher loss image. Bright regions in these images correspond to polymer-rich regions, while the darker regions correspond to fullerene-rich domains.[6] Elastic TEM images were acquired for 2 s using a 10 eV wide energy selecting slit centered at 0 eV.

Nano-Indented Electrical Contact Resistance (ECR): Hysitron TI 950 Triboindenter was used for point measurement of conductivity during indentation of the film. The electron current of the spin-

cast active layer (PffBT4T-2OD:$PC_{71}BM$ or PffBT4T-2OD:copolymer:$PC_{71}BM$) on ITO/ZnO was obtained with a nanoECR (Electrical Contact Resistance) transducer at 50 nm thickness. A Berkovich conductive ceramic probe was used for the indentation. A silver paste was used to secure the sample on the ECR stage with copper as the top surface for better conductivity. The stage is electrically connected to the system for current measurement.

Thin film preparation for triboindentation:

Blends with DIO. Thin films were prepared as described (203) for solar cell fabrication except without the Ag and MoO_3 layers.

Blends with copolymer and DIO. Thin films were prepared as described above (203) for solar cell fabrication except without the Ag and MoO_3 layers.

A2.4 Small Molecule Synthetic Procedures

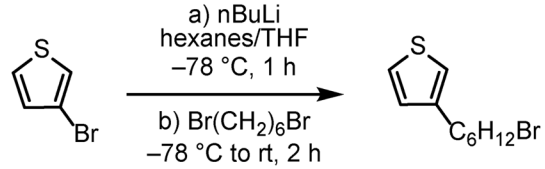

S1

3-(6-bromohexyl)thiophene (S1). An oven-dried Schlenk flask equipped with a stir bar and septum was cooled under vacuum and refilled with N_2 (3x total). To this flask was added 3-bromothiophene (1.00 mL, 10.7 mmol, 1.00 equiv) and dry hexanes (6.62 mL). This solution was cooled to -78 °C and a 2.5 M solution of *n*BuLi (4.90 mL, 12.3 mmol, 1.15 equiv) was added dropwise over 5 min. The solution was stirred for 10 min before adding dry THF (7.95 mL) dropwise. The resulting solution was stirred for 1 h before adding 1,6-dibromohexane (4.90 mL, 32.1 mmol, 3.00 equiv), warming to rt, and stirring for 2 h. The solution was quenched with sat. $NaHCO_3$ (10 mL), and the aqueous layer was extracted with Et_2O (2 x 5 mL). The organic layers were combined and washed with H_2O (1 x 15 mL) and brine (1 x 15 mL), dried over $MgSO_4$, filtered, and concentrated in vacuo to yield an orange oil. The excess 1,6-dibromohexane was removed by distillation. The remaining orange oil was purified by silica gel column chromatography (100% hexanes) to yield a colorless oil, which was heated to 55 °C in vacuo for 10 h to remove excess 1,6-dibromohexane (379 mg, 14%). HRMS (EI): Calcd. for $[M]^+$ 246.0078; found 246.0068.

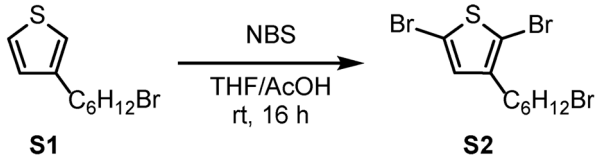

S1 **S2**

2,5-dibromo-3-(6-bromohexyl)thiophene (S2). To a 20 mL vial equipped with a septum were added **S1** (275 mg, 1.11 mmol, 1.00 equiv) and THF (2.78 mL). The resulting solution was sparged with N_2 for 10 min. To this vial was added AcOH (2.78 mL) and recrystallized NBS (494 mg, 2.78

mmol, 2.50 equiv). The solution was stirred in the dark under N_2 at rt for 16 h. The reaction solution was quenched using saturated aq. $NaHCO_3$ (5 mL) and extracted with Et_2O (3 x 5 mL). The combined organic layers were washed with water (15 mL) and brine (15 mL), dried over $MgSO_4$, filtered, and concentrated in vacuo. The resulting orange oil was purified by silica gel column chromatography (100% hexanes) to obtain a colorless oil (158 mg, 35%). HRMS (EI): Calcd. for $C_{10}H_{13}Br_3S$ $[M]^+$ 401.8288; found, 401.8278.

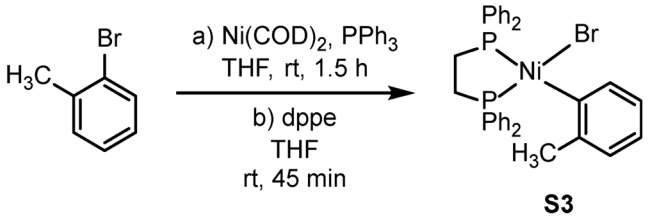

S3

(o-tolyl)(1,2-bis(diphenylphosphino)ethane)nickel bromide (S3). In a glovebox, to a 20 mL vial equipped with a stir bar was added $Ni(COD)_2$ (77.3 mg, 0.281 mmol, 1.00 equiv), PPh_3 (151 mg, 0.574 mmol, 2.04 equiv), and dry THF (1.4 mL). The resulting mixture was stirred for 5 min before 2-bromotoluene (36.7 µL, 0.309 mmol, 1.10 equiv) was added. The solution was stirred for 90 min at rt, yielding an opaque orange suspension. Then dppe (114 mg, 0.286 mmol, 1.02 equiv) was added and the mixture was stirred for 45 min at rt. Hexanes (15 mL) were added as the top layer and the mixture was cooled to –35 °C for 24 h. The resulting yellow-orange solid was isolated via filtration inside the glovebox, washed with hexanes (3 x 5 mL), and recrystallized from DCM/hexanes at –35 °C to yield a yellow crystalline solid (88 mg, 51%). HRMS (EI): Calcd. for $[M]^+$ 626.0438; found 626.0422.

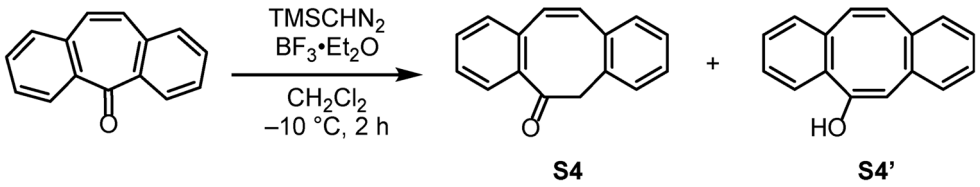

6*H*-Dibenzo[a,e]cyclooctatrien-5-one (S4). In a N_2 flushed 100 mL round-bottom flask was added dibenzosuberenone (3.10 g, 15.0 mmol, 1.00 equiv) and $BF_3 \cdot OEt_2$ (2.80 mL, 22.7 mmol, 1.50 equiv), and DCM (30 mL). The solution was cooled to –10 °C. A 0.75 M solution of trimethylsilyl diazomethane in DCM (32.0 mL, 24.0 mmol, 1.60 equiv) was added to the solution dropwise over 1 h and then stirred at –10 °C for an additional 2 h. Then AcOH (0.2 mL) was added to quench the reaction solution. The mixture was poured into ice water (150 mL). The aqueous layer was extracted with DCM (3 x 100 mL) and the combined organic layers were washed with brine (100 mL), dried over $MgSO_4$, and filtered. The filtrate was concentrated in vacuo and the crude product was purified by silica gel column chromatography (10–70% DCM in hexanes) to give dibenzocyclooctenone (**S4**) as a white solid (1.13 g, 34%) and dibenzocyclooctadienol (**S4'**) as a viscous transparent liquid (2.10 g, 63%). HRMS (EI): Calcd. For $C_{16}H_{12}O$ $[M]^+$ 220.0888; found, 220.0884.

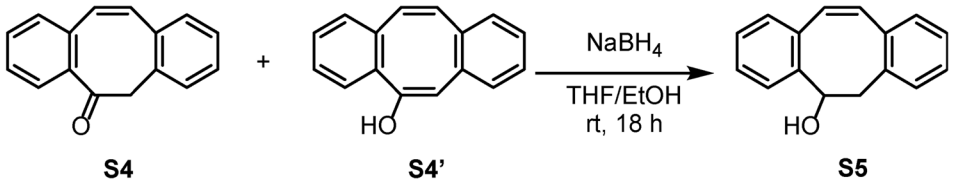

5,6-Dihydro-dibenzo[a,e]cycloocten-5-ol (S5). Sodium borohydride (0.388 g, 10.3 mmol, 2.00 equiv) was slowly added to a stirred solution of **S4/S4'** (1.13 g, 5.13 mmol, 1.00 equiv) in THF/EtOH (1/1, v/v, 60 mL). The solution was stirred at rt for 18 h, then quenched by slow addition of AcOH (0.5 mL). The mixture was concentrated in vacuo, and the yellow residue was dissolved in DCM (50 mL) and washed with brine (50 mL). The aqueous layer was extracted with DCM (4 x 50 mL). The combined organic layers were dried over $MgSO_4$, treated with decolorizing

carbon, filtered and concentrated in vacuo to give a white solid (723 mg, 63%). HRMS (EI): Calcd. For $C_{16}H_{14}O$ $[M]^+$ 222.1045; found, 222.1046.

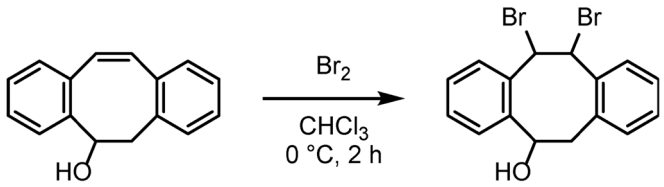

S5 **S6**

11,12-Dibromo-5,6,11,12-tetrahydro-dibenzo[a,e]cycloocten-5-ol (S6). Into a N_2-filled round-bottom flask was added **S5** (0.642 g, 2.89 mmol, 1.00 equiv) and $CHCl_3$ (15 mL) and the resulting solution was cooled to 0 °C using an ice-water bath. A solution of Br_2 (0.150 mL, 2.93 mmol, 1.01 equiv) in $CHCl_3$ (5 mL) was added dropwise over 3 min. After stirring for 2 h, the resulting solution was quenched with saturated aq. $Na_2S_2O_3$ (20 mL) and washed with H_2O (20 mL) and brine (20 mL). The organic layer was dried over $MgSO_4$, filtered, and concentrated in vacuo, affording a yellow oil. The crude product was purified by silica gel column chromatography (5–70% DCM in hexanes) to obtain a viscous, colorless oil (480 mg, 44%). HRMS (EI): Calcd for $C_{16}H_{13}BrO$ $[M–HBr]^+$ 300.0150; found, 300.0156

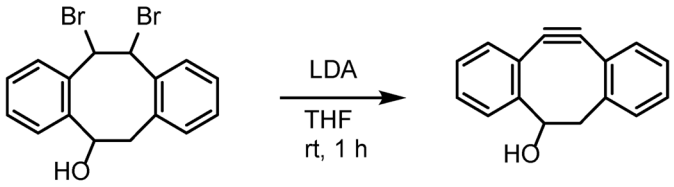

S6 **S7**

5,6-Dihydro-11,12-didehydro-dibenzo[a,e]cycloocten-5-ol (S7). To an oven-dried 10 mL Schlenk flask under N_2 that was equipped with a stir bar and septum was added a solution of **S6** (304 mg, 0.796 mmol, 1.00 equiv) dissolved in dry DCM (0.5 mL). The DCM was removed in vacuo and dry THF (7.96 mL) was added. The solution was cooled to 0 °C and a 1.75 M solution of LDA in THF/heptane/ethylbenzene (59/28/13, v/v) (1.82 mL, 3.18 mmol, 4.00 equiv) was added

dropwise. The resulting solution was stirred for 5 min at 0 °C, then warmed to rt and stirred for 1 h. The reaction solution was slowly quenched with H_2O (1.50 mL) and the solvent was removed in vacuo. The resulting brown oil was purified by silica gel chromatography (25–100% DCM in hexanes) to yield a white solid (158 mg, 90%). HRMS (CI): Calcd. For $[M+H]^+$ 221.0961; found 221.0958

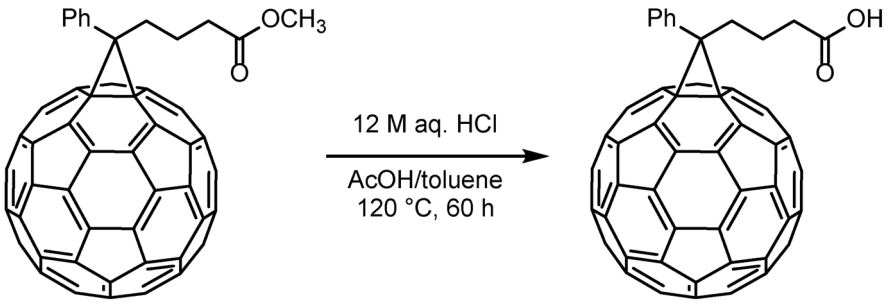

$PC_{61}BM$ **S8**

phenyl-C_{61}-butyric acid (S8). Phenyl-C_{61}-butyric acid methyl ester (PCBM) (550 mg, 0.604 mmol, 1.00 equiv) was dissolved in toluene (80 mL) and AcOH (40 mL) in a 350 mL bomb flask. Then aq. HCl (12 M, 20 mL) was added. The flask was sealed and heated to 120 °C for 60 h with vigorous stirring. The mixture was then cooled to rt. The now heterogeneous organic layer was separated from the aqueous layer and filtered. The resulting brown solid was washed sequentially with MeOH, acetone, toluene, and Et_2O (30 mL each), to afford a brown powder (541 mg, quant). The product was carried to the next step without further purification. HRMS (ESI-): Calcd. For $C_{71}H_{11}O_2$ $[M–H]^-$ 895.0765; found, 895.0750.

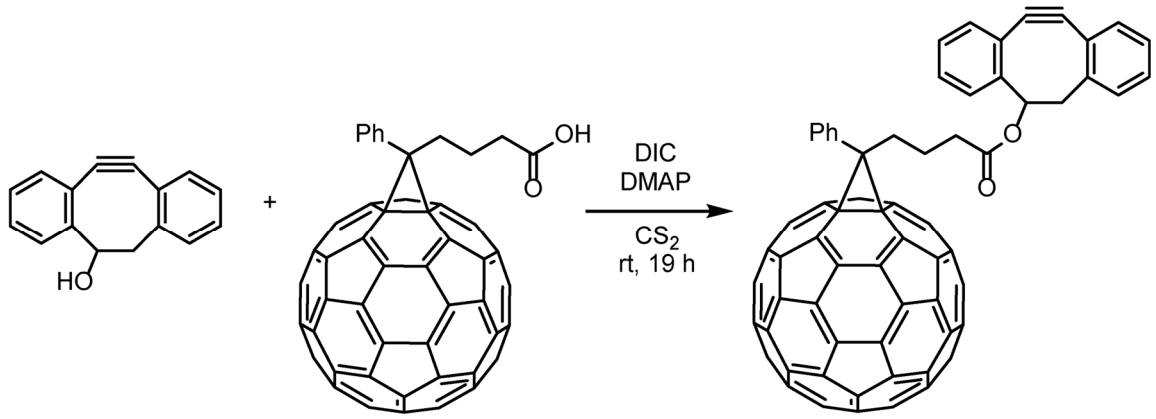

S7 S8 S9

PCB-DIBO (S9). To a flame dried 50 mL round-bottom flask equipped with a stir bar was added **S8** (314 mg, 0.350 mmol, 1.00 equiv) and DMAP (53.6 mg, 0.438 mmol, 1.25 equiv). To this flask was then added CS_2 (24 mL), DIC (82.4 μL, 0.526 mmol, 1.50 equiv), and a 0.015 M solution of **S7** in CS_2 (36 mL, 0.526 mmol, 1.50 equiv). The solution was stirred for 19 h at rt. The reaction solution was quenched with water (5 mL) and extracted with DCM (3 x 10 mL). The organic layers were washed with water (20 mL) and brine (20 mL), dried over $MgSO_4$, filtered, and concentrated in vacuo. The resulting solid was purified by silica gel chromatography (10-40% DCM in hexanes) to yield a brown solid (184 mg, 48%). MALDI-TOF-MS: Calcd. For $C_{87}H_{22}O_2$ [M] = 1099.162; found,1097.508.

A2.5 Polymerization and Post-Polymerization Modifications

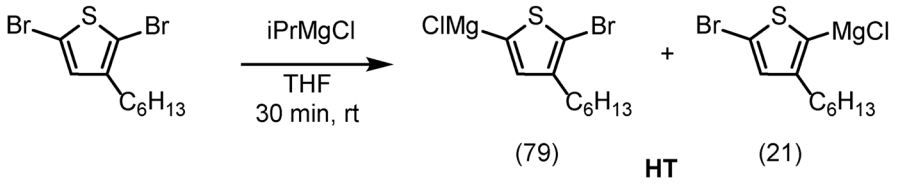

HT monomer activation. In a N_2-filled glovebox, 2,5-dibromo-3-hexylthiophene (193 mg, 0.593 mmol, 1.00 equiv) was dissolved in THF (5 mL) in an 8 mL vial equipped with a stir bar. To this vial was added a 2.10 M solution of iPrMgCl in THF (250 µL, 0.525 mmol, 0.890 equiv) and the resulting solution was stirred for 30 min at rt. An aliquot (0.1 mL) was quenched with 12 M aq. HCl (0.1 mL), extracted with $CHCl_3$ (2 x 1 mL), dried over $MgSO_4$, filtered, and analyzed by GC, showing a mixture of **HT** regioisomers in a 79:21 ratio and active Grignard concentration of 0.080 M.

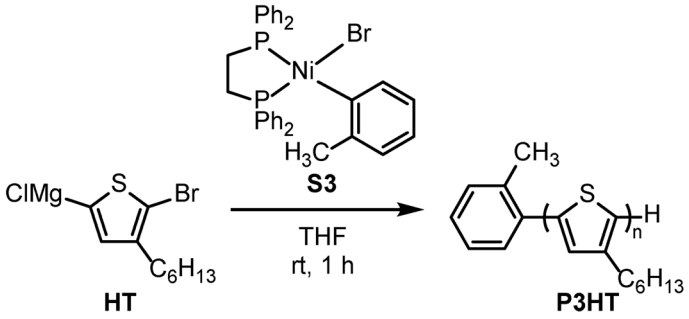

P3HT. In a N_2-filled glovebox, to a 50 mL Schlenk flask equipped with a stir bar and septum was added a 0.080 M solution of **HT** in THF (5.00 mL, 0.400 mmol, 180 equiv), and additional THF (25 mL). Outside of the glovebox under N_2, the solution was cooled to 0 °C and to the flask was added a 0.85 mM solution of **S3** in THF (2.82 mL, 2.2 µmol, 1.0 equiv) via syringe pump at 0.26 mL/min. Once catalyst addition was complete, the resulting solution was stirred for 70 min at 0 °C. The polymerization was quenched with 12 M aq. HCl (20 mL) while stirring, then precipitated

into MeOH (100 mL) and the solids were collected on filter paper. Sequential Soxhlet extraction of the solids with acetone, MeOH, hexane, and $CHCl_3$ afforded a purple solid (47 mg, 70%). $M_{n,SEC}$ = 28.1 kg/mol, $M_{n,NMR}$ = 26.7, Đ = 1.23, regioregularity = 99%. The M_n obtained by SEC is an overestimation, in reasonable agreement with a previous report.[7]

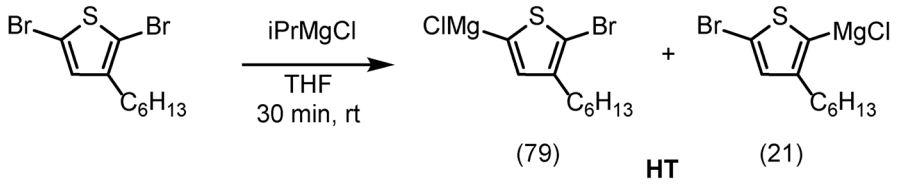

HT monomer activation. In a N_2-filled glovebox, 2,5-dibromo-3-hexylthiophene (234 mg, 0.719 mmol, 1.00 equiv) was dissolved in THF (6.89 mL) in a 20 mL vial equipped with a stir bar. To this vial was added a 1.93 M solution of iPrMgCl in THF (298 µL, 0.575 mmol, 0.800 equiv) and the resulting solution was stirred for 30 min at rt after which the active Grignard concentration was 0.089 M. An aliquot (0.1 mL) of this solution was quenched with 12 M aq. HCl (0.1 mL), extracted with $CHCl_3$ (2 x 1 mL), dried over $MgSO_4$, filtered, and analyzed by GC, showing a mixture of **HT** regioisomers in a 79:21 ratio and 92% monomer activation.

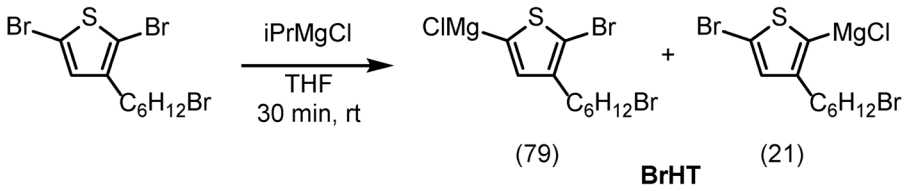

BrHT monomer activation. In a N_2-filled glovebox, 2,5-dibromo-3-(6-bromohexyl)thiophene (148 mg, 0.365 mmol, 1.00 equiv) was dissolved in THF (3.53 mL) in an 8 mL vial equipped with a stir bar. To this vial was added a 1.93 M solution of iPrMgCl in THF (160 µL, 0.309 mmol, 0.850 equiv) and the resulting solution was stirred for 30 min at rt after which the Grignard concentration was 0.091 M. An aliquot (0.1 mL) was quenched with 12 M aq. HCl (0.1 mL),

extracted with $CHCl_3$ (2 x 1 mL), dried over $MgSO_4$, filtered, and analyzed by GC, showing a mixture of **BrHT** regioisomers in a 79:21 ratio and 97% monomer activation.

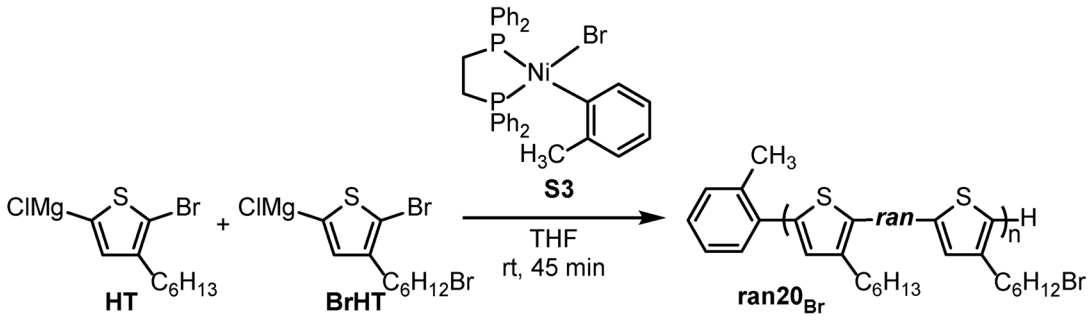

ran20$_{Br}$. In a N_2-filled glovebox, to a 25 mL Schlenk flask equipped with a stir bar was added a 0.089 M solution of **HT** (5.00 mL, 0.445 mmol, 88.0 equiv) in THF, a 0.091 M solution of **BrHT** (1.22 mL, 0.111 mmol, 22.0 equiv) and additional THF (20.6 mL). An aliquot (0.10 mL) was removed for GC analysis. Then to the reaction flask was quickly added a 0.005 M solution of **S3** in THF (1.01 mL, 5.05 μmol, 1.00 equiv) and the solution was stirred for 45 min at rt. The polymerization was removed from the glovebox and quenched with 12 M aq. HCl (6 mL) while stirring. The biphasic mixture was extracted with $CHCl_3$ (3 x 10 mL) and the combined organic layers were dried over $MgSO_4$ and filtered. An aliquot (0.25 mL) was removed and diluted with $CHCl_3$ for GC analysis. The remaining solution was concentrated in vacuo to yield a purple solid. The solid was dissolved in a minimal amount of $CHCl_3$ and precipitated into cold MeOH and centrifuged for 15 min. The supernatant was decanted and the solid was re-suspended in cold MeOH with sonication and centrifuged. This procedure was repeated 3 times. The supernatant was removed a final time and the remaining pellet was dried in vacuo to yield a purple solid (65 mg, 64%).

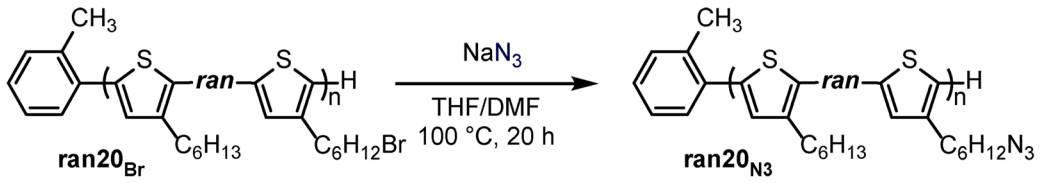

ran20$_{N3}$. To an oven-dried 100 mL RBF was added **ran20Br** (91 mg, 0.10 mmol, 1.0 equiv Br) and dry THF (70 mL). The mixture was stirred for 5 min at 60 °C to dissolve the polymer then to this flask was added DMF (35 mL) and NaN_3 (325 mg, 5.00 mmol, 48.0 equiv wrt Br) in one portion with stirring. The flask was equipped with a reflux condenser and the solution was stirred under N_2 for 20 h at 100 °C. The flask was cooled to rt and the THF was removed in vacuo. The polymer was dissolved in a minimal amount of $CHCl_3$, precipitated into cold MeOH (30 mL), and centrifuged for 15 min. The supernatant was decanted and the polymer was resuspended in MeOH with sonication and centrifuged. This procedure was repeated 3 times. The supernatant was removed a final time and the remaining pellet was dried in vacuo to yield a purple solid (83 mg, 95%).

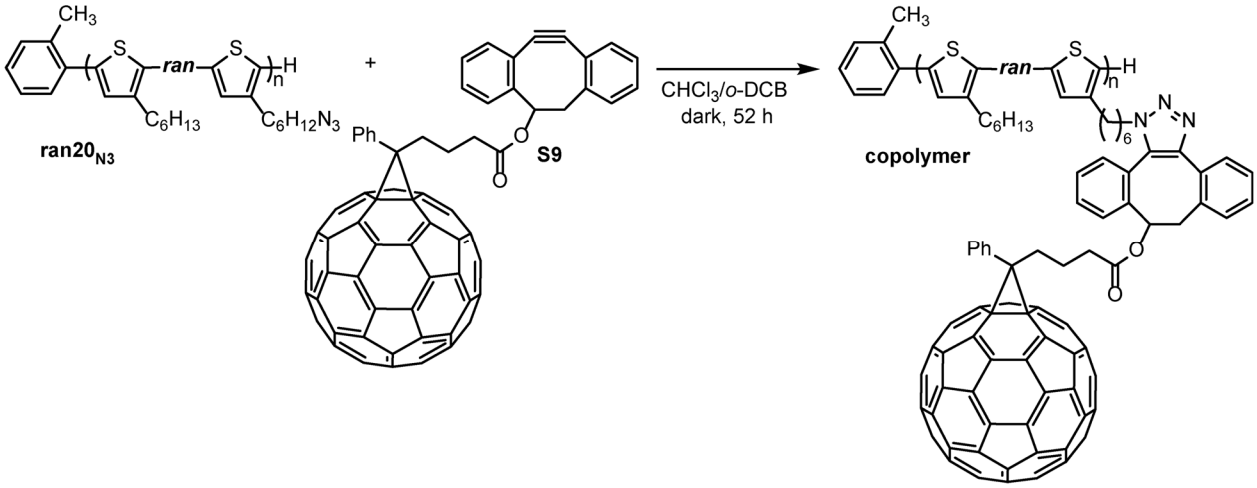

copolymer. To a 100 mL oven-dried round-bottomed flask was added **ran20$_{N3}$** (49.0 mg, 56.0 μmol N_3, 1.00 equiv N_3), $CHCl_3$ (45 mL), *o*-DCB (3 mL), and a stir bar. To this vial was added **S9** (79 mg, 72 μmol, 1.3 equiv wrt N_3). The flask was covered in foil and the solution was stirred under N_2 for 52 h at rt. The $CHCl_3$ was then removed in vacuo until only a minimal amount

remained and the polymer was precipitated into cold MeOH. The mixture was cooled for 15 min at –30 °C and the solids were collected via filtration and purified by sequential Soxhlet extraction with DCM (19 h), $CHCl_3$ (6.5 h), and $CHCl_3/CS_2$ (50/50, v/v) (13 h). The polymer was in the $CHCl_3$ fraction and the solvent was removed in vacuo to yield a reddish orange solid (90 mg, 82%).

Table A 2.1 Characterization data for all copolymer syntheses.

polymer	functionalization ^{1}H NMR (%)	M_n ^{1}H NMR (kg/mol)	M_n SEC (kg/mol)[a]	Đ	RR (%)[b]	conversion ^{1}H NMR (%)	conversion FTIR (%)	yield (%)
ran20Br	21	14.0	18.4	1.22	94	-	-	64
ran20N3	21	14.2	19.0	1.42	99	quant.	-	95
copolymer	21	-	21.0	1.15		-	quant.	82

[a] The M_n obtained by SEC is an overestimation, in reasonable agreement with a previous report for rod polymers[7]
[b] RR = regioregularity

A2.6 Nuclear Magnetic Resonance Spectra

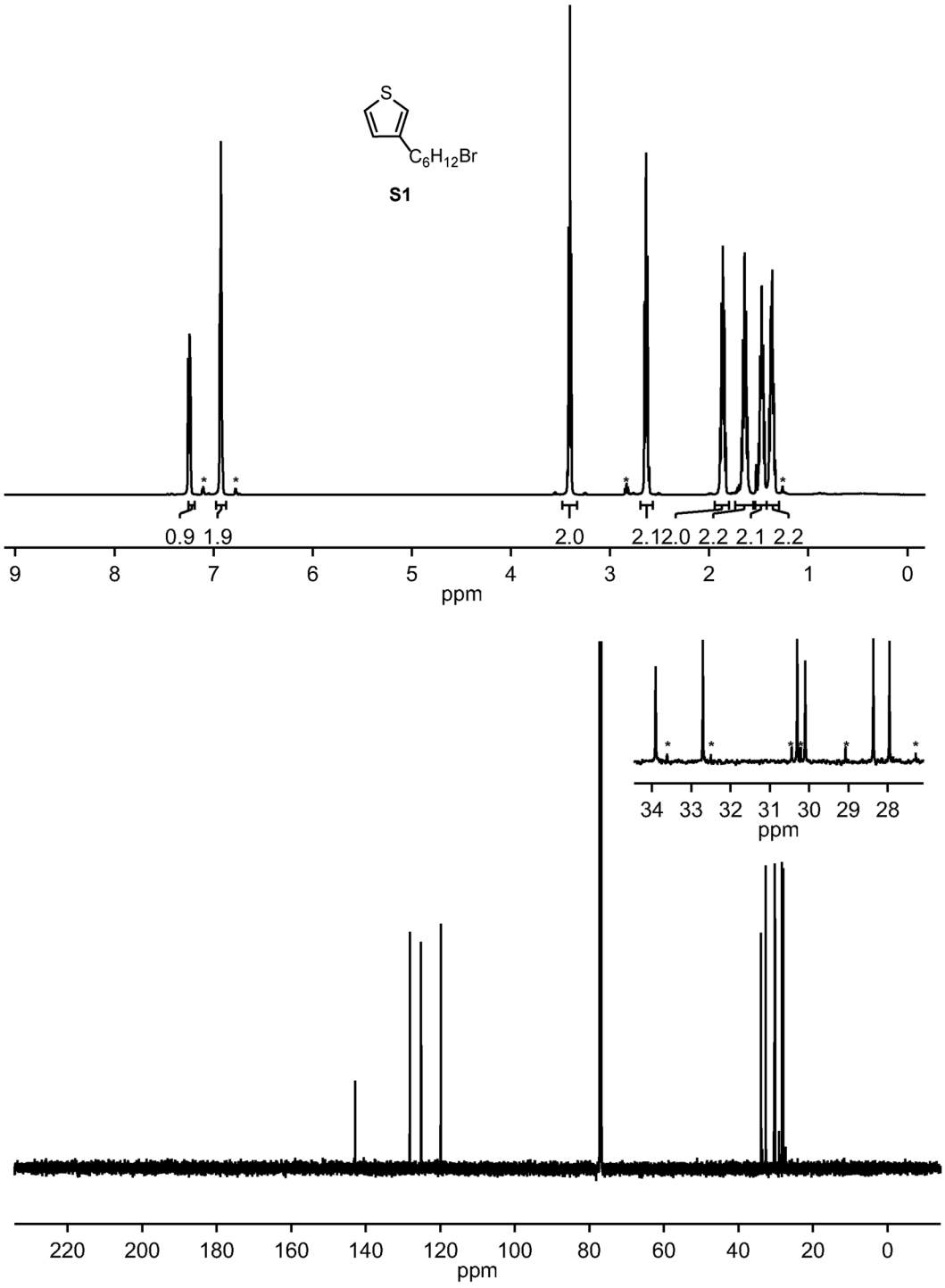

Figure A2.1 ^{1}H and ^{13}C NMR spectra of **S1**. ^{1}H NMR (500 MHz, $CDCl_3$) δ 7.25–7.21 (m, 1H), 6.97–6.87 (m, 2H), 3.40 (t, J = 6.8 Hz, 2H), 2.64 (t, J = 7.7 Hz, 2H), 1.86 (p, J = 7.0 Hz, 2H), 1.64 (p, J = 7.6 Hz, 2H), 1.52–1.42 (m, 2H), 1.41–1.32 (m, 2H). ^{13}C NMR (126 MHz, $CDCl_3$) δ 142.84, 128.18, 125.14, 119.88, 33.91, 32.71, 30.30, 30.10, 28.37, 27.95. *unknown impurity

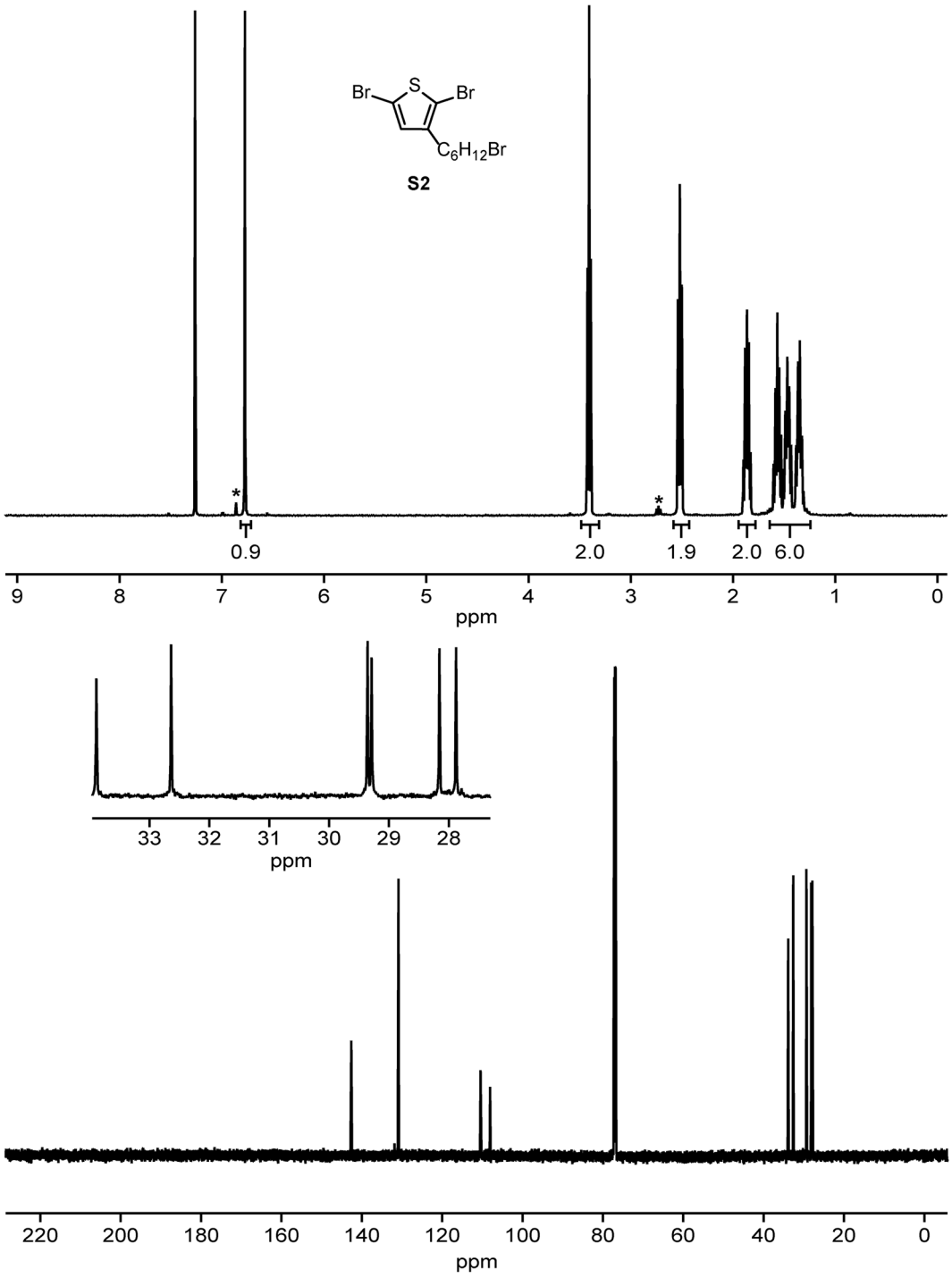

Figure A2.2 ^{1}H and ^{13}C NMR spectra of **S2**. ^{1}H NMR (700 MHz, $CDCl_3$) δ 6.77 (s, 1H), 3.41 (t, J = 6.8 Hz, 2H), 2.52 (t, J = 7.6 Hz, 2H), 1.86 (p, J = 7.0 Hz, 2H), 1.56 (p, J = 7.7 Hz, 2H), 1.46 (p, J = 7.7 Hz, 2H), 1.34 (p, J = 7.7 Hz, 2H). ^{13}C NMR (176 MHz, $CDCl_3$) δ 142.60, 130.87, 110.44, 108.87, 33.89, 32.64, 29.36, 29.29, 28.16, 27.88.*unknown impurity

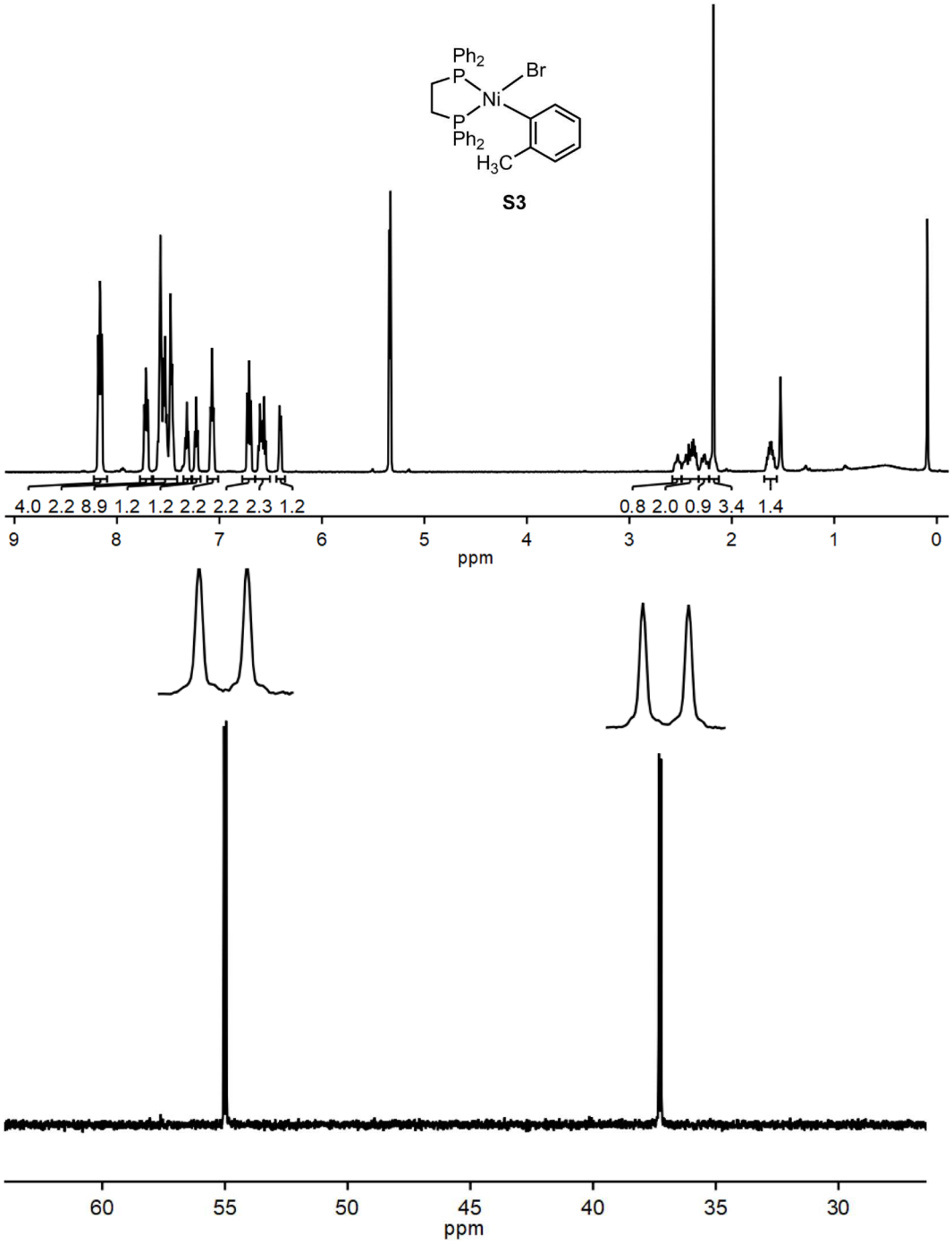

Figure A2.3 ^{1}H and ^{31}P NMR spectra of **S3**. ^{1}H NMR (500 MHz, CD_2Cl_2) δ 8.21–8.11 (m, 4H), 7.75–7.68 (m, 2H), 7.63–7.50 (m, 6H), 7.50–7.43 (m, 3H), 7.32 (t, J = 7.6 Hz, 1H), 7.23 (t, J = 6.8 Hz, 1H), 7.07 (t, J = 7.9 Hz, 2H), 6.71 (t, J = 9.3 Hz, 2H), 6.58 (dt, J = 21.0, 7.4 Hz, 2H), 6.41 (d, J = 7.2 Hz, 1H), 2.59–2.49 (m, 1H), 2.49–2.33 (m, 1H), 2.33–2.23 (m, 1H), 2.18 (s, 3H), 1.70–1.56 (m, 1H). ^{31}P NMR (202 MHz, CD_2Cl_2) δ 55.00 (d, J = 18.3 Hz), 37.28 (d, J = 18.3 Hz).

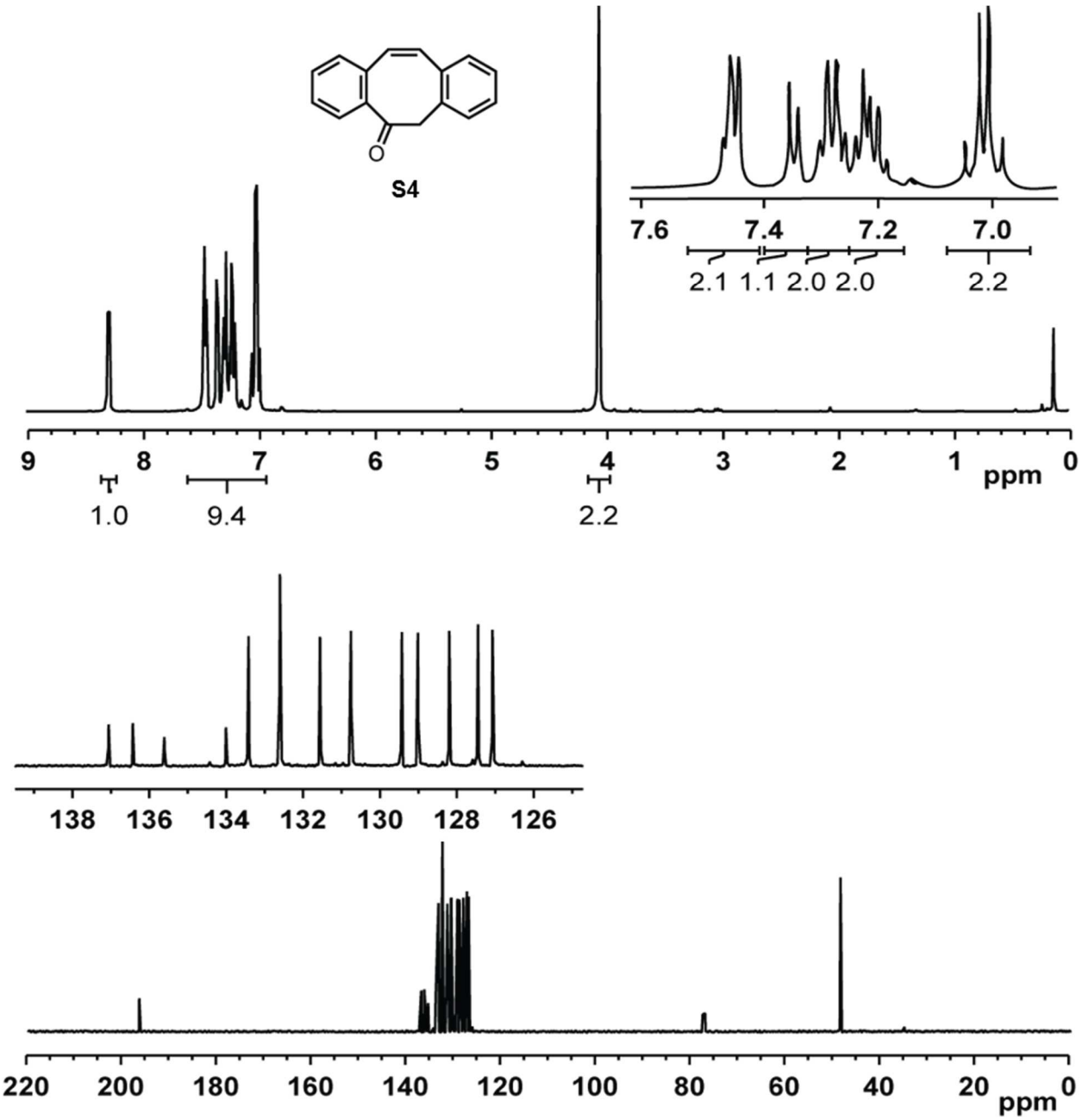

Figure A2.4 ^{1}H and ^{13}C NMR spectra of **S4**. ^{1}H NMR (500 MHz, $CDCl_3$) δ 8.29 (d, J = 8.0 Hz, 1H), 7.46 (m, 2H), 7.35 (d, J = 7.7 Hz, 1H), 7.28 (m, 2H), 7.21 (m, 2H), 7.02 (m, 2H), 4.06 (s, 2H). ^{13}C NMR (126 MHz, $CDCl_3$) δ 196.58, 137.06, 136.43, 135.61, 134.01, 133.42, 132.60, 131.56, 130.76, 129.43, 129.01, 128.20, 127.45, 127.07, 48.60.

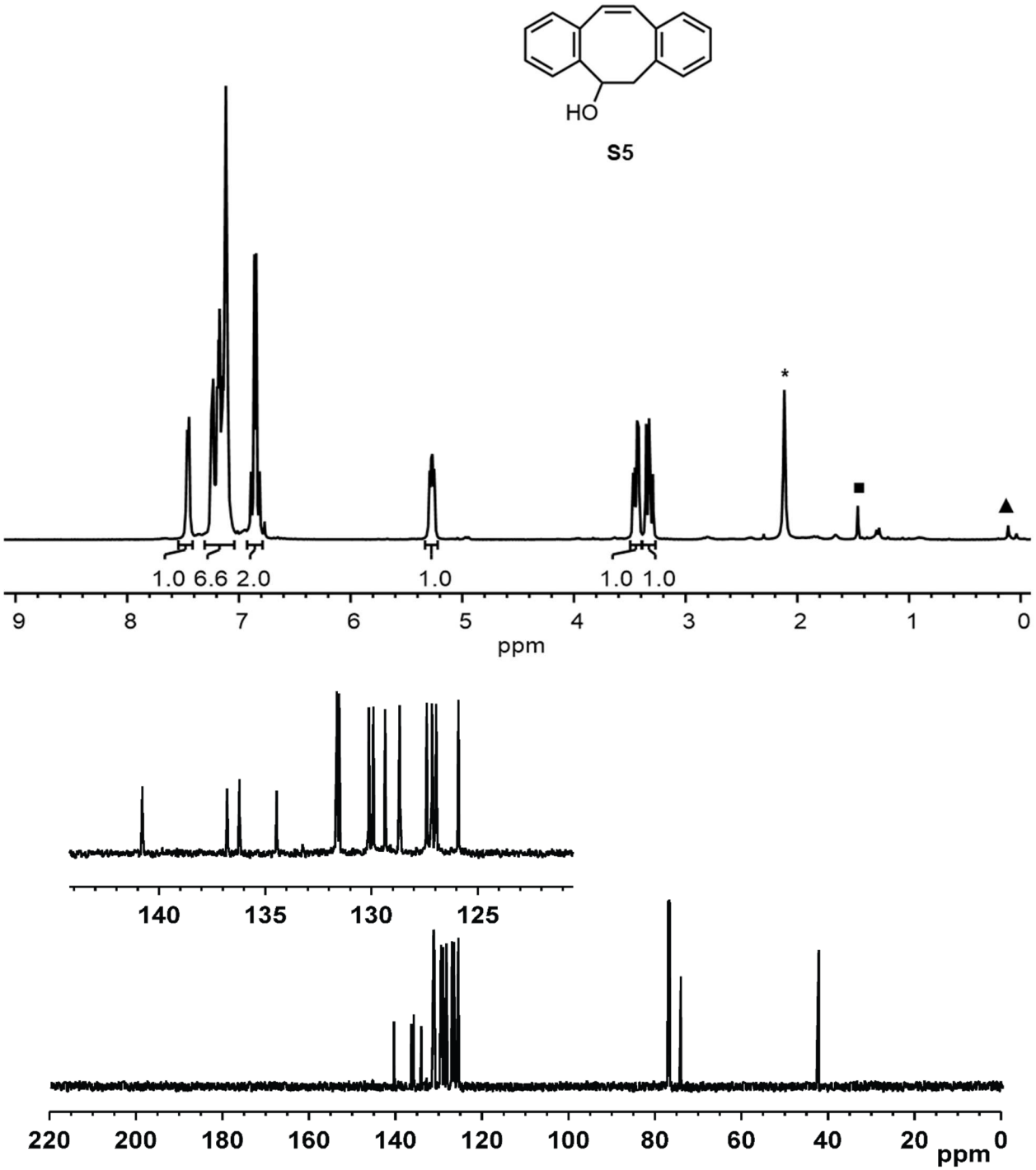

Figure A2.5 ^{1}H and ^{13}C NMR spectra of **S5**. ^{1}H NMR (400 MHz, $CDCl_3$) δ 7.48 (m, 1H), 7.17 (m, 7H), 6.84 (m, 2H), 5.27 (dd, *J* = 9.6, 6.3 Hz, 1H), 3.45 (dd, *J* = 13.7, 6.1 Hz, 1H), 3.32 (dd, *J* = 13.6, 10.2 Hz, 1H). *Acetone, ■ H_2O, ▲ grease. ^{13}C NMR (100 MHz, $CDCl_3$) δ 140.78, 136.79, 136.21, 134.46, 131.63, 131.53, 130.12, 129.91, 129.36, 128.67, 127.40, 127.15, 126.96, 125.91, 74.46, 42.59.

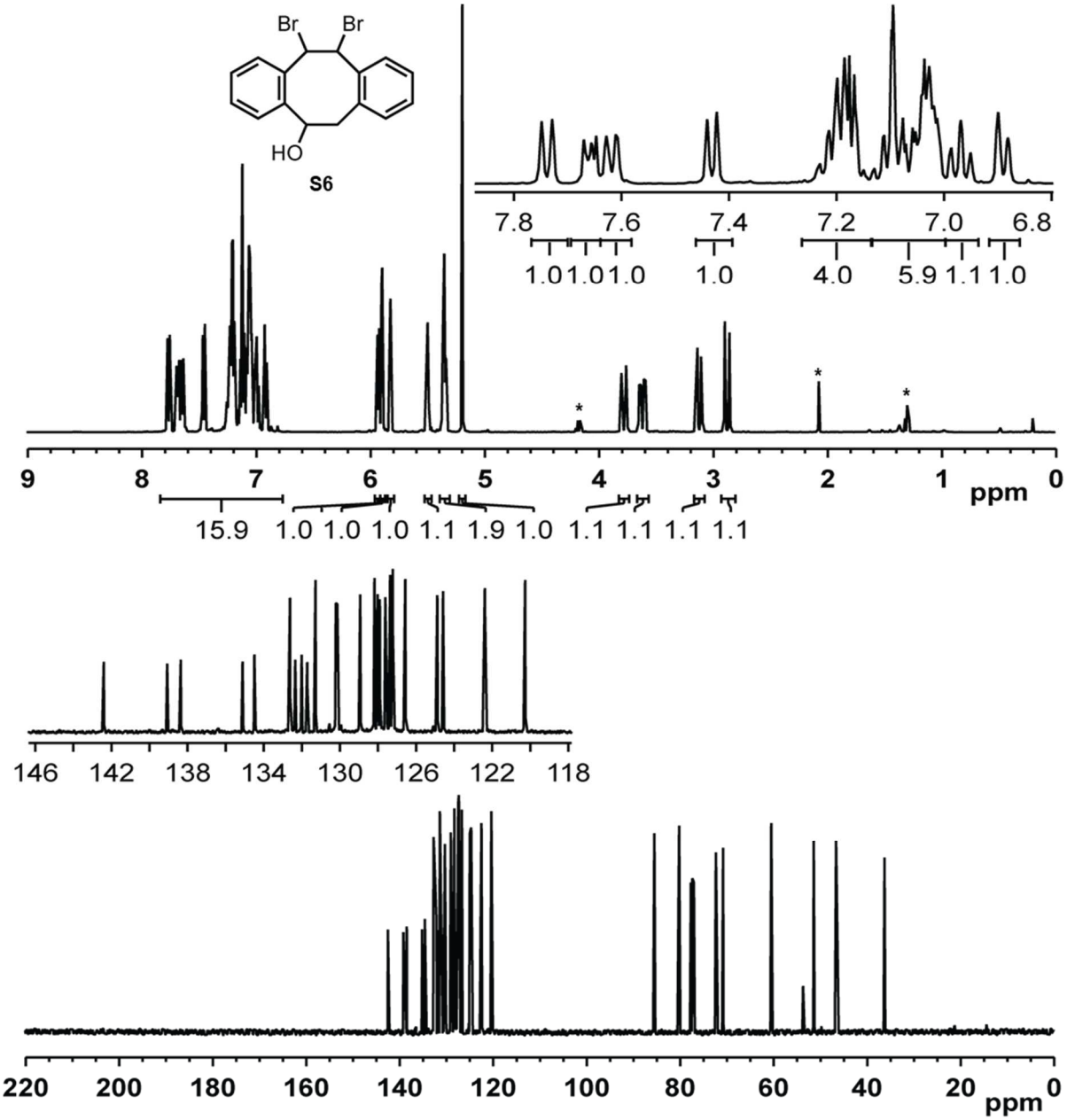

Figure A2.6 ^{1}H and ^{13}C NMR spectra of **S6** (a 1:1 mixture of diastereomers). ^{1}H NMR (400 MHz, CD_2Cl_2) δ 7.74 (d, *J* = 7.8 Hz, 1H), 7.66 (m, 1H), 7.62 (d, *J* = 7.0 Hz, 1H), 7.43 (d, *J* = 7.2 Hz, 1H), 7.23–7.18 (m, 4H), 7.01–7.11 (m, 6H), 6.97 (t, *J* = 7.2 Hz, 1H), 6.89 (d, *J* = 7.4 Hz, 1H), 5.90 (d, *J* = 5.5 Hz, 1H), 5.87 (d, *J* = 2.2 Hz, 1H), 5.80 (s, 1H), 5.47 (t, *J* = 3.2 Hz, 1H), 5.33 (t, *J* = 5.0 Hz, 2H), 5.17 (s, 1H), 3.75 (dd, *J* = 16.1, 1.2 Hz, 1H), 3.59 (dd, *J* = 16.4, 6.2 Hz, 1H), 3.10 (dd, *J* = 16.1, 3.7 Hz, 1H), 2.85 (d, *J* = 16.4 Hz, 1H). ^{13}C NMR (100 MHz, $CDCl_3$) δ 142.40, 139.07, 138.36, 135.11, 134.49, 132.62, 132.35, 132.01, 131.72, 131.28, 130.21, 130.14, 128.93, 128.18, 128.01, 127.90, 127.61, 127.36, 127.22, 126.57, 124.88, 124.58, 122.39, 120.27, 85.40, 80.09, 72.24, 70.70, 60.40, 51.31, 46.53, 36.16. *EtOAc

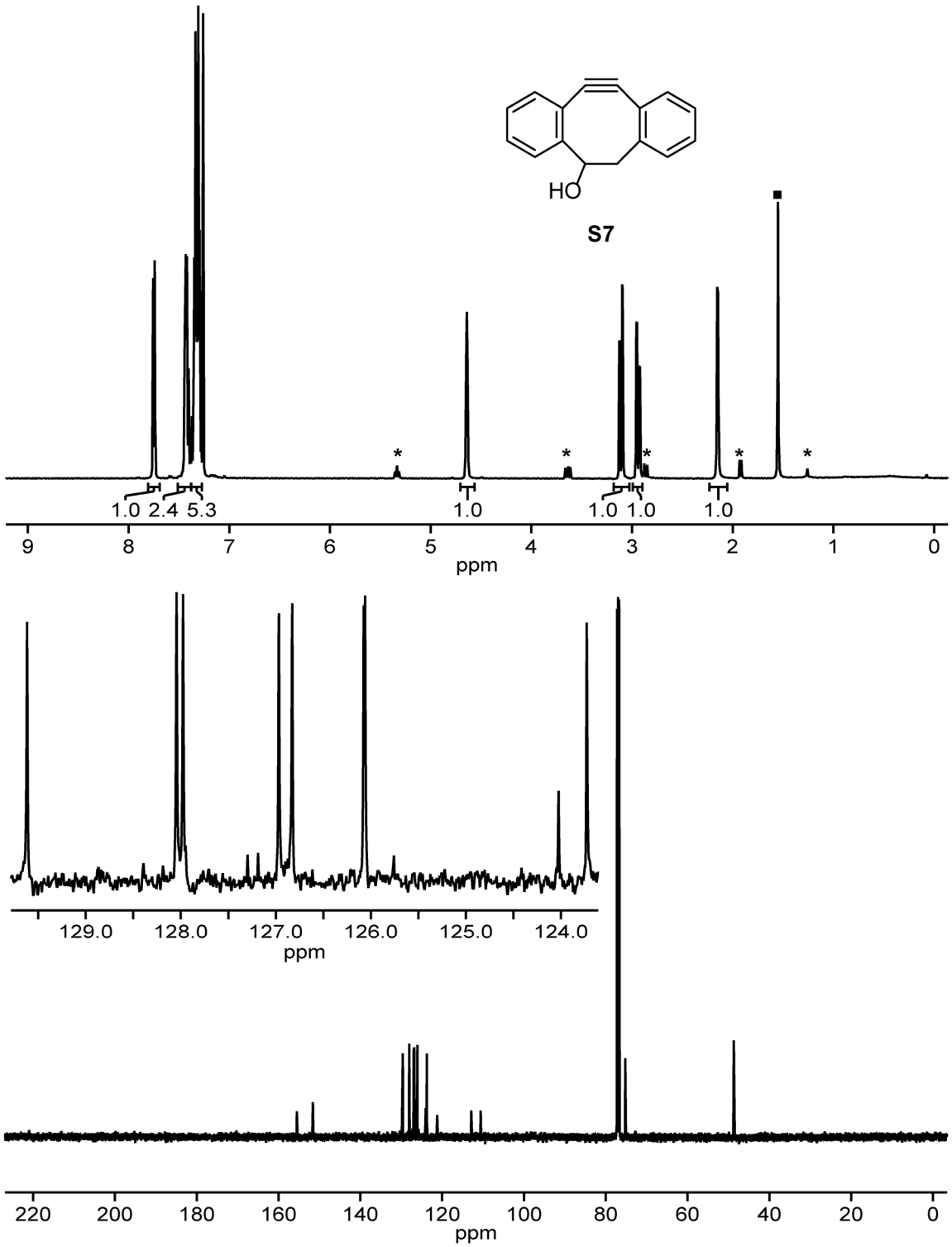

Figure A2.7 ^{1}H and ^{13}C NMR spectra of **S7**. ^{1}H NMR (500 MHz, $CDCl_3$) δ 7.75 (d, J = 7.8 Hz, 1H), 7.48–7.38 (m, 2H), 7.38–7.27 (m, 5H), 4.64 (s, 1H), 3.11 (dd, J = 14.8, 2.2 Hz, 1H), 2.94 (dd, J = 14.7, 3.8 Hz, 1H), 2.15 (d, J = 4.4 Hz, 1H). ^{13}C NMR (126 MHz, $CDCl_3$) δ 155.53, 151.61, 129.62, 128.04, 127.98, 126.97, 126.83, 126.07, 126.06, 124.03, 123.73, 121.21, 112.89, 110.58, 75.23, 48.70. *unknown impurity ■H_2O

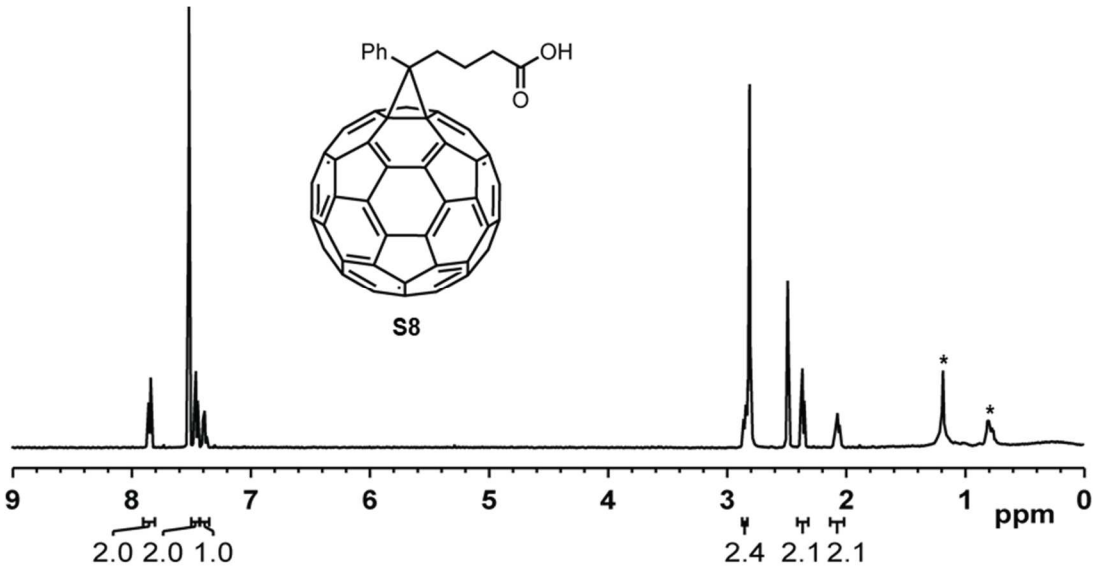

Figure A2.8 ^{1}H NMR spectrum of **S8**. ^{1}H NMR (500 MHz, $CDCl_3$/DMSO-d_6/CS_2 3:1:1) δ 7.84 (d, J = 7.3 Hz, 2H), 7.46 (m, 2H), 7.38 (m, 1H), 2.84 (m, 2H), 2.36 (t, J = 7.6 Hz, 2H), 2.07 (m, 2H). *grease

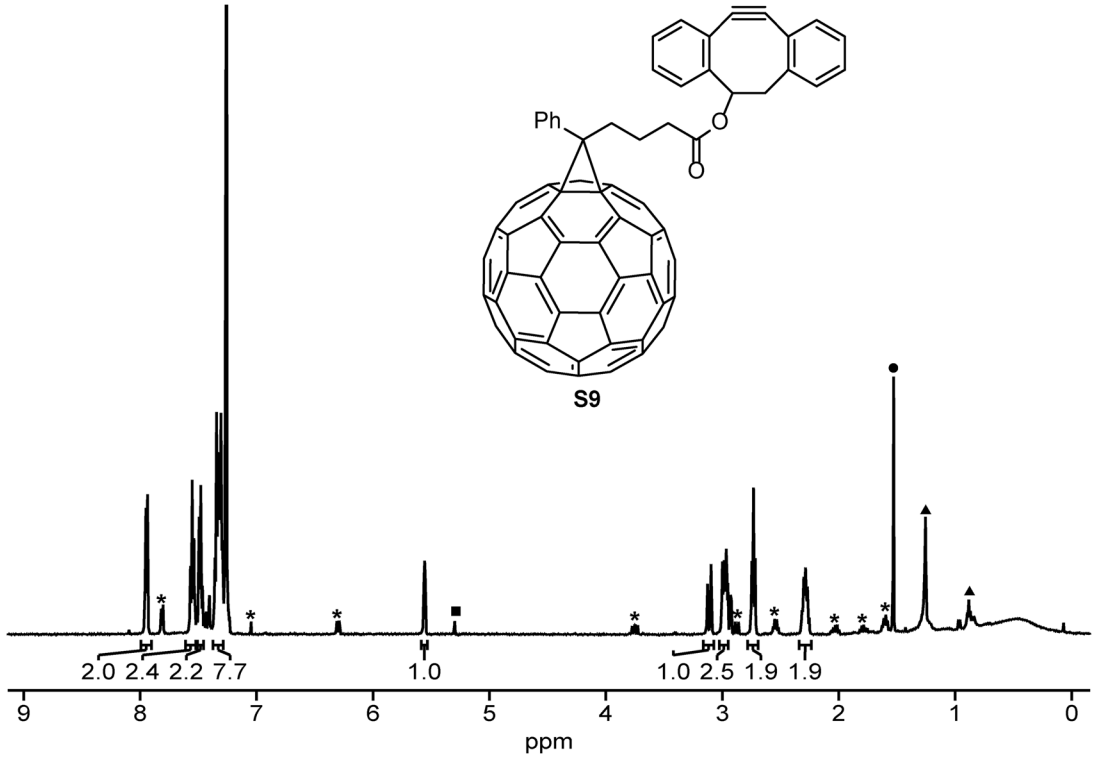

Figure A2.9 ^{1}H NMR Spectrum of S9. ^{1}H NMR ^{1}H NMR (500 MHz, $CDCl_3$) δ 7.99–7.90 (m, 2H), 7.60–7.52 (m, 2H), 7.52–7.46 (m, 2H), 7.37–7.28 (m, 7H), 5.56 (s, 1H), 3.11 (dd, J = 15.2, 2.2 Hz, 1H), 3.04 – 2.94 (m, 2H), 2.73 (t, J = 7.5 Hz, 2H), 2.35–2.23 (m, 2H). *unknown impurity ■DCM ●H_2O ▲grease

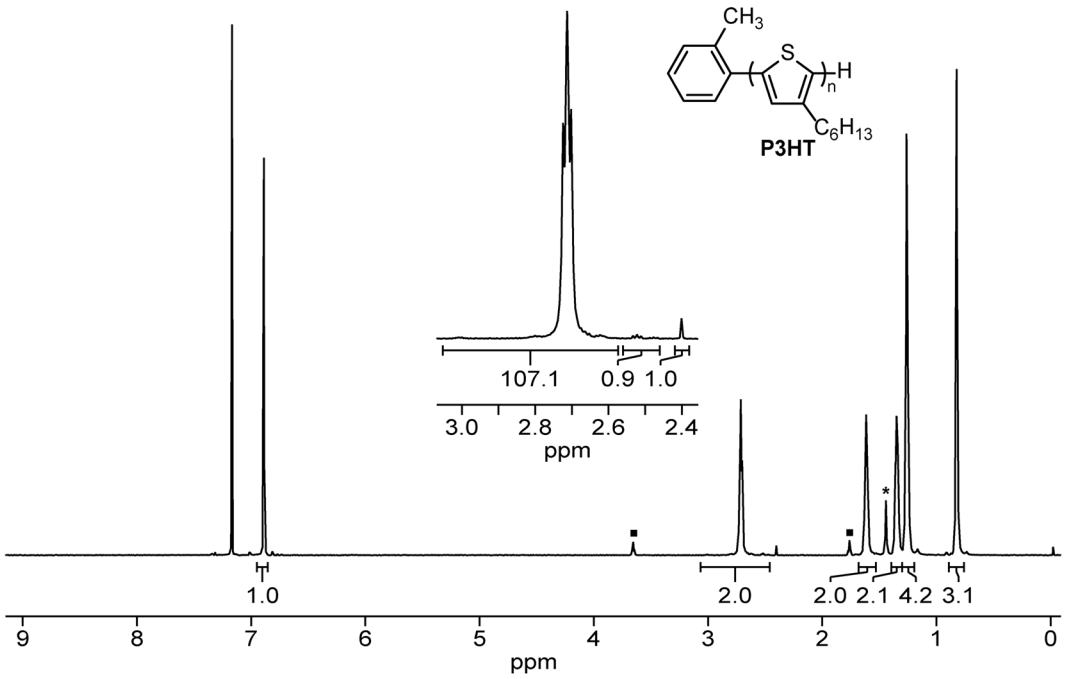

Figure A2.10 ^{1}H NMR spectrum of **P3HT**. ^{1}H NMR (700 MHz, $CDCl_3$) δ 6.98 (s, 1H), 2.80 (t, J = 7.9 Hz, 2H), 1.75–1.67 (m, 2H), 1.47–1.41 (m, 2H), 1.39–1.30 (m, 4H), 0.94–0.88 (m, 3H). *cyclohexane, ■ THF. The inset integrals were used to calculate M_n and regioregularity.

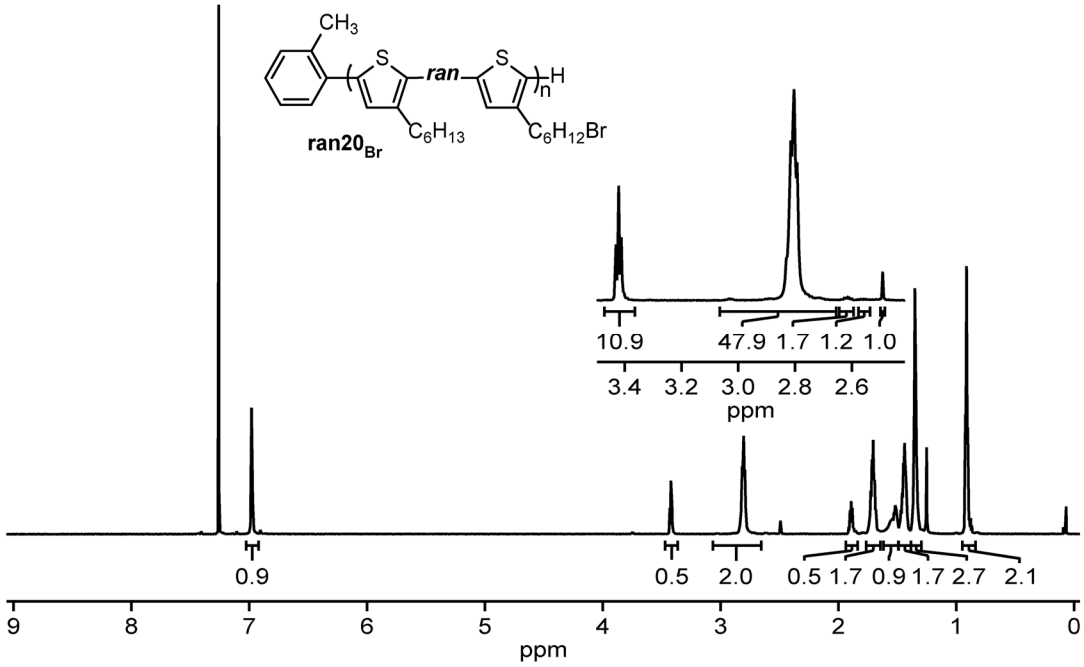

Figure A2.11 ^{1}H NMR spectrum of **ran20$_{Br}$**. ^{1}H NMR (700 MHz, $CDCl_3$) δ 6.98 (s, 1H), 3.42 (t, J = 6.8 Hz, 0.5H), 2.80 (t, J = 8.2 Hz, 2H), 1.89 (p, J = 7.0 Hz, 0.5H), 1.78–1.67 (m, 2H), 1.60–1.49 (m, 1H), 1.49–1.39 (m, 2H), 1.38–1.31 (m, 3H), 0.96–0.88 (m, 3H). The inset integrals were used to calculate the degree of Br functionalization (21%), the $M_{n,NMR}$ (14.0 kg/mol), and to determine regioregularity (94%).

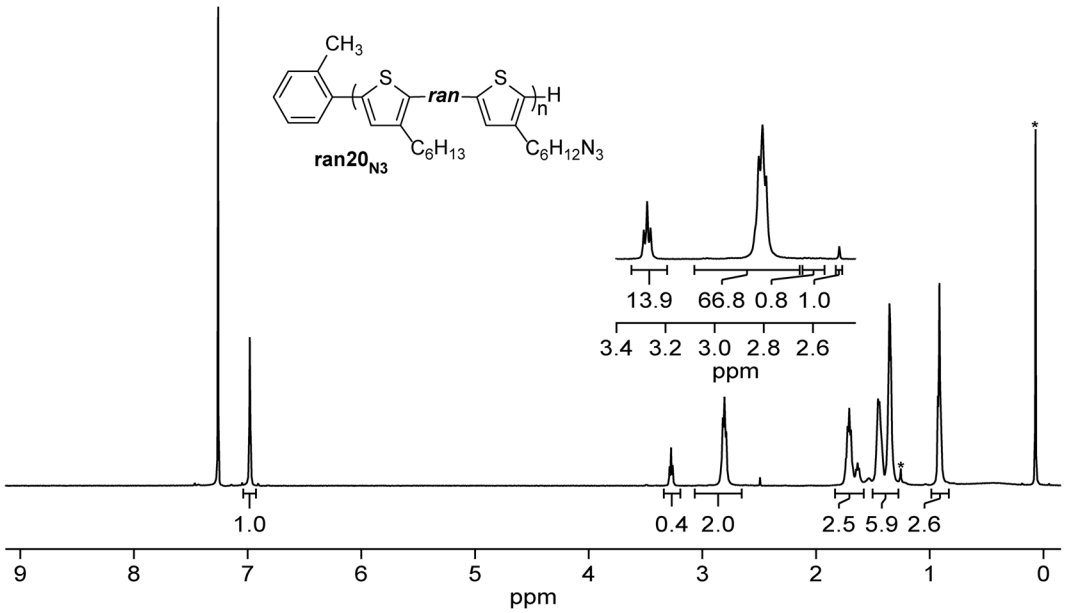

Figure A2.12 ^{1}H NMR spectrum of **ran20$_{N3}$**. ^{1}H NMR (500 MHz, $CDCl_3$) δ 6.98 (s, 1H), 3.27 (t, J = 7.0 Hz, 0.5H), 2.80 (t, J = 8.1 Hz, 2H), 1.76–1.60 (m, 2.5H), 1.48–1.29 (m, 6H), 0.98–0.85 (m, 2.5H). *grease. The inset integrals were used to calculate $M_{n,NMR}$ (14.2 kg/mol) and to determine regioregularity (99%).

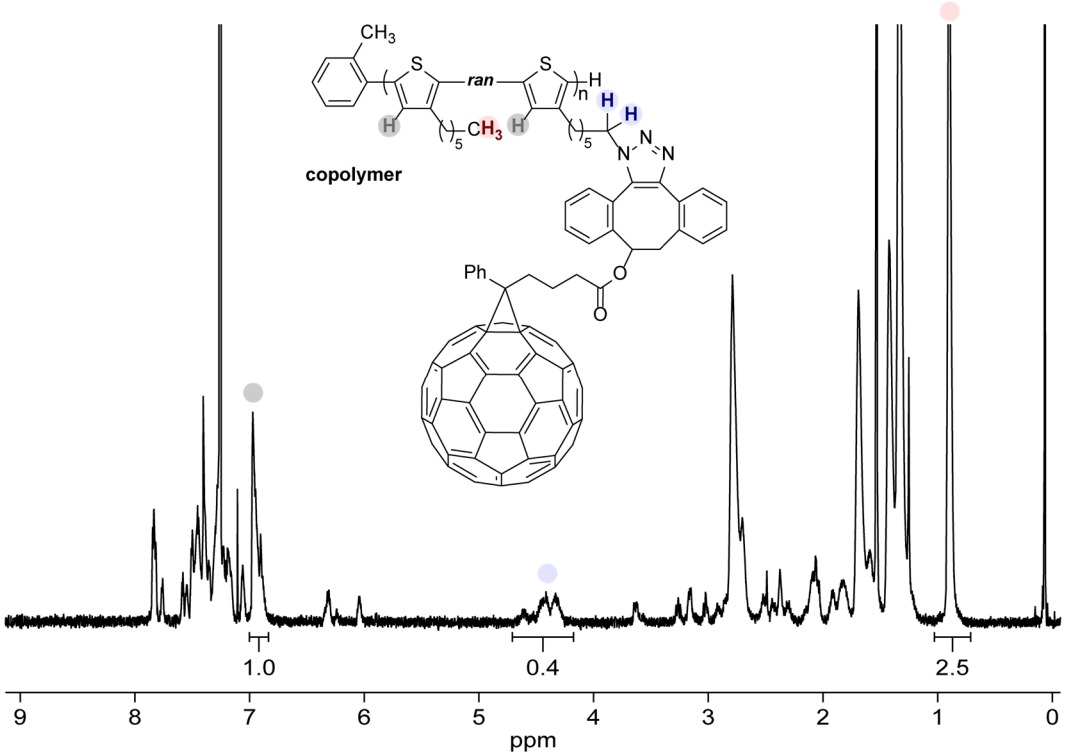

Figure A2.13 ^{1}H NMR spectrum of **copolymer**. (700 MHz, $CDCl_3$) δ 7.00–6.85 (m, 1H), 4.70–4.21 (m, 0.4H), 0.96–0.83 (m, 2.5H).

A2.7 Fourier-Transform Infrared Spectroscopy

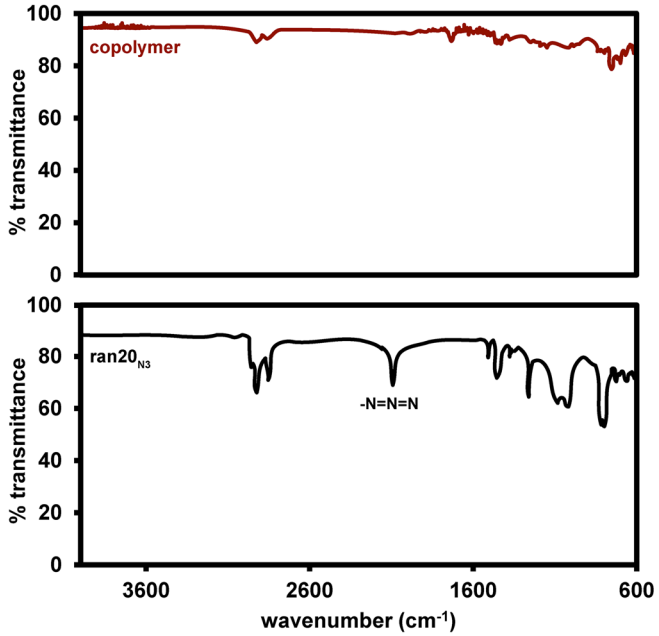

Figure A2.14 Fourier-transform infrared spectra of neat copolymer (red, top) and ran20$_{N3}$ (black, bottom) showing the disappearance of the azide peak at 2092 cm^{-1}.

A2.8 Size Exclusion Chromatography Traces

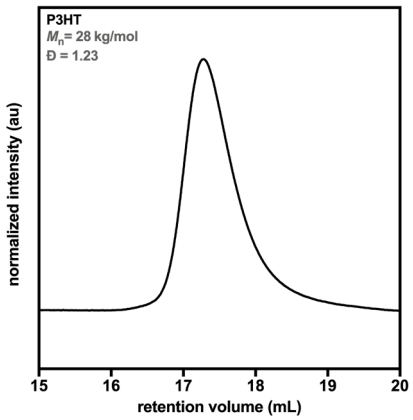

Figure A2.15 Size-exclusion chromatography trace for **P3HT**.

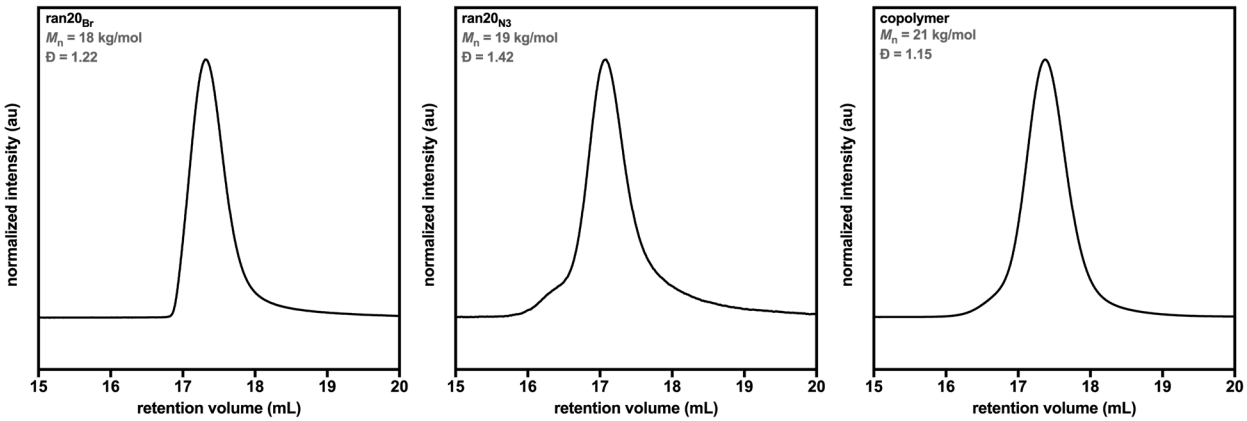

Figure A2.16 Size-exclusion chromatography traces for **ran20$_{Br}$**, **ran20$_{N3}$**, and the **copolymer**.

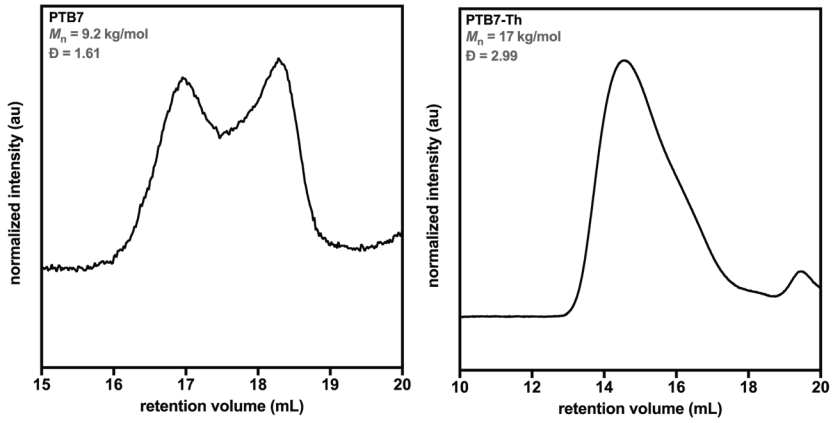

Figure A2.17 Size-exclusion chromatography traces for commercially available polymers **PTB7** and **PTB7-Th**. **PffBT4T-2OD** was not soluble in THF and was not characterized via SEC.

A2.9 Thin Film Preparation for Optical Microscopy

A2.9.1 Blends without Additives

Table A2.2 Quantities of donor polymers, $PC_{71}BM$, and solvents used to prepare blends without additives.

donor	donor mass (mg)	$PC_{71}BM$ mass (mg)	volume o-DCB (μL)	volume CB (μL)
PTB7	7.711	11.569	771	
PTB7-Th	7.585	11.42	759	
PffBT4T-2OD	6.675	7.992	370	370

PTB7 and PTB7-Th. The donor polymer (PTB7 or PTB7-Th) and $PC_{71}BM$ were weighed into a 4 mL vial in a donor:$PC_{71}BM$ ratio 1.0:1.5. To this vial was added a stir bar and *o*-DCB to obtain an overall photoactive solids concentration of 25 mg/mL. The resulting solution was sonicated at rt for 15 min and stirred at 60 °C for 16 h. For each solution, an aliquot (100 μL) was spin-casted onto a glass or fused silica substrate for 120 s at 1000 RPM.

PffBT4T-2OD. PffBT4T-2OD and $PC_{71}BM$ were weighed into a 4 mL vial in a donor:$PC_{71}BM$ ratio of 1.0:1.2. To this vial was added a stir bar and CB/*o*-DCB (50/50 v/v) to obtain an overall photoactive solids concentration of 19.8 mg/mL. The resulting solution was sonicated at rt for 15 min, stirred at 60 °C for 16 h, and stirred an additional 2 h at 110 °C. An aliquot (100 μL) of the solution was spin-cast onto hot glass or fused silica substrates (heated to 110 °C until loading onto spin-coater) for 180 s at 800 RPM.

A2.9.2 Blends with 8 wt% Copolymer

Table A2.3 Quantities of donor polymers, $PC_{71}BM$, and copolymer stock solution used to prepare blends with 8 wt% copolymer.

donor	donor mass (mg)	$PC_{71}BM$ mass (mg)	volume copolymer stock solution (µL)	volume *o*-DCB (µL)
PTB7	4.971	9.347	603	19.5
PTB7-Th	4.851	9.082	588	16.5
PffBT4T-2OD	5.577	8.278	760	

PTB7 and PTB7-Th. The donor polymer (PTB7 or PTB7-Th) and $PC_{71}BM$ were weighed into a 4 mL vial. To this vial was added a stir bar, a 2.06 mg/mL solution of the copolymer in *o*-DCB, and *o*-DCB to obtain a resulting solution with a polymer:$PC_{71}BM$ ratio of 1.0:1.5 and overall photoactive solids concentration of 25 mg/mL. The resulting solution was sonicated at rt for 15 min and stirred at 60 °C for 16 h. For each solution, an aliquot (100 µL) was spin-casted onto a glass or fused silica substrate for 120 s at 1000 RPM.

PffBT4T-2OD. PffBT4T-2OD and $PC_{71}BM$ were weighed into a 4 mL vial. To this vial was added a stir bar and a 1.58 mg/mL solution of the copolymer in *o*-DCB/CB (50/50 v/v) to obtain a solution with a polymer:$PC_{71}BM$ ratio of 1.0:1.2 and an overall photoactive solids concentration of 19.8 mg/mL. The resulting solution was sonicated at rt for 15 min and stirred at 60 °C for 16 h and an additional 2 h at 110 °C. An aliquot (100 µL) of the solution was spin-cast onto a hot glass or fused silica substrate (heated to 110 °C until loading onto spin-coater) for 180 s at 800 RPM.

A2.9.3 Blends with 4 wt% Copolymer

Table A2.4 Quantities of donor polymers, $PC_{71}BM$, and copolymer stock solution used to prepare blends with 4 wt% copolymer.

donor	donor mass (mg)	$PC_{71}BM$ mass (mg)	volume copolymer stock solution (µL)
PTB7	5.916	9.862	0.657
PTB7-Th	5.823	9.715	0.647
PffBT4T-2OD	5.935	7.951	0.731

PTB7 and PTB7-Th. The donor polymer (PTB7 or PTB7-Th) and $PC_{71}BM$ were weighed into a 4 mL vial. To this vial was added a stir bar, a 1.00 mg/mL solution of the copolymer in *o*-DCB, and *o*-DCB to obtain a resulting solution with a polymer:$PC_{71}BM$ ratio of 1.0:1.5 and overall photoactive solids concentration of 25 mg/mL. The resulting solution was sonicated at rt for 15 min and stirred at 60 °C for 16 h. For each solution, an aliquot (100 µL) was spin-casted onto a glass substrate for 120 s at 1000 RPM.

PffBT4T-2OD. PffBT4T-2OD and $PC_{71}BM$ were weighed into a 4 mL vial. To this vial was added a stir bar and a 0.792 mg/mL solution of the copolymer in *o*-DCB/CB (50/50 v/v) to obtain a solution with a polymer:$PC_{71}BM$ ratio of 1.0:1.2 and an overall photoactive solids concentration of 19.8 mg/mL. The resulting solution was sonicated at rt for 15 min and stirred at 60 °C for 16 h and an additional 2 h at 110 °C. An aliquot (100 µL) of the solution was spin-cast onto a hot glass substrate (heated to 110 °C until loading onto spin-coater) for 180 s at 800 RPM.

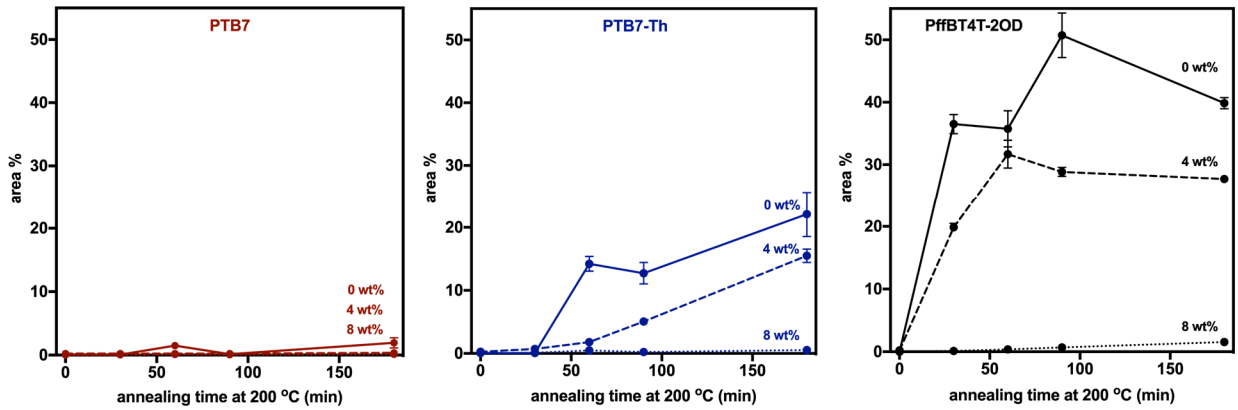

Figure A2.18 The effect of copolymer loading on aggregate area percent for thin film blends of PTB7 (red, left), PTB7-Th (blue, center), or PffBT4T-2OD (black, right) blended with $PC_{71}BM$. The copolymer loading was 0 wt% (solid), 4 wt% (long dashes), or 8 wt% (short dashes) in each case.

A2.9.4 Blends with Diiodooctane (DIO)

Table A2.5 Quantities of donor polymers, $PC_{71}BM$, and solvents used to prepare blends with DIO.

donor	donor mass (mg)	$PC_{71}BM$ mass (mg)	volume o-DCB (µL)	volume CB (µL)	volume DIO (µL)
PTB7	10.115	15.127	979		30.0
PTB7-Th	10.053	15.185	979		30.0
PffBT4T-2OD	6.776	8.143	365	365	19.0

PTB7 and PTB7-Th. The donor polymer (PTB7 or PTB7-Th) and $PC_{71}BM$ were weighed into a 4 mL vial in a donor:$PC_{71}BM$ ratio 1.0:1.5. To this vial was added a stir bar, and *o*-DCB, and DIO to obtain an overall photoactive solids concentration of 25 mg/mL. The resulting solution was sonicated at rt for 15 min and stirred at 60 °C for 16 h. For each solution, an aliquot (100 µL) was spin-casted onto a glass or fused silica substrate for 120 s at 1000 RPM.

PffBT4T-2OD. PffBT4T-2OD and $PC_{71}BM$ were weighed into a 4 mL vial in a PffBT4T-2OD:$PC_{71}BM$ ratio of 1.0:1.2. To this vial was added a stir, *o*-DCB, and CB. The resulting solution was sonicated at rt for 15 min, stirred at 60 °C for 16 h, and stirred for an additional 2 h at 110 °C.

To the hot solution was added DIO 10 minutes prior to spin-casting, yielding an overall photoactive solids concentration of 19.9 mg/mL. An aliquot (100 μL) of the solution was spin-cast onto hot glass or fused silica substrates (heated to 110 °C until loading onto spin-coater) for 180 s at 800 RPM.

A2.9.5 Blends with Copolymer and DIO

Table A2.6 Quantities of donor polymers, $PC_{71}BM$, copolymer stock solution, and solvents used to prepare blends with the copolymer and DIO.

donor	donor mass (mg)	$PC_{71}BM$ mass (mg)	volume copolymer stock solution (μL)	volume DIO (μL)
PTB7	4.677	8.787	567	18.5
PTB7-Th	4.578	8.568	555	17.0
PffBT4T-2OD	5.561	8.131	729	23.0

PTB7 and PTB7-Th. The donor polymer (PTB7 or PTB7-Th) and $PC_{71}BM$ were weighed into a 4 mL vial. To this vial was added a stir bar and a 2.06 mg/mL solution of copolymer in *o*-DCB to obtain a resulting solution with a polymer:$PC_{71}BM$ ratio of 1.0:1.5. The resulting solution was sonicated at rt for 15 min and stirred at 60 °C for 16 h. To the hot solution was added DIO 10 min prior to spin-casting, yielding an overall photoactive solids concentration of 25 mg/mL. For each solution, an aliquot (100 μL) was spin-casted onto a glass or fused silica substrate for 120 s at 1000 RPM.

PffBT4T-2OD. PffBT4T-2OD and $PC_{71}BM$ were weighed into a 4 mL vial. To this vial was added a stir bar and a 1.58 mg/mL solution of the copolymer in *o*-DCB/CB (50/50 v/v) to obtain a solution with a polymer:$PC_{71}BM$ ratio of 1.0:1. The resulting solution was sonicated at rt for 15 min and stirred at 60 °C for 16 h and an additional 2 h at 110 °C. To the hot solution was added DIO 10 min prior to spin casting, yielding an overall photoactive solids concentration of 19.8 mg/mL. An

aliquot (100 µL) of the solution was spin-cast onto hot glass or fused silica substrates (heated to 110 °C until loading onto spin-coater) for 180 s at 800 RPM.

A2.9.6 Blends with P3HT

Table A2.7 Quantities of donor polymers, $PC_{71}BM$, and P3HT stock solution used to prepare blends with P3HT.

donor	donor mass (mg)	$PC_{71}BM$ mass (mg)	volume P3HT stock solution (µL)	volume *o*-DCB (µL)
PTB7	4.922	9.241	596	19.5
PTB7-Th	4.950	9.284	600	19.0
PffBT4T-2OD	5.519	8.204	753	

PTB7 and PTB7-Th. The donor polymer (PTB7 or PTB7-Th) and $PC_{71}BM$ were weighed into a 4 mL vial. To this vial was added a stir bar, a 2.06 mg/mL solution of P3HT in *o*-DCB, and *o*-DCB to obtain a resulting solution with a polymer:$PC_{71}BM$ ratio of 1.0:1.5 and overall photoactive solids concentration of 25 mg/mL. The resulting solution was sonicated at rt for 15 min and stirred at 60 °C for 16 h. For each solution, an aliquot (100 µL) was spin-casted onto a glass or fused silica substrate for 120 s at 1000 RPM.

PffBT4T-2OD. PffBT4T-2OD and $PC_{71}BM$ were weighed into a 4 mL vial. To this vial was added a stir bar and a 1.58 mg/mL solution of P3HT in *o*-DCB/CB (50/50 v/v) to obtain a solution with a polymer:$PC_{71}BM$ ratio of 1.0:1.2 and an overall photoactive solids concentration of 19.8 mg/mL. The resulting solution was sonicated at rt for 15 min and stirred at 60 °C for 16 h and an additional 2 h at 110 °C. An aliquot (100 µL) of the solution was spin-cast onto hot glass or fused silica substrates (heated to 110 °C until loading onto spin-coater) for 180 s at 800 RPM.

Table A2.8 Summary of the blend ratios and solvents used in donor:acceptor thin film blends.

additive	donor	polymer:solid additive:$PC_{71}BM$ mass ratio	polymer:$PC_{71}BM$ mass ratio	o-DCB/CB/DIO (v/v/v)	[solids] (mg/mL)
(A) without additives	PTB7	40:0:60	1.0:1.5	100/0/0	25
	PTB7-Th	40:0:60	1.0:1.5	100/0/0	25
	PffBT4T-2OD	45:0:55	1.0:1.2	50/50/0	19.8
(B) 8 wt% copolymer	PTB7	32:8:60	1.0:1.5	100/0/0	25
	PTB7-Th	32:8:60	1.0:1.5	100/0/0	25
	PffBT4T-2OD	37:8:55	1.0:1.2	50/50/0	19.8
(C) 4 wt% copolymer	PTB7	36:4:50	1.0:1.5	100/0/0	25
	PTB7-Th	36:4:50	1.0:1.5	100/0/0	25
	PffBT4T-2OD	41:4:55	1.0:1.2	50/50/0	19.8
(D) DIO	PTB7	40:0:60	1.0:1.5	97/0/3	25
	PTB7-Th	40:0:60	1.0:1.5	97/0/3	25
	PffBT4T-2OD	45:0:55	1.0:1.2	48.5/48.5/3	19.9
(E) copolymer and DIO	PTB7	32:8:60	1.0:1.5	97/0/3	25
	PTB7-Th	32:8:60	1.0:1.5	97/0/3	25
	PffBT4T-2OD	37:8:55	1.0:1.2	48.5/48.5/3	19.8
(F) P3HT	PTB7	32:8:60	1.0:1.5	100/0/0	25
	PTB7-Th	32:8:60	1.0:1.5	100/0/0	25
	PffBT4T-2OD	37:8:55	1.0:1.2	50/50/0	19.8

A2.9.7 Blends of $PC_{71}BM$ with Copolymer or P3HT

copolymer. To a 4 mL vial was added a stir bar, $PC_{71}BM$ (13.413 mg), and a 1.58 mg/mL solution of the copolymer in *o*-DCB/CB (50/50 v/v) (736 μL) to obtain a solution with polymer:$PC_{71}BM$ ratio of 8:92 and an overall photoactive solids concentration of 19.8 mg/mL. The resulting solution was stirred at 60 °C for 18 h. An aliquot (100 μL) of the solution was spin-cast onto a glass substrate for 120 s at 1000 RPM.

P3HT. To a 4 mL vial was added a stir bar, $PC_{71}BM$ (12.556 mg), and a 1.58 mg/mL solution of P3HT in *o*-DCB/CB (50/50 v/v) (689 μL) to obtain a solution with polymer:$PC_{71}BM$ ratio of 8:92 and an overall photoactive solids concentration of 19.8 mg/mL. The resulting solution was stirred

at 60 °C for 18 h. An aliquot (100 µL) of the solution was spin-cast onto a glass substrate for 120 s at 1000 RPM.

A2.9.8 Thin Film Annealing

After spin-casting, all films were dried in vacuo for 24 h. The films were then annealed at 200 °C in vacuo, unless otherwise noted.

A2.10 Optical Microscopy Images of Thin Films

A2.10.1 Without Copolymer

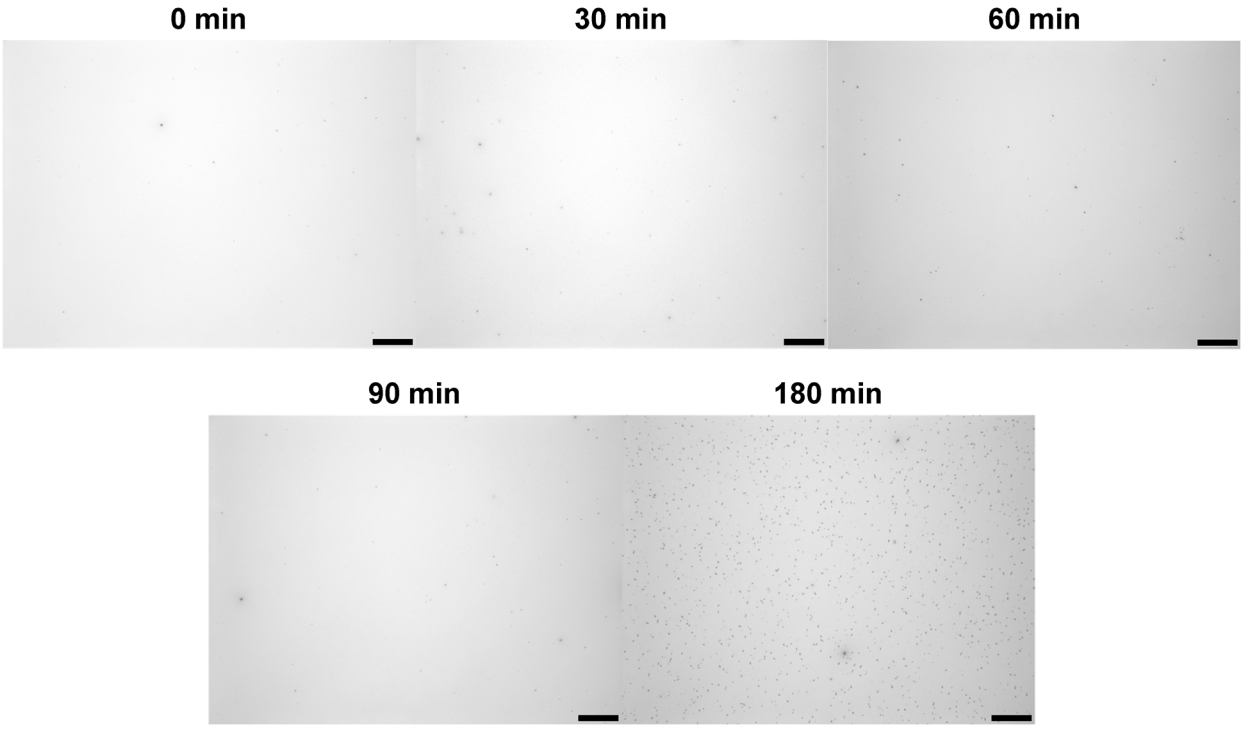

Figure A2.19 Optical microscopy images of PTB7:$PC_{71}BM$ films annealed at 200 °C for a given time. Scale bars represent 30 µm.

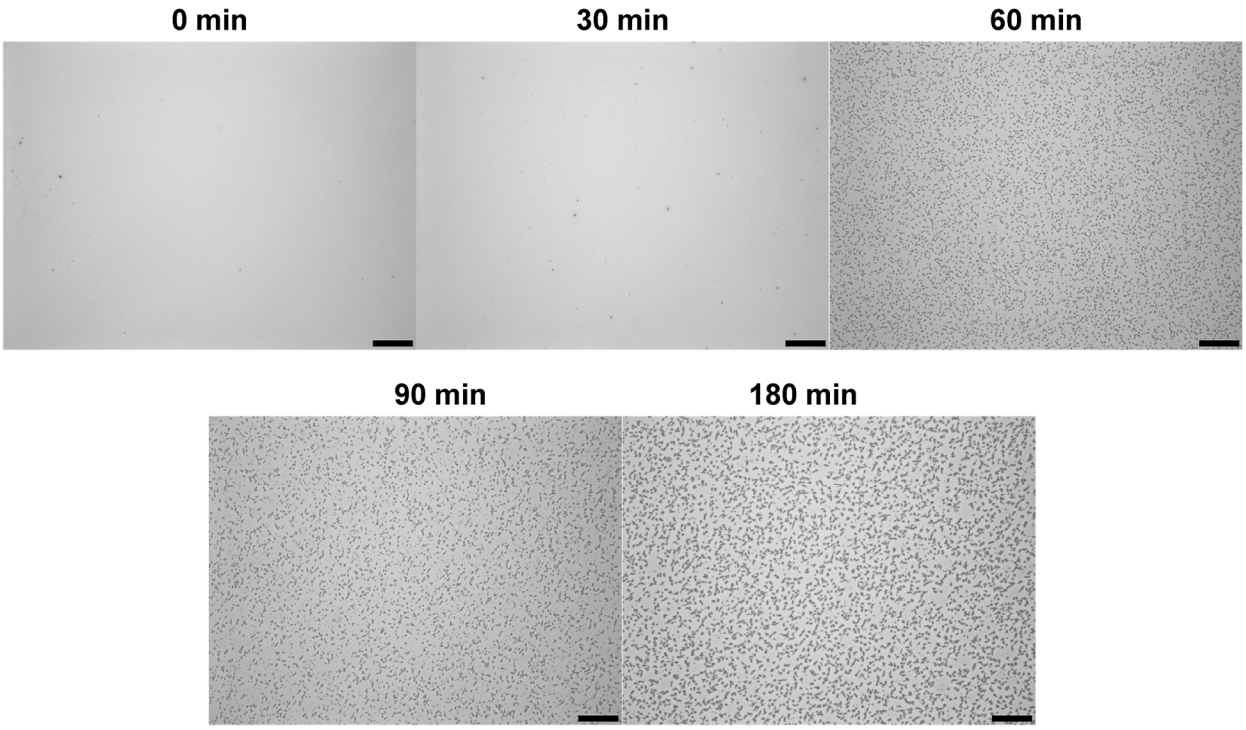

Figure A2.20 Optical microscopy images of **PTB7-Th**:$PC_{71}BM$ films annealed at 200 °C for a given time. Scale bars represent 30 μm.

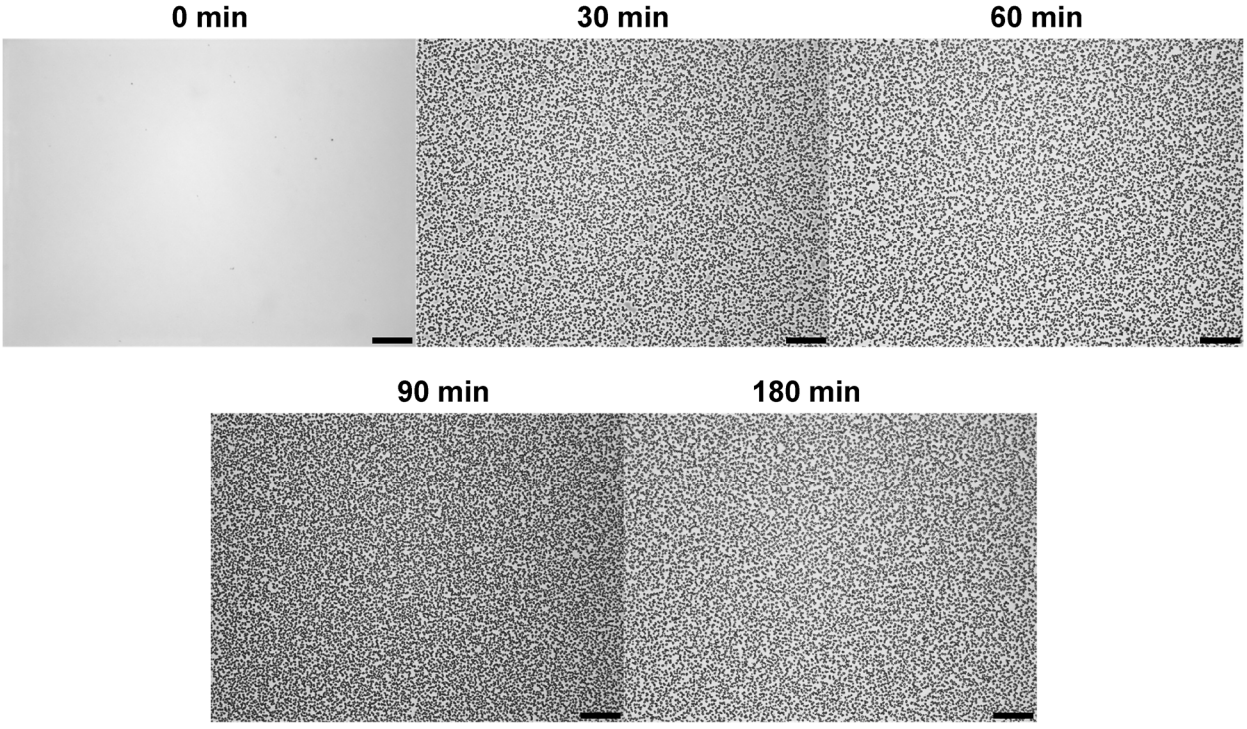

Figure A2.21 Optical microscopy images of **PffBT4T-2OD**:$PC_{71}BM$ films annealed at 200 °C for a given time. Scale bars represent 30 μm.

A2.10.2 With 8 wt% Copolymer

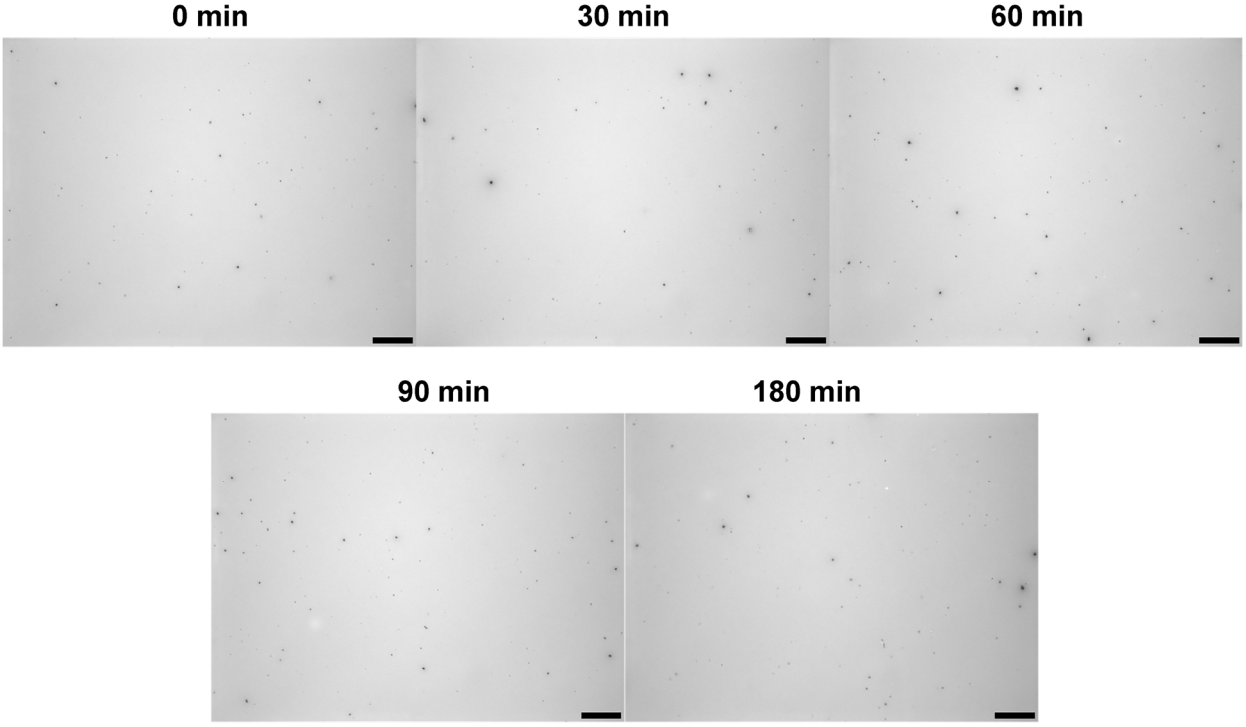

Figure A2.22 Optical microscopy images of **PTB7**:$PC_{71}BM$ films with 8 wt% copolymer annealed at 200 °C for a given time. Scale bars represent 30 μm.

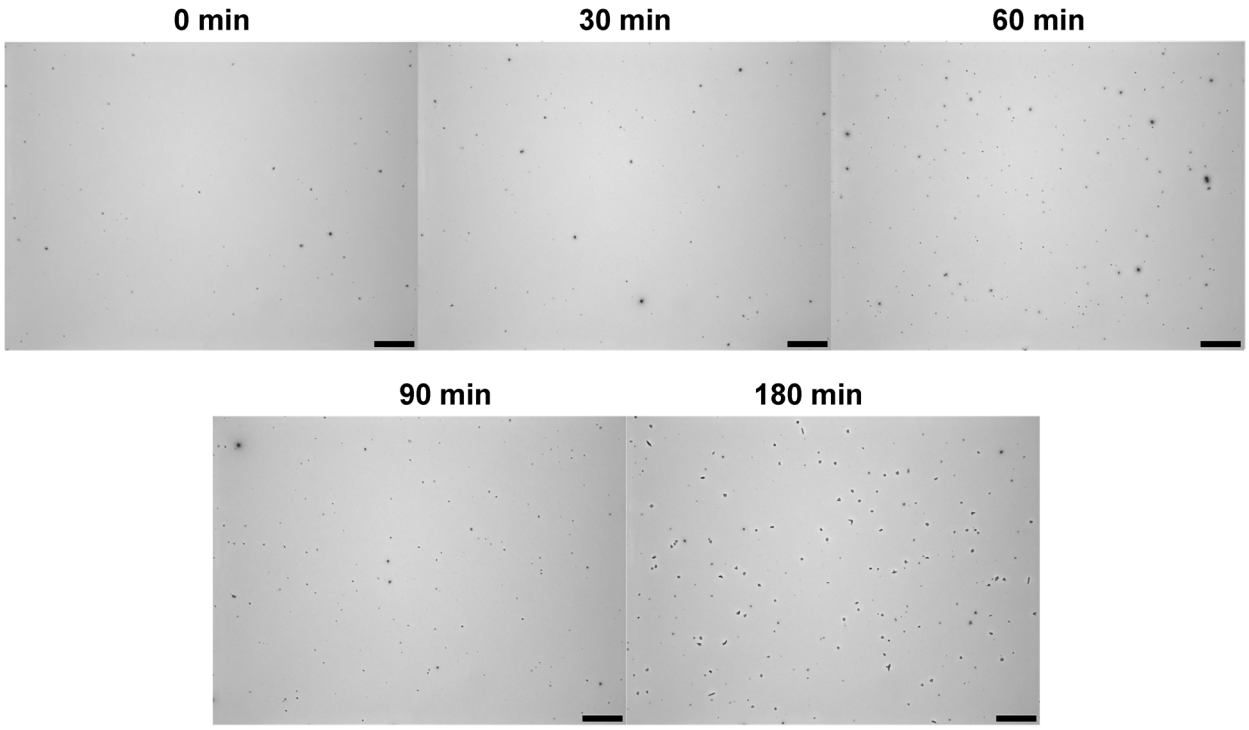

Figure A2.23 Optical microscopy images of **PTB7-Th**:$PC_{71}BM$ films with 8 wt% copolymer annealed at 200 °C for a given time. Scale bars represent 30 μm.

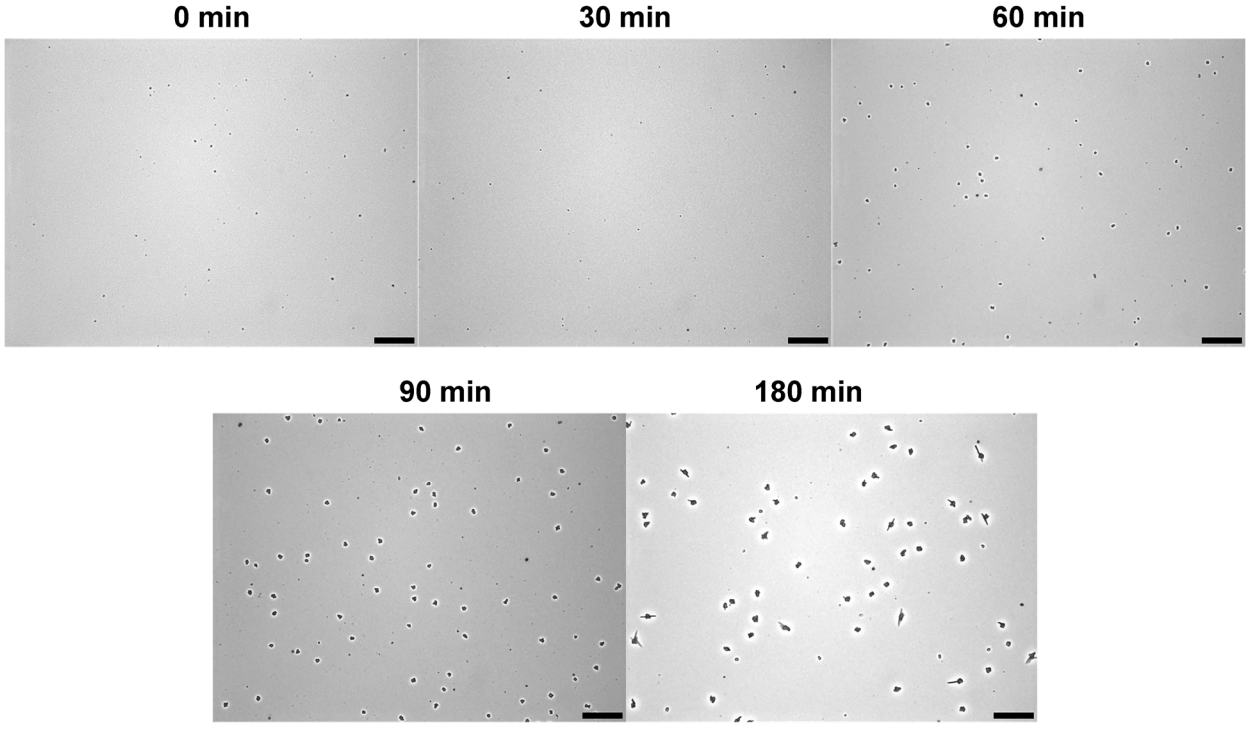

Figure A2.24 Optical microscopy images of **PffBT4T-2OD**:$PC_{71}BM$ films with 8 wt% copolymer annealed at 200 °C for a given time. Scale bars represent 30 μm.

A2.10.3 With 4 wt% Copolymer

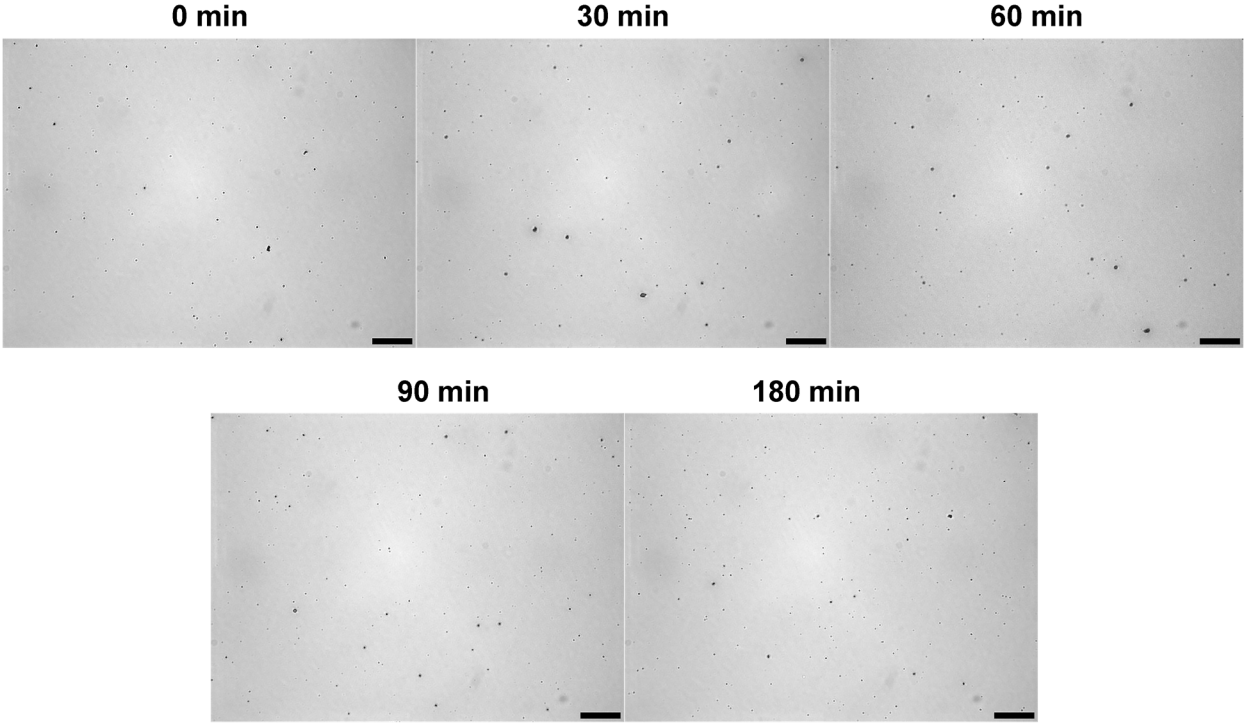

Figure A2.25 Optical microscopy images of **PTB7**:$PC_{71}BM$ films with 4 wt% copolymer annealed at 200 °C for a given time. Scale bars represent 30 μm.

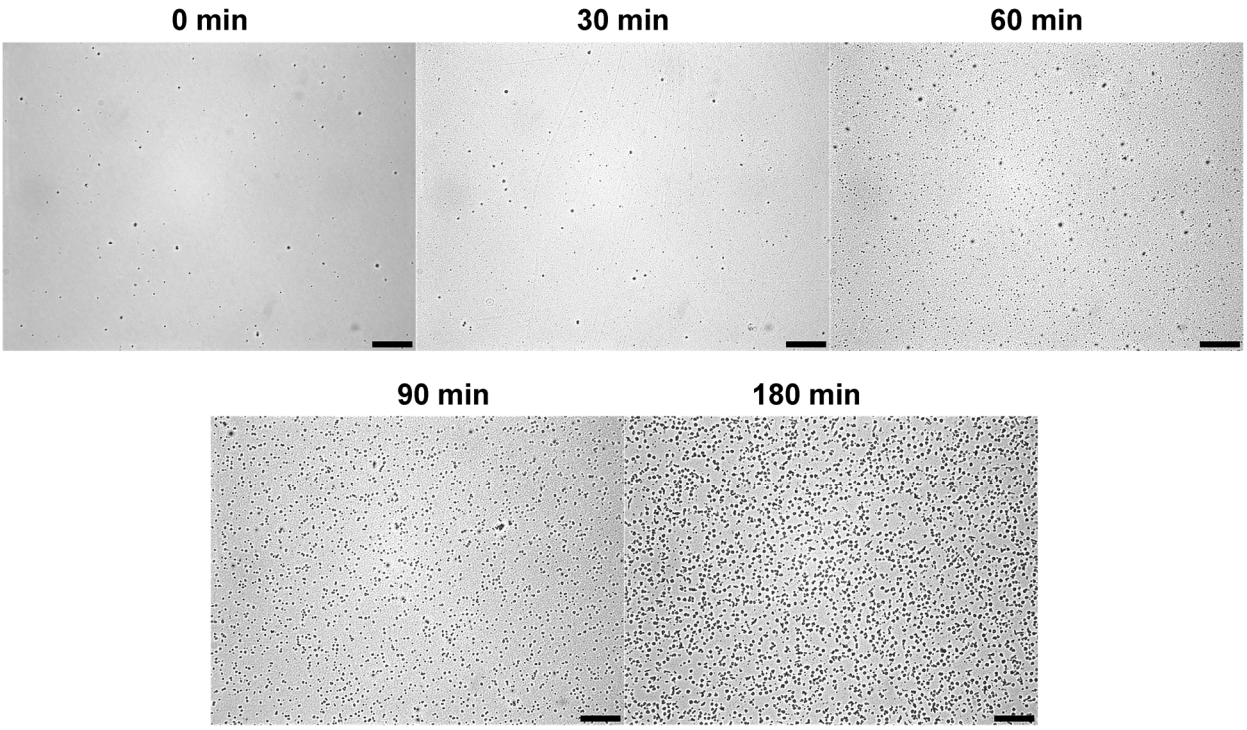

Figure A2.26 Optical microscopy images of **PTB7-Th**:$PC_{71}BM$ films with 4 wt% copolymer annealed at 200 °C for a given time. Scale bars represent 30 μm.

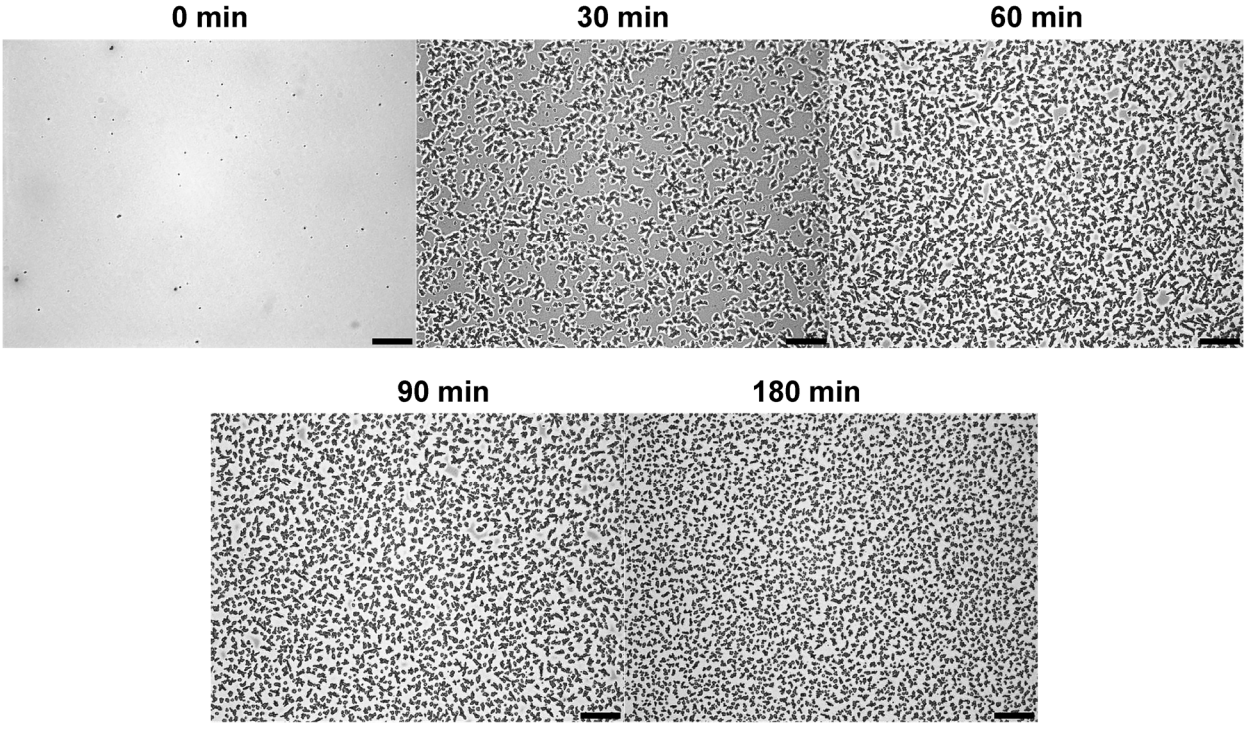

Figure A2.27 Optical microscopy images of **PffBT4T-2OD**:$PC_{71}BM$ films with 4 wt% copolymer annealed at 200 °C for a given time. Scale bars represent 30 μm.

A2.10.4 With DIO

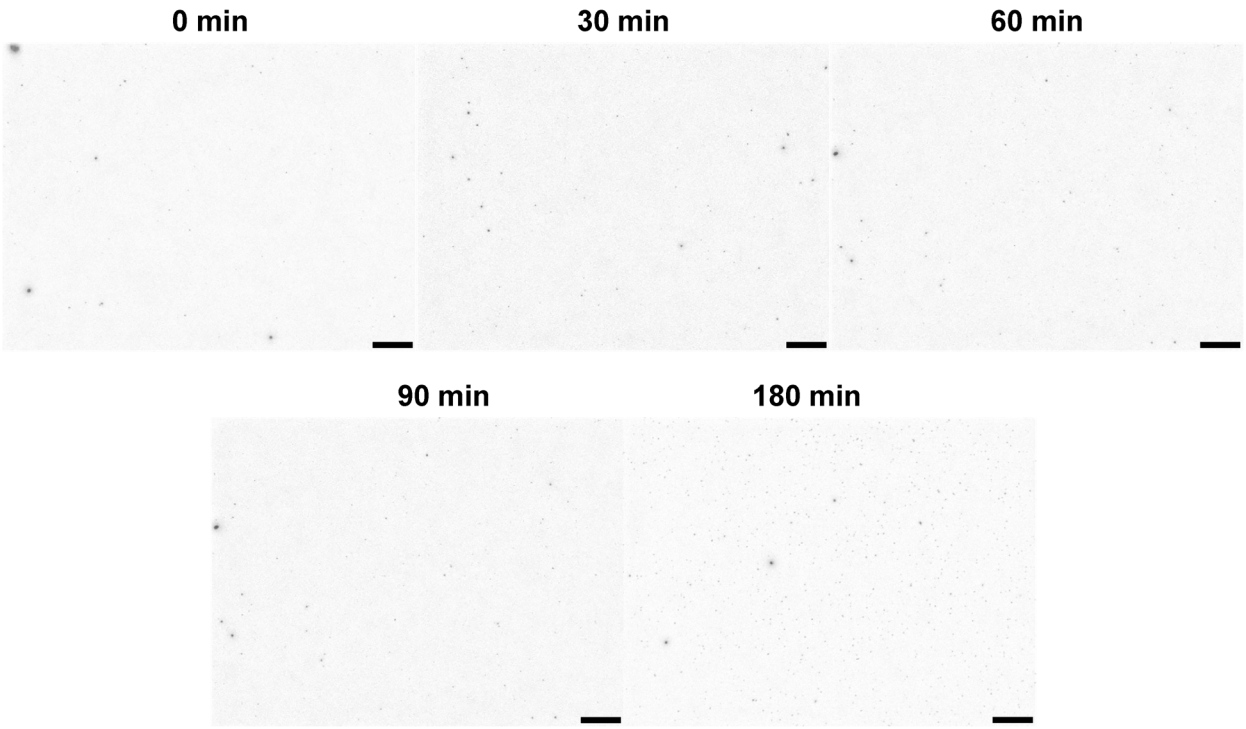

Figure A2.28 Optical microscopy images of **PTB7**:$PC_{71}BM$ films with 3 vol% DIO annealed at 200 °C for a given time. Scale bars represent 30 μm.

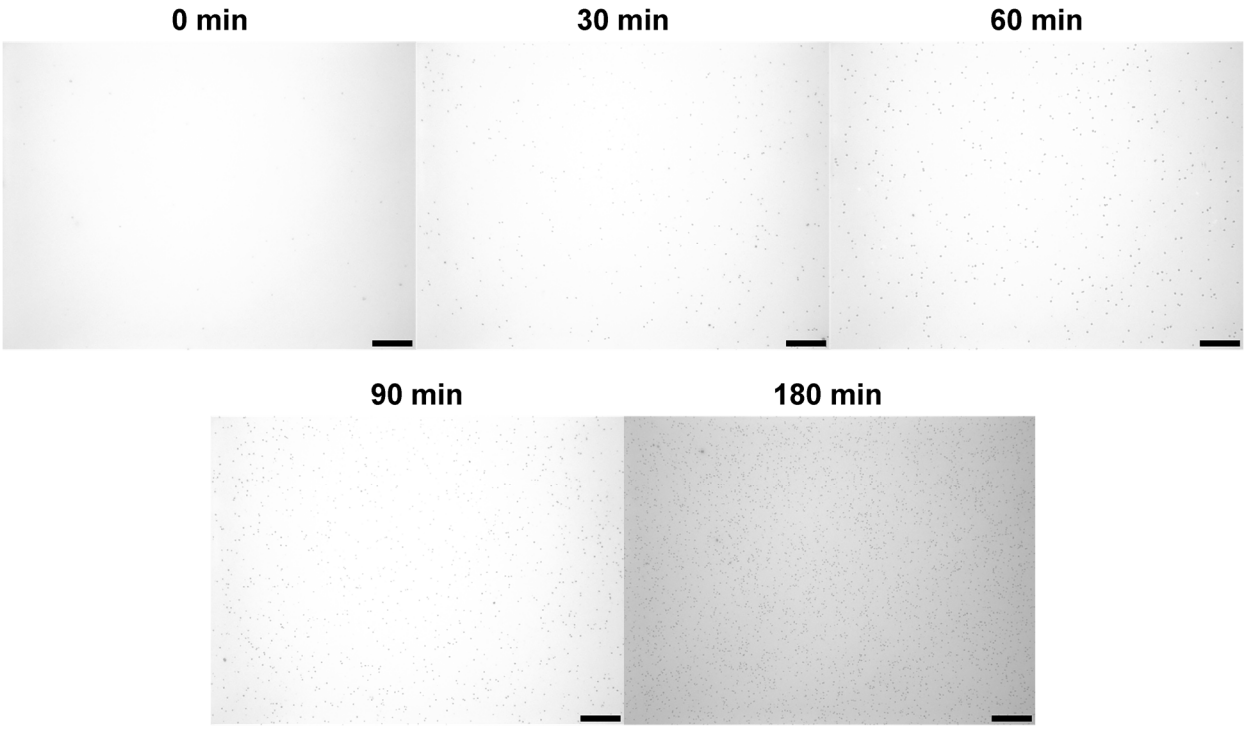

Figure A 2.29 Optical microscopy images of **PTB7-Th**:$PC_{71}BM$ films with 3 vol% DIO annealed at 200 °C for a given time. Scale bars represent 30 μm.

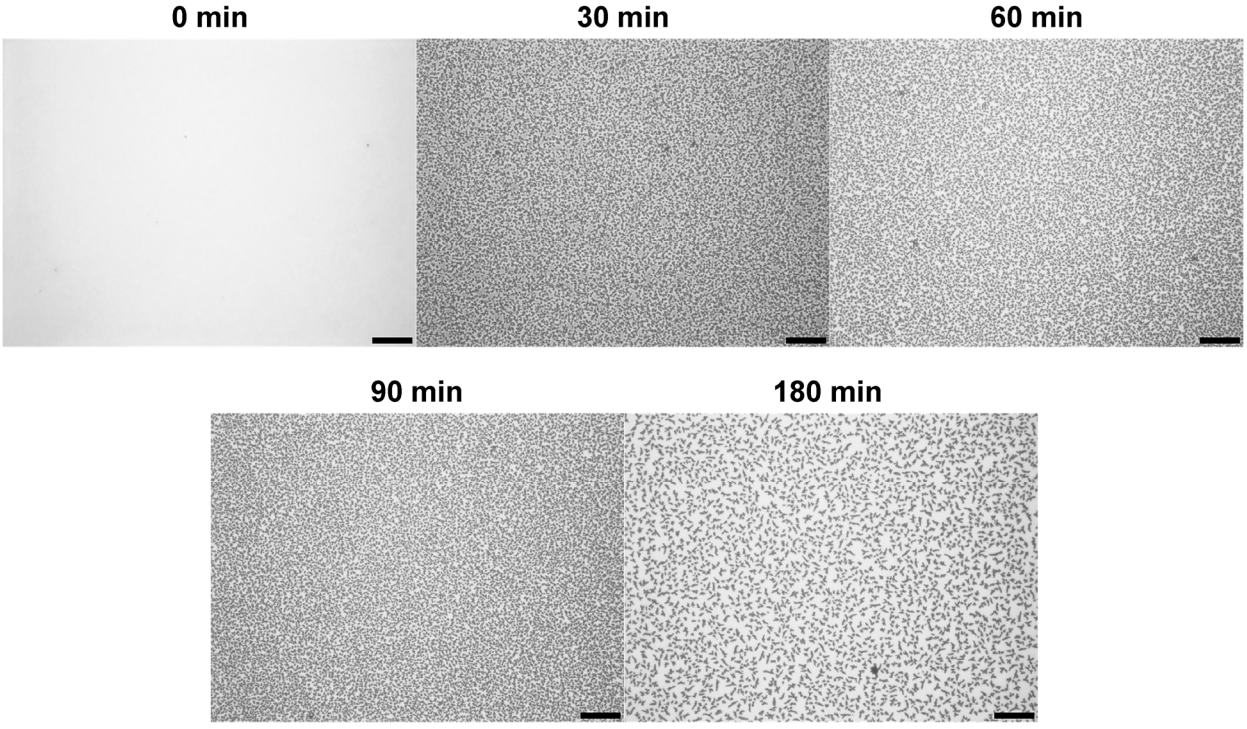

Figure A2.30 Optical microscopy images of **PffBT4T-2OD**:$PC_{71}BM$ films with 3 vol% DIO annealed at 200 °C for a given time. Scale bars represent 30 μm.

A2.10.5 With Copolymer and DIO

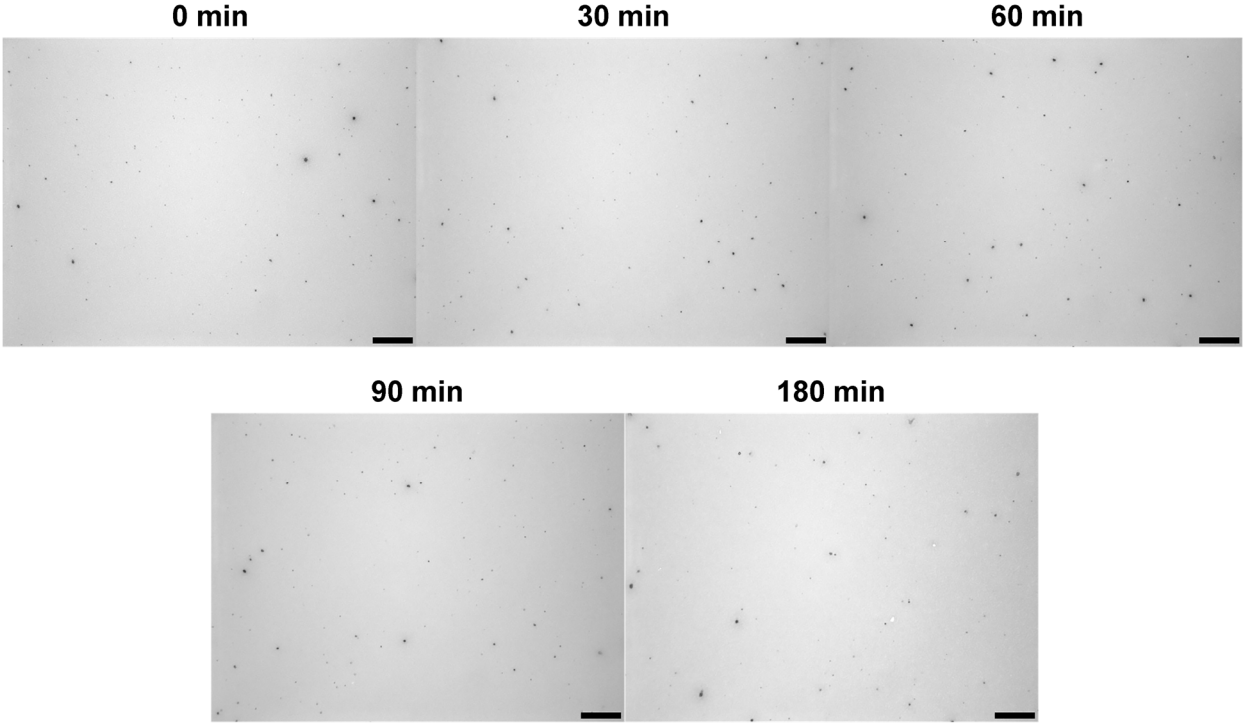

Figure A2.31 Optical microscopy images of **PTB7**:$PC_{71}BM$ films with 8 wt% copolymer and 3 vol% DIO annealed at 200 °C for a given time. Scale bars represent 30 μm.

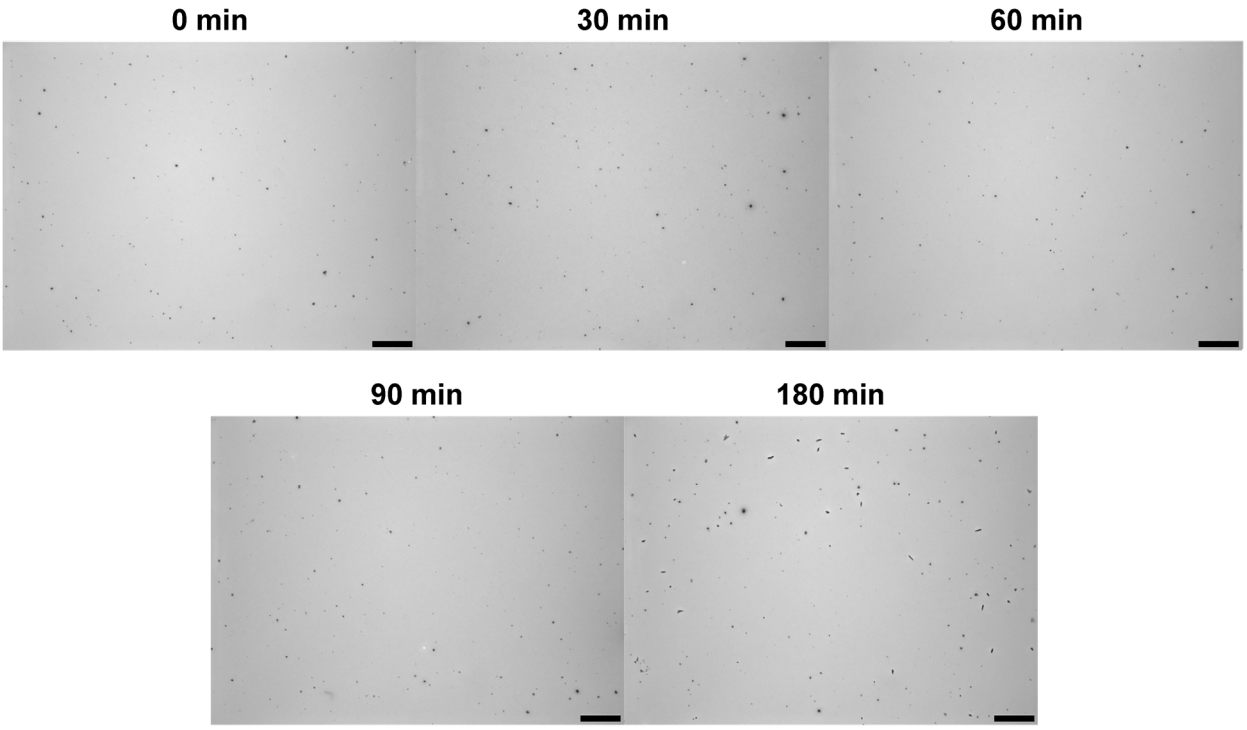

Figure A2.32 Optical microscopy images of **PTB7-Th**:$PC_{71}BM$ films with 8 wt% copolymer and 3 vol% DIO annealed at 200 °C for a given time. Scale bars represent 30 μm.

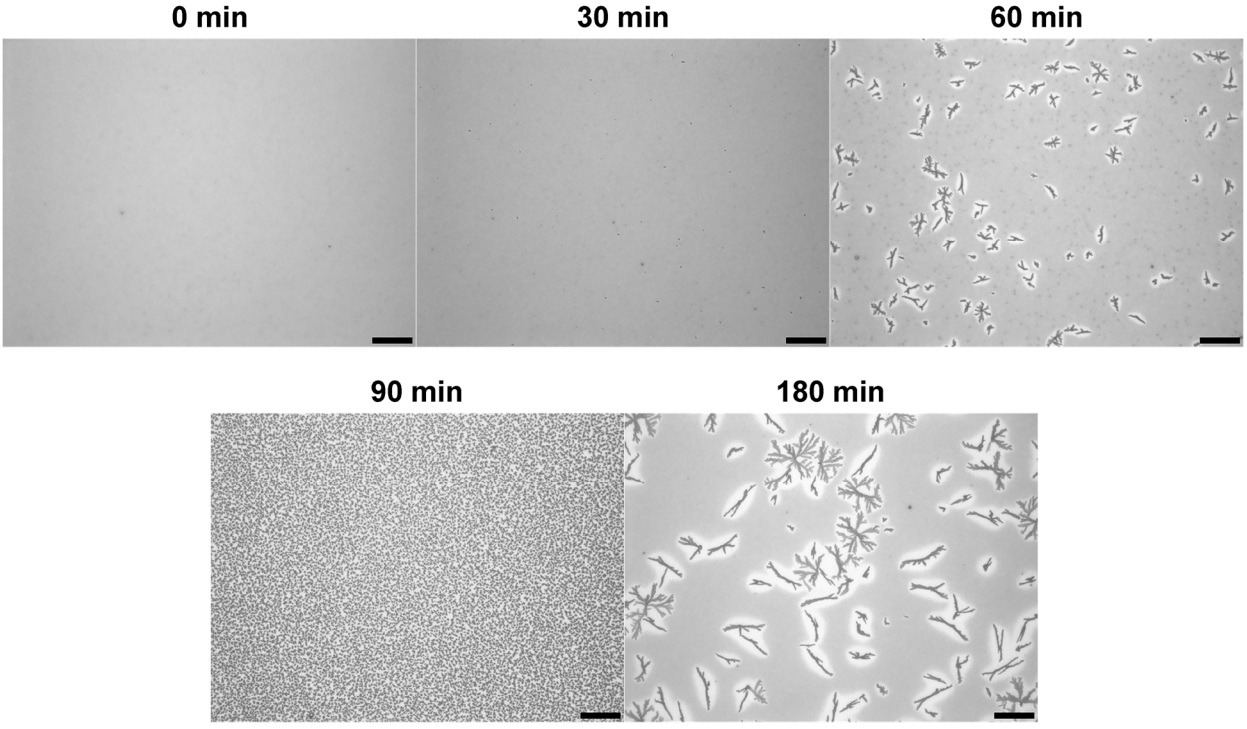

Figure A2.33 Optical microscopy images of **PffBT4T-2OD**:$PC_{71}BM$ films with 8 wt% copolymer and 3 vol% DIO annealed at 200 °C for a given time. Scale bars represent 30 μm.

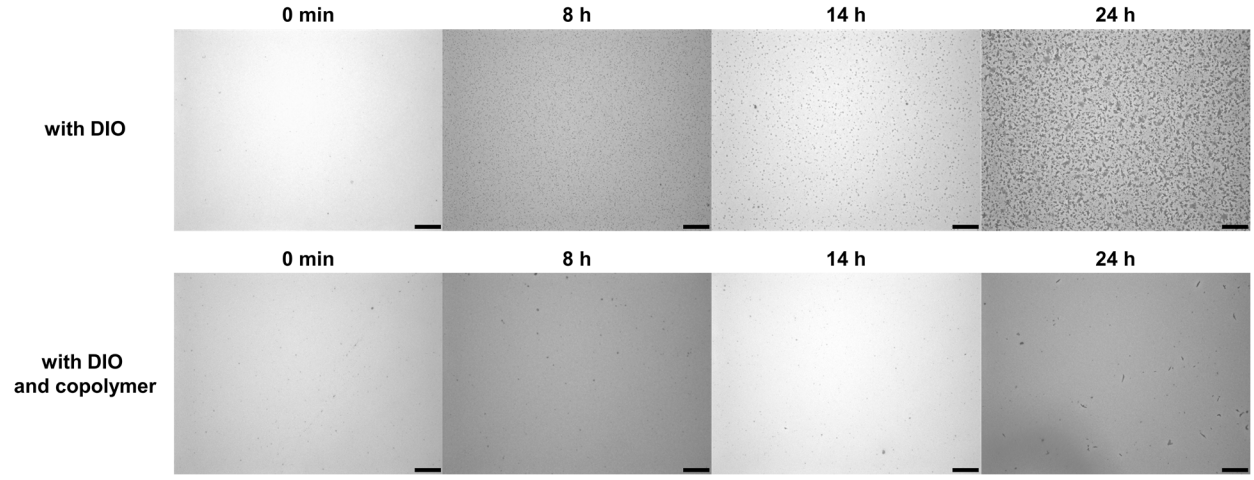

Figure A2.34 Optical microscopy images of **PffBT4T-2OD**:$PC_{71}BM$ films with 3 vol% **DIO** (top) and with 3 vol% **DIO** and 8 wt% **copolymer** (bottom) annealed at 150 °C under N_2. Scale bars represent 30 μm.

A2.10.6 With P3HT

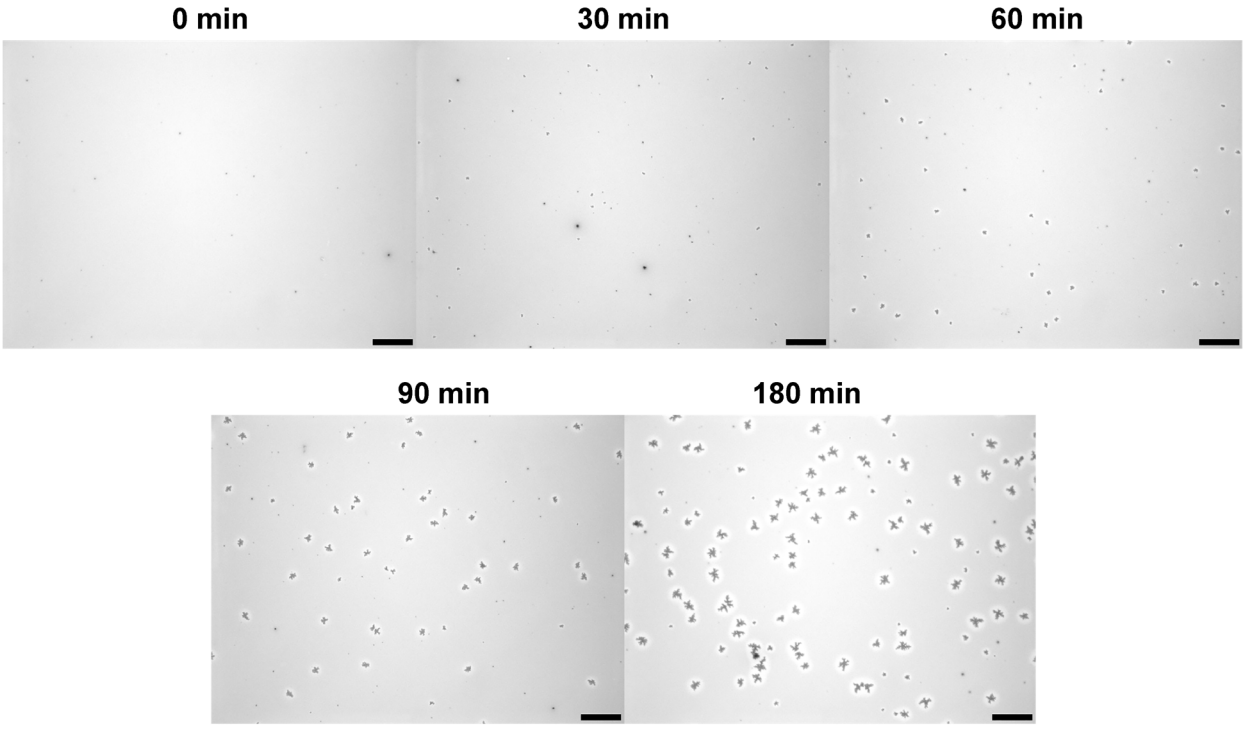

Figure A2.35 Optical microscopy images of **PTB7**:$PC_{71}BM$ films with 8 wt% P3HT annealed at 200 °C for a given time. Scale bars represent 30 μm.

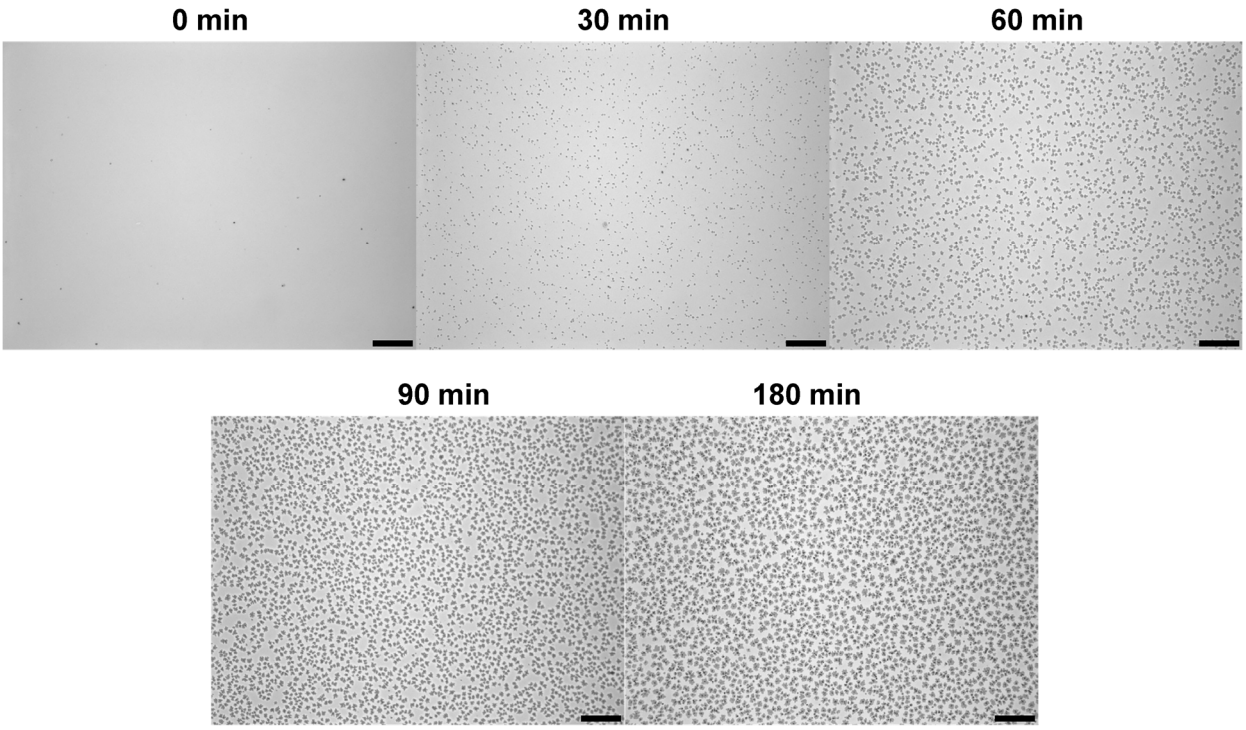

Figure A2.36 Optical microscopy images of **PTB7-Th**:$PC_{71}BM$ films with 8 wt% P3HT annealed at 200 °C for a given time. Scale bars represent 30 μm.

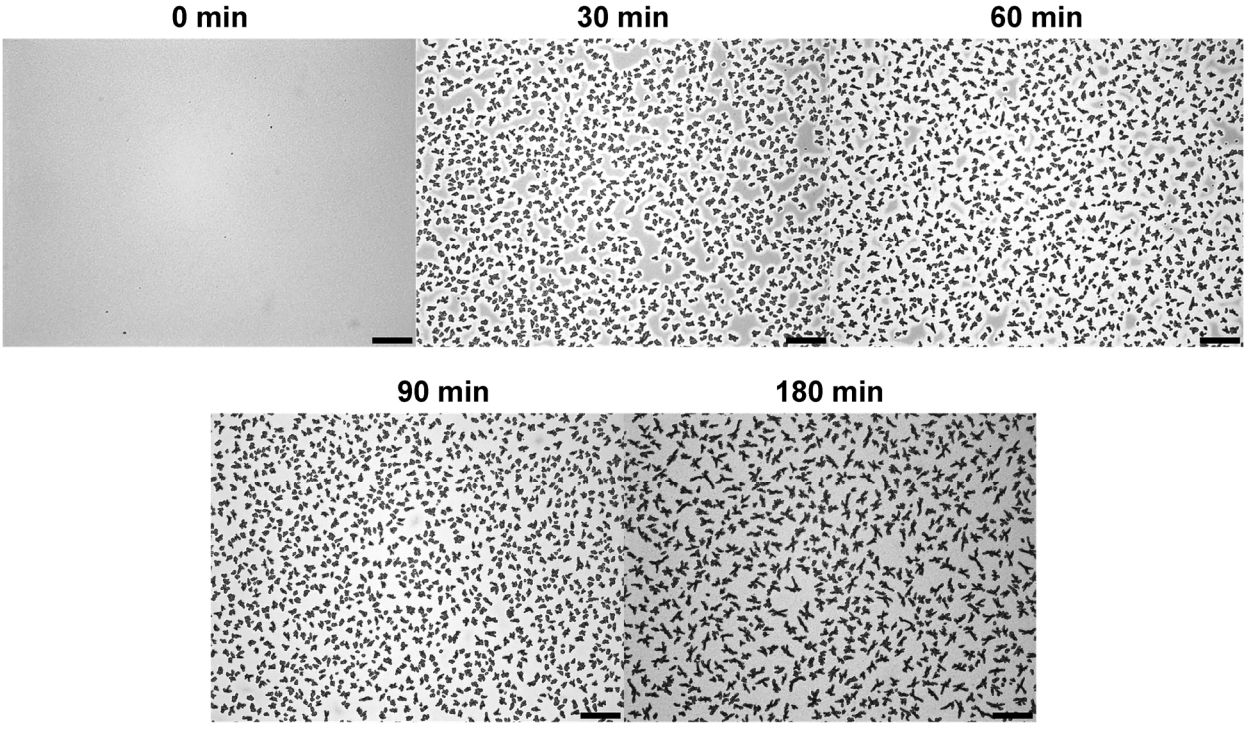

Figure A2.37 Optical microscopy images of **PffBT4T-2OD**:$PC_{71}BM$ films with 8 wt% P3HT annealed at 200 °C for a given time. Scale bars represent 30 μm.

A2.10.7 Blends of $PC_{71}BM$ with Copolymer or P3HT

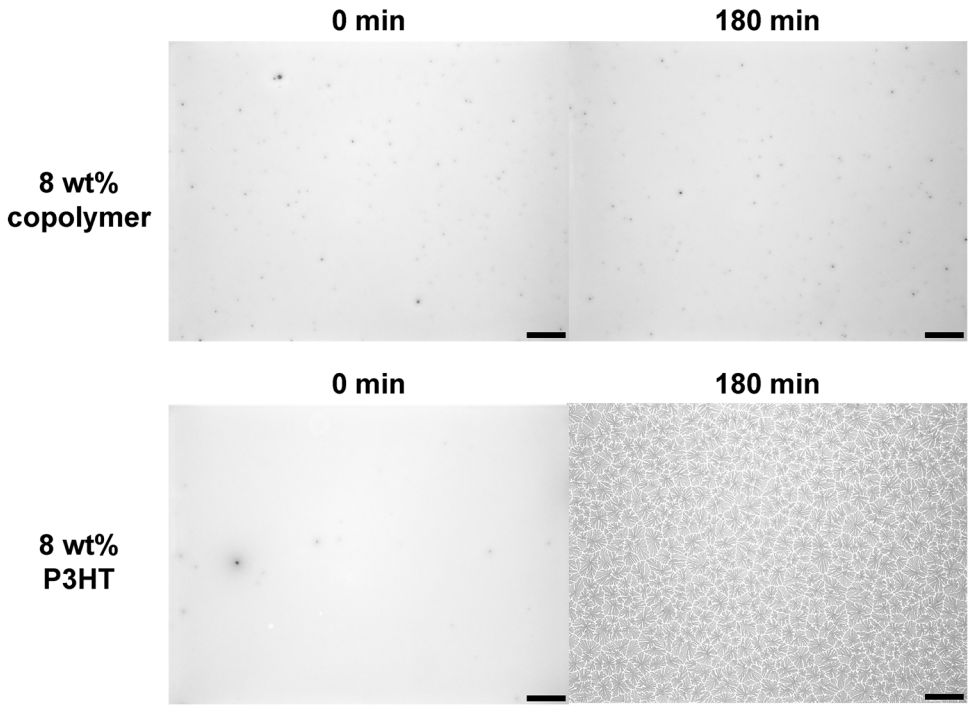

Figure A2.38 Optical microscopy images of **$PC_{71}BM$** films with 8 wt% **copolymer** (top) or **P3HT** (bottom) annealed at 200 °C for a given time. Scale bars represent 30 μm.

A2.11 Surface Contact Angle Data

A2.11.1 Thin Film Preparation

PTB7. To a 4 mL vial equipped with a stir bar was added PTB7 (6.917 mg) and *o*-DCB (277 μL) to yield a final solution with a concentration of 25 mg/mL. The resulting solution was stirred at 60 °C for 18 h. An aliquot of hot solution (100 μL) was spin-cast onto a fused silica substrate at 1000 RPM for 120 s.

PTB7-Th. To a 4 mL vial equipped with a stir bar was added PTB7-Th (6.530 mg) and *o*-DCB (261 μL) to yield a final solution with a concentration of 25 mg/mL. The resulting solution was stirred at 60 °C for 18 h. An aliquot of hot solution (100 μL) was spin-cast onto a fused silica substrate at 1000 RPM for 120 s.

PffBT4T-2OD.To a 4 mL vial equipped with a stir bar was added PffBT4T-2OD (6.013 mg) and *o*-DCB (300 µL) to yield a final solution with a concentration of 20 mg/mL. The resulting solution was stirred at 60 °C for 18 h and at 110 °C for an additional 1.5 h. An aliquot of hot solution (100 µL) was spin-cast onto a fused silica substrate at 1500 RPM for 120 s.

$PC_{71}BM$. To a 4 mL vial equipped with a stir bar was added $PC_{71}BM$ (6.397 mg) and $CHCl_3$ (256 µL) to yield a final concentration of 25 mg/mL. The resulting solution was stirred at 60 °C for 18 h. An aliquot of hot solution (100 µL) was spin-cast onto a fused silica substrate at 1000 RPM for 120 s.

Copolymer. To a 4 mL vial equipped with a stir bar was added the copolymer (3.204 mg) and *o*-DCB (214 µL) to yield a final concentration of 15 mg/mL. The resulting solution was stirred at 60 °C for 18 h. An aliquot of hot solution (100 µL) was spin-cast onto a fused silica substrate at 1000 RPM for 120 s.

P3HT. To a 4 mL vial was added P3HT (0.551 mg) and *o*-DCB (344 µL) to give a 1.60 mg/mL solution. This solution was stirred for 16 h at 60 °C starting at 18:30.

A2.11.2 Surface Contact Angle Measurements

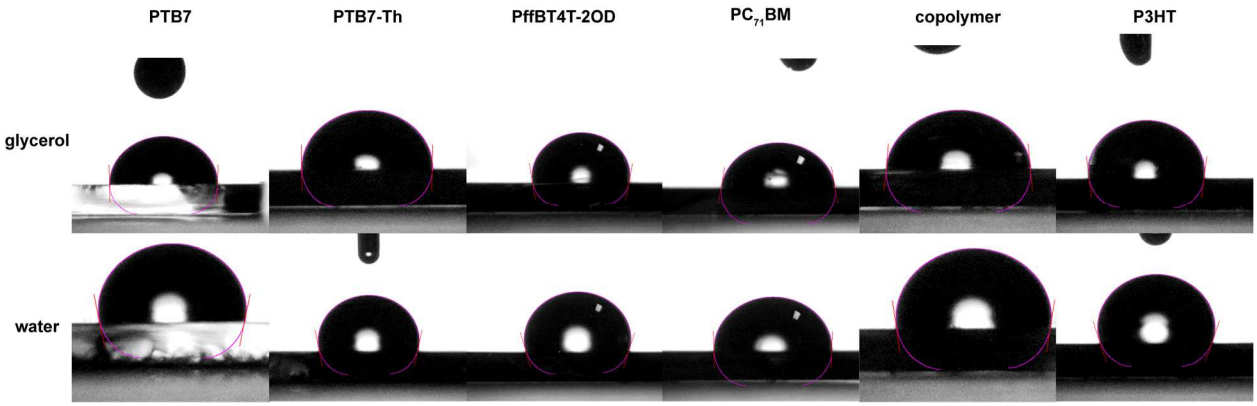

Figure A2.39 Surface contact angles for **PTB7**, **PTB7-Th**, **PffBT4T-2OD**, **$PC_{71}BM$**, and the **copolymer**.

Table A2.9 Water and glycerol contact angles for thin films of the donor polymers, the copolymer, and $PC_{71}BM$.

compound	water contact angle	glycerol contact angle
PTB7	99 ± 2°	91 ± 1°
PTB7-Th	101 ± 3°	91 ± 2°
PffBT4T-2OD	108 ± 2°	97 ± 2°
$PC_{71}BM$	90 ± 2°	78 ± 2°
copolymer	98 ± 1°	84 ± 1°
P3HT	108.3 ± 0.5°	96.4 ± 0.7°

A2.11.3 Surface Energy Calculations

The polar and dispersive components of the surface energy for each material (*i*) were calculated with the Wu harmonic mean method (Eq 1).[3,4] Literature values were used for the surface energy of water and glycerol.[8]

$$\begin{cases} \gamma_1(\cos\theta+1)=\dfrac{4\gamma_1^d\gamma_i^d}{\gamma_1^d+\gamma_i^d}+\dfrac{4\gamma_1^p\gamma_i^p}{\gamma_1^p+\gamma_i^p} \\ \gamma_2(\cos\theta+1)=\dfrac{4\gamma_2^d\gamma_i^d}{\gamma_2^d+\gamma_i^d}+\dfrac{4\gamma_2^p\gamma_i^p}{\gamma_2^p+\gamma_i^p} \end{cases} \quad (1)$$

where γ_1 = 72.8 mJ/m^2 (water), and γ_2 = 64.0 mJ/m^2 (glycerol)

The polar and dispersive components of the surface energy were used to calculate the total surface energy with Eq 2:[9]

$$\gamma_i = \gamma_i^d + \gamma_i^p \quad (2)$$

Table A2.10 Surface energies for thin films of the donor polymers the copolymer, and $PC_{71}BM$.

compound	γ_i^d (mj/m^2)	γ_i^p(mj/m^2)	γ_i^{total}(mj/m^2)
PTB7	14	7.9	21.9
PTB7-Th	15	6.4	21.4
PffBT4T-2OD	15	4.2	19.2
$PC_{71}BM$	18	10	28.0
copolymer	23	4.8	27.8
P3HT	18	2.8	20.8

A2.11.4 Interfacial Surface Energy Calculations

The interfacial surface energy between two components (i, j) was calculated with Eq 3:[9]

$$\gamma_{i\text{-}j} = \gamma_i + \gamma_j - 2\sqrt{\gamma_i \gamma_j}\, e^{-\beta\left(\gamma_i - \gamma_j\right)^2} \quad \beta = 1.15\times10^{-4} \quad (3)$$

Table A2.11 Interfacial surface energies for each donor polymer, $PC_{71}BM$, or the copolymer with each of the other blend components.

compound	$\gamma_{polymer\text{-}PCBM}$ (mj/m^2)	$\gamma_{donor\text{-}copolymer}$ (mj/m^2)	$\gamma_{PCBM\text{-}copolymer}$ (mj/m^2)
PTB7	0.586	0.548	-
PTB7-Th	0.688	0.647	-
PffBT4T-2OD	1.24	1.18	-
$PC_{71}BM$	-	-	0.000615

Table A2.12 Interfacial surface energies for each donor polymer, $PC_{71}BM$, or P3HT with each of the other blend components.

compound	$\gamma_{polymer\text{-}PCBM}$ (mj/m^2)	$\gamma_{donor\text{-}P3HT}$ (mj/m^2)	$\gamma_{PCBM\text{-}P3HT}$ (mj/m^2)
PTB7	0.586	0.0201	-
PTB7-Th	0.688	0.00601	-
PffBT4T-2OD	1.24	0.0438	-
$PC_{71}BM$	-	-	0.821

A2.11.5 Wetting Coefficient Calculations

The wetting coefficient for the copolymer as the third component (*k*) in a three-component mixture (*i*, *j*, *k*) was calculated with Eq 4:[10]

$$\omega_k = \frac{(\gamma_{k\text{-}j} - \gamma_{k\text{-}i})}{\gamma_{i\text{-}j}} \quad (4)$$

Table A2.13 Wetting coefficients (ω_c) for the copolymer or P3HT in various donor:$PC_{71}BM$ blends.

donor	copolymer ω_c	P3HT ω_c
PTB7	-0.94	1.37
PTB7-Th	-0.94	1.19
PffBT4T-2OD	-0.96	0.63

A2.11.6 Flory-Huggins Interaction Parameter (χ) Calculations

The Flory-Huggins interaction parameter (χ) between the copolymer and the different blend components can be estimated by taking advantage of the relationship between the surface energy (γ) and the Hildebrand solubility parameter (δ) (Eq 5):

$$\delta = A\sqrt{\gamma} \quad (5)$$

where A is a proportionality constant (e.g., 116×10^3 $m^{-1/2}$ for P3HT).[11,12]

The relationship between the Flory-Huggins interaction parameter (χ) and Hildebrandt solubility parameters of the copolymer and a blend component, *i*, is shown in Eq 6:

$$\chi_{copolymer,i} = \frac{V_0}{RT}\left(\delta_{copolymer} - \delta_i\right)^2 \quad (6)$$

where V_0 is the molar volume of the copolymer.

Substituting Eq 5 into Eq 6 yields Eq 7:[12]

$$X = K\left(\sqrt{\gamma_{copolymer}} - \sqrt{\gamma_i}\right)^2 \quad (7)$$

where $K=\frac{V_o A^2}{RT}$. Reporting the Flory-Huggins interaction parameter in terms of K enables numerical values to be generated without determining the molar volume of the copolymer segment (V_0).

Table A2.14 Flory-Huggins interaction parameters (χ) calculated from surface energies of the copolymer with various donors and acceptors.

material	γ_i^{total}(mj/m^2)	$\chi_{i,copolymer}K$
PTB7	21.9	0.36
PTB7-Th	21.4	0.50
PffBT4T-2OD	19.2	0.87
$PC_{71}BM$	28.0	0.0036
copolymer	27.8	-

A2.12 Differential Scanning Calorimetry

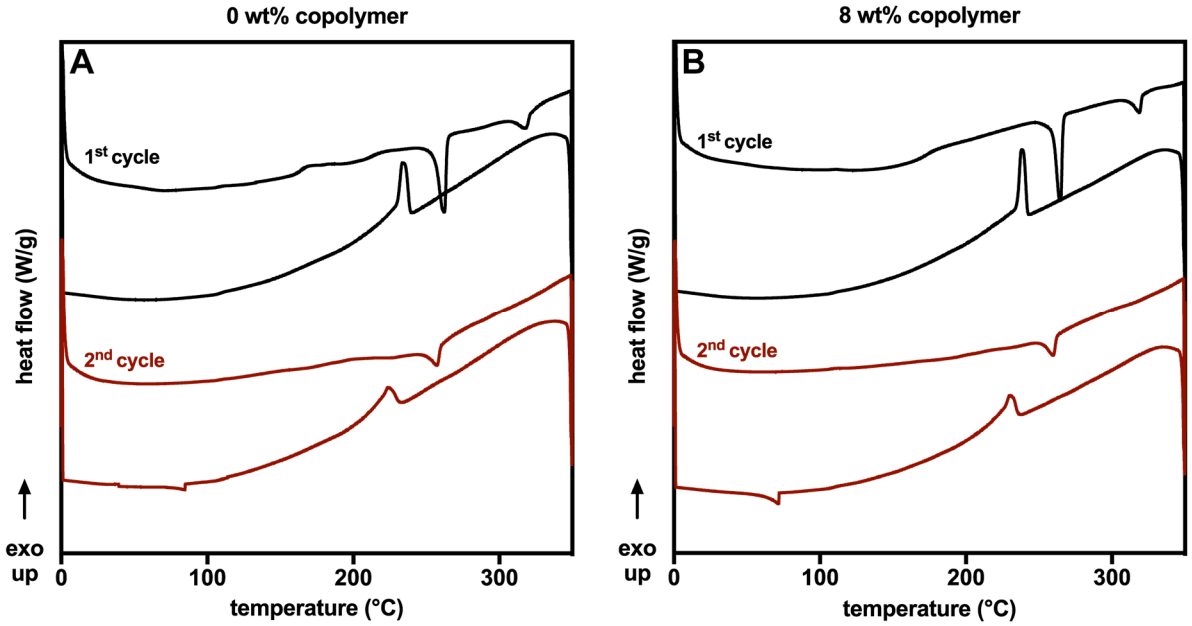

Figure A2.40 DSC thermograms **PffBT4T-2OD**:$PC_{71}BM$ blends with (A) 0 wt% or (B) 8 wt% **copolymer** showing both the first cycle (black) and the second cycle (red). The melting point for $PC_{71}BM$ (T_m = 318 °C) is evident only on the 1st heating cycle and $PC_{71}BM$ crystallization is not observed from the melt.

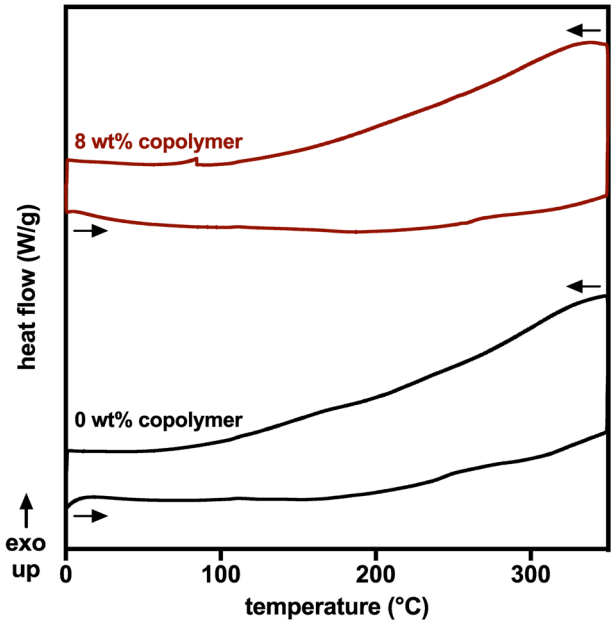

Figure A2.41 Thermogram of the 2nd cycle for $PC_{71}BM$ blended with 0 wt% (black) or 8 wt% (red) **copolymer**. Arrows indicate direction of heating (pointing right) and cooling (pointing left). No $PC_{71}BM$ crystallization is observed.

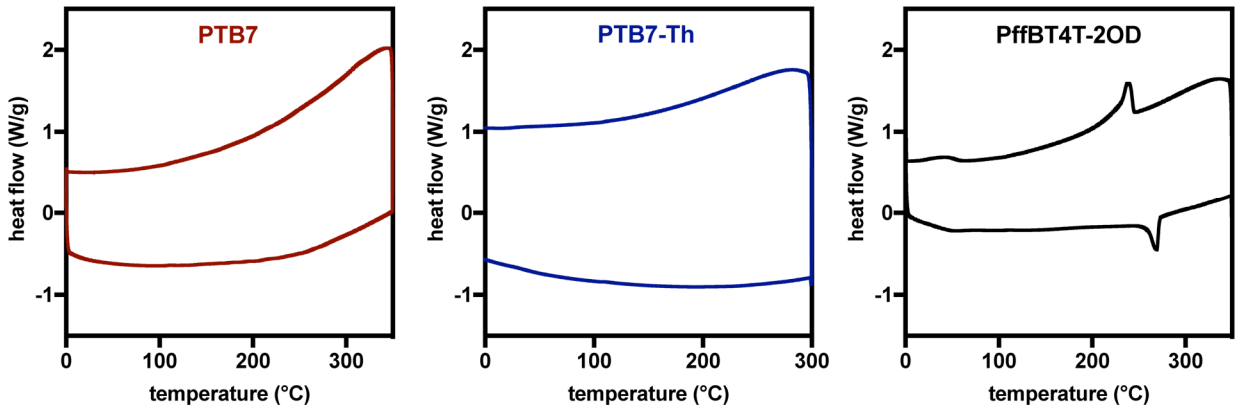

Figure A2.42 Thermograms of the 2nd cycle for neat **PTB7** (left), **PTB7-Th** (middle), and **PffBT4T-2OD** (right).

A2.13 Photocurrent and Device Performance Data

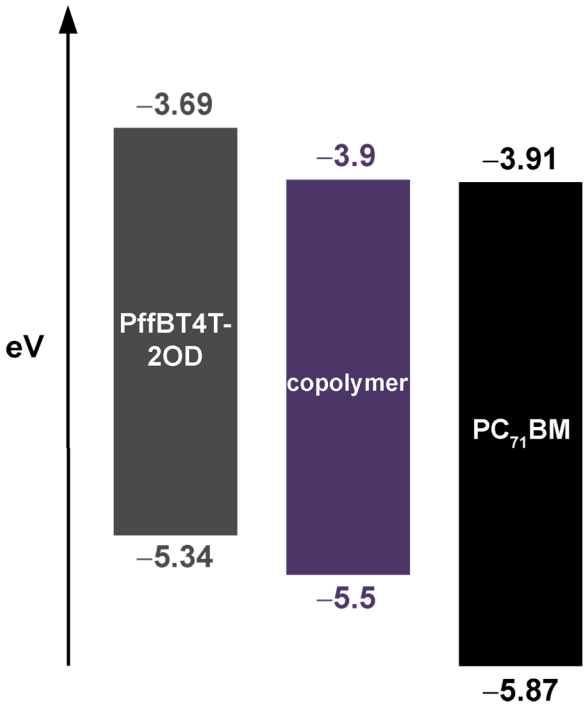

Figure A2.43 Energy level diagram for the active layer materials PffBT4T-2OD (grey),[13] copolymer (purple),[1] and $PC_{71}BM$ (black).[14]

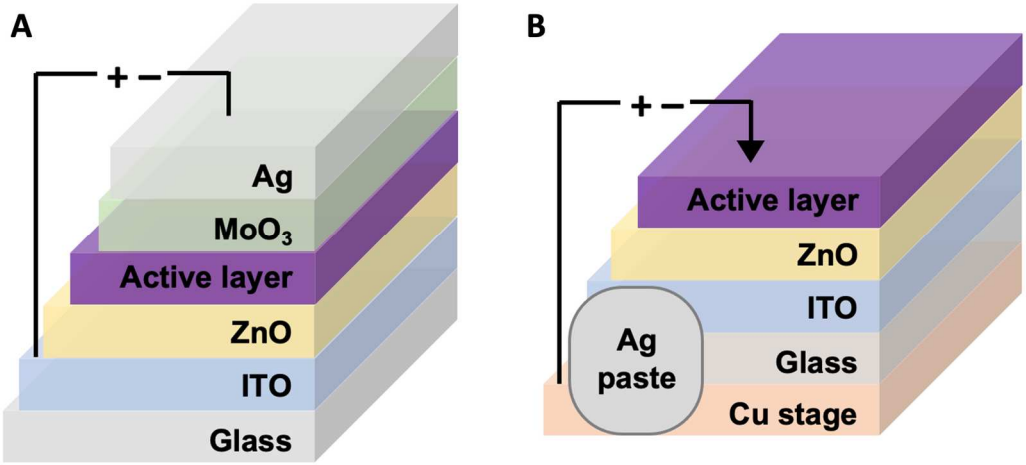

Figure A2.44 (A) Inverted structure of bulk heterojunction solar cell device and (B) structure of samples for triboindentation measurements; Ag paste connects the ITO layer to the copper stage.

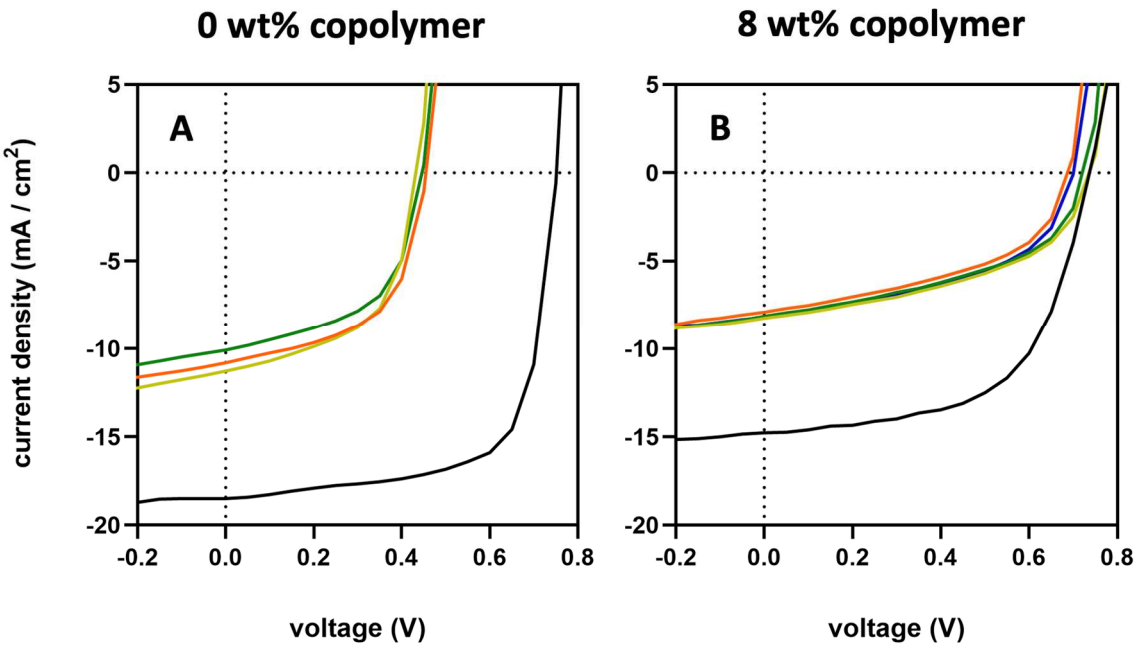

Figure A2.45 Representative current-voltage data for the bulk he terojunction devices. The device active layer is composed of **PffBT4T-2OD**:$PC_{71}BM$ blend with (A) 0 wt% or (B) 8 wt% **copolymer** additive. Thermal annealing at 150 °C for 0 min (black), 30 min (orange), 60 min (yellow), 90 min (green), 180 min (blue, B only).

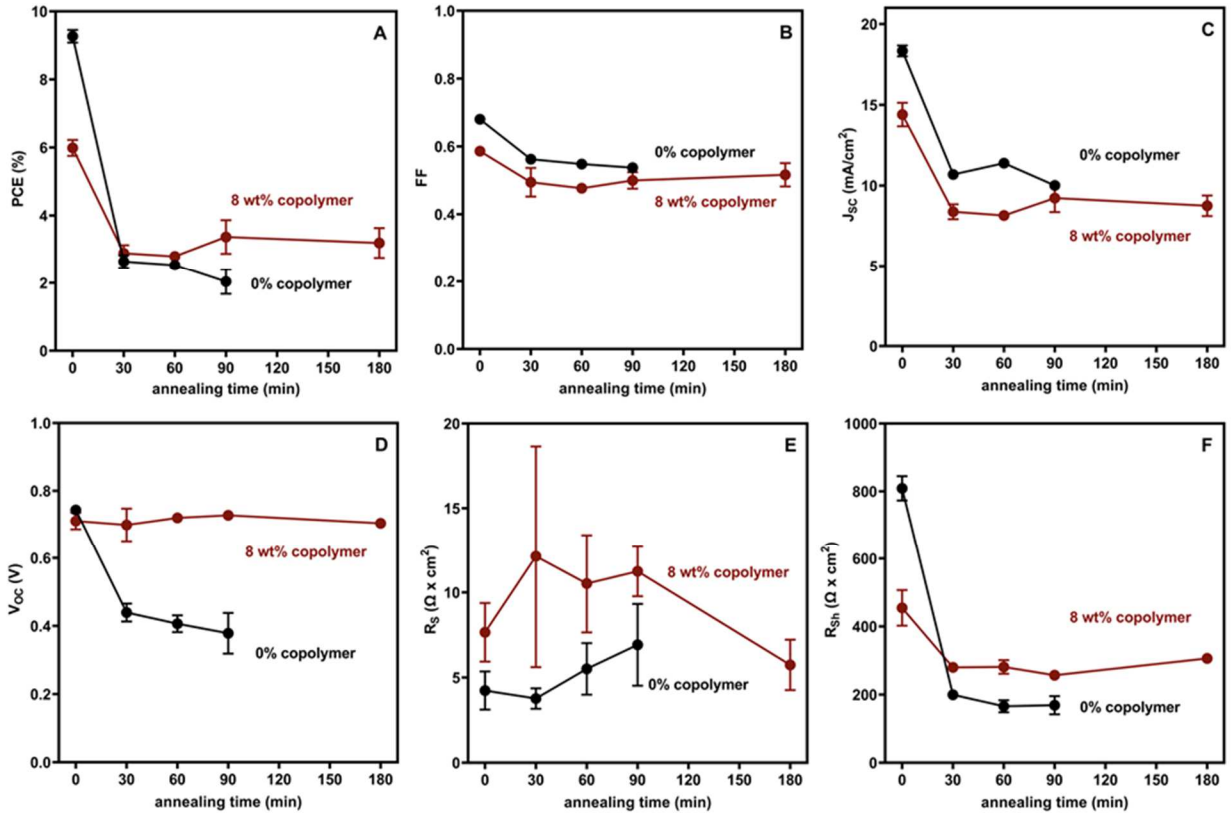

Figure A2.46 Performance data for bulk heterojunction devices with active layers composed **PffBT4T-2OD**:$PC_{71}BM$ blend with 0 wt% (black) or 8 wt% (red) **copolymer** additive. (A) power conversion efficiency (PCE), (B) fill factor (FF) (C) short circuit current (J_{SC}), (D) open circuit voltage (V_{OC}) (E) series resistance (R_S) (F) shunt resistance (R_{sh}) as a function of annealing time at 150 °C. Each data point represents an average of six measurements obtained from three different devices fabricated on two different substrates.

Table A2.15 All measured parameters for annealed bulk heterojunction devices with active layers composed **PffBT4T-2OD**:$PC_{71}BM$ blend with or without copolymer.

copolymer	Annealing temp & time	PCE (%)	FF	J_{SC} (mA/cm^2)	V_{OC} (V)	R_S (Ω x cm^2)	R_{Sh} (Ω x cm^2)
0 wt%	not annealed	9.3 ± 0.2	0.7 ± 0.0	18.3 ± 0.3	0.7 ± 0.0	4.2 ± 1.1	808.8 ± 36.1
	150 °C, 30min	2.6 ± 0.2	0.6 ± 0.0	10.7 ± 0.1	0.4 ± 0.0	3.8 ± 0.6	199.5 ± 7.4
	150 °C, 60min	2.5 ± 0.1	0.5 ± 0.0	11.4 ± 0.1	0.4 ± 0.0	5.5 ± 1.5	166.0 ± 17.7
	150 °C, 90min	2.0 ± 0.4	0.5 ± 0.0	10.0 ± 0.2	0.4 ± 0.1	6.9 ± 2.4	168.9 ± 26.6
	150 °C, 180min	-	-	-	-	-	-
8 wt%	not annealed	6.0 ± 0.2	0.6 ± 0.0	14.4 ± 0.7	0.7 ± 0.0	7.7 ± 1.7	454.4 ± 52.3
	150 °C, 30min	2.9 ± 0.2	0.5 ± 0.0	8.4 ± 0.5	0.7 ± 0.0	12.1 ± 6.5	279.8 ± 12.9
	150 °C, 60min	2.8 ± 0.1	0.5 ± 0.0	8.1 ± 0.2	0.7 ± 0.0	10.5 ± 2.9	281.3 ± 20.1
	150 °C, 90min	3.4 ± 0.5	0.5 ± 0.0	9.2 ± 0.9	0.7 ± 0.0	11.2 ± 1.5	256.7 ± 13.3
	150 °C, 180min	3.2 ± 0.4	0.5 ± 0.0	8.7 ± 0.6	0.7 ± 0.0	5.7 ± 1.5	306.1 ± 11.1
0 wt%	200 °C, 90min	0.6 ± 0.1	0.6 ± 0.0	1.8 ± 0.3	0.6 ± 0.0	55.3 ± 12.3	-
8 wt%		0.5 ± 0.0	0.5 ± 0.0	2.3 ± 0.2	0.5 ± 0.0	46.8 ± 4.6	-

A2.14 Optical Microscopy Images of Devices

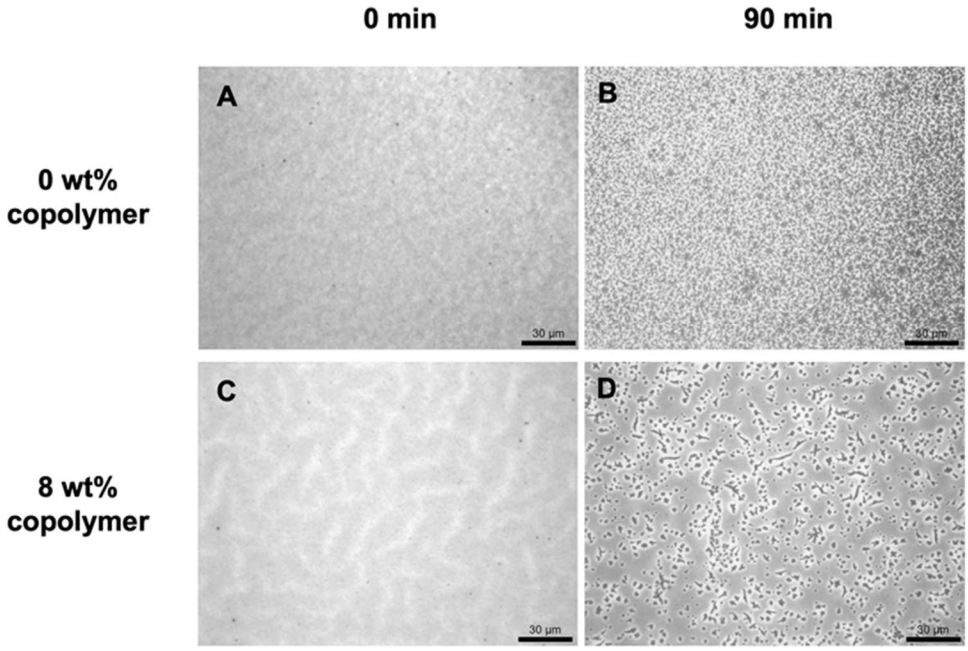

Figure A2.47 Optical microscopy images of **PffBT4T-2OD**:$PC_{71}BM$ devices with 3 vol% **DIO** annealed for 0 min (A, C) or 90 min (B, D) at 200 °C with 0 wt% (top) or 8 wt% (bottom) **copolymer**.

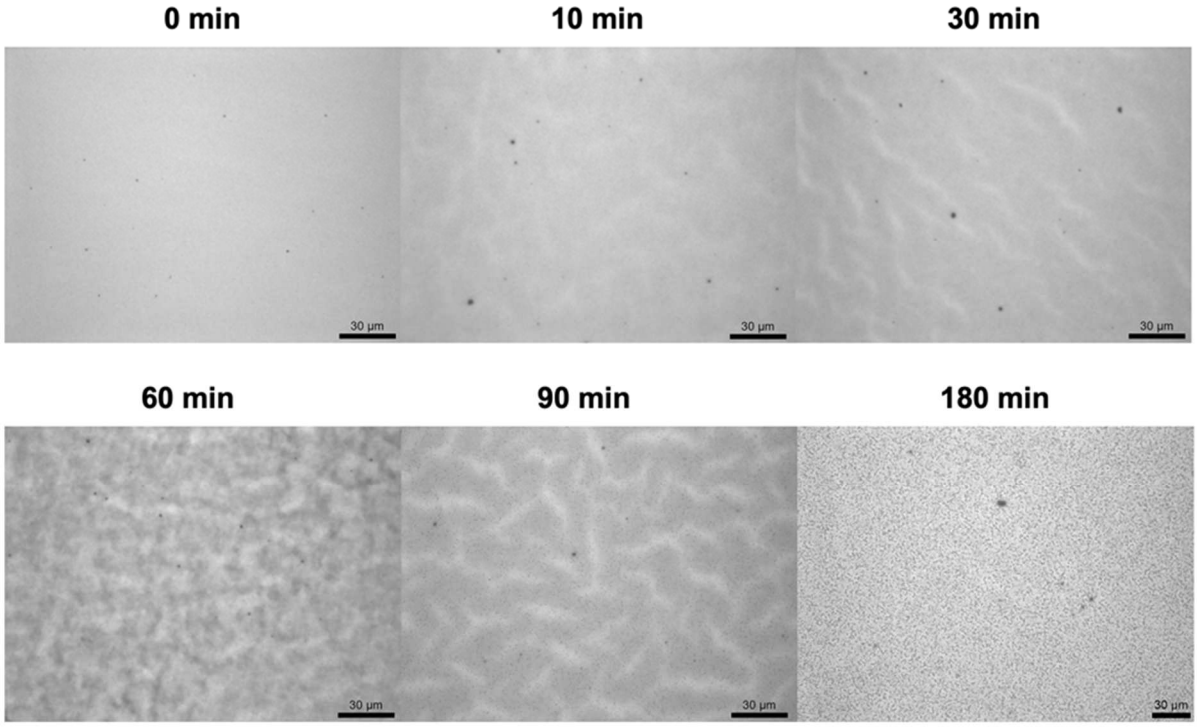

Figure A2.48 Optical microscopy images of **PffBT4T-2OD**:$PC_{71}BM$ devices with 3 vol% **DIO** annealed at 150 °C for a given time. Scale bars represent 30 µm.

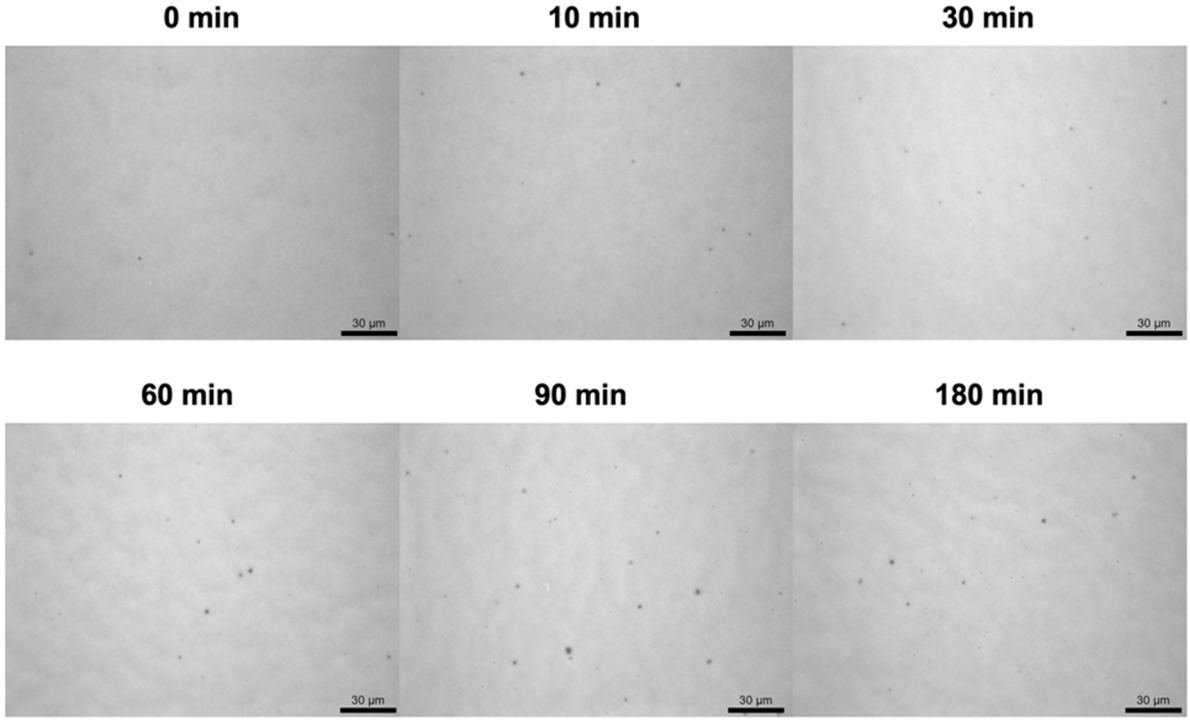

Figure A2.49 Optical microscopy images of **PffBT4T-2OD**:$PC_{71}BM$ devices with 8 wt% **copolymer** and 3 vol% **DIO** annealed at 150 °C for a given time. Scale bars represent 30 µm.

A2.15 UV-vis Spectroscopic Data

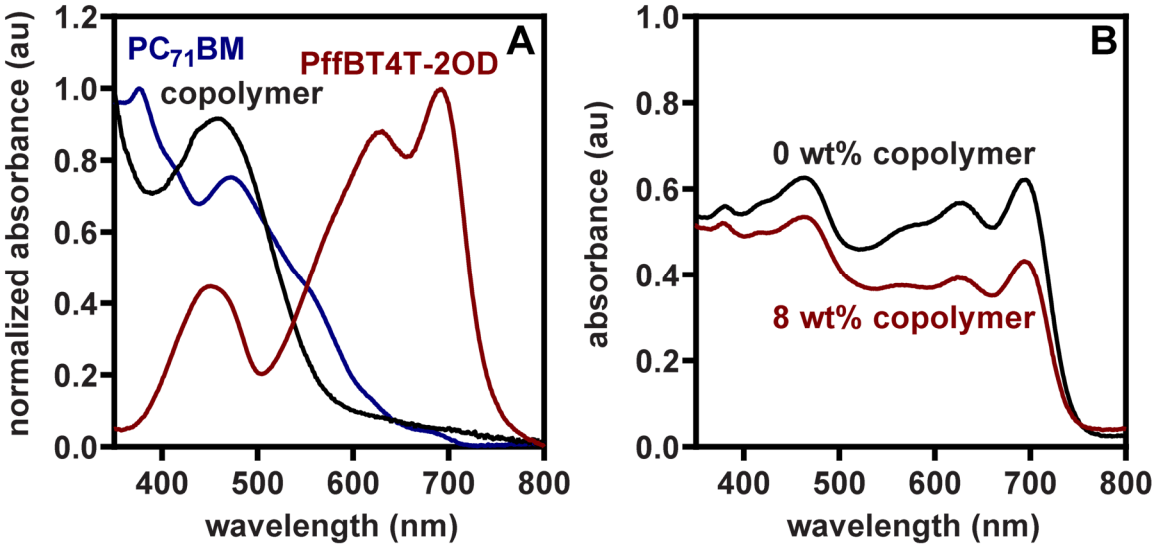

Figure A2.50 A) UV-vis spectra of films of PffBT4T-2OD (red), $PC_{71}BM$ (blue), and copolymer (black). B) Uncorrected UV-vis spectra of films of PffBT4T-2OD:$PC_{71}BM$ with 0 (black) or 8 (red) wt% copolymer.

A2.16 Energy-Filtered Transmission Electron Microscopy (EF-TEM) Images

A2.16.1 Thin Film Preparation

PEDOT:PSS coated substrates. An aliquot of PEDOT:PSS (100 µL, 3–4% suspension in H_2O) was spin-cast onto a glass substrate at 2000 RPM for 120 s.

Blends with DIO or DIO and copolymer. Blend solutions were prepared as described for optical microscopy (S27–S28). Solutions were spin-cast onto hot PEDOT:PSS-coated substrates (heated to 110 °C before loading onto spin-coater) at 800 RPM for 180 s. Immediately after spin-casting the films were delaminated from the substrates by removing a section of film at substrate edge with a razor blade then submerging the scraped substrate in deionized water at a ~15° angle. The delaminated film was lifted onto a 400-mesh Pure-C on copper TEM grid and dried for 24 h in vacuo before analysis.

A2.16.2 EF-TEM Images

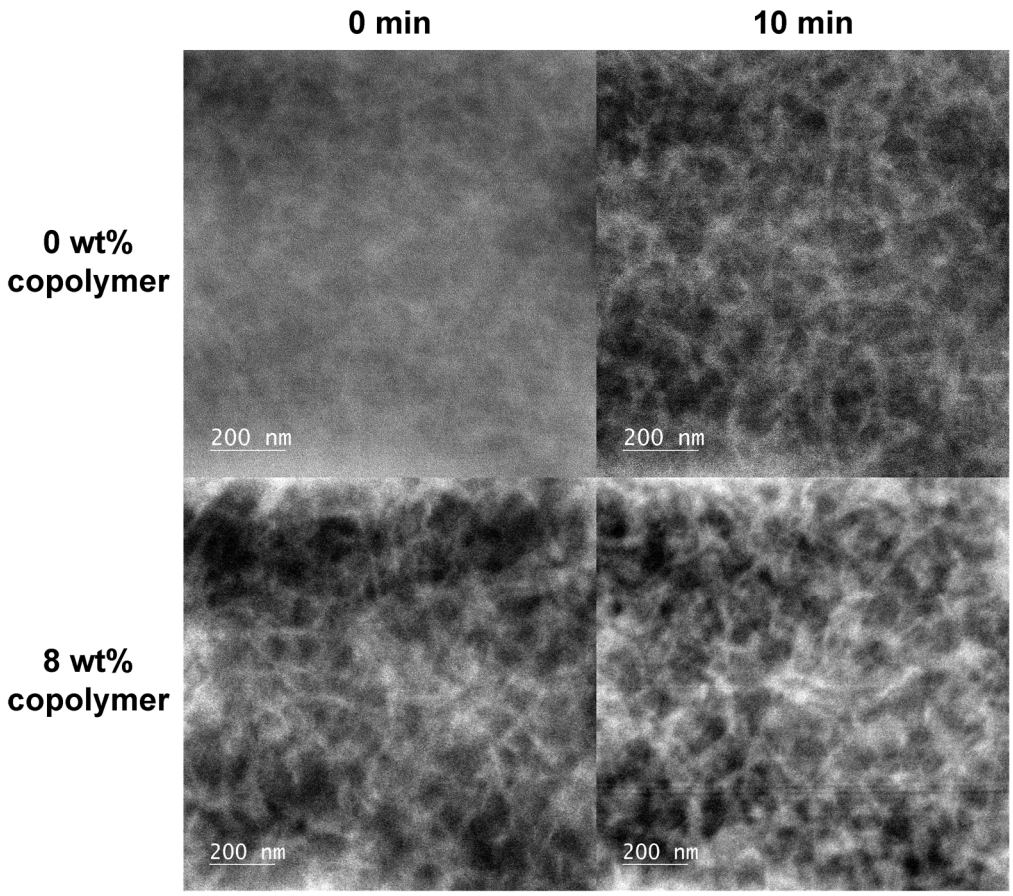

Figure A2.51 EF-TEM images for **PffBT4T-2OD**:$PC_{71}BM$ thin film blends with 0% (top) or with (bottom) 8 wt% **copolymer** and before (left) or after (right) annealing at 150 °C for 10 min.

A2.17 References

[1] Kong, C.; Song, B.; Mueller, E. A.; Kim, J.; McNeil, A. J. Random Copolymers Outperform Gradient and Block Copolymers in Stabilizing Organic Photovoltaics. *Adv. Funct. Mater*. **2019**, 1900467.

[2] Love, B. E.; Jones, E. G. The Use of Salicylaldehyde Phenylhydrazone as an Indicator for the Titration of Organometallic Reagents. *J. Org. Chem.* **1999**, *64*, 3755–3756.

[3] Wu, S. Calculation of Interfacial Tension in Polymer Systems. *J. Polym. Sci.: Part C* **1971**, *34*, 19–30.

[4] Wu, S. Polar and Nonpolar Interactions in Adhesion. *J. Adhesion* **1973**, *5*, 39–55.

[5] White, M. S.; Olson, D. C.; Shaheen, S. E.; Kopidakis, N.; Ginley, D. S. Inverted Bulk-heterojunction Organic Photovoltaic Device Using a Solution-derived ZnO Underlayer. *Appl. Phys. Lett.* **2006**, *89*, 143517.

[6] Kozub, D. R.; Vakhshouri, K.; Orme, L. M.; Wang, C.; Hexemer, A.; Gomez, E. D. Polymer Crystallization of Partially Miscible Polythiophene/Fullerene Mixtures Controls Morphology. *Macromolecules* **2011**, *44*, 5722–5726.

[7] Wong, M.; Hollinger, J.; Kozycz, L. M.; McCormick, T. M.; Lu, Y.; Burns, C. D.; Seferos, D. S. An Apparent Size-Exclusion Quantification Limit Reveals a Molecular Weight Limit in the Synthesis of Externally Initiated Polythiophenes. *ACS Macro Lett.* **2012**, *1*, 1266–1269.

[8] van Oss, C. J. *Interfacial Forces in Aqueous Media, 2nd Ed.* **2006**, Taylor & Frances Group: Boca Raton, FL, pp 96, 146.

[9] Li, D.; Neumann, A. W. Equation of State for Interfacial Tensions of Solid-liquid Systems. *Adv. Colloid Interface Sci.* **1992**, *39*, 299–345.

[10] Sumita, M.; Sakata, K.; Asai, S.; Miyasaka, K.; Nakagawa, H. Dispersion of Fillers and the Electrical Conductivity of Polymer Blends Filled with Carbon Black. *Polym. Bull.* **1991**, *25*, 265–271.

[11] Clark, M. D.; Jespersen, M. L.; Patel, R. J.; Leever, B. J. Predicting Vertical Phase Segregation in Polymer-Fullerene Bulk Heterojunction Solar Cells by Free Energy Analysis. *ACS Appl. Mater. Interfaces* **2013**, *5*, 4799−4807.

[12] Nilsson, S.; Bernasik, A.; Budkowski, A.; Moons, E. Morphology and Phase Segregation of Spin-Casted Films of Polyfluorene/PCBM Blends. *Macromolecules* **2007**, *40*, 8291−8301.

[13] Liu, Y.; Zhao, J.; Li, Z.; Mu, C.; Ma, W.; Hu, H.; Jiang, K.; Lin, H.; Ade, H.; Yan, H. Aggregation and Morphology Control Enables Multiple Cases of High-Efficiency Polymer Solar Cells *Nat. Commun.* **2014**, *5*, 5293.

[14] He, Y.; Zhao, G.; Peng, B.; Li, Y. High-Yield Synthesis and Electrochemical and Photovoltaic Properties of Indene-C70 Bisadduct. *Adv. Funct. Mater.* **2010**, *20*, 3383–3389.

Appendix 3 for Evaluating the Degree of Unsaturation Needed for Alkane Metathesis-Cyclodepolymerization of Polyethylene

A3.1 Materials

Flash chromatography was performed on SiliCycle silica gel (40–63 μm). Thin layer chromatography was performed on MACHEREY-NAGEL TLC plates (pre-coated with 0.20 mm silica gel 60 with fluorescent indicator UV254). $[Ir(COE)_2Cl]_2$, $[Ir(COD)Cl]_2$, and 2,6-Diisopropylphenylimidoneophylidene molybdenum(VI) bis(hexafluoro-t-butoxide) (**Mo-1**) (Schrock's catalyst) were purchased from Strem Chemicals. Grubbs 1st generation catalyst was purchased from Sigma Aldrich. Grubbs 2nd generation catalyst was purchased from Fisher Scientific. Catalyst **M1001** was generously donated by One Materials Inc. Catalysts ***t*BuPOCOP**, ***t*BuPCP**, and ***i*PrPCP** were generously donated by the Goldman group at Rutgers University. All Grignard reagents were titrated with salicylaldehyde phenylhydrazone to obtain the active Grignard concentration.[1] Tosyl chloride (10 g) was purified by dissolving in $CHCl_3$ (25 mL) and filtering. To the filtrate was added petroleum ether (125 mL) and the resulting suspension was filtered. The resulting filtrate was again filtered over decolorizing carbon and the solvent was removed in vacuo. The resulting solid was recrystallized from cold petroleum ether. 1,13-Tetradecadiene was purchased in 90% purity from Alfa Aesar and purified via column chromatography (silica gel, 100% petroleum ether). Low molecular weight polyethylene (PE, approx. M_n = 1.1 kg/mol) and *cis*-and-*trans*-1,4-polybutadiene (*ct*PBD, 36% *cis* 1,4; 55% *trans* 1,4; 9% vinyl 1,2, approx. M_w = 200 kg/mol) were purchased from Scientific Polymer Products. *Cis*-1,4-polybutadiene (*c*PBD, approx. M_w = 200 kg/mol) and a 0.5 M solution of 4-

pentenylmagnesium bromide in THF were purchased from Sigma Aldrich. All other reagent grade materials and solvents were purchased from Sigma Aldrich, Acros Organics, Alfa Aesar, or Fisher and used without further purification unless otherwise noted. THF and toluene were dried and deoxygenated using an MBraun solvent purification system with Innovative Technology columns composed of activated alumina, a copper catalyst, and molecular sieves under N_2. All solvents for reactions with Ir catalysts were dried over $CaCl_2$, distilled, degassed, and backfilled with Ar and all reactions with Ir catalysts were performed under Ar. Any water used for reactions or workups was deionized. The gloveboxes in which specified procedures were carried out were either a MBraun LABMaster 130 with an N_2 atmosphere and H_2O levels below 4.0 ppm or a MBraun LABStar 1200 with an Ar atmosphere and H_2O levels below 0.1 ppm. All air-free reactions were performed with standard Schlenk techniques. Compounds **S1** and **S2** were prepared using modified literature procedures.[2]

A3.2 General Experimental

NMR Spectroscopy: ^{1}H, ^{13}C and ^{31}P spectra for all compounds were acquired in deuterated solvents. For ^{1}H NMR spectra, a relaxation delay of 1 s was used for small molecules and 10 s was used for polymers. For ^{13}C NMR spectra, a relaxation delay of 0.1 s was used for small molecules and 1 s was used for polymers. All NMR spectra were recorded at room temperature unless otherwise noted. For ^{1}H and ^{13}C spectra, the chemical shift data are reported in units of δ (ppm) relative to tetramethylsilane (TMS) and referenced with residual solvent. For ^{31}P spectra, the chemical shift data are reported in units of δ (ppm) relative to 85% H_3PO_4 in H_2O. Multiplicities are reported as follows: singlet (s), doublet (d), doublet of doublets (dd), triplet (t), quartet (q), multiplet (m), broad signal (br).

Gas Chromatography: Gas chromatography was carried out with a Shimadzu GC 2010 containing a Shimadzu SHRX5 (crossbound 5% diphenyl–95% dimethyl polysiloxane; 15 m, 0.25 mm ID, 0.25 μm df) column and a FID detector or a Shimadzu QP20105 quadrupole mass spectrometer.

GC Method

Start temperature: 100 °C

Time at start temperature: 0 min

Ramp rate: 15 °C/min

End temperature: 270 °C

Time at end temperature: 35 min

Flow rate (He): 0.96 mL/min for column, 22.1 mL/min total

Split ratio: 11.3

Inlet temperature: 285 °C

Detector temperature: 285 °C

GCMS Method 1

Start temperature: 100 °C

Time at start temperature: 1 min

Ramp rate: 15 °C/min

End temperature: 270 °C

Time at end temperature: 10 min

Flow rate (He):

0.96 mL/min (column), 22.1 mL/min (total)

Split ratio: 11.3

Inlet temperature: 285 °C

MS cutoff time: 2 min

GCMS Method 2

Start temperature: 100 °C

Time at start temperature: 1 min

Ramp rate: 15 °C/min

End temperature: 270 °C

Time at end temperature: 35 min

Flow rate (He):

0.96 mL/min (column), 22.1 mL/min (total)

Split ratio: 11.3

Inlet temperature: 285 °C

MS cutoff time: 3.1 min

Size-Exclusion Chromatography (SEC): For SEC analysis, all polymers were dried under vacuum overnight, dissolved (~0.5 mg polymer/mL) in THF spiked with trace toluene (<1 vol%), with mild heating if necessary, and filtered through a 0.2 μm PTFE filter. SEC was performed with THF as the eluent at 40 °C and at a flow rate of 1.0 mL/min on two different instruments. The data presented correspond to the refractive index of the sample relative to THF with the maximum intensity normalized to 1.

SEC #1: Malvern Viscotek GPCMax VE2001 equipped with two Viscotek LT-5000L 8 mm (ID) × 300 mm (L) columns, and Viscotek TDA 305 and Viscotek PDA detectors. Apparent molar masses were calculated using 9 polystyrene standards from 377,400 g/mol to 580 g/mol.

SEC #2: Shimadzu GPC/SEC equipped with three Phenomenex Phenogel™ 10 µm Linear (2), LC 7.8 mm (ID) × 300 mm (L) columns and a Shimadzu SPD-M20A detector. Apparent molar masses were calculated using polystyrene standards from 1,000,000 g/mol to 92 g/mol.

High-temperature Size-Exclusion Chromatography (HT-SEC): For high-temperature SEC analysis, all polymers were suspended (~ 1 mg/mL) in 1,2,4-trichlorobenzene and placed in the heated sample holder (135 °C) for at least 1 h before analysis. SEC was performed with 1,2,4-trichlorobenzene as the eluent at 135 °C and a flow rate of 1.0 mL/min on a Tosoh HT-GPC8321 with one TSKgel 13 µm H_{HR} HT-RC 7.8 mm (ID) × 300 mm (L) and one TSKgel 20 µm GMH_{HR}-H(20) HT2 7.8 mm (ID) × 300 mm (L) column. The data presented correspond to the refractive index of the sample relative to 1,2,4-trichlorobenzene with the maximum intensity normalized to 1. Apparent molar masses were calculated using Tosoh TSKgel polystyrene standards 1,110,000 kg/mol to 589 kg/mol.

A3.3 Small Molecule Syntheses

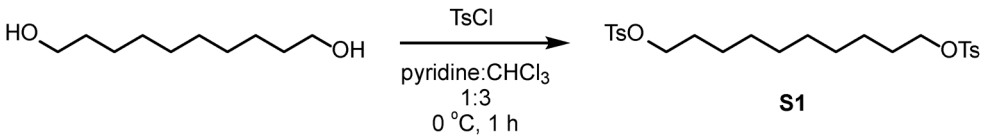

decane-1,10-diyl bis(4-methylbenzenesulfonate) (S1). A 20 mL vial was equipped with a stir bar and purged with N_2 for 15 min. To this vial was added 1,10-decanediol (506 mg, 2.90 mmol, 1.00 equiv), anhydrous pyridine (2.40 mL), and $CHCl_3$ (7.30 mL). The mixture was cooled to 0 °C and p-toluenesulfonyl chloride (1.22 g, 6.40 mmol, 2.20 equiv) was added gradually in small portions. The mixture was stirred at 0 °C for 1 h, after which time the mixture was homogeneous. The resulting solution was warmed to rt, diluted with DCM (4 mL), and washed successively with

10% aq HCl (4×5 mL) and 10% aq NaCl (1×10 mL). The organic layer was dried over $MgSO_4$, filtered, and the solvent was removed *in vacuo*. The resulting solid was recrystallized from EtOH to yield a colorless crystalline solid (1.212 g, 86%).

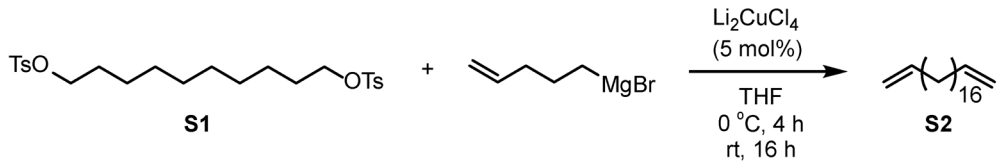

1,19-eicosadiene (S2).

preparation of Li_2CuCl_4: In an N_2-filled glovebox to a 10 mL Schlenk flask equipped with a stir bar was added Cu(II)Cl_2 (48.9 mg, 0.364 mmol, 1.00 equiv), LiCl (30.6 mg, 0.722 mmol, 1.98 equiv), and THF (3.65 mL). This mixture was stirred for 10 min at rt to yield a 0.10 M solution of Li_2CuCl_4.

preparation of diene: To an oven-dried 10 mL Schlenk flask equipped with a stir bar and septum was added **S1** (502 mg, 1.04 mmol, 1.00 equiv). To this flask was added anhydrous THF (5.20 mL) and a 0.10 M solution of Li_2CuCl_4 in THF (0.520 mL, 0.052 mmol, 0.050 equiv). The resulting mixture was cooled to 0 °C and stirred for 5 mins followed by addition of a 0.46 M solution of 4-pentenylmagnesium bromide in THF (6.8 mL, 3.1 mmol, 3.0 equiv). The resulting mixture was stirred for at 0 °C for 4 h and then at rt for 16 h. The reaction was slowly quenched with sat. NH_4Cl (5 mL). The aqueous layer was extracted with DCM (3 x 5 mL) and the combined organic layers were washed with brine (10 mL), dried over $MgSO_4$, filtered, and the solvent was removed *in vacuo*. The resulting colorless solid was purified via column chromatography (silica gel, 100% petroleum ether) to yield a colorless solid (244 mg, 84%).

A3.4 Polymer Syntheses

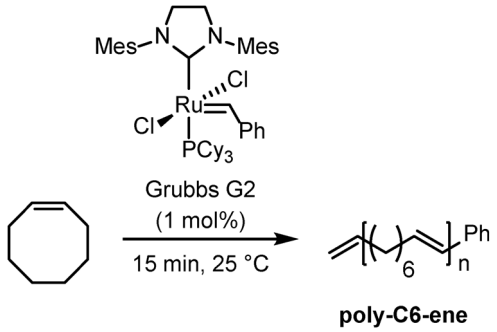

poly-C6-ene

poly-C6-ene. To an oven-dried Schlenk flask equipped with a stir bar and septum was added cyclooctene (0.300 mL, 2.30 mmol, 100. equiv) which was subsequently degassed by freeze-pump-thawing until no bubbling was observed (3 cycles). The flask contents were placed under a strong stream of N_2 and **Grubbs G2** (19 mg, 23 μmol, 1.0 equiv) was added via long-stem funnel. The flask was equipped with a septum and the contents were stirred at rt for 15 min. To the flask was added a 10% solution of ethyl vinyl ether (2 mL) in THF. The resulting mixture was sonicated for 5 min to dissolve the polymer and was then stirred vigorously at 50 °C for 30 min. The polymer was precipitated into cold MeOH (30 mL), the solvent was decanted and the resulting solid was transferred to a centrifuge tube. The solid was resuspended in MeOH (30 mL), sonicated for 10 min, centrifuged, and the supernatant was decanted (5x total). The resulting pellet was dried *in vacuo* to yield an off-white solid (196 mg, 77%).

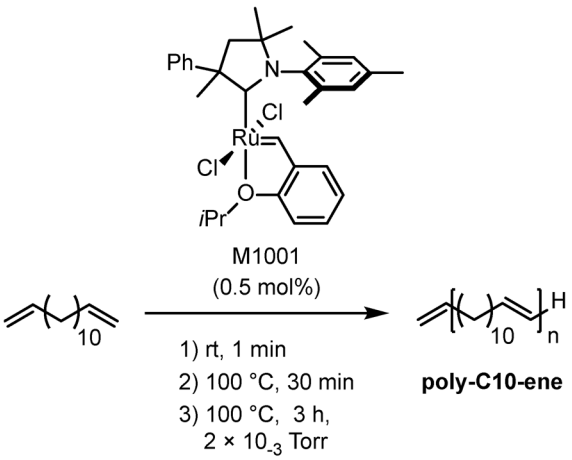

poly-C10-ene. To an oven-dried Schlenk flask equipped with a stir bar and septum was added 1,13-tetradecadiene (0.750 mL, 3.28 mmol, 1.00 equiv) which was subsequently degassed by freeze-pump-thawing until no bubbling was observed. The flask contents were placed under a strong stream of N_2 and **M1001** (10 mg, 16 μmol, 0.5 mol%) was added via a long-stem funnel with stirring. The flask contents were stirred for 1 min at rt, after which time they solidified. The solid was then heated to 100 °C and was stirred in the melt at 100 °C for 30 min under N_2. The flask was then evacuated (2×10^{-3} Torr) and the solution was stirred for 3 h at 100 °C in vacuo. The solution was cooled to rt, after which it solidified, and to the flask was added a 10% solution of ethyl vinyl ether in THF (2 mL). The resulting mixture was stirred vigorously at 45 °C for 35 min. The polymer was precipitated into cold MeOH (30 mL) to yield a viscous orange solid. The solid was resuspended in MeOH (30 mL), centrifuged, and the supernatant was decanted (4x total). The resulting pellet was dried in vacuo to yield a brownish white solid. The resulting solid was dissolved in a minimal amount of chloroform and passed through a silica plug to yield a white solid (366 mg, 81%).

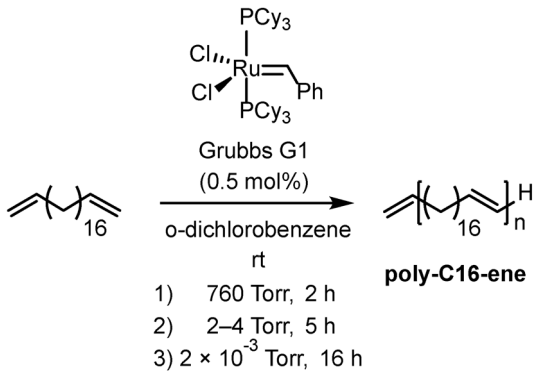

poly-C16-ene.

catalyst stock solution: In a N_2-filled glovebox into a 20 mL vial was weighed **Grubbs G1** (7.2 mg, 8.8 μmol, 0.5 mol%). To this vial was added *o*-dichlorobenzene (*o*-DCB) (8.75 mL) to give a 0.001 M solution. The vial was capped with a septum, sealed with copper wire, and removed from the glovebox.

polymerization: To a 25 mL oven-dried Schlenk tube equipped with a stir bar was added **S2** (101 mg, 0.359 mmol, 200. equiv) in DCM (5 mL) and the solvent was removed in vacuo. To this flask was added a 0.001 M solution of **Grubbs G1** in *o*-DCB (1.80 mL, 1.80 μmol, 1.0 equiv). The reaction was stirred at rt under N_2 for 2 h, then under low vacuum (~2-4 Torr, fluctuating) for 5 h, and under high vacuum 2.0 x 10^{-3} Torr for 16 h. Then, to the reaction flask was added toluene (2 mL) to dissolve reaction products, then ethyl vinyl ether (1.0 mL) was added and the reaction mixture was stirred vigorously for 5 min. In a centrifuge tube, the polymer was precipitated into cold MeOH (30 mL) to yield a light brown solid. The solid was resuspended in MeOH, centrifuged, and the supernatant was decanted (4x total). The resulting pellet was dried *in vacuo* to yield a white solid (58 mg, 29%).

A3.5 Nuclear Magnetic Resonance Spectra

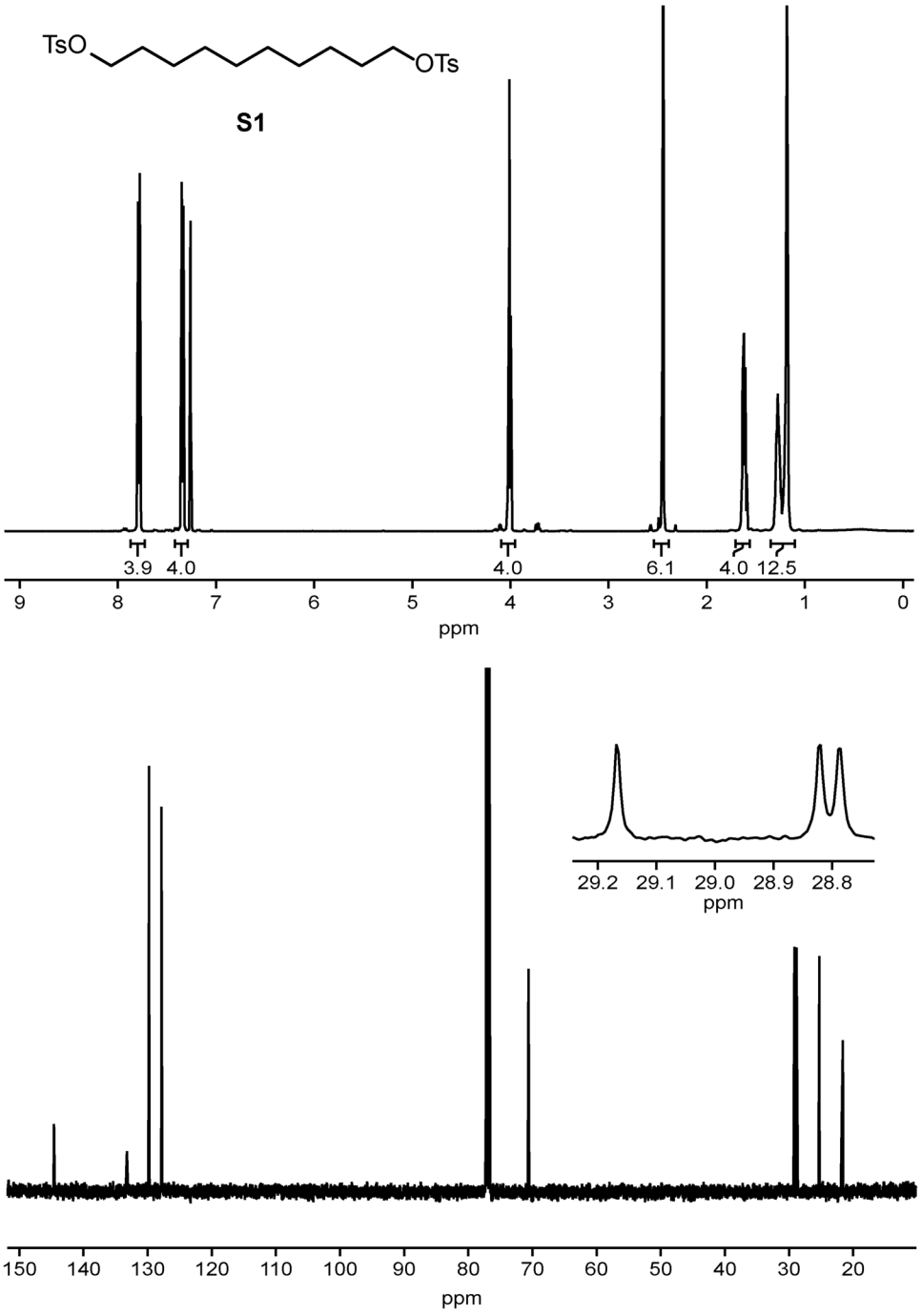

Figure A3.1 NMR spectra for **S1**. ^{1}H NMR (500 MHz, $CDCl_3$) δ 7.78 (d, J = 8.0 Hz, 4H), 7.34 (d, J = 8.0 Hz, 4H), 4.01 (t, J = 6.5 Hz, 4H), 2.45 (s, 6H), 1.68–1.53 (m, 4H), 1.35–1.10 (m, 12H). ^{13}C NMR (126 MHz, $CDCl_3$) δ 144.60, 133.23, 129.77, 127.85, 70.63, 29.17, 28.82, 28.79, 25.28, 21.62.

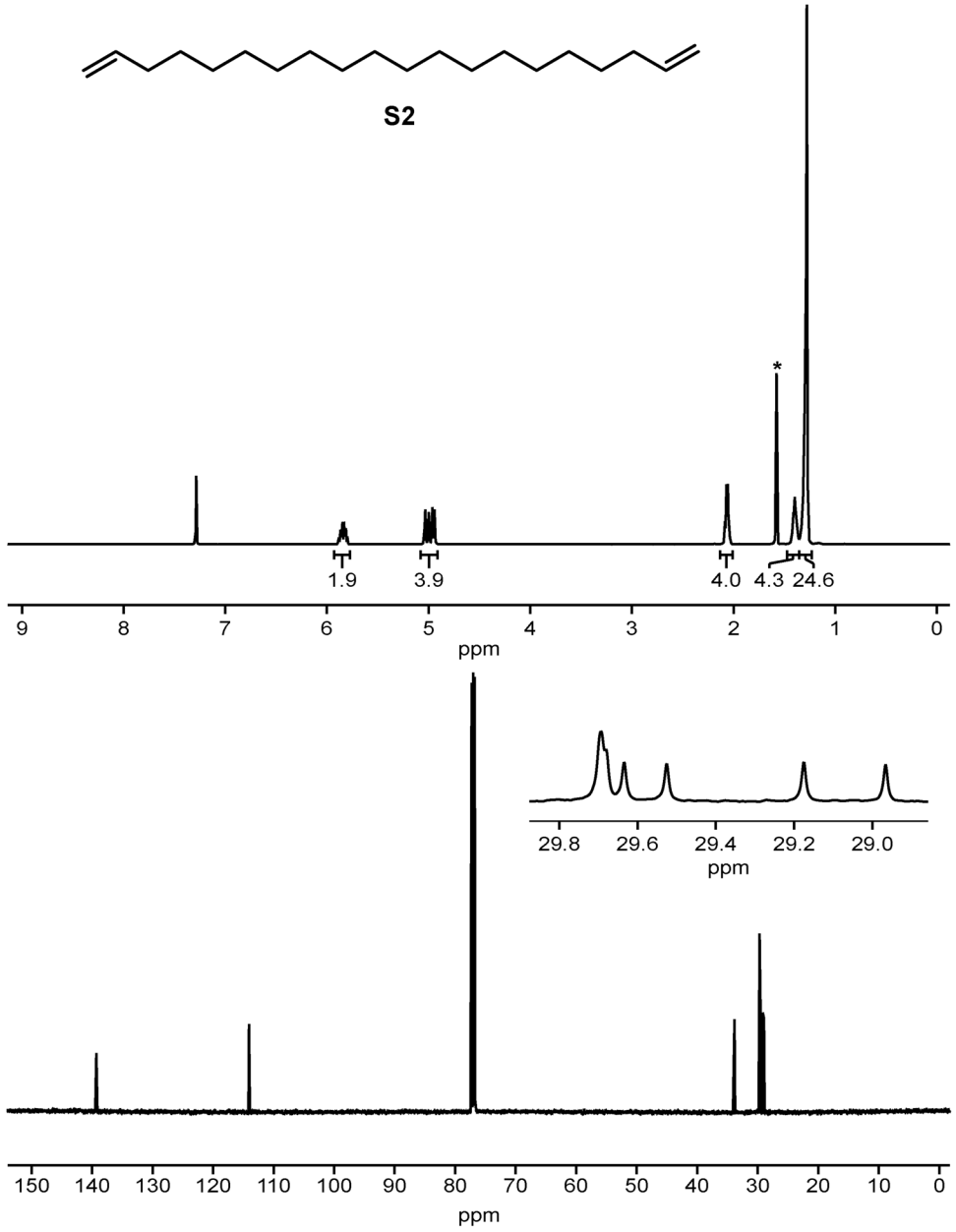

Figure A3.2 NMR spectra for **S2.** ^{1}H NMR (500 MHz, $CDCl_3$) δ 5.84 (ddt, J = 16.9, 10.2, 6.7 Hz, 2H), 4.98 (dd, J = 16.8, 10.1 Hz, 4H), 2.06 (q, J = 7.2 Hz, 4H), 1.48–1.35 (m, 4H), 1.35–1.21 (m, 24H). ^{13}C NMR (126 MHz, $CDCl_3$) δ 139.29, 114.07, 33.84, 29.69, 29.68, 29.63, 29.53, 29.18, 28.97.

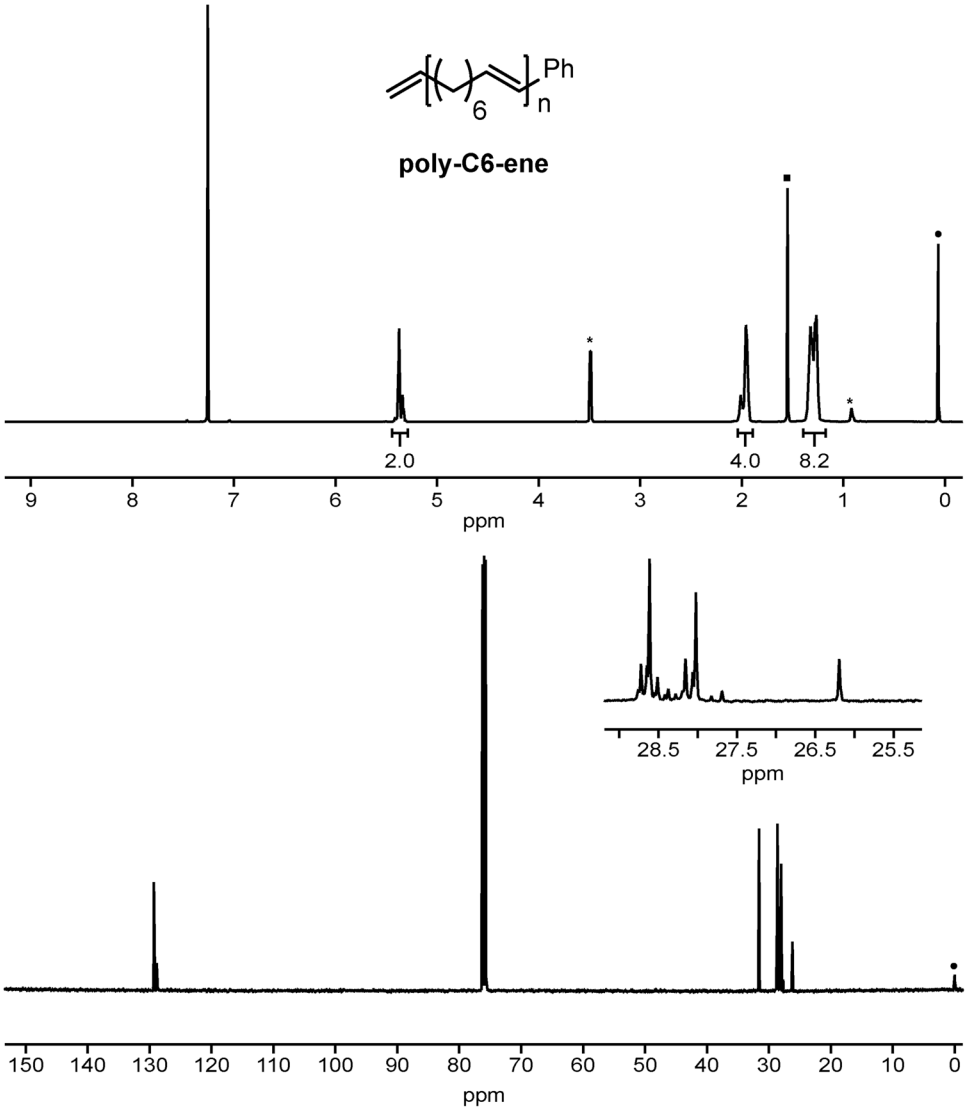

Figure A3.3 NMR spectra for **poly-C6-ene**.[1]H NMR (500 MHz, $CDCl_3$) δ 5.44–5.30 (m, 2H), 2.05–1.89 (m, 4H), 1.41–1.12 (m, 8H). [13]C NMR (126 MHz, $CDCl_3$) δ 129.34, 129.32, 129.30, 128.86, 128.84, 128.82, 31.59, 28.72, 28.61, 28.51, 28.38, 28.16, 28.06, 28.02, 27.69, 26.19. *unknown impurity, ■ H_2O, •grease

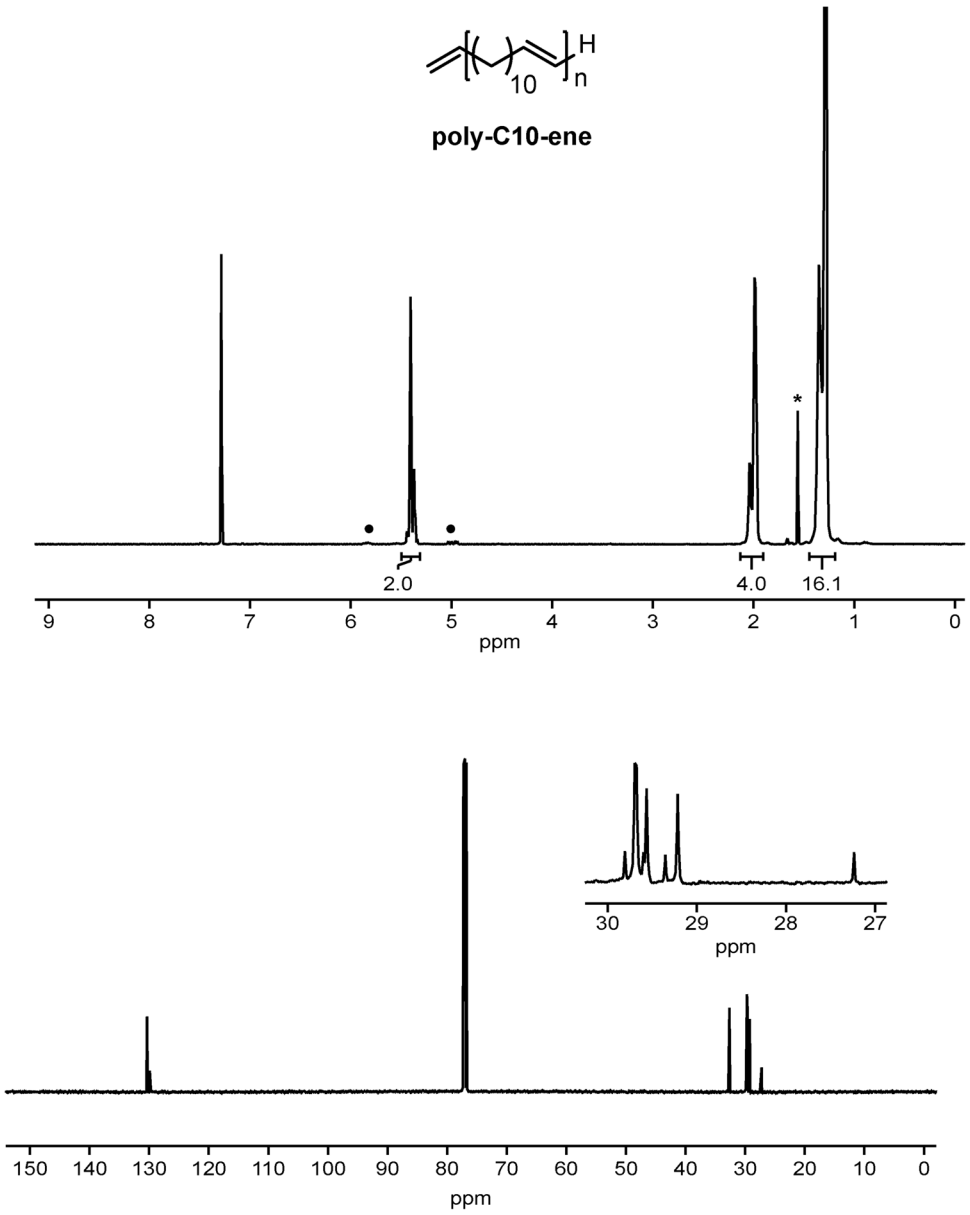

Figure A3.4 NMR spectra for **poly-C10-ene**. ^{1}H NMR (500 MHz, $CDCl_3$) δ 5.50–5.31 (m, 2H), 2.12–1.91 (m, 4H), 1.44–1.20 (m, 16H). ^{13}C NMR (126 MHz, $CDCl_3$) δ 130.35, 129.89, 32.64, 29.80, 29.70, 29.68, 29.60, 29.56, 29.35, 29.21, 27.24. *H_2O, •terminal alkene end-group

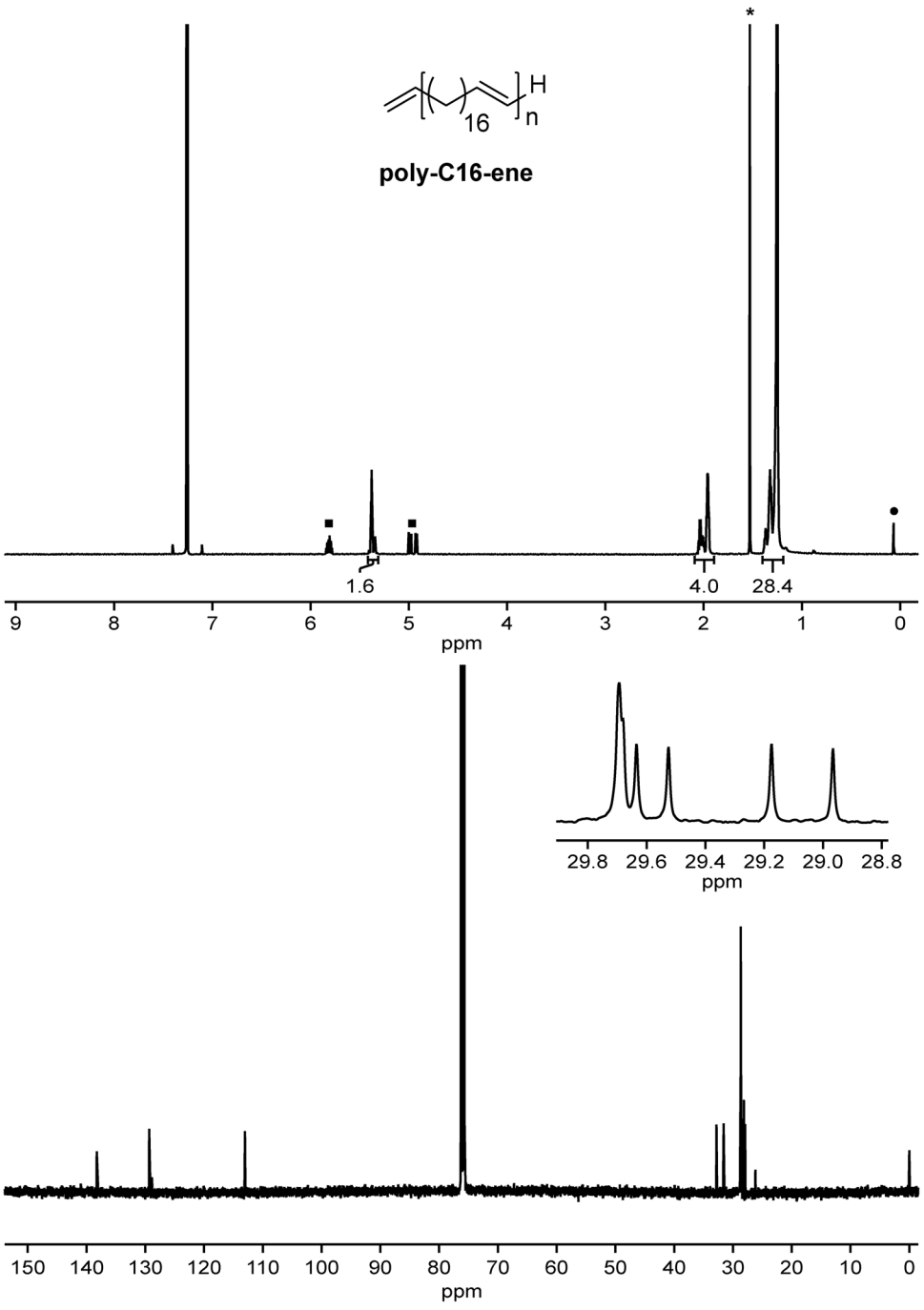

Figure A3.5 NMR spectra for **poly-C16-ene.** ^{1}H NMR (700 MHz, $CDCl_3$) δ 5.42–5.29 (m, 2H), 2.09–1.89 (m, 4H), 1.42–1.18 (m, 28H). ^{13}C NMR (126 MHz, $CDCl_3$) δ 138.25, 129.33, 128.87, 113.04, 32.81, 31.59, 28.76, 28.68, 28.65, 28.61, 28.56, 28.52, 28.50, 28.31, 28.15, 27.93, 26.19. ■ terminal alkene end-groups, *H_2O, •grease

A3.6 Size-Exclusion Chromatography Traces

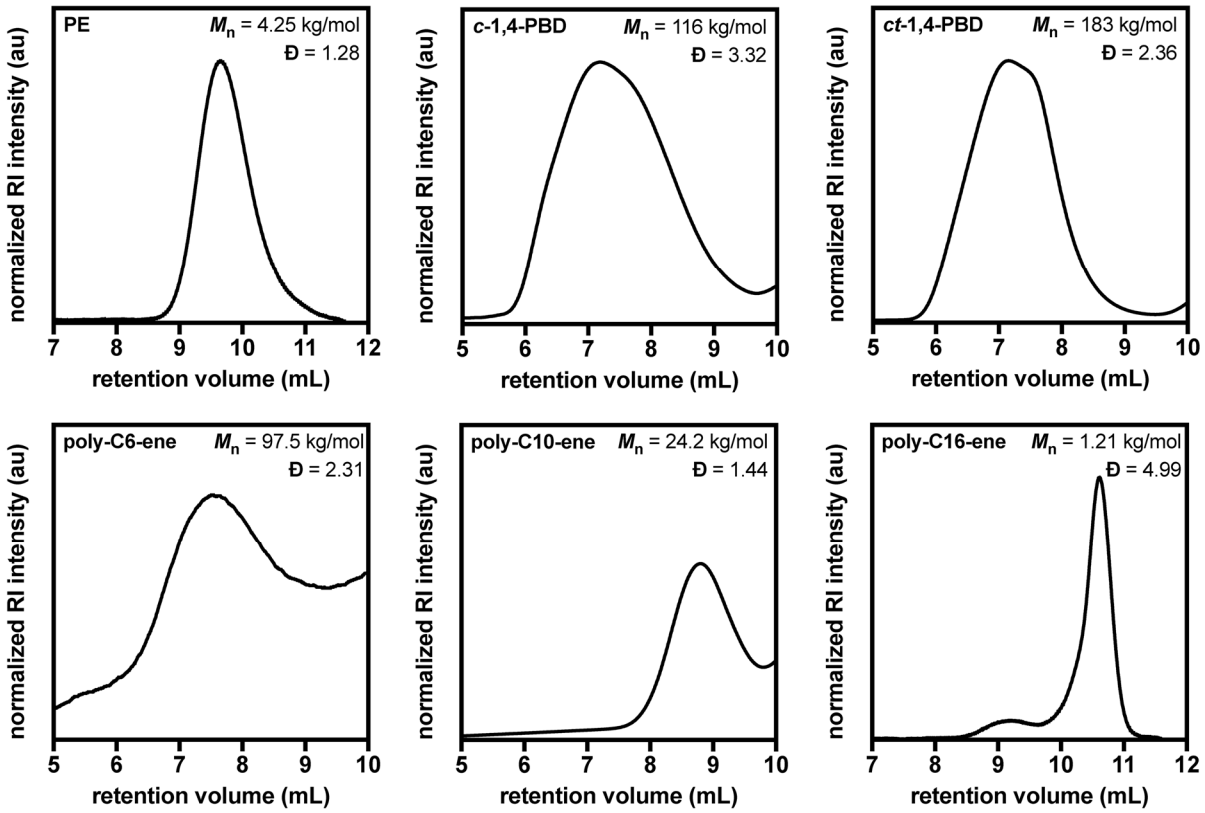

Figure A3.6 SEC traces for all commercial (top) and synthesized (bottom) polymers used in this work.

A3.7 PE Dehydrogenations and Data

A3.7.1 General Procedures

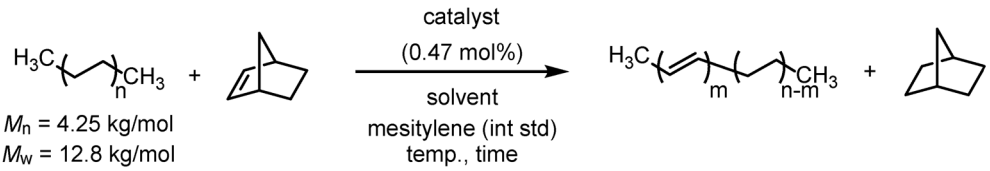

This modified procedure is based on a previous literature report for dehydrogenation of PE.[3]

Dehydrogenation with NBE. In an Ar-filled glovebox to a J-Young NMR tube was added polyethylene (~66 mg, ~2.3 mmol repeat units, 1.0 equiv), a 0.10 M stock solution of Ir-catalyst (~ 0.1 mL, 0.7 mol% or 0.005 equiv) in d_6-benzene or d_{10}-p-xylene, a 1.0 M stock solution of norbornene (~0.15 mL, 0.15 mmol, 0.066 equiv) in d_6-benzene or d_{10}-p-xylene, mesitylene (~33 µL, 0.24 mmol, 0.10 equiv - int standard), and d_6-benzene or d_{10}-p-xylene (~0.5 mL). The tube was sealed, removed from the glovebox and stirred at 150 °C or 175 °C for 18–54 h.

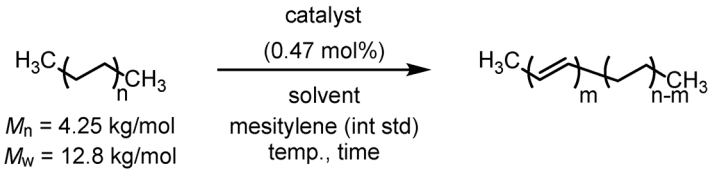

Acceptorless dehydrogenation. In an Ar-filled glovebox to a J-Young NMR tube was added polyethylene (~66 mg, ~2.3 mmol repeat units, 1.0 equiv), a 0.10 M stock solution of Ir-catalyst in d_6-benzene (~0.11 mL, 0.70 mol% or 0.0047 equiv), mesitylene (~33 µL, 0.23 mmol, 0.10 equiv - int standard), and d_6-benzene (~0.5 mL). The tube was sealed, removed from the glovebox and stirred at 150 °C for 54 h.

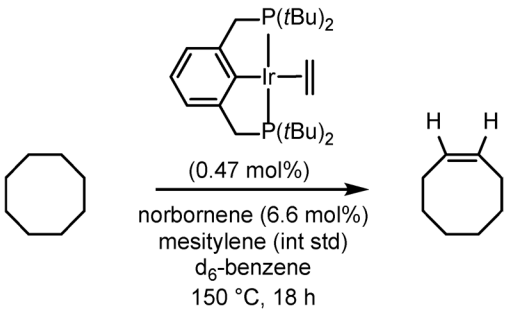

Dehydrogenation of cyclooctane (COA). In an Ar-filled glovebox to a J-Young NMR tube was added cyclooctane (250 µL, 1.86 mmol, 1.00 equiv), a 0.010 M stock solution of ***t*BuPCPIr** in d_6-benzene (871 µL, 0.00871 mmol, 0.070 mol% or 0.00469 equiv), and a 1.0 M solution of norbornene in d_6-benzene (123 µL, 0.123 mmol, 0.066 equiv), and mesitylene (26 µL, 0.19 mmol, 0.10 equiv - int std). The tube was sealed, removed from the glovebox and stirred at 150 °C for 18 h.

Table A3.1 Condition optimization for dehydrogenation of PE

entry	substrate	catalyst	solvent	H_2 acceptor	eq. H_2 acceptor	temp. (°C)	time (h)	dehydrogenation (%)[a]	H_2 acceptor conversion (%)
1	PE	tBuPOCOP	d_6-benzene	NBE	0.066	150	44	2.4	70
2	PE	tBuPOCOP	d_6-benzene	NBE	0.066	175	54	3.6	83
3	PE	tBuPOCOP	d_6-benzene	NBE	0.132	175	54	1.6	34
4	PE	tBuPOCOP	d_6-benzene	TBE	0.066	150	24	2.8	82
5	PE	tBuPCP	d_6-benzene	NBE	-	150	16	0.4	-
6	PE	tBuPCP	d_6-benzene	NBE	0.066[b]	150	54	2.2	quant
7	PE	iPrPCP	d_6-benzene	NBE	-	150	16	0.2	-
8	PE	iPrPCP	d_6-benzene	NBE	0.061[b]	150	54	0.4	quant
9	PE	tBuPCP	d_{10}-*p*-xylene	NBE	0.066	150	24	10.9	quant
10	PE	iPrPCP	d_{10}-*p*-xylene	NBE	0.066	150	24	2.0	quant
11	-	tBuPCP	d_6-benzene	NBE	0.066	150	24	-	47
12	COA	tBuPCP	d_6-benzene	NBE	0.066	150	18	4.8	quant

[a] *from ^{1}H NMR*
[b] *added after 16 h*

A3.7.2 NMR Data for PE Dehydrogenation Experiments

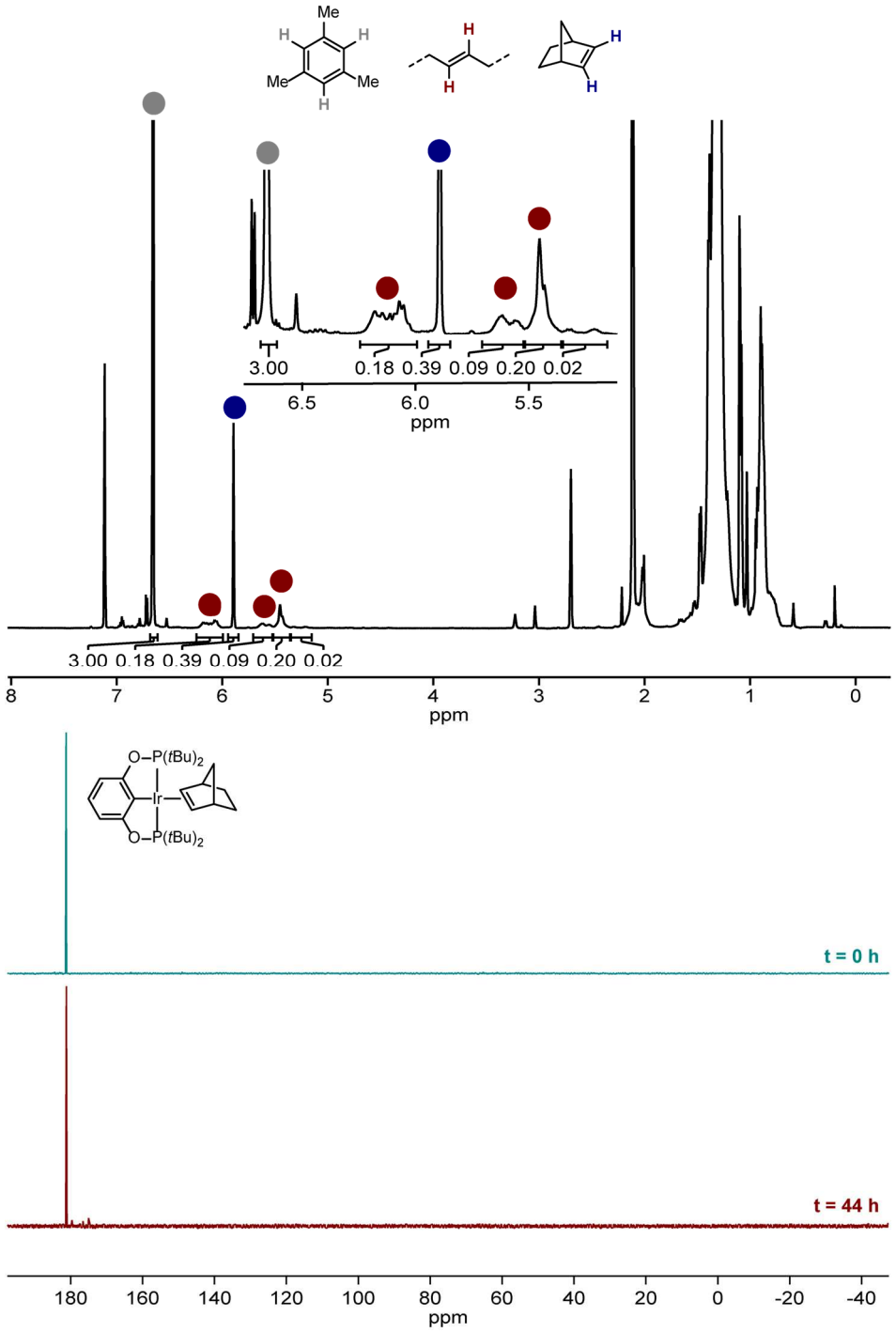

Figure A 3.7 ^{1}H and ^{31}P NMR spectra for **Table A1.1, entry 1**. ^{1}H NMR (600 MHz, C_6D_6, 70 °C) δ 6.66 (s, 3H), 6.25–6.00 (m, 0.18H, PE HC=CH), 5.95–5.84 (m, 0.39H, NBE HC=CH), 5.71–5.52 (m, 0.09H, PE HC=CH), 5.51–5.37 (m, 0.02H, PE HC=CH). ^{31}P NMR, t = 0 h (243 MHz, C_6D_6, 70 °C) δ 181.19. ^{31}P NMR, t = 44 h (243 MHz, C_6D_6, 70 °C) δ 181.19, 179.64, 176.56, 175.05 (d, J = 12.8 Hz).

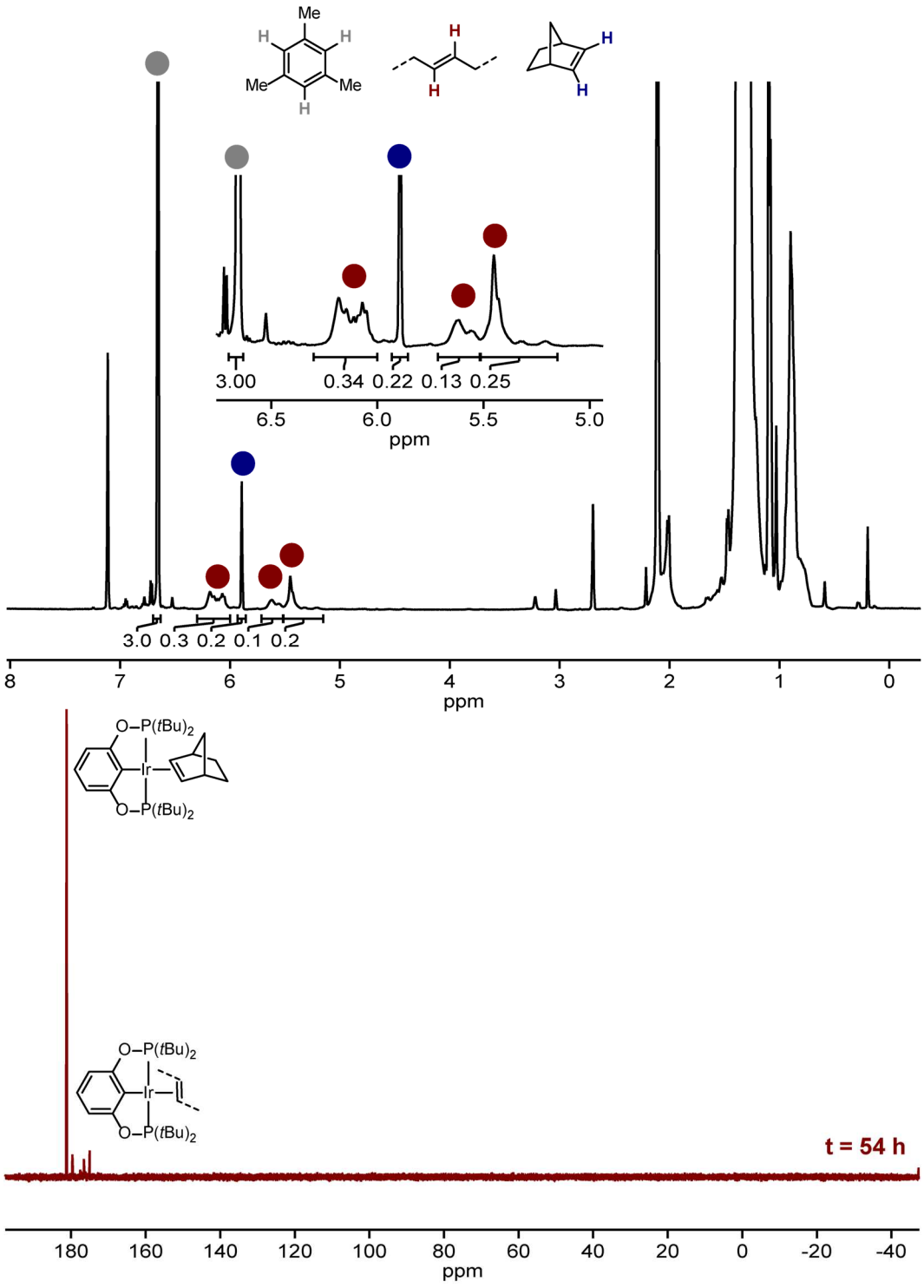

Figure A3.8 ^{1}H and ^{31}P NMR spectra for **Table A1.1, entry 2**. ^{1}H NMR (600 MHz, C_6D_6, 70 °C) δ 6.66 (s, 3H), 6.31–6.00 (m, 0.34H, PE HC=CH), 5.94–5.85 (m, 0.22H, NBE HC=CH), 5.72–5.52 (m, 0.13H, PE HC=CH), 5.51–5.14 (m, 0.25H, PE HC=CH. ^{31}P NMR, t = 54 h (243 MHz, C_6D_6, 70 °C) δ 181.26, 179.65, 176.56, 175.04 (d, J = 13.1 Hz).

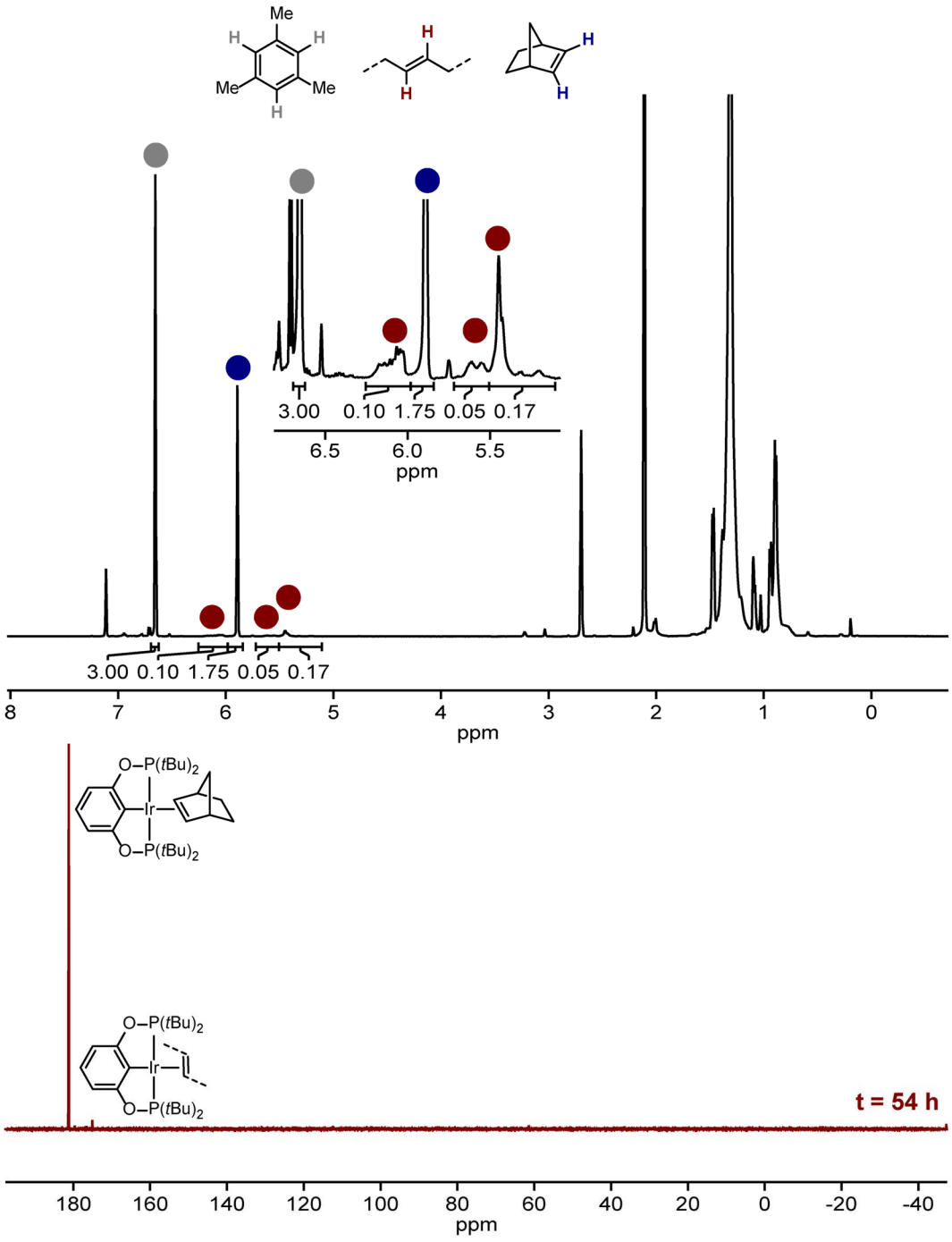

Figure A3.9 ^{1}H and ^{31}P NMR spectra for **Table A1.1, entry 3**. ^{1}H NMR (600 MHz, C_6D_6, 70 °C) δ 6.66 (s, 3H), 6.24–5.99 (m, 0.1H, PE HC=CH), 5.99–5.83 (m, 1.75H, NBE HC=CH), 5.71–5.51 (m, 0.05H, PE HC=CH), 5.51–5.09 (m, 0.17H, PE HC=CH). ^{31}P NMR, t = 54 h (243 MHz, C_6D_6, 70 °C) δ 181.17, 175.05.

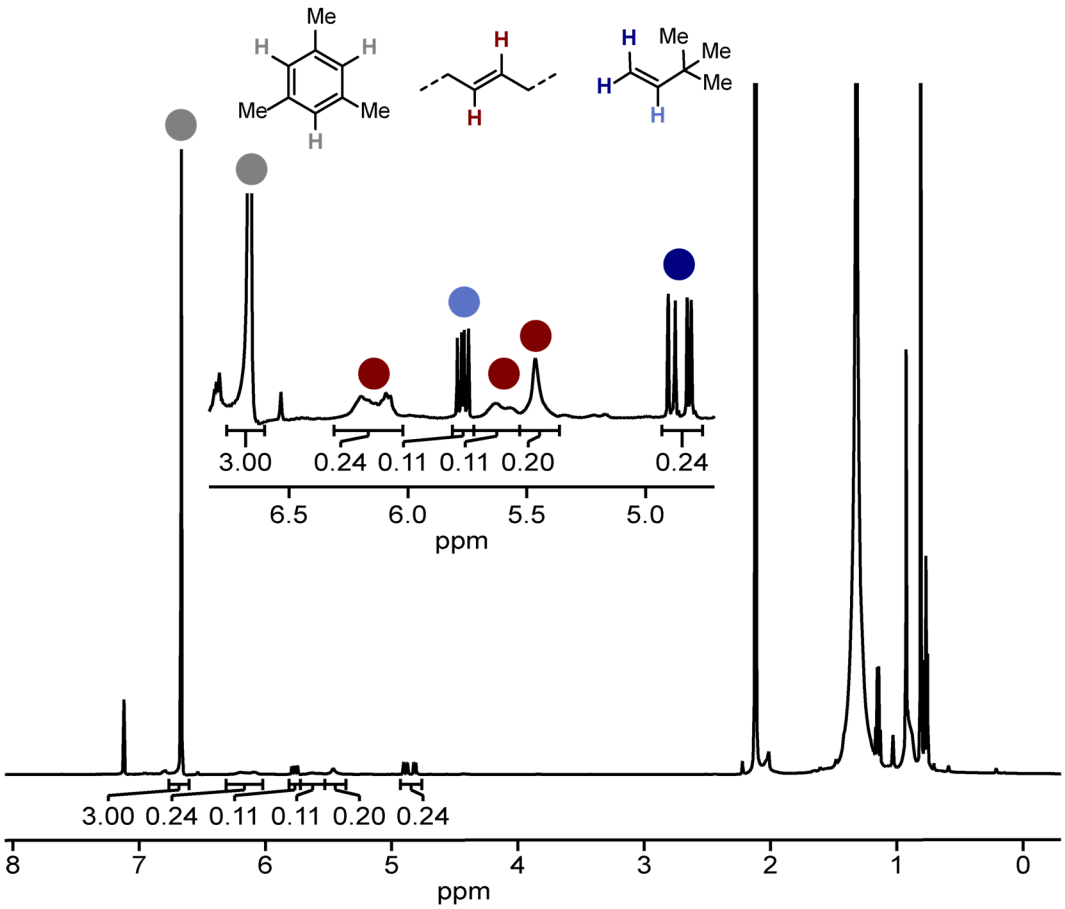

Figure A3.10 ^{1}H NMR spectra for **Table A1.1, entry 4**. ^{1}H NMR (600 MHz, C_6D_6, 70 °C) δ 6.67 (s, 3H), 6.33–6.03 (m, 0.24H, PE HC=CH), 5.77 (dd, J = 17.4, 10.8 Hz, 0.11H, TBE, *t*Bu**H**C=CH_2), 5.69–5.55 (m, 0.11H, PE HC=CH), 5.46 (s, 0.20H, PE HC=CH), 4.85 (dd, J = 17.6, 10.6 Hz, 0.24H, *t*BuHC=C**H**$_2$).

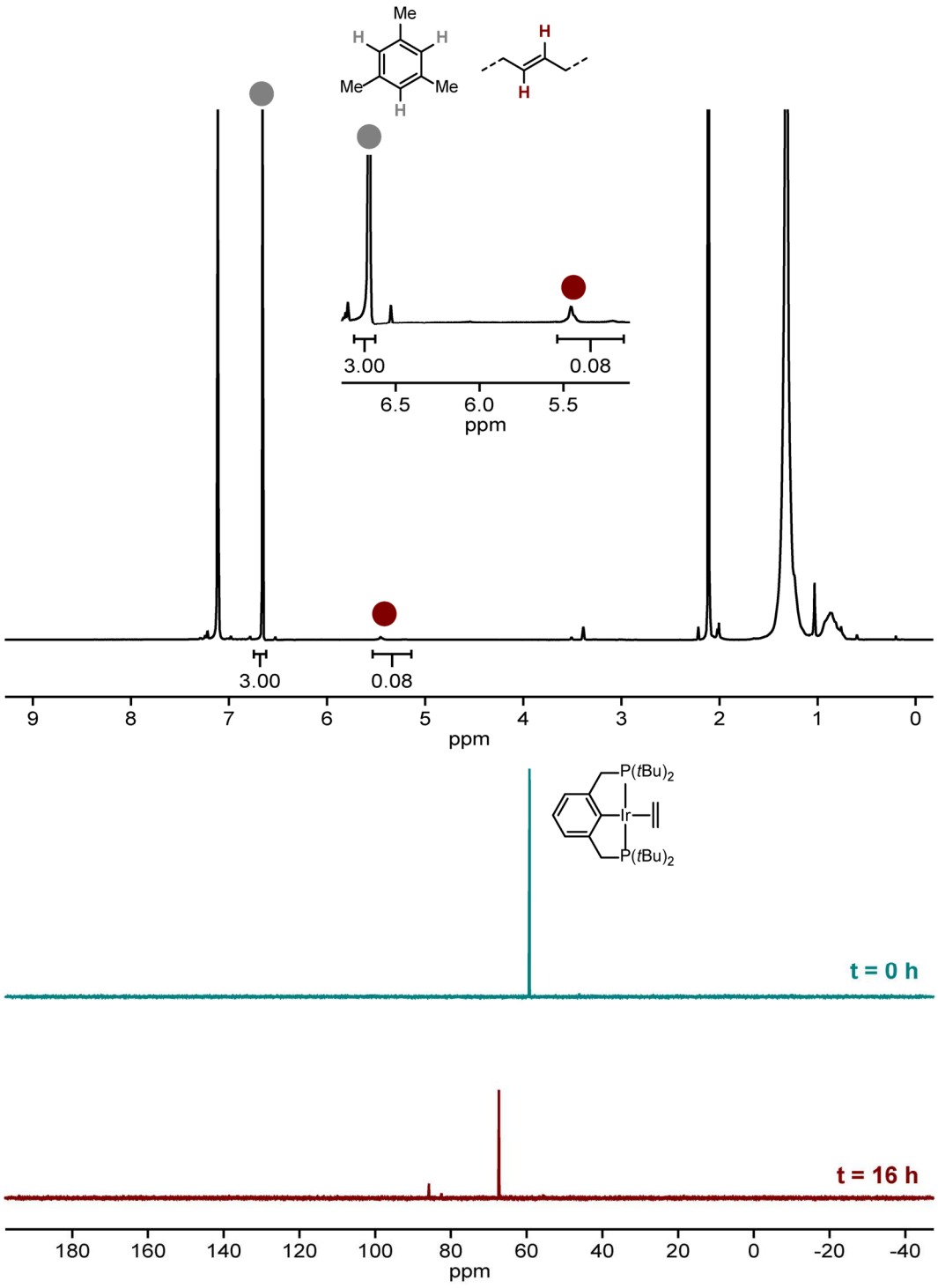

Figure A3.11 ^{1}H and ^{31}P NMR spectra for **Table A1.1, entry 5**. ^{1}H NMR (600 MHz, C_6D_6, 70 °C) δ 6.66 (s, 3H), 5.54–5.14 (m, 0.08H, PE HC=CH). ^{31}P NMR, t = 0 h (243 MHz, C6D6, 70 °C) δ 59.22. ^{31}P NMR, t = 16 h (243 MHz, C_6D_6, 70 °C) δ 85.80, 82.45, 67.32.

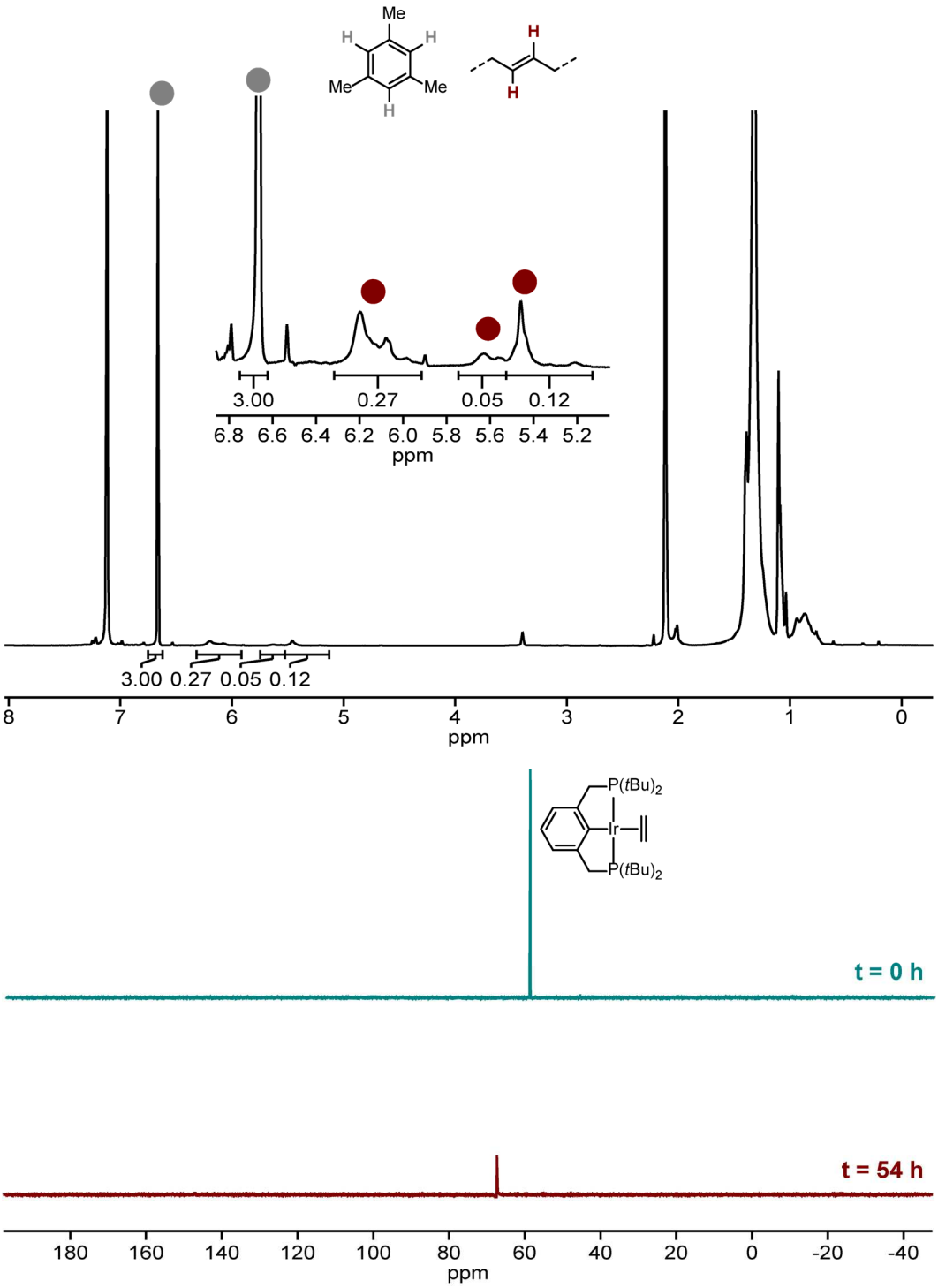

Figure A3.12 ^{1}H and ^{31}P NMR spectra for **Table A1.1, entry 6**. ^{1}H NMR (600 MHz, C_6D_6, 70 °C) δ 6.66 (s, 3H), 6.33–5.93 (m, 0.27H, PE HC=CH), 5.74–5.53 (m, 0.05H, PE HC=CH), 5.53–5.14 (m, 0.12H, PE HC=CH). ^{31}P NMR, t = 0 h (243 MHz, C_6D_6, 70 °C) δ 59.22. ^{31}P NMR, t = 54 h (243 MHz, C_6D_6, 70 °C) δ 67.33.

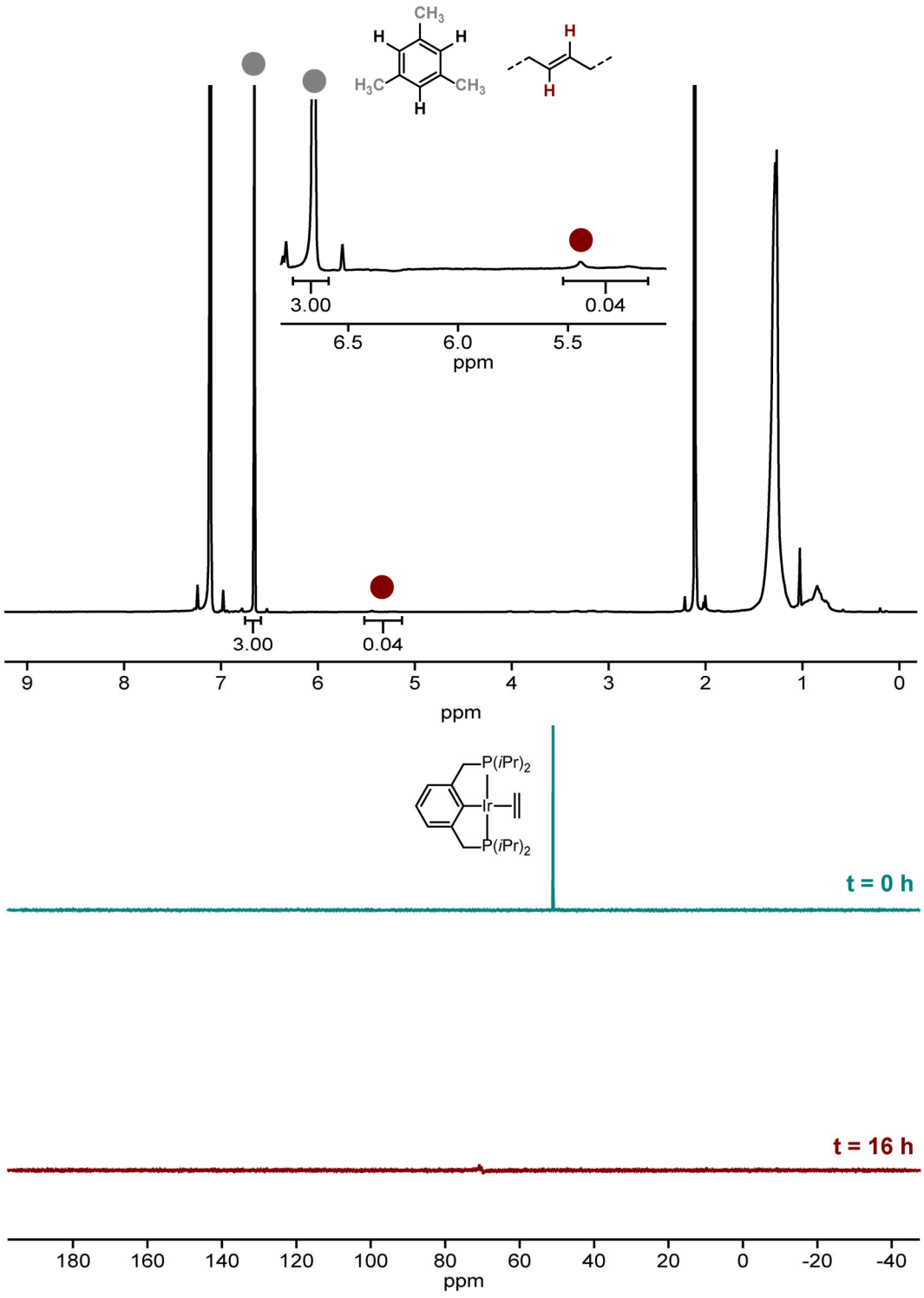

Figure A3.13 ^{1}H and ^{31}P NMR spectra for **Table A1.1, entry 7.** ^{1}H NMR (600 MHz, C_6D_6, 70 °C) δ 6.66 (s, 3H), 5.53–5.13 (m, 0.4H, PE HC=CH). ^{31}P NMR, t = 0 h (243 MHz, C_6D_6, 70 °C) δ 50.97.

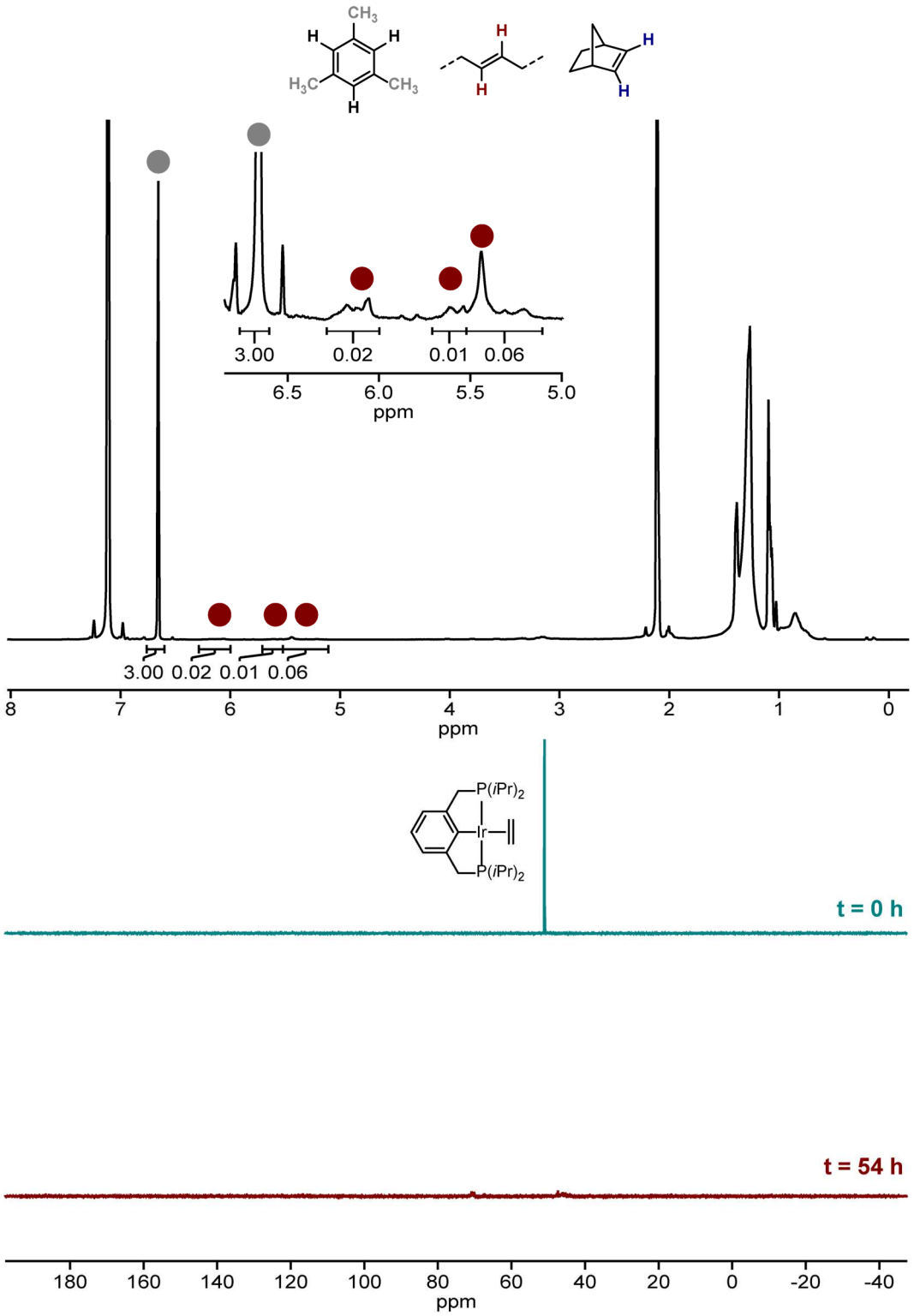

Figure A3.14 ^{1}H and ^{31}P NMR spectra for **Table A1.1, entry 8.** ^{1}H NMR (600 MHz, C_6D_6, 70 °C) δ 6.66 (s, 3H), 6.28–6.01 (m, 0.02H, PE HC=CH), 5.72–5.52 (m, 0.01H, PE HC=CH), 5.52–5.11 (m, 0.06H, PE HC=CH). ^{31}P NMR, t = 0 h (243 MHz, C_6D_6, 70 °C) δ 50.97.

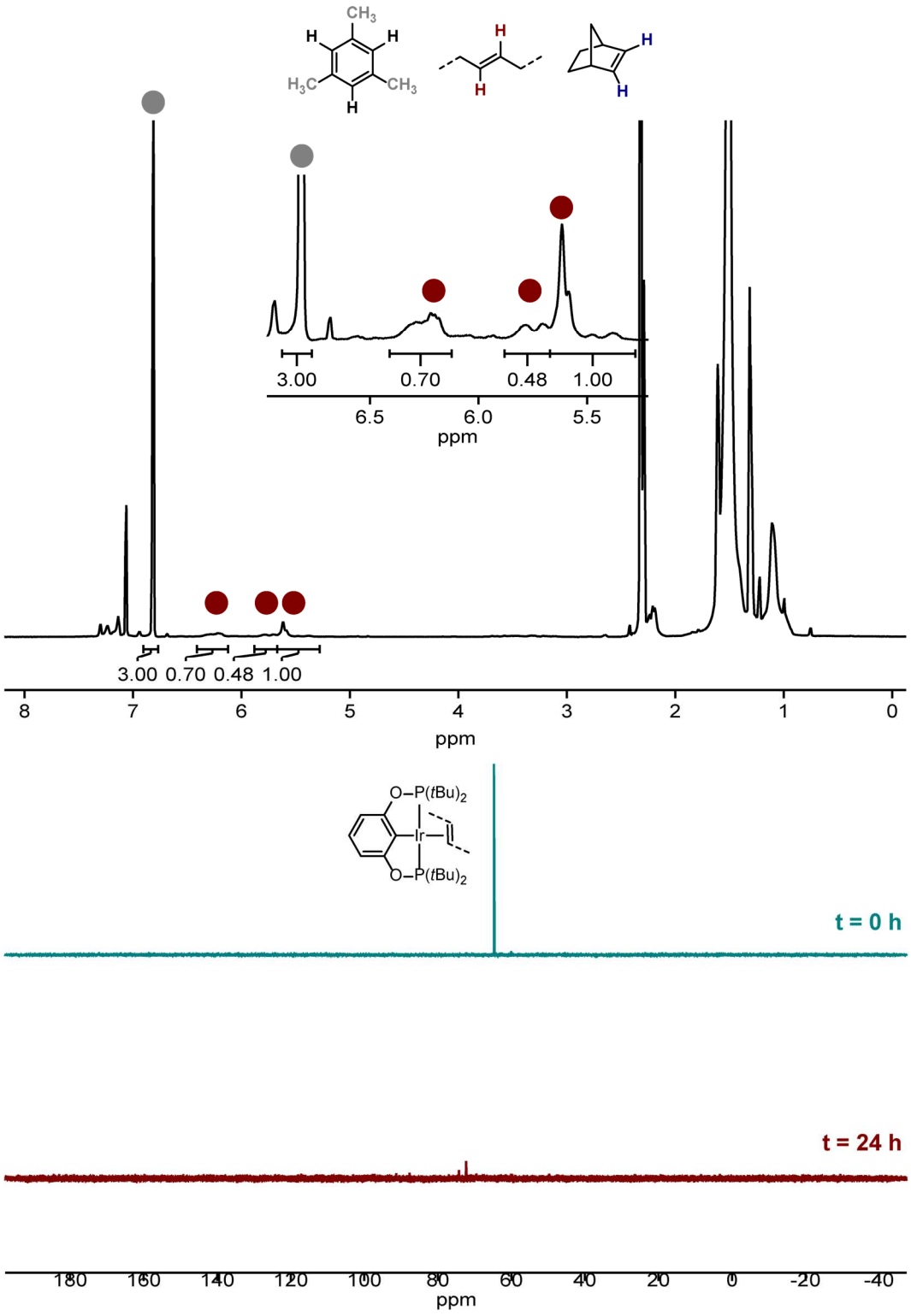

Figure A 3.15 ^{1}H and ^{31}P NMR spectra for **Table A1.1, entry 9.** ^{1}H NMR (600 MHz, d_{10}-*p*-xylene, 90 °C) δ 6.81 (s, 3H), 6.41–6.11 (m, 0.7H, PE HC=CH), 5.89–5.68 (m, 0.48H, PE HC=CH), 5.68–5.24 (m, 1H, PE HC=CH). ^{31}P NMR, t = 0 h (243 MHz, d_{10}-*p*-xylene, 90 °C) δ 64.73. ^{31}P NMR, t = 24 h (243 MHz, d_{10}-*p*-xylene, 90 °C) δ 74.22, 72.30.

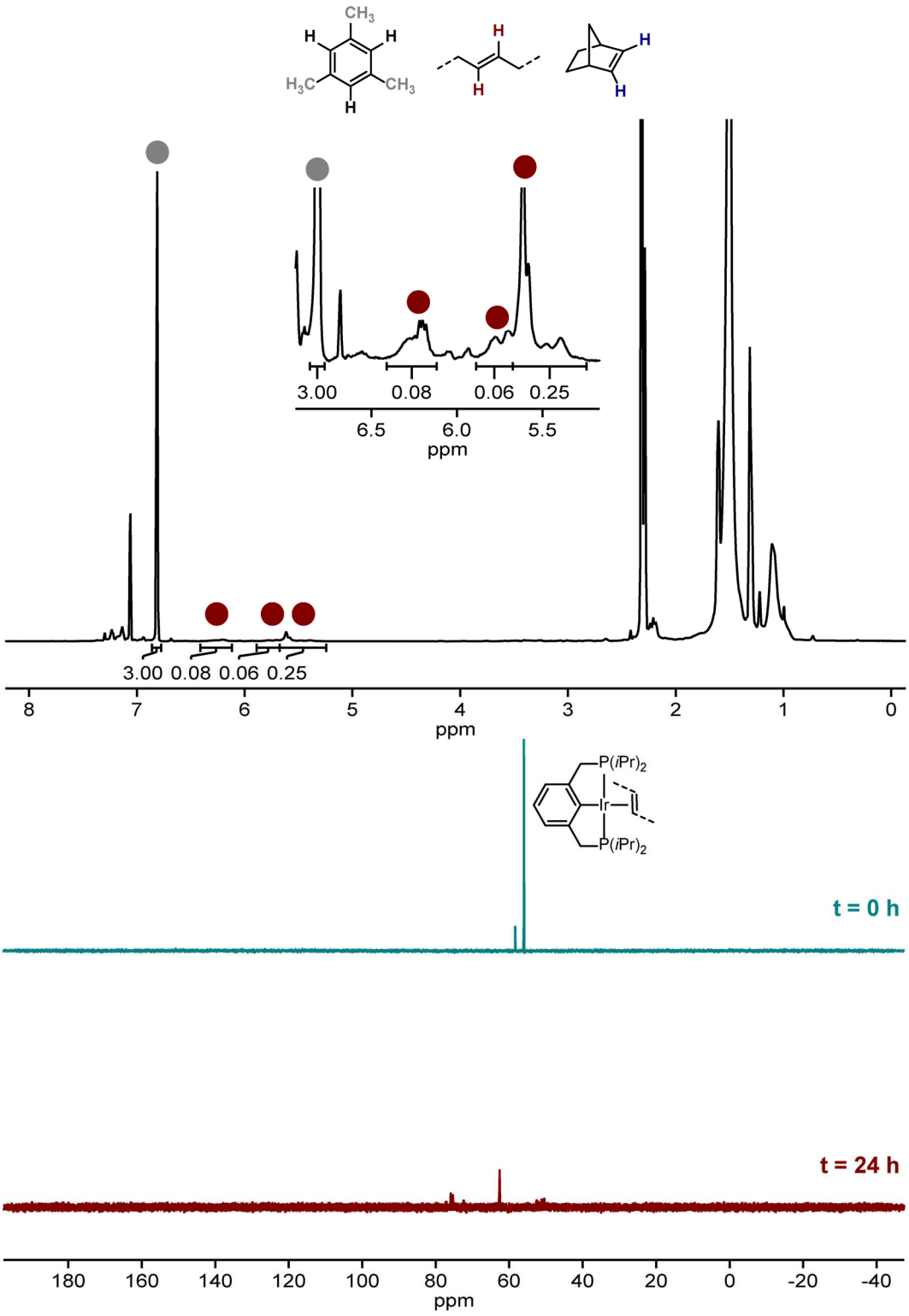

Figure A 3.16 ^{1}H and ^{31}P NMR spectra for **Table A1.1, entry 10.** ^{1}H NMR (600 MHz, d_{10}-*p*-xylene, 90 °C) δ 6.81 (s, 3H), 6.41–6.13 (m, 0.08H, PE HC=CH), 5.88–5.68 (m, 0.06H, PE HC=CH), 5.68–5.27 (m, 0.25H, PE HC=CH). ^{31}P NMR, t = 0 h (243 MHz, d_{10}-*p*-xylene, 90 °C) δ 58.37, 55.99. ^{31}P NMR, t=24 h (243 MHz, d_{10}-*p*-xylene, 90 °C) δ 75.90, 75.32, 62.62, 51.16, 50.46.

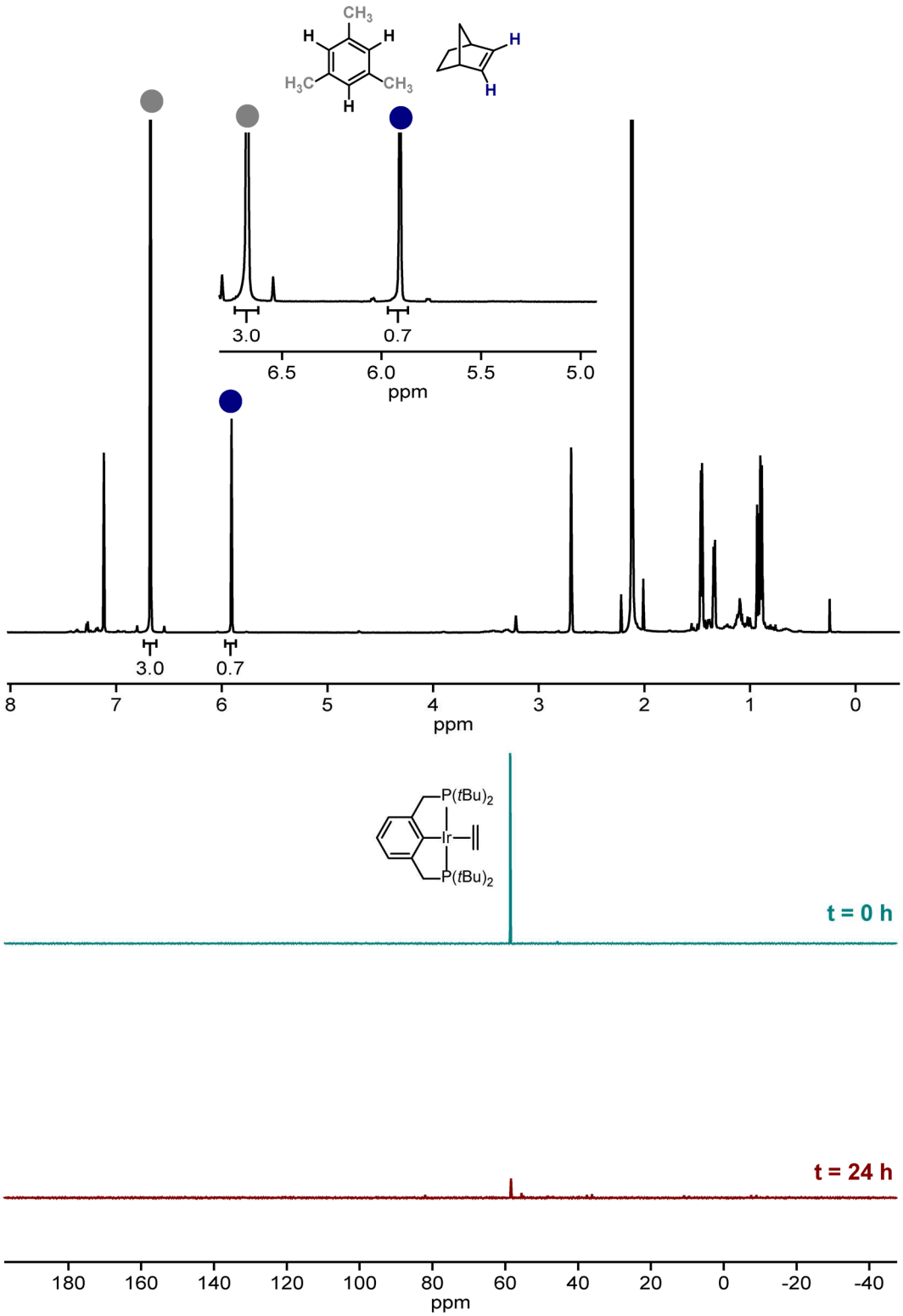

Figure A 3.17 ^{1}H and ^{31}P NMR spectra for **Table A1.1, entry 11.** ^{1}H NMR (600 MHz, C_6D_6,) δ 6.67 (s, 3H), 5.91 (t, J = 1.9 Hz, 0.7H, NBE HC=CH). ^{31}P NMR, t = 0 h (243 MHz, C_6D_6) δ 58.65. ^{31}P NMR, t = 24 h (243 MHz, C_6D_6) δ 82.00, 58.43, 55.54, 52.96, 48.25, 46.84, 37.63, 36.18.

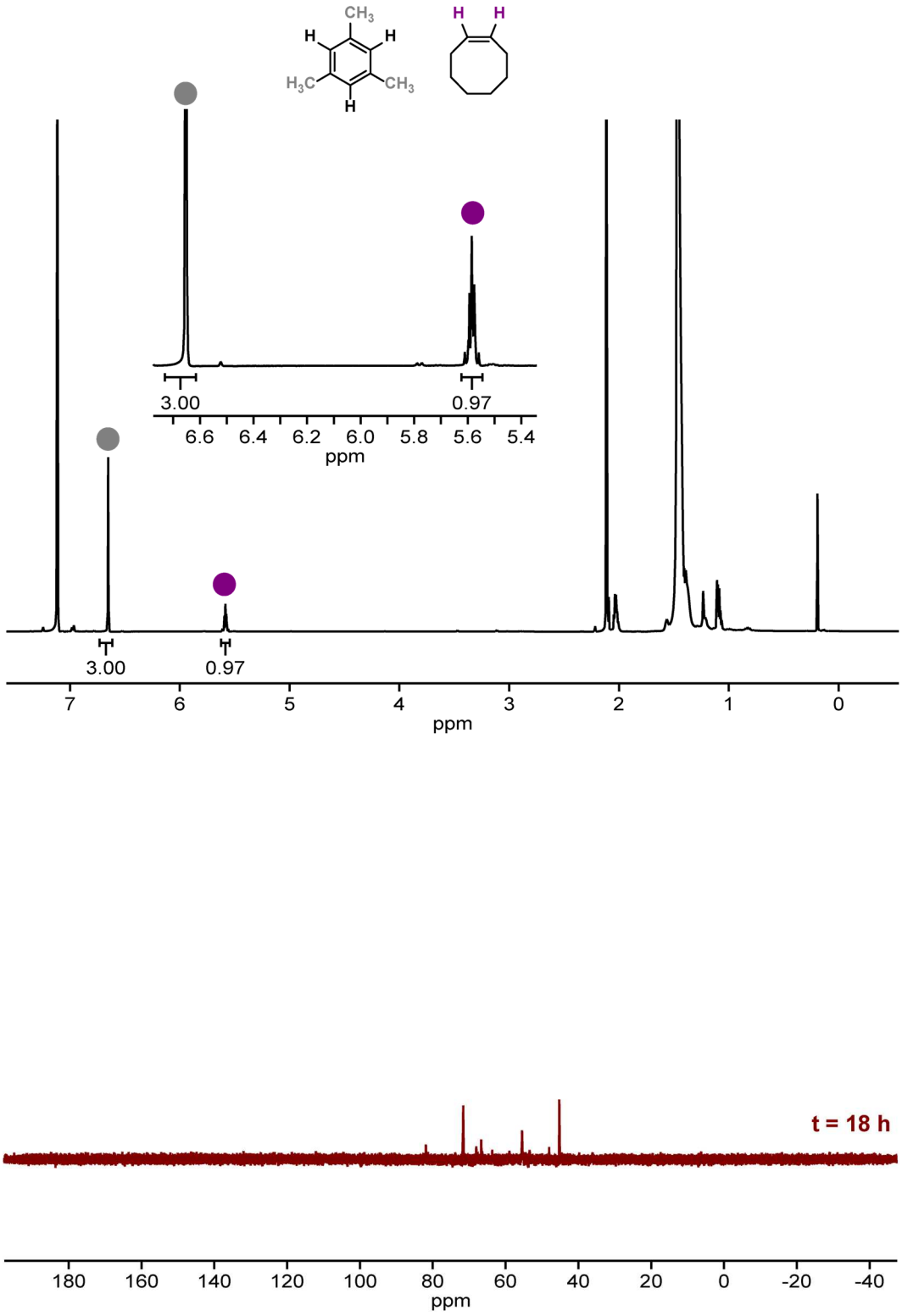

Figure A 3.18 ^{1}H and ^{31}P NMR spectra for **Table A1.1, entry 12**. ^{1}H NMR (600 MHz, C_6D_6) δ 6.65 (s, 3H), 5.58 (td, *J* = 5.2, 2.7 Hz, 0.97H, COE HC=CH. ^{31}P NMR t = 18 h (243 MHz, C_6D_6) δ 71.64, 66.69, 55.46, 45.24.

A3.8 Alkane Metathesis of PE and Data

A3.8.1 Procedure

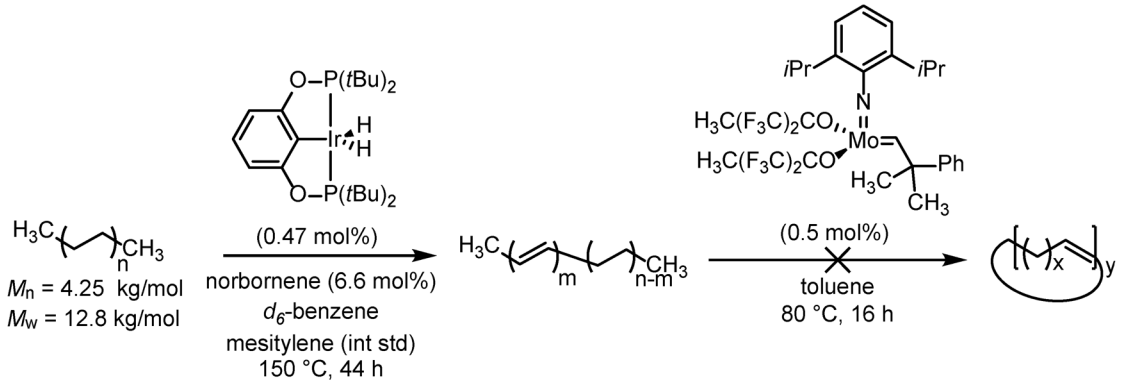

In an Ar-filled glovebox to a J-Young NMR tube was added polyethylene (67.8 mg, 2.42 mmol repeat units, 1.00 equiv), a 0.5 M stock solution of norbornene in d_6-benzene (0.318 mL, 0.159 mmol, 0.066 equiv), a 0.10 M stock solution of $^{t\text{Bu}}$POCOPIrH$_2$ in d_6-benzene (0.114 mL, 0.0114 mmol, 0.7 mol% or 0.00469 equiv), and mesitylene (33.7 μL, 0.240 mmol, 0.10 equiv - int standard) and d_6-benzene (0.563 mL). The tube was sealed, removed from the glovebox and stirred at 150 °C for 44 h. The solution was cooled to rt, returned to an Ar-filled glovebox and transferred to a 100 mL Schlenk flask with toluene (12 mL) to ensure transfer of all solid material. Additional toluene (24 mL) was added and the resulting mixture was stirred at 80 °C for 16 h. The resulting hot solution was filtered through a plug of silica. An aliquot (0.1 mL) was removed, cooled, and diluted with toluene (2 mL), and filtered through a 0.2 μm syringe filter for GCMS analysis. The solvent was removed from the remaining filtrate in vacuo. The resulting solid was dissolved in hot toluene (~1 mL) and precipitated into MeOH (30 mL), centrifuged, and the supernatant was removed. This process (dissolve, precipitate, centrifuge, remove supernatant), was repeated 5 times total. The resulting pellet was dried *in vacuo* to yield a light-yellow solid (48 mg).

A3.8.2 Data for Alkane Metathesis of PE

NMR Spectra

See Figure A3.7.

Size Exclusion Chromatography Traces

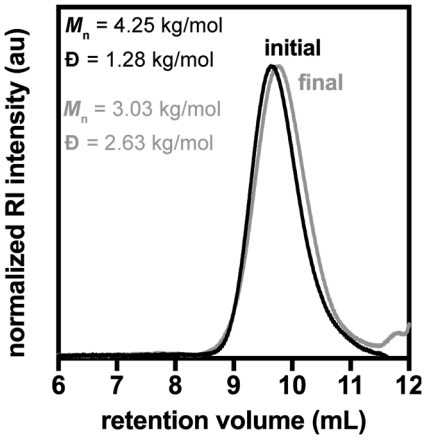

Figure A3.19 Size-Exclusion Chromatography traces for commercial PE (black) and the product after sequential reaction with ***t*BuPOCOP** and **Mo-1** under dilute conditions (see pg 292) (grey).

Gas-Chromatography Mass-Spectroscopy

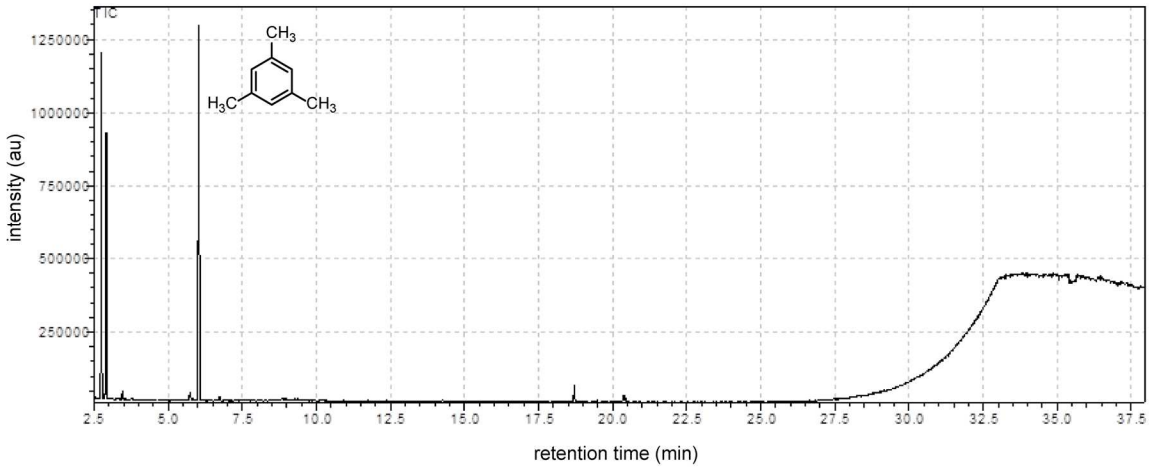

Figure A3.20 GC-MS trace for attempted cyclodepolymerization of dehydrogenated PE. The peaks at retention times 2.55 min and 2.80 min correspond to ethylbenzene and *m*-xylene impurities from the toluene solvent.

A3.9 Cyclodepolymerization of Unsaturated Alkenes and Data

A3.9.1 General Procedure

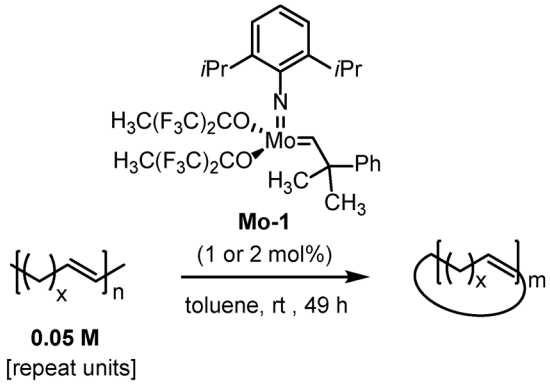

catalyst stock solution: In an N_2 filled glovebox, into a 4 mL vial was weighed Schrock's catalyst (from STREM) (7.2 mg, 9.4 μmol) which was dissolved in toluene (0.943 mL) to give a 10 μM solution.

durene stock solution: In an N_2 filled glovebox, into a 4 mL vial was weighed durene (165.3 mg, 1.232 μmol) was dissolved in toluene (1.232 mL) to give a 1.0 M solution.

cyclodepolymerization: In an N_2 filled glovebox, the poly-CX-ene (~25 mg, 0.23 mmol, 1.0 equiv) was weighed into an 8 mL vial. To this vial was added a stir bar, a 1.0 M solution of durene in toluene (~0.23 mL, 0.23 mmol, 1.0 equiv), toluene (~8.5 mL), and a 0.010 mmol solution of Schrock's catalyst (~0.23 mL, 2.3 μmol, 1.0 mol%). After 22 h, an additional aliquot of 0.010 M Schrock catalyst (0.236 mL, 2.36 μmol, 1.00 mol% of original polymer) in toluene was added. The reaction was stirred for an additional 26 h (49 h total) at rt.

sample prep for GC: The vial was removed from the glove box and water (0.50 mL) was added to deactivate the catalyst. The organic layer was removed via pipette and the aqueous layer was extracted with hexanes (3 x 1 mL). The combined organic layers were filtered through $MgSO_4$ and silica gel (to remove water and catalyst, respectively), and dried *in vacuo* to yield an oily solid. The solid was then dissolved in toluene (2 mL) and filtered through a 0.2 μm PTFE syringe filter into a GC vial.

SEC workup: The solvent was removed from the GC sample *in vacuo.* To the resulting residue was added THF (Table A3.2, entries 1–4) or *o*-DCB (Table A3.2, entry 5) to make a 1 mg/mL solution. Data for entries 1–4 was obtained on SEC#1 or SEC#2, using the same instrument for both initial and final samples in each case. Data for entry 5 was obtained with HT-SEC.

Table A3.2 Cyclodepolymerization conditions and molar mass data for polyolefins with **x** methylene units per repeat unit.

entry	x	conc. (M)	temp (°C)	cat.	cat. mol%	initial M_n (kg/mol)	initial M_w (kg/mol)	final M_n (kg/mol)	final M_w (kg/mol)
1	2[a]	0.05	25	**Mo-1**	2	116	338	0.671	0.968
2	2[b]	0.05	25	**Mo-1**	2	183	434	0	0
3	6	0.05	25	**Mo-1**	2	102	208	0.792	2.02
4	10	0.05	25	**Mo-1**	2	24.2	34.8	0	0
5	16	0.1	25	**Mo-1**[c]	1	2.48	3.38	1.03	2.42

a *c*PBD

b *ct*1,4-PBD

c in paraffin wax

A3.9.2 Cyclodepolymerization SEC Data

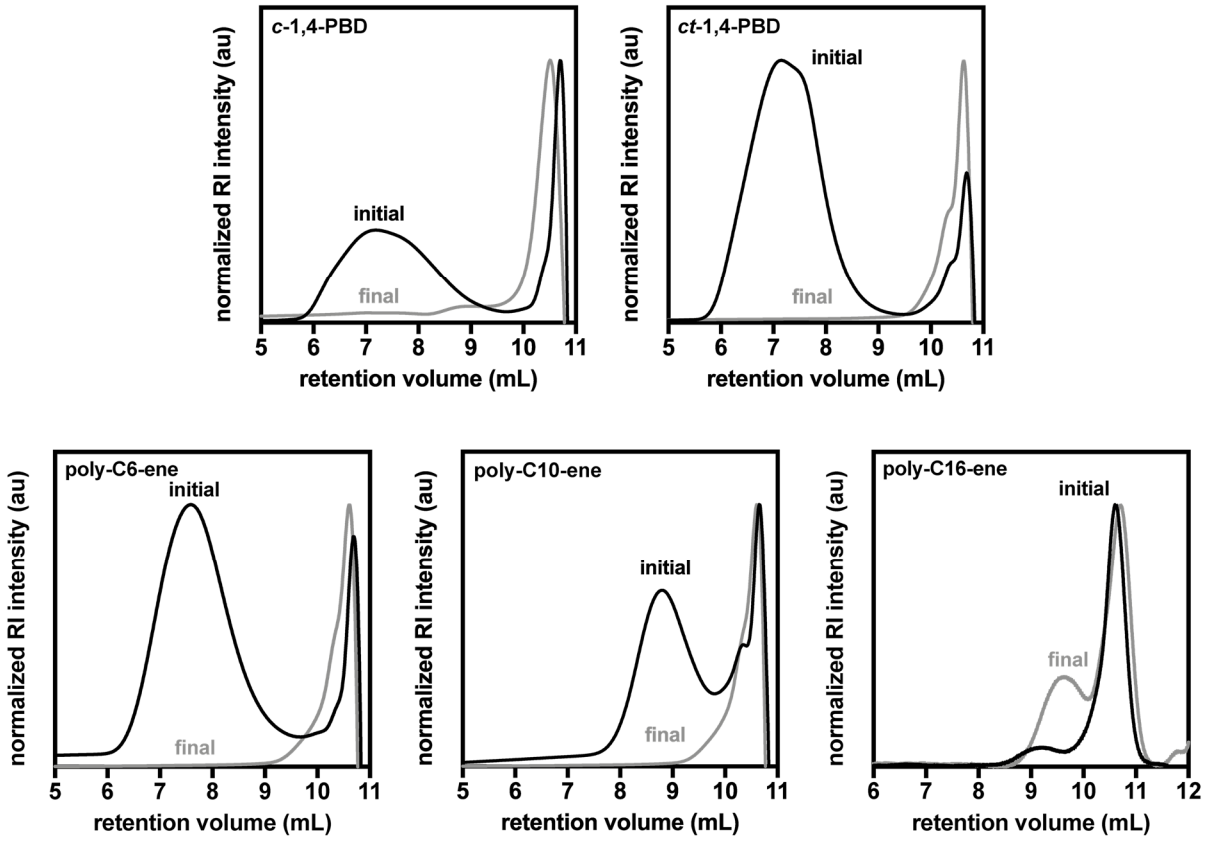

Figure A3.21 SEC data for all polymers before (black) and after (grey) attempted cyclodepolymerization. All traces are normalized to the maximum of the highest peak intensity and do not include the solvent peak.

A3.9.3 Cyclodepolymerization GC Data

Table A3.3 GC peak area data for all cyclodepolymerization reactions of polyolefins with **x** methylene units per repeat unit.

x	rt time (min)	cyclic oligomer	# of C atoms	peak area relative to int. std.
2 (*cPBD)*	3.092	trimer	12	0.340
			total	***0.340***
2 *(ctPBD)*	3.085	trimer	12	0.290
			total	***0.290***
6	5.549	dimer – CH_2	15	0.008
	6.282	dimer	16	0.026
	6.335	dimer	16	0.064
			subtotal	*0.090*
	7.694	dimer + $2CH_2$	18	0.018
	10.735	trimer – CH_2	23	0.014
	11.247	trimer	24	0.053
	11.287	trimer	24	0.042
			subtotal	*0.095*
	11.776	trimer + CH_2	25	0.021
	11.831	trimer + CH_2	25	0.020
			subtotal	*0.040*
	12.393	trimer	26	0.009
			total	***0.275***
10	3.376	monomer	12	0.002
	3.488	monomer	12	0.001
			subtotal	*0.003*
	9.047	dimer – $2CH_2$	22	0.002
	10.18	dimer – $2CH_2$	22	0.002
	10.225	dimer – $2CH_2$	22	0.001
			subtotal	*0.006*
	10.729	dimer – CH_2	23	0.011
	10.781	dimer – CH_2	23	0.005
	10.84	dimer – CH_2	23	0.001
			subtotal	*0.016*
	11.233	dimer	24	0.032
	11.304	dimer	24	0.026
	11.368	dimer	24	0.004
			subtotal	*0.063*
	11.781	dimer + CH_2	25	0.003
	11.856	dimer + CH_2	25	0.002
			total	***0.088***
16	-	-	-	-

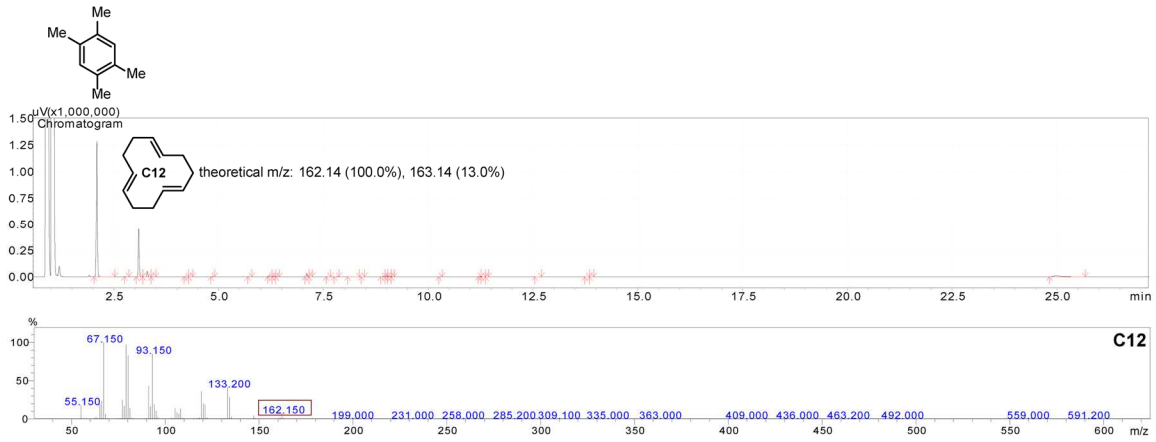

Figure A3.22 GC and MS traces for cyclodepolymerization of ***c*PBD**. The major product was 1,5,7-cyclododecatriene.

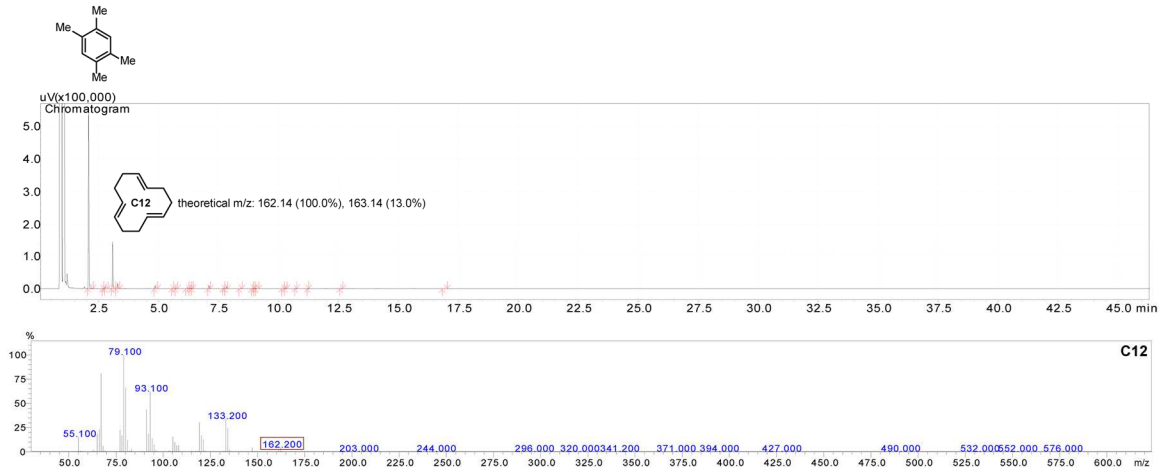

Figure A3.23 GC and MS traces for cyclodepolymerization of ***ct*PBD**. The major product was 1,5,7-cyclododecatriene

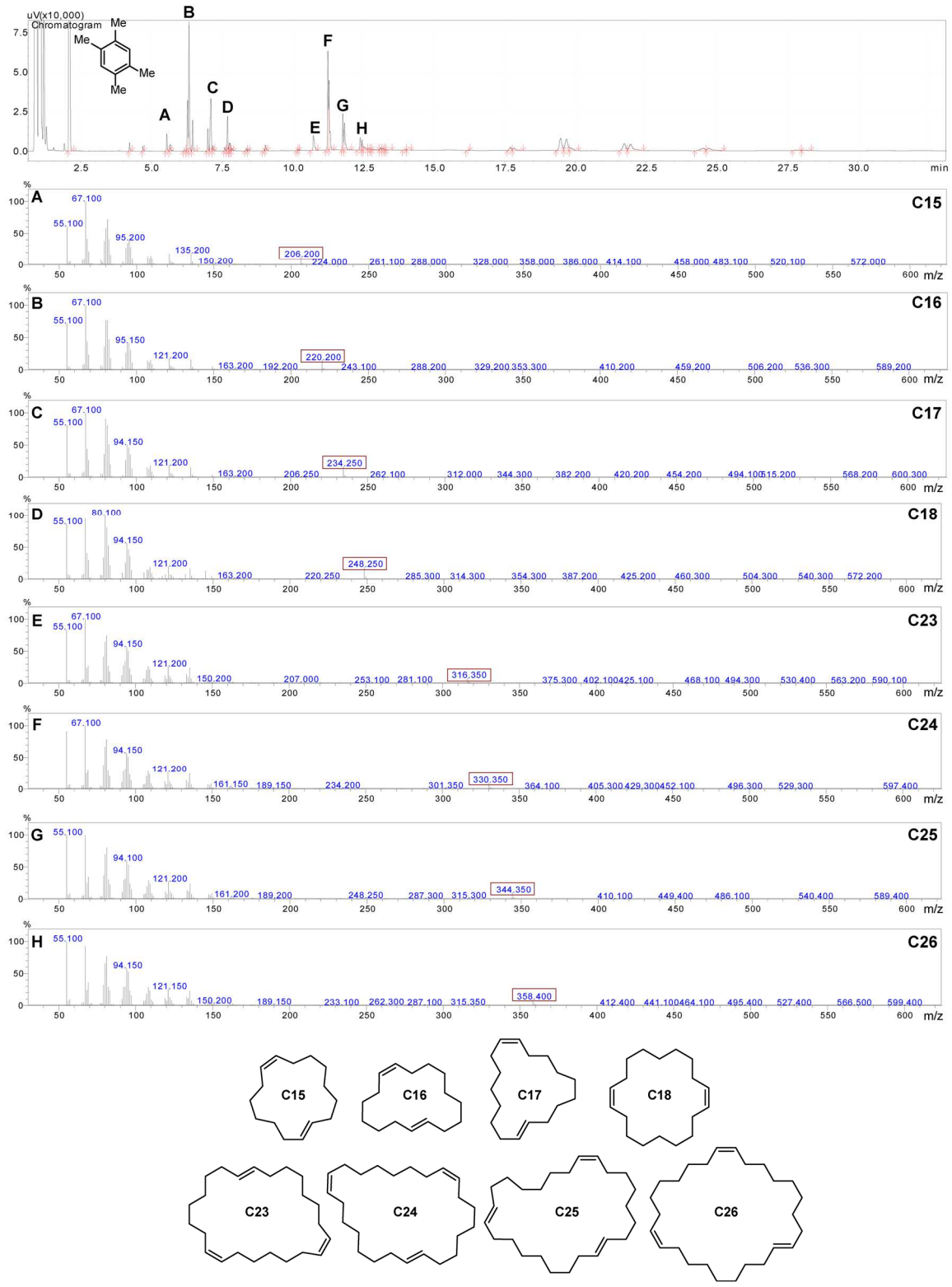

Figure A3.24 GC trace for depolymerization of **poly-C6-ene**. From GC-MS, it was determined that dimers and trimers as well as species with ± one or two methylene units were formed.

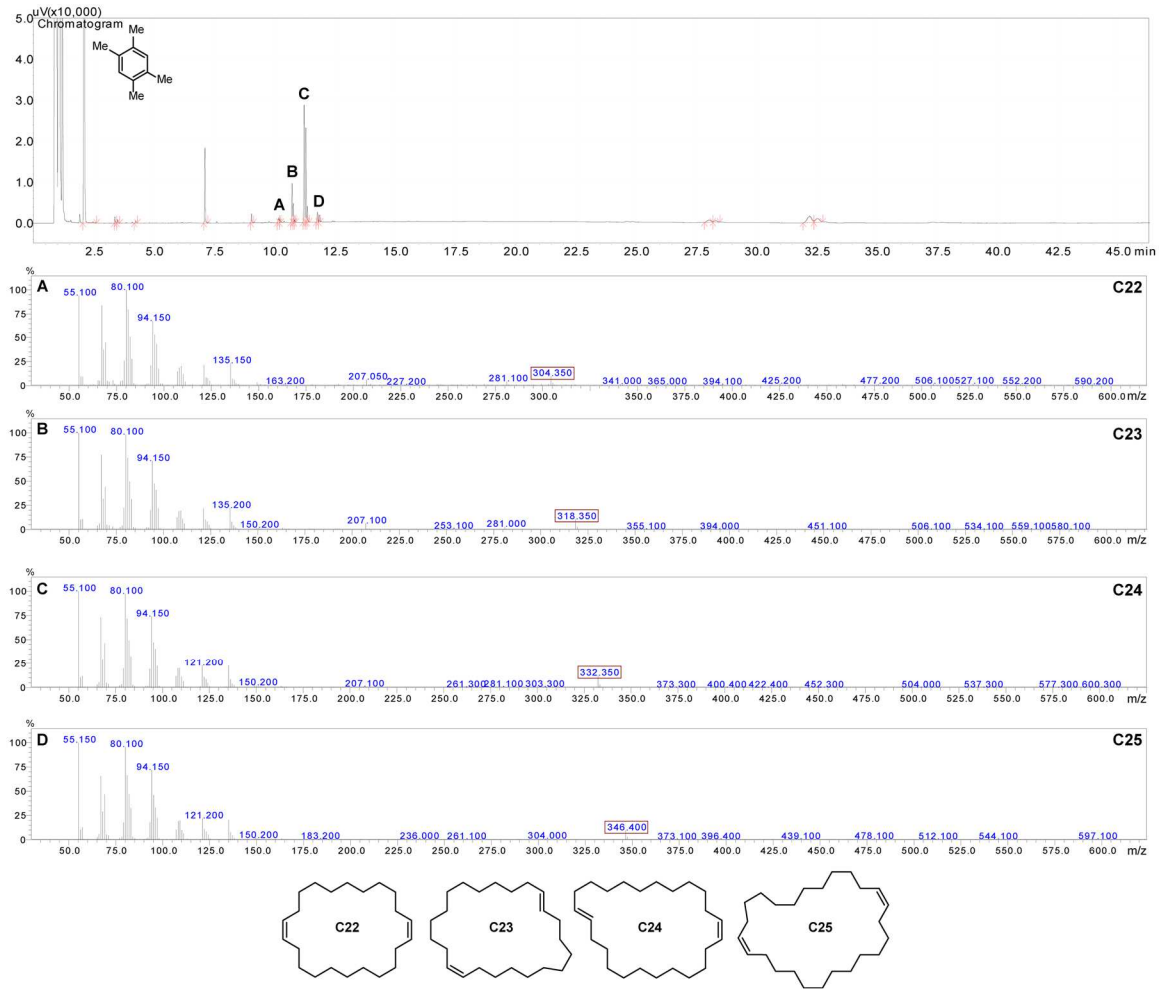

Figure A3.25 GC and MS traces GC and MS traces for cyclodepolymerization of **poly-C10-ene**. The major product was the cyclic dimer, but species with up to +/– 2 methylene units were also observed.

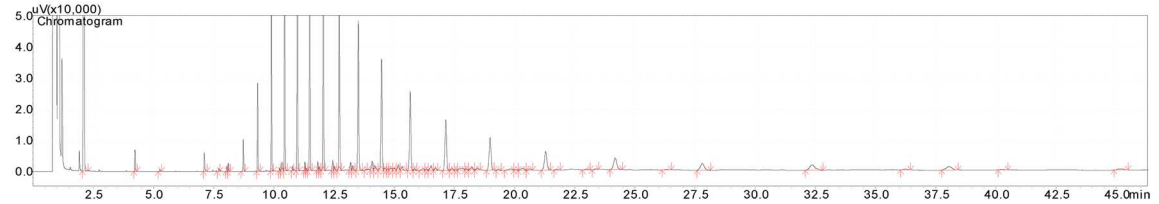

Figure A3.26 GC trace for cyclodepolymerization of **poly-C16-ene**. Due to overlapping peaks from the paraffin wax pellet that the catalyst was loaded in, analysis of cyclodepolymerization products could not be performed.

A3.10 References

[1] Love, B. E.; Jones, E. G. The Use of Salicylaldehyde Phenylhydrazone as an Indicator for the Titration of Organometallic Reagents. *J. Org. Chem.* **1999**, *64*, 3755–3756.

[2] Schlosser, M.; Bossert, H. The "Two-Fold Reaction" Benchmark Applied to the Copper Catalyzed Assembling of 1ω-Difunctional Hydrocarbon Chains. *Tetrahedron* **1991**, *47*, 6287–6292.

[3] Ray, A.; Zhu, K.; Kissin, Y. V.; Cherian, A. E.; Coates, G. W.; Goldman, A. S. Dehydrogenation of Aliphatic Polyolefins Catalyzed by Pincer-Ligated Iridium Complexes. *Chem. Commun.* **2005**, *27*, 3388–3390.